UNIVERSITEIT VAN PRETORIA
UNIVERSITY OF PRETORIA
YUNIBESITHI YA PRETORIA

HIGH STRENGTH, DUCTILE WIDE GAP BRAZE JOINTS FOR STATIONARY TURBINE COMPONENT REPAIRS

by

Warren Martin Andre Miglietti

Submitted in partial fulfillment of the requirements for the degree

Philosophiae Doctor

in the Faculty of Engineering, the Built Environment and Information Technology
University of Pretoria

April 2008

ABSTRACT

Wide cracks in land-based Ni- or Co-base superalloy turbine components are difficult to repair successfully using conventional welding or brazing techniques. This project examined the feasibility of liquid phase diffusion brazing using novel Ni- and Co-base braze alloys containing Hf or Zr as melt point depressant for the repair of wide cracks in turbine components. An optimized braze cycle was developed and the joints were evaluated using various metallographic techniques and mechanical tests (elevated temperature tensile tests, creep rupture tests and low cycle fatigue tests). Microstructural examination revealed the presence of Hf- or Zr-rich intermetallic phases (most likely Ni_7Hf_2 or Ni_5Zr) in Ni-base braze joints. These intermetallic compounds were, however, observed to be significantly softer than the boride phases routinely found in commercially available braze alloys with boron as melt point depressant. As a result, the novel wide gap brazed joints displayed excellent mechanical properties (ranging from 80% to 100% of the base metal's properties). The low cycle fatigue properties of wide gap braze joints performed using a combination of MarM247 superalloy powder and Ni-Cr-Hf or Ni-Cr-Zr braze filler metals were found to be superior to those of the widely used Ni-Cr-B braze filler metals. Wide gap braze repair of FSX-414 Co-base superalloy using novel MarM509/MarM509B and MarM509/Co-Hf braze alloys resulted in high temperature tensile properties equivalent to those of weld repairs in the same parent material (using Nozzalloy filler metal). The creep rupture and low cycle fatigue (LCF) properties of the braze joints were superior to those of welds performed using MarM918 filler metal.

TABLE OF CONTENTS

CHAPTER 10 - EXPERIMENT 8

CHARACTERIZATION OF THE MICROSTRUCTURE AND PROPERTIES OF HYPO-EUTECTIC Ni-Cr-Hf AND Ni-Cr-Hf-B ALLOYS

CHAPTER 11 - EXPERIMENT 9

MICROPROBE ANALYSIS OF INTERMETALLIC PHASES

CHAPTER 12 - EXPERIMENT 10

DEVELOPMENT OF COMPLEX Ni-Cr-Hf BRAZE ALLOYS

CHAPTER 13 - EXPERIMENT 11

CHARACTERIZATION OF THE MICROSTRUCTURE AND MECHANICAL PROPERTIES OF ADH BRAZE JOINTS IN FSX-414 COBALT-BASE SUPERALLOY NOZZLE SEGMENTS USING NOVEL BRAZE ALLOYS

LIST OF FIGURES

LIST OF TABLES

ACKNOWLEDGEMENTS

Thank you to my wife Portia who had to endure me working many weekends to undertake the experiments and write up the thesis. Thank you to Kevin Pelletier and Jan Williams of Dirats Laboratories for the Scanning Electron Microscope analyses and tensile/stress rupture testing, respectively. In addition thanks to the people at Metcut and Westmoreland for the low cycle fatigue testing. Thanks to Joe Foroughi of the M&P lab and Louis Peluso of GRC for help with the Electron Microprobe analyses and a tremendous thanks to Ann Ritter of GRC for the help in developing and analyzing the phases that formed in the hypo-eutectic alloys and for help in developing and characterizing the microstructures of novel “near-eutectic” braze alloys in the as-cast condition

Thank you also to Prof Lugscheider of the RWTH Institute in Aachen, Germany, for introducing me to the concept of using Hf as a melt point depressant in Ni-base braze filler alloys, and similarly thank you to Dr Khorunov of the Paton Institute in Kiev, Ukraine, for introducing me to the concept of using Zr as a melt point depressant in Ni-base braze filler alloys.

CHAPTER 1 - LITERATURE SURVEY

THE APPLICATION OF BRAZING, WIDE GAP BRAZING AND LIQUID PHASE SINTERING IN THE REPAIR OF NICKEL-BASE SUPERALLOY COMPONENTS FOR GAS TURBINE ENGINES

1.1) Introduction

A gas turbine engine, be it for an aircraft application or for power generation, typically ingests air from the atmosphere. The air is then compressed by the compressor and mixed with fuel. The mixture is combusted in a combustion chamber, usually referred to as the combustor can or the burner can, following which the hot gas is expanded through the turbine section, producing thrust. In essence, thermal energy is converted to mechanical energy.

Components within the turbine section of a gas turbine engine are generally identified as 'blades' and 'vanes', with 'blades' referring to rotating components and 'vanes' to stationary components. Some original engine manufacturers (OEM's), such as General Electric, refer to blades as 'buckets' and vanes as 'nozzles', while a number of European OEM's, such as ABB and Alstom, further confuse matters by referring to vanes as 'stator blades'.

Blades and vanes are not only exposed to high service temperatures (typically 1000^{o}C to 1200^{o}C), but also experience severe stresses and strains, oxidation and corrosive attack during service. As a result of the high temperatures that the turbine section is exposed to during service, the blades and vanes are usually manufactured from materials referred to as superalloys. By definition a superalloy is a material that can operate at 75% and higher of its melting point, while maintaining adequate mechanical strength. Steels have little mechanical strength within the temperature range mentioned above and are therefore not used in the manufacture of turbine components.

Materials used in the production of turbine components include iron-base superalloys, cobalt-base superalloys and nickel-base superalloys. In the early days of engine manufacture, iron-base alloys were widely utilized, but nowadays the majority of blades and vanes are produced from nickel- and cobalt-base superalloys. These alloys exhibit outstanding mechanical strength over the entire operating temperature range in a gas turbine engine and maintain good mechanical integrity, including high creep rupture strength, over long periods of time (up to 20000 hours). The nickel- and cobalt-base superalloys have close packed face centred cubic (FCC) austenitic crystal structures. Of significance in determining the properties of superalloys is the solubility of alloying elements in the austenite matrix and the precipitation of intermetallic compounds (such as gamma prime, γ') and various carbide phases. The cobalt-base superalloys are generally solid solution strengthened, whereas the nickel-base alloys used in engines today are typically γ' strengthened. Gamma prime, γ', is a face centred cubic intermetallic compound of composition $Ni_3(Al,Ti)$. Primary γ' exhibits a cuboidal structure, whereas secondary γ' has a more spheroidal morphology (as demonstrated in **Figure 1**). Although the γ' particle size varies depending on the heat treatment that the alloy receives, the typical size of the primary γ' particles is 0.5 μm to 0.8 μm, and that of the secondary γ' phase is between 0.1 μm and 0.2 μm. The two main heat treatments performed in industry are the solution heat treatment, which is performed above the γ' solvus temperature, and the aging heat treatment, which induces the precipitation of the cuboidal and

spheroidal γ' precipitates shown in **Figure 1**. Carbide phases may form intergranularly or intragranularly, as shown in **Figure 2**. Intergranular carbides prevent grain boundary sliding.

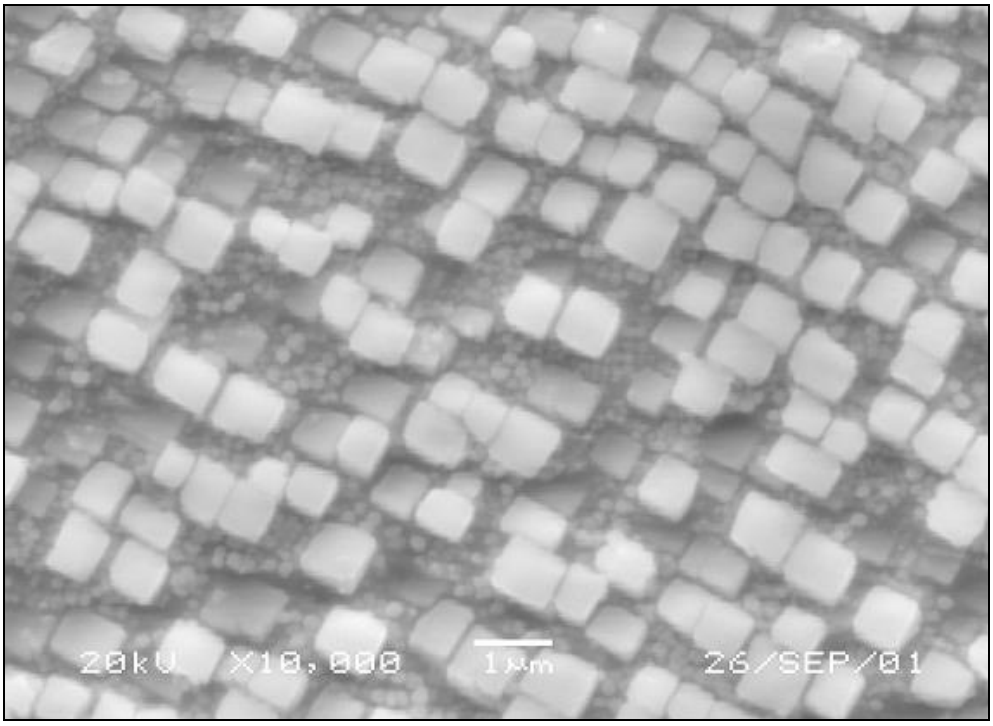

Figure 1 – The cuboidal and spheroidal structure of primary and secondary γ' precipitates (10% oxalic acid etch, magnification: 10000X).

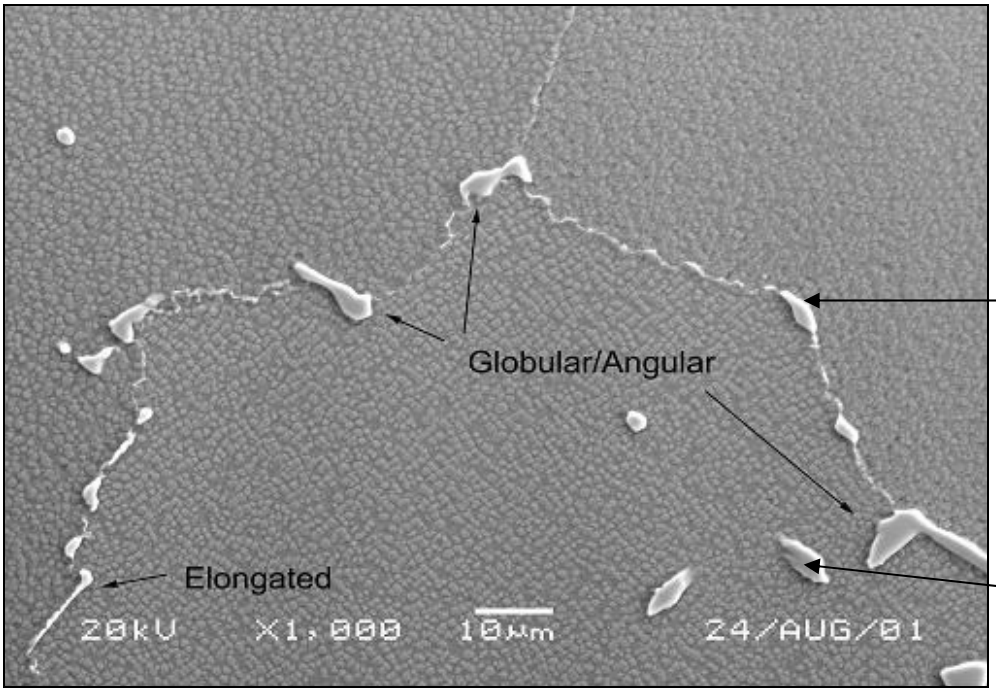

Figure 2 - Intergranular and intragranular carbide phases (10% oxalic acid etch, magnification: 1000X).

Table 1 displays the typical chemical compositions and commercial trade names of superalloys used in the casting of blades and vanes. These alloys usually consist of at least fourteen major alloying elements, in addition to some minor trace elements. Aluminium and titanium are added to form the γ' phase, while chromium is added for corrosion resistance and to promote the formation of carbides. Other carbide formers include molybdenum, tungsten, vanadium, niobium, tantalum and titanium. Nickel, cobalt, iron, molybdenum, tungsten and chromium may be found in the austenite (γ) matrix of the alloy.

Table 1 - Nominal chemical compositions (wt.%, balance Ni) of some Ni-base superalloys.

Alloy	C	Co	Cr	Mo	Al	W	Ta	Nb	Ti	Zr	Fe	Hf	B
In738	0.17	8.5	16.0	1.7	3.4	2.6	1.7	2.0	3.4	0.1	0	0	0.001
In939	0.15	19.0	22.5	0	1.9	2.0	1.4	0	3.7	0.1	0	0	0.001
Rene 80	0.17	9.5	14.0	4.0	3.0	4.0	0	0	5.0	0.03	0	0	0.001
MarM247	0.15	10.0	8.25	0.7	5.5	10.0	3.0	0	1.0	0.05	0.5	1.5	0.001

1.2) The brazing of superalloys and the influence of brazing parameters on joint quality

Fusion welding served as the main fabrication technique for joining these materials for many years. The solid solution family of nickel-base superalloys has been extensively welded using arc welding processes (mainly gas tungsten arc welding and plasma arc welding) and high energy density welding processes (such as electron beam welding). The solid solution alloys, however, do not contain significant amounts of Al and Ti, hence welding problems are seldom encountered. With the addition of Al and Ti (see **Table 1** above), the γ' strengthened alloys become unweldable due to heat-affected zone (HAZ) microfissuring and fusion zone (FZ) cracking (including liquation cracking, ductility dip cracking and strain age cracking).

As a result of these welding-related problems, designers and welding engineers examined brazing as an alternative method of joining these "difficult-to-weld" superalloys. Brazing is defined as a process that produces bonding of materials at the brazing temperature in the presence of a filler metal with a liquidus above 450^{o}C and below the solidus of the parent metal. Unlike welding, the parent metal does not melt. The filler metal is distributed between the closely fitted mating surfaces of the joint through capillary action.

The brazing parameters have been shown to have a significant influence on the properties of the brazed joint. Five main factors, listed below and considered in more detail in the remainder of this chapter, affect the quality of a brazed joint. These factors are:

- the braze gap and joint design,
- the braze filler metal and its flow characteristics,
- the braze temperature and the holding time at temperature,
- the surface preparation and cleanliness of the joint, and
- the rate and source of heating (for example, induction brazing versus furnace brazing).

In the late 1960's, OEM's mainly used gold-base braze filler metals to join airfoils to stator rings to form nozzles. Au/Ni and Au/Cu alloys were used because Au flows well into joints at elevated temperatures. The braze temperatures for these filler metals varied from 900^{o}C to 1100^{o}C, depending on the alloying elements present. The Au-based filler metals resulted in

very ductile joints, but with the price of Au increasing, OEM's started replacing Au with less expensive precious metals such as palladium.

Regardless of the type of precious metal used, however, the high prices on the world market prompted inventors to develop Ni-base braze filler metals with alternative melt point depressants. In the early 1970's, three main melt point depressants were introduced, namely boron, silicon and phosphorus. It should be noted that the melting point of pure Ni is 1455^{o}C. In 1976, Sheward and Bell [1] evaluated several braze filler metals doped with P for joining nuclear parts and components. Boron was considered undesirable in this application because of its high neutron capture cross section and the fact that it transmutes to He. During long term exposure this results in voids and possibly swelling within the joints. Shear test results, corrosion test results and oxidation test results revealed that acceptable braze joints can be achieved on using a braze filler metal with composition Ni-25Cr-10P. The liquidus temperature was in the range of 927^{o}C to 950^{o}C. According to Lee and Nash, quoted in the ASM Handbook [2], a eutectic point exists in the Ni-P system at 11% P and a temperature of 870^{o}C. Many commercial manufacturers of braze filler metals have subsequently successfully produced braze filler metals with P contents ranging from 7% to 14%.

It is important to note that one of the most important factors in achieving a high strength joint is the **joint gap**. When brazing Ni-base superalloys, studies by Sulzer Metco (a popular supplier and manufacturer of Ni-base filler metals) have shown that the joint gap should be between 0.03 mm and 0.25 mm. Because of the difficulty in maintaining a joint gap of close tolerance, many manufacturers and fabricators intensely dislike the brazing process. If the recommended joint gap is exceeded, brittle centreline eutectic phases can form. In joints produced using Ni/P filler metal, wide gaps promote the formation of brittle Ni_3P and Ni_5P_2 phases. In joints with large clearances, soaking for long periods of time at elevated temperature promotes the diffusion of the melt point depressant, such as P, into the parent metal, preventing the formation of brittle phases. This has the distinct disadvantage that braze times on the order of several hours are required to achieve this, which may be uneconomical. Nevertheless, diffusing melt point depressants into the parent metal is often performed when high strength joints are required in turbine components. This process is referred to as diffusion brazing, and will be considered in more detail later.

Ni-base filler metals with Si as melt point depressant display a eutectic point at 30% Si according to Nash and Nash, quoted in the ASM Handbook [2]. Braze filler metals with 30% Si, however, result in brittle joints, as Si has a large atomic diameter and is not readily diffused into the parent metal. Hypoeutectic compositions containing between 8 and 12% Si are commercially manufactured and produce sound, reliable joints in the gas turbine industry. Ni_4Si and Ni_3Si silicide phases have, however, been found in joints with large clearances, resulting in severe embrittlement.

Similarly, for Ni-base filler metals with B as melt point depressant, Liao and Spear [2] reported a eutectic point in the Ni-B system at ±11% B, with a eutectic temperature of 1018^{o}C. However, braze filler metals containing 11% B also result in brittle joints. Nevertheless, the small atomic diameter of B allows rapid diffusion into the parent metal, and joints with gaps as wide as 0.3 mm to 0.6 mm have been brazed successfully using filler metals with B as melt point depressant. A hypoeutectic composition of 3.6% B, corresponding to a melting temperature of 1100^{o}C, is widely used, because it is easier to diffuse a small amount of B into the parent metal. Where filler metals containing 3.6% B are used, the joint is almost indistinguishable from the parent metal after brazing. Joints

produced with filler metals containing between 2% and 5% B are commercially manufactured and produce sound, reliable joints in the gas turbine industry. Nevertheless, if the joint gap is too wide, a variety of boride phases can form. Some of the brittle phases found to date include Ni_3B, Ni_2B and NiB.

In the majority of applications, braze filler metals do not contain a single melt point depressant, but a combination. The most popular Ni-base braze filler metals contain both B and Si. The Aerospace Materials Specification (AMS) introduced four Ni-base braze filler metals containing both B and Si. These are:

a) AMS 4776, with a composition Ni-14Cr-3.3B-4.5Si-4Fe and a liquidus temperature of 1077^{o}C,
b) AMS 4777, with a composition Ni-7Cr-3.2B-4.5Si-3Fe and a liquidus temperature of 1000^{o}C,
c) AMS 4778, with a composition Ni-3.2B-4.5Si and a liquidus temperature of 1038^{o}C, and
d) AMS 4779, with a composition Ni-2B-3.5Si and a liquidus temperature of 1066^{o}C.

These filler metals are the most popular braze filler metals used in the aircraft industry and are produced by many suppliers throughout the world.

During the course of an investigation into Ni-base braze filler metals containing Si and P as melt point depressants, Lugscheider and Kim [3] considered four braze filler metals with the following compositions:

1) Ni-24Cr-15Fe-11.5Si-0.6P
2) Ni-24Cr-15Fe-8.5Si-3.0P
3) Ni-24Cr-15Fe-7.5Si-0.6P
4) Ni-24Cr-15Fe-11.5Si-1.8P

Brazing experiments were conducted to enable the brazing parameters (particularly temperature and time) to be optimized with regards to a suitable joint microstructure, and to determine the maximum allowable joint gap. Mechanical tests and corrosion tests revealed that the joints possessed high tensile strengths and excellent corrosion resistance.

Lugscheider and Partz [4] examined the effect of two filler metal compositions on the maximum allowable joint gap during the brazing of Ni-base superalloys. BNi-2 has a composition of Ni-7Cr-3.2B-4.5Si-3Fe and contains Si and B as melt point depressants, and BNi-5 has a composition of Ni-19Cr-10Si and contains only Si as melt point depressant. The authors reported that when BNi-2 was used as filler metal, the maximum allowable joint gap ranged between 0.03 mm and 0.04 mm for a brazing time of 10 minutes at a temperature of between 1010^{o}C and 1120^{o}C. Increasing the brazing time to 60 minutes, however, increased the maximum allowable joint gap to between 0.05 mm and 0.1 mm. When BNi-5 was used as filler metal, the maximum joint gap was between 0.018 mm and 0.022 mm for a brazing time of 10 minutes at a temperature of 1150^{o}C to 1210^{o}C. Increasing the brazing time to 60 minutes increased the maximum allowable joint gap to between 0.035 mm and 0.05 mm. The authors also reported that brazing for either 10 minutes or 60 minutes at temperatures between 980^{o}C and 1100^{o}C reduced the maximum joint gap to 0.01 mm. The narrow gap required for producing quality joints limits the wider application of braze filler metals containing P as melt point depressant. In this author's opinion, the most popular melt point depressants used for joining Ni-base superalloy turbine components are those containing B or Si, or a combination of these two elements, as melt point depressants.

In a similar study, Johnson [5] examined the hard, brittle centreline eutectic phases in a joint brazed with BNi-4 filler metal (with a composition of Ni-2B-3.5Si), shown in **Figure 3**. In **Figure 3A**, the wide centreline eutectic component contains multiple cracks. Even the narrow, but continuous, centreline eutectic phase evident in **Figure 3B** promotes crack propagation. The centreline phases are probably a combination of boride and silicide phases, although this was not stated in the document.

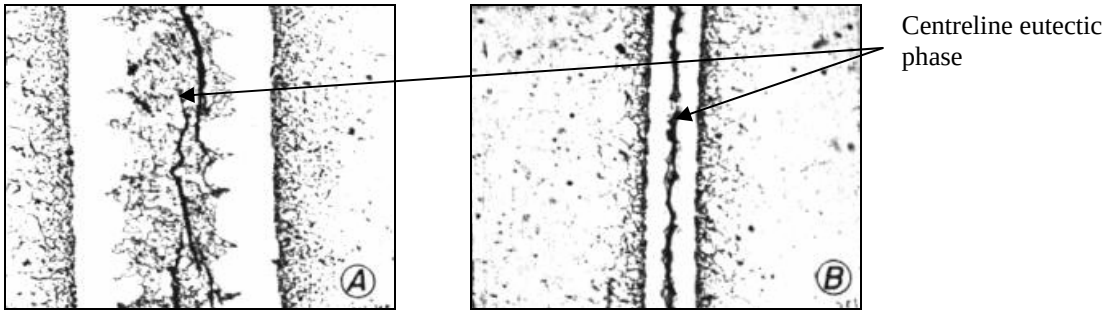

Figure 3 – Centreline cracking in a joint brazed with BNi-4 (with a composition of Ni-2B-3.5Si) [5].

Figure 4 shows the different microstructures that exist within braze joints produced using four braze filler metals with compositions shown below. The brittle centreline phases are clearly visible.

BNi-2: Ni-7Cr-3.2B-4.5Si-3Fe
BNi-3: Ni-3.2B-4.5Si
BNi-4: Ni-2B-3.5Si
NK10: Ni-15Cr-1.5Fe-3.6B

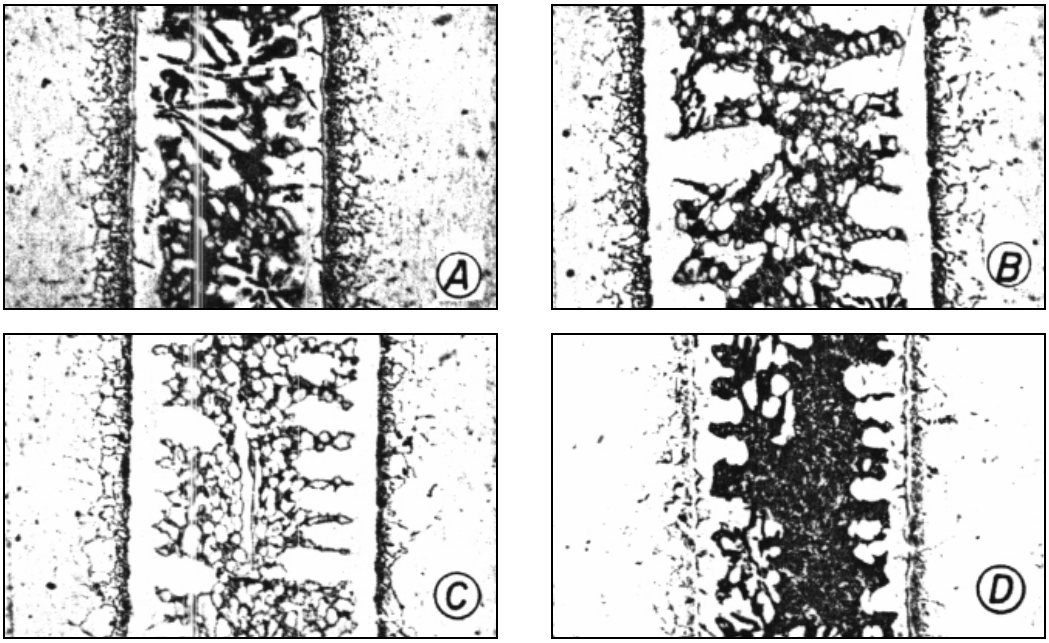

Figure 4 – Typical joint microstructures in four filler metals. A: BNi-2; B: BNi-3; C: BNi-4; and D: NK10. Magnification: 200X [5].

Figure 5 depicts the manner in which the joint microstructures vary as a function of the joint gap. In **Figure 5E**, the joint gap is wide and a continuous eutectic centreline phase is evident.

When the joint gap is narrow, however, as shown in **Figure 5H**, only isolated eutectic phases are present. Continuous centreline eutectic phases facilitate crack propagation.

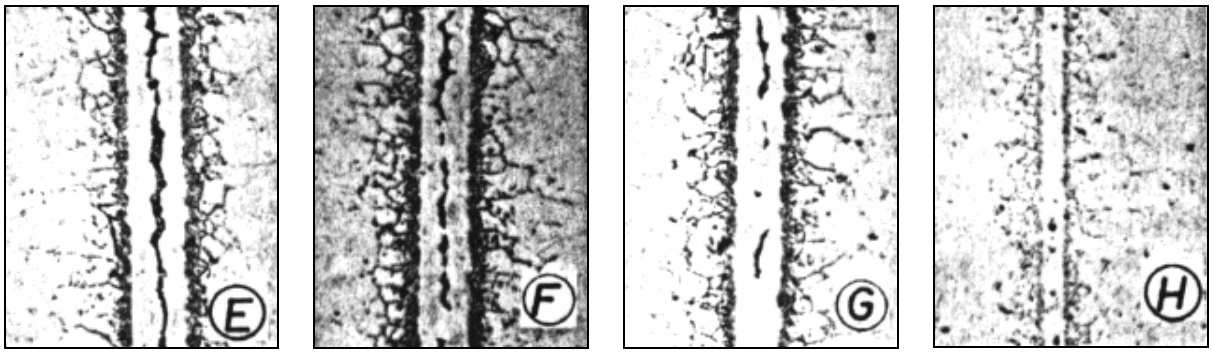

Figure 5 – Variation in microstructure with decreasing gap width. Magnification: 200X [5].

As shown in **Figure 5**, the joint gap needs to be controlled in order to ensure brazed joints with good mechanical properties. It is, however, often difficult to control the joint gap in practice. In the event of a wide gap, a longer brazing time can be used to remove continuous centreline phases. This is illustrated in **Figure 6** for brazing times between 10 minutes and 640 minutes. As the brazing time increases, the centreline eutectic component shrinks, and would probably become discontinuous at holding times exceeding 640 minutes.

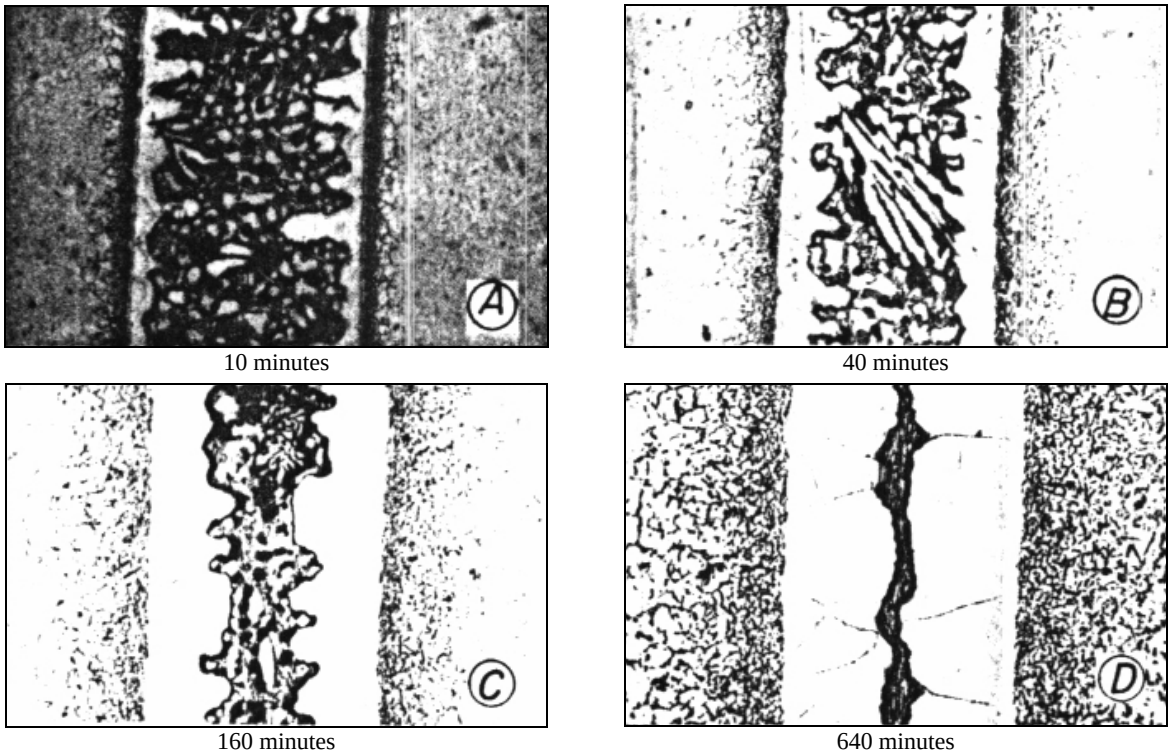

Figure 6 – Effect of holding time on the brazed joint microstructure. A: 10 minutes; B: 40 minutes; C: 160 minutes; and D: 640 minutes. Magnification: 200X [5].

In the event of a wide joint gap, **temperature** can also be used to render a braze joint free of continuous centreline phases. **Figure 7** shows the effect of increasing temperature on the joint microstructure. The microstructures shown in the first three micrographs (A, B and C in **Figure 7**) are comparable with those in **Figure 6** showing the effect of increasing braze time.

At 1250°C, however, the microstructure changes considerably. As a result of isothermal diffusion, elements from the parent metal also diffuse into the joint at the high braze temperature and a new type of eutectic forms in the joint. This new eutectic is believed to be less brittle than the more typical boride or silicide centreline phases.

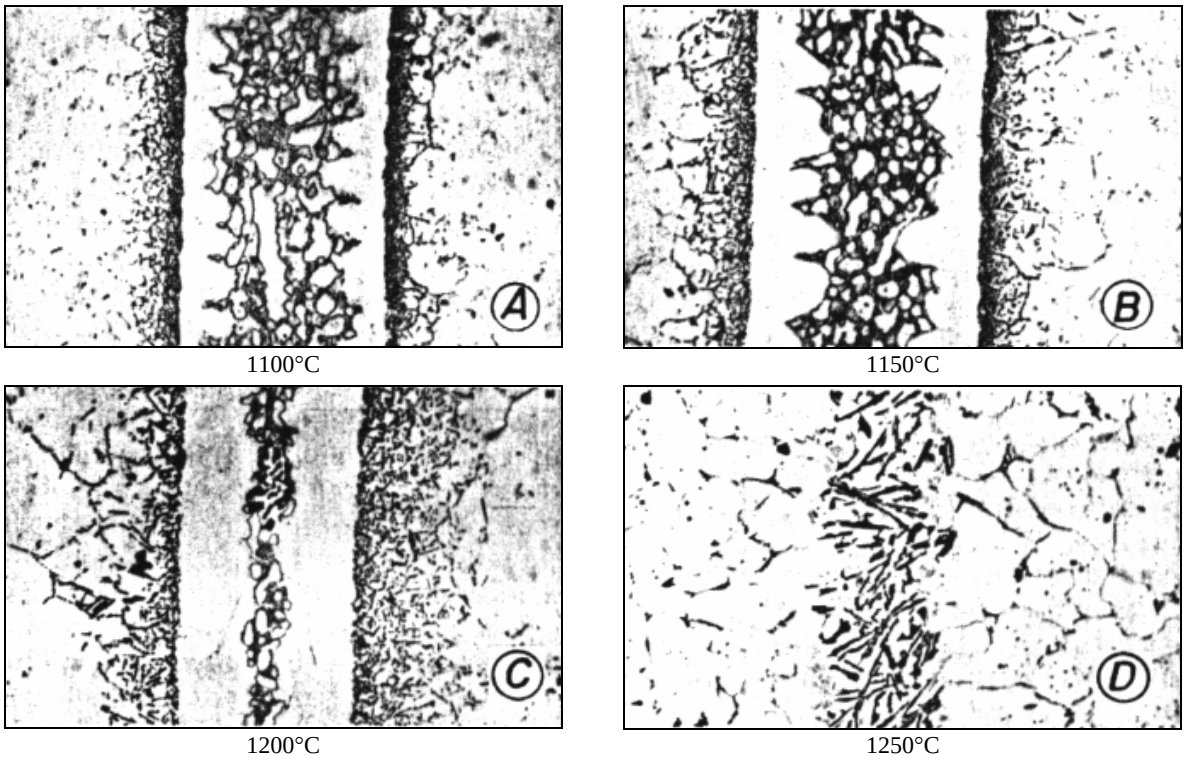

Figure 7 – Effect of brazing temperature on joint microstructure. A: 1100°C; B: 1150°C; C: 1200°C; and D: 1250°C. Magnification: A, B and C = 200X, and D = 100X [5].

Sakamoto *et al* [6] performed a similar investigation in 1989, and found that increasing the time at the brazing temperature or increasing the brazing temperature can result in joints without eutectic phases. **Figure 8A** displays the characteristic continuous brittle eutectic centreline component in a 0.05 mm wide joint, held for 10 minutes at 1075°C. On increasing the braze temperature to 1175°C, a braze joint free of eutectic phases was obtained, as seen in **Figure 8B**. Similarly, **Figure 8C** shows irregular centreline eutectic phases in a 0.05 mm wide joint, held for 30 minutes at 1075°C. On increasing the holding time to 90 minutes at 1075°C, a braze joint free of eutectic phases was obtained (**Figure 8D**).

It is evident from the published research described above that the type of braze filler metal, the joint gap, the time at the brazing temperature, and the brazing temperature are important variables associated with the braze process.

These variables also play a major role in determining the mechanical properties of the braze joint. Miyazawa and Ariga [7] reported the effect of brazing time and temperature on the shear strength of brazed joints produced using BNi-1 braze foil (Ni-14Cr-3.3B-4.5Si-3Fe). As demonstrated in **Figure 9**, the shear strength of the joint increased with an increase in braze time and temperature. After 60 minutes at 1275°C the brazed joint displayed the highest shear strength (320 MPa).

Similarly, when using BNi-2 braze foil (Ni-7Cr-3.2B-4.5Si-3Fe), the shear strength of the joint increased with an increase in braze time and temperature, as shown in **Figure 10**. After 60 minutes at 1275°C the brazed joint displayed the highest shear strength (320 MPa). When joining steel to nickel, it is therefore more desirable to use BNi-2, rather than BNi-1, because the same shear strength can be achieved at a lower brazing temperature (1150°C compared to 1275°C).

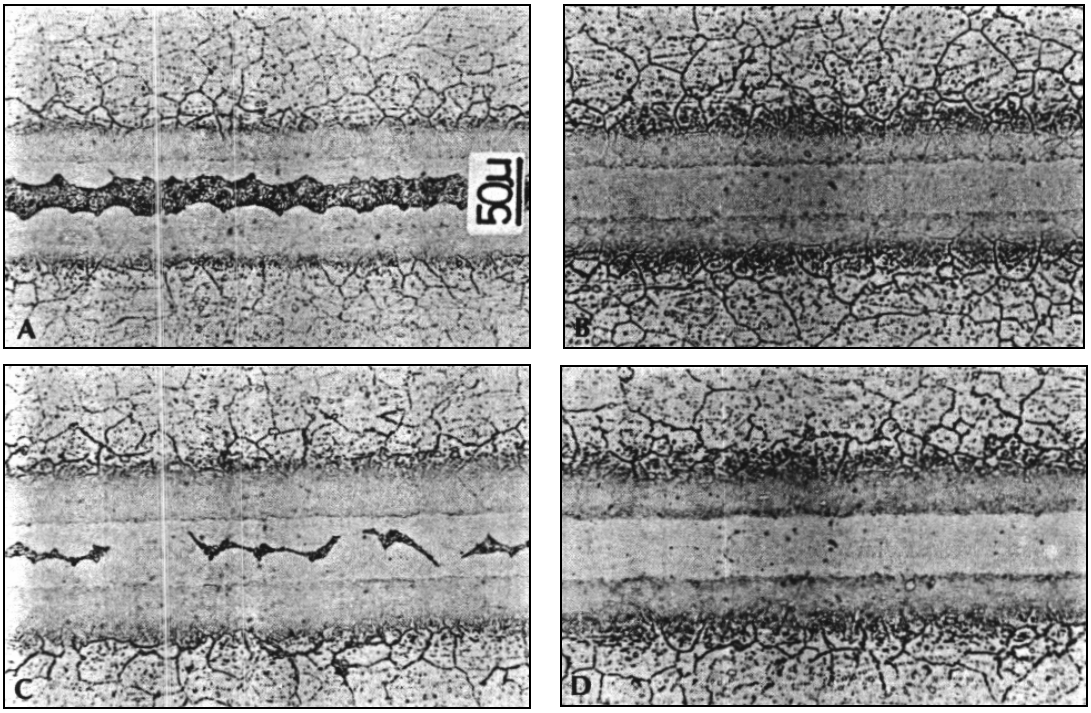

Figure 8 – Microstructure of brazed joints with a 0.05 mm gap. A: 1075°C for 10 minutes; B: 1175°C for 10 minutes; C: 1075°C for 30 minutes; and D: 1075°C for 90 minutes [6].

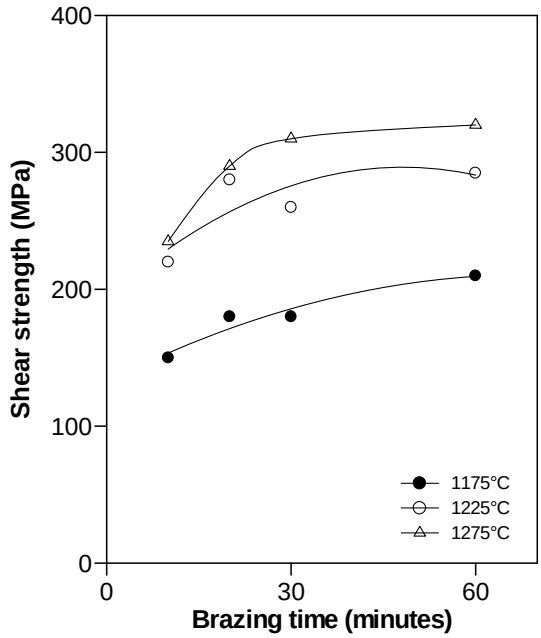

Figure 9 – The effect of brazing time and brazing temperature on joint shear strength (brazing foil BNi-1) [7].

The same trend is evident on using BNi-3 braze foil (Ni-3.2B-4.5Si), **Figure 11**. After 60 minutes at 1190°C the brazed joint displayed the highest shear strength of 250 MPa, 70 MPa less than that achieved when using BNi-1 or BNi-2 braze filler metals. The lower shear strength can be attributed to the absence of Cr and Fe in the BNi-3 filler metal. The joint therefore relies on diffusion of Cr from the nickel-base parent metal for solid solution strengthening, and a brazing time of 60 minutes is too short to allow sufficient Cr diffusion from the parent metal into the joint.

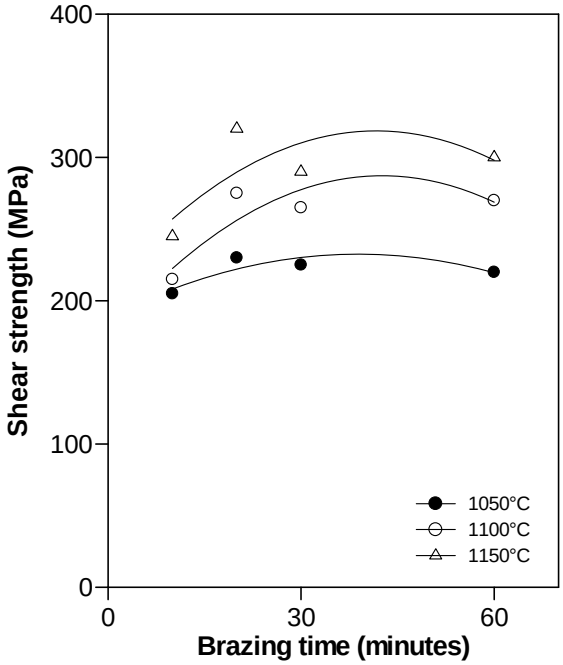

Figure 10 - Effect of brazing time and brazing temperature on the joint shear strength (brazing foil BNi-2) [7].

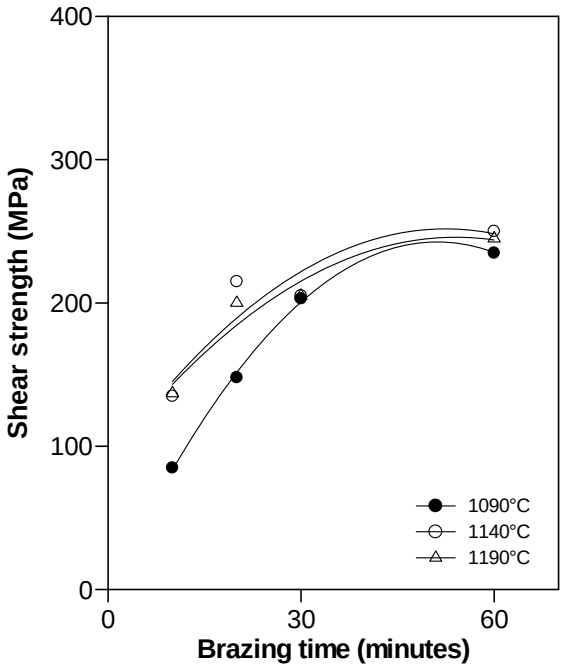

Figure 11 - Effect of brazing time and brazing temperature on the joint shear strength (brazing foil BNi-3) [7].

In a similar study undertaken by Kavishe and Baker [8], an increase in tensile strength with decreasing gap width was reported for copper brazed alloy steel joints, as shown in **Figure 12(a)**. **Figure 12(b)** demonstrates a corresponding increase in the percentage elongation with an increase in gap width.

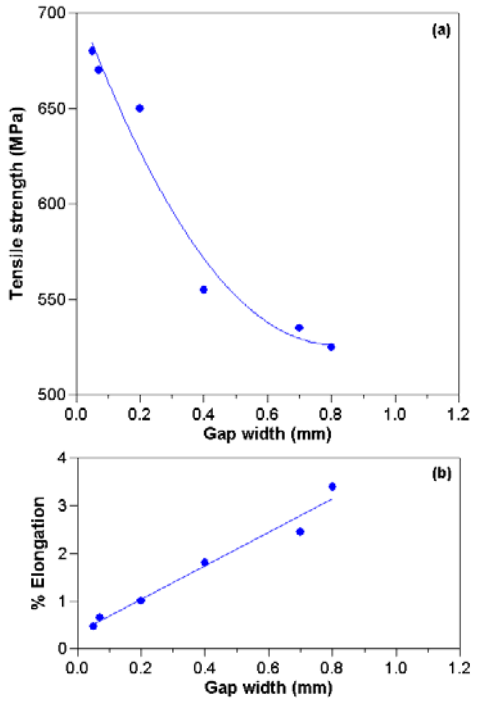

Figure 12 – Influence of joint gap on (a) tensile strength, and (b) percentage elongation of copper brazed alloy steel joints [8].

These authors also reported that the proof stress of the joints was slightly lower than the yield strength of mild steel for narrow gaps, but that the tensile strength was significantly greater than the yield strength of mild steel, as seen in **Figure 13.** The fracture toughness of the steel brazed joints decreased with a decrease in joint gap, as shown in **Figure 14.** This is associated with the increase in joint strength.

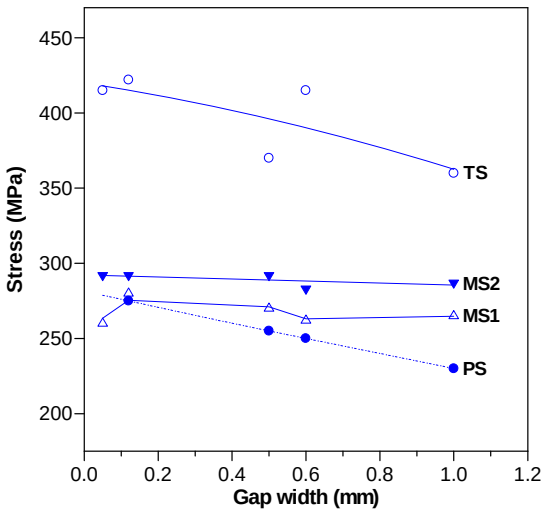

Figure 13 – Influence of gap width on the tensile strength (TS) and proof stress (PS) of copper brazed mild steel joints. MS1 and MS2 are the yield points of mild steel [8].

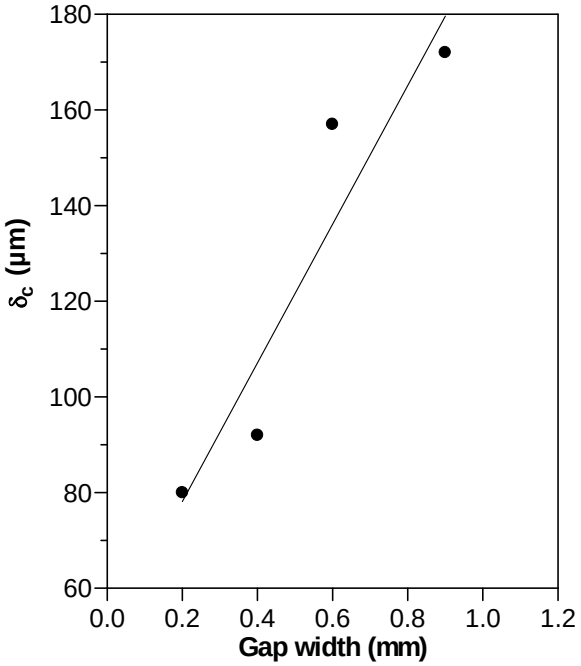

Figure 14 – The influence of gap width on the fracture toughness, as characterized by δ_c (the crack tip opening displacement), for copper brazed mild steel joints [8].

Lugscheider and Krappitz [9] studied the influence of gap width on the impact strength of Inconel 625 joints brazed with Au-6 filler metal. These authors reported a maximum notch impact energy at a joint gap of 12 μm, as illustrated in **Figure 15**.

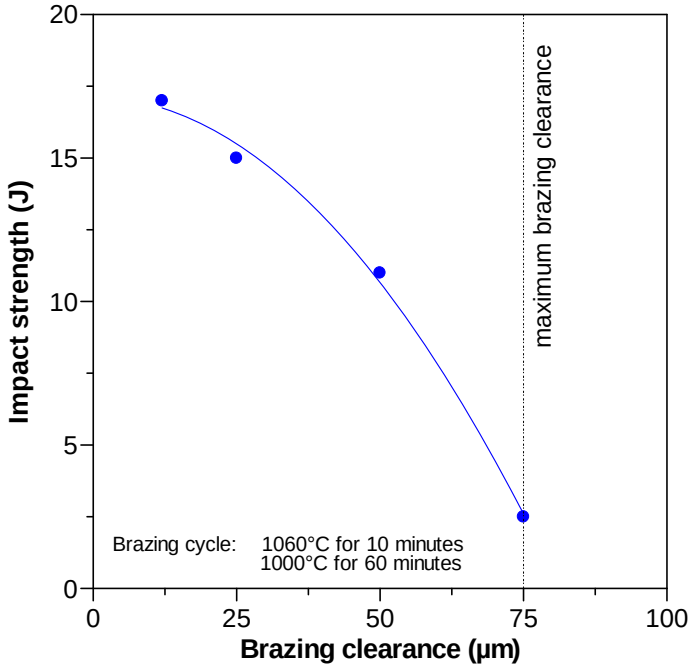

Figure 15 – Dependence of impact strength on joint clearance for Inconel 625 brazed with Au-6 (Ni-20.5Au-5.6Cr-2.3Fe-3.4Si-2.3B) filler metal [9].

Draugelates and Hartmann [10] studied the fatigue properties of a Nimonic 80 Ni-base superalloy, brazed with BNi-5 (Ni-19Cr-10Si-0.1C) filler metal. They found that the braze cycle, particularly braze temperature and time, had a significant influence on the fatigue properties of the joint. As seen in **Figure 16**, brazing at 1190^{o} C for 5 minutes, followed by

soaking at 1100°C for 8 hours and aging at 710°C for 16 hours, resulted in a 40% increase in fatigue life, when compared to brazing at 1190° C for 5 minutes, followed by aging at 710°C for 16 hours. The increase in fatigue life was attributed to the removal of brittle Cr-silicide phases from the joint during the extended heat treatment. Since Si has a large atomic diameter, extended times at temperature are required to diffuse the silicon into the parent metal and to reduce the occurrence of brittle phases.

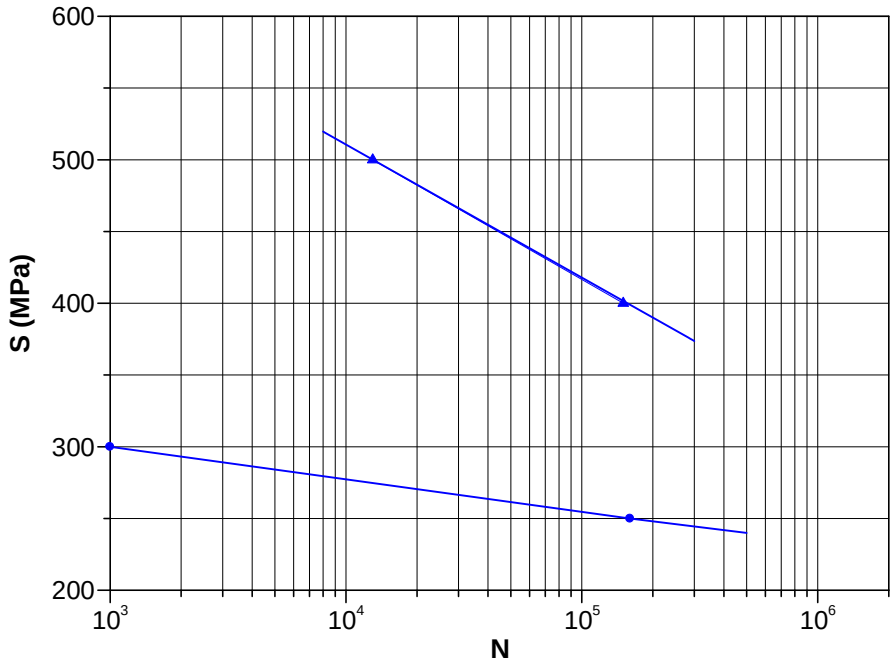

Figure 16 – Fatigue behavior of brazed joints (tested at room temperature, R = 0.1).
• brazing at 1190° C for 5 minutes, followed by aging at 710°C for 16 hours.
▲ brazing at 1190° C for 5 minutes and 1100°C for 10 hours, followed by aging at 710°C for 16 hours [10].

The preceding discussion illustrates that four important parameters need to be controlled in order to achieve high-strength joints free of brittle centreline eutectic phases. These parameters are:

- brazing time,
- brazing temperature,
- gap width/joint gap, and
- braze filler metal.

It is also apparent from the preceding discussion that metallurgical reactions which take place during the braze cycle affect the properties of the joints. During the braze cycle the melt point depressants in the nickel-base braze filler metal (such as P, B and/or Si) diffuse into the parent metal, thereby increasing the remelt temperature of the brazed joint and making the joint capable of higher temperature service. The diffusion of elements from the braze filler metal also affects the ductility of the completed joint. During the braze cycle a limited amount of parent metal may dissolve in the liquid braze filler metal, which increases the melt liquidus temperature. Diffusion of alloying elements from the parent metal into the joint has a similar effect.

As mentioned earlier, the main melt point depressants in use today are B, Si and P. Consideration of the alloy phase diagrams [2], however, suggests that Zn and Cd may also act as melt point depressants. Due to the high vapour pressures of these elements, however, they are unsuitable for use in vacuum brazing. Many Ag- and Cu-base braze filler metals are doped with Zn or Cd, but use of these fillers is restricted to flame brazing, induction brazing or inert atmosphere brazing.

1.3) Characterization of the eutectic phases that form in brazed joints

As stated earlier, Ni-base braze filler metals typically contain melt point depressants, such as B, Si and P. These elements tend to form hard, brittle structures in the joint. If the melt point depressants diffuse into the parent metal during the braze cycle, brittle phases may also form adjacent to the joint, depending on the composition of the parent metal. **Figure 17** displays hardness profiles across brazed joints in Inconel 625 (a Ni-base superalloy) for three different filler metals, BNi-2, BNi-5 and Au-6. The highest hardness was observed in the joint brazed with BNi-5, which contains Si as melt point depressant and forms brittle silicide phases even after an extended brazing cycle at 1150^{o}C for 10 minutes, followed by holding at 1100^{o}C for 60 minutes. As a result of this braze cycle, the hardness of the parent metal was increased to a level exceeding that of the brazed region. The joint with the next highest hardness was BNi-2, containing both Si and B as melt point depressants. Brittle silicide and boride phases formed even after brazing at 1065^{o}C for 10 minutes, followed by holding at 1000^{o}C for 60 minutes. The joint with the lowest hardness was Au-6, containing 20.55% Au, as well as B and Si. Au is known for its ductility and softness. The B and Si in Au-6 still resulted in the formation of some silicide and boride phases after brazing at 1060^{0}C for 60 minutes, but the joint hardness was considerably lower.

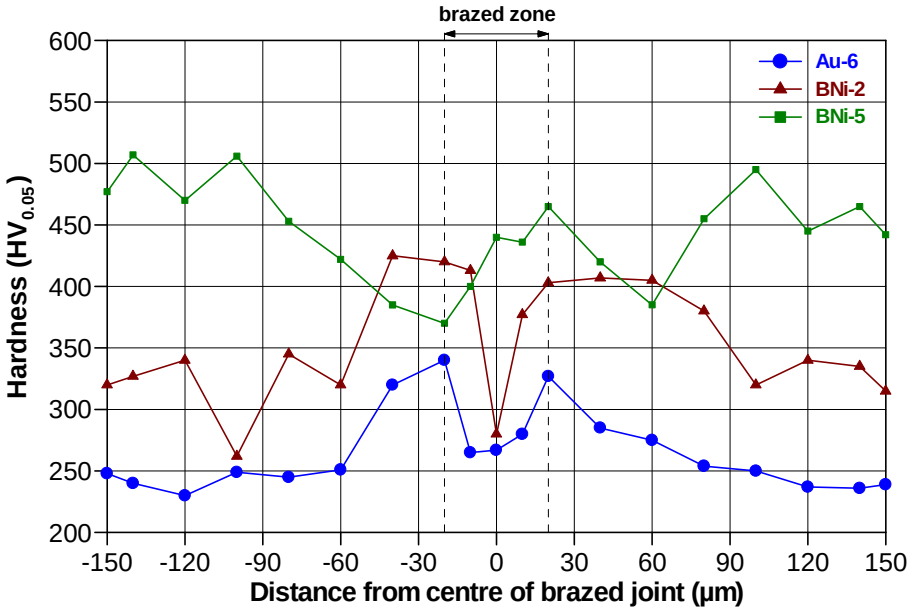

Figure 17 – Hardness profiles across brazed joints in Inconel 625 [7].

Tung, Lim and Lai [11] examined four braze filler metals, BNi-5 (Ni-19Cr-10.2Si), Nicrobraz 150 (Ni-15Cr-3.5B), BNi-4 (Ni-3.5Si-1.5B) and BNi-1 (Ni-14Cr-4.5Si-4.5Fe-3B), and concluded that the braze melt point depressants tend to form hard and brittle intermetallic compounds with nickel, and that the presence of these compounds is detrimental to the mechanical properties of the brazed joints. An incentive therefore exists to control the

microstructures that develop in brazed joints and to develop brazing alloys that are less sensitive to the formation of detrimental phases. **Figure 18** shows the typical microstructure of a 0.5 mm wide joint brazed with BNi-5. The only intermetallic compound observed in this braze was nickel silicide, which appears white in the micrograph. It solidified as a component phase of the binary eutectic with γ-nickel, the latter appearing as the dark phase in **Figure 18**. The microstructure of a joint brazed with Nicrobraz 150 is shown in **Figure 19(a).** The phase marked G1 in this micrograph is nickel boride, while the phase marked G2 is the nickel-rich γ solid solution. In the centreline region of the joint a ternary eutectic of γ-nickel, nickel boride and chromium boride was present, as shown in **Figure 19(b).**

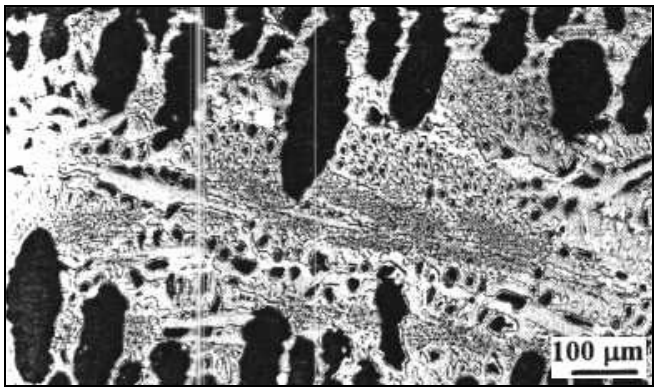

Figure 18 – Typical microstructure of a joint brazed with BNi-5 [11].

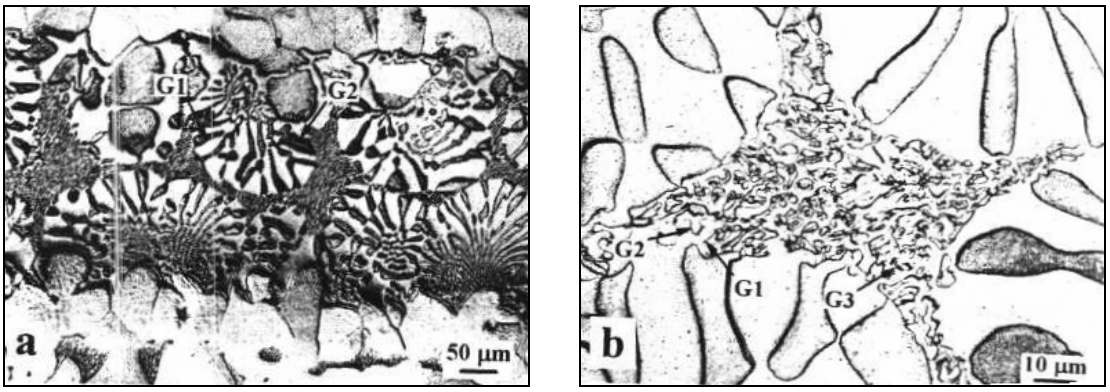

Figure 19 - (a) Microstructure of a joint brazed with Nicrobraz 150 at 1125^{o}C; and (b) a magnified view showing the details of the ternary eutectic component [11].

Typical microstructures of joints brazed with BNi-4 filler metal are shown in **Figure 20**. The various phases formed in this joint, shown in **Figure 20(a)**, include γ-nickel solid solution layers (marked M*) found adjacent to the joint mating surfaces, γ-nickel nodules (marked M), bulky nickel borides (marked R), binary eutectics of γ-nickel and nickel boride, and ternary eutectics of γ-nickel, nickel boride and nickel silicide (marked X). The binary eutectic of normal morphology (marked N) formed adjacent to the layers of single-phase γ-nickel. **Figure 20(b)** shows details of the ternary eutectic (X). The phases designated X1, X2 and X3, are nickel silicide, γ-nickel and nickel boride, respectively. Nickel silicide (marked m), which precipitates in the solid state, was found in the outer regions of the γ-nickel nodules, especially those in the centreline region of the joint.

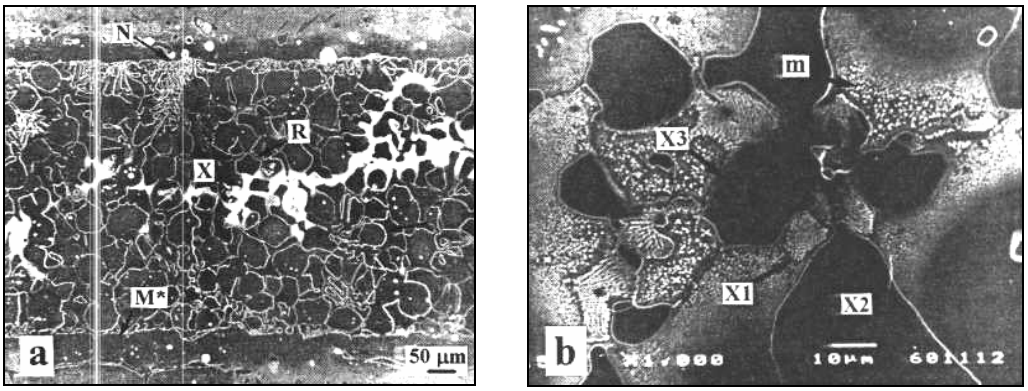

Figure 20 - (a) The constituents and component phases in a joint brazed with BNi-4; and (b) details of the ternary eutectic and nickel silicide precipitates in the joint centreline [11].

The microstructure resulting from the solidification of the molten filler metal in the joint brazed with BNi-1 was found to be extremely complex. Three intermetallic compounds formed in this braze, namely nickel boride, nickel silicide and chromium boride. The typical microstructure of a BNi-1 joint is shown in **Figure 21(a).** The phases marked L1a, L1b and L1c are nickel borides, L2a and L2b are γ-nickel, L3 is nickel silicide, and L4 is chromium boride. Three eutectic constituents were identified: a binary eutectic of γ-nickel and nickel boride (L2a/L1a), a binary eutectic of γ-nickel and chromium boride (L2a/L4), and a ternary eutectic of γ-nickel, nickel boride and nickel silicide (L2a/L1c/L3). Details of the ternary eutectic are given in **Figure 21(b).** It is interesting to note that in the presence of silicon, the formation of the ternary eutectic of γ-nickel, nickel boride and chromium boride was suppressed, in that chromium boride solidified with γ-nickel as a binary eutectic. The fine precipitates in γ-nickel (L2a) are nickel silicide particles, which formed in the solid state on cooling to room temperature.

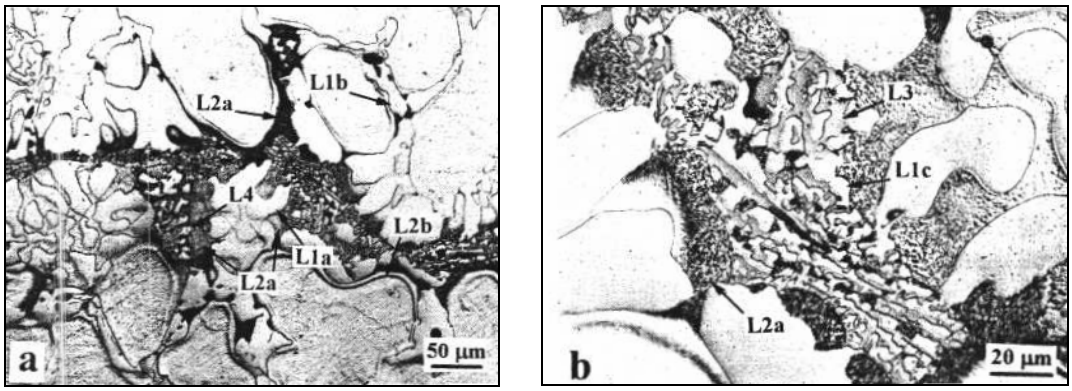

Figure 21 - (a) Microstructure of a joint brazed with BNi-1 at 1125°C; and (b) a magnified view showing the details of the eutectic phases [11].

It can therefore be concluded that the intermetallic compounds formed in brazed joints using nickel-base filler metals containing chromium, boron and silicon, are nickel boride, nickel silicide and chromium boride. These intermetallic compounds form as constituents of binary or ternary eutectics with γ-nickel. The binary eutectics are γ-nickel/nickel boride, γ-nickel/nickel silicide and γ-nickel/chromium boride, whereas the ternary eutectics are γ-nickel/nickel boride/chromium boride and γ-nickel/nickel boride/nickel silicide.

Johnson [12] performed microprobe analyses to identify the phases formed on brazing ferritic steel using various gap widths. The braze filler metals evaluated were the popular BNi-2 (Ni-7Cr-3.2B-4.5Si-3Fe) and BNi-4 (Ni-3.5Si-1.5B). The phases identified were α-nickel (containing Si, but no B), nickel boride, nickel silicide and chromium boride. As the joint gap narrowed, the number of phases was reduced, as shown in **Figures 22 to 25**. The first phase to disappear was nickel boride, followed by nickel silicide, and lastly chromium boride. Finally only α-nickel remained, as seen in **Figure 25**.

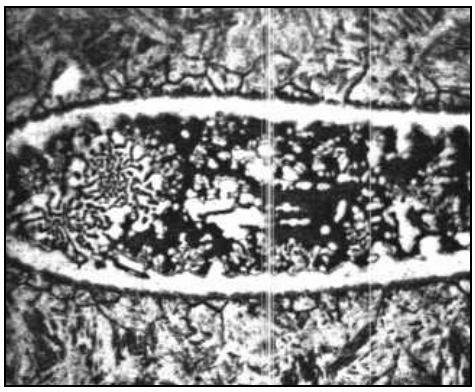

Figure 22 – Brazed joint of BNi-2 with 4 phases present. Magnification: 200X (reduced 50% on reproduction) [12].

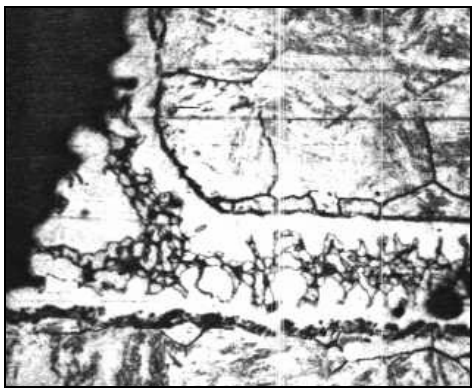

Figure 23 – Brazed joint of BNi-4 with 3 phases present. Magnification: 200X (reduced 50% on reproduction) [12].

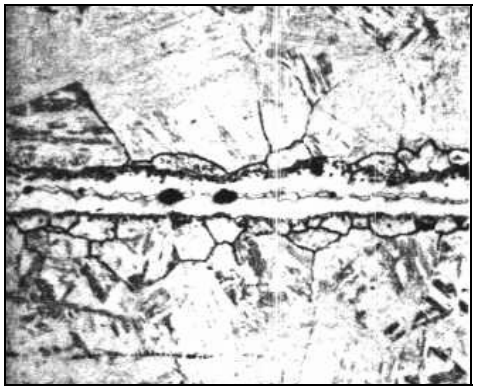

Figure 24 – Brazed joint of BNi-4 with 2 phases present. Magnification: 200X (reduced 50% on reproduction) [12].

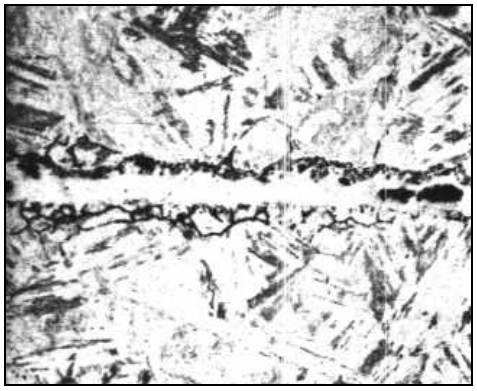

Figure 25 – Brazed joint of BNi-4 with 1 phase present. Magnification: 200X (reduced 50% on reproduction) [12].

While the braze filler metal was enriched in elements from the steel parent metal through erosion and diffusion, filler metal alloying elements were also entering the parent metal. In BNi-4, nickel and silicon entered by bulk diffusion into the parent metal to a distance of about 15 μm, but boron (which diffuses along the grain boundaries) migrated to a maximum distance of 140 μm. In BNi-2, the corresponding diffusion distances were 8 μm and 60 μm. It is evident in **Figures 26 and 27** that the B formed almost continuous stringers of iron boride along the grain boundaries.

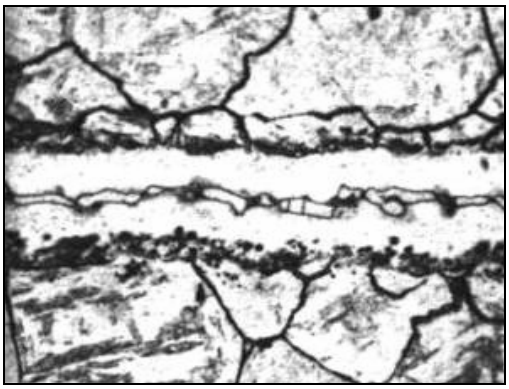

Figure 26 – Boride particles in the steel parent metal (BNi-4 braze). Magnification: 500X (reduced 50% on reproduction) [12].

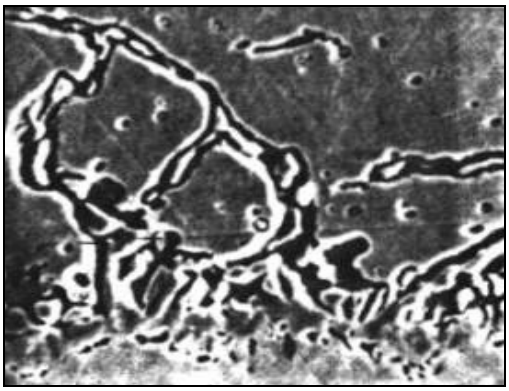

Figure 27 – Boride particles in the steel parent metal (BNi-4 braze). Magnification: 2000X (reduced 50% on reproduction) [12].

The implication of Johnson's research is that in order to make serviceable brazed joints, the braze filler metal should be ductile and contain no regions of weakness or brittleness. With the nickel-base filler metals investigated, this ideal was realized in narrow joints less than 40 to 50 μm in width, containing only α-nickel. Wider joint gaps allowed the formation of boride and silicide eutectics along the centreline of the joint. As these phases have high hardness values, in the region of 900 HV (hardness on the Vickers scale), they possess only limited ductility and may crack if high tensile stresses are generated along or across the joint. These hard particles may also rupture to form fatigue crack nuclei. While a long brazing time facilitated the diffusion of B into the steel parent metal to some extent, such an extended high temperature soak is generally not a viable option if liquation of the grain boundaries is to be avoided.

Gale and Wallach [13] studied Ni-Cr joints brazed with BNi-3 (Ni-3.2B-4.5Si) and observed $Ni_{23}B_6$ within the joints. This phase formed intragranularly in the proeutectic nickel phase immediately adjacent to the eutectic mixture. These boride phases generally formed as platelets along $<001>_{Ni}$ directions, although cuboidal morphologies were also observed. The origin of $Ni_{23}B_6$ precipitation remains uncertain, especially as this phase does not appear on the available phase diagrams for the Ni-Si-B system. Nevertheless, $Ni_{23}B_6$ formation occurred reproducibly in samples held for 3 minutes at 1065°C, but not in those subjected to longer soaking times. The Ni_3Si phase formed throughout the joint within the nickel component of the filler metal eutectic, and had a cuboidal structure aligned along the <100> directions. The most pronounced precipitation in the eutectic phase occurred in samples not subjected to long holding times.

Gale and Wallach concluded that:

- for Ni and Ni-5Cr substrates, Ni_3B formed at the original substrate/filler interface and $M_{23}B_6$ formed in the bulk substrate,
- for Ni-10Cr substrates, $M_{23}B_6$ formed throughout the substrate,
- for Ni-15Cr substrates, $M_{23}B_6$ and Cr_5B_3 formed throughout the substrate, and
- for Ni-20Cr substrates, $M_{23}B_6$, Cr_5B_3 and Ni_3Si formed at the original substrate/filler interface, while $M_{23}B_6$ and Cr_5B_3 formed throughout the substrate.

Similarly, Lasalmonie [14] examined the phases precipitated during the brazing of DS 247 (Ni-9.5Co-8Cr-3.3Ta-0.5Mo-9.5W-5.5Al-0.6Ti-0.07C) and ATGP 3 (Ni-15Co-15Cr-5.2Mo-4.4Al-3.5Ti-0.06C) using 120 μm thick BNi-3 (Ni-4.5Si-3.2B) braze filler metal. Brazing was performed at 1040°C for 3 hours. The phases present in the structure (shown in **Figure 28**) were reported as:

- $M_{23}B_6$ with a hardness in the region of 1000 HV (with M consisting of Ni, Cr, Co, Al and Ti),
- Cr_5B_3, with a hardness of 3000 HV,
- W_2B,
- Ta-Hf carbides, and
- MB_{12} (with M consisting of Cr, Mo and W).

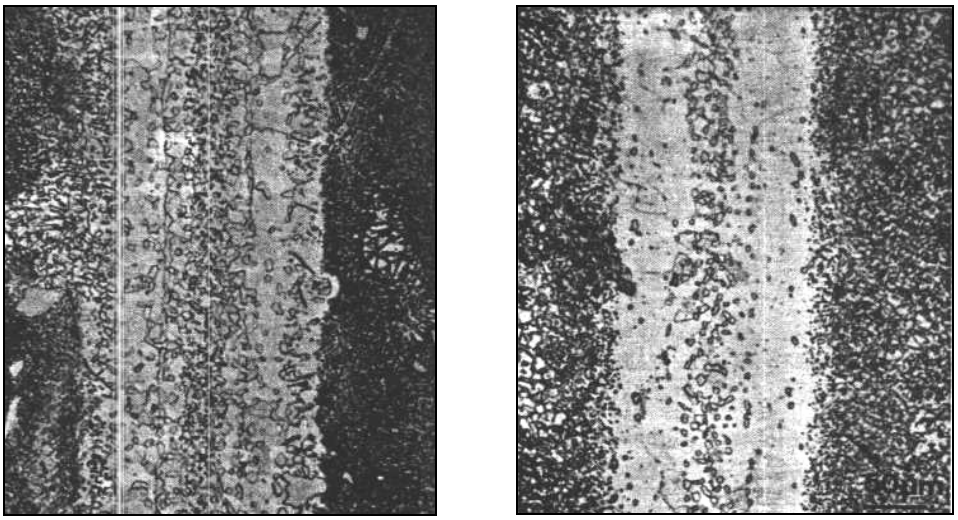

(a) DS 247 (b) ATGP 3

Figure 28 - Brazed joints in two nickel-base superalloys produced with BNi-3 filler metal at 1040°C for 3 hours [14].

Savage and Kane [15] attributed a number of field failures observed during the joining of Nickel 201 tubing to Nickel 201 plate stock using BNi-3 filler metal to the formation of nickel silicide and nickel boride phases in the joint. The braze cycle of 1093°C for 30 minutes resulted in rapid grain boundary diffusion of B from the braze joint into the base metal. This sensitized the grain boundaries, causing the tubing to undergo intergranular corrosion. The authors reported that quenching, as opposed to slow cooling from the braze temperature, changed the boride morphology in the joint. After quenching the boride phase displayed a needle-like morphology and no intergranular corrosion attack was observed. Failure was primarily as a result of crevice corrosion involving attack of this needle-like boride phase, with the corrosion rate determined by the joint gap. The quench rate from the brazing temperature is therefore also an important parameter that needs to be controlled, since a different boride or silicide morphology can affect the mechanical and corrosion properties of the brazed joints.

Tung, Lim and Lai [16] evaluated the intermetallic phases that form in Ni-base brazed joints, and reported the presence of bulky nickel boride and nickel silicide phases in a solid solution area referred to as γ-nickel. The compositions and hardness values of the phases observed are as follows:

- γ-nickel, consisting of Ni and 3.0 to 4.8% Si, with a hardness between 108 and 188 HV,
- nickel boride, consisting of Ni and 0.2 to 0.3% Si, with a hardness between 776 and 906 HV, and
- nickel silicide, consisting of Ni and 8.0 to 13.1% Si (the hardness was not measured).

The relative nickel and silicon weight percentages listed above were obtained by means of standardless EDS analysis. Since the EDS system employed could not measure B contents accurately, the B concentrations were not reported. Despite this deficiency, the information given above was sufficient to distinguish the different phases. The general direction of solidification was from the base metal towards the centreline of the joint. The first phase to form was primary γ-nickel, solidifying in the form of solid solution layers next to the joint faying surfaces. This caused the melt to become enriched in B. As solidification proceeded, eutectics of nickel boride solidified. Higher brazing temperatures and faster cooling rates facilitated the formation of binary γ-nickel/nickel boride eutectics. Higher cooling rates also promoted the formation of ternary eutectics of γ-nickel, nickel boride and nickel silicide in the last remaining liquid. On further cooling to room temperature, solid state precipitation of nickel silicide occurred within the γ-nickel nodules, especially those formed in the latter stages of solidification near the centreline of the joint. Bands of nickel boride precipitates were observed in the base metal adjacent to the joint interface in joints brazed at 1090^{o}C, below the eutectic temperature of the binary Ni-B system.

1.4) Repair of turbine components using brazing

Degradation of engine components during service may result from thermal cracking and distortion, oxidation, sulphidation, corrosion, erosion, fretting, wear, foreign object damage (FOD, i.e. objects ingested into the engine) and creep. Degraded components are replaced not only because of their loss of structural integrity, but because there is a loss of operating efficiency in the engine. In many instances, especially in the land-based industry (turbines used to generate electrical power) it is more cost effective to carry out repairs to return the components to serviceable condition for a fraction of the cost of a new component. Typically, repair costs are approximately 10 to 50% of the cost of a new component. This is a very lucrative business and there are numerous companies throughout the world whose primary business is to repair turbine components.

As shown in §1.2 and §1.3, the major variables which need to be controlled in order to achieve a high quality brazed joint are gap width, braze alloy/filler metal, braze temperature and time, cooling rate and cleanliness. When it comes to braze repair of turbine components, however, controlling the joint gap is near impossible. This is because components have predefined and precise crack widths after service exposure. In the early era of crack repair using brazing, only cracks with widths between 0.025 mm and 0.254 mm were repaired. Once the combustion products were removed by processes such as fluoride ion cleaning (a process that uses a combination of H_2 gas and HF gas to reduce the aluminum oxide and titanium oxide present in the crack), capillary action would draw the molten braze filler metal into the crack. Braze filler metals containing B and/or Si as melt point depressants were initially evaluated for crack repair, but as a result of the brittle silicide and boride phases that form in the repaired joint, the braze joint would re-crack when returned to service. Since Si has a large atomic diameter and do not readily diffuse into the parent metal, investigators concluded that only braze filler metals with B as melt point depressant could be used for crack repair. This encouraged the introduction of a number of new filler metals into the market. Some of these braze alloys are listed below:

- DF3 - (Ni-20Cr-20Co-3Ta-3B-0.05La)
- DF4B – (Ni-14Cr-10Co-2.5Ta-3.5Al-2.7B-0.02Y)
- DF5 – (Ni-13Cr-3Ta-4Al-2.7B-0.02Y)
- DF6 – (Ni-20Cr-3Ta-2.8B-0.04Y)
- BRB – (Ni-14Cr-9.5Co-4Al-2.5B)
- 775 – (Ni-15Cr-3.5B)
- S57B – (Co-10Ni-21Cr-5Ta-2.5Al-3B-3Si-0.02Y)

Lecomte-Martens [17] from the repair company C.R.M in Belgium investigated the use of DF4B (with the composition shown above) in the braze repair of In792 nickel-base superalloy vanes, as well as the use of S57B in the braze repair of H188 cobalt-base superalloy vanes. In792 has a composition of Ni-12.7Cr-9Co-2Mo-4.2W-4.1Ti-3.4Al-4.2Ta-1.0Hf-0.05Zr-0.015B-0.14C, and H188 consists of Co-22Cr-22Ni-14W-1.5Fe-0.08La-0.08C. The brazing temperature for the DF4B filler metal was 1200^{o}C and the brazing time 15 minutes, followed by a 3 hour diffusion cycle at 1057^{0}C (to diffuse the B away from the joint). The brazing temperature for the S57B filler metal was 1220^{o}C and the brazing time 15 minutes, followed by a 3 hour diffusion cycle at 1040^{0}C (to diffuse the B and Si away from the joint). For both joints, 18 hour and 30 hour diffusion cycles were also investigated. The joints produced with S57B filler metal displayed evidence of a Co-Ni-Cr solid solution, Cr carbides, W carbides, Ta carbides, Cr borides and Cr-Co-W silicide phases. The joints produced with DF4B filler metal contained a Ni-Co-Cr solid solution, Ta-Ti-Hf carbides, Cr carbides and Cr borides. Fatigue tests were performed on actual braze repaired vanes, as opposed to test specimens. The first engine test showed that new vanes cracked after 441200 cycles, whereas the braze repaired vanes cracked after 324200 cycles. The second engine test showed that new vanes cracked after 409200 cycles, whereas the braze repaired vanes cracked after 270300 cycles. In the third and fourth engine tests, new vanes cracked after 397600 and 417325 cycles, respectively, whereas the braze repaired vanes cracked after 240100 and 280250 cycles. It was concluded that, on average, the number of cycles required to fracture a braze repaired vane is about 2/3 of that required for a new vane. This was acceptable since the price of a repaired vane is typically 10 to 50% of that of a new vane, and hence the braze repair was still economical. The total number of cracks found on the new vanes was 40, the total crack length was 287 mm and the average crack length was 7.2 mm. For the braze repaired vane, 39 cracks were found in total, the total crack length was 218 mm and the average crack length was 5.6 mm. These results suggest that, although cracks initiated earlier in a braze repaired vane, the average crack length was less than in a new vane. The crack propagation rate therefore appeared to be slower in the brazed joint than in the parent metal. **Figure 29** compares cracks detected in a new vane and in a repaired vane after engine testing. An important conclusion reached by the author was that cracks wider than 0.5 mm were not completely filled by the molten braze filler metal and should be repaired using wide gap brazing. The topic of wide gap diffusion brazing is considered in §1.5.

Elder, Thamburaj and Patnaik [18] investigated the repair of narrow cracks in MA 754 (Ni-19.7Cr-0.35Al-0.45Ti-0.37Fe-0.05C-0.57Y_2O_3-0.39O_2) using vacuum brazing with fourteen different braze alloys. The braze filler metals contained either B, or B and Si, as melt point depressants. Microprobe analyses revealed the presence of Cr boride and Ni silicide in brazed joints containing both B and Si as melt point depressants. Joints containing only B as melt point depressant contained Cr-W boride phases. Narrow cracks (0.038 mm in this investigation) resulted in joints free of brittle phases. As the crack width approached 0.762 mm, brittle intermetallic phases formed, reducing joint ductility to 1.3% (compared with the parent metal ductility of 4%). The authors also concluded that these brittle intermetallic

phases act as preferential crack initiation sites, and recommended the use of B as the sole melt point depressant in repair brazing. For joints approaching 0.762 mm in width, wide gap brazing was recommended.

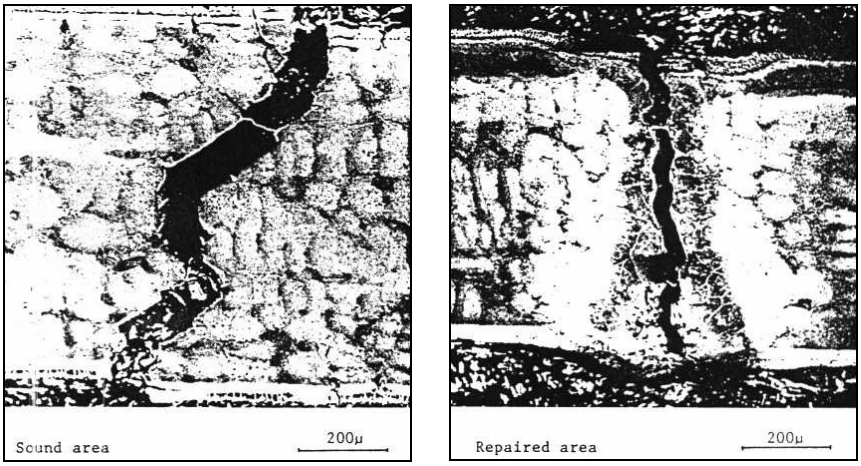

Figure 29 – Cracks in new and repaired vanes after engine testing [17].

It is important to note that when cracks form during engine operation, combustion products are often entrapped within the cracks. The crack surfaces also tend to be covered in Al and Ti oxides. These must be removed before cracks are repaired. As mentioned earlier, cleanliness is important in achieving high quality brazed joints. If the crack is dirty and filled with contaminants, capillary action will not draw the molten braze filler metal into the joint. In order to clean a crack prior to vacuum brazing, a process called FIC (fluoride ion cleaning) was developed to reduce the oxide layers in the crack and to remove dirt and other contaminants. The process is performed at elevated temperature and uses a mixture of HF and H_2 gas. Rose, Price and Thyssen [19], employed by Chromalloy, developed a braze repair process using FIC and a braze filler metal with a composition of Ni-12Cr-4.5Mo-6Al-4Ta-0.6Ti-0.1Zr-0.05C-2.5B. Without the boron alloying addition, the composition of the braze filler metal matches that of In713 nickel-base superalloy. This publication contained the first mention in open literature of a new braze filler metal composition developed by a repair company. The braze temperature and time were not documented and are considered proprietary. An interesting observation reported was that the joints contained a certain percentage of porosity, and that the authors relied on the use of a process referred to as HIP'ing to close the pores. HIP'ing is a process performed at elevated temperature under high isostatic pressure, applied using Ar gas, to plastically close the pores. This repair process using FIC, a proprietary braze filler metal and HIP'ing, was used to repair cracks in the saddle and blade areas of a Garrett GTCP 85 APU component that provides electrical power and compressed air for commercial aircraft such as Boeing 727 and 737 and McDonnell-Douglas DC-9 and MD-80. To qualify the braze repair, tensile tests and fatigue tests were performed at room temperature. After achieving acceptable mechanical test results, the authors performed thermal fatigue tests, and reported satisfactory results.

Lee, McMurray and Miller [20] patented a novel technique, referred to as M-Fill, to repair cracks in stationary components. This process does not rely on capillary action to draw the molten metal into the joint area. The crack is mechanically removed as per a welding process, then the surface of the routed out area is Ni-plated. A braze paste is placed in the groove and the component is processed in a vacuum furnace at 954^{o}C for 1 hour, followed by soaking at 1065^{o}C for 15 minutes and 982^{o}C for 3 hours to diffuse the B and Si into the parent metal.

The braze filler metal contained Ni, 8-10% Cr, 7-9% W, 2.5-4% Fe, 3-4.5% Si, 2-3% B and 0.06% C. Although boride and silicide phases formed, they were inconsequential because the cracks were in low stress areas and hence the braze repair was considered non-structural. The authors showed that the braze joint could be readily coated with an aluminide coating for corrosion and oxidation protection. The joint remained intact during engine testing. This repair is still applied in the TF40 and T55 Allied Signal engines used in helicopters.

1.5) Wide Gap Diffusion Brazing

As mentioned earlier, controlling the joint gap is very important in producing good quality, high-strength joints free of brittle eutectic and intermetallic phases. It is fairly easy to control joint gaps in manufacturing assemblies, but when it comes to repair, the size of the crack cannot be controlled. In the author's experience, cracks in aircraft turbine vanes range from 0.05 mm to 1 mm in width, whereas cracks in industrial turbine engines can range from 1 mm to 6 mm in width. To repair these types of defects, the wide gap diffusion brazing process was invented.

GE, an OEM, invented and patented a process called activated diffusion brazing (ADB). It is also referred to as activated diffusion bonding or activated diffusion healing (ADH). Hoppin and Berry [21] defined this process as a joining method for high strength nickel-base superalloys, involving a combination of the best current knowledge of conventional brazing and solid state diffusion bonding technology. The process combines the manufacturing ease of brazing with the high joint strengths achievable during solid state diffusion bonding. ADB involves vacuum furnace brazing with an ultra high-strength bonding alloy, nearly identical in chemical composition to the base metal being joined. Diffusion and aging heat treatments enable the joint to achieve maximum mechanical strength at the operating temperature of the engine component. The ultra high-strength bonding alloy is a mixture of braze powder and superalloy powder in a 60/40 ratio.

Figure 30 shows the tensile strength properties of 0.25 mm wide ADB joints in Rene 80 base metal at 650^{o}C and 870^{o}C, and indicates that the tensile properties of the joints are equivalent to those of the base metal. Results of creep rupture tests on Rene 80 brazed with AMS 4782 (Ni-19Cr-10Si), AMS 4786 (Au-22Ni-8Pd) and the ultra high-strength bonding alloy can be seen in **Figure 31**. Typical creep rupture strengths of 80 to 90% of the parent metal's creep rupture properties are attained, and the creep rupture properties of the ADB joints are two orders of magnitude greater than those achievable with conventional braze filler metals such as AMS 4782. Fatigue tests were performed at 760^{o}C for the ADB joints and the resultant high cycle fatigue curve is shown in **Figure 32**. The high cycle fatigue properties are approximately 70% of those of the Rene 80 base metal. The elevated temperature tensile, creep rupture and high cycle fatigue tests therefore demonstrated that ADB joint strengths of 70 to 90% of those of the base metal can be achieved, and the authors concluded that the ADB process is suitable for replacing fusion welding in the crack repair of aircraft gas turbine components (Rene 80 base metal displays a tendency towards cracking during fusion welding).

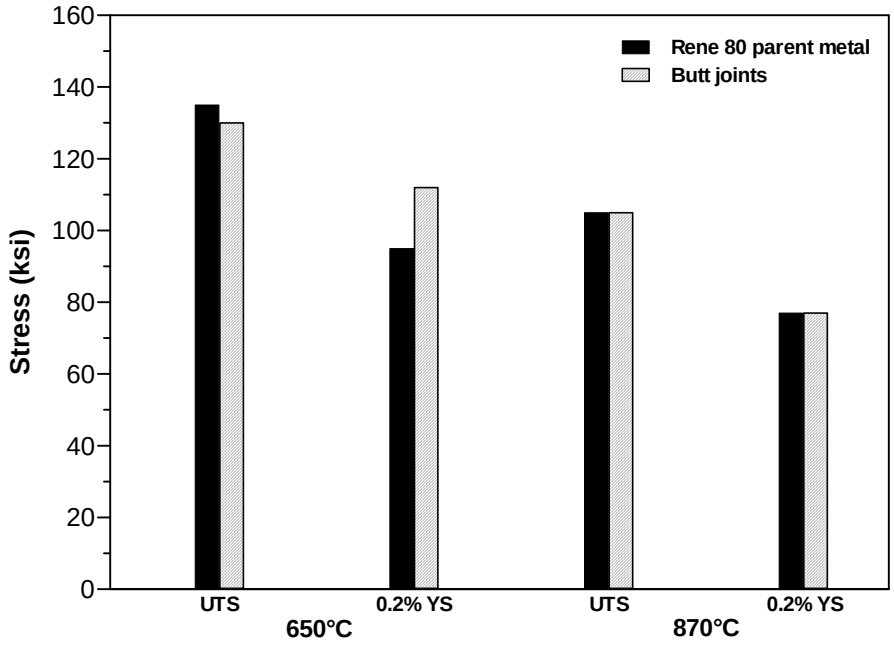

Figure 30 - Tensile properties (UTS: ultimate tensile strength, and 0.2% YS: 0.2% proof stress) of activated diffusion bonded butt joints in Rene 80, compared with those of the base metal [21].

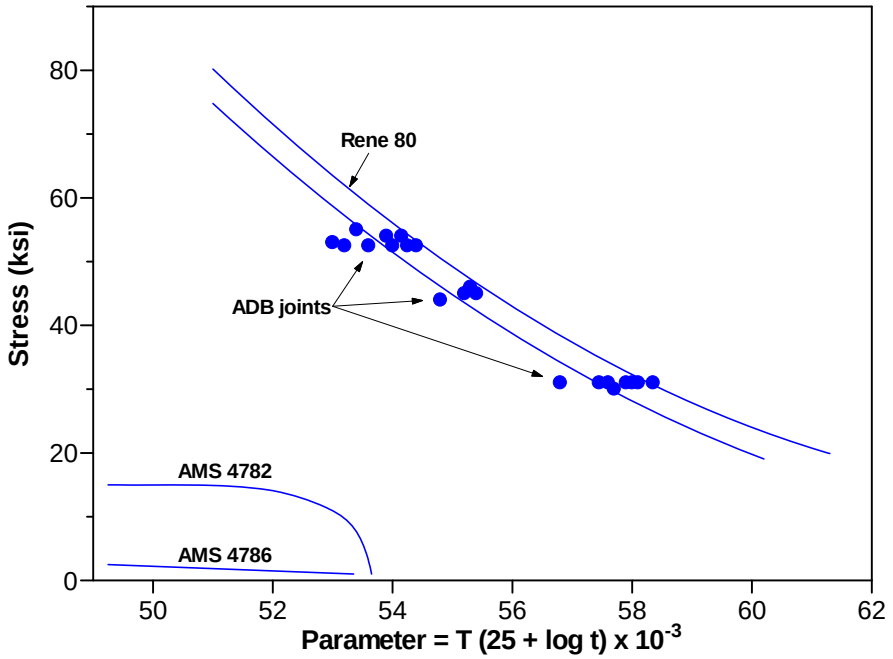

Figure 31 - Creep rupture properties of activated diffusion bonded joints in Rene 80, compared with those of the base metal and conventional brazed joints [21].

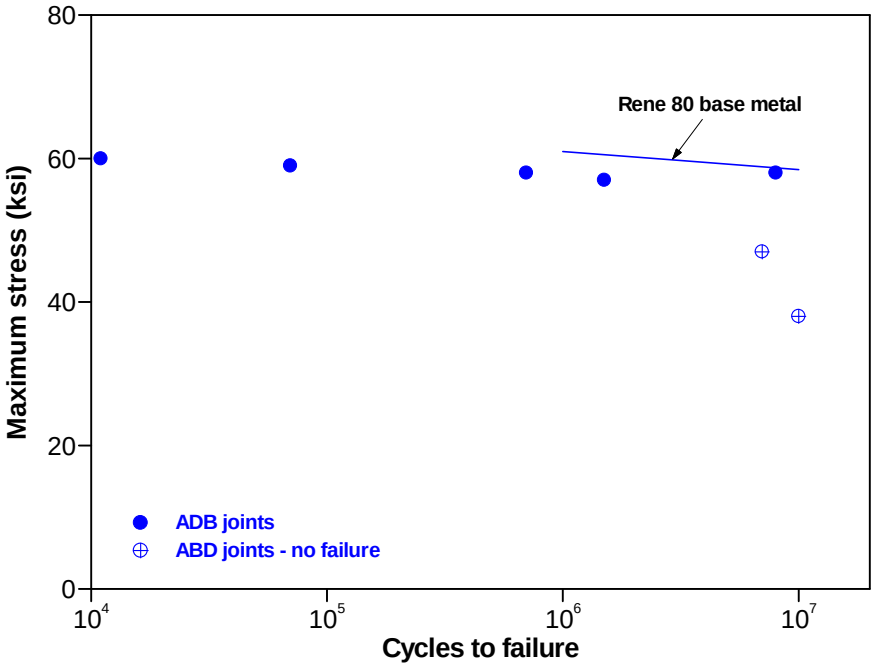

Figure 32 - High cycle fatigue strengths of activated diffusion bonded butt joints in Rene 80 at 760°C [21].

The ADB (or ADH) process was also described by Demo and Ferrigno [22]. As shown in **Figure 33**, the ADH process uses a mixture of superalloy powder and braze powder called a low-melting matrix. The superalloy powder in this low-melting matrix has the same composition as the substrate material. The low-melting braze powder used by Demo and Ferrigno consisted of the elements Ni-Cr-Co-Al-Ta-B, but the relative percentages of the elements were not documented. Brazing was performed at 1205°C for 30 minutes, followed by an undisclosed diffusion cycle and aging treatment. **Figure 34** shows the tensile properties measured at 870°C for various joint gaps ranging from 0.075 mm to 1 mm. The joint tensile strength was approximately 80% of the parent metal tensile strength, and the tensile strength did not appear to vary significantly over the range of joint gaps tested. The creep rupture properties, however, varied significantly with joint gap, as shown in **Figure 35**. Joints with gaps of 0.075 mm achieved approximately 90% of the creep rupture properties of the parent metal, whereas joint gaps of 0.5 mm and 1.0 mm resulted in only 60% and 50% of the parent metal creep rupture properties, respectively.

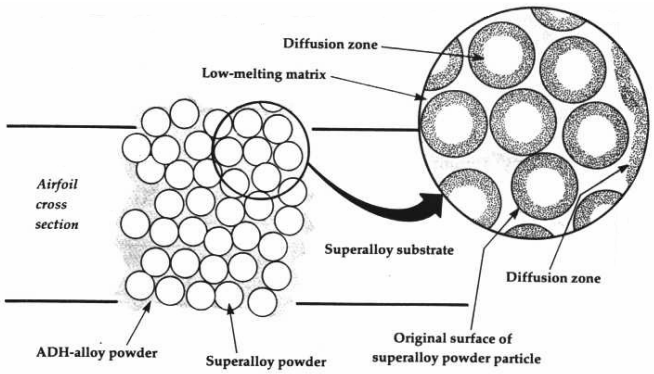

Figure 33 - In the ADH repair process, a superalloy is "cast" into the crack using a lower melting point bonding alloy [22].

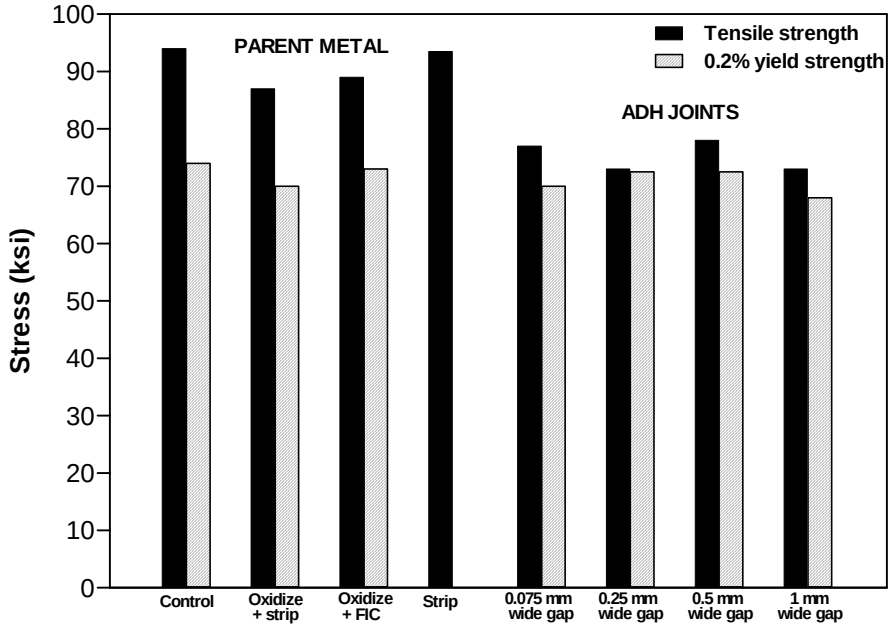

Figure 34 - Tensile strength data at 870°C (1600°F) for the parent metal and brazed joints in Rene 80 base metal. ('Oxidised' refers to a simulated engine run; 'Strip' refers to chemical stripping simulating the removal of the aluminide coating; and 'FIC' refers to fluoride ion cleaning) [22].

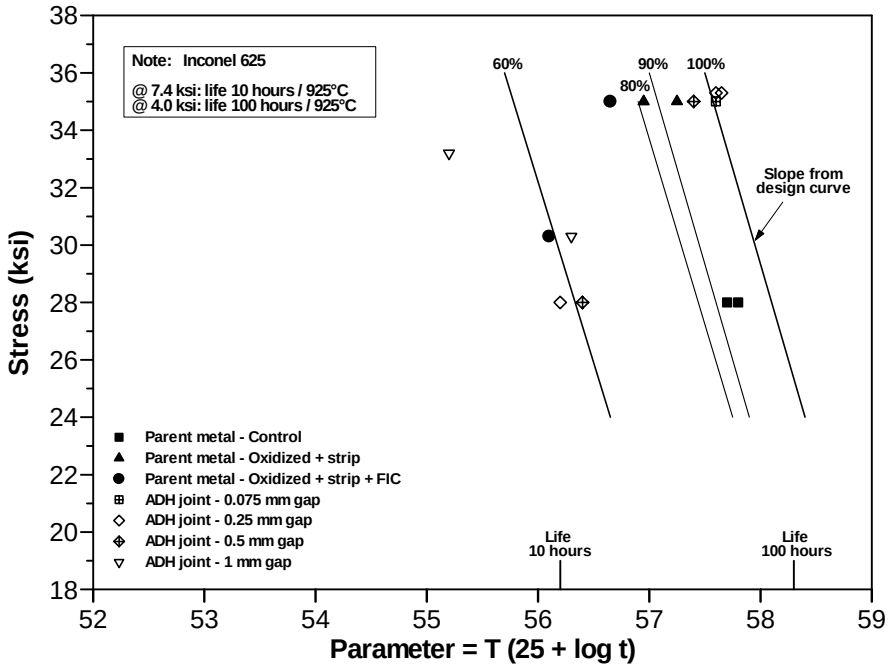

Figure 35 - Creep rupture curves for different width ADH joints in Rene 80 base metal [22].

Young [23] evaluated the ADH process by determining the nil strength temperature, defined as the temperature at which the bonded joint is incapable of sustaining a constant load of 0.86 MPa (125 psi), for two ADH alloys. An ADH joint consisting of 50% D-15 braze alloy and 50% X-40 cobalt-base superalloy powder attained a room temperature tensile strength of 82.4 ksi (569 MPa) and a nil strength temperature of 1260°C, whereas an ADH mixture consisting of 80% H-33 braze alloy and 20% X-40 cobalt-base superalloy powder had a room temperature tensile strength of 658 MPa (95.4 ksi) and a nil strength temperature of 1232°C. This compares well with the X-40 parent metal, which has a room temperature tensile strength

of 794 MPa (115 ksi) and a nil strength temperature of 1329°C. For ADH processing of nickel-base superalloys such as Rene 80, a 50% D-15 braze alloy and 50% Rene 80 powder mixture was evaluated. The braze cycle consisted of holding at 1204°C for 30 minutes, followed by a boron diffusion cycle at 1093°C for 2 hours, 1149°C for 2 hours, and 1190°C for 2 hours. The first aging cycle was performed at 1093°C for 4 hours, followed by a second aging cycle at 843°C for 24 hours. The 1 mm wide joints attained 80% of the Rene 80 parent metal tensile strength measured at 870°C. Creep rupture testing at 925°C demonstrated a 10% reduction in rupture life for a joint gap of 0.025 mm, a 20% reduction in rupture life for a 0.075 mm gap, and a 30% reduction in rupture life for a 0.25 mm gap. A 1 mm gap resulted in a 40% reduction in creep rupture life. It is evident that a wider joint gap results in a reduction in mechanical properties. Despite this, the ADH process has been used successfully for the past two decades to repair cracks in aircraft turbine blades, and the FAA (Federal Aviation Authority) has never reported an engine failure as a result of an inappropriate ADH braze application. This shows that, although the mechanical properties are not equivalent to the base metal properties, ADH braze joints can perform reliably in an engine. For this reason, the process has replaced conventional gas tungsten arc welding (GTAW) with In625 filler metal in this application.

Knotek and Lugscheider [24] mixed stainless steel powder and Ni-base braze filler metal of composition Ni-10Cr-4.2Si-6.3Fe-3B in three different ratios: 45:55, 50:50 and 55:45, and performed brazing at a temperature of 1000°C with a joint gap of 0.1 mm. The results of tensile tests carried out at 20°C, 800°C, 1000°C and 1200°C are shown in **Figure 36**. The last two test temperatures are higher than the solidus temperature of the braze alloy in the mixture. As shown in **Figure 36**, all three mixtures had similar tensile strengths at elevated temperature. At room temperature the tensile strengths ranged from 480 MPa to 540 MPa, and at 1000°C the tensile strengths were in the region of 70 MPa. These tensile strengths are higher than those of the popular Ni-Cr-B-Si braze filler metals such as AMS 4777 and AMS 4776. No significant change in the tensile strength values at 1000°C was observed after a 1 hour diffusion heat treatment, as shown in **Table 2**.

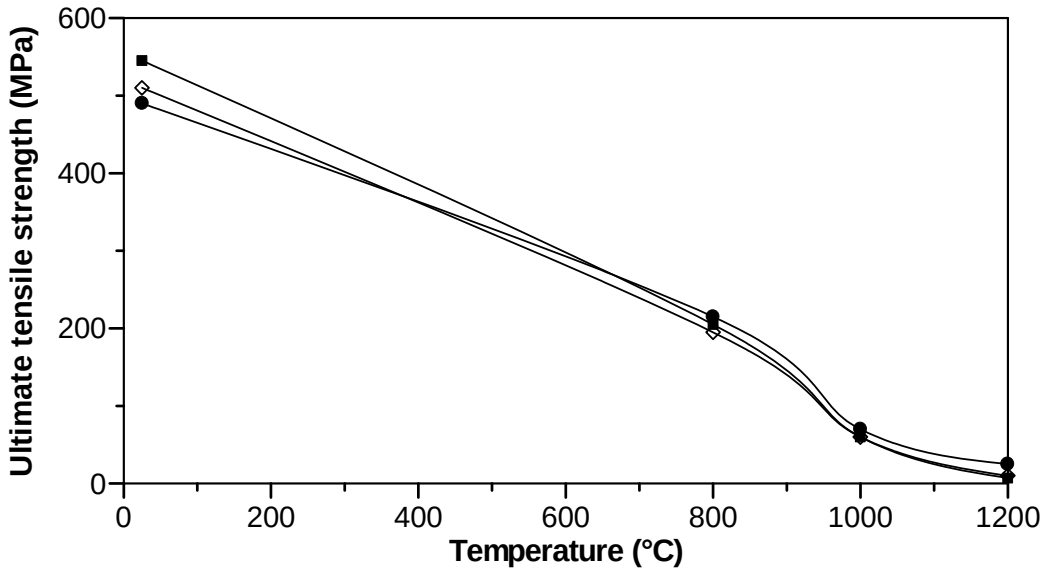

Figure 36 - Tensile strength at elevated temperature for various ratios of superalloy powder to braze powder [24].

Table 2 – Influence of heat treatment on the tensile strength (1000°C) of reacting brazed joints [24].

Component (wt.%)		Composition after reaction (wt.%, balance Ni)				Tensile strength at 1000°C			
						As-brazed		Brazed + 1 hr @ 800°C	
A	B	Cr	B	Si	Fe	MPa	ksi	MPa	ksi
55	45	8.25	1.65	2.30	2.00	74.6	10.8	66.7	9.7
50	50	7.50	1.50	2.10	1.85	68.7	10.0	68.6	10.0
45	55	6.75	1.35	1.90	1.70	64.8	9.4	67.6	9.8

Van Esch [25] from Elbar, a repair vendor in Holland, developed a proprietary wide gap braze process to repair blades from the Industrial Gas Turbine engine referred to as GE Frame 5. The compositions of the two alloys used, the mix ratio and the braze temperature and time were not documented. Since the wide gap braze process was used to repair blades, not vanes, the butt joints were not tested. Instead, samples with gauge diameters consisting of 20% braze build-up and 80% parent metal were tested. Creep rupture tests were performed using In738 nickel-base superalloy parent material. **Figure 37** shows the creep rupture properties of the joints. The joints displayed creep rupture lives ranging from 62% to 100% of that of the In738 alloy. Because of the comparatively low amount of boron in the wide gap braze joint, the borides could be rounded and distributed more evenly by an annealing heat treatment, as seen in **Figures 38 and 39**. This improved the joint ductility.

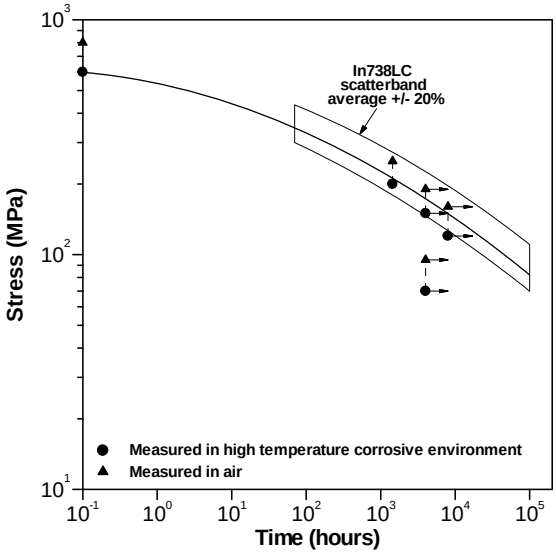

Figure 37 - Creep rupture tests performed at 850°C (base material is In738 and the wide gap braze is a proprietary material referred to as Elniment 100) [25].

Su, Chou, Wu and Lih [26] evaluated the phases that formed in ADB joints in In738 base metal. Three braze alloys, namely Nicrobraz 150, BRB and DF4B, were evaluated. The chemical compositions of these alloys are given in **Table 3**.

Table 3 - Nominal compositions of powders and base metal (wt.%, balance Ni).

Alloy	Cr	Co	Al	Ti	W	Mo	Ta	Nb	B	C	Zr	Y
In738	16.0	8.4	3.4	3.4	2.7	1.7	1.7	0.8	0.01	0.1	0.03	-
Nicrobraz 150	15.0	-	-	-	-	-	-	-	3.50	0.1	-	-
BRB	13.5	9.5	4.0	-	-	-	-	-	2.50	N/A	-	-
DF4B	14.0	10.0	3.5	-	-	-	2.5	-	2.70	N/A	-	0.02

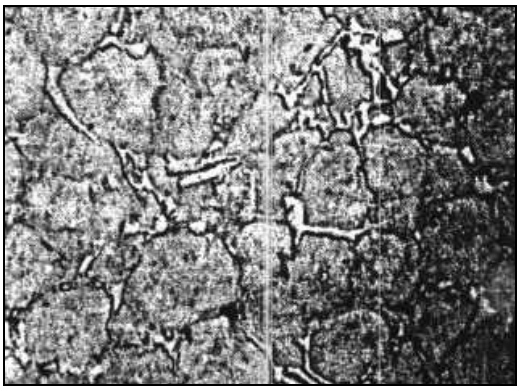

Figure 38 - Elniment 10 wide gap braze, as-brazed without subsequent heat treatment. The borides have an oblong shape [25].

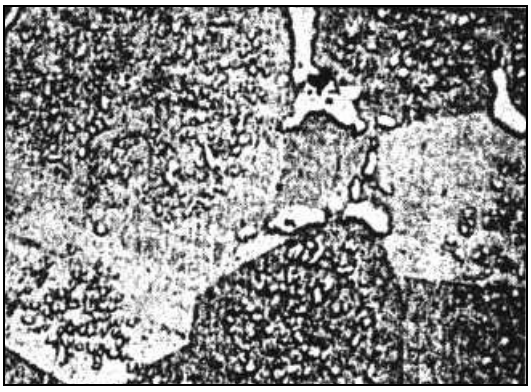

Figure 39 - Elniment 10 wide gap braze, as-brazed with annealing heat treatment. The borides appear more rounded [25].

Brazing mixtures, consisting of brazing alloy and In738 superalloy powder, were prepared in weight percentage ratios of 30:70, 40:60 and 50:50. Microstructural observations were made using optical microscopy, scanning electron microscopy (SEM) and electron probe x-ray microanalysis (EPMA). The percentage porosity detected in the ADB joints is shown in **Figure 40** as a function of the filler metal ratio for the BRB and DF4B braze alloys. It is evident that joints containing 30% BRB or 30% DF4B mixed with In738 powder exhibited very high porosity levels after brazing at temperatures of 1180^{o}C and 1190^{o}C. Powder mixes containing 40% or 50% DF4B brazing alloy exhibited no porosity. The interstitial voids were small and randomly distributed in the 40% and 50% joints containing BRB as braze alloy.

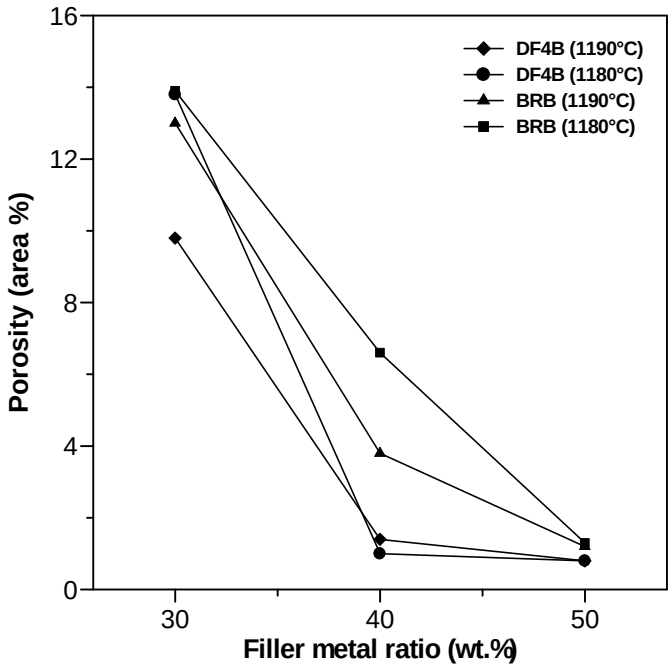

Figure 40 - Percentage porosity as a function of braze alloy content [26].

Figure 41(a) shows the microstructure of a 40% Nicrobraz 150 specimen after ADB processing. No pores are evident. The microstructure at high magnification is shown in **Figure 41(b)**. The matrix and secondary (blocky) phases are more evident, and island-like blocky boride phases are present in the In738 powder particles. **Table 4** shows the chemical

compositions of the two phases observed. Quantitatively, the blocky phase has a higher concentration of light elements (boron and carbon) than the matrix. The results of the quantitative analysis indicate that the blocky phase is Cr(B,C) with low levels of Co, Al, Ni, Ta and Ti in solution, while comparatively rich in Mo and W. The matrix of the Nicrobraz 150 braze alloy is predominantly Ni_3B with reduced amounts of B and C, but with high concentrations of Co, Ti and Ta. Cr boride is thermodynamically stable at all the temperatures evaluated, and its chemistry does not change once it has nucleated. The compound present probably has the stoichiometry CrB. **Figure 41(b**) also shows a Ni-Ni_3B eutectic precipitated in the braze alloy matrix (designated 'N'). This phase contains higher amounts of Co and Ti, derived from the superalloy powder by diffusion. The chain-like structure of the CrB, Ni_3B and Ni-Ni_3B eutectic reduces the ductility and the strength of the joint.

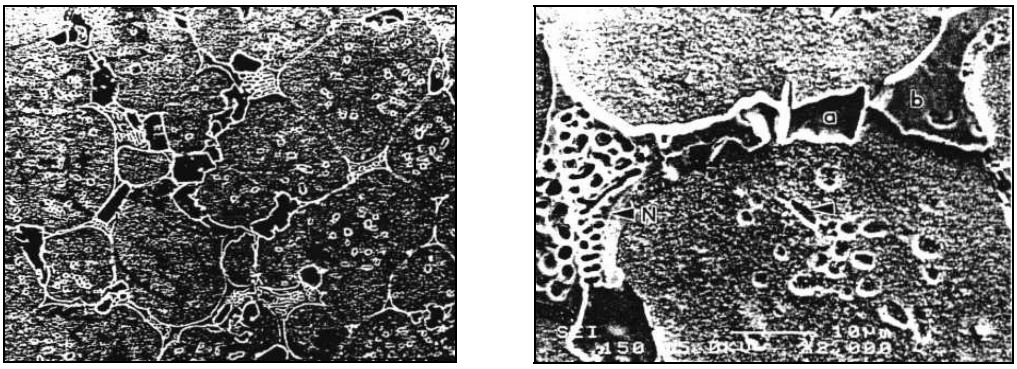

(a) (b)

Figure 41 – SEM micrographs of a brazed joint produced from a mixture containing 40 wt.% Nicrobraz 150: (a) blocky boride phase (magnification: approximately 270X), and (b) Ni-Ni_3B eutectic (N). The arrow highlights the blocky boride phase precipitated within the metal powder particles (magnification: approximately 1800X) [26].

Table 4 – Chemical compositions of phases in specimens containing 40 wt.% Nicrobraz 150 braze filler metal [26].

Element	Matrix		Blocky phase	
	wt.%	at.%	wt.%	at.%
Ni	76.248	67.473	4.753	2.957
Cr	4.789	4.783	68.858	48.349
Co	5.833	5.140	1.917	1.188
Al	0.594	1.144	0.006	0.008
Ti	5.117	5.548	0.257	0.196
Ta	2.276	0.654	0	0
Mo	0.248	0.134	5.978	2.275
Nb	1.394	0.779	0.038	0.015
W	0.366	0.103	4.467	0.887
B	1.447	6.946	7.135	24.083
C	1.687	7.295	6.591	20.041

Figure 42(a) shows the microstructure of a joint containing 40% DF4B and 60% In738 processed at 1190°C. The initial spherical shape of the superalloy powder has disappeared and the blocky phase is still present. However, the matrix is not clearly identifiable, in contrast to **Figure 41(a**). As seen in **Figure 42(b),** the blocky boride phase is present within the superalloy powder particles. Darker matrix phases are also present alongside the blocky phase. The results of compositional analyses are shown in **Table 5**. The blocky boride phase

contains higher concentrations of Mo and W, compared to the Nicrobraz 150 joints. The composition of the irregular lathy dark-etching phase alongside the blocky boride phase revealed it to be γ' phase, containing Al and Ti, which had diffused from the superalloy powder. The results shown in **Figure 42** and **Table 5** indicate that within the superalloy powder particles, the gamma prime (γ') phase had coarsened to form a lathy structure in the boron diffusion direction. Within the DF4B powder, a dark matrix structure and blocky boride phase formed.

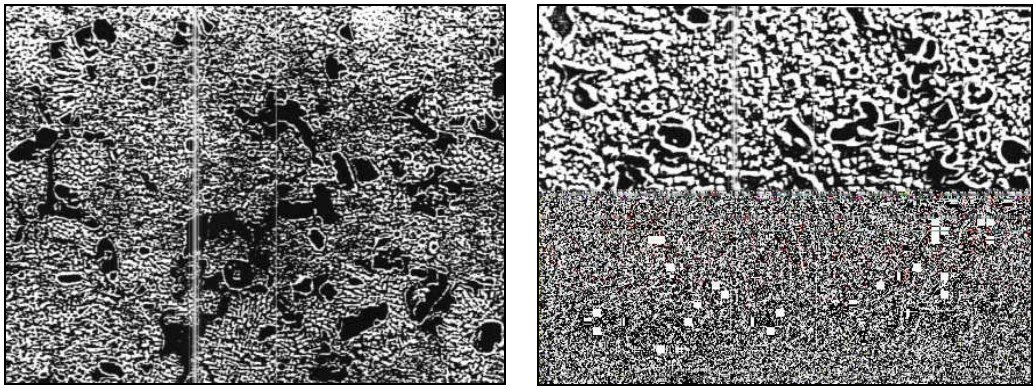

(a) (b)

Figure 42 – SEM micrographs of a brazed joint produced from a mixture containing 40 wt.% DF4B: (a) blocky boride phase (magnification: approximately 350X), and (b) darker γ' phase. The arrow highlights the blocky boride phase precipitated within the metal powder particles (magnification: approximately 1750X) [26].

Table 5 – Chemical compositions of phases in specimens containing 40 wt.% DF4B braze filler metal [26].

Element	Matrix		Blocky phase	
	wt.%	at.%	wt.%	at.%
Ni	73.337	67.269	4.673	3.373
Cr	3.474	3.596	70.230	57.209
Co	6.064	5.539	3.725	2.678
Al	6.844	13.656	0.018	0.028
Ti	4.548	5.111	0.528	0.467
Ta	3.899	1.160	0.684	0.160
Mo	0.256	0.144	5.816	2.568
Nb	0.545	0.316	0.108	0.049
W	0.339	0.099	5.777	1.331
B	0.008	0.040	6.081	23.811
C	0.685	3.070	2.360	8.325

Figure 43 shows the microstructure of a joint consisting of 40% BRB filler metal and 60% In738 powder processed at 1190°C. The blocky boride phase and the darker lathy phase are similar to those observed within the DF4B joint. The compositions of the darker phase and the blocky phase can be found in **Table 6**.

Subsequent tensile investigations of these ADB butt joints showed that the ultimate tensile strength (UTS) of the DF4B/In738 joints attained 85% of the room temperature UTS of the In738 base metal, and 100% of the UTS of the In738 base metal at 980°C. For the Nicrobraz 150/In738 joints, the UTS was 40% of the room temperature UTS of the In738 base metal. The reduction in mechanical strength was attributed to the presence of the Ni-Ni_3B eutectic phase within the joint. This eutectic not observed in the DF4B/In738 or BRB/In738 joints.

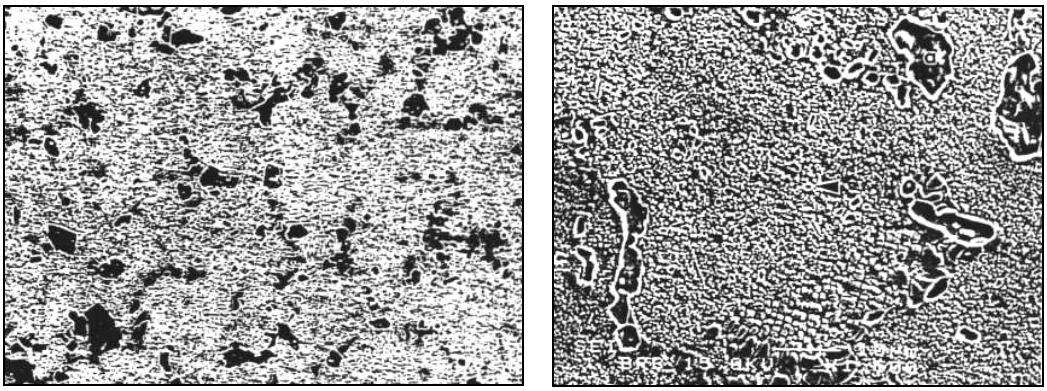

(a) (b)

Figure 43 – SEM micrographs of a brazed joint produced from a mixture containing 40 wt.% BRB: (a) blocky boride phase (magnification: approximately 225X), and (b) darker γ' phase. The arrow highlights the blocky boride phase precipitated within the metal powder particles (magnification: approximately 1325X) [26].

Table 6 – Chemical compositions of phases in specimens containing 40 wt.% BRB braze filler metal [26].

Element	Matrix		Blocky phase	
	wt.%	at.%	wt.%	at.%
Ni	6.724	5.500	73.889	68.778
Cr	67.700	62.494	4.724	4.962
Co	3.028	2.467	6.183	5.731
Al	0.185	0.329	6.511	13.184
Ti	0.445	0.446	4.352	4.964
Ta	0.113	0.030	2.372	0.716
Mo	6.373	3.189	0.308	0.175
Nb	0.073	0.338	0.825	0.485
W	9.893	2.583	0.657	0.195
B	3.099	13.751	0	0
C	2.283	9.126	0.178	0.810

1.6) Sintering of Ni-base superalloys using braze filler metals

As illustrated in §1.5, mixing of braze filler metal powder and base metal powder does not result in adequate joint strength when the joint gap approaches 1 mm in width. The results considered above also indicate a significant loss in creep rupture life when the ADB process is used for joints gaps approaching 1 mm in width. In an aircraft engine, stationary components such as vanes seldom contain cracks approaching 1 mm in width, and the ADB process has therefore been used successfully during the last two decades to repair aircraft engine components. There are many profitable companies throughout the world which offer a service repairing aircraft engine components. South African Airways spent $50 million dollars per annum in the 1990's on the repair of aircraft engine components at repair companies located in Europe and the USA.

With the tremendous growth in global energy consumption, however, the repair of land-based power generation gas turbines has become a lucrative business. A typical land-based turbine blade is ten times the length of an aircraft turbine blade and a land-based vane weighs more than 20 kg as opposed to an aircraft vane that weighs approximately 5 kg. Thermal fatigue

cracks in land-based turbine vanes can be up to 20 cm long, 5 mm wide and 6 mm deep. The ADB process and conventional narrow gap brazing processes cannot be used to repair these large defects successfully. An incentive therefore exists for the development of new joining technologies suitable for repairing wide cracks in land-based turbine components.

In 1979, Chasteen and Metzger [27] developed a sintering process during which a large gap is filled with a metal powder. The powder is then sintered in the gap. Simply stated, sintering is a process involving the compacting and agglomeration of loose powder particles, usually at elevated temperature. The authors sintered gaps varying from 0.025 mm to 2 mm in width in Hastelloy X base metal using four different powders: Hastelloy C (fine and coarse particle size), Rene 80 and a 79%Ni-20%Cr-1%Si powder. The compositions of the powders are given in **Table 7**.

Table 7 – Chemical compositions of the base metal and sinter powders (S1-S4) used in the Chasteen and Metzger investigation [27].

Alloy	Common designation	Nominal chemical composition (wt.%, balance Ni)									Melting temperature (°F)		Mesh size
		Cr	Fe	Co	Mo	W	Si	B	Al	Ti	Solidus	Liquidus	
Base metal	Hastelloy X	22	18	2	9	1	-	-	-	-	2350	2470	-
Sinter filler													
S1	-	20	-	-	-	-	1	-	-	-	2500	2575	-325
S2	Hastelloy C	16	6	2	16	4	-	-	-	-	2320	2380	-150/+325
S3	Hastelloy C	16	6	2	16	4	-	-	-	-	2320	2380	-325
S4	Rene 80	14	-	10	4	4	-	-	3	5	-	-	-100
Braze filler													
B1	-	7	3	-	-	6	4.5	3	-	-	1790	1900	-

The powders were sintered at a temperature of 1129°C for 30 minutes. After sintering, the joints displayed an average of 33% porosity by volume. By adding a braze filler metal, referred to as B1 (see **Table 7**), the porosity could be minimized. The sintering and subsequent brazing process resulted in the joint microstructure shown in **Figure 44**. A few voids are evident in the micrograph and this is believed to be due to the low temperature used during the brazing cycle (1129°C for 2 hours).

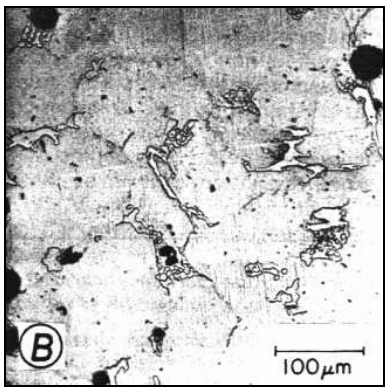

Figure 44 - Braze joint of 1.25 mm clearance using sinter filler metal S1 and braze filler metal B1 (as shown in Table 7) [28].

Figure 45 shows the tensile strength variation as a function of temperature for 0.5 mm joints with sinter powder, joints with no sinter powder, and the base metal. The joints with sinter

powder displayed tensile strengths corresponding to approximately 70% of the base metal strength at temperatures below 650°C, but more than 90% of the base metal strength at temperatures greater than 760°C. The brazed joints without sinter powder displayed very low tensile strength values (about 20% of the base metal tensile strength).

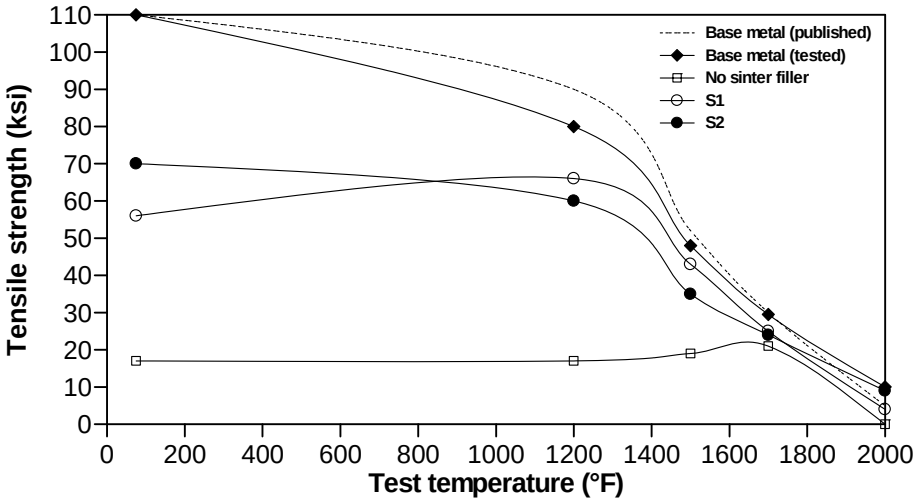

Figure 45 - Tensile strength as a function of temperature for the base metal, and for sintered and brazed joints with 0.5 mm clearance [27].

Figure 46 shows the variation in tensile strength with joint clearance. The results indicate that at low joint clearances, joints brazed without sinter powder had joints strengths comparable with those of joints containing sinter powder and braze powder. At joint clearances greater than 0.15 mm, the joint strength (with no sinter powder) decreased rapidly. Joints containing S2 powder displayed higher strength values at all joint clearances tested than joints with S1 sinter powder. The strength of joints brazed with S1 sinter powder remained fairly constant at about 60 ksi (414 MPa) (54% of the base metal strength), while the curve for the S2 joints displayed a slight decrease in strength with increasing clearance.

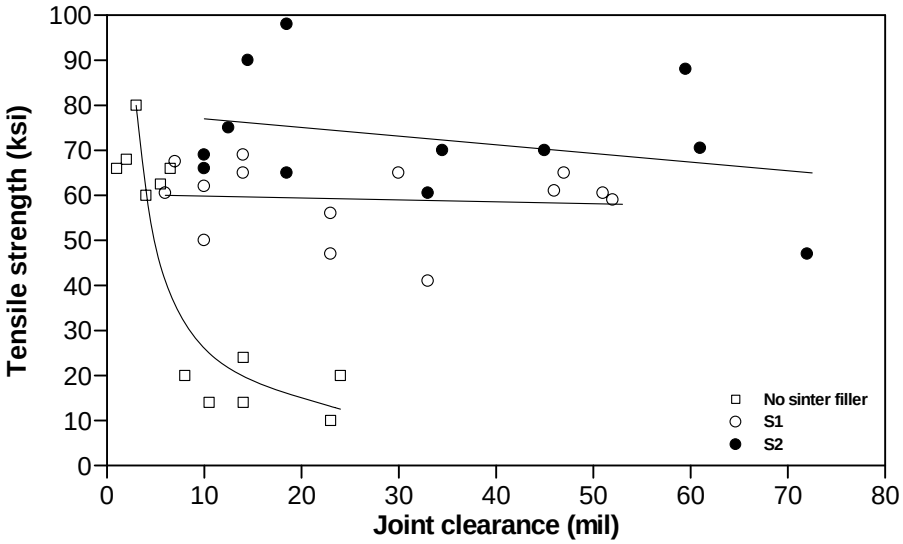

Figure 46 – Room temperature tensile strength as a function of joint clearance for sintered and brazed joints and for the joints containing no sinter powder [27].

The method developed by Chasteen and Metzger for filling wide gaps therefore consists of two steps. The first step involves sintering a nickel-base alloy of high melting point (called the sinter filler metal) in powder form in the joint. Light sintering results in a porous, but not friable, metallic mass in the joint. The second step involves filling the powder interstices by brazing with a nickel-base filler metal (called the braze filler metal) to complete the joint. The results of this investigation encouraged researchers to optimize the process for use in repairing wide cracks in gas turbine components.

In 1992, Liburdi *et al* [28] patented a similar two step process. The first step involved sintering in the solid state at elevated temperatures and for extended times (e.g. 1200^{o}C for 4 hours), resulting in a dense structure. The braze filler metal was therefore only required to close a small number of pores, leading to superior mechanical properties (as shown in **Figure 47**). On average, the creep rupture properties were at least 75% of the base metal properties for a 1.5 mm wide gap (such as those typically found in gas turbine components). Whereas Chasteen and Metzger used conventional, commercially available braze filler metals, Liburdi *et al* used braze filler metal especially designed to match the composition of the base metal being repaired, except for the addition of both B and Si as melt point depressants.

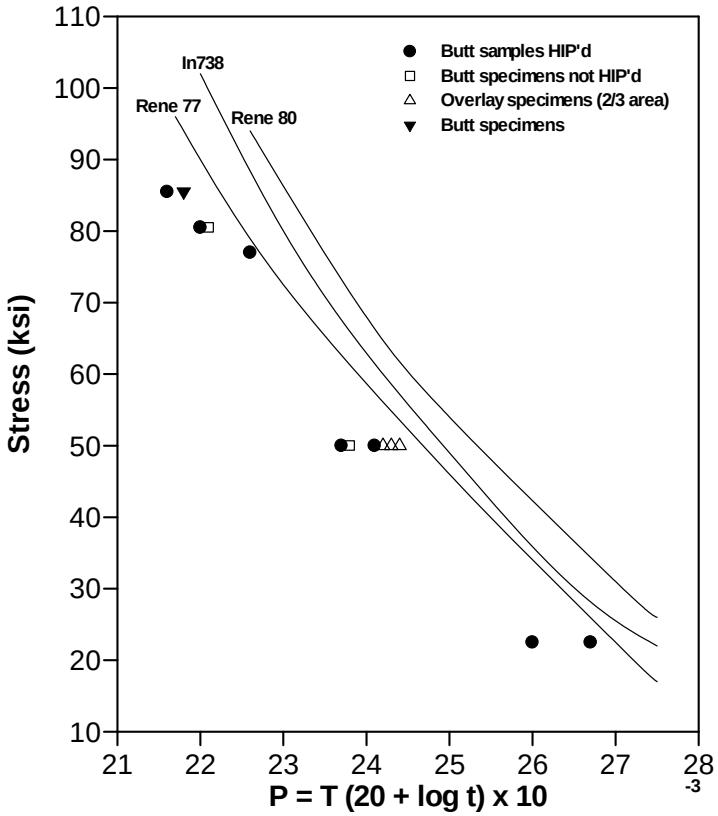

Figure 47 - Larson Miller plot for wide gap joints produced by the Liburdi solid state sintering process [28].

In 1983, Jahnke and Demny [29] developed a process referred to as liquid phase diffusion sintering. They claimed it had potential for closing wide gaps, and for developing improved mechanical strength compared to conventional wide gap brazed joints, such as those produced through the ADH process. The joints produced with this method generally have high thermal fatigue resistance and good hot corrosion properties. The steps involved in this process are listed below, and schematically illustrated in **Figure 48**.

1) Melting of the filler metal on heating above the solidus temperature.
2) Rearrangement of solid grains by sliding on the liquid films separating them.
3) Densification.
4) Melting of the parent metal (powder particles) and dilution until the concentration of the liquid reaches C_L (see **Figure 48**).
5) Diffusion of the melt point depressants (boron and silicon) into the solid, resulting in isothermal solidification.
6) Recession of the solid-liquid interface and a reduction in the liquid zone until the solubility limit in the base metal powder particles is reached.

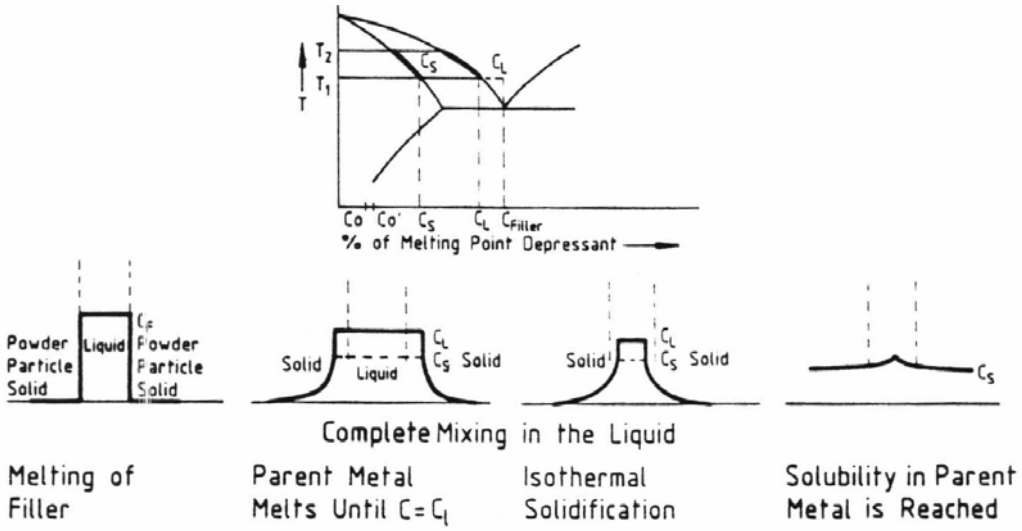

Figure 48 - Liquid phase diffusion sintering: general description of diffusion solidification [29].

In a subsequent development, Miglietti (US patent number US6520401(B1)) developed a liquid phase diffusion bonding process, described in more detail in four technical papers [30-33] supplied in Appendices A to D. During this bonding process, a crack is filled with MarM247 nickel-base superalloy powder. This powder has a solidus temperature in excess of 1315°C, well above the recommended brazing temperature range. The MarM247 powder is then covered with a Ni-base superalloy braze powder or paste. The braze powder or paste is doped with either B, Zr or Hf, or a mixture of all three elements, to lower its melting point. Adding Zr or Hf as melt point depressant to braze filler metals for joining Ni-base superalloys is novel and the results are considered in more detail in subsequent chapters. The braze filler metal is then heated to the brazing temperature of between 1220°C to 1280°C. The braze powder melts to form a liquid, which is carried into the spaces between the MarM247 powder particles to form a solid diffusion bond that joins the powder particles. Thermal processing consists of heating to a brazing temperature between 1220°C to 1280°C and holding at this temperature for a maximum of 30 to 45 minutes. The temperature is then lowered to approximately 1200°C to diffuse the melt point depressants into the parent metal.

The remaining chapters of this document describe the results of a series of experiments aimed at evaluating the potential of novel Ni-Hf and Ni-Zr braze filler metals for joining Ni-base superalloys using the liquid phase diffusion bonding process.

CHAPTER 2 - OBJECTIVES

LIQUID PHASE DIFFUSION BONDING OF NICKEL-BASE SUPERALLOY COMPONENTS USING NOVEL BRAZE FILLER METALS

2.1) Background

Turbine vanes or nozzles operating in power generation engines often develop wide cracks during service. When the engine is overhauled, or when cracks propagate to a specific length during service, a decision has to be made whether new replacement parts should be purchased, or whether the damaged components should be repaired at a fraction of the cost of a new part. On the basis of economic considerations, the majority of users opt for repair.

Many γ'-strengthened nickel-base superalloys are difficult to weld successfully and brazing techniques have gained prominence in the turbine repair industry in the last decades. Since conventional brazing techniques rely on capillary action to draw the molten braze filler metal into the joint gap, these processes are only suitable for repairing narrow cracks (less than 0.25 mm in width). In order to overcome this limitation, wide gap brazing techniques have been developed for repairing cracks up to 1 mm in width. At present these techniques are widely used in applications involving the repair of turbine components for aircraft engines, where wide cracks (more than 1 mm in width) are seldom encountered.

Conventional wide gap brazing techniques, however, find limited application in the repair of land-based turbine components, such as those found in power generation engines, where cracks widths often exceed 1 mm. When wide gap brazing techniques are applied to repair cracks wider than 1 mm, the repaired areas normally achieve only 60 to 70% of the mechanical properties of the base metal, and display a tendency for premature degradation and cracking in service. A need has therefore been identified for a reliable technique suitable for repairing the wide cracks often observed in land-based turbine engine components.

In the past most repair vendors operated independently from the original engine manufacturers (OEM's). As a result of the lucrative nature of the repair market, all the OEM's (including General Electric, Pratt & Whitney (P&W), Siemens and Alstom) have since opened their own repair shops or acquired some of the independent repair vendors. For the end user the most important deciding factor when choosing a repair vendor is often not the cost involved, but the technology utilized during the repair. In order to remain competitive in the repair business, repair vendors therefore have to develop, implement and market new repair techniques for refurbishing degraded turbine components on an ongoing basis.

2.2) Objectives of this investigation

The majority of commercially available Ni-base braze filler metals contain B and/or Si as melt point depressants, and display a tendency for forming brittle intermetallic phases (such as borides and silicides) within the braze joint when used to repair wide gaps. The objective of this investigation was to capitalize on the need for a reliable repair technique for wide cracks in land-based turbine components by developing novel braze filler metals which ensure high strength joints with good ductility when used in conjunction with the liquid sintering process to repair wide cracks. The investigation was designed to:

- evaluate the use of two novel melt point depressants, namely Hf and Zr, in Ni- and Co-base braze filler metals, and
- optimize the liquid phase diffusion bonding process in combination with these novel braze filler metals with the aim of producing high strength joints with good ductility and mechanical properties at elevated temperature approaching those of the base metal.

The results of this investigation are considered in more detail in the remainder of this document.

CHAPTER 3 - EXPERIMENT 1

MICROSTRUCTURAL EXAMINATION OF NOVEL BINARY EUTECTIC Ni-Hf AND Ni-Zr BRAZE ALLOYS

This chapter describes the results of a series of preliminary experiments aimed at determining whether hafnium and zirconium can be used as melt point depressants in novel Ni-base braze filler metals.

3.1) Introduction

Examination of binary phase diagrams with nickel as solvent revealed that hafnium and zirconium may be suitable for use as melt point depressants in novel braze filler metals for repairing Ni-base superalloys. Nash and Nash, as quoted in ASM Handbook [2], reported the existence of an invariant eutectic reaction in the Ni-Hf binary system at a composition of 30.5 wt.% Hf and 69.5 wt.% Ni (see **Figure 49**). The eutectic temperature was quoted as 1190°C. According to Nash and Jayanth, also quoted in ASM Handbook [2], the Ni-Zr binary system contains a eutectic point located at 13 wt.% Zr and 87 wt.% Ni (see **Figure 50**). The eutectic temperature was quoted as 1170°C. In order to determine whether Hf and Zr can be used as melt point depressants in Ni-base braze filler metals, nickel powder was mixed with hafnium powder or zirconium powder to make up the simple binary eutectic compositions obtained from the phase diagrams.

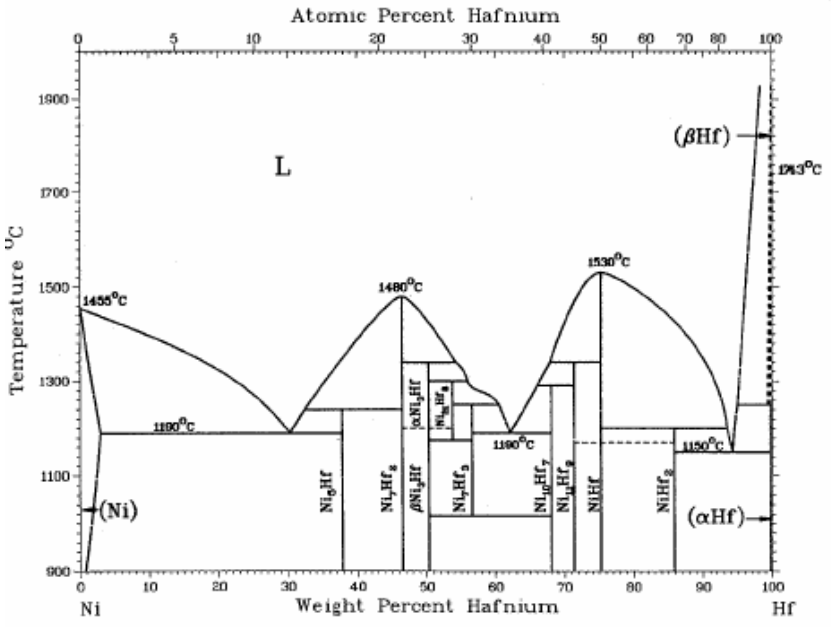

Figure 49 – Binary Ni-Hf phase diagram [2].

The objectives of Experiment 1 were therefore:

- to verify that eutectic Ni-Hf and Ni-Zr braze alloys melt and flow in the same way as the braze alloys currently used in the aerospace and land-based gas turbine repair industries,
- to determine the optimum braze temperatures for both alloys, and
- to examine the microstructures of the braze joints after relatively short brazing times (40 minutes), and to compare the joint microstructures with those obtained after extended times (18 hours) at the braze temperature.

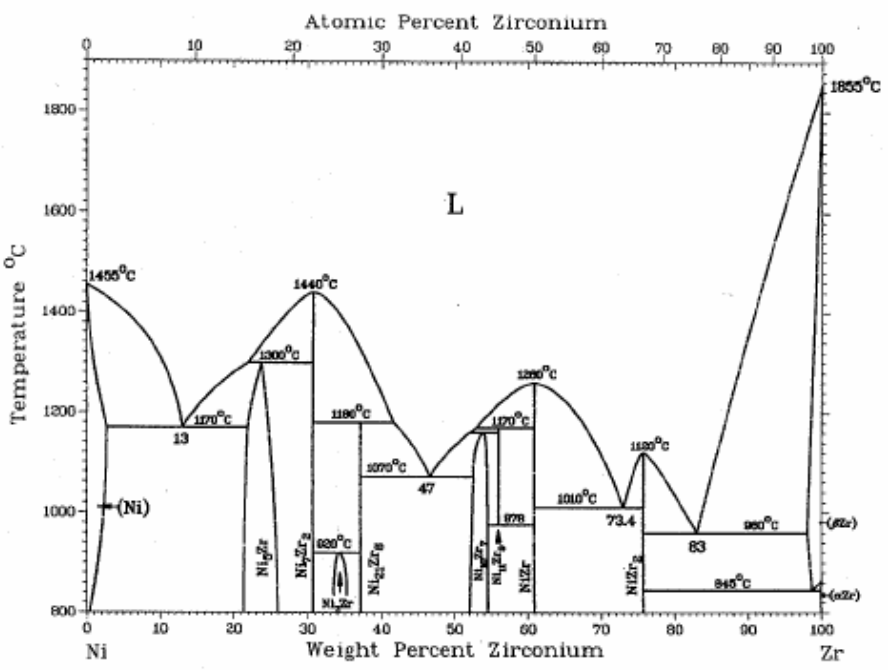

Figure 50 – Binary Ni-Zr phase diagram [2].

3.2) Experimental procedure

Inconel 738 (abbreviated as In738 throughout the remainder of this document), with the nominal chemical composition shown in Table 8, was used as parent metal during the course of this investigation. Flat plate was obtained by sectioning slabs of material from the root of scrap blades using Electric Discharge Machining (EDM). The root of a turbine blade is not exposed to appreciable temperatures or stresses in service, and material removed from this area is often viewed as virgin-like as-cast material. The In738 material was prepared for brazing by grinding to a thickness of 2 mm. The plates were mechanically cleaned by grit blasting with 220 grit silicon carbide media, and then wiped with acetone to remove any surface residue from the grit blasting process.

Table 8 – Nominal chemical composition of the In738 parent metal used during the course of this investigation (wt.%, balance nickel).

B	C	Co	Cr	Mo	Al	W	Ta	Nb	Ti	Zr
0.001	0.17	8.5	16	1.7	3.4	2.6	1.7	2.0	3.4	0.1

The novel Ni-Hf braze filler metal was prepared by mixing 69.5 wt.% Ni and 30.5 wt.% Hf (the eutectic composition) in powder form. The powder mixture was then mixed with a binder to form a braze paste. The Ni-Zr braze paste was produced in a similar way by mixing 87 wt.% Ni powder and 13 wt.% Zr powder with a binder. Following evaporation of the acetone from the In738 plates, a layer of Ni-Hf or Ni-Zr braze paste was applied over the In738 plate or between two In738 plates (like a filling in a sandwich). The samples were dried for an hour before being placed in a laboratory vacuum furnace with a maximum temperature capability of 1260°C. It should be noted that the vacuum furnace used in this investigation did not have any quench facilities. The samples were therefore slow cooled to room temperature in the furnace.

The vacuum braze cycle used for both braze alloys was as follows:

1) Ramp up to a temperature of 450°C at a minimum rate of 9°C/minute.
2) Hold at 450°C for 20 minutes to allow the binder to burn off.
3) Ramp up to a temperature of 1150°C at a minimum rate of 9°C/minute.
4) Hold at 1150°C for 20 minutes to allow the samples to stabilize at this temperature.
5) Ramp up to a temperature of 1190°C, 1214°C or 1238°C at a minimum rate of 9°C/minute to allow the Ni-Hf braze alloy to melt; or ramp up to a temperature of 1170°C, 1204°C or 1238°C to allow the Ni-Zr alloy to melt.
6) Hold at the braze temperature for 40 minutes or 18 hours.
7) Furnace cool to room temperature.

After exposing the samples to the vacuum brazing cycle described above, the brazed samples were sectioned and mounted in resin using conventional metallographic practices. The mounted samples were polished, etched with Marble's reagent to reveal the microstructure and examined using optical and scanning electron microscopy (SEM) techniques. A Nikon Epiphot 200 optical microscope with a maximum magnification of 1000X, and a JOEL-Oxford scanning electron microscope equipped with ZAF software correction, were used. The acceleration voltage was 20 kV, the % dead time approximately 50 seconds, the sample tilt angle 0°, and the total acquisition time 150 seconds.

3.3) Results and discussion

3.3.1 Optimization of the braze temperature:

Neither the Ni-Hf, nor the Ni-Zr braze, melted at their published eutectic temperatures of 1190°C and 1170°C, respectively. This could be as a result of experimental error, such as incorrect weighing of the Ni-Hf or Ni-Zr powders (unlikely), insufficient mixing (resulting in segregated braze powders), or inaccurate furnace calibration. It may also be due to insufficient thermodynamic driving force for melting as a result of the low levels of superheat above the equilibrium eutectic temperatures.

Since neither alloy melted at their published eutectic temperatures, the braze temperatures were raised to 1214°C for the Ni-Hf alloy and 1204°C for the Ni-Zr alloy. Partial melting occurred, suggesting that the braze temperatures used were between the solidus and liquidus temperatures of the filler metals. Since eutectic alloys have congruent melting points, this implies that the compositions of the alloys deviated from the eutectic compositions given on the phase diagrams in **Figures 49 and 50**.

Complete melting was eventually achieved at a furnace temperature of 1238°C for both braze alloys. This is 48°C above the equilibrium eutectic temperature for the Ni-Hf alloy, and 68°C above the published Ni-Zr eutectic temperature. It should be noted that three furnace thermocouples were used to control the temperature within the vacuum furnace. All three thermocouples were within ±3°C of the specified temperature of 1238°C during brazing. Two additional load thermocouples placed in contact with the In738 plate gave readings of 1229°C and 1232°C. The real temperature at which the Ni-Hf and Ni-Zr alloys successfully melted and flowed was therefore closer to 1230°C ± 2°C. This is 40°C higher than the published eutectic temperature of the Ni-Hf alloy and 60°C higher than the eutectic temperature of the Ni-Zr alloy.

In order to clarify this discrepancy between the published and measured melting temperatures, the solidus and liquidus temperatures of both braze alloys were determined using Differential Thermal Analysis (DTA), and the chemical compositions were measured using ICP-OE (Inductively Coupled Plasma-Optical Emission) techniques. The results are summarized in Table 9.

Table 9 – Measured chemical compositions (wt.%) of the Ni-Hf and Ni-Zr braze alloys.

Alloy	Ni	Hf	Zr	Co	Cr	Cu	Fe	P	Mn	Si	C
Ni-Hf braze	69.995	28.87	0.70	0.02	0.04	0.01	0.14	0.007	-	0.20	0.018
Ni-Zr braze	86.212	-	13.26	0.02	0.05	0.01	0.18	-	0.01	0.24	0.018

The measured solidus temperature of the Ni-Hf braze alloy was 1176^{o}C and the liquidus temperature 1208^{o}C. The solidus temperature of the Ni-Zr braze was 1163^{o}C and the liquidus temperature 1206^{o}C.

These results indicate that the measured liquidus temperature of the Ni-Hf braze alloy was approximately 18^{o}C higher than the published eutectic temperature, whereas the liquidus of the Ni-Zr alloy was 36^{o}C higher than the equilibrium eutectic temperature. Since the load thermocouples in contact with the In738 plate measured a temperature of 1230^{o}C ± 2^{o}C, the actual brazing temperature was about 22^{o}C to 24^{o}C higher than the measured liquidus temperatures determined by DTA for the Ni-Hf and Ni-Zr braze alloys used in this investigation. Brazing at a temperature ± 25^{o}C higher than the melting point of the braze alloy is within acceptable braze practice.

The observed differences between the published and measured liquidus temperatures can probably be attributed to deviations in chemical composition from the eutectic compositions specified by the phase diagrams (as indicated in **Table 9**). The conclusion was drawn that the Ni, Hf and Zr powders used to make up the braze alloys were not completely pure, leading to contamination of the braze alloys by various residual elements. These elements shifted the compositions of the braze powders away from the eutectic points, leading to higher melting temperatures and incongruent melting points.

3.3.2 Microstructures of the Ni-Hf and Ni-Zr joints after brazing at 1230°C for 40 minutes:

Optical micrographs of the Ni-Hf brazed joint after 40 minutes at 1230^{o}C are shown in **Figures 51 to 53** at various magnifications. **Figure 51** indicates that the Ni-Hf braze alloy melts and flows adequately when processed at 1230^{o}C for 40 minutes, and that a satisfactory bond forms with the In738 substrate material. The braze microstructure, shown in **Figures 52 and 53**, consists of a mixture of coarse and fine dendrites (probably γ), and a second phase that is most likely the Ni_5Hf or Ni_7Hf_2 intermetallic compound.

Figures 54 to 57 display optical micrographs at various magnifications of the Ni-Zr brazed joint after 40 minutes at 1230^{o}C. Like the Ni-Hf braze alloy, the Ni-Zr braze melts and flows satisfactorily when processed at 1230^{o}C for 40 minutes, and an acceptable bond forms with the In738 substrate material (see **Figures 54 and 55**). The braze microstructure, shown in **Figures 55 to 57**, consists of γ dendrites, a Ni_5Zr intermetallic phase, and a γ/γ' flower-shaped eutectic component.

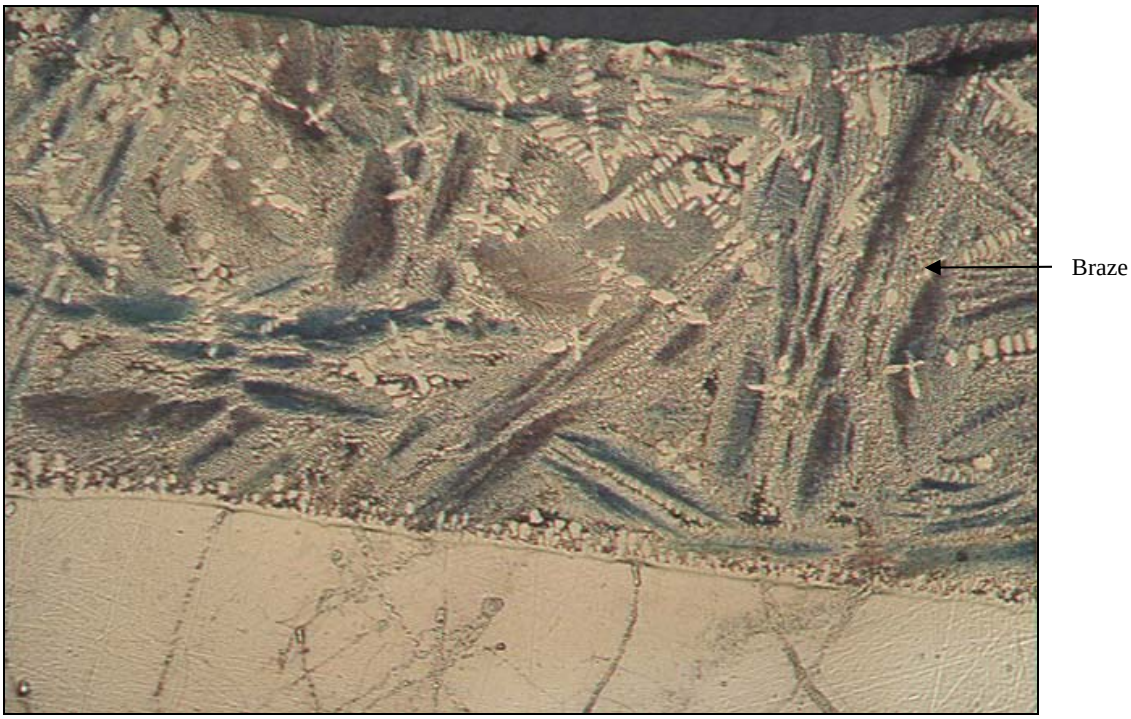

Figure 51 – Optical micrograph of a Ni-Hf brazed joint in In738 parent metal after brazing at 1230°C for 40 minutes. Magnification: 50X.

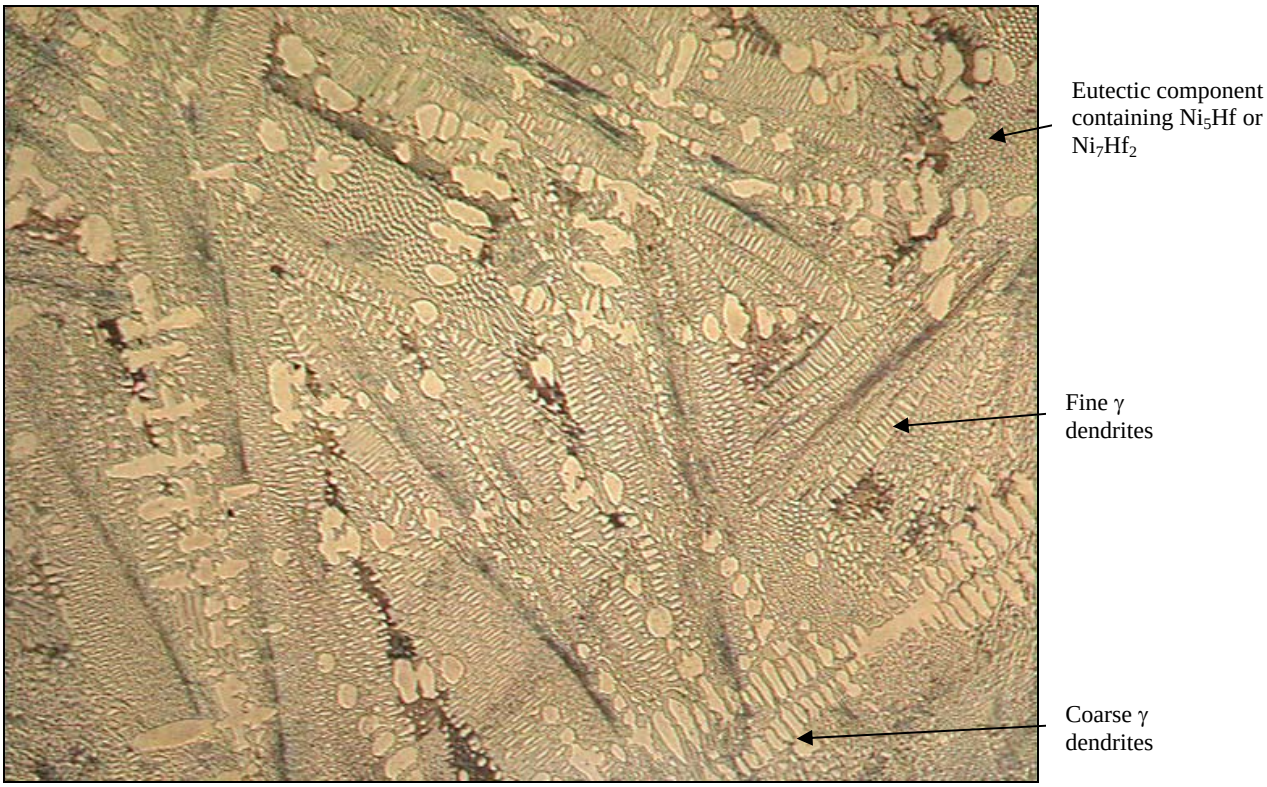

Figure 52 – Optical micrograph of a Ni-Hf brazed joint in In738 parent metal after brazing at 1230°C for 40 minutes. Magnification: 100X.

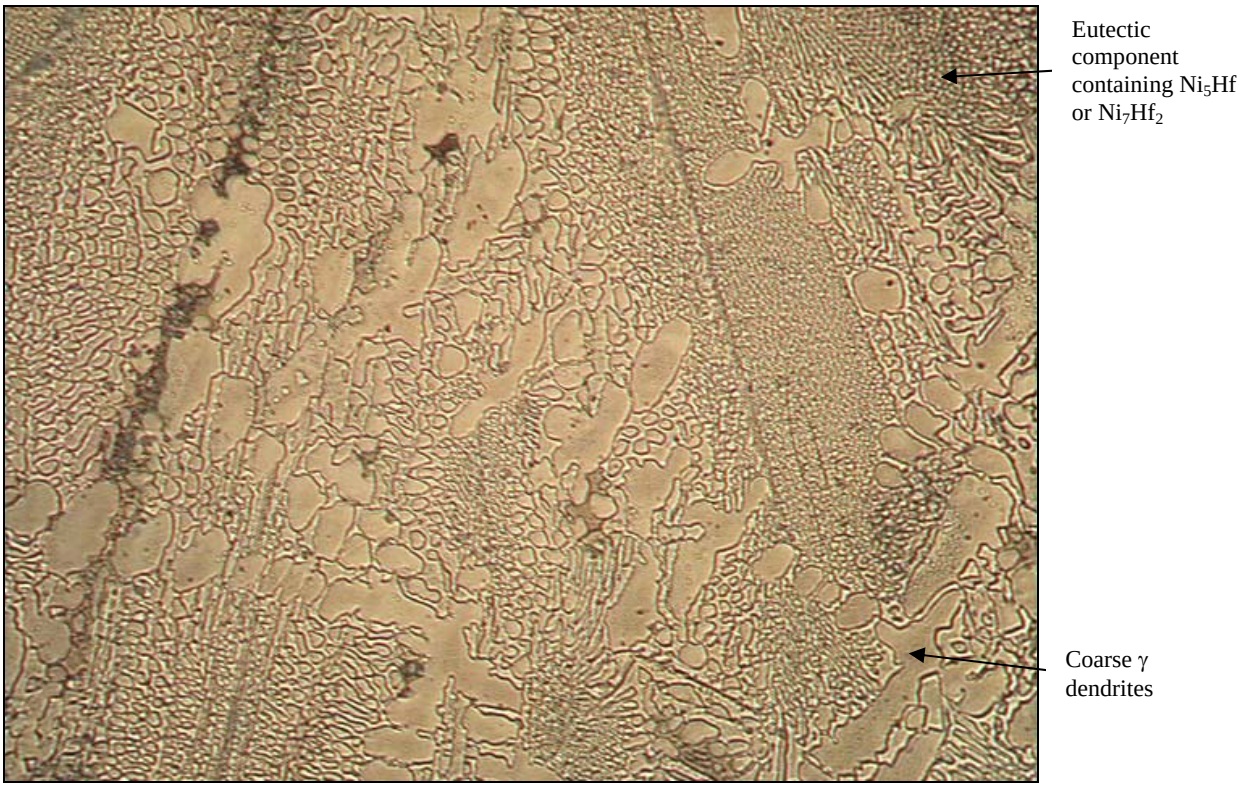

Figure 53 – Optical micrograph of a Ni-Hf brazed joint in In738 parent metal after brazing at 1230°C for 40 minutes. Magnification: 200X.

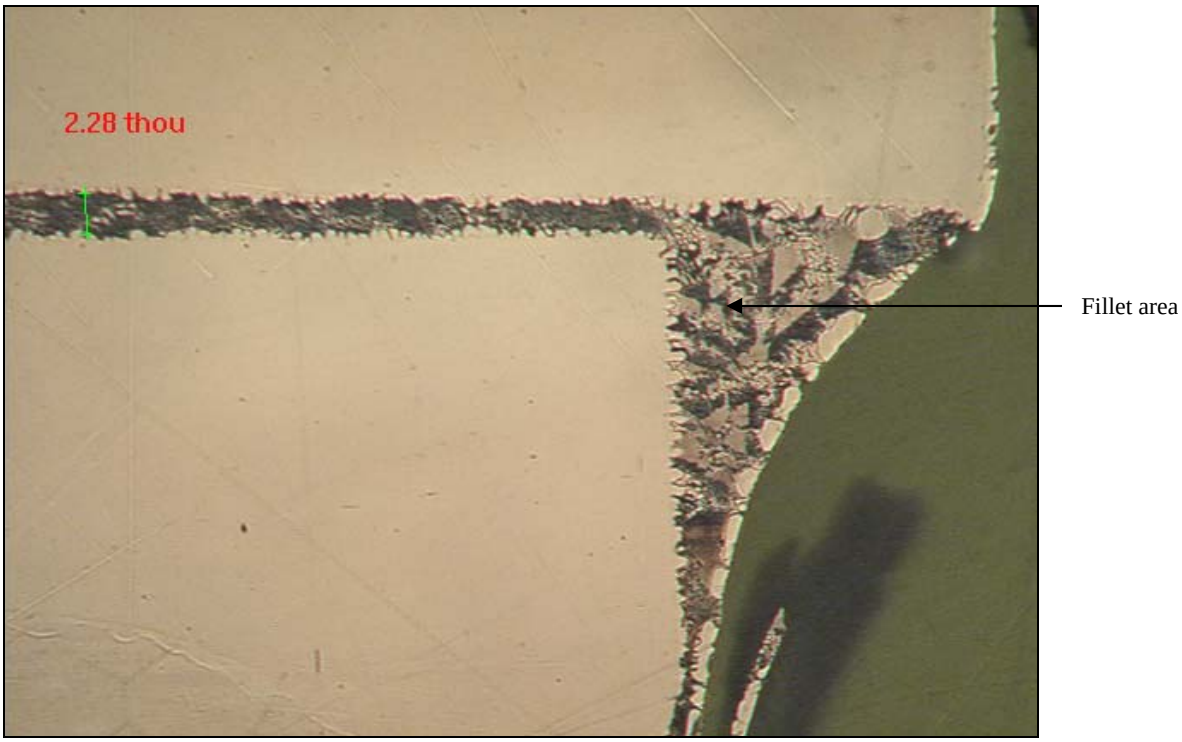

Figure 54 – Optical micrograph of a Ni-Zr brazed joint in In738 parent metal after brazing at 1230°C for 40 minutes. Magnification: 50X.

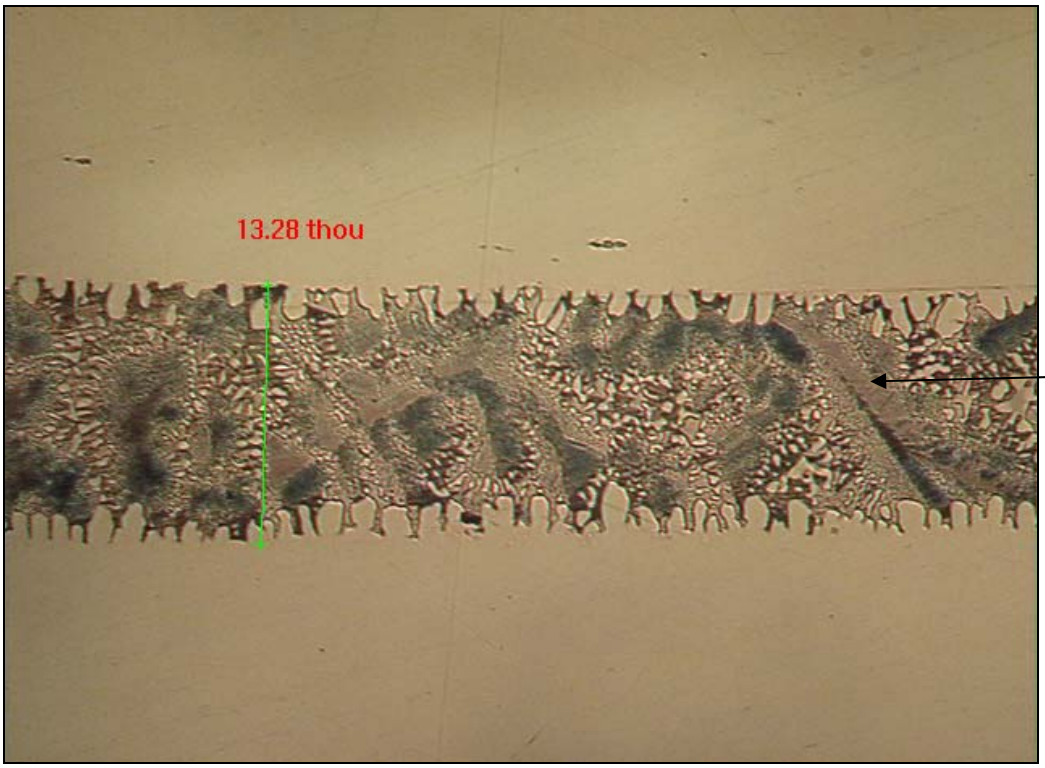

Figure 55 – Optical micrograph of a Ni-Zr brazed joint in In738 parent metal after brazing at 1230°C for 40 minutes. Magnification: 100X.

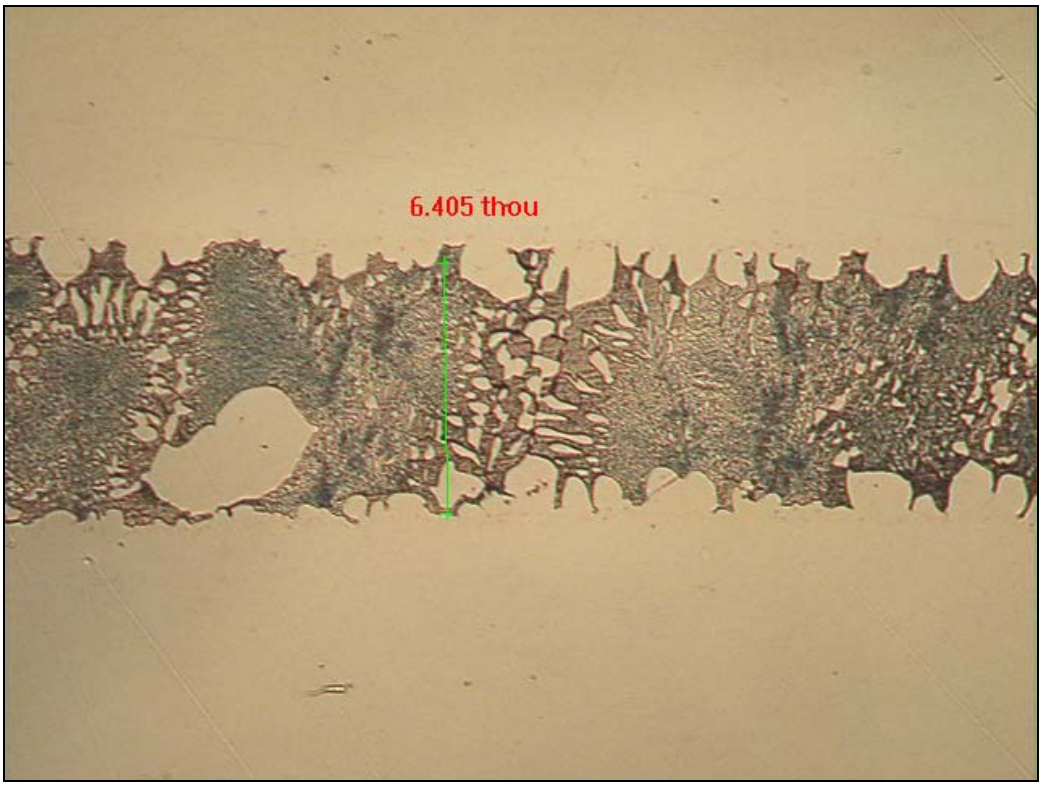

Figure 56 – Optical micrograph of a Ni-Zr brazed joint in In738 parent metal after brazing at 1230°C for 40 minutes. Magnification: 200X.

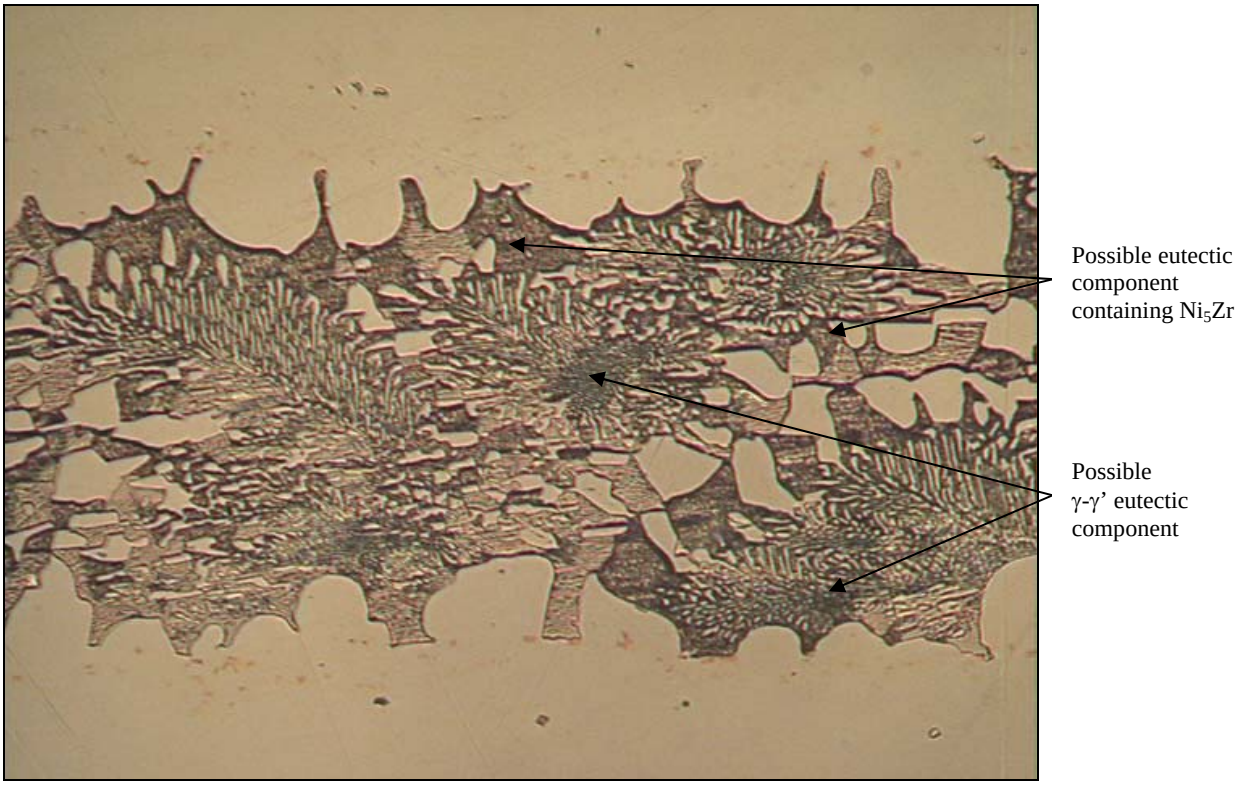

Figure 57 – Optical micrograph of a Ni-Zr brazed joint in In738 parent metal after brazing at 1230°C for 40 minutes. Magnification: 500X.

3.3.3 Microstructures of the Ni-Hf and Ni-Zr joints after brazing at 1230°C for 18 hours:

Optical micrographs of the Ni-Hf braze joint after 18 hours at 1230°C are shown in **Figures 58 to 62** at various magnifications. A brazed joint between two In738 plates is shown in **Figures 58 and 59**. An acceptable fillet area, indicating good braze flow, is evident and an acceptable bond forms with the In738 substrate material. The braze microstructure, shown in **Figures 58 to 61**, consists of mixture of coarse and fine γ dendrites, and a γ/γ' flower-shaped eutectic component that is often observed in Ni-based superalloys. The formation of the γ/γ' eutectic component is probably promoted by the high solubility of Hf in γ' (Hf is a good γ' former). Higher levels of the γ/γ' eutectic component most likely suppress the formation of Hf-rich intermetallic phases in the joint. Nevertheless, the Ni_5Hf or Ni_7Hf_2 intermetallic phase is evident, as shown in **Figure 62**.

A Ni-Zr brazed joint between two In738 plates is shown at various magnifications in **Figures 63 to 66** after brazing at 1230°C for 18 hours. Adequate bonding of the braze alloy to the In738 substrate is evident from **Figures 63 and 64**. The braze microstructure, shown in **Figures 63 to 66**, consists of a mixture of coarse and fine γ dendrites and a Ni_5Zr intermetallic phase.

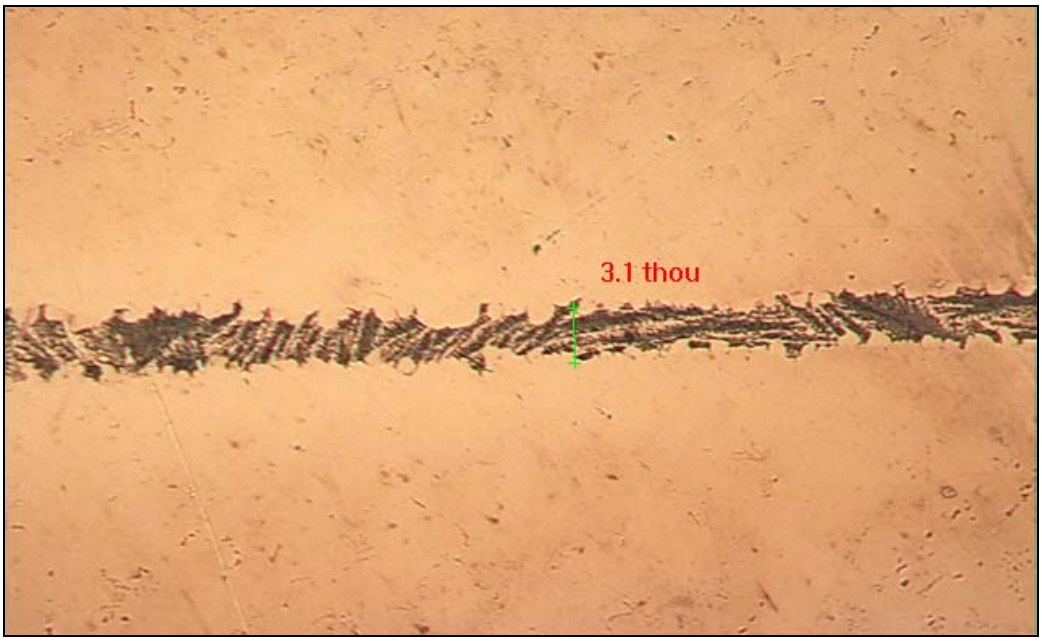

Figure 58 – Optical micrograph of a Ni-Hf brazed joint in In738 parent metal after brazing at 1230°C for 18 hours. Magnification: 50X.

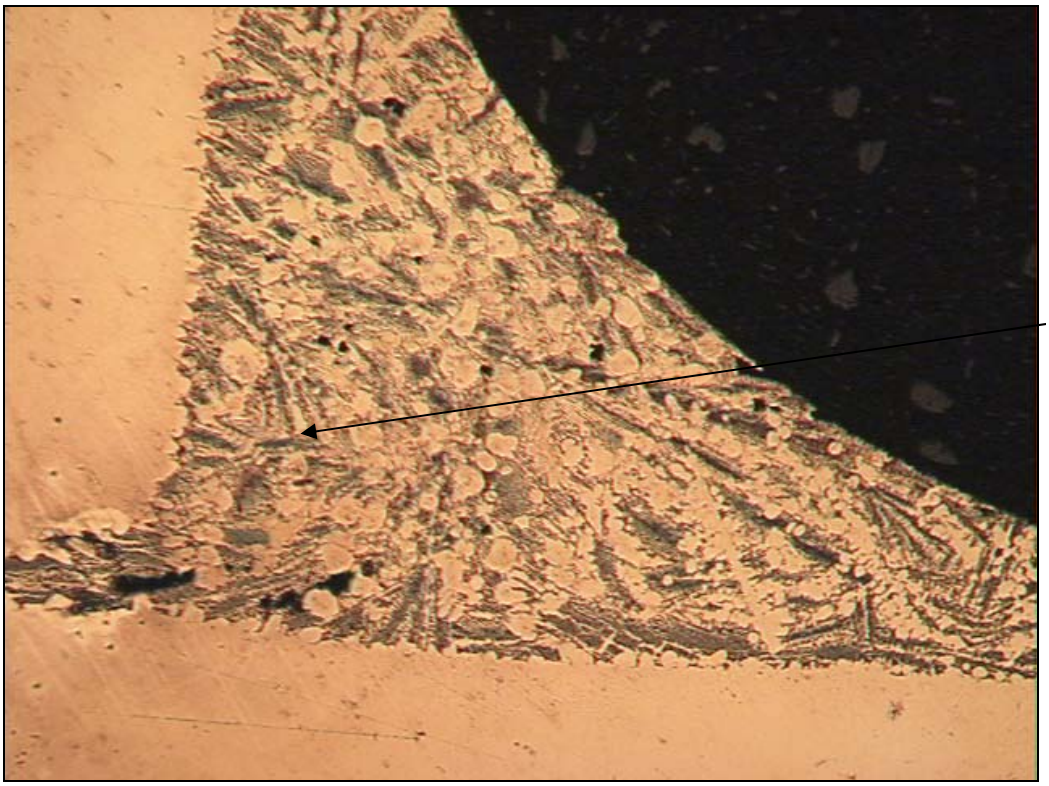

Figure 59 – Optical micrograph of a Ni-Hf brazed joint in In738 parent metal after brazing at 1230°C for 18 hours. Magnification: 50X.

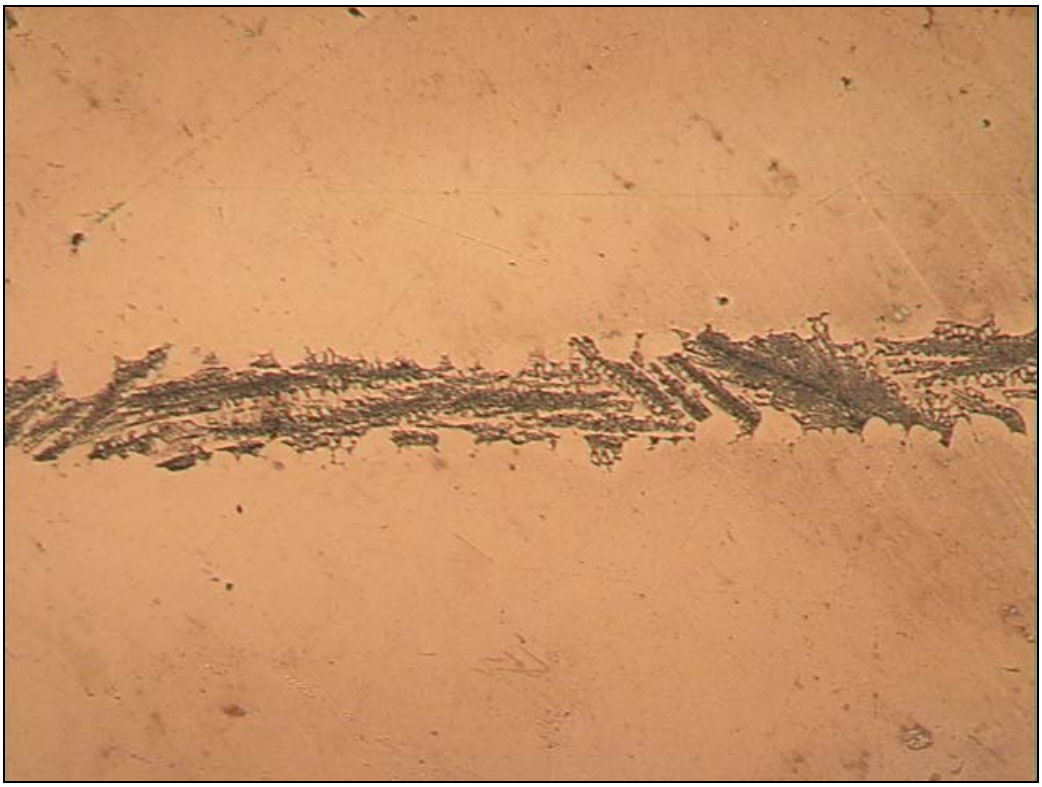

Figure 60 – Optical micrograph of a Ni-Hf brazed joint in In738 parent metal after brazing at 1230°C for 18 hours. Magnification: 100X.

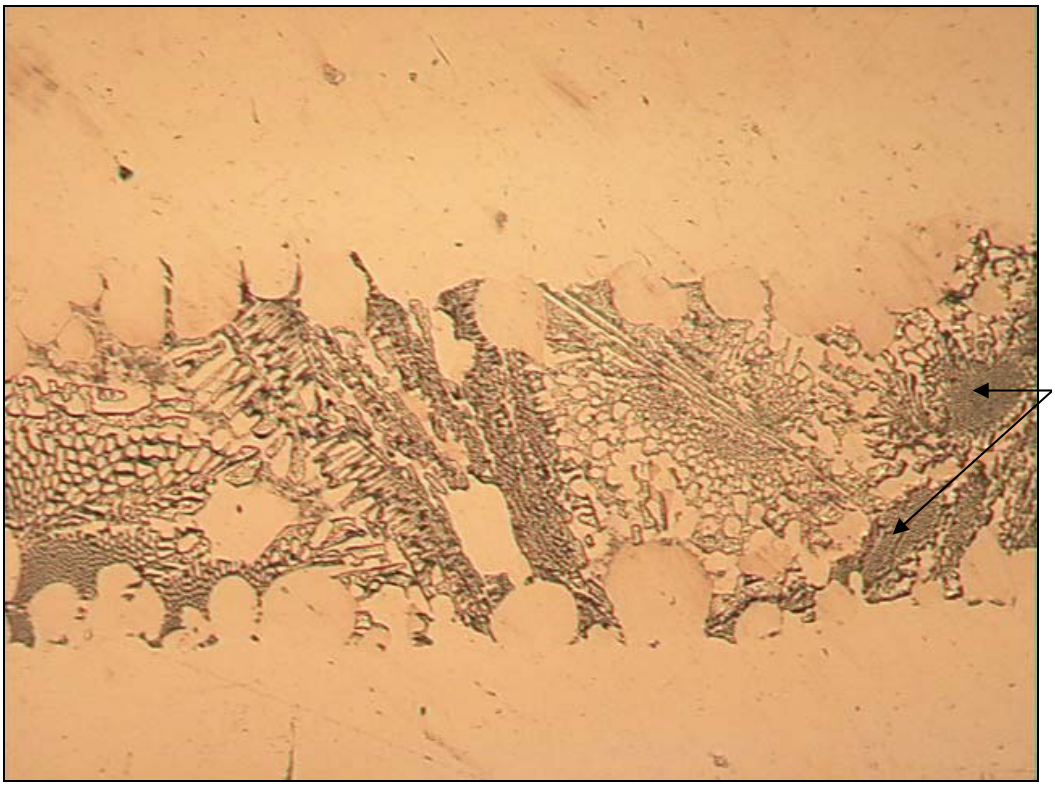

Figure 61 – Optical micrograph of a Ni-Hf brazed joint in In738 parent metal after brazing at 1230°C for 18 hours. Magnification: 200X.

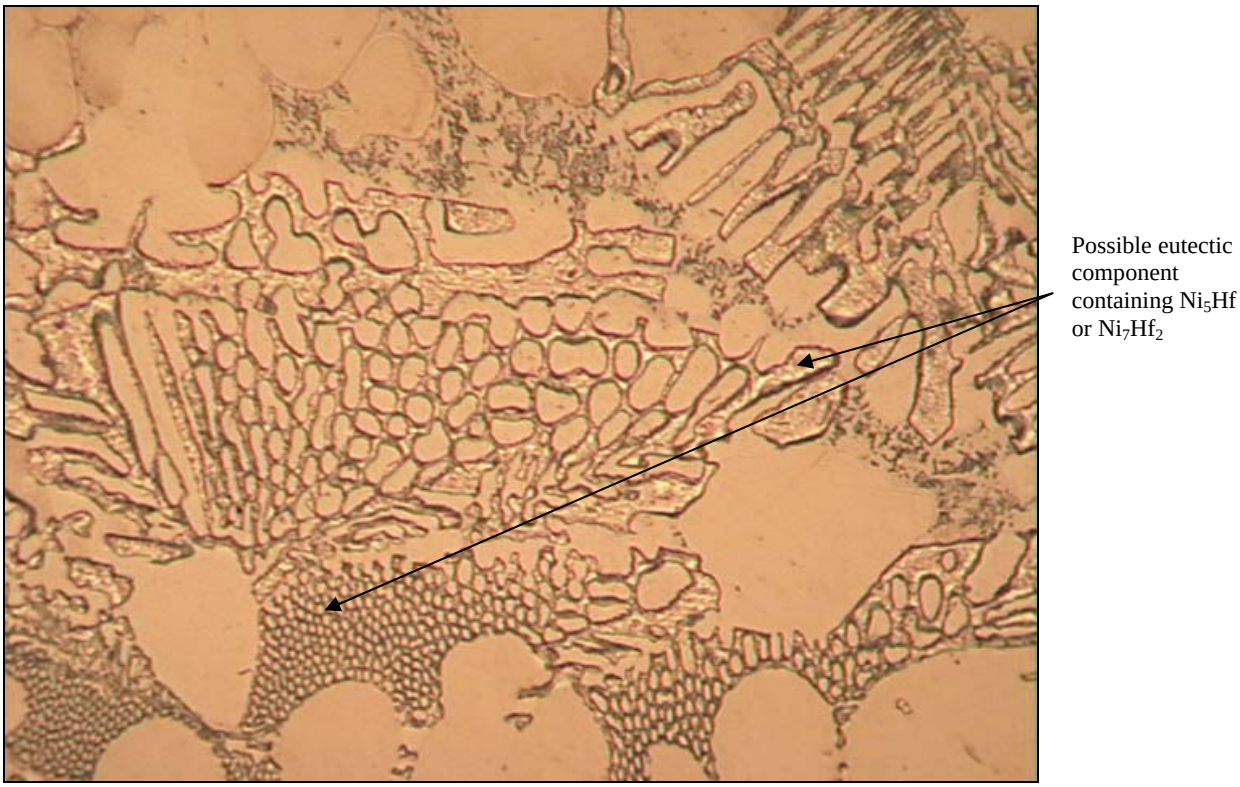

Figure 62 – Optical micrograph of a Ni-Hf brazed joint in In738 parent metal after brazing at 1230°C for 18 hours. Magnification: 500X.

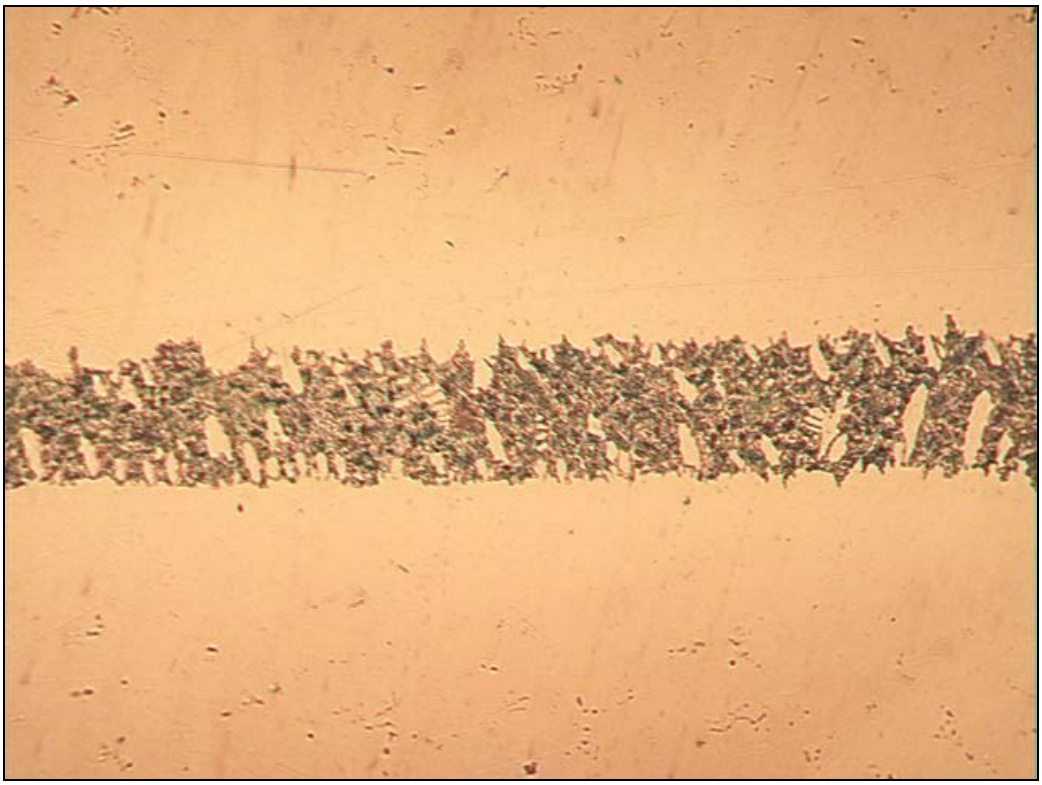

Figure 63 – Optical micrograph of a Ni-Zr brazed joint in In738 parent metal after brazing at 1230°C for 18 hours. Magnification: 50X.

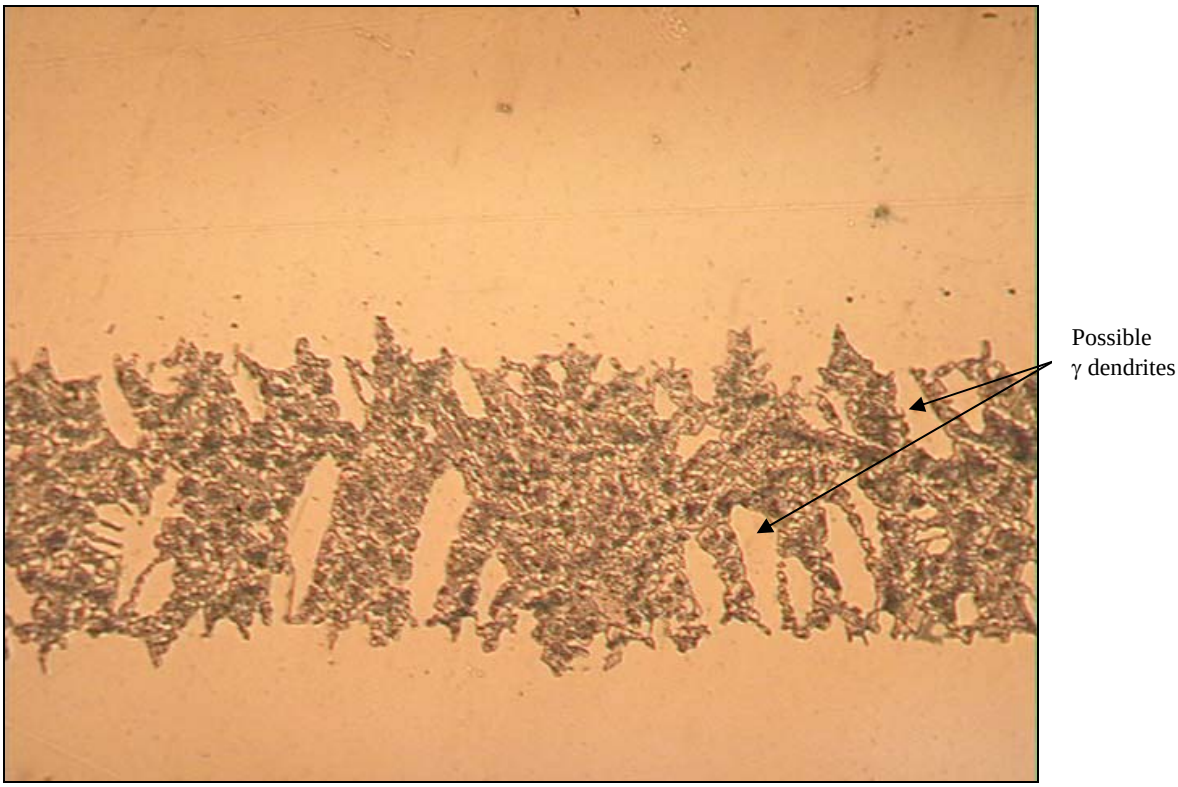

Figure 64 – Optical micrograph of a Ni-Zr brazed joint in In738 parent metal after brazing at 1230°C for 18 hours. Magnification: 100X.

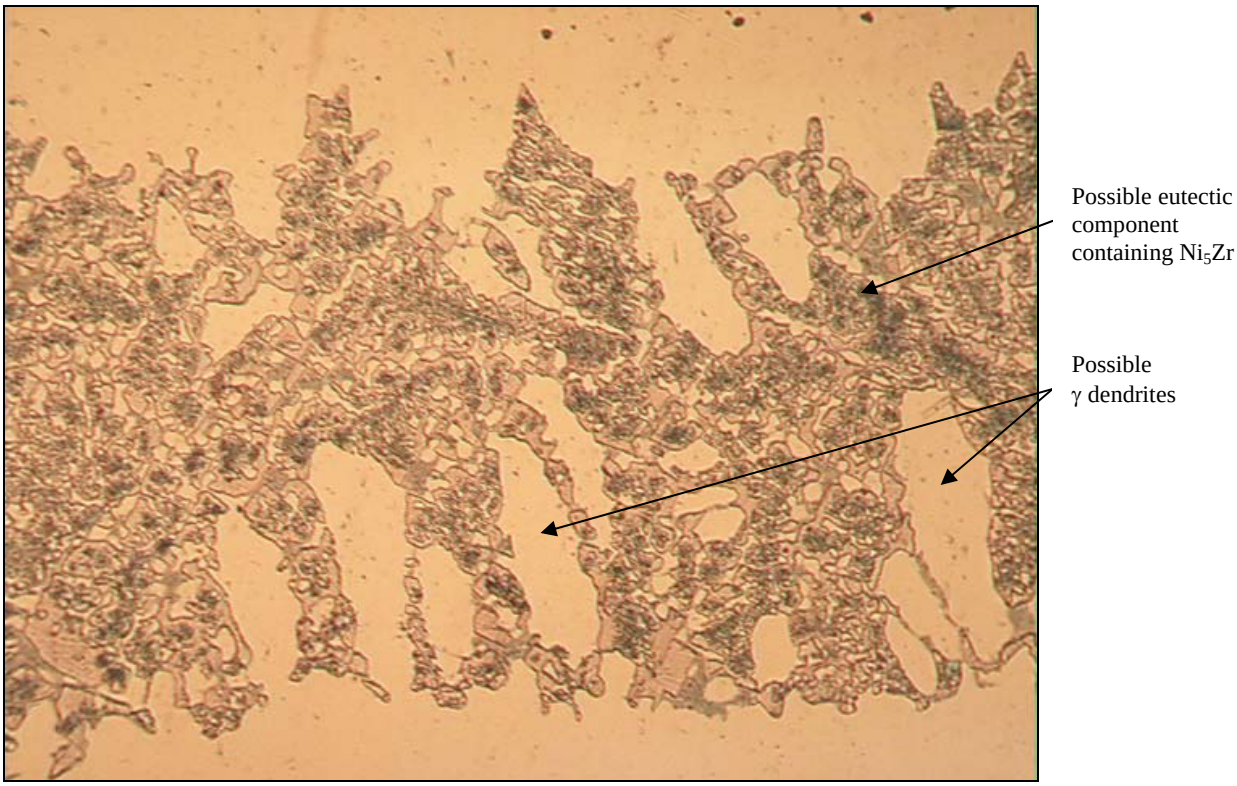

Figure 65 – Optical micrograph of a Ni-Zr brazed joint in In738 parent metal after brazing at 1230°C for 18 hours. Magnification: 200X.

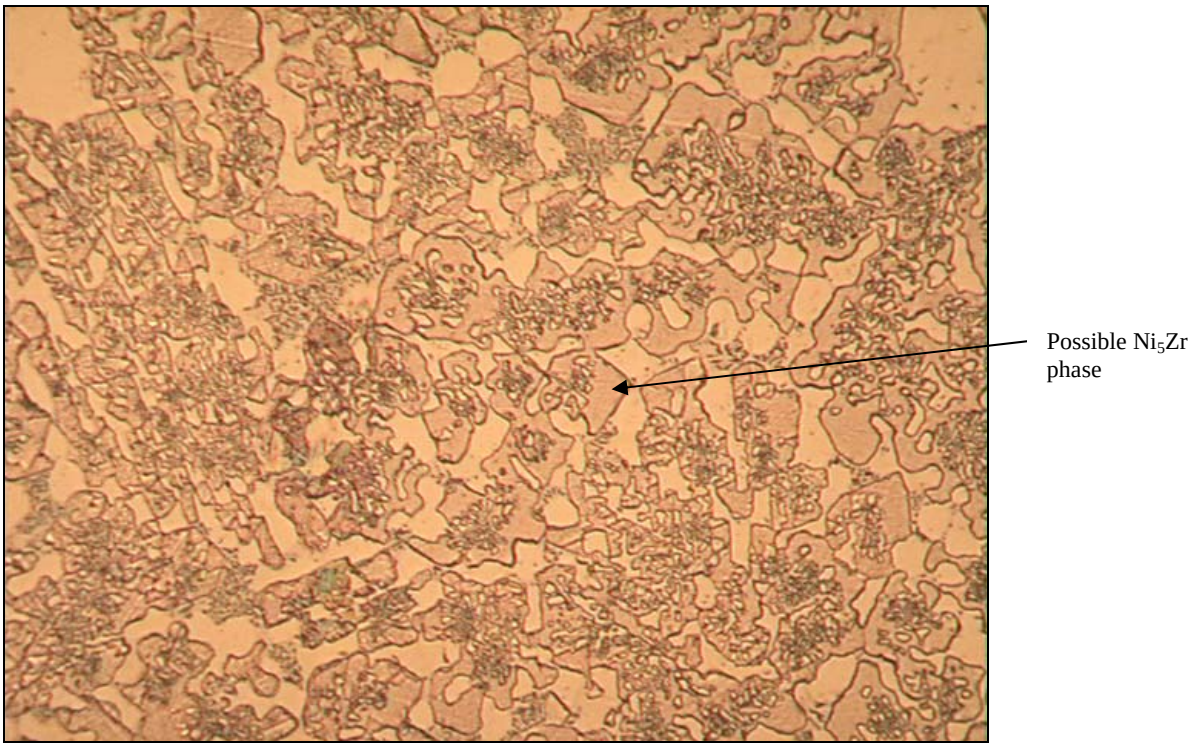

Figure 66 – Optical micrograph of a Ni-Zr brazed joint in In738 parent metal after brazing at 1230°C for 18 hours. Magnification: 500X.

A SEM micrograph of the Ni-Hf joint brazed at 1230°C for 18 hours is shown in **Figure 67.** SEM-EDS analysis was performed on the two phases highlighted by the arrows in **Figure 67**. One phase was arbitrarily labelled "grain boundary particle". The energy dispersive x-ray analysis revealed a composition of 78.72Ni-5.97Co-4.47Cr-4.00Al-2.82W-2.53Fe-0.53Mo-0.38Ti (wt.%) for this phase, identifying it as the γ phase. The second phase was arbitrarily designated "grain boundary film", and had a composition of 49.21Ni-45.74Hf-2.32W-1.94Co-0.37Cr-0.28Al-0.14Ti. The binary Ni-Hf phase diagram, shown in **Figure 49**, indicates that the Ni_7Hf_2 intermetallic phase contains 46.5% Hf, whereas the Ni_5Hf phase has a nominal Hf content of 37.9% Hf. The "grain boundary film" phase was therefore provisionally identified as the Ni_7Hf_2 intermetallic compound. The SEM-EDS analysis also indicates that small amounts of W, Co, Cr, Al and Ti are soluble in this phase. The presence of coarse γ dendrites in the Ni-Hf braze alloy suggests that the alloy may be slightly hypoeutectic, resulting in the formation of a proeutectic γ phase on solidification. The existence of Ni_7Hf_2 in the braze alloy was, however, unexpected, since the phase diagram (**Figure 49**) predicts a γ-Ni_5Hf eutectic component. It is not clear why the formation of the Ni_5Hf intermetallic compound was suppressed on solidification. The cooling rate after brazing may have been too fast to achieve true equilibrium, or the published phase diagram may be incorrect. In-depth investigation into the cause of this deviation from the predictions of the phase diagram falls outside the scope of this experiment and further speculation is therefore not justified at this time.

Figure 68 displays a SEM micrograph of the Ni-Zr joint brazed at 1230°C for 18 hours. Two phases, highlighted by the arrows in **Figure 68**, were analyzed. The phase arbitrarily labelled "grain boundary particle" had a composition of 78.82Ni-9.00Zr-3.08Co-2.97Cr-3.05Al-1.24Fe-1.57Mo-0.26Ti (wt.%) and was identified as the γ phase. This braze alloy also appears to be slightly hypoeutectic, forming a proeutectic γ phase on solidification. The

second phase, arbitrarily labelled "grain boundary film", had a composition of 71.24Ni-24.91Zr-1.45W-1.47Co-0.57Cr-0.38Mo. According to the Ni-Zr phase diagram shown in **Figure 50**, the Ni_5Zr phase contains between 21.32 and 25.95% Zr, suggesting that the phase labelled "grain boundary film" is the Ni_5Zr intermetallic compound that forms as part of the γ-Ni_5Zr eutectic component. Small amounts of W, Co, Cr and Mo are soluble in this phase.

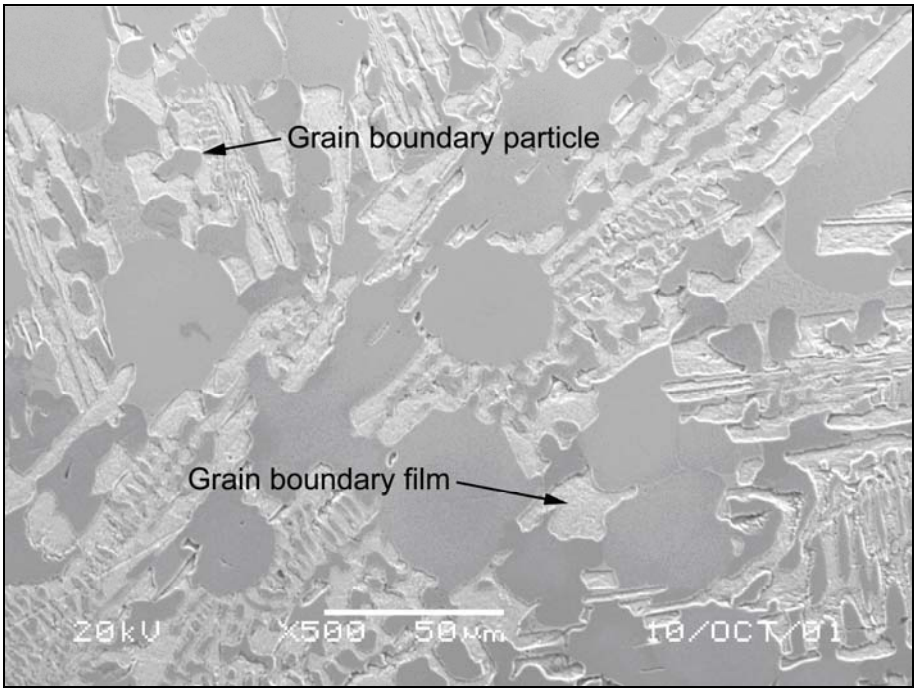

Figure 67 – SEM micrograph of the Ni-Hf braze, showing the phases identified as γ (labelled "grain boundary particle") and Ni_7Hf_2 (labelled "grain boundary film").

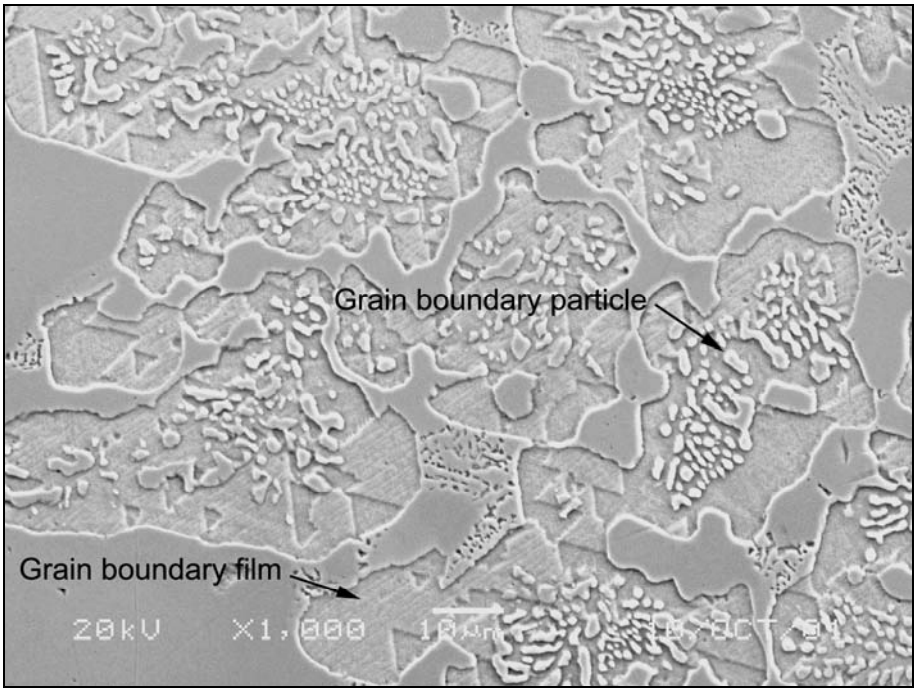

Figure 68 – SEM micrograph of the Ni-Zr braze, showing the phases identified as γ (labelled "grain boundary particle") and Ni_5Zr (labelled "grain boundary film").

3.4) Conclusions

- The eutectic Ni-Hf and Ni-Zr braze alloys did not melt at the equilibrium eutectic temperatures predicted by the binary phase diagrams. This was attributed to a shift in chemical composition away from the eutectic point due to contamination of the powders used to mix the braze alloys. The brazing temperature for both alloys was optimized at $1230^{o}C \pm 2^{o}C$. This temperature is approximately 25°C higher than the measured liquidus temperatures of the alloys.

- The Ni-Hf and Ni-Zr braze alloys exhibited good flow and wetting of the substrate at a brazing temperature of $1230^{o}C$. Narrow gaps in In738 parent metal can be repaired successfully using either of the novel braze alloys. The joints produced at $1230^{o}C$ appeared to consist of:

    1) coarse and fine γ dendrites,
    2) a flower-shaped γ-γ' eutectic component (in the Ni-Hf joints), and
    3) a γ-Ni_7Hf_2 or γ-Ni_5Zr eutectic component.

- The mechanical properties of the joints were not evaluated during the course of Experiment 1. Based on the chemistry (simple binary eutectic Ni-Hf or Ni-Zr alloys), it is reasonable to assume that wide joints with clearances greater than 0.10 mm will not exhibit strength levels approaching those of the base metal. In order to determine whether high strength joints can be produced using the novel braze alloys, liquid phase diffusion bonds were produced using the Ni-Hf and Ni-Zr braze powders in combination with Ni-base superalloy powder within the joint. The results are presented in Chapter 4.

CHAPTER 4 - EXPERIMENT 2

CHARACTERIZATION OF THE MICROSTRUCTURE AND MECHANICAL PROPERTIES OF LIQUID PHASE DIFFUSION BONDS USING EUTECTIC Ni-Hf AND Ni-Zr BRAZE ALLOYS AFTER SHORT PROCESSING TIMES (40 MINUTES)

This chapter examines the microstructure and mechanical properties of liquid phase diffusion bonds, produced by mixing the novel eutectic Ni-Hf or Ni-Zr braze alloys with MarM247 Ni-base superalloy powder, after short processing times (40 minutes) at 1230°C.

4.1) Introduction

As shown in the preceding chapter, simple binary eutectic Ni-Hf and Ni-Zr braze alloys can be used to successfully join In738 Ni-base superalloy. The joint gap must, however, be narrow (less than 0.15 mm in width) to allow capillary action to draw the filler metal into the joint. Such narrow joint gaps are usually only found in the manufacturing industry. In the repair industry, especially in IGT (industrial gas turbine) engine components, cracks are frequently wider than 0.15 mm and the simple eutectic Ni-Hf and Ni-Zr brazes will most likely not deliver adequate mechanical properties if used independently. In order to improve the mechanical properties of the In738 braze joints, the Ni-Hf or Ni-Zr eutectic braze alloy was mixed with MarM247 Ni-base superalloy powder, and processed using the liquid phase diffusion bonding (LPDB) process described in §1.6 of the literature survey.

The objectives of Experiment 2 were therefore:

- to demonstrate that the novel Ni-Hf and Ni-Zr braze alloys can be used in conjunction with MarM247 Ni-base superalloy powder to successfully join In738 using the liquid phase diffusion bonding (LPDB) process, and
- to examine the microstructure and mechanical properties of the LPDB joints after short processing times (40 minutes).

4.2) Experimental procedure

In738 plate material was produced and prepared as described in §3.2. A mixture of coarse (+325 mesh) and fine (–325 mesh) MarM247 Ni-base superalloy powder with a nominal composition shown in Table 10 was mixed with braze binder to form a paste. MarM247 powder, as opposed to In738, was selected because MarM247 is recognized as the equiaxed Ni-base superalloy with the highest mechanical integrity. The MarM247 paste was applied to the In738 plate over an area of approximately 2500 mm^2 and allowed to dry. A layer of eutectic Ni-Hf or Ni-Zr braze alloy in paste form (produced as described in §3.2) was then applied over the dry MarM247 powder. The samples were dried for one hour, and placed into a laboratory vacuum furnace.

Table 10 – Nominal chemical composition of the MarM247 powder used in this investigation (wt.%, balance Ni).

B	C	Co	Cr	Hf	Mo	Al	W	Ta	Ti	Zr	Fe
0.001	0.15	10.0	8.25	1.50	0.70	5.50	10.0	3.0	1.0	0.05	0.5

The vacuum braze cycle used for both braze alloys was as follows:

1) Ramp up to a temperature of 450°C at a minimum rate of 9°C/minute.
2) Hold at 450°C for 20 minutes to allow the binder to burn off.
3) Ramp up to a temperature of 1150°C at a minimum rate of 9°C/minute.
4) Hold at 1150°C for 20 minutes to allow the samples to stabilize at this temperature.
5) Ramp up to a temperature of 1230°C at a minimum rate of 9°C/minute to melt the Ni-Hf and Ni-Zr braze alloys and to allow the melt to infiltrate the MarM247 powder.
6) Hold at 1230°C for 40 minutes.
7) Furnace cool to room temperature.

After exposing the In738 plates to the vacuum LPDB cycle described above, samples were sectioned and mounted using conventional metallographic practices. The mounted samples were polished and etched with Marble's reagent to reveal the microstructure. Optical and scanning electron microscopy techniques were then used to characterize the microstructures.

Tensile tests were performed at room temperature (21°C) and at temperatures of 540°C, 650°C, 760°C, 870°C and 980°C. In order to produce the tensile specimens, MarM247 plate material was joined using the procedure described earlier. The tensile test samples were aged at 870°C for 20 hours, as is typical during a normal braze repair cycle. The tensile test specimens were prepared in a butt joint configuration, shown schematically in **Figure 69**. The LPDB joint was 1.5 mm wide to simulate the typical crack widths found in Industrial Gas Turbine (IGT) components, and was located in the centre of the sample gauge length.

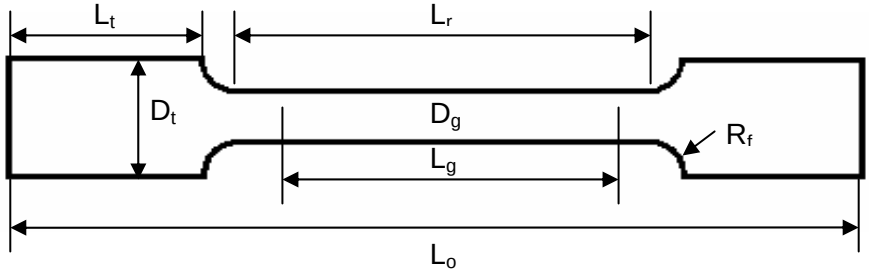

Figure 69 – Configuration of tensile and creep rupture specimens: D_g = 4.6 mm; L_g = 18.3 mm; L_r = 21.8 mm; L_o = 46.5 mm; R_f = 3.2 mm; L_t = 9.5 mm; and D_t = 8 mm.

4.3) Results and discussion

4.3.1 Microstructural investigation:

The microstructure of the LPDB joint produced with Ni-Hf braze filler metal and MarM247 powder is shown in **Figures 70 to 75**. The equiaxed, light-etching particles are the original MarM247 powder particles, and the darker areas consist of eutectic Ni-Hf braze alloy. The variation in MarM247 particle size, evident in **Figures 71 and 72**, is due to the mixture of coarse and fine MarM247 powders used in producing the superalloy powder. Such a mixture results in a denser, less porous structure, provided the braze temperature is high enough and the Ni-Hf braze alloy has sufficient time to flow.

Figures 72 and 73 indicate that the Ni-Hf joint is composed of MarM247 powder particles, interspersed with a thick layer consisting of γ dendrites and an intermetallic Ni_5Hf or Ni_7Hf_2

phase. It is expected that the mechanical properties of this joint will fall between those of the MarM247 superalloy and the Ni-Hf braze alloy. The dark etching component in **Figures 74 and 75** most likely consists of proeutectic γ, and the γ-Ni_5Hf or γ-Ni_7Hf_2 eutectic component. The γ dendrites and the Ni_5Hf or Ni_7Hf_2 phase surround each MarM247 powder particle, resembling a film or coating around the particles. If this film is brittle, cracks can propagate around each powder particle and connect to form what is referred to in industry as craze-cracked areas.

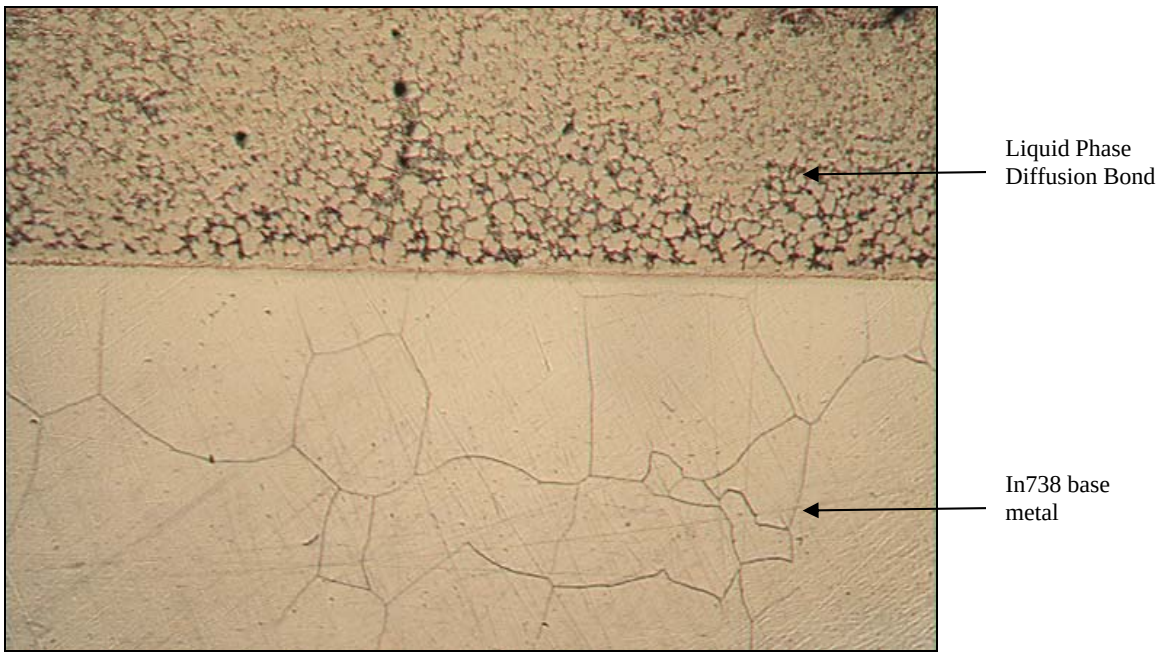

Figure 70 – Ni-Hf braze dispersed between MarM247 powder particles after brazing at 1230°C for 40 minutes. Magnification: 50X.

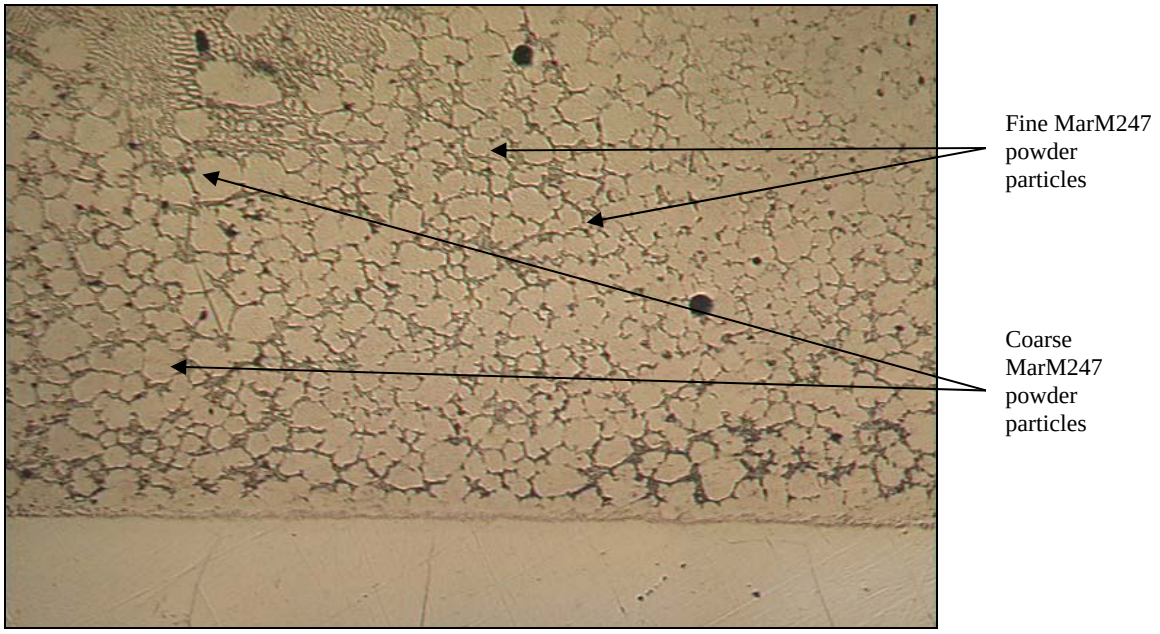

Figure 71 - Ni-Hf braze dispersed between MarM247 powder particles after brazing at 1230°C for 40 minutes. Magnification: 100X.

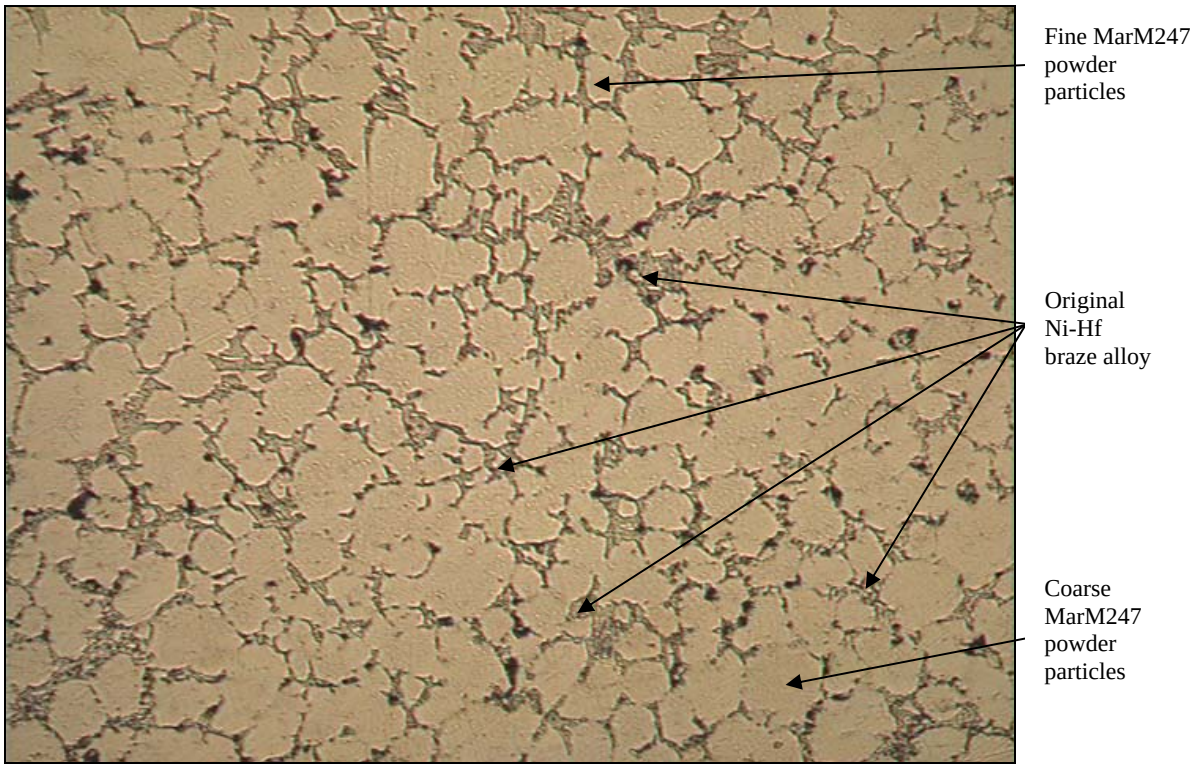

Figure 72 - Ni-Hf braze dispersed between MarM247 powder particles after brazing at 1230°C for 40 minutes. Magnification: 200X.

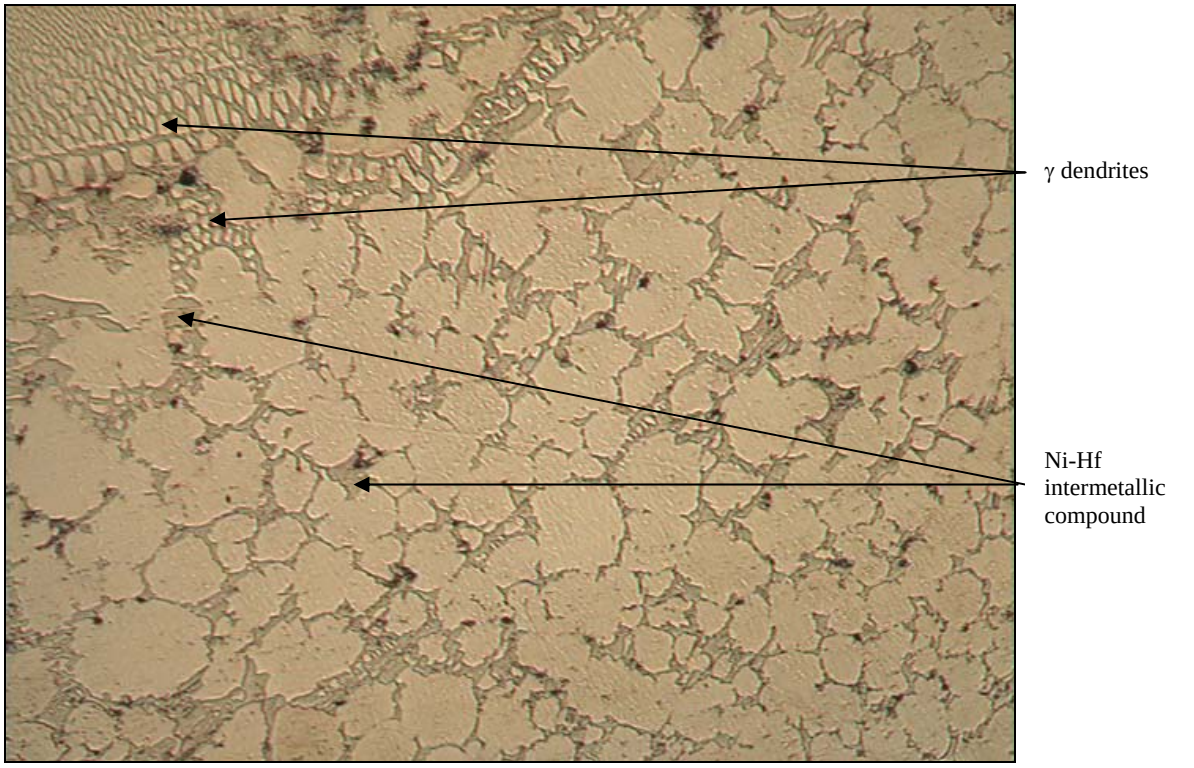

Figure 73 - Ni-Hf braze dispersed between MarM247 powder particles after brazing at 1230°C for 40 minutes. Magnification: 200X.

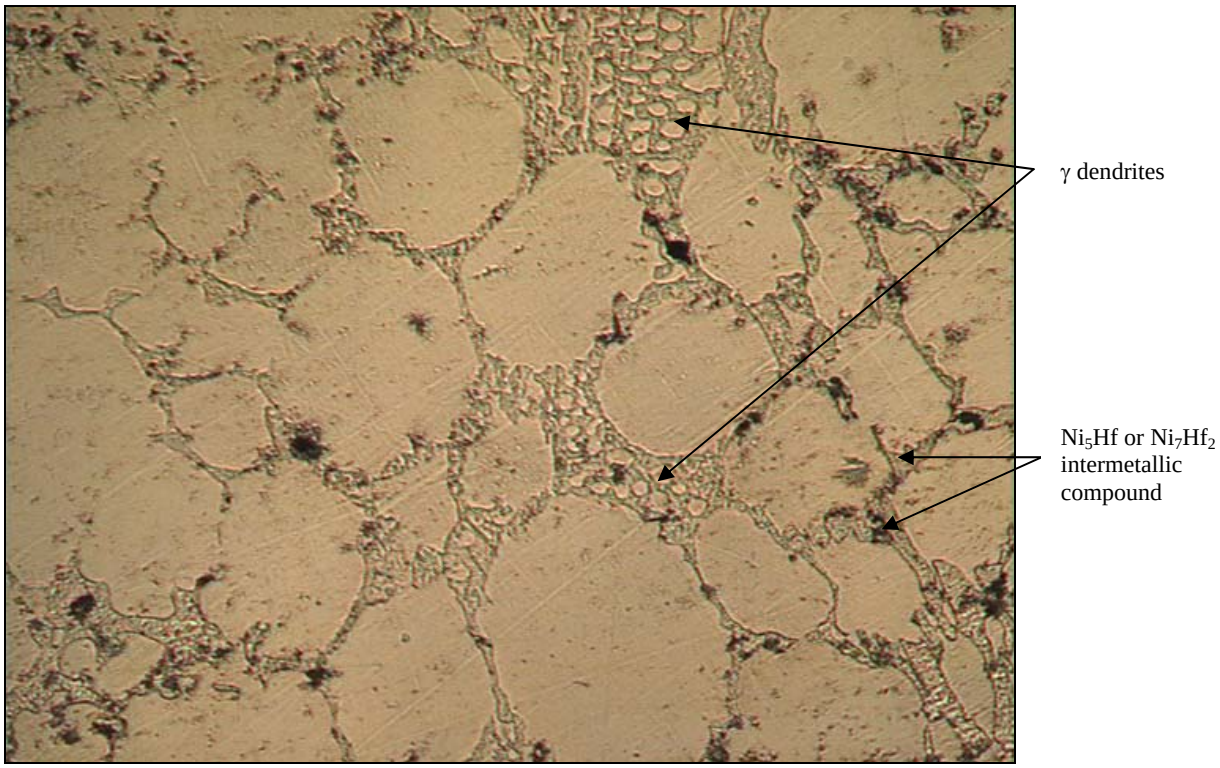

Figure 74 - Ni-Hf braze dispersed between MarM247 powder particles after brazing at 1230°C for 40 minutes. Magnification: 500X.

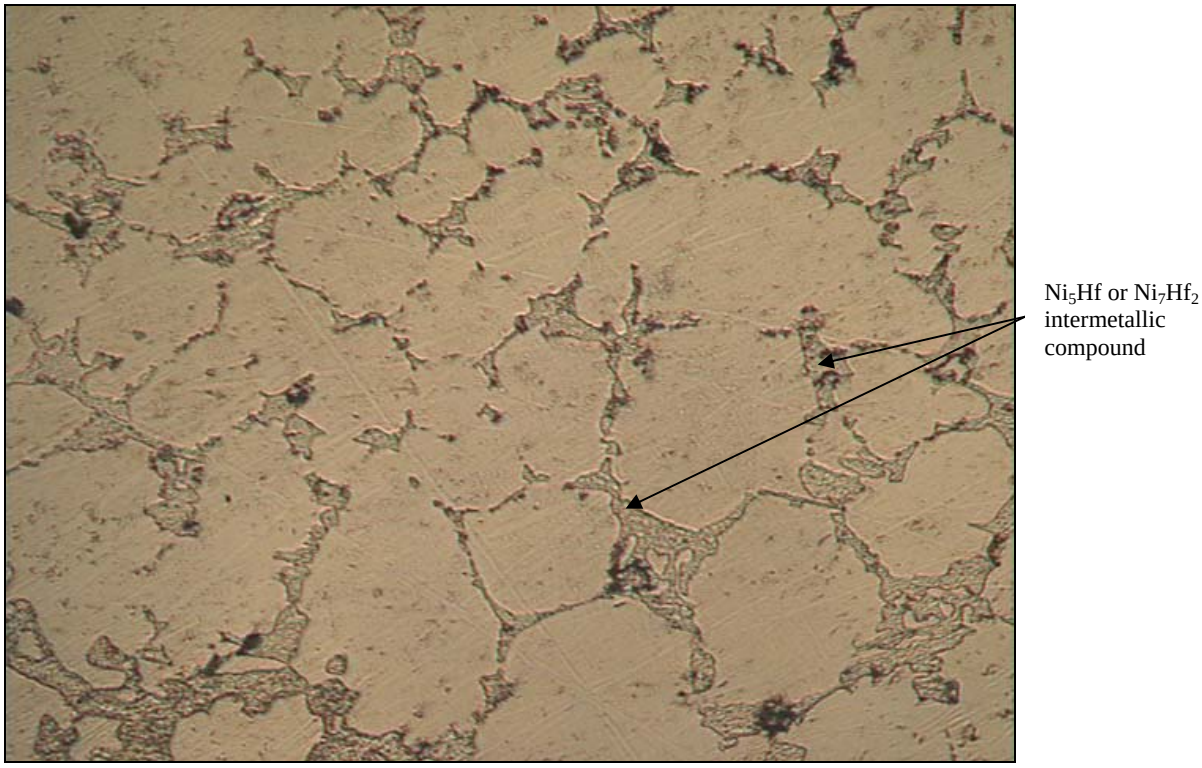

Figure 75 - Ni-Hf braze dispersed between MarM247 powder particles after brazing at 1230°C for 40 minutes. Magnification: 500X.

The microstructure of the LPDB joint produced using MarM247 powder and Ni-Zr braze paste is shown in **Figures 76 to 81** at various magnifications. The original MarM247 powder particles are evident as the lighter, more equiaxed component, while the darker regions consist of eutectic Ni-Zr braze alloy. As explained earlier, the variation in MarM247 particle size is due to the mixture of coarse and fine powders in the joint. This ensure a denser, less porous structure, provided the braze temperature is high enough and the Ni-Zr braze alloy has sufficient time to flow during the braze cycle.

Figures 78 to 81 illustrate that the joint is composed of individual MarM247 powder particles, separated by a layer consisting of γ dendrites and Ni_5Zr intermetallic compound (darker regions). Since this layer surrounds each MarM247 particle, its properties will most likely influence the properties of the joint. A brittle film will promote the propagation of cracks and may lead to the development of craze-cracked areas in service.

Figure 82 displays a SEM micrograph of the MarM247/Ni-Hf joint after brazing at 1230^{o}C for 40 minutes. SEM-EDS analysis was performed on two phases, highlighted by the arrows in **Figure 82**. One phase was arbitrarily labelled "grain boundary particle", and was shown to consist of 78.06Ni-6.68Co-3.74Cr-4.22Al-2.42W-3.01Fe-0.79Mo-0.81Ti-0.27Zr (wt.%). On the basis of this composition, the "grain boundary particle" phase was identified as γ. The second phase was arbitrarily labelled "grain boundary film", and contained 50.31Ni-43.93Hf-2.32W-2.50Co-0.40Cr-0.39Al-0.14Ti (wt.%). According to the Ni-Hf phase diagram (shown in **Figure 49**), the Ni_7Hf_2 intermetallic phase contains approximately 46.5% Hf, whereas the Ni_5Hf phase contains about 37.9% Hf. On the basis of the SEM-EDS analysis, the "grain boundary film" phase was therefore provisionally identified as the Ni_7Hf_2 intermetallic phase, with some W, Co, Cr, Al and Ti in solution.

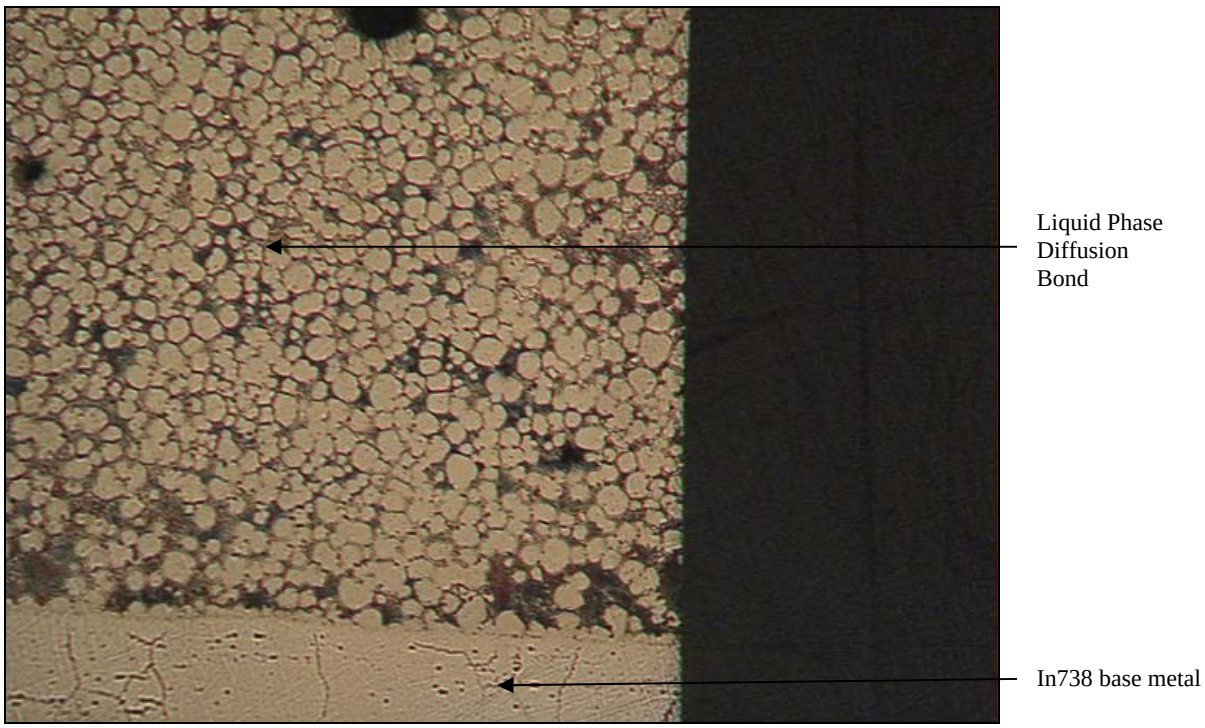

Figure 76 - Ni-Zr braze dispersed between MarM247 powder particles after brazing at 1230°C for 40 minutes. Magnification: 50X.

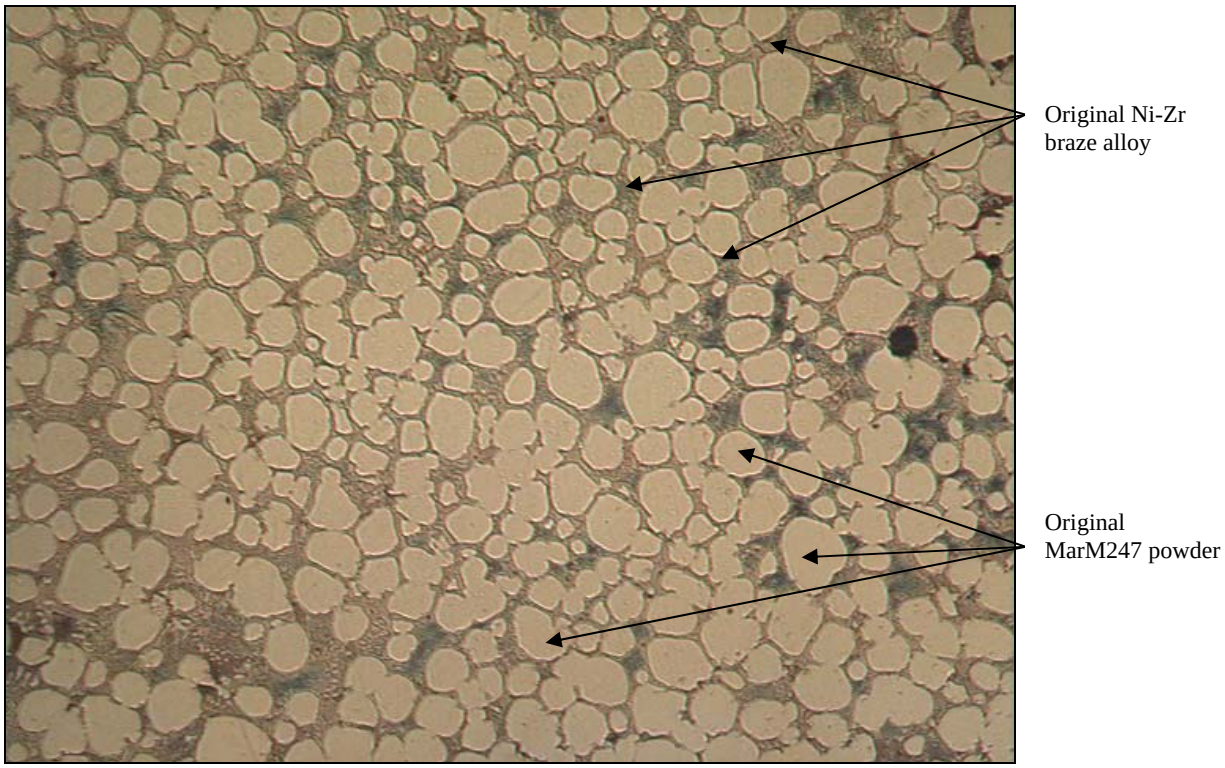

Figure 77 - Ni-Zr braze dispersed between MarM247 powder particles after brazing at 1230°C for 40 minutes. Magnification: 100X.

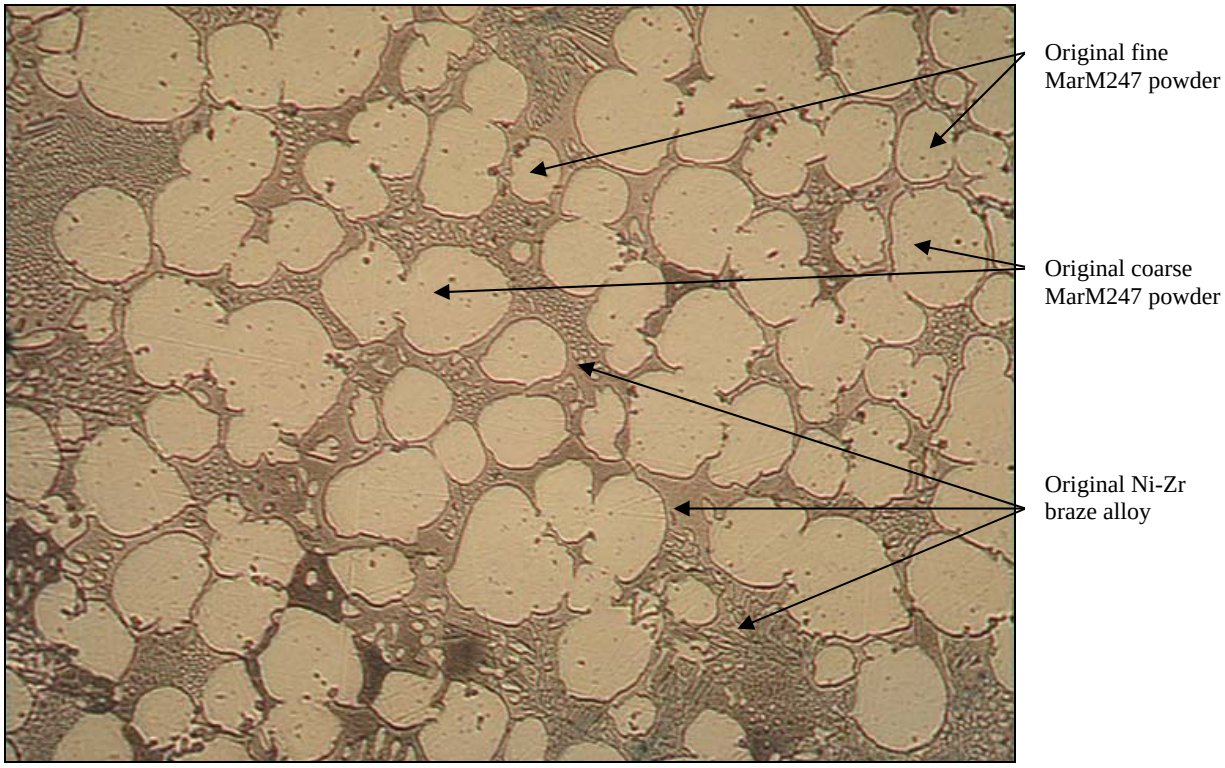

Figure 78 - Ni-Zr braze dispersed between MarM247 powder particles after brazing at 1230°C for 40 minutes. Magnification: 200X.

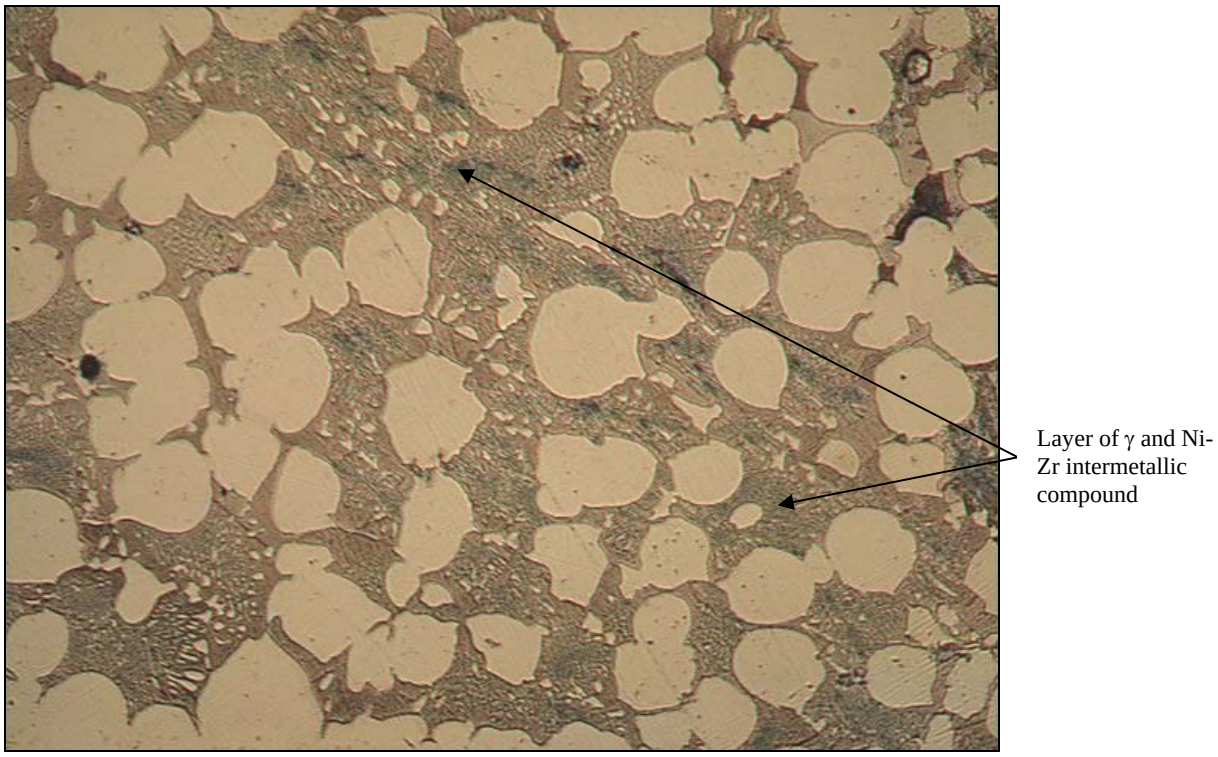

Figure 79 - Ni-Zr braze dispersed between MarM247 powder particles after brazing at 1230°C for 40 minutes. Magnification: 200X.

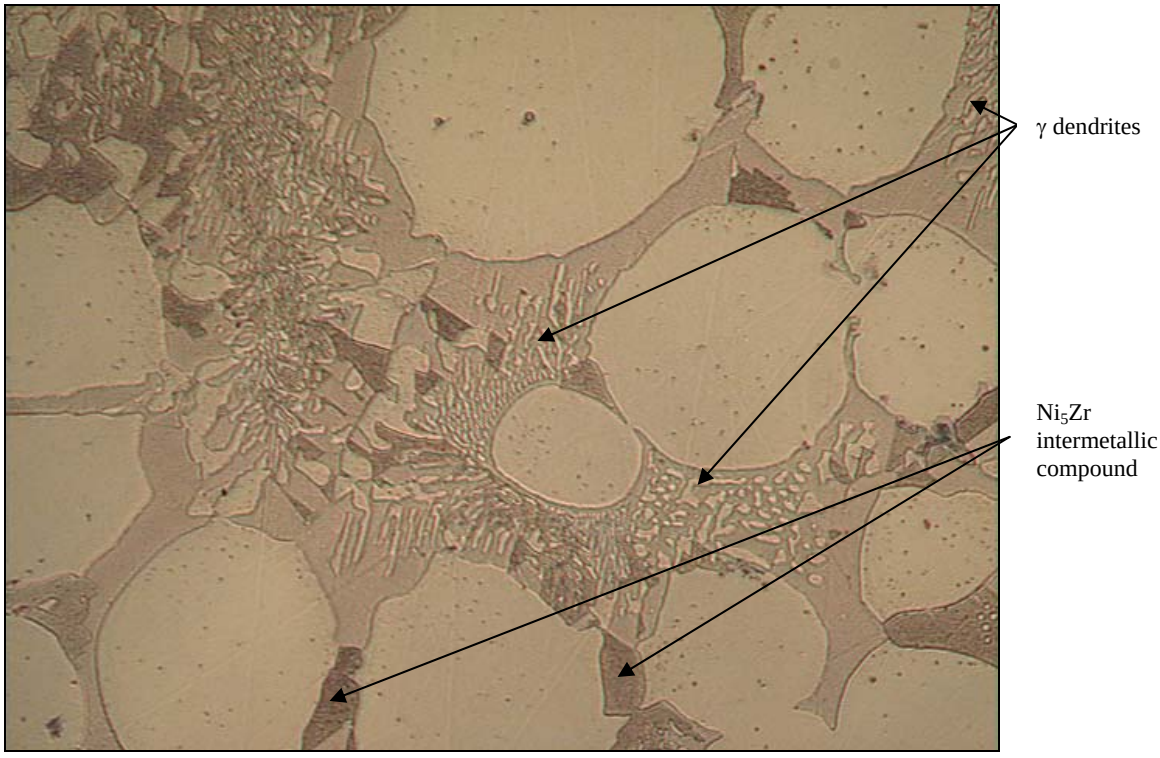

Figure 80 - Ni-Zr braze dispersed between MarM247 powder particles after brazing at 1230°C for 40 minutes. Magnification: 500X.

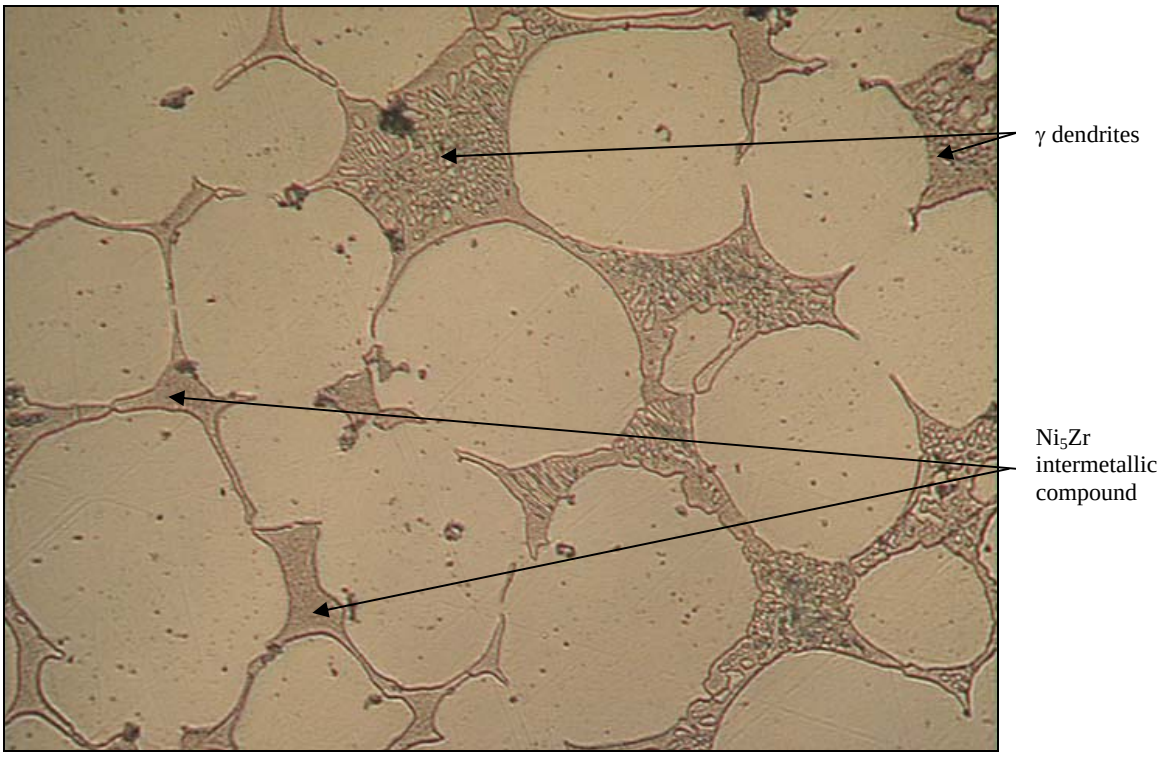

Figure 81 - Ni-Zr braze dispersed between MarM247 powder particles after brazing at 1230°C for 40 minutes. Magnification: 500X.

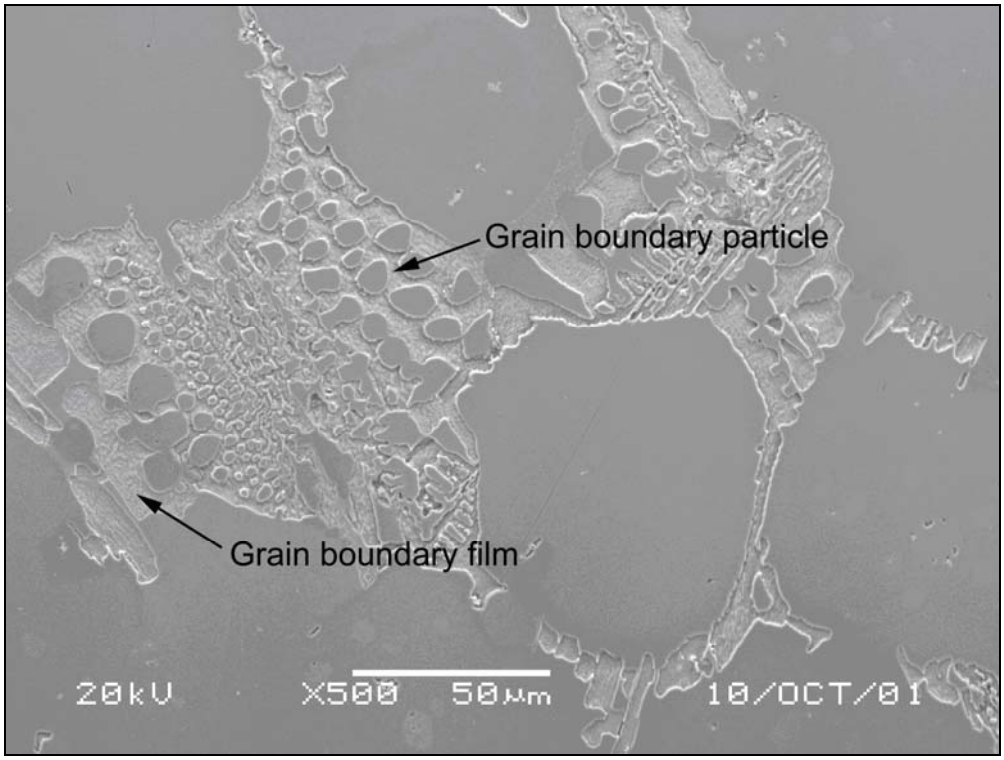

Figure 82 – SEM micrograph of the Ni-Hf braze, showing the phases identified as γ (labelled "grain boundary particle") and Ni_7Hf_2 (labelled "grain boundary film").

Figure 83 displays a SEM micrograph of the MarM247/Ni-Zr joint brazed at 1230°C for 40 minutes. Two phases, highlighted by the arrows in **Figure 83,** were analyzed using the SEM-EDS technique. The phase arbitrarily labelled "grain boundary particle" was identified as γ dendrites (with a composition of 74.48Ni-8.76Zr-5.64Co-3.21Cr-3.27Al-2.26W-1.86Mo-0.52Ti). The second phase, arbitrarily labelled "grain boundary film", had a composition of 69.49Ni-24.24Zr-2.03W-2.99Co-0.62Cr-0.41Mo-0.21Ti (wt.%). This phase was identified as the Ni_5Zr intermetallic phase, with small amounts of W, Co, Cr and Mo in solution.

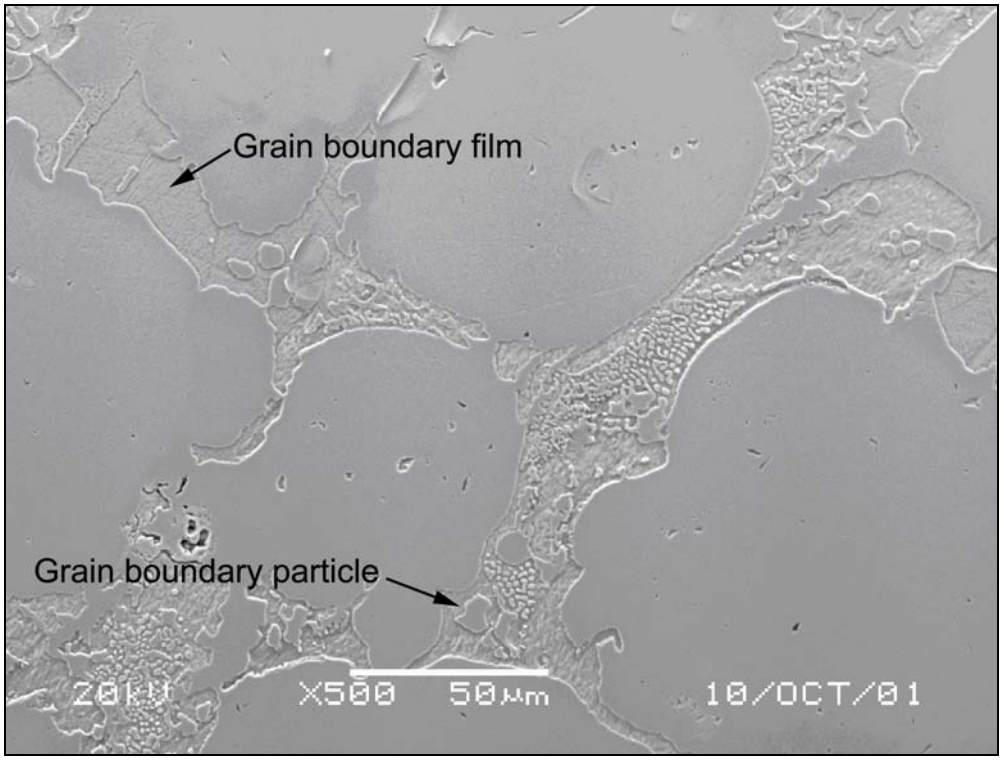

Figure 83 – SEM micrograph of the Ni-Zr braze, showing the phases identified as γ (labelled "grain boundary particle") and Ni_5Zr (labelled "grain boundary film").

4.3.2 Tensile test results:

The results of tensile tests performed at various temperatures are shown in **Tables 11 to 16**, and displayed graphically in **Figures 84 and 85**. The values shown represent the average of three tests.

Table 11 – Joint tensile properties measured at 21°C.

Tensile properties	Ni-Hf joints	Ni-Zr joints	MarM247 base metal
Tensile Strength (UTS)	323 MPa (46.8 ksi)	557 MPa (80.7 ksi)	960 MPa (139 ksi)
Yield Strength (YS)	239 MPa (34.7 ksi)	505 MPa (73.2 ksi)	800 MPa (116 ksi)
Elongation (%)	4.7	3.0	7.9
Reduction in area (RA) %	6.3	4.4	10.0

Table 12 – Joint tensile properties measured at 540°C.

Tensile properties	Ni-Hf joints	Ni-Zr joints	MarM247 base metal
Tensile Strength (UTS)	328 MPa (47.6 ksi)	619 MPa (89.7 ksi)	1014 MPa (147 ksi)
Yield Strength (YS)	243 MPa (35.2 ksi)	539 MPa (78.1 ksi)	801 MPa (116 ksi)
Elongation (%)	3.8	2.7	7.8
Reduction in area (RA) %	4.2	3.2	9.9

Table 13 – Joint tensile properties measured at 650°C.

Tensile properties	Ni-Hf joints	Ni-Zr joints	MarM247 base metal
Tensile Strength (UTS)	343 MPa (49.7 ksi)	562 MPa (81.4 ksi)	1040 MPa (151 ksi)
Yield Strength (YS)	265 MPa (38.4 ksi)	513 MPa (74.4 ksi)	805 MPa (117 ksi)
Elongation (%)	2.8	2.2	7.0
Reduction in area (RA) %	3.6	2.9	9.7

Table 14 – Joint tensile properties measured at 760°C.

Tensile properties	Ni-Hf joints	Ni-Zr joints	MarM247 base metal
Tensile Strength (UTS)	333 MPa (48.3 ksi)	593 MPa (85.9 ksi)	1000 MPa (145 ksi)
Yield Strength (YS)	282 MPa (40.8 ksi)	553 MPa (80.1 ksi)	815 MPa (118 ksi)
Elongation (%)	2.5	1.2	6.0
Reduction in area (RA) %	3.2	5.9	8.4

Table 15 – Joint tensile properties measured at 870°C.

Tensile properties	Ni-Hf joints	Ni-Zr joints	MarM247 base metal
Tensile Strength (UTS)	289 MPa (41.9 ksi)	444 MPa (64.4 ksi)	790 MPa (115 ksi)
Yield Strength (YS)	211 MPa (30.5 ksi)	414 MPa (60.0 ksi)	650 MPa (94 ksi)
Elongation (%)	2.0	1.0	5.0
Reduction in area (RA) %	3.0	2.4	7.7

Table 16 – Joint tensile properties measured at 980°C.

Tensile properties	Ni-Hf joints	Ni-Zr joints	MarM247 base metal
Tensile Strength (UTS)	195 MPa (28.3 ksi)	261 MPa (37.8 ksi)	506 MPa (73 ksi)
Yield Strength (YS)	141 MPa (20.4 ksi)	245 MPa (35.5 ksi)	312 MPa (45 ksi)
Elongation (%)	1.8	0.8	4.7
Reduction in area (RA) %	2.9	1.9	7.5

As shown in **Table 11**, the room temperature tensile and yield strengths of the Ni-Hf LPDB joints were 34% and 30%, respectively, of those of the MarM247 base metal, whereas the tensile and yield strengths of the Ni-Zr joints were 58% and 63%, respectively, of those of the MarM247 base metal. The Ni-Hf joints therefore exhibited considerably lower strength than the Ni-Zr joints after short processing times (40 minutes). The Ni-Hf joints, however, exhibited approximately 60% of the ductility of the MarM247 base metal, whereas the Ni-Zr joints only displayed about 40% of the base metal's ductility. It should be noted that, after

short processing times, the ductility of the Ni-Zr and Ni-Hf joints was significantly higher than the ductility of similar joints containing boron as melt point depressant. Boron-containing joints typically exhibit ductility values in the range of 0.5 to 1.0% after short processing times [35-37]. This observation provides initial evidence that, if higher strength joints can be achieved by increasing the processing time and similar levels of ductility are obtained, the use of Zr or Hf as melt point depressant in Ni-base braze alloys (instead of B) holds considerable potential for crack repair in the IGT industry.

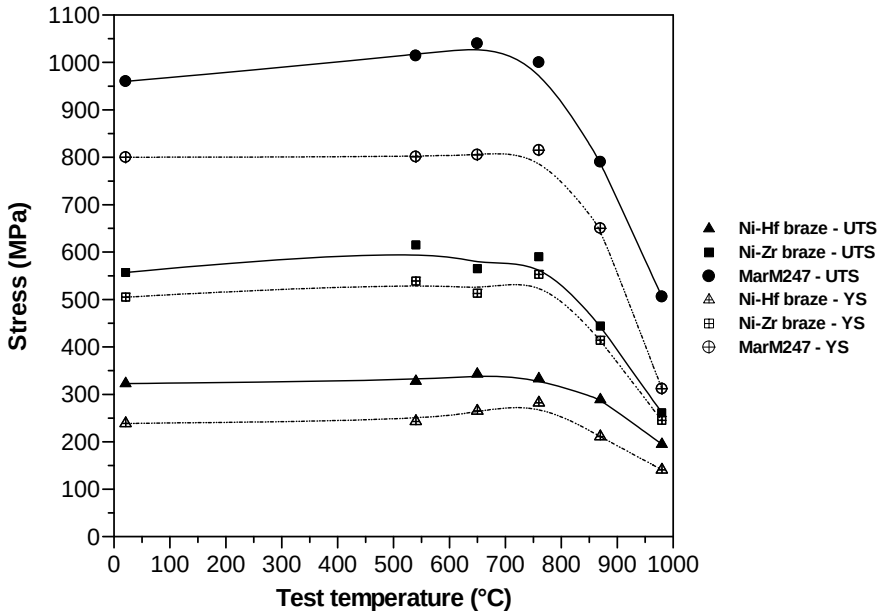

Figure 84 – The tensile strength (UTS) and yield strength (YS) of the Ni-Hf and Ni-Zr braze joints and the MarM247 parent metal as a function of the test temperature (each data point shown represents the average of three tests).

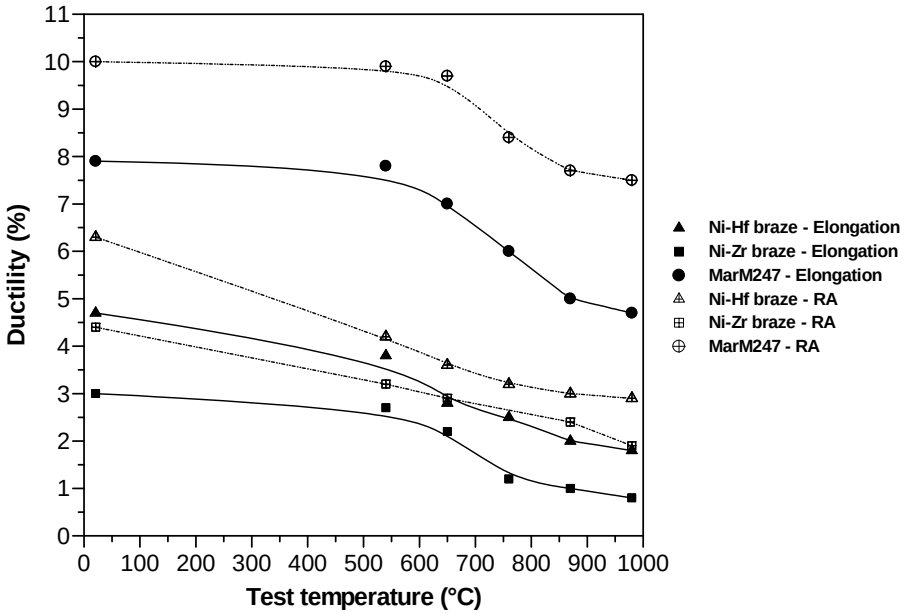

Figure 85 – The ductility of the Ni-Hf and Ni-Zr braze joints and the MarM247 parent metal expressed as % elongation and % reduction in area (RA) as a function of the test temperature (each data point shown represents the average of three tests).

As shown in **Table 12**, the tensile and yield strengths of the Ni-Hf joints at 540°C were 32% and 30%, respectively, of the MarM247 base metal properties, whereas the tensile and yield strengths of the Ni-Zr joints were 55% and 67%, respectively, of those of the MarM247 base metal. The same trend is evident at 650°C, shown in **Table 13**, which indicates that the tensile and yield strengths of the Ni-Hf joints were approximately 33% of the MarM247 base metal properties, and those of the Ni-Zr joints 54% and 64%, respectively, of the MarM247 strength levels. The Ni-Hf joints were therefore considerably weaker than the Ni-Zr joints at 540°C and 650°C. As was the case at room temperature, however, the Ni-Hf joints displayed higher ductility than the Ni-Zr joints. At 540°C, the Ni-Hf joint had approximately 50% of the MarM247 ductility, compared to about 35% for the Ni-Zr joint. At 650°C, the ductility changed to 40% and 32% of the MarM247 ductility for the Ni-Hf and the Ni-Zr joints, respectively.

At higher temperatures, the tensile and yield strengths of the Ni-Hf LPDB joints increased slightly relative to those of the base metal, as shown in **Figure 84** and **Tables 14 to 16** for test temperatures of 760°C, 870°C and 980°C, respectively. The Ni-Hf joint tensile strength increased from 33% of the base metal strength at 760°C, to 37% at 870°C and 39% at 980°C. This trend was not observed for the Ni-Zr joints, with the tensile strength changing from 59% of the base metal strength, to 56% and finally to 52% as the test temperature increased. The yield strength of the Ni-Hf joints changed from 35% of the base metal yield strength at 760°C, to 33% at 870°C and 45% at 980°C. Corresponding yield strength values for the Ni-Zr joint were at 68%, 64% and 79% of the base metal yield strength at 760°C, 870°C and 980°C, respectively. After short processing times (40 minutes), the Ni-Hf joints therefore remained considerably weaker than the Ni-Zr joints as the test temperature increased. The ductility of the Ni-Hf joints was, however, higher than that of the Ni-Zr joints, regardless of test temperature. Ductility values for the Ni-Hf joints changed from 42% of the base metal ductility at 760°C, to 40% at 870°C and 38% at 980°C. Corresponding ductility values for the Ni-Zr joints were approximately 20% of the base metal ductility at 760°C and 870°C, and about 17% at 980°C.

4.4) Conclusions

- A relatively dense, low porosity LPDB joint, with a microstructure consisting of MarM247 powder particles surrounded by Ni-Hf or Ni-Zr braze alloy, formed during processing at 1230°C for 40 minutes. The braze microstructure consisted of γ dendrites and Ni_5Zr or Ni_7Hf_2 intermetallic compound in the form of thick layers surrounding each MarM247 powder particle.

- At all test temperatures (room temperature and at elevated temperatures of 540°C, 650°C, 760°C, 870°C and 980°C), the tensile and yield strengths of the Ni-Zr joints exceeded those of the Ni-Hf joints after short processing times (40 minutes). The tensile and yield strengths of the Ni-Hf joints were typically only about 30 to 40% of those of the MarM247 base metal. For the Ni-Zr joints, the tensile and yield strengths were in the range of 52 to 62% of the MarM247 base metal properties.

- The Ni-Hf joints, however, displayed superior ductility compared to the Ni-Zr joints. Depending on the test temperature, the Ni-Hf joints exhibited ductility on the order of 38 to 60% of that of the MarM247 base metal, whereas the Ni-Zr joints had ductility values in the region of 17 to 40% of the ductility of the MarM247 base metal.

- The ductility of the novel braze alloys containing Hf or Zr as melt point depressant was significantly higher than the ductility of similar joints containing boron as melt point depressant. Boron-containing joints typically exhibit ductility values in the range of 0.5 to 1.0% after short processing times.

- The results described in this chapter were obtained after short processing times of 40 minutes. Longer brazing cycles are frequently used to diffuse melt point depressants into the parent metal and to reduce the occurrence of brittle eutectic phases in the braze joint (as described in Chapter 1). In order to determine whether such an extended brazing cycle will reduce or even eliminate the eutectic films of γ and Ni_5Zr or Ni_7Hf_2 intermetallic compound around the MarM247 powder particles, the brazing time was increased to 4 hours at 1230^{o}C. The results obtained after extended brazing cycle are described in Chapter 5.

CHAPTER 5 - EXPERIMENT 3

CHARACTERIZATION OF THE MICROSTRUCTURE AND MECHANICAL PROPERTIES OF LIQUID PHASE DIFFUSION BONDS USING EUTECTIC Ni-Hf AND Ni-Zr BRAZE ALLOYS AFTER LONGER PROCESSING TIMES (4 HOURS)

5.1) Introduction

The results described in Chapter 4 revealed that a reasonably dense, low porosity LPDB joint, consisting of Ni-Hf or Ni-Zr braze filler metal and MarM247 Ni-base superalloy powder, can be produced using a short brazing cycle (40 minutes at 1230^{o}C). The braze joints consisted of the original MarM247 powder particles encircled by a layer of braze alloy containing γ phase and a Ni_5Zr or Ni_7Hf_2 intermetallic compound.

Experiment 3, described in this chapter, aimed at determining whether a longer brazing time (4 hours at 1230^{o}C) leads to an improvement in the mechanical properties of the brazed joint due to diffusion of the melt point depressant (Hf or Zr) from the braze alloy into the parent metal. If diffusion of the melt point depressant is promoted by the longer brazing cycle, the layers of eutectic braze alloy around the MarM247 powder particles may be reduced in thickness or even eliminated.

5.2) Experimental procedure

In order to study the influence of a longer brazing time, LPDB samples joining In738 parent material were prepared using the procedure described in §4.2. The vacuum brazing cycle, shown below, differed from that used in Experiment 2 (Chapter 4) only in the extended brazing time (4 hours).

1) Ramp up to a temperature of 450^{o}C at a minimum rate of 9^{o}C/minute.
2) Hold at 450^{o}C for 20 minutes to allow the binder to burn off.
3) Ramp up to a temperature of 1150^{o}C at a minimum rate of 9^{o}C/minute.
4) Hold at 1150^{o}C for 20 minutes to allow the samples to stabilize at this temperature.
5) Ramp up to a temperature of 1230^{o}C at a minimum rate of 9^{o}C/minute to melt the Ni-Hf and Ni-Zr braze alloys and to allow the melt to infiltrate the MarM247 powder.
6) Hold at 1230^{o}C for 4 hours.
7) Furnace cool to room temperature.

After exposing the samples to the vacuum LPDB cycle described above, the samples were sectioned, mounted and polished using conventional metallographic practices. The polished metallographic samples were etched with Marble's reagent, and characterized using optical and scanning electron microscopy techniques.

In order to characterize the mechanical properties of the joints, tensile tests were performed at room temperature, and at temperatures of 540^{o}C, 650^{o}C, 760^{o}C, 870^{o}C and 980^{o}C. The tensile samples were prepared by joining MarM247 plate material using the LPDB process and the vacuum brazing cycle described above. After brazing, the tensile test samples were aged at 870^{o}C for 20 hours. The dimensions of the tensile test samples used in this investigation were previously given in **Figure 69**. The LPDB joint was 1.5 mm wide to simulate typical crack widths found in Industrial Gas Turbine (IGT) components, and was located in the centre of the sample gauge length.

5.3) Results and discussion

5.3.1 Microstructural investigation:

The microstructure of the Ni-Hf LPDB joint processed at 1230°C for 4 hours is shown in **Figures 86 to 89.** The joint consists of the original MarM247 powder particles, separated by layers of Ni-Hf braze alloy. It is evident from **Figures 87 and 88** that the layers of γ and Ni_7Hf_2 intermetallic compound between the MarM247 powder particles are finer and less continuous (compared with those shown in **Figures 72 and 73** for a brazing time of 40 minutes). This supports the premise stated in §5.1 that an extended brazing cycle promotes the diffusion of the melt point depressant (Hf) into the parent metal and minimizes the occurrence of intermetallic-containing eutectic component in the braze. This should lead to an improvement in mechanical properties.

The microstructure of the LPDB joint produced using MarM247 powder and Ni-Zr braze paste is shown in **Figures 90 to 93** at various magnifications. The original MarM247 powder particles are evident as the lighter, more equiaxed component, while the darker regions consist of Ni-Zr braze alloy. The braze alloy contains γ dendrites and Ni_5Zr intermetallic compound, but the layers of braze metal around each MarM247 particle appear less continuous and considerably finer than those observed after processing for 40 minutes at 1230°C (**Figures 79 to 81**).

The islands of braze alloy retained between the MarM247 particles resemble the intergranular carbides often observed in Ni-base superalloys (see **Figure 2**). The structures shown in **Figures 86 to 93** can be viewed as consisting of a mixture of fine and coarse-grained material, dispersed with intergranular γ and Ni_7Hf_2 or Ni_5Zr compounds. It is hoped that the mixture of coarse and fine grains within the braze joint will ensure a good combination of high tensile strength (promoted by a fine grain size) and good creep rupture strength (promoted by a coarse grain structure).

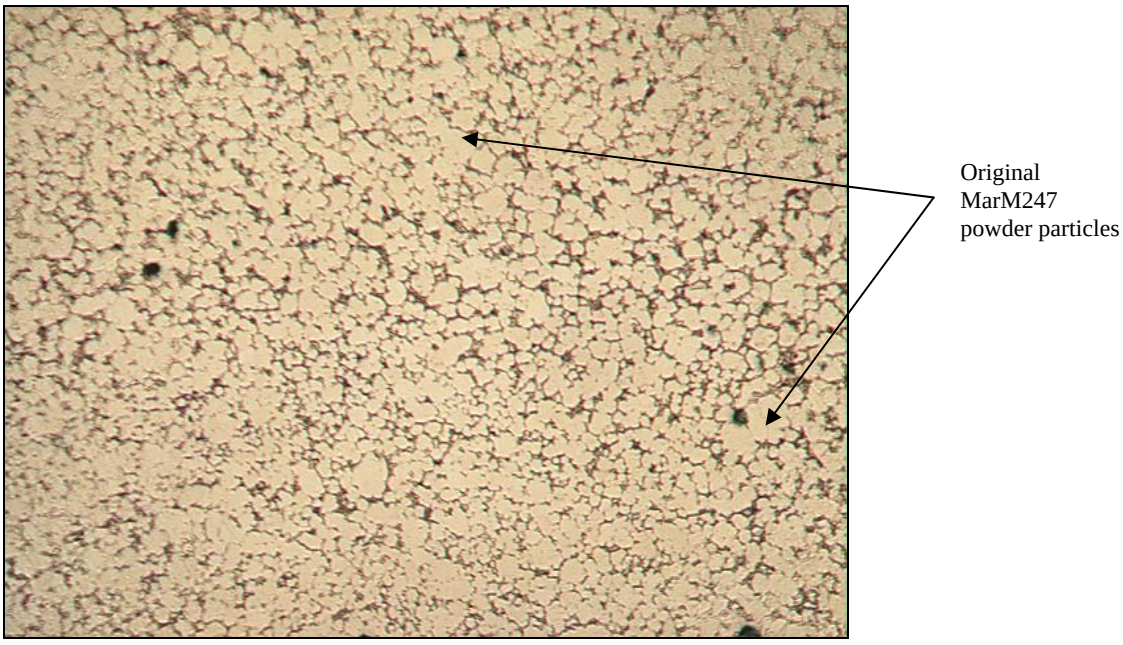

Figure 86 - Ni-Hf braze dispersed between MarM247 powder particles after brazing at 1230°C for 4 hours. Magnification: 50X.

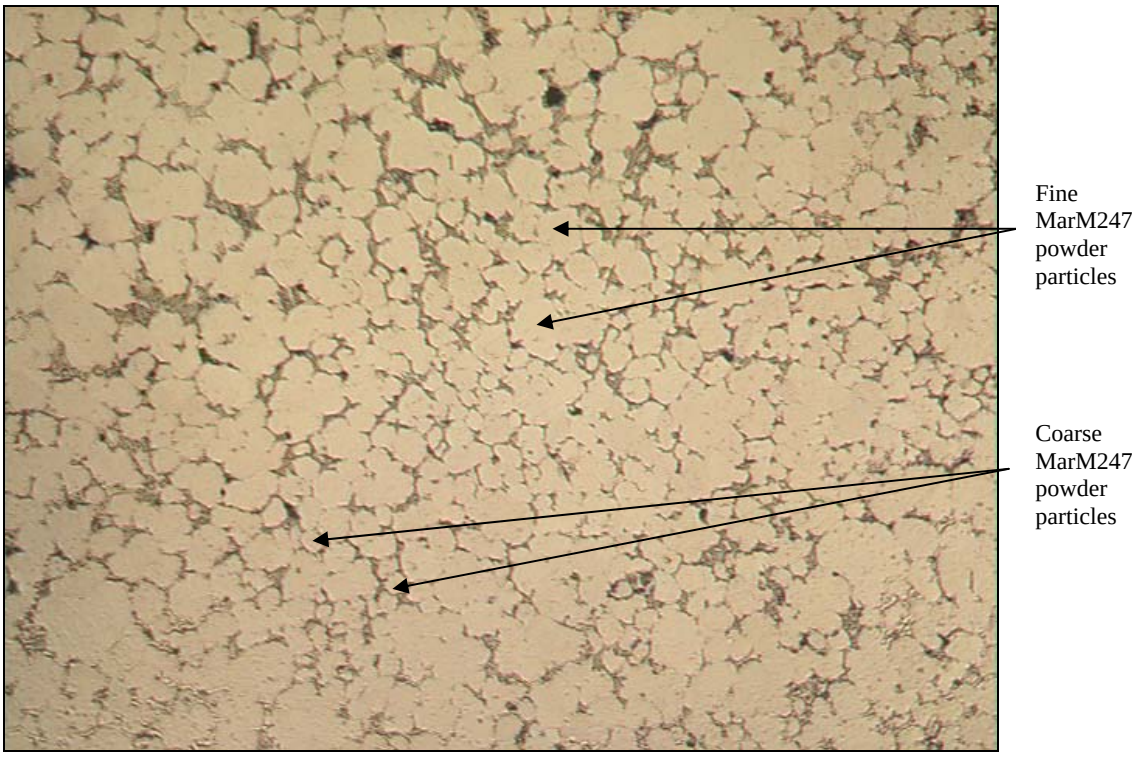

Figure 87 - Ni-Hf braze dispersed between MarM247 powder particles after brazing at 1230°C for 4 hours. Magnification: 100X.

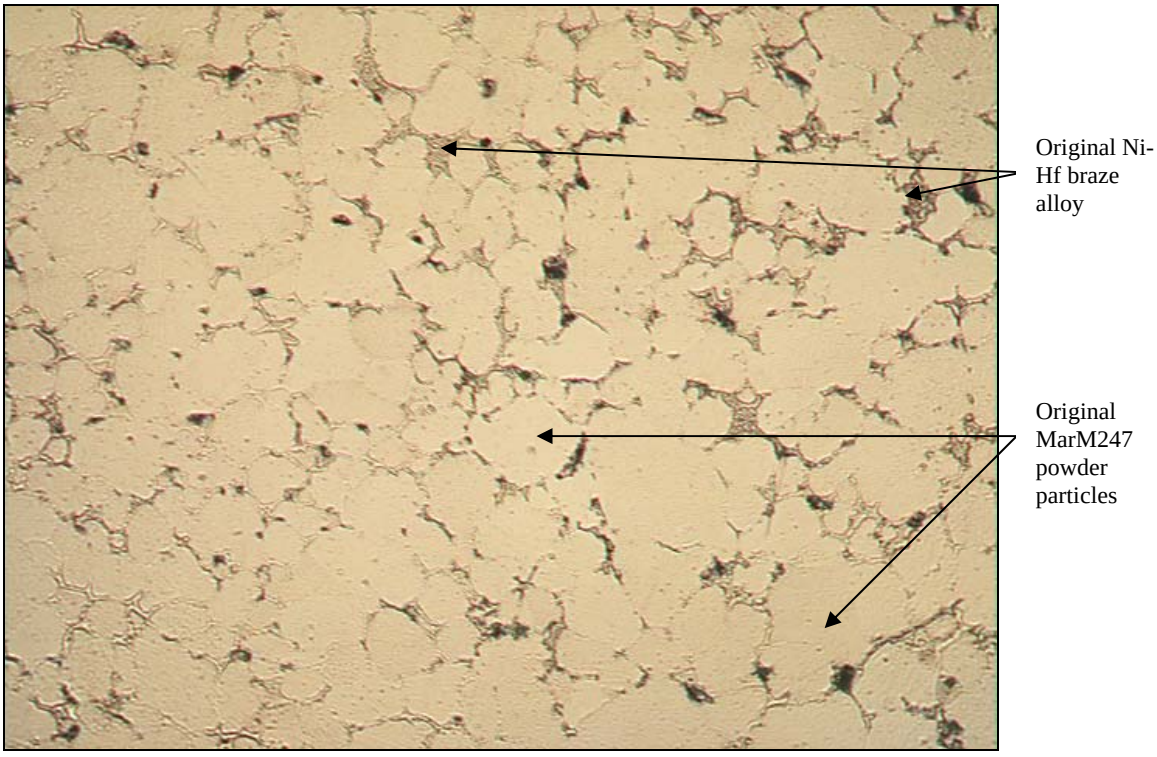

Figure 88 - Ni-Hf braze dispersed between MarM247 powder particles after brazing at 1230°C for 4 hours. Magnification: 200X.

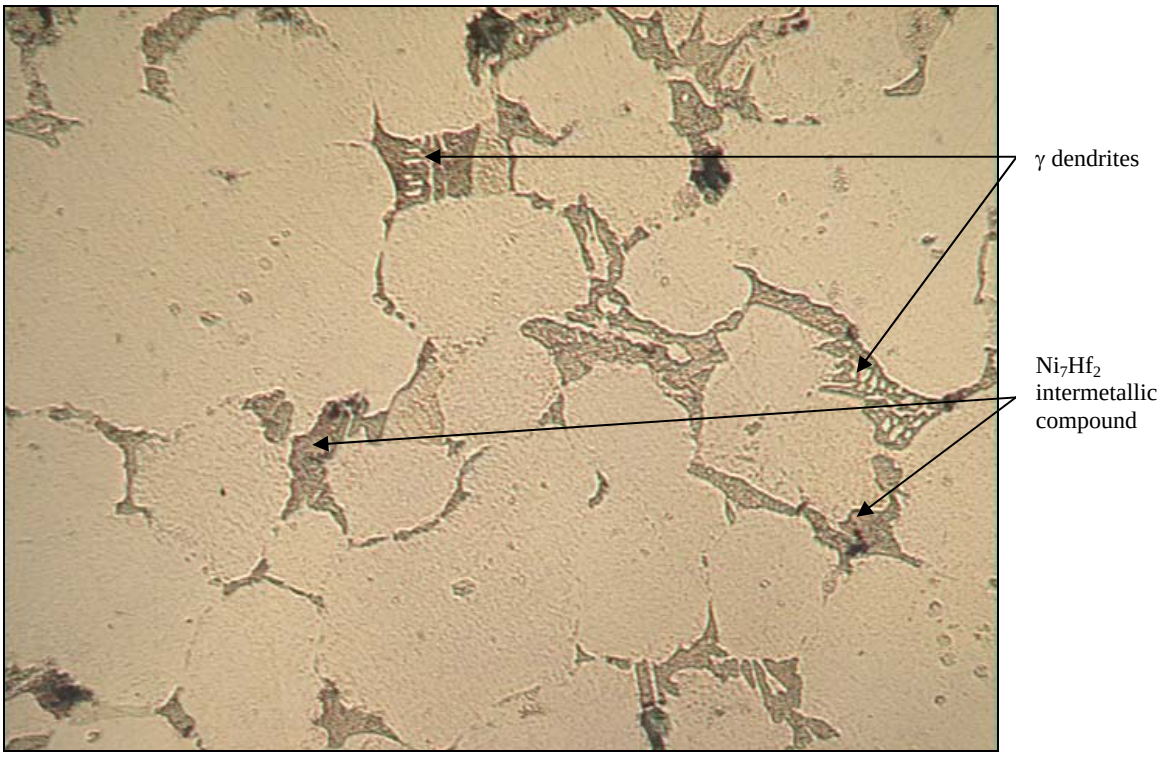

Figure 89 - Ni-Hf braze dispersed between MarM247 powder particles after brazing at 1230°C for 4 hours. Magnification: 500X.

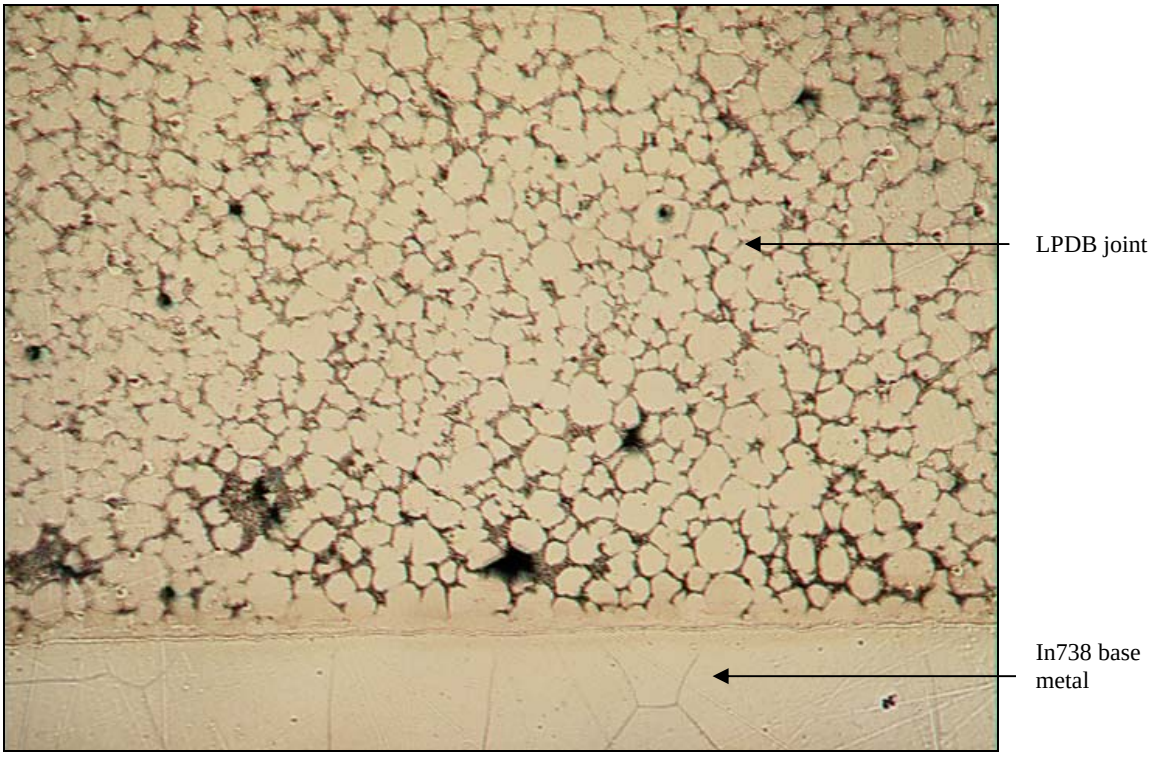

Figure 90 - Ni-Zr braze dispersed between MarM247 powder particles after brazing at 1230°C for 4 hours. Magnification: 50X.

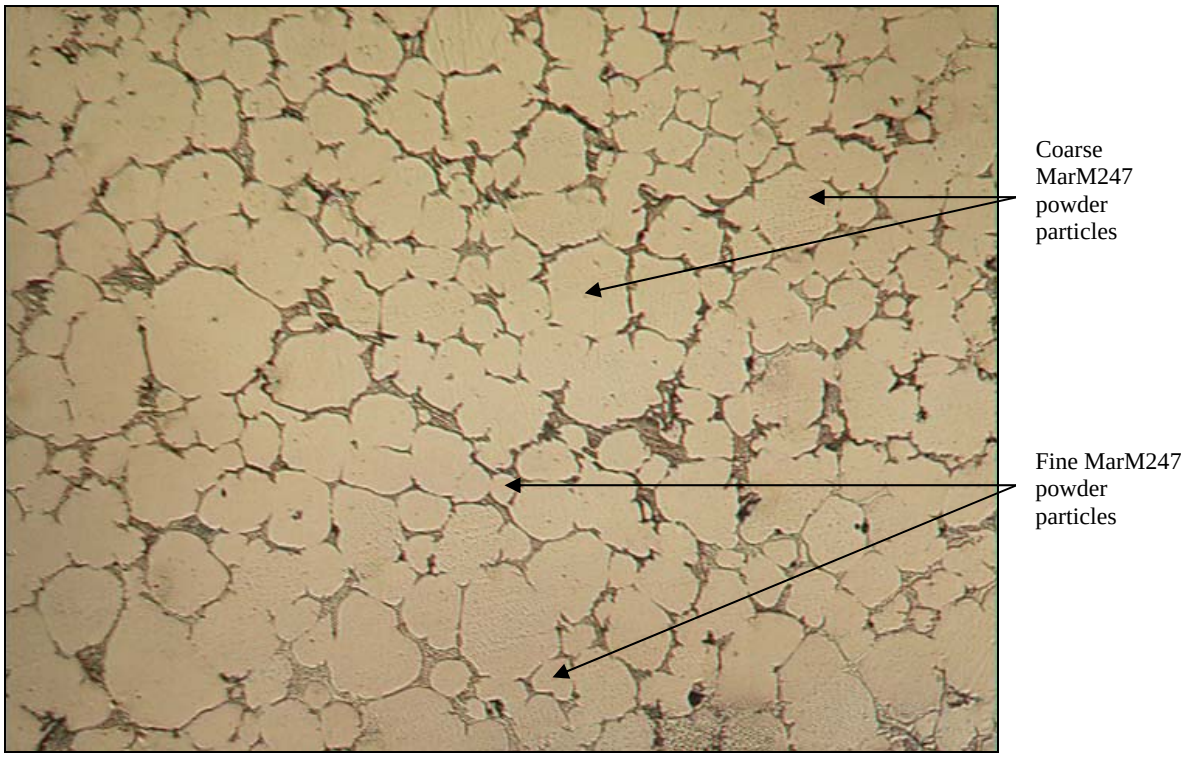

Figure 91 - Ni-Zr braze dispersed between MarM247 powder particles after brazing at 1230°C for 4 hours. Magnification: 100X.

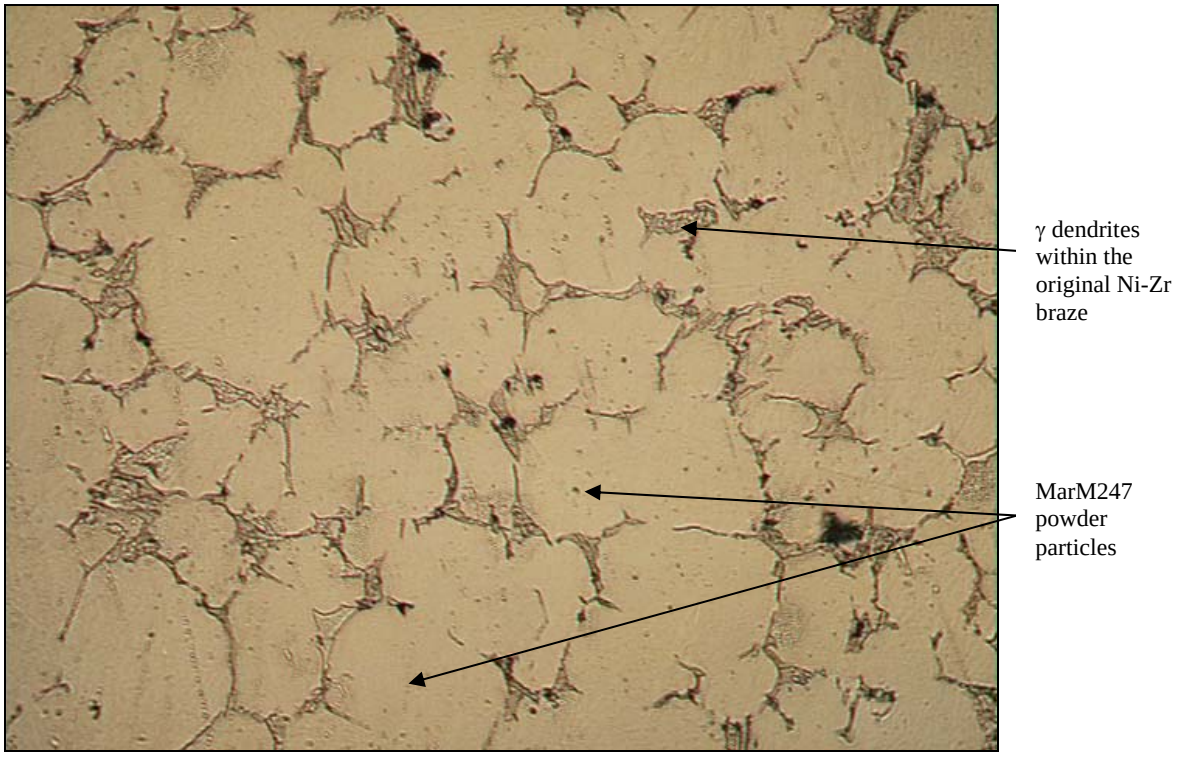

Figure 92 - Ni-Zr braze dispersed between MarM247 powder particles after brazing at 1230°C for 4 hours. Magnification: 200X.

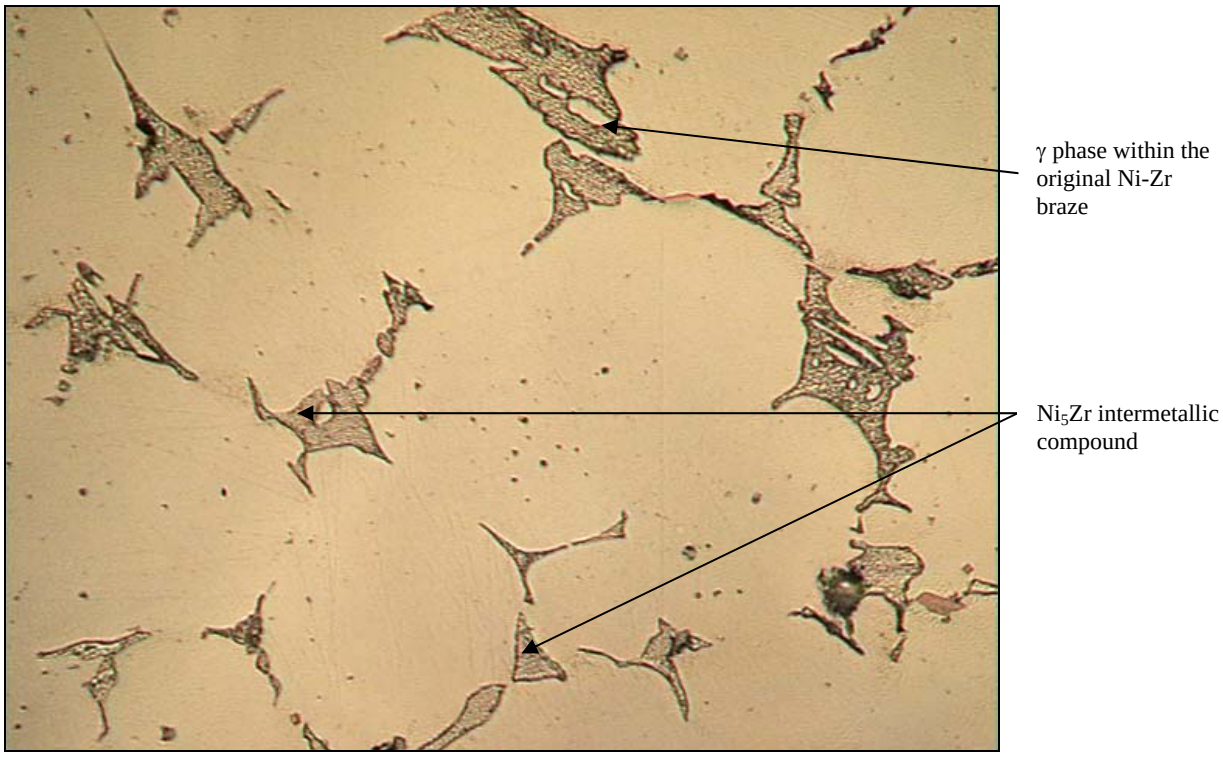

Figure 93 - Ni-Zr braze dispersed between MarM247 powder particles after brazing at 1230°C for 4 hours. Magnification: 500X.

Figure 94 displays a SEM micrograph of the MarM247/Ni-Hf joint brazed at 1230°C for 4 hours. Two phases, highlighted by the arrows in **Figure 94,** were analyzed using the SEM-EDS technique. The phase arbitrarily labelled "grain boundary particle" was identified as γ dendrites (with a composition of 75.27Ni-6.26Co-6.88Cr-3.67Al-2.29W-2.22Fe-1.93Mo-0.73Ti-0.74Zr) (wt. %). The second phase, arbitrarily labelled "grain boundary film", had a composition of 49.50Ni-46.56Hf-1.36W-2.01Co-0.38Cr-0.19Ti (wt.%). This phase was provisionally identified as the Ni_7Hf_2 intermetallic phase, with small amounts of W, Co, Cr and Ti in solution.

A SEM micrograph of the MarM247/Ni-Zr joint after brazing at 1230°C for 4 hours is shown in **Figure 95**. SEM-EDS analysis revealed that the phase arbitrarily labelled "grain boundary particle" consisted of 79.54Ni-5.90Co-5.34Cr-3.98Al-1.81W-11.11Fe-0.85Mo-0.64Ti-0.83Zr (wt.%). On the basis of this composition, the "grain boundary particle" phase was identified as γ. The second phase was arbitrarily labelled "grain boundary film", and consisted of 71.35Ni-24.47Zr-0.70W-2.28Co-0.61Cr-0.16Mo-0.43Al (wt.%). This phase was identified as the Ni_5Zr intermetallic phase, with some W, Co, Cr, Mo and Al in solution.

5.3.2 Tensile test results:

The results of tensile tests performed at various temperatures are shown in **Tables 17 to 22** and presented graphically in **Figures 96 to 99**. The values shown represent the average of three tests.

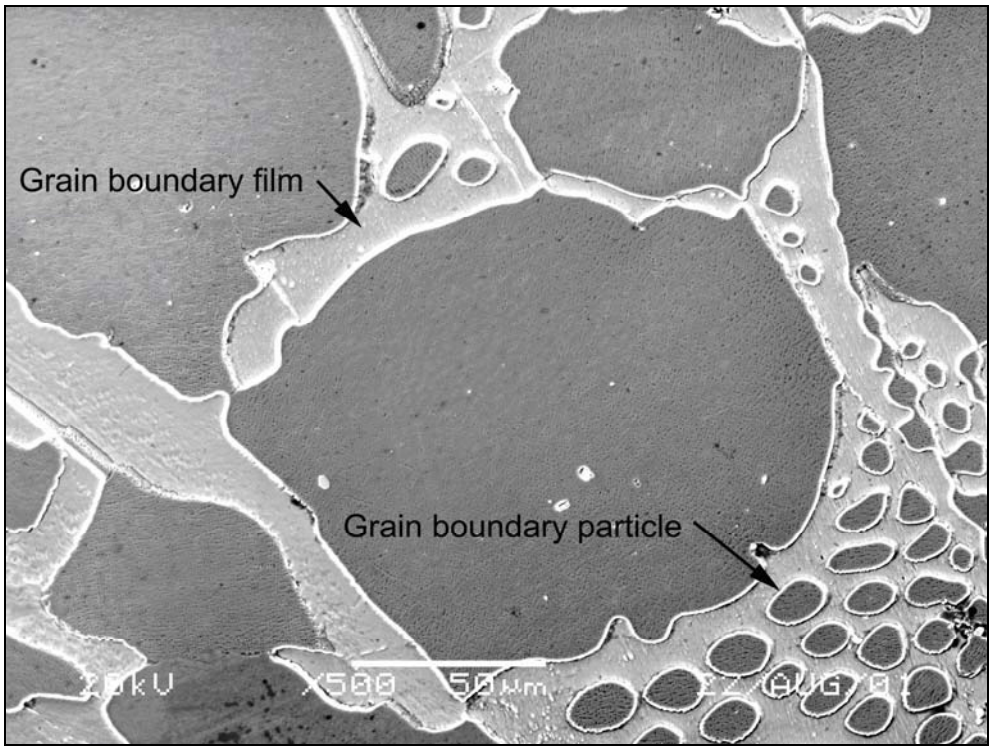

Figure 94 – SEM micrograph of the Ni-Hf braze, showing the phases identified as γ (labelled "grain boundary particle") and Ni_7Hf_2 (labelled "grain boundary film").

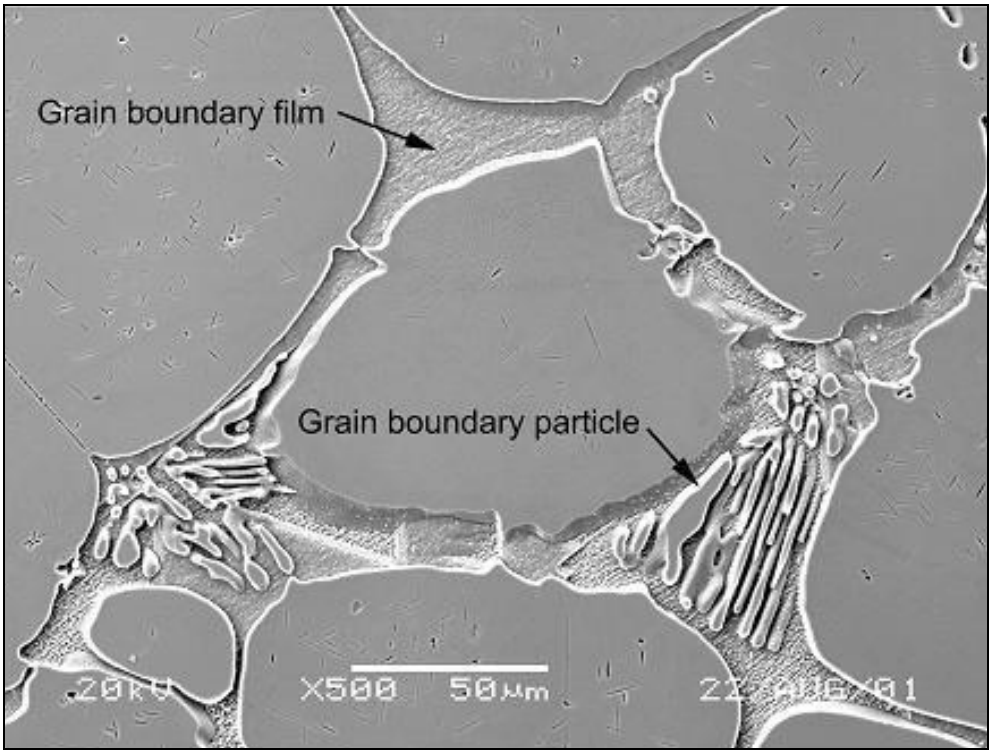

Figure 95 – SEM micrograph of the Ni-Zr braze, showing the phases identified as γ (labelled "grain boundary particle") and Ni_5Zr (labelled "grain boundary film").

Table 17 – Joint tensile properties measured at 21°C.

Tensile properties	**Ni-Hf joints** 1230°C for 40 min.	**Ni-Hf joints** 1230°C for 4 hours	**Ni-Zr joints** 1230°C for 40 min.	**Ni-Zr joints** 1230°C for 4 hours	**MarM247 Base metal**
Tensile strength	323 MPa (46.8 ksi)	344 MPa (49.8 ksi)	557 MPa (80.7 ksi)	564 MPa (81.7 ksi)	960 MPa (139 ksi)
Yield strength	239 MPa (34.7 ksi)	302 MPa (43.8 ksi)	505 MPa (73.2 ksi)	511 MPa (74.0 ksi)	800 MPa (116 ksi)
Elongation (%)	4.7	2.7	3.0	3.0	7.9
Reduction in area (%)	6.3	3.9	4.4	4.5	10.0

Table 18 – Joint tensile properties measured at 540°C.

Tensile properties	**Ni-Hf joints** 1230°C for 40 min.	**Ni-Hf joints** 1230°C for 4 hours	**Ni-Zr joints** 1230°C for 40 min.	**Ni-Zr joints** 1230°C for 4 hours	**MarM247 Base metal**
Tensile strength	328 MPa (47.6 ksi)	406 MPa (58.9 ksi)	619 MPa (89.7 ksi)	625 MPa (90.6 ksi)	1014 MPa (147 ksi)
Yield strength	243 MPa (35.2 ksi)	329 MPa (47.7 ksi)	539 MPa (78.1 ksi)	556 MPa (80.6 ksi)	801 MPa (116 ksi)
Elongation (%)	3.8	3.0	2.7	2.8	7.9
Reduction in area (%)	4.2	3.8	3.2	3.4	10.0

Table 19 – Joint tensile properties measured at 650°C.

Tensile properties	**Ni-Hf joints** 1230°C for 40 min.	**Ni-Hf joints** 1230°C for 4 hours	**Ni-Zr joints** 1230°C for 40 min.	**Ni-Zr joints** 1230°C for 4 hours	**MarM247 Base metal**
Tensile strength	343 MPa (49.7 ksi)	408 MPa (59.1 ksi)	562 MPa (81.4 ksi)	569 MPa (82.5 ksi)	1040 MPa (151 ksi)
Yield strength	265 MPa (38.4 ksi)	308 MPa (44.7 ksi)	513 MPa (74.4 ksi)	501 MPa (72.6 ksi)	805 MPa (117 ksi)
Elongation (%)	2.8	3.1	2.2	2.3	7.0
Reduction in area (%)	3.6	3.8	2.9	2.9	9.7

Table 20 – Joint tensile properties measured at 760°C.

Tensile properties	**Ni-Hf joints** 1230°C for 40 min.	**Ni-Hf joints** 1230°C for 4 hours	**Ni-Zr joints** 1230°C for 40 min.	**Ni-Zr joints** 1230°C for 4 hours	**MarM247 Base metal**
Tensile strength	333 MPa (48.3 ksi)	464 MPa (67.2 ksi)	593 MPa (85.9 ksi)	602 MPa (87.3 ksi)	1000 MPa (145 ksi)
Yield strength	282 MPa (40.8 ksi)	380 MPa (55.1 ksi)	553 MPa (80.1 ksi)	524 MPa (75.9 ksi)	815 MPa (118 ksi)
Elongation (%)	2.5	2.9	1.2	2.2	6.0
Reduction in area (%)	3.2	3.0	5.9	4.3	8.4

Table 21 – Joint tensile properties measured at 870°C.

Tensile properties	**Ni-Hf joints** 1230°C for 40 min.	**Ni-Hf joints** 1230°C for 4 hours	**Ni-Zr joints** 1230°C for 40 min.	**Ni-Zr joints** 1230°C for 4 hours	**MarM247 Base metal**
Tensile strength	289 MPa (41.9 ksi)	342 MPa (49.6 ksi)	444 MPa (64.4 ksi)	480 MPa (69.6 ksi)	790 MPa (115 ksi)
Yield strength	211 MPa (30.5 ksi)	277 MPa (40.1 ksi)	414 MPa (60.0 ksi)	404 MPa (58.6 ksi)	650 MPa (94 ksi)
Elongation (%)	2.0	2.2	1.0	2.1	5.0
Reduction in area (%)	3.0	3.2	2.4	3.1	7.7

Table 22 – Joint tensile properties measured at 980°C.

Tensile properties	**Ni-Hf joints** 1230°C for 40 min.	**Ni-Hf joints** 1230°C for 4 hours	**Ni-Zr joints** 1230°C for 40 min.	**Ni-Zr joints** 1230°C for 4 hours	**MarM247 Base metal**
Tensile strength	195 MPa (28.3 ksi)	266 MPa (38.6 ksi)	261 MPa (37.8 ksi)	308 MPa (44.7 ksi)	506 MPa (73 ksi)
Yield strength	141 MPa (20.4 ksi)	206 MPa (29.9 ksi)	245 MPa (35.5 ksi)	214 MPa (31.0 ksi)	312 MPa (45 ksi)
Elongation (%)	1.8	2.7	0.8	3.1	4.7
Reduction in area (%)	2.9	3.1	1.9	6.2	7.5

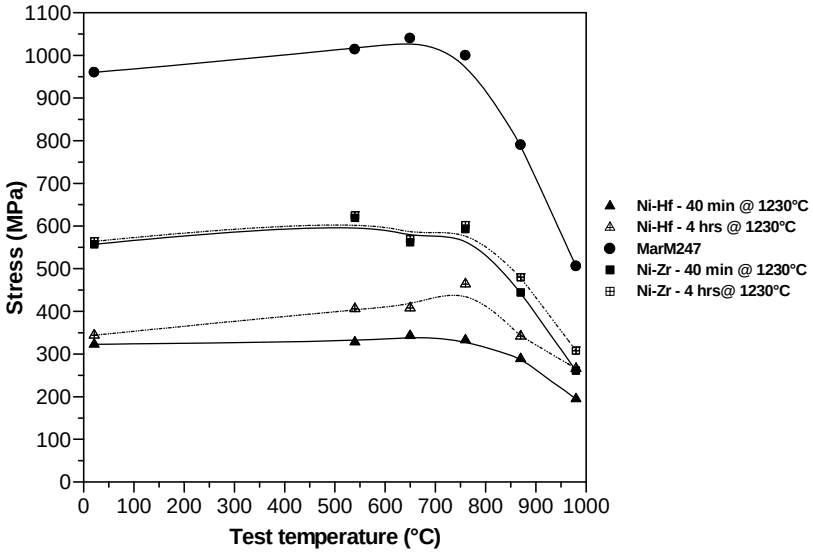

Figure 96 – The tensile strength (UTS) of the Ni-Hf and Ni-Zr braze joints and the MarM247 parent metal as a function of the test temperature and braze time (each data point shown represents the average of three tests).

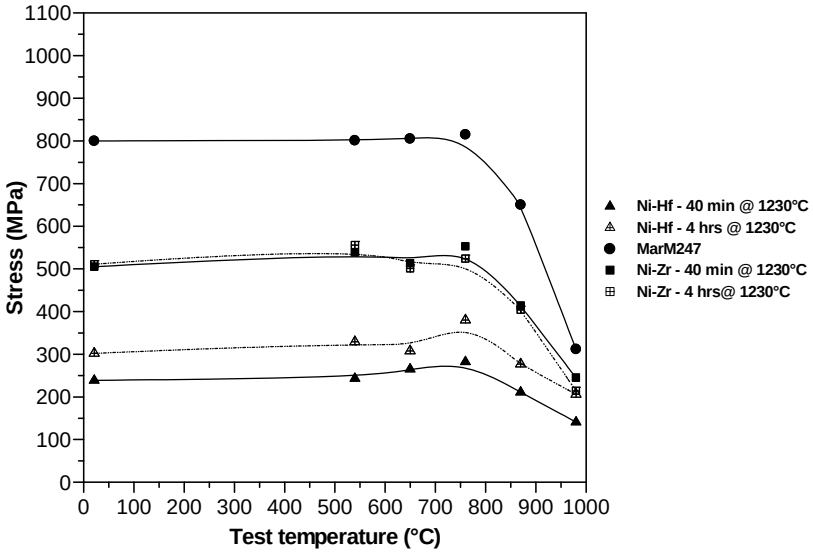

Figure 97 – The yield stress of the Ni-Hf and Ni-Zr braze joints and the MarM247 parent metal as a function of the test temperature and braze time (each data point shown represents the average of three tests).

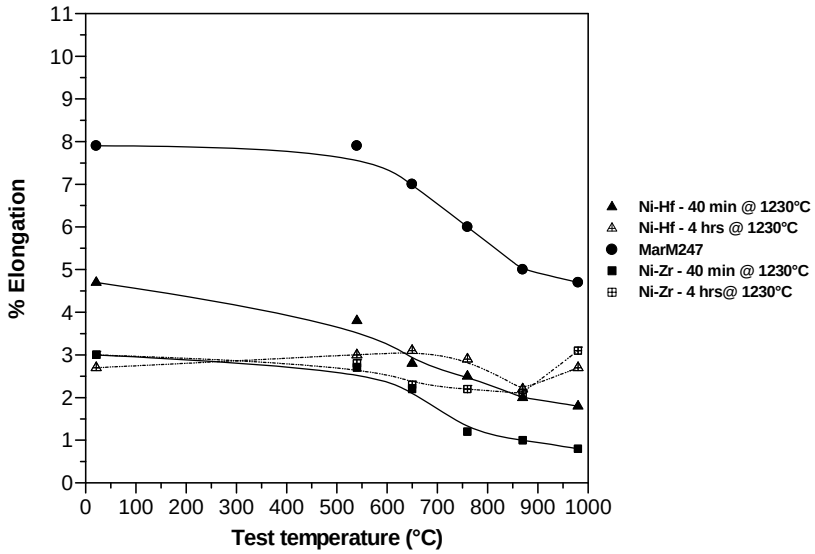

Figure 98 – The % elongation measured for the Ni-Hf and Ni-Zr braze joints and the MarM247 parent metal as a function of the test temperature and braze time (each data point shown represents the average of three tests).

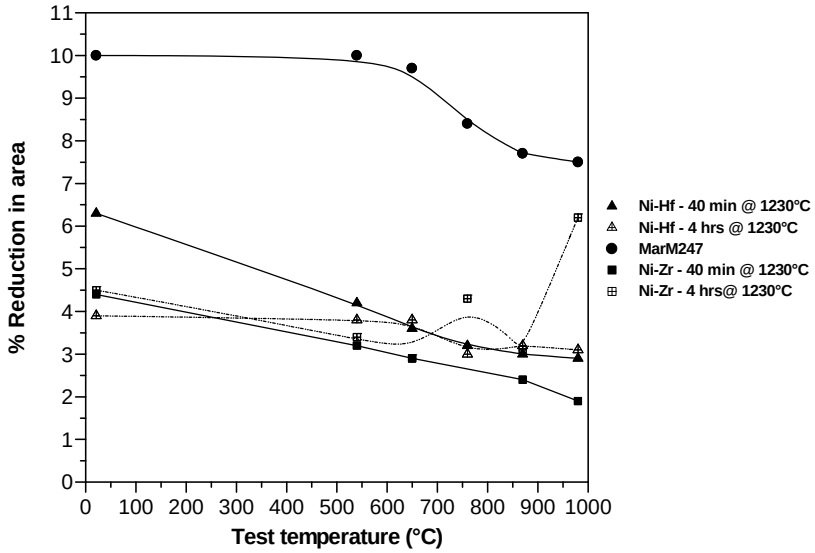

Figure 99 – The % reduction in area measured for the Ni-Hf and Ni-Zr braze joints and the MarM247 parent metal as a function of the test temperature and braze time (each data point shown represents the average of three tests).

As shown in **Figures 96 and 97**, the tensile and yield strengths of the Ni-Hf braze alloy were improved considerably over the entire range of tensile test temperatures by increasing the brazing time. The measured joint tensile strength values ranged from approximately 36% of the base metal tensile strength at room temperature, to about 53% at a test temperature of 980°C. The measured yield strength values ranged from about 38% (at room temperature) to 56% of the base metal yield strength (at 980°C). This suggests that the longer braze cycle facilitated the diffusion of the melt point depressant into the parent metal (as suggested by **Figures 87 to 89**), reducing the amount of brittle intermetallic compound in the joint and allowing the mechanical properties of the braze joint to approach those of the MarM247

superalloy powder. The longer braze time reduced the ductility of the joint at lower test temperatures, but at higher temperatures the ductility was improved (**Figures 98 and 99**).

The tensile and yield strength values of the Ni-Zr braze joint exceeded those of the Ni-Hf joint at all test temperatures, attaining levels of approximately 60% of the base metal tensile strength, and up to 70% of the base metal yield strength after brazing for 4 hours (**Figures 96 and 97**). The longer braze time, however, did not improve the joint strength to any significant extent. A significant improvement in ductility was, however, evident after 4 hours at 1230°C, particularly at higher test temperatures. The measured joint ductility ranged from about 38% of the base metal ductility at room temperature, to approximately 74% at 980°C (**Figures 98 and 99**).

5.4) Conclusions

- A relatively dense, low porosity LPDB joint, with a microstructure consisting of MarM247 powder particles surrounded by Ni-Hf or Ni-Zr braze alloy, formed during processing at 1230°C for 4 hours. The braze microstructure consisted of γ dendrites and Ni_5Zr or Ni_7Hf_2 intermetallic compound.

- Brazing at 1230°C for 4 hours, compared to 40 minutes, decreased the amount of Ni_5Zr/Ni_7Hf_2 intermetallic compound, and reduced the thickness of the layers of braze alloy surrounding the MarM247 powder particles. The regions of braze alloy between the powder particles appeared less continuous after 4 hours, and in many areas only isolated γ dendrites and Ni_5Zr/Ni_7Hf_2 phases existed between the superalloy particles.

- At all test temperatures, the tensile and yield strength values of the Ni-Zr joints exceeded those of the Ni-Hf joints. The measured Ni-Hf joint strength ranged from approximately 36% of the base metal tensile strength and 38% of the yield strength at room temperature, to about 53% of the tensile strength and 56% of the yield strength at a test temperature of 980°C. The Ni-Zr joint attained strength levels of approximately 60% of the base metal tensile strength, and up to 70% of the base metal yield strength after a braze time of 4 hours.

- A longer braze cycle (4 hours compared to 40 minutes at 1230°C) significantly improved the strength of the Ni-Hf joint, but had little effect on the strength of the Ni-Zr joint. Both joints exhibited a significant improvement in ductility after the extended braze cycle, particularly at higher test temperatures.

- The ductility of the novel braze alloys containing Hf or Zr as melt point depressant was significantly higher than the ductility of similar joints containing boron as melt point depressant. Boron-containing joints typically exhibit ductility values in the range of 0.5 to 1.0% after short processing times.

- The results described in this chapter were obtained after processing times of 4 hours. In order to determine whether an even longer brazing cycle will further reduce or even eliminate the eutectic films of γ and Ni_5Zr or Ni_7Hf_2 intermetallic compound around the MarM247 powder particles, the brazing time was increased to 12 hours at 1230°C. The results of this experiment are described in Chapter 6.

CHAPTER 6 - EXPERIMENT 4

CHARACTERIZATION OF THE MICROSTRUCTURE AND MECHANICAL PROPERTIES OF LIQUID PHASE DIFFUSION BONDS USING EUTECTIC Ni-Hf AND Ni-Zr BRAZE ALLOYS AFTER EXTENDED BRAZING TIMES (12 HOURS)

6.1) Introduction

The results described in Chapter 5 revealed that a reasonably dense, low porosity LPDB joint, consisting of Ni-Hf or Ni-Zr braze filler metal and MarM247 Ni-base superalloy powder, can be produced by brazing for 4 hours at 1230°C. After processing the braze joints consisted of the original MarM247 powder particles surrounded by a layer of γ phase and Ni_5Zr or Ni_7Hf_2 intermetallic compound. Increasing the braze time from 40 minutes to 4 hours reduced the thickness of the braze layer around the MarM247 powder particles and increased the tensile and yield strengths of the Ni-Hf braze joint at all test temperatures. The strength of the Ni-Zr joint was not improved significantly by extending the braze cycle, but the ductility of both braze joints was improved, particularly at higher test temperatures. These results suggest that the extended braze cycle promoted the diffusion of the melt point depressants from the braze metal into the parent plate, partially decomposing the brittle eutectic phases within the braze joints, and resulting in improved mechanical properties.

Since extending the braze cycle from 40 minutes to 4 hours yielded promising results, Experiment 4 aimed at determining whether an even longer braze cycle (12 hours at 1230°C, followed by solution annealing at the same temperature for an additional 4 hours) promotes further decomposition of the layers of γ and Ni_7Hf_2/Ni_5Zr surrounding the MarM247 powder particles. Creep rupture tests were also performed at various stress levels at three elevated temperatures in order to obtain preliminary creep/stress rupture properties for the MarM247/Ni-Zr and MarM247/Ni-Hf braze formulations.

6.2) Experimental procedure

Liquid phase diffusion bonding was used to join In738 parent material using the eutectic Ni-Hf and Ni-Zr braze alloys described in earlier chapters. The braze samples were prepared using the procedure presented in §4.2. The vacuum brazing cycle, shown below, differed from those described in Chapters 4 and 5 only in the extended brazing time (12 hours) used.

1) Ramp up to a temperature of 450°C at a minimum rate of 9°C/minute.
2) Hold at 450°C for 20 minutes to allow the binder to burn off.
3) Ramp up to a temperature of 1150°C at a minimum rate of 9°C/minute.
4) Hold at 1150°C for 20 minutes to allow the samples to stabilize at this temperature.
5) Ramp up to a temperature of 1230°C at a minimum rate of 9°C/minute to melt the Ni-Hf and Ni-Zr braze alloys and to allow the melt to infiltrate the MarM247 powder.
6) Hold at 1230°C for 12 hours.
7) Furnace cool to room temperature.

After joining the samples using the LPDB cycle described above, the brazed samples were placed in a production vacuum furnace equipped with quenching facilities in order to solution anneal the joints. Gas quenching, using 2 bar argon pressure, was utilized on completion of

the solution annealing cycle. A conventional vacuum solution heat treatment cycle, similar to that applied in industry to MarM247 Siemens Westinghouse blades operating in W501F turbine engines, was applied. The solution heat treatment used in this experiment was as follows:

1) Ramp up to a temperature of 1230°C at a minimum rate of 14°C per minute.
2) Hold at 1230°C for 4 hours.
3) Quench to room temperature at a rate of 50°C per minute.

After exposing the plates to the vacuum LPDB and solution heat treatment cycles described above, samples were sectioned, mounted and polished using conventional metallographic techniques. The polished metallographic samples were then etched with Marble's reagent, and characterized using optical and scanning electron microscopy.

In order to obtain preliminary creep/stress rupture properties for the novel braze formulations, creep rupture tests were performed at three temperatures: 845°C, 900°C and 980°C. Samples were subjected to three different applied stress levels at each test temperature, as indicated in **Table 23**. The creep rupture test samples were prepared by joining In738 plate material using the LPDB process and the vacuum brazing and solution heat treatment cycles described above. The dimensions of the test specimens used in this investigation were identical to those given in **Figure 69**. The joint was located in the centre of the gauge length and the joint gap was maintained at 1.5 mm to simulate typical crack widths found in Industrial Gas Turbine (IGT) components.

Table 23 - Creep rupture test conditions.

Test temperature	Stress level #1	Stress level #2	Stress level #3
845°C	345 MPa (50 ksi)	276 MPa (40 ksi)	228 MPa (33 ksi)
900°C	242 MPa (35 ksi)	186 MPa (27 ksi)	152 MPa (22 ksi)
980°C	138 MPa (20 ksi)	104 MPa (15 ksi)	76 MPa (11 ksi)

The metallographic examination and creep rupture tests were performed on samples in the solution annealed condition. In industry, In738 turbine components normally receive an aging heat treatment after solution annealing – typically at a temperature of approximately 1120°C for 2 hours, followed by an additional 24 hours at 845°C. Not aging the samples used in this experiment was an oversight on the author's part due to a misunderstanding. Even though the samples were not aged, the results presented in this chapter still allow a comparison between the Ni-Zr and Ni-Hf braze compositions. It must be borne in mind, however, that since the samples were tested in the solution heat treated condition without any aging, the material is likely to be softer and to exhibit enhanced ductility and reduced creep rupture strength compared to fully aged specimens.

6.3) Results and discussion

6.3.1 Microstructural investigation:

The microstructure of the Ni-Hf LPDB joint processed at 1230°C for 12 hours, followed by solution annealing, is shown in **Figures 100 to 103.** The joint consists of the original MarM247 powder particles, surrounded by layers of Ni-Hf braze alloy. This microstructure resembles the microstructure of the Ni-Hf joint processed at 1230°C for 4 hours, shown in

Figures 86 to 89. The layers of γ and Ni_7Hf_2 between the MarM247 powder particles appear finer and less continuous (compared with those shown in **Figures 72 and 73** for a brazing time of 40 minutes), supporting the conclusion that an extended brazing cycle promotes the diffusion of the melt point depressant (Hf) into the parent metal and minimizes the amount of brittle intermetallic compound in the braze.

The microstructure of the LPDB joint produced with MarM247 powder and Ni-Zr braze paste is shown in **Figures 104 to 107** at various magnifications. The original MarM247 powder particles are evident as the lighter, more equiaxed component, while the darker regions consist of retained eutectic Ni-Zr braze alloy. The microstructure of the MarM247/Ni-Zr joint processed at 1230°C for 12 hours, followed by solution heat treatment, resembles the microstructure shown in **Figures 90 to 93** for a braze cycle of 4 hours. The braze alloy contains γ dendrites and Ni_5Zr intermetallic compound, but the layers of braze metal around each MarM247 particle are less continuous and significantly finer than those observed after processing for 40 minutes at 1230°C (**Figures 79 to 81**). The islands of braze alloy retained between the MarM247 powder particles resemble the intergranular carbides often observed in Ni-base superalloys (see **Figure 2**). The structures shown in **Figures 100 to 107** can be viewed as consisting of a mixture of fine and coarse-grained superalloy material, dispersed with intergranular γ and Ni_7Hf_2/Ni_5Zr intermetallic compound. It is hoped that the mixture of coarse and fine grains within the braze joint will ensure a good combination of high tensile strength (promoted by a fine grain size) and good creep rupture strength (promoted by a coarse grain structure).

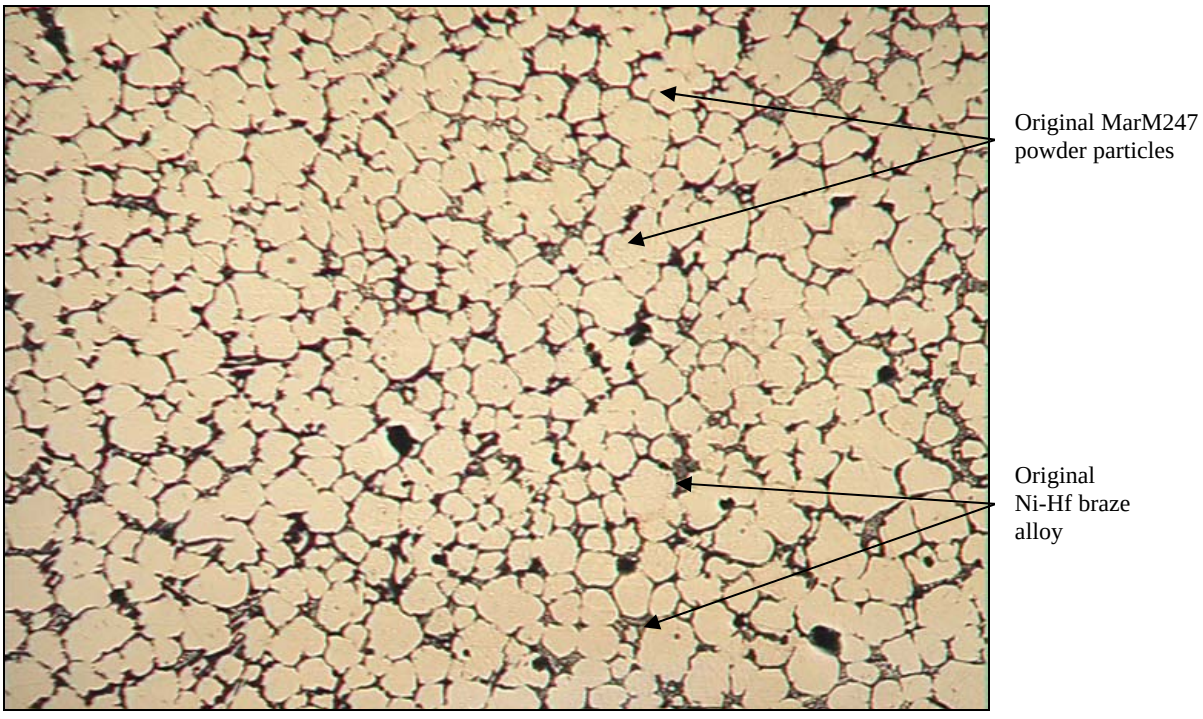

Figure 100 - Ni-Hf braze dispersed between MarM247 powder particles after brazing at 1230°C for 12 hours, followed by solution heat treatment at 1230°C for 4 hours and quenching. Magnification: 50X.

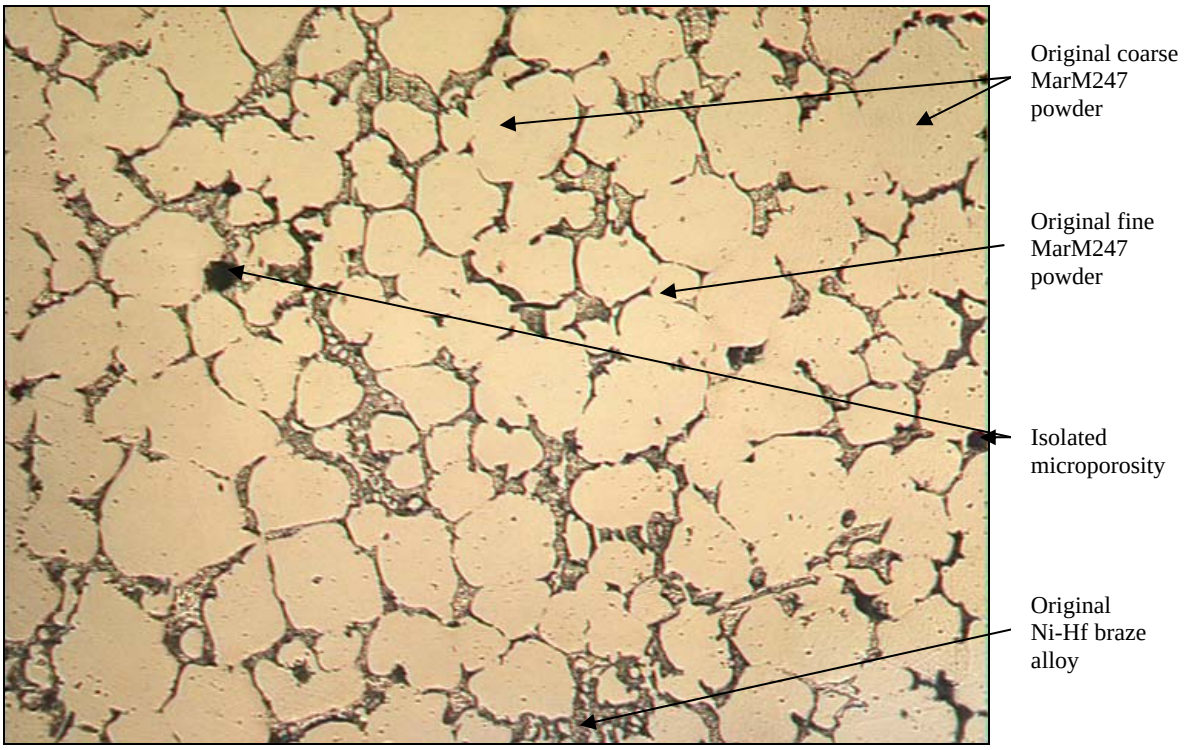

Figure 101 - Ni-Hf braze dispersed between MarM247 powder particles after brazing at 1230°C for 12 hours, followed by solution heat treatment at 1230°C for 4 hours and quenching. Magnification: 100X.

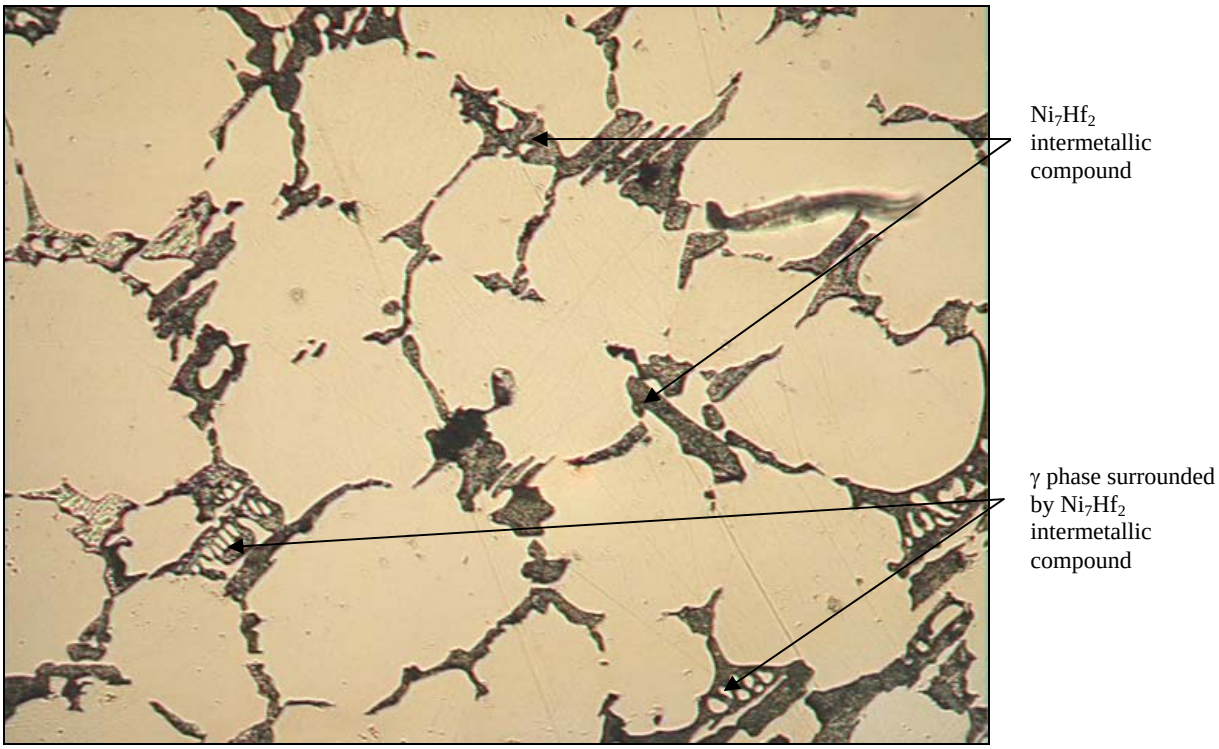

Figure 102 - Ni-Hf braze dispersed between MarM247 powder particles after brazing at 1230°C for 12 hours, followed by solution heat treatment at 1230°C for 4 hours and quenching. Magnification: 200X.

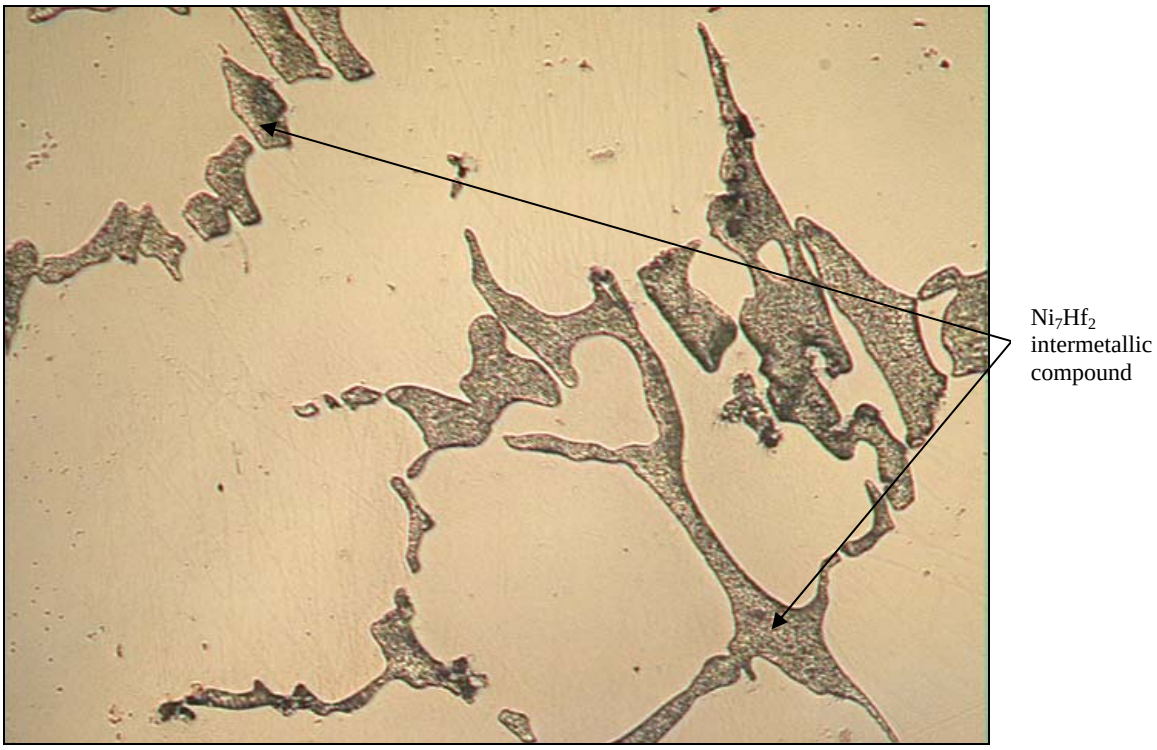

Figure 103 - Ni-Hf braze dispersed between MarM247 powder particles after brazing at 1230°C for 12 hours, followed by solution heat treatment at 1230°C for 4 hours and quenching. Magnification: 500X.

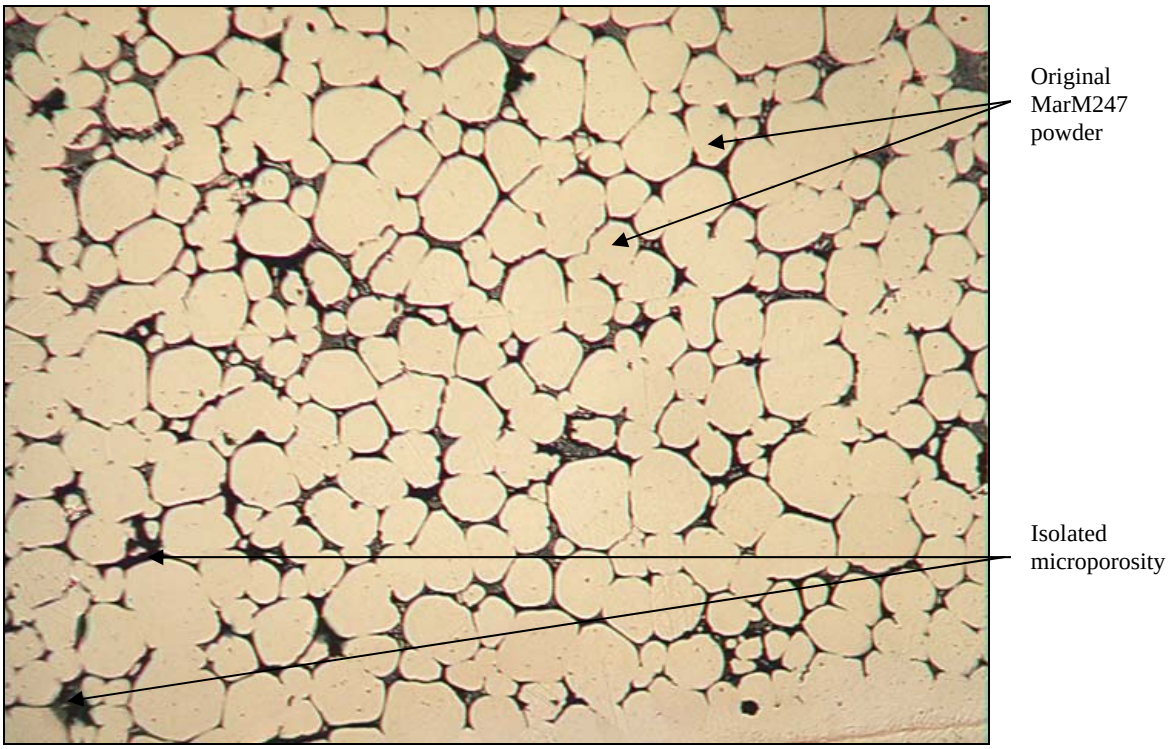

Figure 104 - Ni-Zr braze dispersed between MarM247 powder particles after brazing at 1230°C for 12 hours, followed by solution heat treatment at 1230°C for 4 hours and quenching. Magnification: 50X.

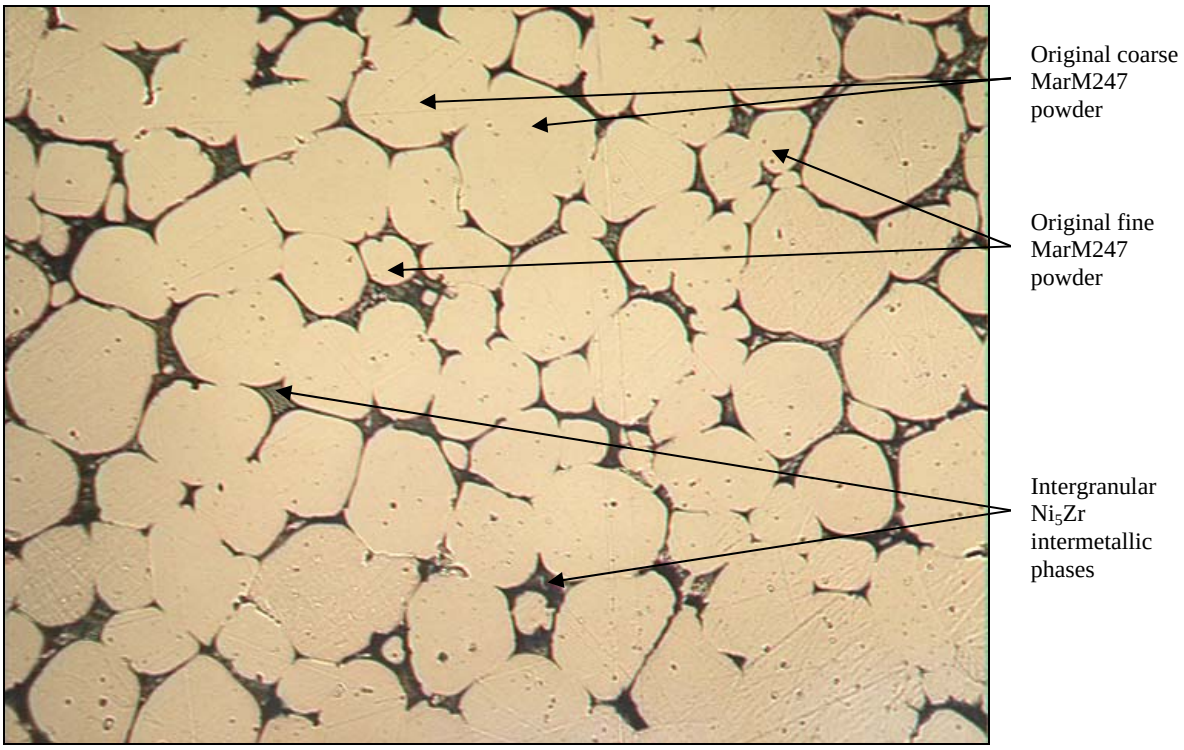

Figure 105 - Ni-Zr braze dispersed between MarM247 powder particles after brazing at 1230°C for 12 hours, followed by solution heat treatment at 1230°C for 4 hours and quenching. Magnification: 100X.

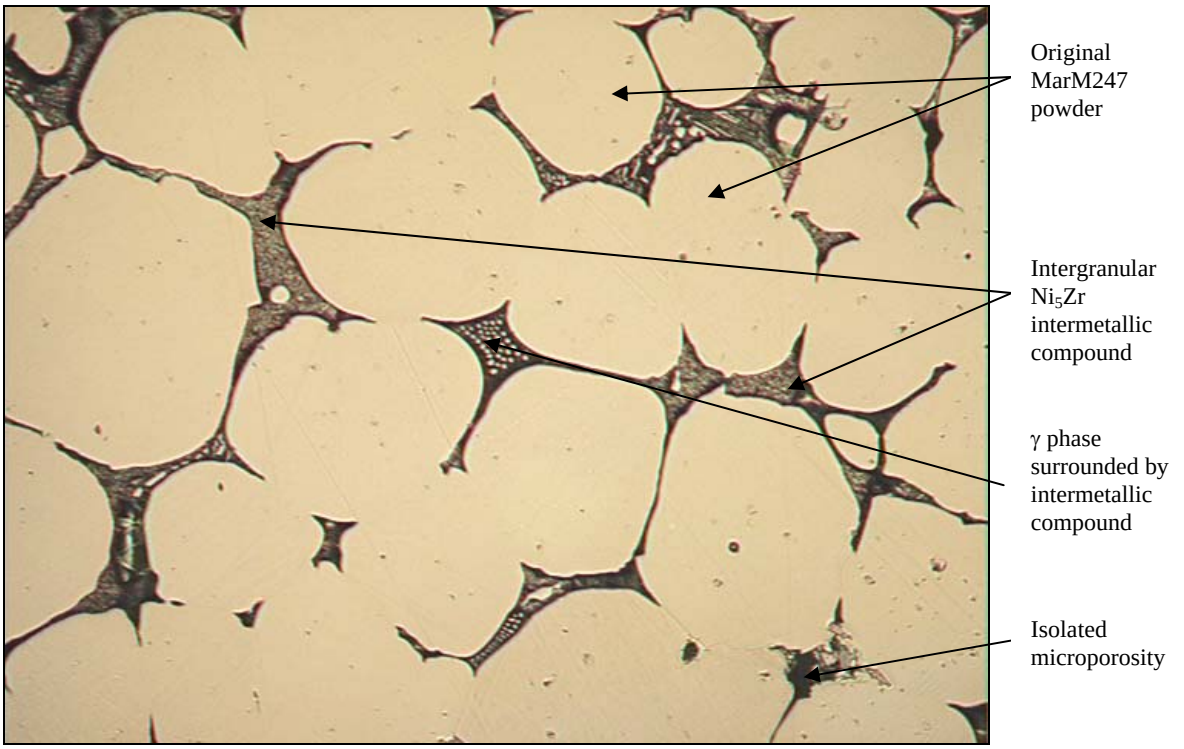

Figure 106 - Ni-Zr braze dispersed between MarM247 powder particles after brazing at 1230°C for 12 hours, followed by solution heat treatment at 1230°C for 4 hours and quenching. Magnification: 200X.

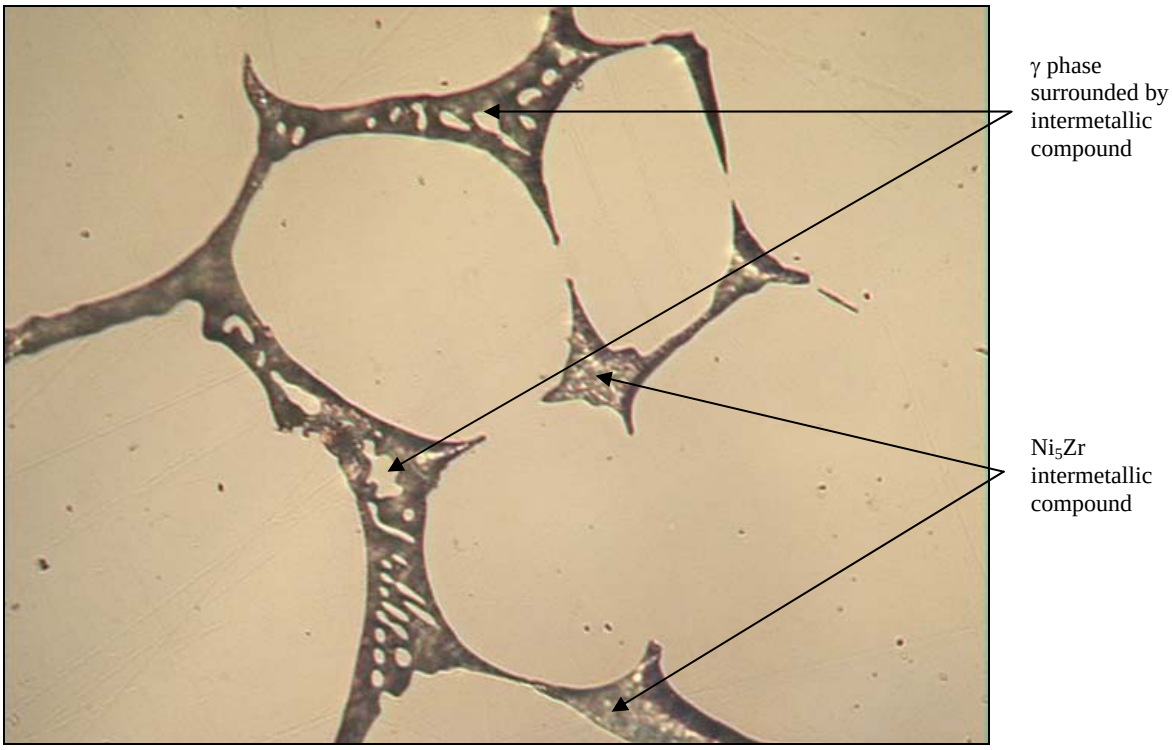

Figure 107 - Ni-Zr braze dispersed between MarM247 powder particles after brazing at 1230°C for 12 hours, followed by solution heat treatment at 1230°C for 4 hours and quenching. Magnification: 500X.

SEM micrographs of the Ni-Hf joint, processed at 1230°C for 12 hours, followed by solution heat treatment at 1230°C for 4 hours, are shown in **Figures 108 and 109**. Two phases within the original braze alloy were analyzed, indicated by the arrows in **Figure 108**. As indicated on the micrograph, one of these phases was identified as γ, consisting of 73.14Ni-6.33Co-7.37Cr-2.73Al-6.10W-1.49Mo-0.65Ti (wt.%). The phase surrounding the γ particles was identified as Ni_7Hf_2, with a composition of 52.96Ni-43.90Hf-2.18Co-0.46Cr-0.16Ti-0.34W (wt.%). The more angular intergranular phase, highlighted by the arrows in **Figure 109**, was shown to consist of 53.01Ni-43.09Hf-2.43Co-0.82Cr-0.20Ti-0.45W (wt.%), and was therefore also identified as Ni_7Hf_2.

Figures 110 and 111 display SEM micrographs of the Ni-Zr joint after processing at 1230°C for 12 hours, followed by solution annealing at 1230°C for 4 hours. Two of the intergranular phases in **Figure 110** were analyzed, as indicated by the arrows. One of these phases, consisting of 75.46Ni-5.27Co-5.23Cr-3.42Al-7.17W-1.16Fe-0.92Mo-0.70Ti-0.68Zr (wt%.), was identified as γ phase. The second phase had a composition of 73.63Ni-23.75Zr-2.09Co-0.53Al (wt.%), and was identified as Ni_5Zr. The intergranular phase highlighted by the arrows in **Figure 111** had a similar composition (70.78Ni-25.44Zr-2.27Co-0.81Cr-0.44Al-0.25W), and was therefore also identified as Ni_5Zr intermetallic compound.

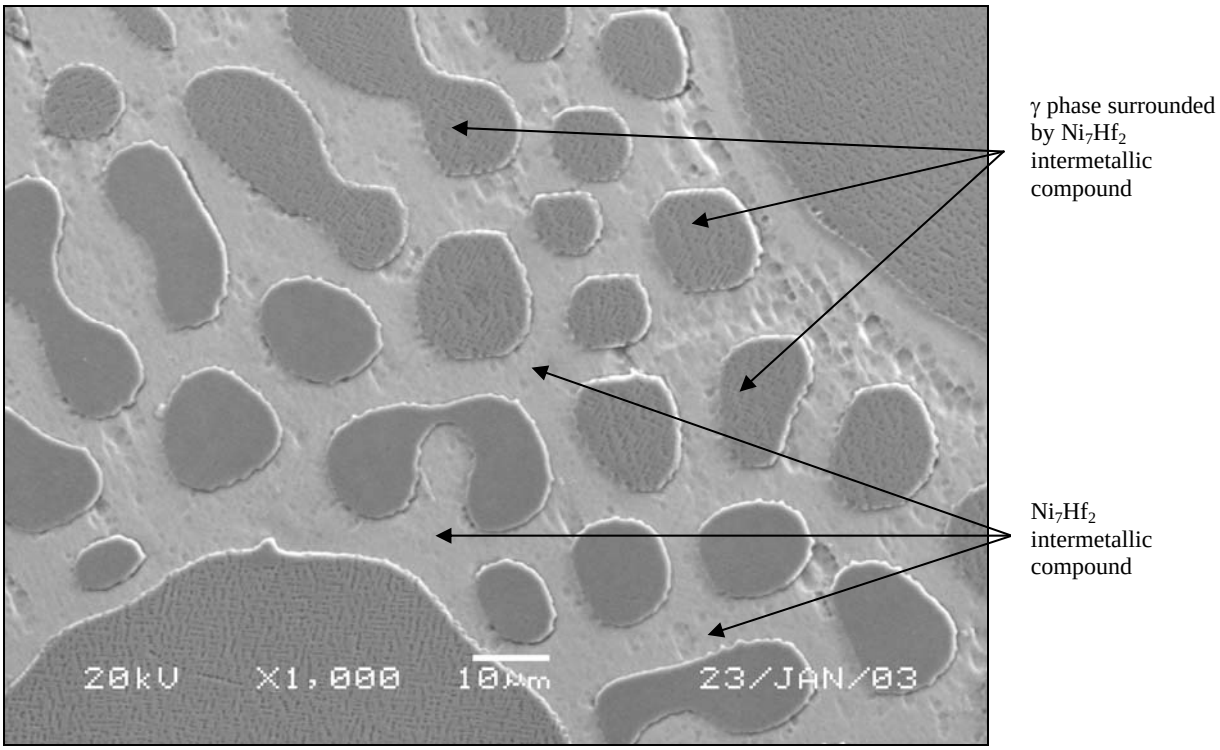

Figure 108 – SEM micrograph of the Ni-Hf braze, showing the phases identified as γ and Ni_7Hf_2.

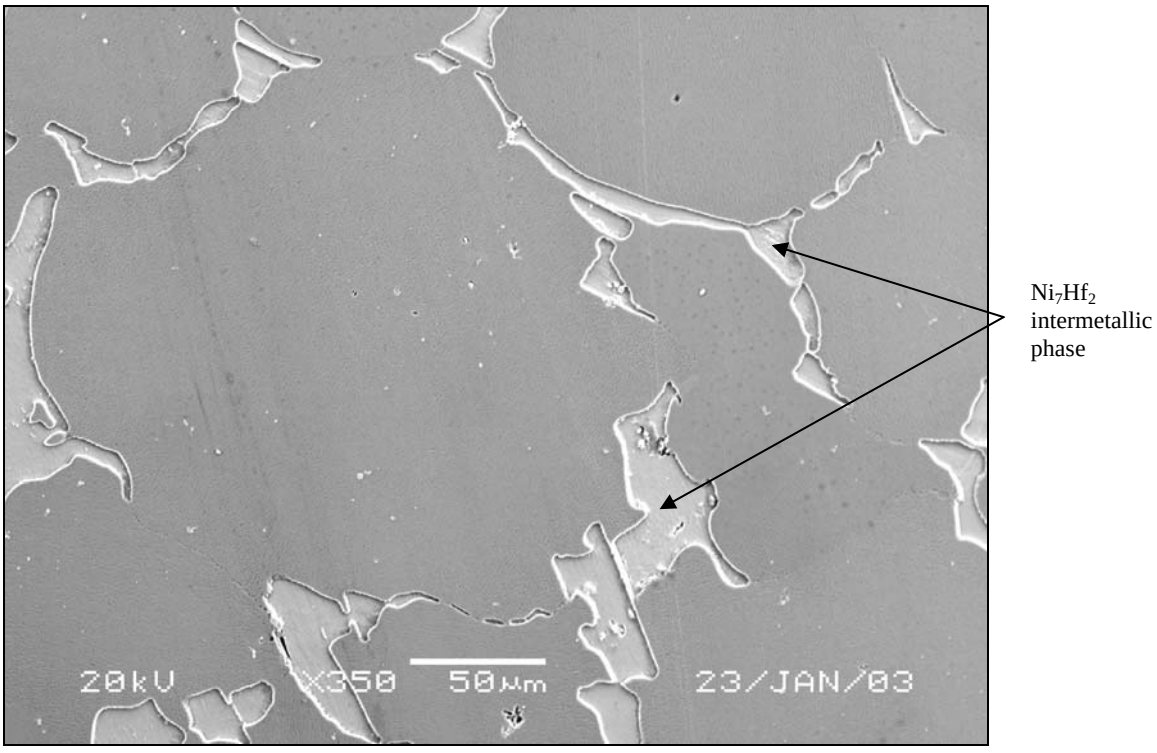

Figure 109 – SEM micrograph of the Ni-Hf braze, showing islands of intergranular Ni_7Hf_2 intermetallic compound.

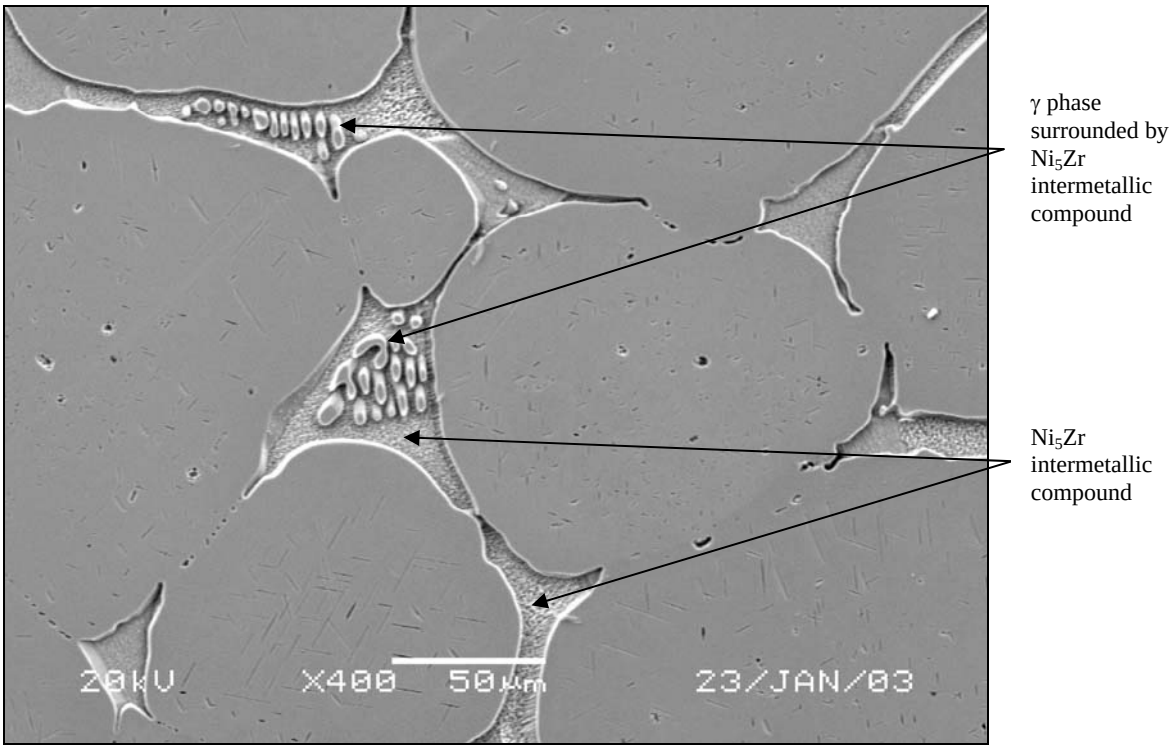

Figure 110 – SEM micrograph of the Ni-Zr braze, showing the phases identified as γ and Ni_5Zr.

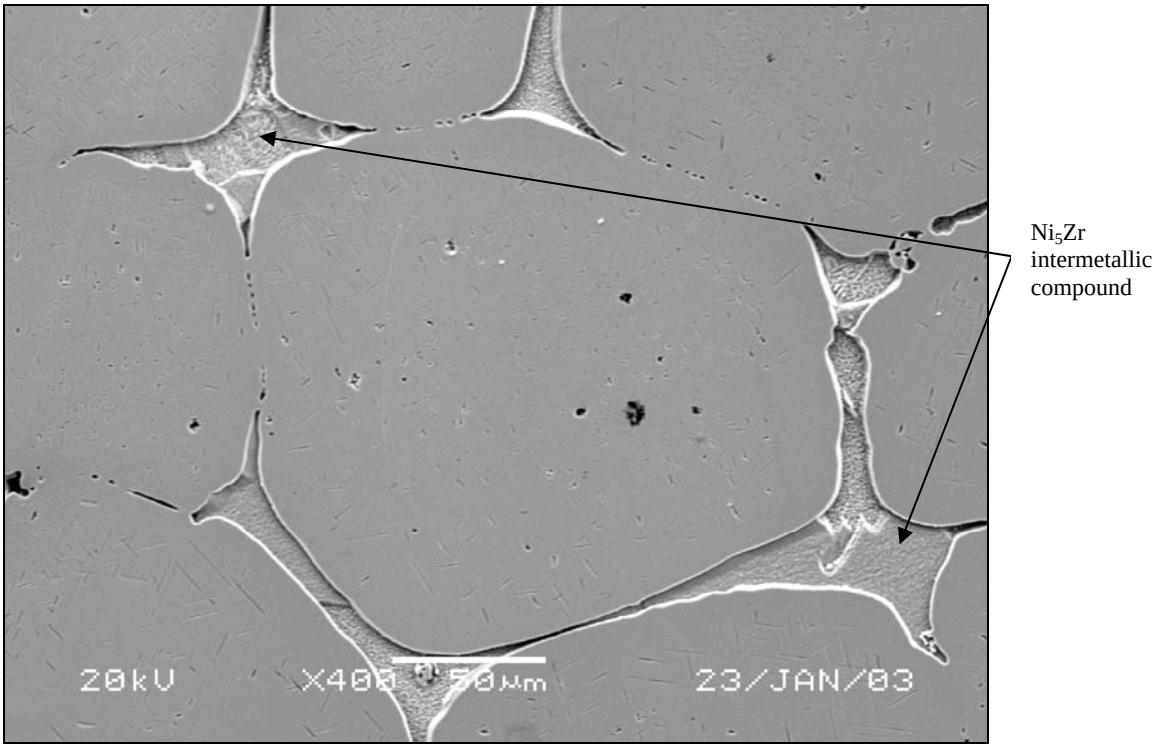

Figure 111 – SEM micrograph of the Ni-Zr braze, showing islands of intergranular Ni_5Zr intermetallic compound.

6.3.2 Creep rupture test results:

The results of creep rupture tests performed at three different stress levels at a temperature of 845°C are documented in **Table 24**, and displayed graphically in the form of a Larson-Miller plot in **Figure 112**. In **Table 24**, the creep rupture properties of the MarM247/Ni-Hf and MarM247/Ni-Zr joints are compared with those of the In738 base metal in the solution annealed condition.

Table 24 - Creep rupture properties at 845°C of the In738 base metal, and LPDB joints produced with MarM247 superalloy powder and Ni-Hf or Ni-Zr braze alloy. The test samples were produced with a joint gap of 1.5 mm to simulate a worst-case crack repair scenario.

Specimen identification	Failure location	Hours to failure	% Elongation	% Reduction in area
APPLIED STRESS 345 MPa (50 ksi)				
BM-1T (In738 as-cast base metal)	Base metal	30.0	5.0	7.0
BM-2T (In738 as-cast base metal)	Base metal	24.7	6.0	7.5
Average for the In738 as-cast base metal		**27.4**	**5.5**	**7.3**
738-1 (In738 brazed with MarM247/Ni-Zr)	Joint	20.5	3.6	4.6
738-2 (In738 brazed with MarM247/Ni-Zr)	Joint	21.8	3.0	4.0
738-3 (In738 brazed with MarM247/Ni-Zr)	Joint	20.9	3.7	4.7
Average for the MarM247/Ni-Zr joint		**21.1**	**3.4**	**4.4**
738-A (In738 brazed with MarM247/Ni-Hf)	Joint	20.6	3.7	5.8
738-B (In738 brazed with MarM247/Ni-Hf)	Joint	18.2	3.0	4.5
738-C (In738 brazed with MarM247/Ni-Hf)	Joint	17.0	4.5	6.5
Average for the MarM247/Ni-Hf joint		**18.6**	**3.7**	**5.6**
APPLIED STRESS 276 MPa (40 ksi)				
BM-3T (In738 as-cast base metal)	Base metal	100.0	6.2	8.7
BM-4T (In738 as-cast base metal)	Base metal	137.8	6.1	8.4
Average for the In738 as-cast base metal		**118.9**	**6.2**	**8.6**
738-4 (In738 brazed with MarM247/Ni-Zr)	Joint	75.2	5.7	8.6
738-5 (In738 brazed with MarM247/Ni-Zr)	Joint	78.8	3.9	7.9
738-6 (In738 brazed with MarM247/Ni-Zr)	Joint	70.1	4.9	7.2
Average for the MarM247/Ni-Zr joint		**74.7**	**4.8**	**7.9**
738-D (In738 brazed with MarM247/Ni-Hf)	Joint	73.2	4.9	7.6
738-E (In738 brazed with MarM247/Ni-Hf)	Joint	70.9	5.9	8.9
738-F (In738 brazed with MarM247/Ni-Hf)	Joint	68.9	5.2	8.4
Average for the MarM247/Ni-Hf joint		**71.0**	**5.3**	**8.3**
APPLIED STRESS 228 MPa (33 ksi)				
BM-5T (In738 as-cast base metal)	Base metal	200.0	6.6	8.8
BM-6T (In738 as-cast base metal)	Base metal	344.6	6.0	8.6
Average for the In738 as-cast base metal		**272.3**	**6.3**	**8.7**
738-7 (In738 brazed with MarM247/Ni-Zr)	Joint	253.6	4.2	6.0
738-8 (In738 brazed with MarM247/Ni-Zr)	Joint	240.0	4.4	6.3
738-9 (In738 brazed with MarM247/Ni-Zr)	Joint	232.2	4.9	6.7
Average for the MarM247/Ni-Zr joint		**241.9**	**4.5**	**6.3**
738-G (In738 brazed with MarM247/Ni-Hf)	Joint	209.8	5.3	7.5
738-H (In738 brazed with MarM247/Ni-Hf)	Joint	220.8	4.9	6.9
738-I (In738 brazed with MarM247/Ni-Hf)	Joint	214.3	5.2	7.0
Average for the MarM247/Ni-Hf joint		**215.0**	**5.1**	**7.1**

As shown in **Table 24**, the creep life to failure of the braze joints at 845°C was well below that of the In738 base metal at all three applied stress levels. At an applied stress level of 345 MPa, the MarM247/Ni-Zr and the MarM247/Ni-Hf braze joints achieved average creep lives to failure of approximately 77% and 68%, respectively, of that of the In738 base metal. At an applied stress level of 276 MPa, the creep life to failure of the joints was 63% and 60% of that of the base metal for the MarM247/Ni-Zr and MarM247/Ni-Hf joints, respectively. At 228 MPa, these values were 89% (Ni-Zr joints) and 79% (Ni-Hf joints) of the creep life determined for the In738 base metal. The Larson-Miller plot shown in **Figure 112** confirms that, compared to the MarM247/Ni-Hf joints, the MarM247/Ni-Zr braze joints displayed superior creep rupture properties at 845°C at all applied stress levels evaluated. In spite of the lower creep rupture properties of the MarM247/Ni-Hf braze joints, the ductility of these joints was marginally higher than that of the MarM247/Ni-Zr joints (as shown in **Table 24**).

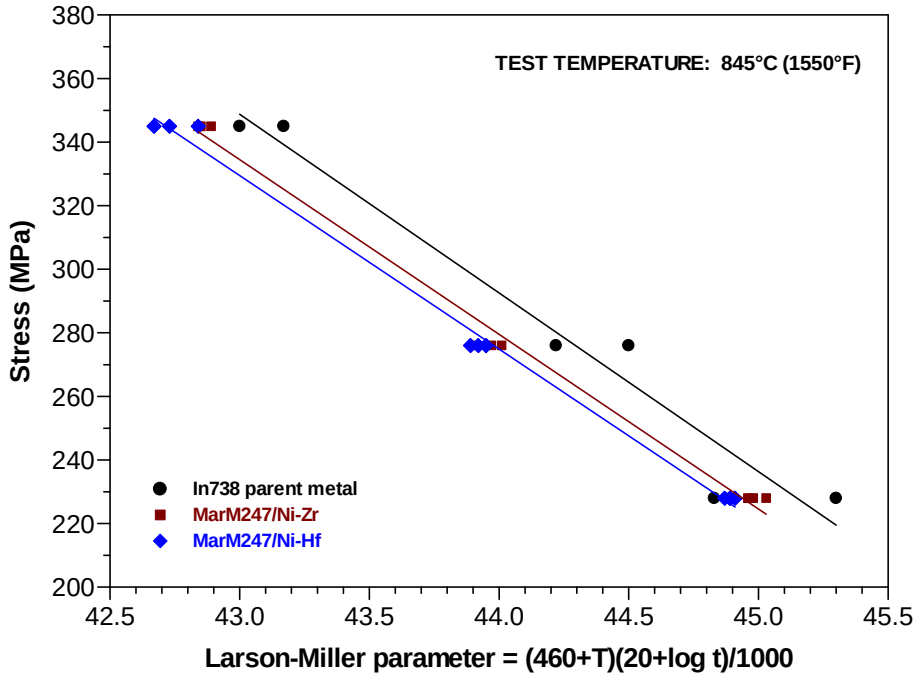

Figure 112 – Larson-Miller plot at 845°C for creep rupture tests performed at three applied stress levels: 345 MPa (50 ksi), 276 MPa (45 ksi) and 228 MPa (33 ksi) (where: *T* is temperature (°F) and *t* is time (hours)).

The creep rupture properties of the In738 base metal and the MarM247/Ni-Hf and MarM247/Ni-Zr joints at 900°C are shown in **Table 25**, and displayed graphically in the form of a Larson-Miller plot in **Figure 113**. The creep rupture lives of both braze joints were well below that of the parent metal at all three stress levels tested. At an applied stress of 242 MPa, the creep rupture life of the MarM247/Ni-Zr braze joint was 69% of that of the In738 base metal, whereas that of the MarM247/Ni-Hf braze joint was 64% of the base metal creep rupture life. At an applied stress of 186 MPa, the MarM247/Ni-Zr joint achieved 71%, and the MarM247/Ni-Hf joint 65%, of the creep rupture life of the In738 base metal. At 152 MPa, the creep rupture lives of the braze joints were 77% of the life of the base metal for the Ni-Zr braze, and 66% for the Ni-Hf braze. The Larson-Miller plot shown in **Figure 113** confirms that the MarM247/Ni-Zr braze joints outperformed the MarM247/Ni-Hf braze joints during creep rupture testing at 900°C. In spite of the lower creep rupture properties of the MarM247/Ni-Hf braze joints, the ductility of these joints was superior to that of the MarM247/Ni-Zr braze joints.

Table 25 - Creep rupture properties at 900°C of the In738 base metal, and LPDB joints produced with MarM247 superalloy powder and Ni-Hf or Ni-Zr braze alloy. The test samples were produced with a joint gap of 1.5 mm to simulate a worst-case crack repair scenario.

Specimen identification	Failure location	Hours to failure	% Elongation	% Reduction in area
APPLIED STRESS 242 MPa (35 ksi)				
BM-7T (In738 as-cast base metal)	Base metal	30.0	5.5	7.8
BM-8T (In738 as-cast base metal)	Base metal	29.5	5.9	7.9
Average for the In738 as-cast base metal		**29.8**	**5.7**	**7.9**
738-10 (In738 brazed with MarM247/Ni-Zr)	Joint	22.9	3.7	4.4
738-11 (In738 brazed with MarM247/Ni-Zr)	Joint	20.3	4.2	5.6
738-12 (In738 brazed with MarM247/Ni-Zr)	Joint	18.2	4.5	6.0
Average for the MarM247/Ni-Zr joint		**20.5**	**4.1**	**5.3**
738-J (In738 brazed with MarM247/Ni-Hf)	Joint	17.1	4.5	5.9
738-K (In738 brazed with MarM247/Ni-Hf)	Joint	19.4	4.6	6.1
738-L (In738 brazed with MarM247/Ni-Hf)	Joint	20.5	4.7	6.2
Average for the MarM247/Ni-Hf joint		**19.0**	**4.6**	**6.1**
APPLIED STRESS 186 MPa (27 ksi)				
BM-9T (In738 as-cast base metal)	Base metal	100.0	7.0	10.0
BM-10T (In738 as-cast base metal)	Base metal	109.1	6.9	9.9
Average for the In738 as-cast base metal		**104.6**	**7.0**	**9.9**
738-13 (In738 brazed with MarM247/Ni-Zr)	Joint	75.5	4.2	7.3
738-14 (In738 brazed with MarM247/Ni-Zr)	Joint	72.0	4.0	6.8
738-15 (In738 brazed with MarM247/Ni-Zr)	Joint	76.2	4.6	7.7
Average for the MarM247/Ni-Zr joint		**74.6**	**4.3**	**7.3**
738-M (In738 brazed with MarM247/Ni-Hf)	Joint	70.3	5.0	6.8
738-N (In738 brazed with MarM247/Ni-Hf)	Joint	69.2	5.6	8.0
738-O (In738 brazed with MarM247/Ni-Hf)	Joint	64.2	5.8	8.2
Average for the MarM247/Ni-Hf joint		**67.9**	**5.5**	**7.7**
APPLIED STRESS 152 MPa (22 ksi)				
BM-11T (In738 as-cast base metal)	Base metal	200.0	8.5	10.8
BM-12T (In738 as-cast base metal)	Base metal	404.2	8.0	10.0
Average for the In738 as-cast base metal		**302.1**	**8.3**	**10.4**
738-16 (In738 brazed with MarM247/Ni-Zr)	Joint	242.2	4.8	7.6
738-17 (In738 brazed with MarM247/Ni-Zr)	Joint	238.6	4.4	6.4
738-18 (In738 brazed with MarM247/Ni-Zr)	Joint	217.4	4.0	6.1
Average for the MarM247/Ni-Zr joint		**232.7**	**4.6**	**6.7**
738-G (In738 brazed with MarM247/Ni-Hf)	Joint	205.9	5.0	7.7
738-H (In738 brazed with MarM247/Ni-Hf)	Joint	198.4	5.5	7.8
738-I (In738 brazed with MarM247/Ni-Hf)	Joint	192.8	5.7	8.0
Average for the MarM247/Ni-Hf joint		**199.0**	**5.4**	**7.8**

The creep rupture properties of the In738 base metal, and the MarM247/Ni-Zr and MarM247/Ni-Hf joints measured at 980°C are displayed in **Table 26**, and shown graphically in the form of a Larson-Miller plot in **Figure 114**. At an applied stress level of 138 MPa, the creep rupture life of the MarM247/Ni-Zr joint was 79% of the creep rupture life of the base metal, and that of the MarM247/Ni-Hf joint 64%. These values decreased to 70% and 61% of the creep rupture life of the base metal, respectively, for the MarM247/Ni-Zr and

MarM247/Ni-Hf joints at an applied stress level of 104 MPa. The creep rupture life of the Ni-Zr joint at an applied stress of 76 MPa was 81% of that of the In738 base metal, whereas that of the Ni-Hf braze joint achieved 78% of creep rupture life of the base metal. The Larson-Miller plot shown in **Figure 114** indicates that the creep rupture properties of the MarM247/Ni-Zr braze joints were superior to those of MarM247/Ni-Hf brazed joints. The MarM247/Ni-Hf joints, however, displayed superior ductility at all stress levels. The average percentage elongation and percentage reduction in area of the MarM247/Ni-Hf brazed joints were 73% and 70% of those of the base metal, respectively, whereas the MarM247/Ni-Zr brazed joints displayed approximately 60% of the ductility of the base metal.

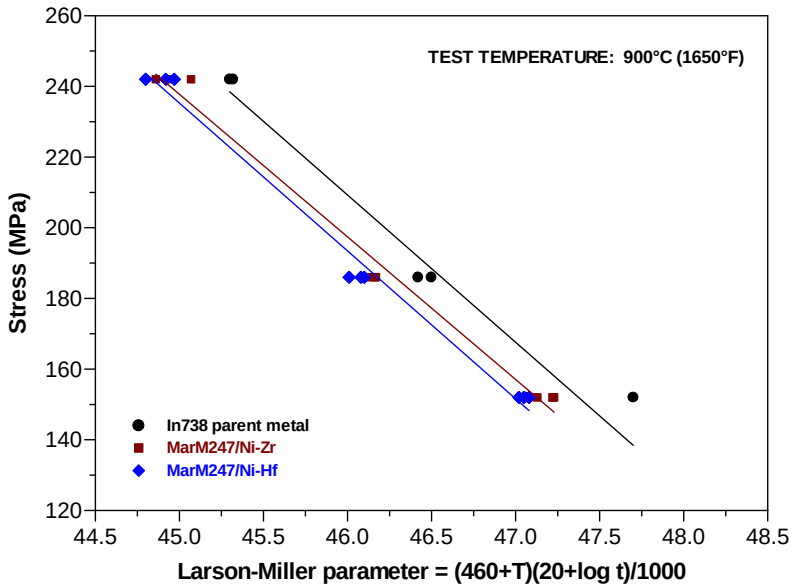

Figure 113 –Larson-Miller plot at 900°C for creep rupture tests performed at three applied stress levels: 242 MPa (35 ksi), 186 MPa (27 ksi) and 152 MPa (22 ksi) (where: *T* is temperature (°F) and *t* is time (hours)).

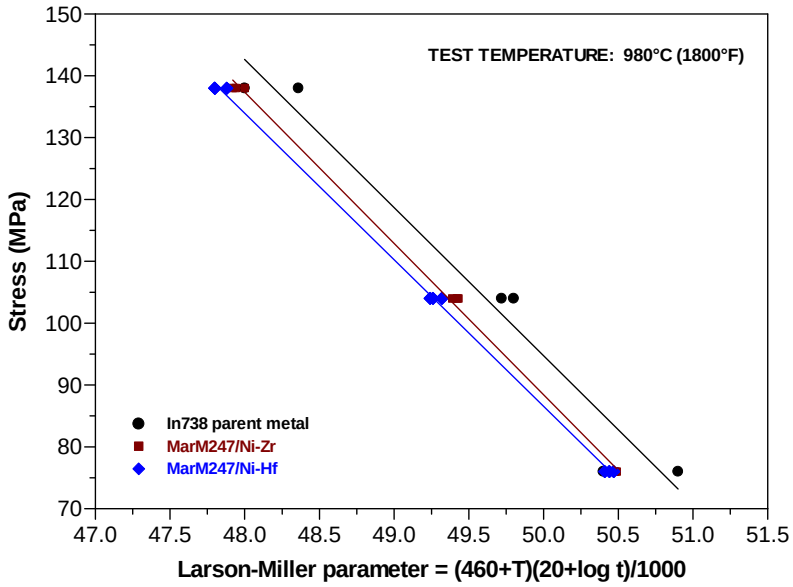

Figure 114 –Larson-Miller plot at 980°C for creep rupture tests performed at three applied stress levels: 138 MPa (20 ksi), 104 MPa (15 ksi) and 76 MPa (11 ksi) (where: *T* is temperature (°F) and *t* is time (hours)).

Table 26 - Creep rupture properties at 980°C of the In738 base metal, and LPDB joints produced with MarM247 superalloy powder and Ni-Hf or Ni-Zr braze alloy. The test samples were produced with a joint gap of 1.5 mm to simulate a worst-case crack repair scenario.

Specimen identification	Failure location	Hours to failure	% Elongation	% Reduction in area
APPLIED STRESS 138 MPa (20 ksi)				
BM-13T (In738 as-cast base metal)	Base metal	25.0	8.0	11.6
BM-14T (In738 as-cast base metal)	Base metal	17.3	8.2	11.9
Average for the In738 as-cast base metal		**21.2**	**8.1**	**11.8**
738-19 (In738 brazed with MarM247/Ni-Zr)	Joint	15.9	5.6	7.5
738-20 (In738 brazed with MarM247/Ni-Zr)	Joint	16.3	5.2	7.0
738-21 (In738 brazed with MarM247/Ni-Zr)	Joint	17.3	4.5	6.9
Average for the MarM247/Ni-Zr joint		**16.5**	**5.1**	**7.1**
738-S (In738 brazed with MarM247/Ni-Hf)	Joint	15.3	6.1	8.8
738-T (In738 brazed with MarM247/Ni-Hf)	Joint	14.1	6.7	9.3
738-U (In738 brazed with MarM247/Ni-Hf)	Joint	11.3	6.9	9.9
Average for the MarM247/Ni-Hf joint		**13.6**	**6.6**	**9.3**
APPLIED STRESS 104 MPa (15 ksi)				
BM-15T (In738 as-cast base metal)	Base metal	100.0	8.1	11.9
BM-16T (In738 as-cast base metal)	Base metal	108.5	8.2	12.1
Average for the In738 as-cast base metal		**104.3**	**8.2**	**12.0**
738-22 (In738 brazed with MarM247/Ni-Zr)	Joint	73.3	4.3	7.0
738-23 (In738 brazed with MarM247/Ni-Zr)	Joint	74.2	4.0	6.8
738-24 (In738 brazed with MarM247/Ni-Zr)	Joint	71.4	4.9	7.4
Average for the MarM247/Ni-Zr joint		**73.0**	**4.4**	**7.1**
738-V (In738 brazed with MarM247/Ni-Hf)	Joint	61.5	5.7	7.6
738-W (In738 brazed with MarM247/Ni-Hf)	Joint	66.6	5.1	7.0
738-X (In738 brazed with MarM247/Ni-Hf)	Joint	62.5	5.6	7.4
Average for the MarM247/Ni-Hf joint		**63.5**	**5.5**	**7.3**
APPLIED STRESS 76 MPa (11 ksi)				
BM-17T (In738 as-cast base metal)	Base metal	200.0	8.8	12.9
BM-18T (In738 as-cast base metal)	Base metal	332.8	8.6	12.4
Average for the In738 as-cast base metal		**266.4**	**8.7**	**12.7**
738-25 (In738 brazed with MarM247/Ni-Zr)	Joint	214.7	5.9	8.2
738-26 (In738 brazed with MarM247/Ni-Zr)	Joint	218.8	5.0	7.0
738-27 (In738 brazed with MarM247/Ni-Zr)	Joint	216.1	5.4	7.3
Average for the MarM247/Ni-Zr joint		**216.5**	**5.4**	**7.5**
738-Y (In738 brazed with MarM247/Ni-Hf)	Joint	202.6	6.2	8.9
738-Z (In738 brazed with MarM247/Ni-Hf)	Joint	214.8	6.0	8.6
738-ZZ (In738 brazed with MarM247/Ni-Hf)	Joint	208.0	6.1	8.7
Average for the MarM247/Ni-Hf joint		**208.5**	**6.1**	**8.7**

The Larson-Miller plots shown in **Figures 112 to 114** were constructed individually for each of the three test temperatures. In order to compare the creep rupture test data at all three test temperatures, the data shown in **Tables 24 to 26** were combined into a single Larson-Miller plot, shown in **Figure 115**. Based on this figure, the three materials were ranked in descending order of creep rupture properties: In738 base metal, the MarM247/Ni-Zr braze joint, and the MarM247/Ni-Hf joint. It must be emphasized, however, that linear regression

methods revealed no statistically relevant differences between the Larson-Miller plots of the MarM247/Ni-Zr and MarM247/Ni-Hf braze joints.

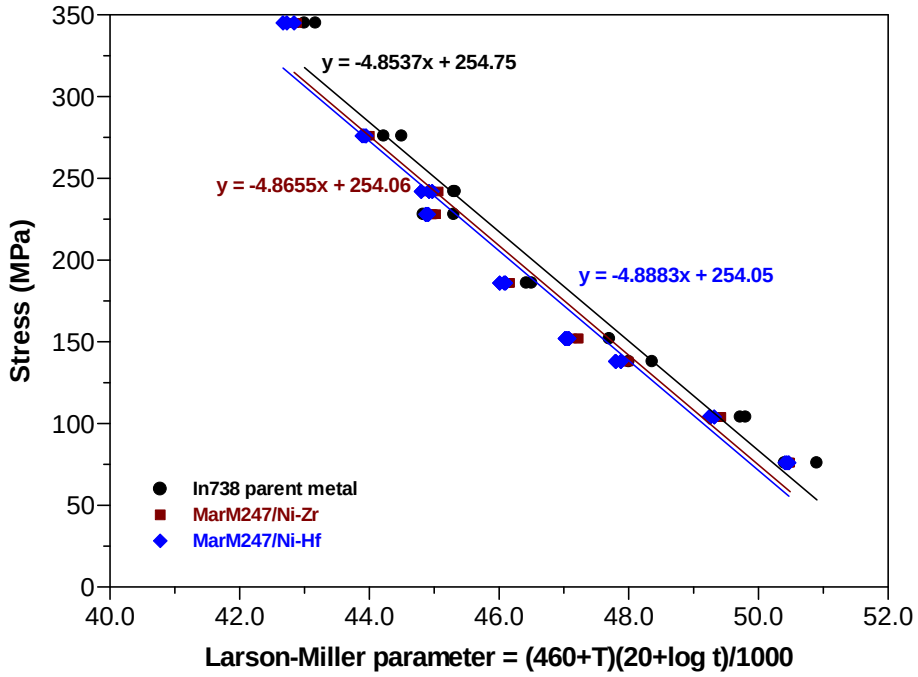

Figure 115 – Larson-Miller plot for the In738 base metal, the MarM247/Ni-Zr joint and the MarM247/Ni-Hf braze joints in the solution annealed condition.

6.4) Conclusions

- A relatively dense, low porosity LPDB joint, with a microstructure consisting of MarM247 powder particles surrounded by Ni-Hf or Ni-Zr braze alloy, formed during processing at 1230°C for 12 hours, followed by solution heat treatment at 1230°C for 4 hours. The braze microstructure consisted of γ dendrites, surrounded by Ni_5Zr or Ni_7Hf_2 intermetallic compound, interspersed with more continuous regions of Ni_5Zr or Ni_7Hf_2 intermetallic compound.

- The extended brazing cycle further reduced the amount of γ and Ni_5Zr/Ni_7Hf_2 intermetallic compound, and decreased the thickness of the layers of braze alloy surrounding the MarM247 powder particles.

- Creep rupture tests performed at 845°C, 900°C and 980°C at various stress levels revealed that the MarM247/Ni-Zr brazed joints have superior creep rupture properties compared with the MarM247/Ni-Hf joints. A combined Larson Miller plot, however, showed little statistically relevant difference between the creep rupture properties of the two braze filler metals in the solution annealed condition.

- The creep rupture properties described in this chapter were measured in the solution annealed condition and should improve following a suitable aging heat treatment. In the solution heat treated condition, the creep rupture properties of the Ni-Hf and Ni-Zr joints achieved between 65% and 75% of the creep rupture properties of the In738 base metal. Based on past experience with brazed joints using a Ni-B braze alloy, the aging treatment is expected to improve the creep rupture properties by between 15% and 20%.

- The ductility of the Ni-Hf braze joints was higher than that of the Ni-Zr joints. The joint ductility is expected to decrease marginally following aging heat treatment.

- The results presented in this chapter were obtained after processing times of 12 hours, followed by solution heat treatment for an additional 4 hours. Promising joint microstructures and creep rupture properties were obtained, but isolated microporosity was observed in the Ni-Zr and Ni-Hf joints. In order to improve the joint quality, Hot Isostatic Pressing (HIP'ing) was used in an attempt to close the micropores that form during the braze cycle. Chapter 7 describes the influence of such a HIP cycle on the microstructure and amount of microporosity in MarM247/Ni-Hf and MarM247/Ni-Zr joints after brazing for 12 hours at 1230°C, followed by a solution annealing treatment.

CHAPTER 7 - EXPERIMENT 5

CHARACTERIZATION OF THE MICROSTRUCTURE AND MECHANICAL PROPERTIES OF LIQUID PHASE DIFFUSION BONDS USING EUTECTIC Ni-Hf AND Ni-Zr BRAZE ALLOYS AFTER BRAZING FOR 12 HOURS, FOLLOWED BY SOLUTION ANNEALING AND HOT ISOSTATIC PRESSING

7.1) Introduction

The results considered in Chapter 6 revealed that a braze microstructure consisting of γ dendrites, surrounded by Ni_5Zr or Ni_7Hf_2 intermetallic compound, formed during an extended braze cycle of 12 hours at 1230°C, followed by solution annealing at the same temperature for 4 hours. These joints displayed promising creep rupture properties, but contained a significant volume fraction of microporosity.

In order to determine whether the properties of the braze joints could be improved by reducing the amount of microporosity, a Hot Isostatic Pressing (HIP) cycle was introduced after solution annealing. During the HIP cycle, the joint was subjected to pressurized argon gas at elevated temperature. The high isostatic gas pressure is known to induce plastic deformation in the material, causing the collapse of any micropores. The success of the HIP cycle was assessed by examining the joint microstructures and by performing elevated temperature tensile and creep rupture tests.

7.2) Experimental procedure

The liquid phase diffusion bonding technique was used to join In738 parent material using the novel eutectic Ni-Hf and Ni-Zr braze alloys. The In738 plate material and the experimental braze pastes were prepared using the techniques presented in §4.2, and braze samples were produced using the vacuum braze cycle described in §6.2. After joining the brazed samples were placed in a production vacuum furnace equipped with quenching facilities, and solution annealed at 1230°C for 4 hours, followed by gas quenching at a rate of 50°C per minute.

The solution heat treatment was followed by a HIP cycle at an isostatic pressure of 104 MPa (15 000 psi), using the following procedure:

1) Ramp up to a temperature of 1080°C at a minimum rate of 11°C per minute.
2) Hold at 1080°C for 4 hours.
3) Quench to room temperature at a rate of 50°C per minute.

After exposing the plates to the vacuum LPDB, solution heat treatment and HIP cycles described above, samples were sectioned, mounted and polished using conventional metallographic techniques. The polished metallographic samples were then etched with Marble's reagent, and characterized using optical and scanning electron microscopy techniques.

In order to characterize the tensile properties of the braze joints after solution annealing and HIP'ing, tensile tests were performed at room temperature, 540°C, 870°C and 980°C using the tensile test procedure described in §4.2. Creep rupture tests were performed (as described in

§6.2) using the following combinations of temperature and applied stress: 345 MPa at 845°C; 242 MPa at 900°C; and 138 MPa at 980°C.

7.3) Results and discussion

7.3.1 Microstructural investigation:

The microstructure of the Ni-Hf LPDB joint processed at 1230°C for 12 hours, followed by solution annealing and HIP'ing, is shown in **Figures 116 to 119** at various magnifications. The joint consists of MarM247 powder particles, surrounded by layers of Ni-Hf braze alloy. Isolated γ particles are evident within the Ni-Hf braze, but the braze microstructure between the MarM247 powder particles appears to be dominated by Ni_7Hf_2 intermetallic compound.

The microstructure of the LPDB joint produced with MarM247 powder and Ni-Zr braze paste is shown in **Figures 120 to 123** at various magnifications. The original MarM247 powder particles are evident as the lighter, more equiaxed component, while the darker regions consist of eutectic Ni-Zr braze alloy. The braze alloy contains isolated γ dendrites and Ni_5Zr intermetallic compound.

Isolated micropores were observed in both the Ni-Hf and Ni-Zr joints, suggesting that the HIP cycle was not effective in eliminating microporosity from the braze joints. A higher temperature may be required during the HIP treatment to close the pores formed during the brazing cycle.

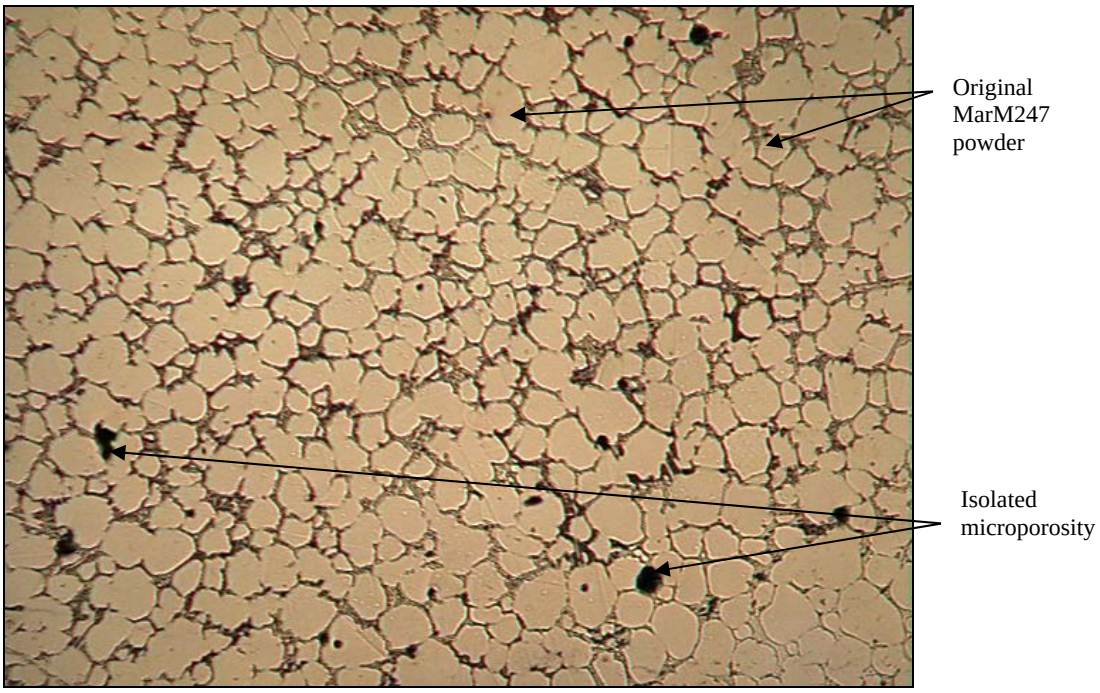

Figure 116 - Ni-Hf braze dispersed between MarM247 powder particles after brazing at 1230°C for 12 hours, followed by solution heat treatment at 1230°C for 4 hours and a HIP cycle at 1080°C for 4 hours. Magnification: 50X.

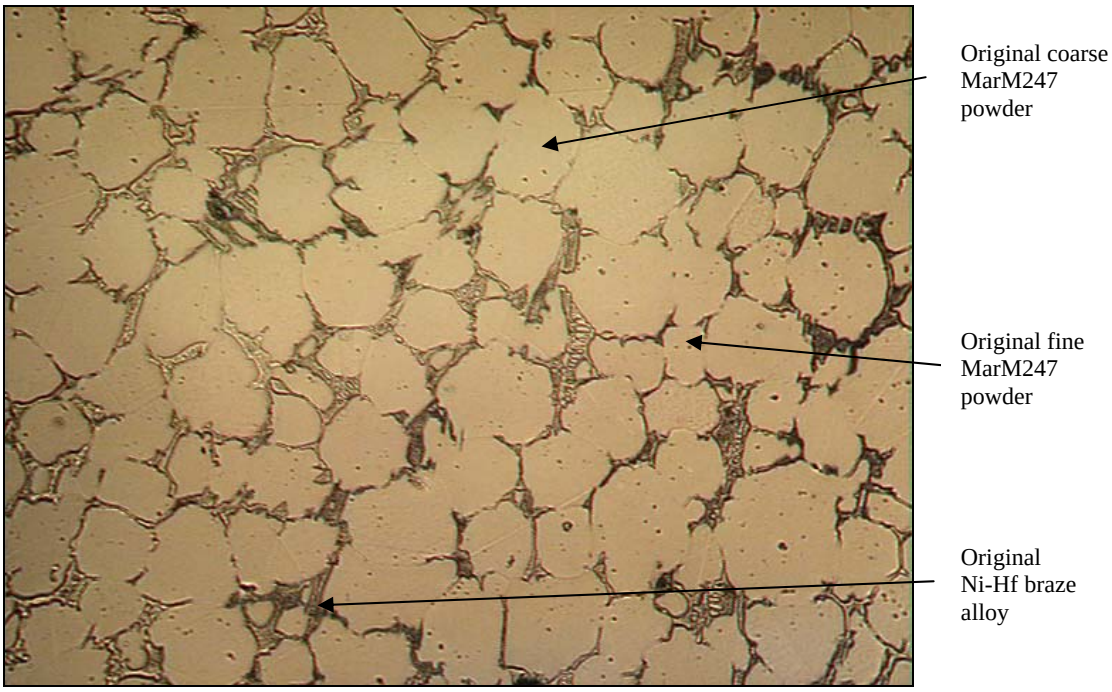

Figure 117 - Ni-Hf braze dispersed between MarM247 powder particles after brazing at 1230°C for 12 hours, followed by solution heat treatment at 1230°C for 4 hours and a HIP cycle at 1080°C for 4 hours. Magnification: 100X.

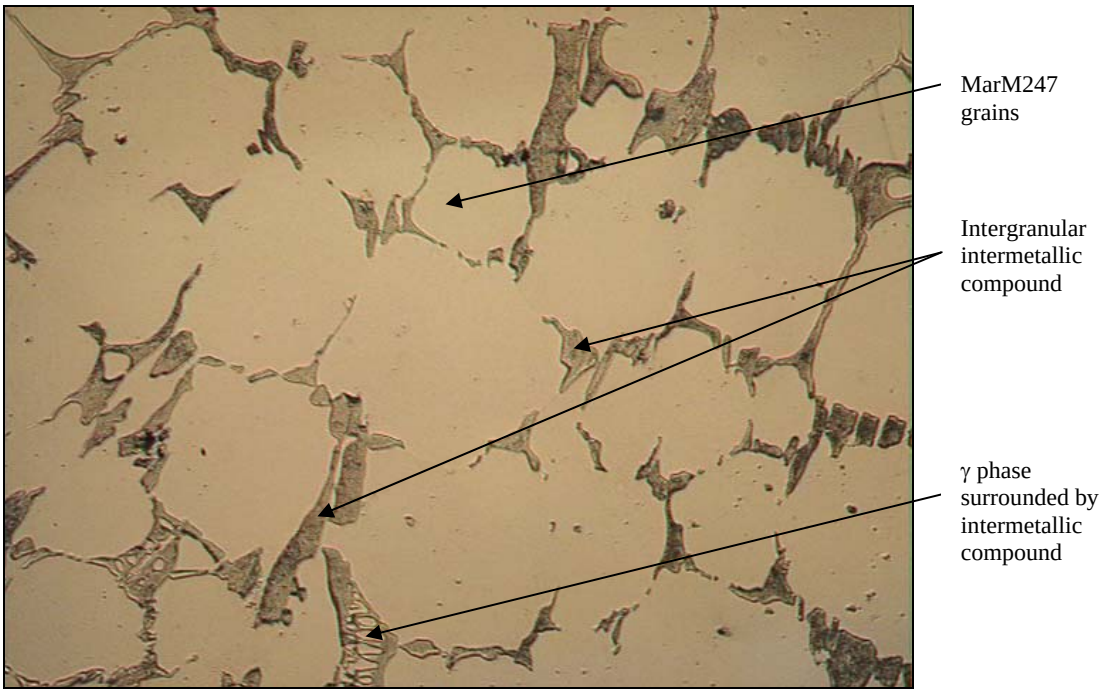

Figure 118 - Ni-Hf braze dispersed between MarM247 powder particles after brazing at 1230°C for 12 hours, followed by solution heat treatment at 1230°C for 4 hours and a HIP cycle at 1080°C for 4 hours. Magnification: 200X.

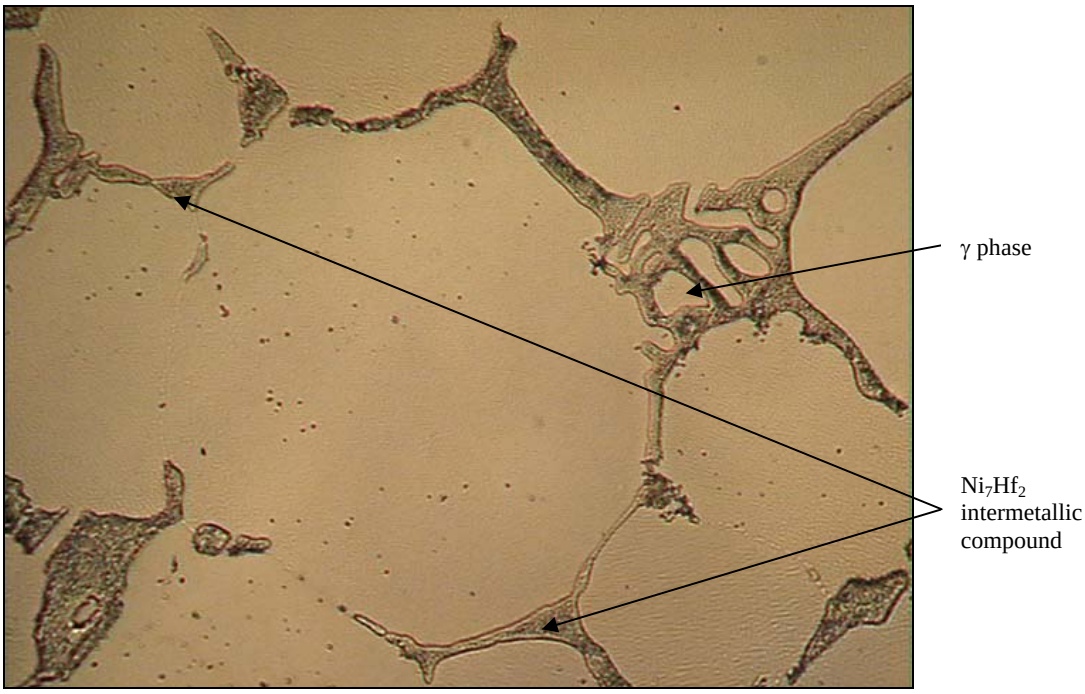

Figure 119 - Ni-Hf braze dispersed between MarM247 powder particles after brazing at 1230°C for 12 hours, followed by solution heat treatment at 1230°C for 4 hours and a HIP cycle at 1080°C for 4 hours. Magnification: 500X.

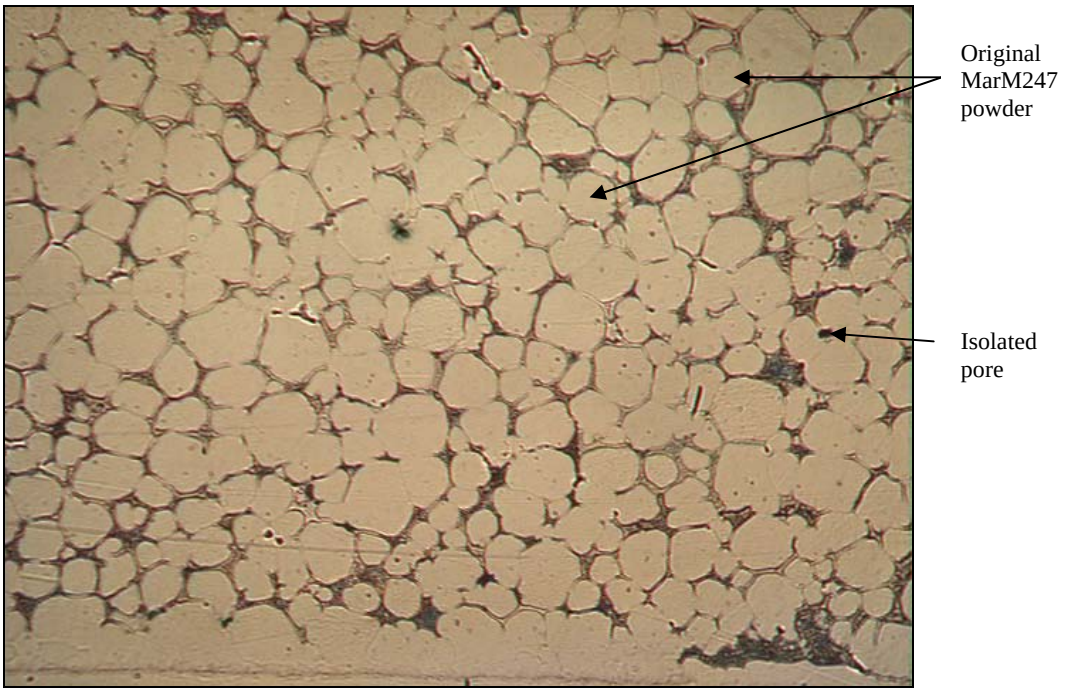

Figure 120 - Ni-Zr braze dispersed between MarM247 powder particles after brazing at 1230°C for 12 hours, followed by solution heat treatment at 1230°C for 4 hours and a HIP cycle at 1080°C for 4 hours. Magnification: 50X.

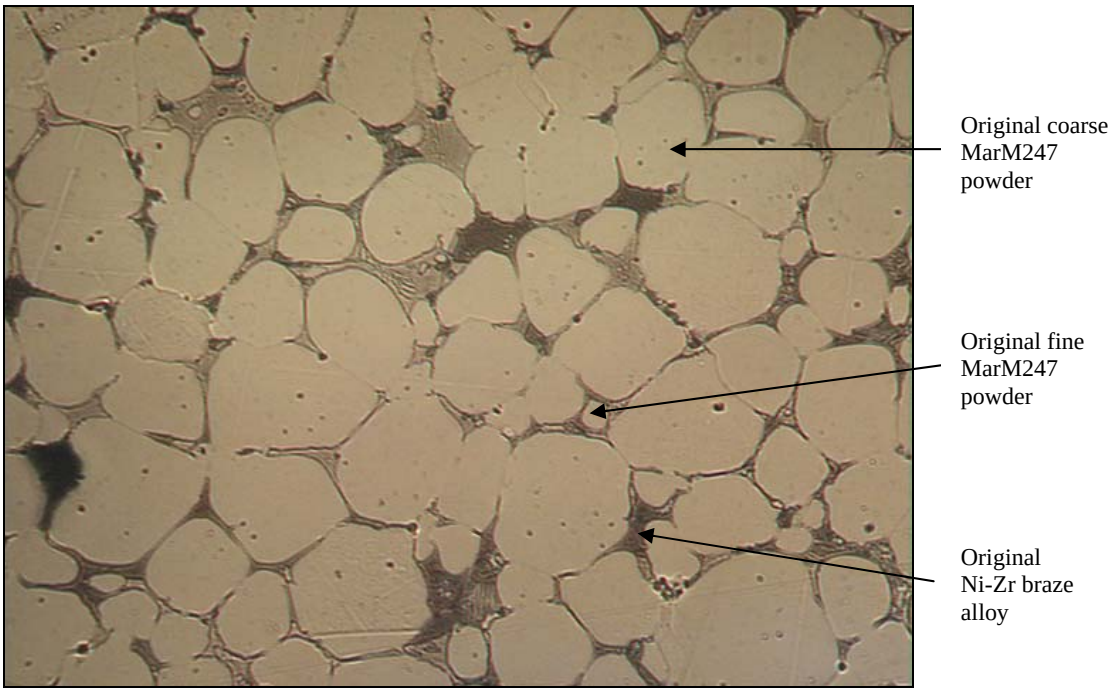

Figure 121 - Ni-Zr braze dispersed between MarM247 powder particles after brazing at 1230°C for 12 hours, followed by solution heat treatment at 1230°C for 4 hours and a HIP cycle at 1080°C for 4 hours. Magnification: 100X.

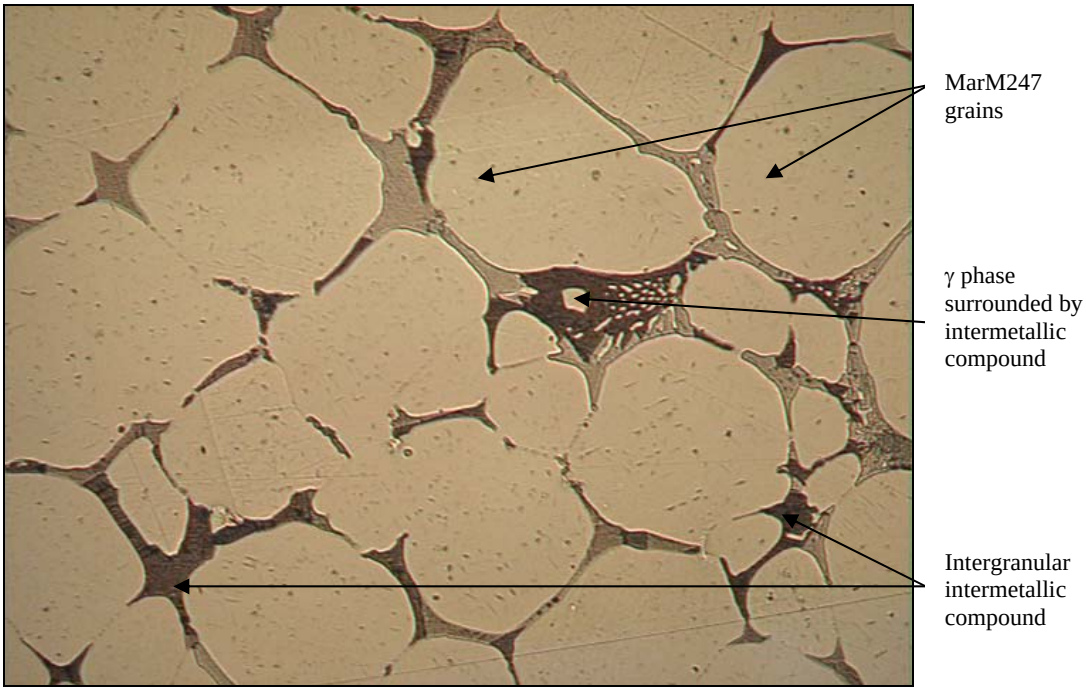

Figure 122 - Ni-Zr braze dispersed between MarM247 powder particles after brazing at 1230°C for 12 hours, followed by solution heat treatment at 1230°C for 4 hours and a HIP cycle at 1080°C for 4 hours. Magnification: 200X.

Figure 123 - Ni-Zr braze dispersed between MarM247 powder particles after brazing at 1230°C for 12 hours, followed by solution heat treatment at 1230°C for 4 hours and a HIP cycle at 1080°C for 4 hours. Magnification: 500X.

SEM micrographs of the Ni-Hf joint, processed at 1230°C for 12 hours, followed by solution heat treatment and HIP'ing, are shown in **Figures 124 and 125**. The intergranular phase highlighted by the arrow in **Figure 124** was shown to have a composition of 52.21Ni-44.72Hf-2.11Co-0.53Cr-0.17Ti-0.26W (wt. %), and was provisionally identified as the Ni_7Hf_2 intermetallic compound. The micrograph shown in **Figure 125** indicates that a fine, cuboidal gamma prime (γ') phase had precipitated within the MarM247 γ matrix. The cuboidal and spheroidal γ' precipitates in MarM247 generally form during primary and secondary aging cycles at 1080°C for 4 hours, followed by soaking at 870°C for 24 hours. The HIP cycle used in this investigation therefore overlapped with the primary aging treatment for MarM247, resulting in some γ' precipitation within the γ phase.

Figure 126 displays a SEM micrograph of the Ni-Zr joint after processing at 1230°C for 12 hours, followed by solution annealing and HIP'ing. The phase identified by the arrow had a composition of 72.18Ni-24.43Zr-2.18Co-0.64Cr-0.45Al-0.28W (wt. %), and was identified as Ni_5Zr. Although not evident in **Figure 126**, cuboidal γ' precipitates were observed in the MarM247 powder particles at higher magnification.

7.3.2 Tensile test results:

The results of tensile tests performed at various temperatures are shown in **Tables 27 to 30**, and presented graphically in **Figures 127 to 130**. The values shown represent the average of three tests at each temperature.

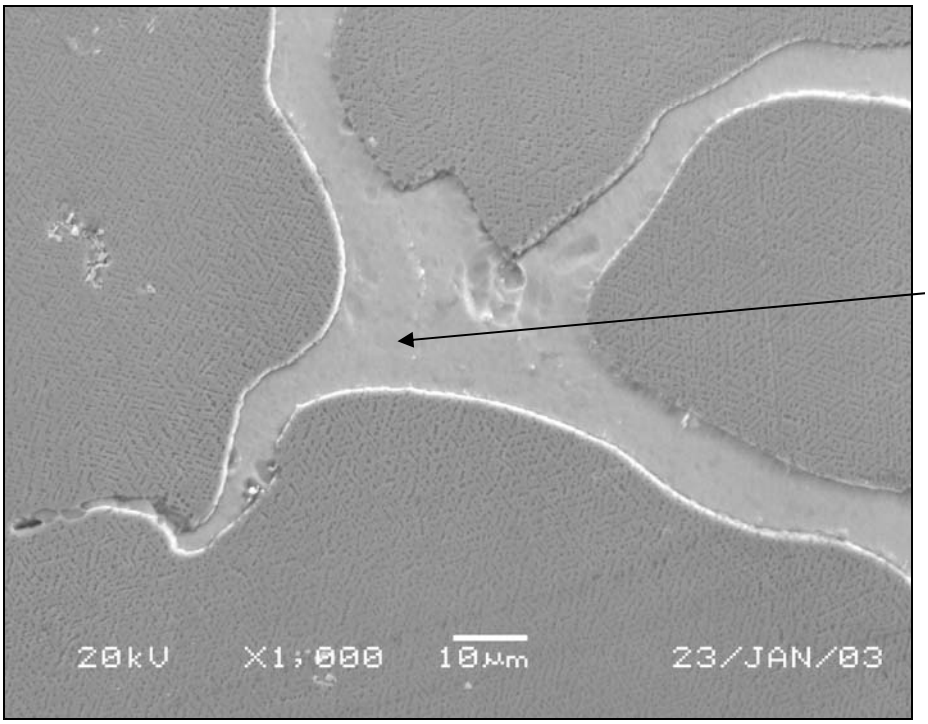

Figure 124 – SEM micrograph of the Ni-Hf braze, showing the intergranular Ni_7Hf_2 intermetallic phase and γ' precipitates within the MarM247 particles.

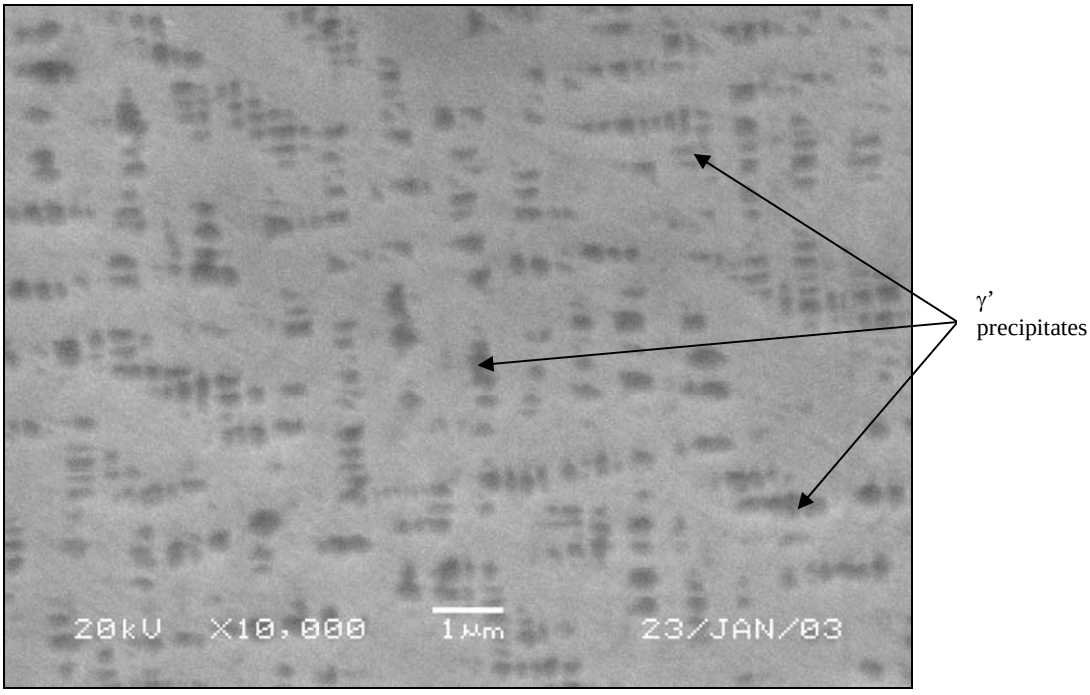

Figure 125 – Higher magnification SEM micrograph of the Ni-Hf braze, showing cuboidal γ' precipitates within the MarM247 powder particles.

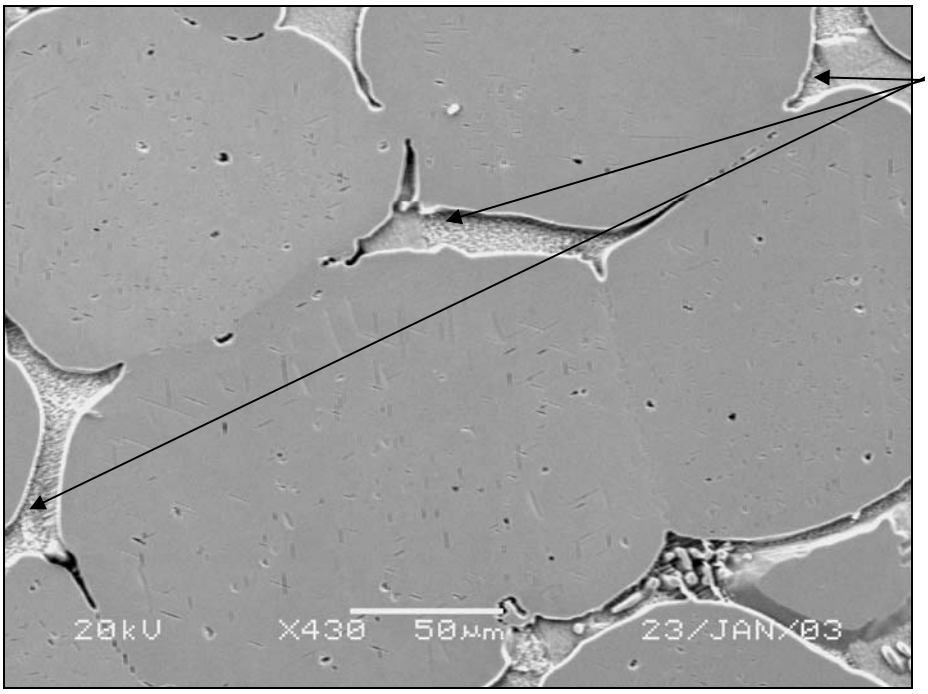

Figure 126 – SEM micrograph of the Ni-Zr braze, showing intergranular Ni_5Zr intermetallic compound.

Table 27 – Joint tensile properties measured at 21°C.

Tensile properties	**Ni-Hf joints** 1230°C for 40 minutes	**Ni-Zr joints** 1230°C for 40 minutes	**Ni-Hf joints** 1230°C for 4 hours	**Ni-Zr joints** 1230°C for 4 hours	**Ni-Hf joints** 1230°C for 12 hours + SHT + HIP	**Ni-Zr joints** 1230°C for 12 hours + SHT + HIP	**MarM247 base metal**
Tensile strength	323 MPa	557 MPa	344 MPa	564 MPa	713 MPa	736 MPa	960 MPa
Yield strength	239 MPa	505 MPa	302 MPa	511 MPa	644 MPa	622 MPa	800 MPa
Elongation (%)	4.7	3.0	2.7	3.0	2.5	3.7	7.9
Reduction in area (%)	6.3	4.4	3.9	4.5	5.6	8.0	10.0

SHT: Solution heat treatment.

Table 28 – Joint tensile properties measured at 540°C.

Tensile properties	**Ni-Hf joints** 1230°C for 40 minutes	**Ni-Zr joints** 1230°C for 40 minutes	**Ni-Hf joints** 1230°C for 4 hours	**Ni-Zr joints** 1230°C for 4 hours	**Ni-Hf joints** 1230°C for 12 hours + SHT + HIP	**Ni-Zr joints** 1230°C for 12 hours + SHT + HIP	**MarM247 base metal**
Tensile strength	328 MPa	619 MPa	406 MPa	625 MPa	740 MPa	999 MPa	1014 MPa
Yield strength	243 MPa	539 MPa	329 MPa	556 MPa	647 MPa	707 MPa	801 MPa
Elongation (%)	3.8	2.7	3.0	2.8	2.7	3.7	7.8
Reduction in area (%)	4.2	3.2	3.8	3.4	5.3	7.9	9.9

SHT: Solution heat treatment.

Table 29 – Joint tensile properties measured at 870°C.

Tensile properties	**Ni-Hf joints** 1230°C for 40 minutes	**Ni-Zr joints** 1230°C for 40 minutes	**Ni-Hf joints** 1230°C for 4 hours	**Ni-Zr joints** 1230°C for 4 hours	**Ni-Hf joints** 1230°C for 12 hours + SHT + HIP	**Ni-Zr joints** 1230°C for 12 hours + SHT + HIP	**MarM247 base metal**
Tensile strength	289 MPa	444 MPa	342 MPa	480 MPa	544 MPa	743 MPa	790 MPa
Yield strength	211 MPa	414 MPa	277 MPa	404 MPa	458 MPa	650 MPa	650 MPa
Elongation (%)	2.0	1.0	2.2	2.1	2.4	3.4	5.0
Reduction in area (%)	3.0	2.4	3.2	3.1	4.2	6.0	7.7

SHT: Solution heat treatment.

Table 30 – Joint tensile properties measured at 980°C.

Tensile properties	**Ni-Hf joints** 1230°C for 40 minutes	**Ni-Zr joints** 1230°C for 40 minutes	**Ni-Hf joints** 1230°C for 4 hours	**Ni-Zr joints** 1230°C for 4 hours	**Ni-Hf joints** 1230°C for 12 hours + SHT + HIP	**Ni-Zr joints** 1230°C for 12 hours + SHT + HIP	**MarM247 base metal**
Tensile strength	195 MPa	261 MPa	266 MPa	308 MPa	282 MPa	311 MPa	506 MPa
Yield strength	141 MPa	245 MPa	206 MPa	214 MPa	223 MPa	239 MPa	312 MPa
Elongation (%)	1.8	0.8	2.7	3.1	4.3	4.8	4.7
Reduction in area (%)	2.9	1.9	3.1	6.2	5.7	2.9	7.5

SHT: Solution heat treatment.

The tensile strength and yield stress of the MarM247 base metal, and the MarM247/Ni-Hf and MarM247/Ni-Zr joints in various conditions, are shown in **Figures 127 and 128** as a function of test temperature. It is evident that the HIP cycle improved the tensile and yield strengths of both joints at all test temperatures, with the strength values approaching those of the base metal at elevated temperatures. The MarM247/Ni-Zr joints displayed higher tensile and yield strengths than the Ni-Hf joints at almost all test temperatures. With an increase in test temperature, the tensile strength of the MarM247/Ni-Zr joints after the HIP cycle varied from 98% of the base metal tensile strength at 540°C, to 94% at 870°C, and 62% at 980°C. Measured yield strength values ranged from 88% of the base metal yield stress at 540°C, to 100% at 870°C, and 77% at 980°C for the Ni-Zr joints following the HIP cycle. Corresponding strength measurements for the MarM247/Ni-Hf joints ranged from 73% and 81% of the base metal properties (for tensile strength and yield stress, respectively) at 540°C, to 69% and 71% at 870°C, and 56% and 72% at 980°C. The increase in strength after the HIP cycle can most likely be attributed to precipitation hardening linked to the formation of fine γ' precipitates in the MarM247 powder particles during the HIP treatment.

As shown in **Figures 129 and 130**, the HIP cycle generally resulted in an improvement in the ductility of the braze joints, particularly at elevated temperatures. The MarM247/Ni-Hf braze joints displayed approximately 45% of the ductility of the base metal at 540°C, increasing to 51% at 870°C, and finally to 84% at 980°C. The ductility of the MarM247/Ni-Zr joints ranged from approximately 64% of the base metal ductility at 540°C, to 73% at 870°C, and almost 100% at 980°C (calculation based on the percentage elongation). The increase in ductility measured at elevated test temperatures is probably associated with the observed decrease in strength.

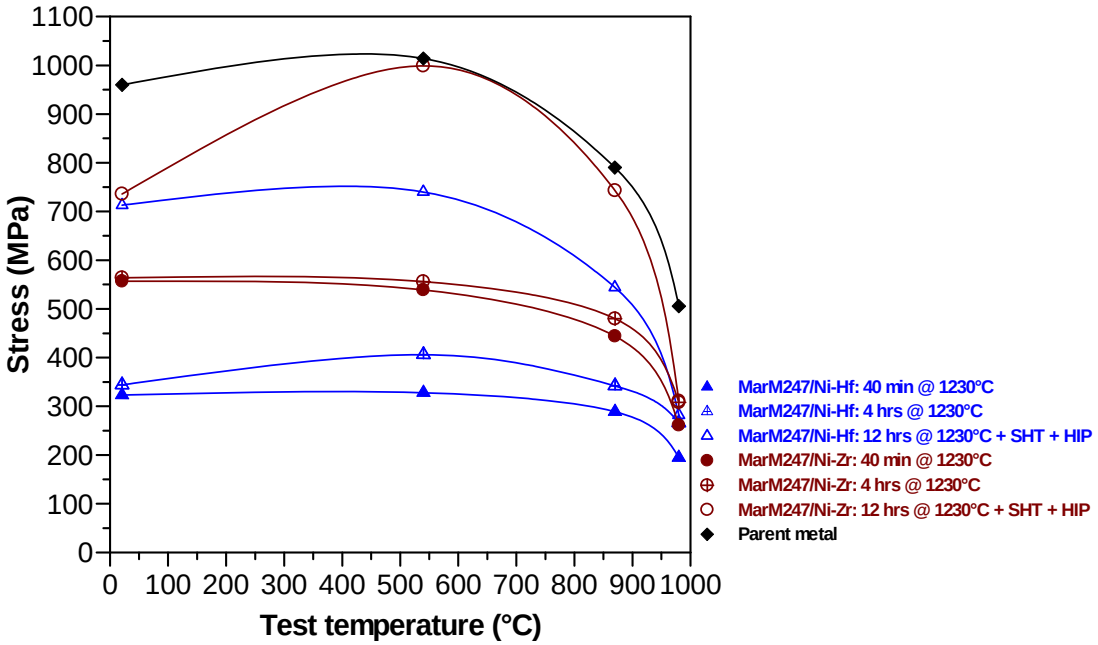

Figure 127 – The tensile strength of the MarM247 base metal, and the MarM247/Ni-Hf and MarM247/Ni-Zr braze joints after brazing for 40 minutes and 4 hours at 1230°C, and after brazing for 12 hours at 1230°C, followed by solution heat treatment and a HIP cycle.

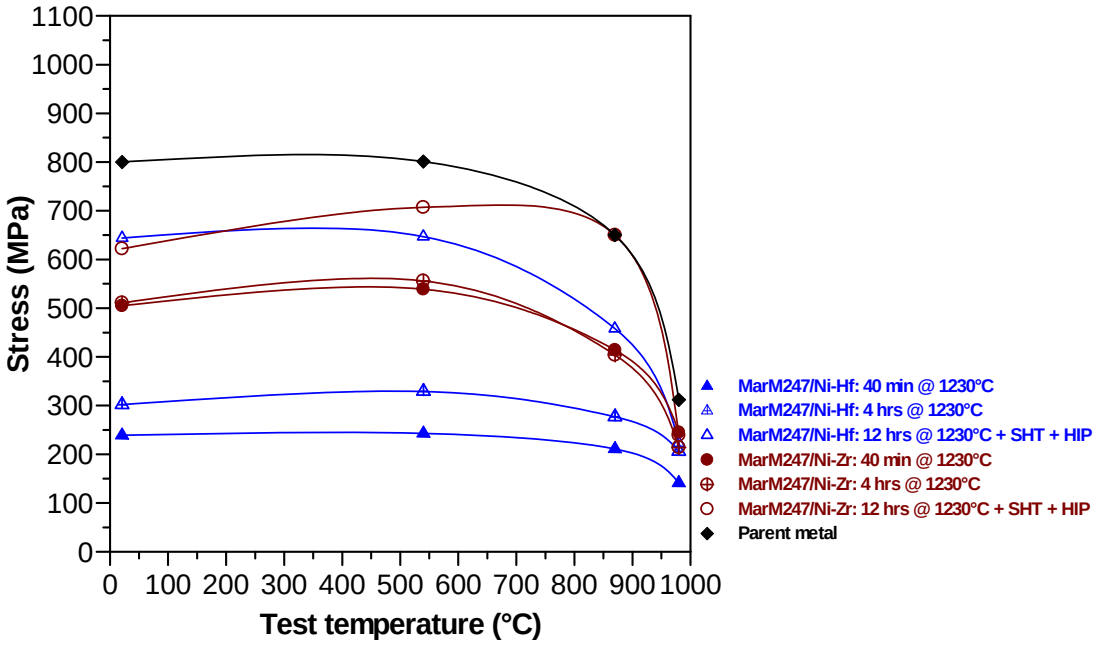

Figure 128 – The yield stress of the MarM247 base metal, and the MarM247/Ni-Hf and MarM247/Ni-Zr braze joints after brazing for 40 minutes and 4 hours at 1230°C, and after brazing for 12 hours at 1230°C, followed by solution heat treatment and a HIP cycle.

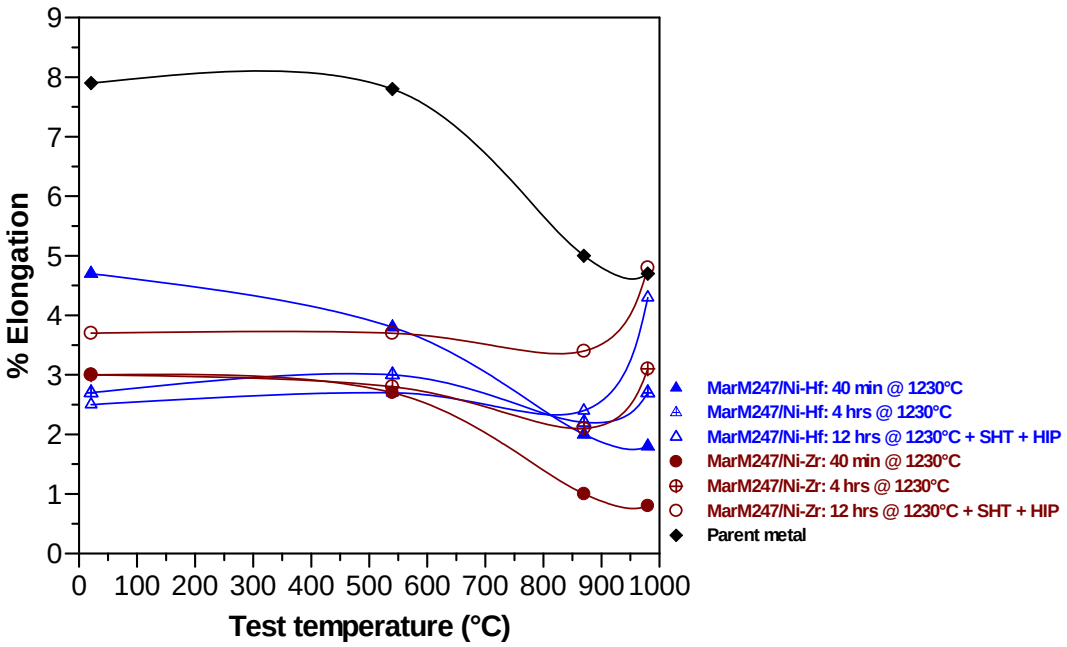

Figure 129 – The percentage elongation of the MarM247 base metal, and the MarM247/Ni-Hf and MarM247/Ni-Zr braze joints after brazing for 40 minutes and 4 hours at 1230°C, and after brazing for 12 hours at 1230°C, followed by solution heat treatment and a HIP cycle.

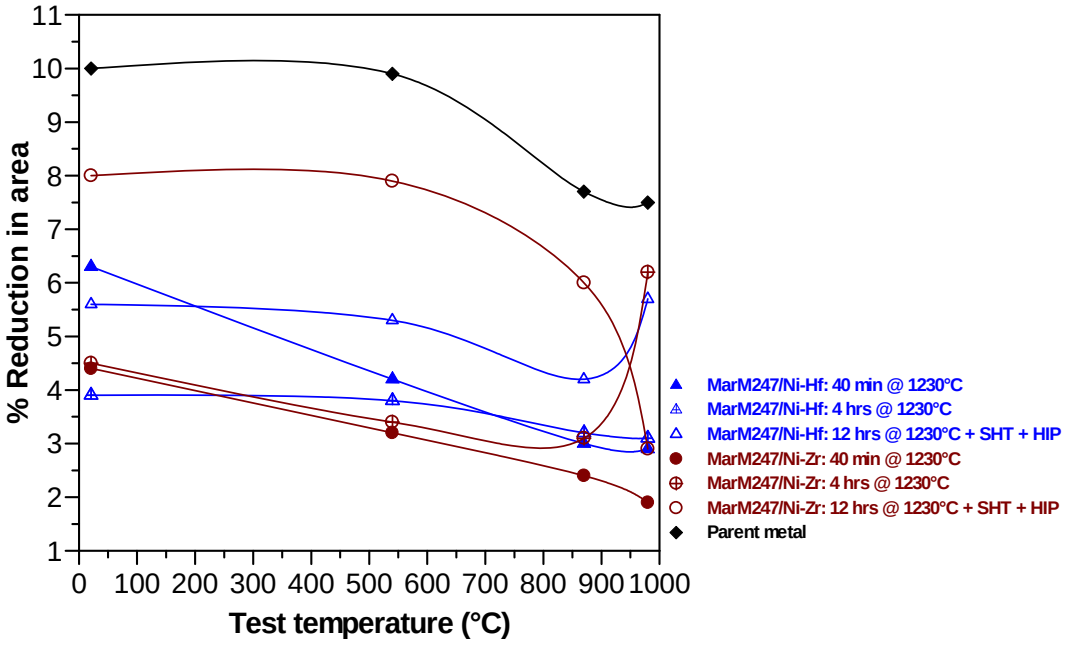

Figure 130 – The percentage reduction in area of the MarM247 base metal, and the MarM247/Ni-Hf and MarM247/Ni-Zr braze joints after brazing for 40 minutes and 4 hours at 1230°C, and after brazing for 12 hours at 1230°C, followed by solution heat treatment and a HIP cycle.

7.3.3 Creep rupture test properties:

The results of creep rupture tests performed at various temperatures and applied stress levels are shown in **Table 31** and presented graphically in the form of a Larson-Miller plot in **Figure 131.**

Table 31 – The influence of a HIP cycle on the creep rupture properties of the In738 base metal and the MarM247/Ni-Hf and MarM247/Ni-Zr joints (1.5 mm joint gap).

Test condition	Property	Ni-Hf 1230°C for 12 hours + SHT	Ni-Hf 1230°C for 12 hours + SHT + HIP	Ni-Zr 1230°C for 12 hours + SHT	Ni-Zr 1230°C for 12 hours + SHT + HIP	In738 base metal
345 MPa at 845°C	**Creep rupture life**	18.6 hours	20.2 hours	21.2 hours	24.4 hours	27.4 hours
	% Elongation	3.7	3.8	3.4	3.9	5.5
	% Reduction in area	5.6	5.6	4.4	4.7	7.3
242 MPa at 900°C	**Creep rupture life**	19.0 hours	19.4 hours	20.5 hours	22.1 hours	29.8 hours
	% Elongation	4.6	4.3	4.1	4.2	5.7
	% Reduction in area	6.1	5.8	5.3	6.7	7.9
138 MPa at 980°C	**Creep rupture life**	13.6 hours	14.8 hours	16.5 hours	17.7 hours	21.2 hours
	% Elongation	6.6	7.0	5.1	8.0	8.1
	% Reduction in area	9.3	24.7	7.1	23.5	11.8

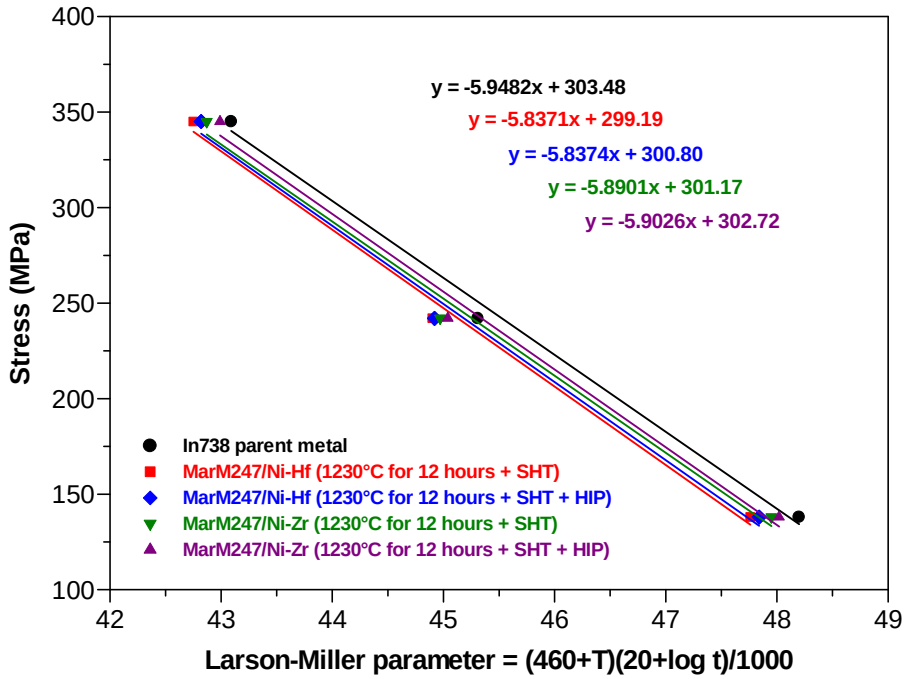

Figure 131 – Larson-Miller plot for the In738 base metal and the MarM247/Ni-Hf and MarM247/Ni-Zr joints after brazing for 12 hours at 1230°C, followed by solution heat treatment (SHT) and a HIP cycle.

The results shown in **Table 31** and in **Figure 131** illustrate that the HIP cycle resulted in an improvement in the creep rupture properties of both the Ni-Hf and Ni-Zr braze joints. The best creep rupture properties were obtained in the MarM247/Ni-Zr joints after brazing at 1230°C for 12 hours, followed by a solution heat treatment at 1230°C for 4 hours and a HIP

cycle at 1080°C for 4 hours. Depending on the test temperature, these joints displayed creep rupture lives between 74% and 89% of that of the base metal. Since the joints were tested in the partially age hardened condition, the creep rupture properties are expected to improve further once the full aging heat treatment is employed.

Although linear regression methods revealed very little statistically relevant difference between the lines representing the braze joints in **Figure 131**, the Larson-Miller plot can be used to rank the braze joints in order of descending creep rupture properties:

- MarM247/Ni-Zr joint brazed at 1230°C for 12 hours, followed by solution heat treatment and a HIP cycle.
- MarM247/Ni-Zr joint brazed at 1230°C for 12 hours, followed by solution heat treatment.
- MarM247/Ni-Hf joint brazed at 1230°C for 12 hours, followed by solution heat treatment and a HIP cycle.
- MarM247/Ni-Hf joint brazed at 1230°C for 12 hours, followed by solution heat treatment.

It is important to note that the improved creep rupture properties displayed by the braze joints after the HIP cycle cannot be attributed to the closure of micropores in the microstructure. The higher creep rupture properties are most likely due to the precipitation of fine γ' precipitates within the MarM247 powder particles during the HIP cycle.

Although equivalent base metal creep properties were not achieved, excellent joint ductility was obtained. For example, during testing at an applied stress level of 138 MPa at 980°C, both the Ni-Zr and Ni-Hf braze joints displayed ductility values in the region of 87% of that of the base metal. This implies that the presence of the Ni_7Hf_2 or Ni_5Zr intermetallic compound within the braze alloy did not embrittle the joints to the same extent as the boride phases observed in Ni-B braze alloys. In boride-containing braze joints, the ductility values rarely exceed 30% of the ductility of the base metal in the case of wide joint gaps.

7.4) Conclusions

- Brazing for 12 hours at 1230°C, followed by solution heat treatment at 1230°C for 4 hours and a HIP cycle at 1080°C for 4 hours, resulted in joint microstructures consisting of MarM247 powder particles, surrounded by eutectic Ni-Hf or Ni-Zr braze alloy containing γ phase and Ni_7Hf_2 or Ni_5Zr intermetallic compound. The extended braze cycle and the solution annealing treatment reduced the fraction of γ phase and the amount of intermetallic compound between the MarM247 particles, resulting in a less continuous film of braze alloy surrounding the MarM247 grains. The HIP cycle induced the precipitation of fine γ' precipitates within the MarM247 powder particles.

- The HIP cycle was not effective in eliminating microporosity from the joint. The HIP temperature may have been too low to close the micropores formed during brazing.

- The HIP cycle significantly improved the tensile and yield strength values of both joints at all test temperatures, with the strength values approaching those of the base metal at elevated temperatures. The MarM247/Ni-Zr joints displayed higher tensile and yield strengths than the Ni-Hf joints at almost all test temperatures. The increase in strength

after the HIP cycle can most likely be attributed to precipitation hardening linked to the formation of fine γ' precipitates in the MarM247 powder particles during the HIP treatment. The HIP cycle generally resulted in an improvement in the ductility of the braze joints, particularly at elevated temperatures. The increase in ductility measured at elevated test temperatures is probably associated with the observed decrease in strength.

- The HIP treatment resulted in an improvement in the creep rupture properties of both the Ni-Hf and Ni-Zr braze joints. The best creep rupture properties were obtained in the MarM247/Ni-Zr joints. Depending on the test temperature, these joints displayed creep rupture properties between 74% and 89% of those of the base metal. Since the joints were tested in the partially age hardened condition, the creep rupture properties are expected to improve further once the full aging heat treatment is employed. Although equivalent base metal creep properties were not achieved, excellent joint ductility was obtained, suggesting that the presence of the Ni_7Hf_2 or Ni_5Zr intermetallic compound within the braze alloy does not embrittle the joints to the same extent as the boride phases observed in Ni-B braze alloys.

- The majority of cracks which form in turbine components during service initiate under low cycle fatigue conditions. The low cycle fatigue properties of braze repaired turbine components therefore ultimately determine whether a braze alloy can be commercialized successfully. Experiment 6, described in Chapter 8, aimed at determining the low cycle fatigue (LCF) properties of the novel braze alloys. In order to obtain representative LCF results, the thermal treatment of the braze joints was optimized based on the results of earlier experiments. The braze time was increased to 24 hours (to promote diffusion of the melt point depressants into the parent metal), the HIP temperature was raised to 1200°C (to eliminate microporosity) and the joints were subjected to the complete primary and secondary aging cycles to precipitate γ' in the MarM247 powder particles.

CHAPTER 8 - EXPERIMENT 6

CHARACTERIZATION OF THE LOW CYCLE FATIGUE PROPERTIES OF LIQUID PHASE DIFFUSION BONDS USING EUTECTIC Ni-Hf AND Ni-Zr BRAZE ALLOYS AFTER BRAZING FOR 24 HOURS, FOLLOWED BY SOLUTION ANNEALING, HOT ISOSTATIC PRESSING AT 1200°C AND A FULL AGING TREATMENT

8.1) Introduction

The results of Experiment 5, described in Chapter 7, revealed that brazing at 1230°C for 12 hours, followed by solution annealing at 1230°C for 4 hours and a HIP treatment at 1080°C for 4 hours, resulted in a microstructure consisting of MarM247 powder particles, interspersed with Ni-Hf or Ni-Zr braze alloy. The layers of braze alloy surrounding the MarM247 powder particles appeared less continuous than those observed during Experiment 4, containing a lower volume fraction of γ phase and Ni_5Zr or Ni_7Hf_2 intermetallic compound. The HIP cycle used in Experiment 5 overlapped with the primary aging cycle for MarM247, resulting in the precipitation of fine γ' particles within the MarM247 grains. The braze joints displayed promising tensile and creep rupture properties, despite being only partially age hardened.

The aim of Experiment 6 was to determine the low cycle fatigue (LCF) properties of the braze joints. Low cycle fatigue testing is essential since cracks in nozzle segments almost always initiate under LCF conditions, and nozzle segments rarely fail under tensile overload or creep rupture conditions. Tensile and creep rupture tests provide the approval authority with an indication of the potential of novel braze alloys, but ultimately it is the low cycle fatigue test results which determine whether a braze alloy will be commercialized. In order to obtain representative LCF results, the thermal treatment of the braze joints was optimized based on the results of earlier experiments. The braze cycle was extended to 24 hours at 1230°C to facilitate diffusion of the melt point depressant (Hf or Zr) into the parent metal, followed by solution annealing at the same temperature for 4 hours. The braze joints were then subjected to a 4 hour HIP treatment. Since the HIP cycle used in Experiment 5 was not effective in eliminating microporosity, the HIP temperature was increased to 1200°C. After the HIP treatment, the specimens were subjected to the full MarM247 aging treatment designed to precipitate a mixture of coarse and fine γ' particles.

8.2) Experimental procedure

During the course of this investigation, In738 plates with dimensions of approximately 240 mm long, 125 mm wide and 15 mm thick were prepared. A 1.5 mm wide groove was machined along the length of the plate, as shown in **Figures 132 and 133**. After machining, the groove was grit blasted with 220 grit silicon carbide media, and wiped with acetone to remove any grit blasting residue.

MarM247 paste was prepared from a mixture of coarse and fine MarM247 powder (as described in §4.2) and used to fill the groove machined in each In738 plate. After drying, a layer of eutectic Ni-Hf braze alloy, Ni-Zr braze alloy or commercially available BRB braze alloy in paste form was applied over the MarM247 powder. As described in Chapter 1, BRB is a B-containing braze of nominal composition Ni-13.5Cr-7.5Co-4Al-2.5B. The plates were dried, and subjected to the following vacuum braze cycle:

1. Ramp up to a temperature of 450°C at a minimum rate of 9°C/minute.
2. Hold at 450°C for 20 minutes to allow the binder to burn off.
3. Ramp up to a temperature of 1150°C at a minimum rate of 9°C/minute.
4. Hold at 1150°C for 20 minutes to allow the samples to stabilize at this temperature.
5. Ramp up to a temperature of 1230°C at a minimum rate of 9°C/minute to melt the Ni-Hf and Ni-Zr braze alloys and to allow the melt to infiltrate the MarM247 powder.
6. Hold at 1230°C for 24 hours.
7. Furnace cool to room temperature.

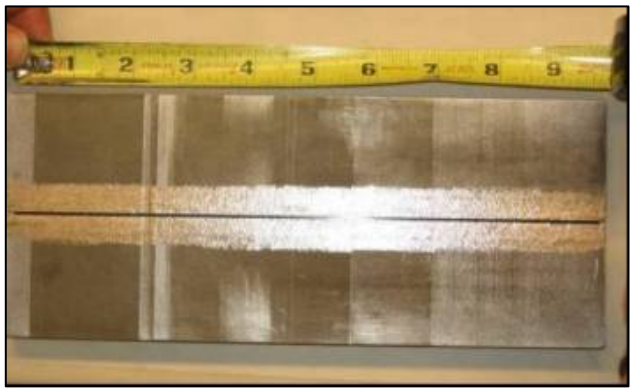

Figure 132 – In738 plate with a 1.5 mm wide groove machined in the center.

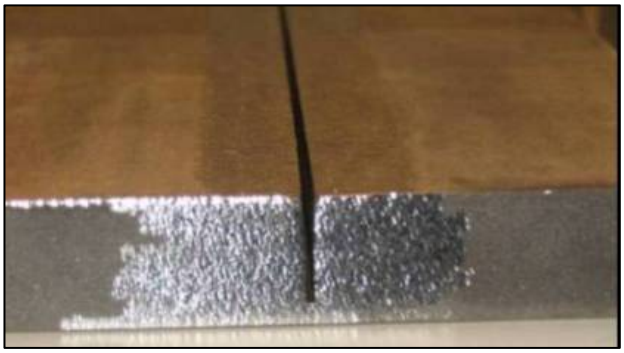

Figure 133 – Enlarged view of the 1.5 mm wide groove machined in the centre of the In738 plate samples.

The brazed plates were transferred to a production furnace and solution annealed at 1230°C for 4 hours, followed by gas quenching. The solution annealed samples were then subjected to a revised HIP cycle at a pressure of 104 MPa (15000 psi), as described below:

1. Ramp up to a temperature of 1200°C at a minimum rate of 11°C/minute.
2. Hold at 1200°C for 4 hours.
3. Gas quench as rapidly as possible using argon gas at 2 bar pressure.

Following the HIP cycle, the plates were subjected to the primary and secondary aging heat treatments used in industry to precipitate a combination of fine and coarse γ' precipitates in MarM247. The primary aging heat treatment involves holding the material at 1080°C for 4 hours, followed by gas quenching. This aging cycle is followed by the secondary aging heat

treatment, during which the samples are held at 870°C for 20 hours, followed by gas quenching.

After thermal processing, 12.7 mm diameter low cycle fatigue test specimens were machined from the plates in such a way that each braze joint formed a full butt joint in the centre of the gauge length. The ends of the samples were threaded and the diameter of the gauge length reduced to 6.35 mm (as shown in **Figure 134**).

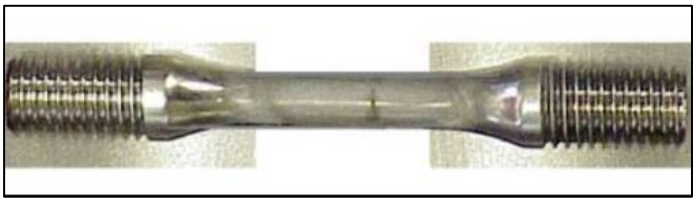

Figure 134 - LCF specimen with the braze joint in the centre of the gauge length.

Low cycle fatigue tests were performed at a test temperature of 870°C under strain control conditions. The tests were performed at a constant strain rate of 0.01 s^{-1} with a symmetrical triangular waveform. The total strain was varied from 0.3% to 2% and the test frequency from 1 Hz to 0.33 Hz. A constant A-ratio (defined below) of +1 was maintained during testing.

A-ratio = (maximum strain – minimum strain) / (maximum strain + minimum strain)

8.3) LCF test results:

The results of the LCF tests for the In738 base metal, and the MarM247/Ni-Hf, MarM247/Ni-Zr and In738/BRB braze joints, are displayed graphically in **Figure 135**.

The In738 base metal displayed the best LCF properties, whereas the In738/BRB braze joint had the lowest LCF properties. BRB is a B-containing braze filler metal with a known tendency to form brittle borides in wide gap brazed joints. These boride phases are hard and brittle, and have a detrimental effect on the LCF properties. The Ni-Hf braze joint displayed slightly higher LCF life than the Ni-Zr braze joint.

The LCF graph shown in **Figure 135** can be divided into three regions:

- Below a strain of 0.4%, the BRB braze joint exhibited 70% of the fatigue life of the base metal, compared to 85% for the MarM247/Ni-Zr braze, and 96% for the MarM247/Ni-Hf braze joint. Different repair authorities normally have different acceptance and rejection criteria, but it is safe to say that if a braze joint displays 70% or more of the base metal's LCF life, the braze filler can be utilized for production braze repairs of cracks in stationary nozzle segments. Unfortunately, only a small number of cracks are normally located in regions of nozzles where the strain is less than 0.4%.

- Between 0.4% and 0.8% strain, the BRB braze joint exhibited only 11% of the base metal's life, whereas the MarM247/Ni-Zr braze displayed 70% and the MarM247/Ni-Hf braze 74% of the base metal's low cycle fatigue life. The majority of cracks in nozzle

segments occur in this strain range, suggesting that both the Ni-Zr and Ni-Hf braze filler metals are likely to outperform the B-containing braze alloy in service.

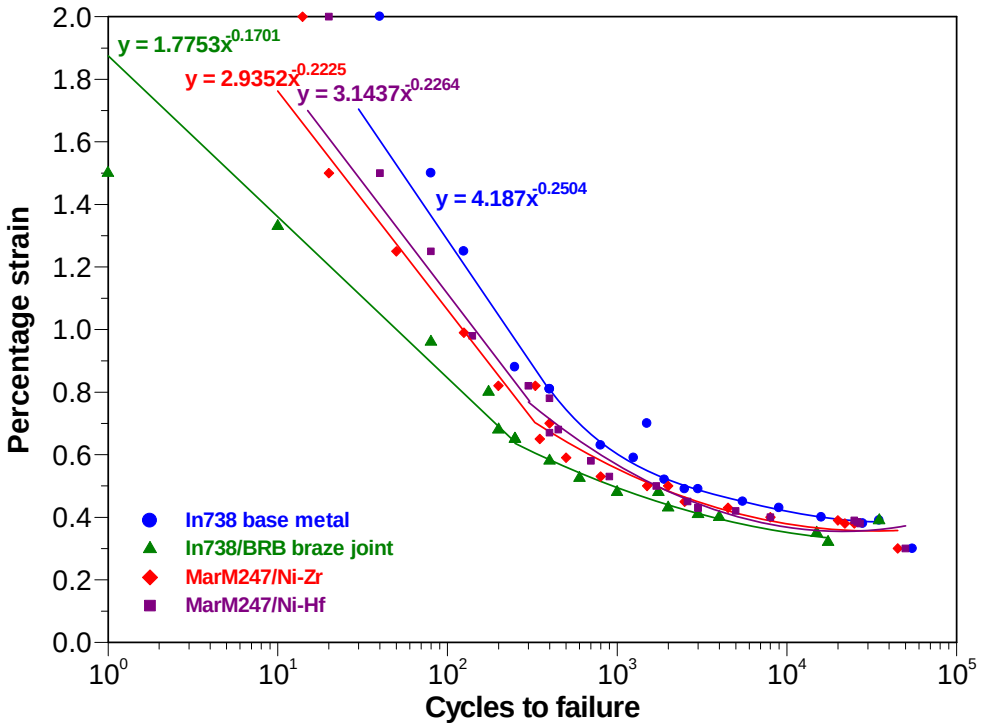

Figure 135 – Low cycle fatigue properties of the In738 base metal, the In738/BRB braze joint, and the MarM247/Ni-Zr and MarM247/Ni-Hf braze joints.

- Between 0.8% and 2% strain, representing the region of a nozzle segment where one or two cracks typically form during service, none of the braze joints evaluated displayed good LCF life. At a strain level of 1.5%, the BRB braze joint failed after only 1 cycle, whereas the Ni-Zr and Ni-Hf braze joints failed after 30 and 40 cycles, respectively. The base metal failed after 80 cycles at this strain level, indicating that none of the three braze filler metals evaluated approach the LCF properties of the base metal at high strains. Nevertheless, the Ni-Zr and Ni-Hf braze joints outperformed the BRB braze joint by an order of magnitude, suggesting improved performance and easier acceptance compared to the commercially available B-containing BRB braze filler metal.

8.4) Conclusions

- Since cracks in nozzle segments generally initiate under low cycle fatigue conditions, a braze joint should ideally display LCF properties equivalent or better than those of the base metal. Since the original cracks in a nozzle segment form in the base metal, a repaired area with inferior LCF properties compared to those of the base metal will result in earlier crack initiation and faster crack propagation.

- The measured LCF properties of the B-containing BRB braze were vastly inferior to those of the base metal, with the In738/BRB braze joint displaying a low cycle fatigue life of only 1 cycle at an applied strain of 1.5%, compared to 80 cycles for the base metal at the same level of strain. Although the Ni-Zr and Ni-Hf braze joints displayed superior LCF properties at high strains compared to the BRB joints, the LCF properties of the

novel braze alloys at high strains were only 27% and 50%, respectively, of the base metal's LCF properties.

- At intermediate strain levels (0.4% to 0.8% strain), the Ni-Zr and Ni-Hf braze joints displayed 70% and 74%, respectively, of the LCF properties of the base metal. At these strain levels, the novel alloys outperformed the BRB braze alloy that displayed only 11% of the base metal's LCF properties.

- At low strain rates (0.2% to 0.4% strain), the Ni-Zr and Ni-Hf braze joints displayed LCF properties equivalent to those of the base metal, whereas the BRB joint exhibited approximately 70% of the base metal's LCF properties.

- Although the Ni-Zr or Ni-Hf braze alloys did not display LCF properties equivalent to those of the base metal at high strain values, the novel braze filler metals outperformed the commercially available B-containing BRB braze alloy. The new alloys should therefore have a distinct advantage over the B-containing braze filler metals in the repair of nozzle segments in industry.

- The good ductility values and promising LCF properties of LPDB joints produced using the novel braze alloys suggested that it may be possible to further improve the joint ductility by combining the braze paste with a ductile solid solution strengthened Ni-base superalloy within the joint, rather than the γ'-strengthened MarM247 powder evaluated in previous chapters. The results of such a change in joint matrix alloy are presented in Chapter 9.

CHAPTER 9 - EXPERIMENT 7

CHARACTERIZATION OF THE MECHANICAL PROPERTIES OF LIQUID PHASE DIFFUSION BONDS PRODUCED BY MIXING A SOLID SOLUTION STRENGTHENED NICKEL-BASE SUPERALLOY POWDER WITH THE EUTECTIC Ni-Hf AND Ni-Zr BRAZE ALLOYS

9.1) Introduction

During the preceding experiments, described in Chapters 4 to 8, a precipitation hardenable, γ'-strengthened Ni-base superalloy powder, known as MarM247, was mixed with the eutectic Ni-Zr or Ni-Hf braze alloy within the joint in an attempt to produce high-strength braze joints with good ductility. As a possible alternative, a ductile solid solution strengthened superalloy powder, such as Haynes 230, may be substituted for the MarM247 powder in an attempt to improve the ductility of the joint.

Experiment 9 therefore aimed to compare the mechanical properties (and in particular the ductility) of MarM247/Ni-Zr joints with Haynes 230/Ni-Zr joints in order to determine whether a braze joint with a solid solution strengthened matrix (in lieu of a γ'-strengthened matrix) displays a higher level of ductility.

9.2) Experimental procedure

In738 plate material was produced and prepared as described in §3.2. A mixture of coarse and fine Haynes 230 Ni-base superalloy powder with a nominal composition shown in **Table 32** was mixed with braze binder to form a paste. The Haynes 230 paste was applied to the In738 plate over an area of approximately 2500 mm^2 and allowed to dry. A layer of eutectic Ni-Zr braze alloy in paste form (produced as described in §3.2) was then applied over the dry Haynes 230 powder. The samples were dried for one hour, and placed in a laboratory vacuum furnace.

Table 32 – Nominal chemical composition of the Haynes 230 powder used in this investigation (wt.%, balance Ni).

B	C	Co	Cr	Mn	Mo	Al	W	La	Si	Fe
0.015	0.1	5.0	22.0	0.5	2.0	0.3	14.0	0.02	0.4	3.0

The vacuum braze cycle used was as follows:

1) Ramp up to a temperature of 450°C at a minimum rate of 9°C/minute.
2) Hold at 450°C for 20 minutes to allow the binder to burn off.
3) Ramp up to a temperature of 1150°C at a minimum rate of 9°C/minute.
4) Hold at 1150°C for 20 minutes to allow the samples to stabilize at this temperature.
5) Ramp up to a temperature of 1230°C at a minimum rate of 9°C/minute to melt the Ni-Zr braze alloy and to allow the melt to infiltrate the Haynes 230 powder particles.
6) Hold at 1230°C for 12 hours.
7) Furnace cool to room temperature.

After brazing, the samples were transferred to a production vacuum furnace equipped with quenching facilities in order to solution anneal the joint. Gas quenching, using 2 bar argon pressure, was utilized on completion of the solution annealing cycle. The solution heat treatment used in this experiment was as follows:

1) Ramp up to a temperature of 1230°C at a minimum rate of 14°C per minute.
2) Hold at 1230°C for 4 hours.
3) Quench to room temperature at a minimum rate of 50°C per minute.

The solution heat treatment was followed by a HIP cycle at an isostatic pressure of 104 MPa (15 000 psi), using the following procedure:

1) Ramp up to a temperature of 1080°C at a minimum rate of 11°C per minute.
2) Hold at 1080°C for 4 hours.
3) Quench to room temperature at a rate of 50°C per minute.

In order to characterize the tensile properties of the braze joint after solution annealing and HIP'ing, tensile tests were performed at room temperature, 95°C, 315°C, 540°C, 650°C, 870°C and 980°C using the tensile test procedure described in §4.2. Creep rupture tests were performed (as described in §6.2) using the combinations of test temperature and applied stress shown in **Table 33**. These temperature/stress combinations were selected because the creep rupture properties of the standard Haynes 230 alloy under these test conditions have been documented.

Table 33 – Creep rupture test conditions.

Test temperature	Applied stress
650°C	385 MPa (56 ksi)
760°C	185 MPa (27 ksi)
870°C	95 MPa (14 ksi)
980°C	41 MPa (6.0 ksi)
1040°C	24 MPa (3.5 ksi)
1095°C	14 MPa (2.1 ksi)

9.3) Results and discussion

9.3.1 Tensile test results:

The results of tensile tests performed at various temperatures are shown in **Tables 34 to 40**, and are presented graphically in **Figures 136 to 138**. The values shown represent the average of three tests at each temperature.

Table 34 – Joint tensile properties measured at 21°C.

Tensile properties	**MarM247/Ni-Zr joint** 1230°C for 12 hours + SHT + HIP	**Haynes 230/Ni-Zr joint** 1230°C for 12 hours + SHT + HIP	**Haynes 230**	**In738**	**MarM247**
Tensile strength	736 MPa (107 ksi)	737 MPa (107 ksi)	860 MPa (125 ksi)	821 MPa (119 ksi)	960 MPa (139 ksi)
Yield strength	622 MPa (90 ksi)	718 MPa (104 ksi)	395 MPa (57 ksi)	683 MPa (99 ksi)	800 MPa (116 ksi)
Elongation (%)	3.7	1.3	50	4.0	7.9

Table 35 – Joint tensile properties measured at 95°C.

Tensile properties	**MarM247/Ni-Zr joint** 1230°C for 12 hours + SHT + HIP	**Haynes 230/Ni-Zr joint** 1230°C for 12 hours + SHT + HIP	**Haynes 230**	**In738**	**MarM247**
Tensile strength	Not tested	739 MPa (107 ksi)	835 MPa (121 ksi)	883 MPa (128 ksi)	1014 MPa (147 ksi)
Yield strength	Not tested	726 MPa (105 ksi)	359 MPa (52 ksi)	752 MPa (109 ksi)	801 MPa (116 ksi)
Elongation (%)	Not tested	2.4	51	5.0	7.8

Table 36 – Joint tensile properties measured at 315°C.

Tensile properties	**MarM247/Ni-Zr joint** 1230°C for 12 hours + SHT + HIP	**Haynes 230/Ni-Zr joint** 1230°C for 12 hours + SHT + HIP	**Haynes 230**	**In738**	**MarM247**
Tensile strength	Not tested	533 MPa (77 ksi)	787 MPa (114 ksi)	856 MPa (124 ksi)	1001 MPa (145 ksi)
Yield strength	Not tested	520 MPa (75 ksi)	324 MPa (47 ksi)	725 MPa (105 ksi)	807 MPa (117 ksi)
Elongation (%)	Not tested	2.0	52	5.0	7.7

Table 37 – Joint tensile properties measured at 540°C.

Tensile properties	**MarM247/Ni-Zr joint** 1230°C for 12 hours + SHT + HIP	**Haynes 230/Ni-Zr joint** 1230°C for 12 hours + SHT + HIP	**Haynes 230**	**In738**	**MarM247**
Tensile strength	999 MPa (145 ksi)	638 MPa (92 ksi)	705 MPa (103 ksi)	876 MPa (127 ksi)	1014 MPa (147 ksi)
Yield strength	707 MPa (103 ksi)	624 MPa (90 ksi)	275 MPa (40 ksi)	745 MPa (108 ksi)	807 MPa (117 ksi)
Elongation (%)	3.7	1.9	53	5.1	7.8

Table 38 – Joint tensile properties measured at 650°C.

Tensile properties	**MarM247/Ni-Zr joint** 1230°C for 12 hours + SHT + HIP	**Haynes 230/Ni-Zr joint** 1230°C for 12 hours + SHT + HIP	**Haynes 230**	**In738**	**MarM247**
Tensile strength	Not tested	511 MPa (74 ksi)	675 MPa (98 ksi)	828 MPa (120 ksi)	1021 MPa (148 ksi)
Yield strength	Not tested	497 MPa (72 ksi)	275 MPa (40 ksi)	690 MPa (100 ksi)	814 MPa (118 ksi)
Elongation (%)	Not tested	1.8	55	5.5	7.2

Table 39 – Joint tensile properties measured at 870°C.

Tensile properties	**MarM247/Ni-Zr joint** 1230°C for 12 hours + SHT + HIP	**Haynes 230/Ni-Zr joint** 1230°C for 12 hours + SHT + HIP	**Haynes 230**	**In738**	**MarM247**
Tensile strength	743 MPa (108 ksi)	555 MPa (80 ksi)	435 MPa (63 ksi)	690 MPa (100 ksi)	790 MPa (115 ksi)
Yield strength	650 MPa (94 ksi)	541 MPa (78 ksi)	255 MPa (37 ksi)	137 MPa (76 ksi)	650 MPa (94 ksi)
Elongation (%)	3.4	1.5	65	7.5	5.0

Table 40 – Joint tensile properties measured at 980°C.

Tensile properties	**MarM247/Ni-Zr joint** 1230°C for 12 hours + SHT + HIP	**Haynes 230/Ni-Zr joint** 1230°C for 12 hours + SHT + HIP	**Haynes 230**	**In738**	**MarM247**
Tensile strength	311 MPa (45 ksi)	267 MPa (39 ksi)	240 MPa (35 ksi)	414 MPa (60 ksi)	506 MPa (73 ksi)
Yield strength	240 MPa (35 ksi)	189 MPa (27 ksi)	145 MPa (21 ksi)	283 MPa (41 ksi)	312 MPa (45 ksi)
Elongation (%)	4.8	1.8	83	8.0	4.7

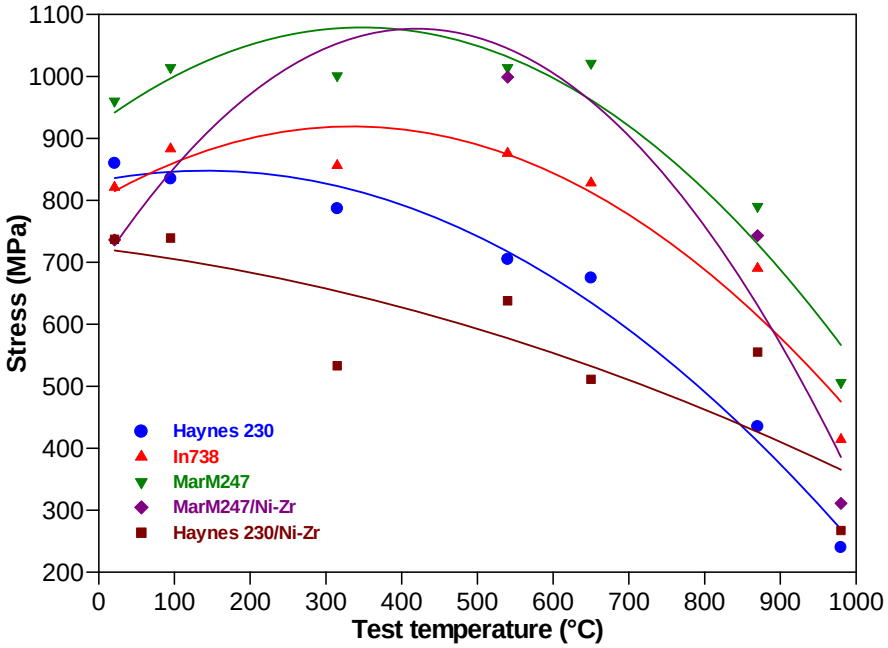

Figure 136 – Tensile strength of Haynes 230, In738, MarM247, the MarM247/Ni-Zr braze joint and the Haynes 230/Ni-Zr braze joint as a function of test temperature.

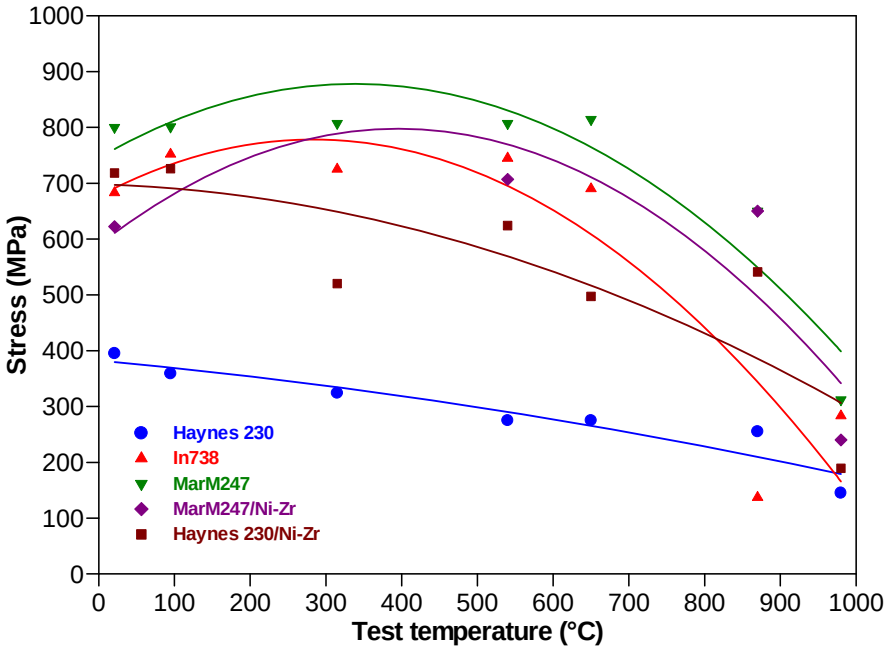

Figure 137 – Yield stress of Haynes 230, In738, MarM247, the MarM247/Ni-Zr braze joint and the Haynes 230/Ni-Zr braze joint as a function of test temperature.

As shown **Table 34** and **Figures 136 and 137**, the room temperature tensile and yield strengths of the Haynes 230/Ni-Zr joint compared well with those of the MarM247/Ni-Zr joint. The high strength of the Haynes 230/Ni-Zr joint relative to that of the MarM247/Ni-Zr joint is attributed to it being in its highest strength condition (i.e. solution heat treated), whereas the MarM247/Ni-Zr joint was in the solution heat treated and partially aged condition. The MarM247/Ni-Zr joint only achieves its highest mechanical strength after secondary aging at 870^{o}C.

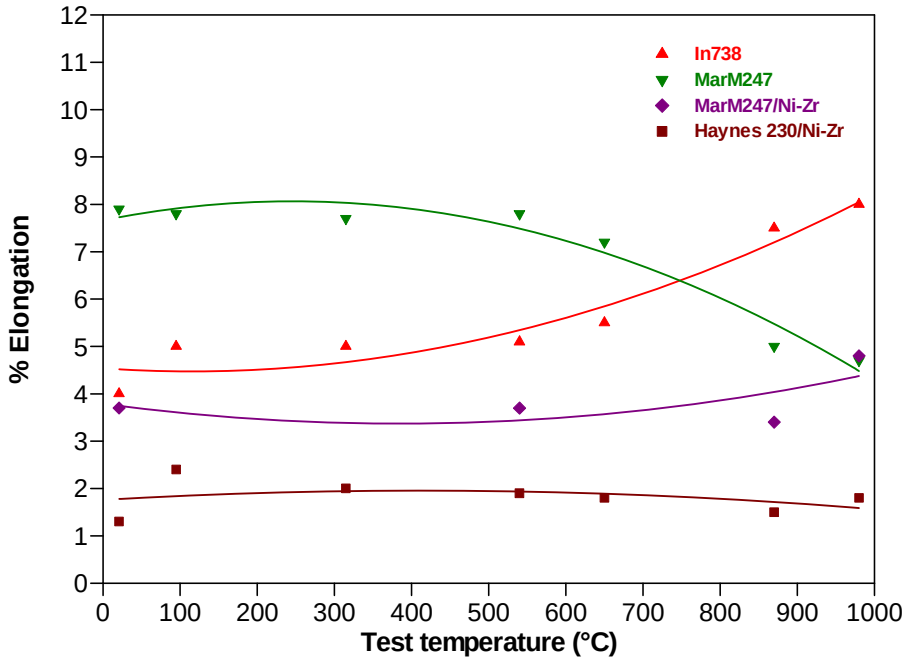

Figure 138 – Percentage elongation of In738, MarM247, the MarM247/Ni-Zr braze joint and the Haynes 230/Ni-Zr braze joint as a function of test temperature.

As shown in **Table 34** and **Figure 138,** the room temperature ductility (expressed as percentage elongation) of the Haynes 230/Ni-Zr joint was surprisingly low, given that Haynes 230 material normally exhibits up to 50% elongation at room temperature. In contrast, the percentage elongation of the MarM247/Ni-Zr joint after solution heat treatment and HIP'ing (representing partial aging) achieved approximately 63% of the ductility of MarM247 and 75% of the measured ductility of the In738 base metal. Although not examined in more detail, it is postulated that the low ductility of the Haynes 230/Ni-Zr joint may be due to the braze alloy disrupting the continuity of the matrix, limiting the ductility of the joint. It is also possible that the majority of the plastic deformation in the joint was concentrated in the more ductile Haynes 230 powder particles, resulting in rapid work hardening of the austenitic matrix and premature failure during testing.

With an increase in the test temperature, the tensile and yield strengths of the MarM247/Ni-Zr joint increased, reaching peak strength values at a test temperature of approximately 540°C. At peak strength, the tensile and yield strength values of the MarM247/Ni-Zr joint attained 98% and 88%, respectively, of the tensile and yield strengths of MarM247 at the same temperature, and exceeded those of the In738 base metal. With a further increase in test temperature above 540°C, the tensile and yield strengths of the MarM247/Ni-Zr joint gradually decreased, following the same general trend as that observed for the MarM247 and In738 samples. The tensile and yield strengths of the Haynes 230/Ni-Zr joint gradually decreased with an increase in test temperature, following the same general trend as that of the Haynes 230 samples.

As shown in **Figure 138**, the ductility values (expressed as percentage elongation) of both joints were well below the ductility of the MarM247 and In738 samples at all test temperatures. The ductility of the MarM247/Ni-Zr joint increased slightly with an increase in test temperature, probably associated with the observed decrease in strength at higher temperatures. The measured ductility of the Haynes 230/Ni-Zr joint remained very low and did not vary to any significant extent with an increase in test temperature. It is postulated that

most of the plastic deformation during tensile testing was concentrated in the more ductile Haynes 230 powder particles, resulting in rapid work hardening and premature failure.

9.3.2 Creep rupture test results:

Creep rupture test results measured at various temperatures and stress levels are shown in **Table 41** and presented graphically in **Figure 139** in the form of a Larson-Miller plot. Also included are the creep rupture properties of In738 base metal and MarM247/Ni-Zr joints (from Chapter 7). Each value shown represents the average of three tests.

Table 41 – Creep rupture properties of In738, Haynes 230 and the MarM247/Ni-Zr and Haynes 230/Ni-Zr joints (1.5 mm joint gap).

Test condition	Property	MarM247/Ni-Zr braze SHT + HIP	Haynes 230/Ni-Zr braze SHT + HIP	In738	Haynes 230
385 MPa at 650°C	**Creep rupture life** **% Elongation** **% Reduction in area**	Not tested	110 hours 1.7 0.7	Not tested	100 hours
185 MPa at 760°C	**Creep rupture life** **% Elongation** **% Reduction in area**	Not tested	212.8 hours 0.3 1.7	Not tested	100 hours
345 MPa at 845°C	**Creep rupture life** **% Elongation** **% Reduction in area**	24.4 hours 3.9 4.7	Not tested	27.4 hours 5.5 7.3	Not tested
95 MPa at 870°C	**Creep rupture life** **% Elongation** **% Reduction in area**	Not tested	114.6 hours 0.6 0.9	Not tested	100 hours
242 MPa at 900°C	**Creep rupture life** **% Elongation** **% Reduction in area**	22.1 hours 4.2 6.7	Not tested	29.8 hours 5.7 7.9	Not tested
41 MPa at 980°C	**Creep rupture life** **% Elongation** **% Reduction in area**	Not tested	252.2 hours 1.7 11.1	Not tested	100 hours
138 MPa at 980°C	**Creep rupture life** **% Elongation** **% Reduction in area**	17.7 hours 8.0 23.5	Not tested	21.2 hours 8.1 11.8	Not tested
24 MPa at 1040°C	**Creep rupture life** **% Elongation** **% Reduction in area**	Not tested	139.3 hours 4.1 6.0	Not tested	100 hours
14 MPa at 1095°C	**Creep rupture life** **% Elongation** **% Reduction in area**	Not tested	126.4 hours 1.8 18.5	Not tested	100 hours

SHT: Solution heat treatment at 1230°C for 4 hours.
HIP: Hot isostatic pressing at 1080°C for 4 hours.

It is evident from **Table 41** and **Figure 139** that the creep rupture properties of the Haynes 230/Ni-Zr joint were equivalent to that of Haynes 230 parent material, but inferior to those of the MarM247/Ni-Zr joint, and well below the creep rupture properties of the In738 base metal. The measured creep rupture life of the MarM247/Ni-Zr joint varied between 74% and 89% of that of the In738 base metal. It must be emphasized that the creep rupture properties of the MarM247/Ni-Zr joints are expected to improve on application of the full aging cycle (the results given in **Table 41** and **Figure 139** are relevant to the partially aged condition).

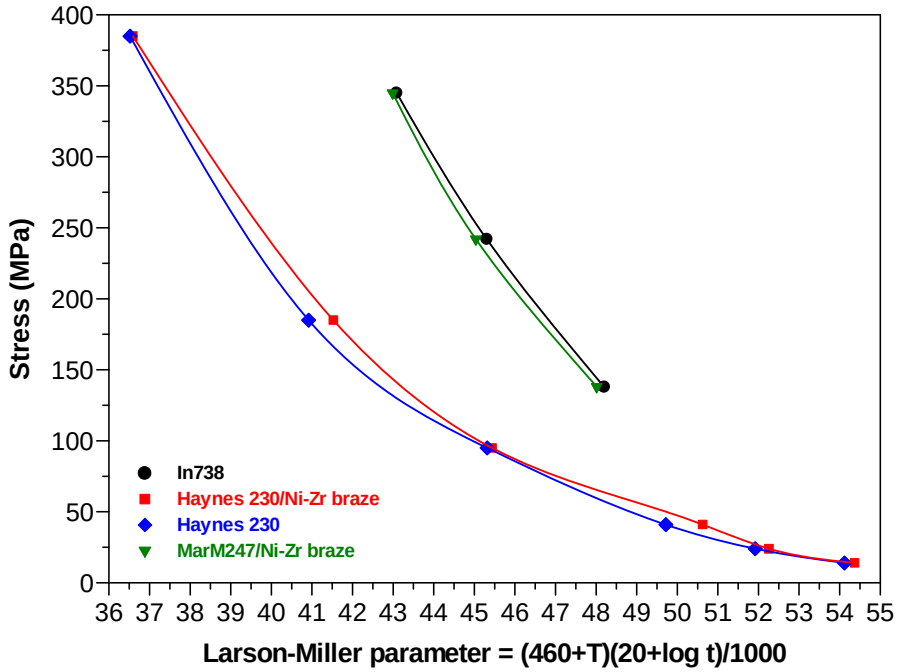

Figure 139 – Creep rupture properties of In738, Haynes 230, the MarM247/Ni-Zr braze joint and the Haynes 230/Ni-Zr braze joint.

The creep rupture test results shown in **Table 41** confirm the observation (described in §9.3.1) of poor ductility in the case of the Haynes 230/Ni-Zr joints. Both the percentage elongation and the percentage reduction in area values were very low, especially in the high stress/low temperature creep regime. At higher test temperatures (such as 1040°C and 1095°), where the applied stress levels were lower, the ductility improved considerably. The MarM247/Ni-Zr joints displayed very good ductility, achieving up to 88% of the percentage elongation and reduction in area of the base metal (at a temperature of 980°C and an applied stress level of 138 MPa). Although equivalent base metal ductility was not obtained, the MarM247/Ni-Zr joints outperformed the commercially available B-containing brazes, for which elongation and reduction in area values below 30% are usually obtained in 1.5 mm wide joints. This suggests that the Ni_5Zr intermetallic phase within the Ni-Zr joints does not embrittle the braze joints to the same extent as the boride phases commonly observed when B-containing braze alloys are used to fill in wide gaps.

9.4) Conclusions

- Although the solid solution strengthened Haynes 230 Ni-base superalloy displays excellent ductility over a temperature range from room temperature to 980°C (well in excess of that documented for cast, γ'-strengthened alloys), Haynes 230/Ni-Zr braze joints displayed very poor ductility during testing. This may be due to the property mismatch between the Haynes 230 powder particles within the joint and the In738 parent material. During tensile testing, most of the plastic deformation is expected to take place in the more ductile Haynes 230 material, resulting in rapid work hardening of the austenitic matrix, and premature failure.

- The room temperature tensile and yield strengths of the Haynes 230/Ni-Zr joint compared well with those of the MarM247/Ni-Zr joint. With an increase in test

temperature, the tensile and yield strengths of the MarM247/Ni-Zr joint increased, reaching peak strength values at a test temperature of approximately 540°C. At peak strength, the tensile and yield strength values of the MarM247/Ni-Zr joint attained 98% and 88%, respectively, of the tensile and yield strengths of MarM247 at the same temperature, and exceeded those of the In738 base metal. With a further increase in test temperature above 540°C, the tensile and yield strengths of the MarM247/Ni-Zr joint gradually decreased, following the same general trend as that observed for the MarM247 and In738 samples. The tensile and yield strengths of the Haynes 230/Ni-Zr joint gradually decreased with an increase in test temperature, following the same trend as Haynes 230.

- The MarM247/Ni-Zr joints displayed excellent creep rupture properties, achieving between 74% and 89% of the creep rupture life of the In738 parent material. The creep rupture properties of the MarM247/Ni-Zr joints are expected to improve further on application of the full aging cycle. The MarM247/Ni-Zr joints also displayed very good ductility, achieving up to 88% of the ductility of the base metal. Although equivalent base metal ductility was not obtained, the MarM247/Ni-Zr joints outperformed the commercially available B-containing brazes.

- The Haynes 230/Ni-Zr joints displayed creep rupture properties equivalent to those of the Haynes 230 base metal, but inferior to those of the In738 parent material and the MarM247/Ni-Zr braze joints. Since the creep rupture properties of solid solution strengthened alloys, such as Haynes 230, are inferior to those of γ'-strengthened alloys, the poor creep rupture properties of the Haynes 230/Ni-Zr joints were not unexpected. The ductility values of the Haynes 230/Ni-Zr joint were, however, disappointingly low, especially in the high stress/low temperature creep regime. These low ductility values are attributed to the property mismatch between the braze joints and the parent material.

- Since the use of a more ductile matrix alloy in the braze joint did not result in any significant improvement in mechanical properties, the next chapter describes preliminary experiments aimed at improving the performance of the braze joints through the addition of chromium and boron to hypo-eutectic Ni-Hf braze alloys.

CHAPTER 10 - EXPERIMENT 8

CHARACTERIZATION OF THE MICROSTRUCTURE AND PROPERTIES OF HYPO-EUTECTIC Ni-Cr-Hf AND Ni-Cr-Hf-B ALLOYS

10.1) Introduction

The experiments described in earlier chapters focused on simple binary eutectic Ni-Zr or Ni-Hf braze alloys. Since the joint ductility could not be improved by using a more ductile solid solution strengthened matrix alloy within the joint (as described in Chapter 9), an attempt was made to improve the performance of the novel braze filler metals by producing a series of ternary and quaternary hypo-eutectic Ni-Hf alloys containing chromium and boron.

The aim of this experiment was therefore to develop ternary and quaternary hypo-eutectic braze alloys containing chromium and boron, and to characterize the microstructures of these alloys using microprobe analysis techniques.

10.2) Experimental procedure

Four off-eutectic experimental alloys were produced by melting various metal powders in a crucible at a temperature of 1500^{o}C. The alloy compositions (in wt.%) are given below:

- Ni-13Cr-15Hf
- Ni-13Cr-20Hf
- Ni-13Cr-25Hf
- Ni-13Cr-25Hf-1B

After cooling, the alloy samples were mounted in resin and prepared using conventional metallographic techniques before being subjected to microstructural analysis using microprobe techniques. The mounted samples were carbon coated using a sputtering technique and electrically grounded with copper tape in order to minimize charging of the specimens by the microprobe electron beam. Calibration was performed using polished pure element standards.

Analysis conditions were established for either a 15 or 20 keV focused electron beam, adjusted to provide 35 nA of specimen current on pure nickel. Desired locations for analysis were selected by generating a backscattered electron (BSE) image before placing the instrument in "spot mode", during which the focused beam was directed to locations within the area shown in the BSE image. The EDS (energy dispersive x-ray spectroscopy) peak identifications were verified using a wavelength dispersive x-ray spectrometer (WDS), tuned to the elements of interest. X-ray intensity data were collected in triplicate at each phase location of interest. Measured x-ray counts were then converted to elemental weight percentages using commercially available algorithms.

A preliminary characterization of the mechanical properties of the alloys was performed by measuring the hardness of each specimen using a micro-Vickers hardness tester.

10.3) Results and discussion

10.3.1 Ternary Ni-Cr-Hf alloys:

The microstructure of the Ni-13Cr-15Hf alloy after cooling is shown in **Figure 140**. The coarse dendritic phase (dark gray areas) was shown to have a composition of Ni-19.2Cr-1.6Hf (wt.%), identifying it as the Ni-rich γ phase. The white areas consisted of 53.7Ni-1.2Cr-45.1Hf (wt.%) and are most likely islands of Ni_7Hf_2 intermetallic compound within the eutectic component. The fine eutectic component had a composition of Ni-9.0Cr-25.8Hf. This microstructure suggests that the alloy was hypo-eutectic, forming a primary Ni-rich γ phase on solidification. On reaching the eutectic temperature, the remaining liquid transformed to the eutectic mixture of γ and the Ni_7Hf_2 intermetallic compound. The majority of the chromium present in this ternary alloy apparently partitioned to the γ phase on solidification.

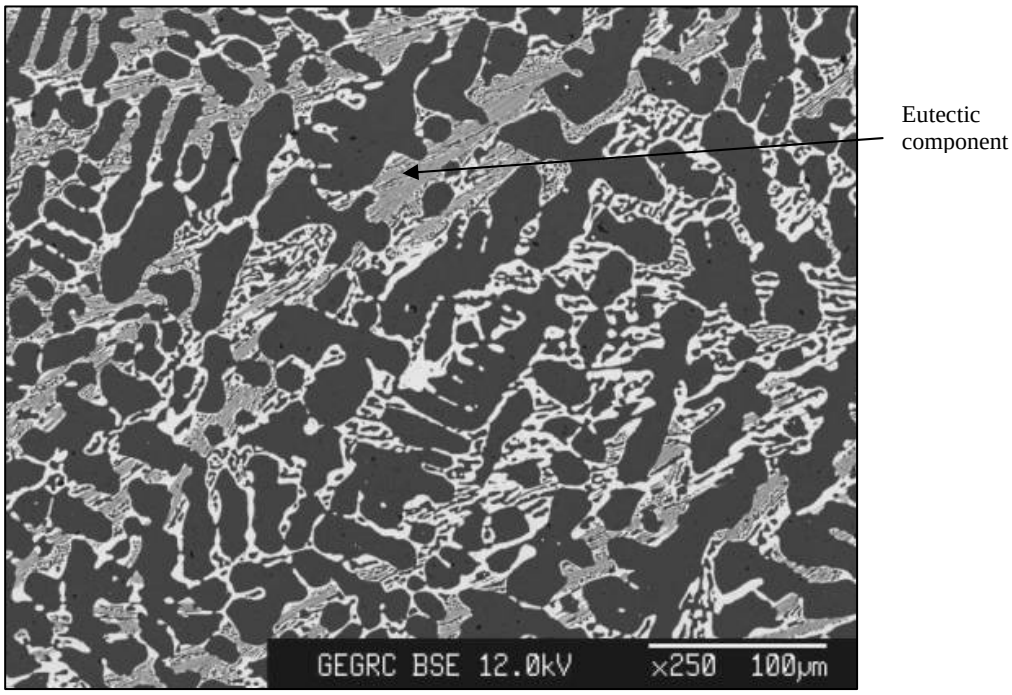

Figure 140 - BSE image of the Ni-13Cr-15 Hf alloy showing primary γ dendrites, and a fine eutectic component consisting of γ phase and the Ni_7Hf_2 intermetallic compound.

The microstructure of the Ni-13Cr-20Hf alloy, shown in **Figure 141**, is very similar to that of the alloy containing 15% Hf. The dark-etching phase was identified as Ni-rich γ dendrites (consisting of Ni-22.4Cr-1.4Hf), the white phase appeared to be the Ni_7Hf_2 intermetallic compound (consisting of 53.8Ni-1.3Cr-44.9Hf), whereas the eutectic component had a composition of Ni-10.5Cr-25.2Hf (all compositions given as wt.%). This alloy also appeared to be hypo-eutectic, although at 20% Hf it is located closer to the eutectic point, resulting in less primary γ phase.

Figure 142 shows the microstructure of the Ni-13Cr-25Hf alloy. The white areas were identified as Ni_7Hf_2 intermetallic compound, with a nominal composition of 53.5Ni-0.8Cr-45.7Hf. The fine eutectic component consisted of Ni_7Hf_2 intermetallic compound and the Ni-rich γ phase (dark gray regions). The eutectic component had a nominal composition of Ni-

15.1Cr-21.8Hf (all compositions given as wt.%). This microstructure suggests that the alloy was hypereutectic, forming a primary Ni_7Hf_2 intermetallic phase on solidification. On reaching the eutectic temperature, the remaining liquid transformed to the eutectic mixture of Ni-rich γ phase and Ni_7Hf_2 intermetallic compound. The majority of the chromium present in the alloy apparently partitioned to the γ phase on solidification.

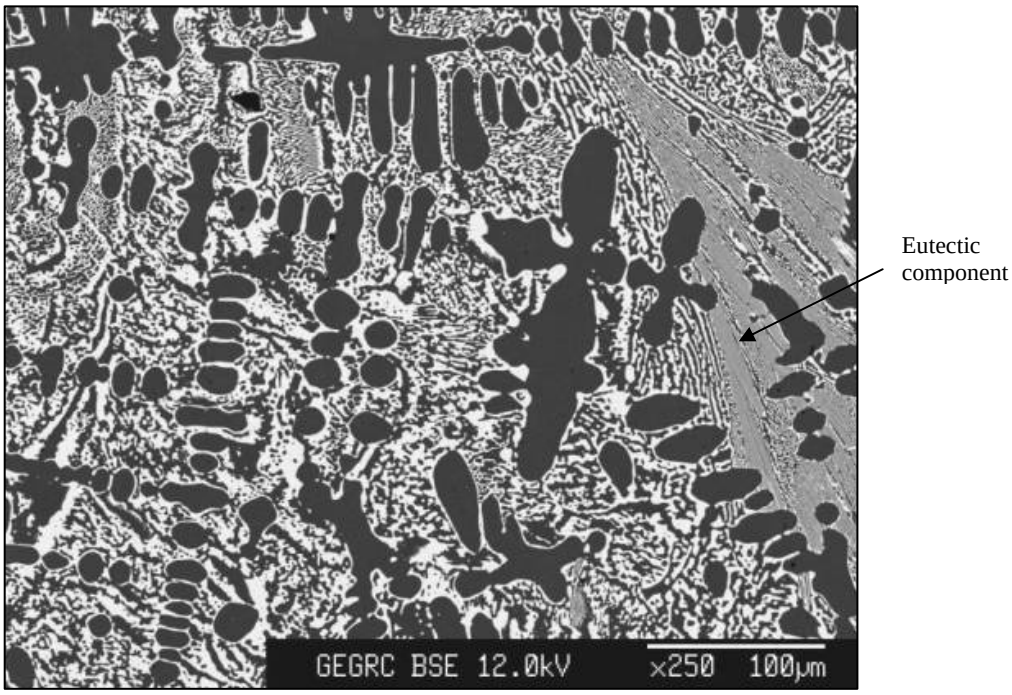

Figure 141 - BSE image of the Ni-13Cr-20 Hf alloy showing primary γ dendrites, and a fine eutectic component consisting of γ phase and the Ni_7Hf_2 intermetallic compound.

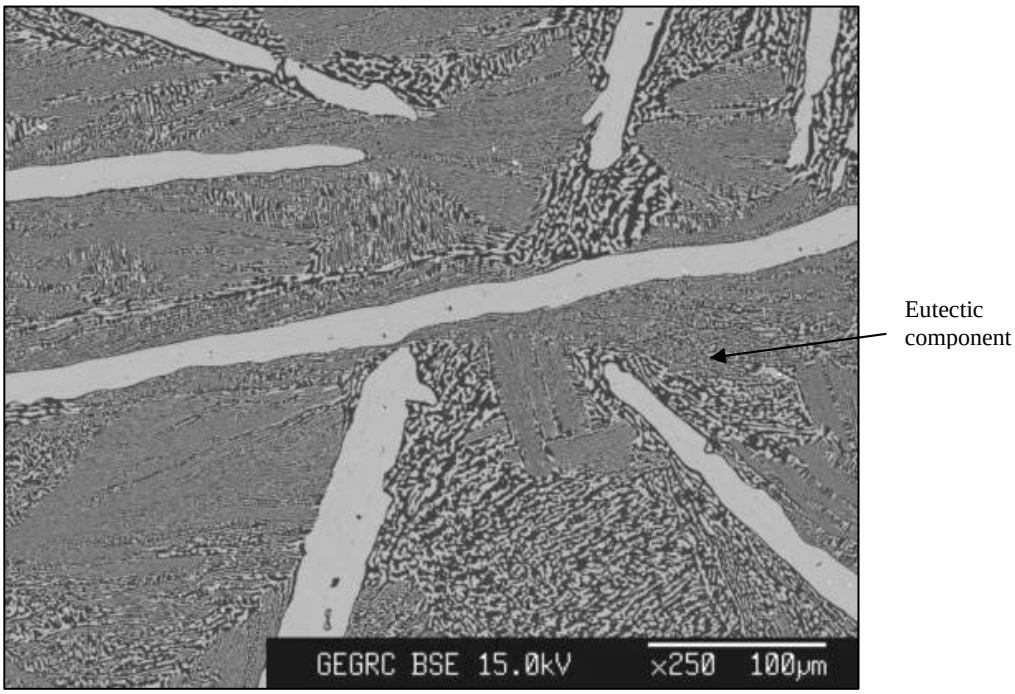

Figure 142 - BSE image of the Ni-13Cr-25 Hf alloy showing primary Ni_7Hf_2, and a fine eutectic component consisting of γ phase and the Ni_7Hf_2 intermetallic compound.

Table 42 summarizes the measured chemical compositions of the eutectic components formed in each alloy on solidification. The binary Ni-Hf phase diagram shown in **Figure 49** indicates that the eutectic point in the binary Ni-Hf system is located at 30.5 wt.% Hf and a temperature of 1190°C. The addition of chromium therefore appears to shift the eutectic composition to lower Hf contents. The measured solidus and liquidus temperatures of the three ternary alloys are shown in **Table 43**. An increase in Hf content decreased the liquidus and increased in the solidus temperatures of the alloys. As expected, the solidus and liquidus temperatures of the ternary alloys were well above the Ni-Hf eutectic temperature of 1190°C.

Table 42 – Chemical composition (wt.%) of the eutectic component observed in the ternary Ni-Cr-Hf alloys.

Alloy	Eutectic formed	Ni	Cr	Hf
Ni-13Cr-15Hf	Ni-rich γ + Ni_7Hf_2	65.2	9.0	25.8
Ni-13Cr-20Hf	Ni-rich γ + Ni_7Hf_2	64.3	10.5	25.2
Ni-13Cr-25Hf	Ni-rich γ + Ni_7Hf_2	63.1	15.1	21.8

Table 43 – Measured liquidus and solidus temperatures of the ternary Ni-Cr-Hf alloys.

Alloy	Solidus temperature	Liquidus temperature
Ni-13Cr-15Hf	1205°C	1337°C
Ni-13Cr-20Hf	1220°C	1304°C
Ni-13Cr-25Hf	1231°C	1291°C

10.3.2 Quaternary Ni-Cr-Hf-B alloy:

The microstructure of the quaternary Ni-13Cr-25Hf-1B alloy is shown in **Figure 143**. The addition of 1% B to the alloy resulted in the formation of a significant volume fraction of brittle borides (black phase). These boride particles were identified as chromium borides, with a composition of Ni-88.3Cr-0.0Hf-13.6B. The white areas were identified as the Ni_7Hf_2 intermetallic phase (with a composition of Ni-0.7Cr-46.1Hf-0.3B), and the dark gray areas were shown to be the Ni-rich γ phase (containing Ni-25.9Cr-1.2Hf-0.2B). Analysis of the eutectic regions yielded compositions of Ni-11.0Cr-20.3Hf-2.0B (coarser eutectic component) and Ni-10.7Cr-16.9Hf-2.7B (fine eutectic regions). (All compositions given in wt.%).

The sequence of phase transformations on solidification of this alloy was probably:

$L_1 \rightarrow Ni_7Hf_2 + L_2$
$L_2 \rightarrow$ Ni-rich γ + L
L (eutectic) $\rightarrow$ Ni-rich γ + Ni_7Hf_2

10.3.3 Microhardness measurements:

In order to characterize the hardness of the phases within the braze alloys, Vickers microhardness tests were performed. The measured hardness values are given in **Table 44**. These results indicate that the chromium boride phase was significantly harder than the Hf-bearing intermetallic phase. This is consistent with the high ductility values obtained during earlier testing of Ni-Hf joints, compared with those typically found in B-containing brazes.

The high hardness of the eutectic component observed in the B-containing alloy suggests that the chromium boride phase participated in the eutectic reaction, possibly resulting in the formation of a ternary Cr boride/γ/Ni_7Hf_2 eutectic component.

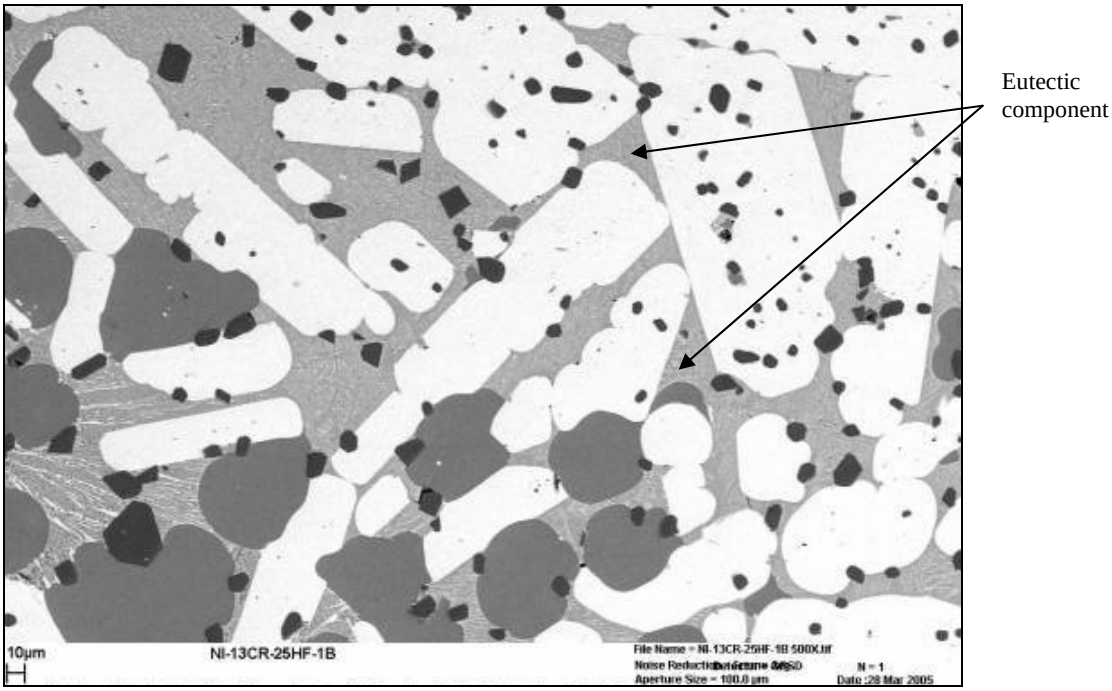

Figure 143 - BSE image of the Ni-13Cr-25 Hf-1B alloy showing the Ni_7Hf_2 phase (white), Ni-rich γ (dark gray), chromium borides (black) and a possible ternary eutectic component consisting of γ phase, Cr boride, and the Ni_7Hf_2 intermetallic compound.

Table 44 – Measured microhardness values of various phases observed in the ternary and quaternary alloys.

Alloy	Microhardness, H_v							
	γ phase		Eutectic constituent		Boride phase		Other	
	Average	Standard deviation	Average	Standard deviation	Average	Standard deviation	Average	Standard deviation
Ni-13Cr-15Hf	242	19	294	56	N/A	N/A	N/A	N/A
Ni-13Cr-20Hf	309	19	322	72	N/A	N/A	N/A	N/A
Ni-13Cr-25Hf	398	32	324	30	N/A	N/A	N/A	N/A
Ni-13Cr-25Hf-1B	326	93	746	108	1150	240	350	43

Table 45 summarizes the microprobe results, and displays the chemical compositions of the microstructural constituents observed within the ternary and quaternary alloys.

10.4) Conclusions

- The ternary Ni-13Cr-15Hf and Ni-13Cr-20Hf alloys appeared to be hypo-eutectic, and consisted of primary Ni-rich γ dendrites (with approximately 20% Cr in solution), and a eutectic component consisting of γ phase and Ni_7Hf_2 intermetallic compound. Increasing the Hf content from 15% to 20% reduced the amount of primary γ phase. The Ni-13Cr-25Hf alloy appeared to be hypereutectic, with a primary Ni_7Hf_2 phase and a eutectic

component consisting of γ and Ni_7Hf_2. Since the eutectic point in binary Ni-Hf alloys is located at approximately 30.5% Hf, the addition of chromium apparently shifted the eutectic composition to lower Hf contents.

Table 45 – The chemical compositions of various phases within the ternary and quaternary alloys (all compositions given as wt.%).

Alloy	Microstructural constituent	Transformation	Weight %			
			Ni	Cr	Hf	B
Ni-13Cr-15Hf	Ni-rich γ	Primary	79	19.2	1.6	-
	Ni_7Hf_2	Eutectic	55.5	1.2	45.1	-
	Eutectic component { Ni_7Hf_2, γ }	Eutectic	65.2	9	25.8	-
Ni-13Cr-20Hf	Ni-rich γ	Primary	75.9	22.4	1.4	-
	Ni_7Hf_2	Eutectic	55.9	1.3	44.9	-
	Eutectic component { Ni_7Hf_2, γ }	Eutectic	64.3	10.5	25.2	-
Ni-13Cr-25Hf	Ni_7Hf_2	Primary	54.9	0.8	45.7	-
	Eutectic component { Ni_7Hf_2, γ }	Eutectic	63.1	15.1	21.8	-
Ni-13Cr-25Hf-1B	Ni_7Hf_2	Primary	54.9	0.7	46.1	0.3
	Ni-rich γ	Primary	73.2	25.9	1.2	0.2
	Cr boride	Primary	2.6	88.3	0.0	13.6
	Eutectic component { Ni_7Hf_2, γ, Cr boride }	Eutectic	65.9 70.2	11.0 10.7	20.3 16.9	2.0 2.7

- An increase in the Hf content of the experimental alloys lowered the liquidus temperature, but increased the solidus temperature. Since single-crystal Ni-base superalloys can be processed at temperatures up to 1310°C, only the Ni-13Cr-25Hf alloy holds any potential for production brazing. The liquidus temperatures of the Ni-13Cr-20Hf and Ni-13Cr-15Hf alloys exceeded 1300°C.

- The quaternary Ni-13Cr-25Hf-1B alloy consisted of a coarse Ni_7Hf_2 phase, islands of Ni-rich γ (with Cr in solution), a ternary eutectic component (Ni_7Hf_2, γ and Cr boride) and a significant volume fraction of chromium boride particles. The boride particles were shown to be considerably harder than the Ni_7Hf_2 intermetallic phase. This difference in hardness may account for the high ductility and good LCF properties of the Ni-Hf braze joints, compared with those of braze alloys containing B as a melt point depressant.

CHAPTER 11 - EXPERIMENT 9

MICROPROBE ANALYSIS OF INTERMETALLIC PHASES

11.1) Introduction

Previous chapters revealed a discrepancy between the equilibrium intermetallic phase predicted by the Ni-Hf binary phase diagram (i.e. Ni_5Hf) for the novel braze alloys, and the intermetallic phase provisionally identified in the Ni-Hf braze joints on the basis of SEM-EDS and preliminary microprobe analyses (Ni_7Hf_2). The SEM-EDS technique is, at best, semi-quantitative, and an attempt was therefore made to determine the chemical make-up of the intermetallic phases in modified Ni-Hf and Ni-Zr braze joints using more detailed electron microprobe analysis (EMPA) techniques. This experiment also aimed at assessing the effect of chromium additions to the Ni-Hf and Ni-Zr braze alloys on the microstructure of the wide gap braze joints.

11.2) Experimental procedure

MarM247/Ni-Hf and MarM247/Ni-Zr braze joints in In738 base metal were produced using two experimental ternary braze alloys with compositions of Ni-7Cr-31Hf and Ni-7Cr-13Zr (wt.%). Brazing was performed using the procedure described in §4.2. The joints were examined, either in the as-brazed condition (without applying an extended diffusion cycle), or after a diffusion treatment to facilitate the diffusion of the melt point depressant into the parent metal.

The brazed samples were mounted in resin and prepared using conventional metallographic techniques before being subjected to microstructural examination using microprobe analysis techniques. The mounted samples were carbon coated using a sputtering technique and electrically grounded with copper tape to minimize charging of the specimens by the microprobe electron beam. Calibration was performed using polished pure element standards.

Analysis conditions were established for either a 15 or 20 keV focused electron beam, adjusted to provide 35 nA of specimen current on pure nickel. Desired locations for analysis were selected by generating a backscatter electron (BSE) image before placing the instrument in "spot mode", during which the focused beam was directed to selected locations within the area shown in the BSE image. The BSE images were annotated to highlight the features subjected to elemental characterization by energy dispersive x-ray spectroscopy (EDS). The EDS peak identifications were verified using a wavelength dispersive x-ray spectrometer (WDS), tuned to the elements of interest. X-ray intensity data were collected in triplicate at each selected location. Measured x-ray counts were then converted to elemental weight percentages using commercially available algorithms.

11.3) Results and discussion

11.3.1 The MarM247/Ni-Hf braze joint produced using Ni-7Cr-31Hf braze filler (as-brazed condition):

Secondary and backscatter electron images of the MarM247/Ni-Hf joint produced using the experimental Ni-7Cr-31Hf braze filler metal are shown in **Figure 144** in the as-brazed

condition. The arrow indicates the location and direction of the 5 µm stepped EPMA line scan. The results of the EMPA scan are shown in **Table 46**.

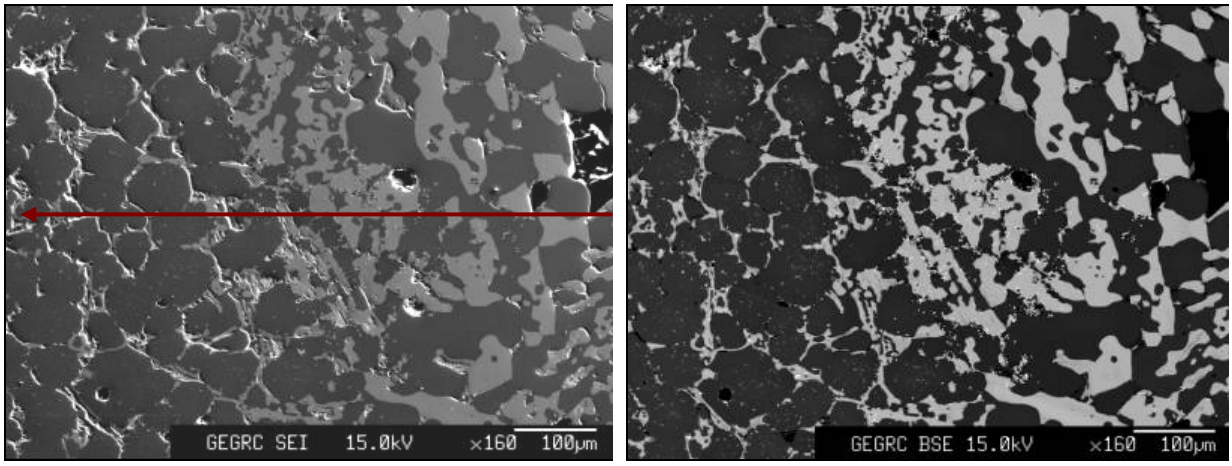

(a) (b)

Figure 144 – Secondary (a) and backscatter (b) electron images of the MarM247/Ni-7Cr-31Hf joint in the as-brazed condition.

Table 46 – The results of the EMPA scan of the MarM247/Ni-7Cr-31Hf braze joint in the as-brazed condition. (All compositions given in wt.%).

X (mm)	Y (mm)	Z (mm)	Al	Hf	Ni	Cr	Zr	Fe	Ta	Mo	Co	W	Ti
74.213	64.158	11.067	4.40	1.71	68.70	9.30	0.30	0.58	3.40	1.04	7.15	2.65	0.01
74.218	64.158	11.067	4.48	1.72	69.15	9.18	0.28	0.58	3.16	1.03	7.14	2.54	0.00
74.223	64.158	11.067	4.48	1.66	68.69	9.25	0.30	0.58	3.43	1.09	7.11	2.59	0.00
74.228	64.158	11.067	4.45	1.64	68.40	9.13	0.30	0.60	3.42	1.03	7.12	2.83	0.00
74.233	64.158	11.066	4.54	1.69	68.41	8.99	0.34	0.57	3.33	1.06	7.08	2.86	0.00
74.238	64.158	11.066	4.55	1.67	68.13	9.07	0.31	0.58	3.23	1.00	7.03	2.66	0.00
74.243	64.158	11.066	4.74	1.64	68.00	8.72	0.30	0.60	3.05	1.00	6.96	2.78	0.01
74.248	64.158	11.068	0.40	27.68	56.16	0.72	9.57	0.09	3.08	0.13	2.98	0.00	0.00
74.253	64.158	11.068	0.63	26.18	56.43	1.41	8.81	0.14	2.61	0.23	3.28	0.00	0.00
74.258	64.158	11.068	4.68	1.69	68.03	8.77	0.31	0.59	3.09	1.07	7.02	2.55	0.00
74.263	64.158	11.068	4.52	1.66	68.11	8.98	0.31	0.61	3.13	1.06	7.16	2.76	0.00
74.268	64.158	11.068	4.50	1.63	67.83	9.03	0.31	0.61	2.97	1.07	7.17	2.75	0.00
74.273	64.158	11.068	4.22	13.37	58.87	7.35	1.30	0.48	5.22	0.86	5.69	1.15	0.01
74.278	64.158	11.066	4.56	1.64	67.57	8.92	0.31	0.62	2.87	1.04	7.17	2.85	0.00
74.283	64.158	11.068	4.64	1.64	68.17	8.84	0.32	0.61	3.00	1.04	7.16	2.66	0.00
74.288	64.158	11.068	4.59	1.60	67.68	8.87	0.32	0.65	2.92	1.01	7.17	2.66	0.00
74.293	64.158	11.066	4.54	1.76	67.77	8.66	0.32	0.60	3.00	1.02	7.12	2.67	0.00
74.298	64.158	11.068	0.88	24.80	57.35	1.81	8.08	0.17	2.92	0.26	3.48	0.00	0.00
74.303	64.158	11.068	0.29	28.34	55.23	0.59	9.36	0.08	2.78	0.16	2.96	0.00	0.00
74.308	64.158	11.068	0.29	28.36	55.77	0.54	9.44	0.06	2.91	0.17	2.96	0.00	0.01
74.313	64.158	11.068	0.29	28.45	55.56	0.57	9.36	0.07	2.76	0.14	2.90	0.00	0.00
74.318	64.158	11.066	3.04	11.30	63.34	5.83	3.30	0.40	2.91	0.76	5.58	1.32	0.01
74.323	64.158	11.068	4.54	1.70	68.45	8.56	0.35	0.56	2.92	1.03	7.17	2.26	0.00
74.328	64.158	11.068	4.53	1.59	68.39	8.69	0.33	0.60	2.81	1.04	7.23	2.55	0.01
74.333	64.158	11.068	4.55	1.63	68.18	8.71	0.29	0.59	2.69	1.08	7.19	2.64	0.01
74.338	64.158	11.067	4.61	1.74	68.19	8.58	0.31	0.56	3.08	1.04	7.05	2.38	0.00
74.343	64.158	11.067	4.47	1.61	68.41	8.86	0.26	0.60	3.07	1.02	7.20	2.47	0.00
74.348	64.158	11.067	4.60	1.77	68.11	8.67	0.36	0.61	3.22	1.03	7.18	2.23	0.00
74.353	64.158	11.067	4.55	1.74	68.08	8.72	0.29	0.59	3.29	1.03	7.16	2.66	0.01
74.358	64.158	11.067	4.52	1.66	68.61	8.67	0.34	0.57	3.24	1.06	7.23	2.35	0.00
74.363	64.158	11.067	4.64	1.73	67.96	8.58	0.32	0.60	3.22	1.05	7.17	2.37	0.00
74.368	64.158	11.067	5.68	3.56	68.87	7.46	0.63	0.51	3.34	0.85	6.36	1.07	0.02
74.373	64.158	11.066	4.81	1.59	67.81	8.58	0.32	0.59	3.09	1.02	7.10	2.43	0.00

Table 46 – (continued).

X (mm)	Y (mm)	Z (mm)	Al	Hf	Ni	Cr	Zr	Fe	Ta	Mo	Co	W	Ti
74.378	64.158	11.066	4.55	1.71	67.21	8.65	0.29	0.58	3.12	1.05	7.17	2.79	0.02
74.383	64.158	11.066	4.60	1.70	67.51	8.60	0.32	0.59	3.36	1.05	7.08	2.43	0.00
74.388	64.158	11.066	4.68	1.75	67.72	8.76	0.37	0.58	3.20	1.02	7.11	2.29	0.00
74.393	64.158	11.066	4.40	3.13	66.37	9.22	0.60	0.61	2.46	1.05	7.33	1.89	0.01
74.398	64.158	11.066	4.72	1.62	68.42	8.81	0.34	0.57	3.12	1.02	7.14	2.38	0.00
74.403	64.158	11.066	4.88	1.61	68.42	8.69	0.35	0.55	3.01	1.04	7.07	2.05	0.00
74.408	64.158	11.068	4.88	1.71	68.67	8.73	0.35	0.54	3.30	1.03	7.10	2.12	0.01
74.413	64.158	11.068	4.87	2.40	68.59	8.63	0.37	0.59	3.03	0.99	6.97	2.11	0.02
74.418	64.158	11.066	4.87	1.71	68.70	8.70	0.35	0.57	3.41	1.00	7.00	1.65	0.00
74.423	64.158	11.068	3.53	9.56	65.11	6.64	3.03	0.44	2.68	0.78	5.90	0.94	0.00
74.428	64.158	11.066	0.32	28.28	55.10	0.69	9.34	0.09	2.99	0.15	2.90	0.00	0.01
74.433	64.158	11.066	0.34	28.32	55.65	0.68	9.21	0.05	2.53	0.15	2.83	0.00	0.00
74.438	64.158	11.066	0.37	26.67	56.91	0.92	9.85	0.11	1.75	0.17	3.07	0.00	0.01
74.443	64.158	11.068	3.03	16.92	62.22	1.44	9.70	0.13	2.14	0.25	3.20	0.00	0.00
74.448	64.158	11.068	0.32	29.43	55.77	0.58	8.15	0.06	2.83	0.12	2.91	0.00	0.00
74.453	64.158	11.068	0.97	45.68	34.07	2.84	5.77	0.22	9.53	0.30	2.80	0.00	0.01
74.458	64.158	11.068	5.33	1.66	69.66	8.51	0.40	0.55	2.95	0.93	6.84	1.39	0.01
74.463	64.158	11.068	5.32	1.62	69.86	8.50	0.35	0.59	2.74	0.98	6.84	1.53	0.01
74.468	64.158	11.066	5.43	15.67	60.91	4.16	3.19	0.30	4.50	0.46	4.10	0.25	0.01
74.473	64.158	11.066	1.63	17.51	58.98	2.26	8.42	0.17	2.10	0.25	3.54	0.00	0.00
74.478	64.158	11.003	2.20	3.35	37.04	7.31	0.76	0.24	5.20	0.73	2.91	1.37	0.00
74.483	64.158	11.067	5.81	5.41	68.75	7.04	0.80	0.46	2.92	0.80	5.89	0.70	0.00
74.488	64.158	11.067	5.06	1.60	69.21	8.59	0.35	0.57	2.61	0.95	6.86	2.51	0.00
74.493	64.158	11.065	5.48	2.09	70.60	8.20	0.49	0.50	2.81	0.91	6.51	1.46	0.01
74.498	64.158	11.067	1.86	16.95	62.21	3.76	8.91	0.25	1.53	0.43	4.36	0.00	0.01
74.503	64.158	11.067	7.86	6.11	71.63	3.87	1.42	0.27	3.64	0.45	4.10	0.29	0.02
74.508	64.158	11.067	0.67	43.17	37.81	1.04	7.89	0.09	9.41	0.15	2.04	0.00	0.01
74.513	64.158	11.066	0.29	34.25	50.08	0.58	8.76	0.06	4.81	0.12	2.54	0.00	0.01
74.518	64.158	11.066	0.35	29.23	55.59	0.74	8.58	0.09	3.02	0.18	2.93	0.00	0.01
74.523	64.158	11.066	0.29	27.62	55.05	0.76	9.13	0.08	2.91	0.16	2.90	0.00	0.00
74.528	64.158	11.064	4.46	1.79	67.89	8.56	0.43	0.53	3.30	1.05	6.85	3.06	0.00
74.533	64.158	11.064	4.69	1.57	68.33	8.52	0.33	0.53	3.02	1.05	6.85	2.77	0.01
74.538	64.158	11.062	3.00	23.04	50.75	6.71	2.44	0.44	6.71	0.73	4.93	0.19	0.00
74.543	64.158	11.064	2.55	27.62	45.92	6.57	2.10	0.36	7.45	0.65	4.84	0.00	0.01
74.548	64.158	11.066	0.29	27.04	55.63	0.63	9.62	0.07	2.61	0.17	2.92	0.00	0.00
74.553	64.158	11.064	0.29	28.52	54.53	0.57	9.16	0.05	2.63	0.16	2.87	0.00	0.00
74.558	64.158	11.064	0.28	28.40	54.96	0.56	9.31	0.07	2.40	0.12	2.83	0.00	0.00
74.563	64.158	11.062	0.28	26.58	53.92	0.62	9.28	0.05	2.32	0.16	2.83	0.00	0.01
74.568	64.158	11.062	0.28	27.48	53.96	0.69	9.39	0.07	3.07	0.14	2.80	0.00	0.02
74.573	64.158	11.066	3.49	21.00	53.49	6.96	0.88	0.46	6.58	0.76	5.35	0.58	0.00
74.578	64.158	11.066	4.49	1.63	68.45	9.00	0.35	0.56	2.82	1.04	7.10	2.25	0.00
74.583	64.158	11.064	4.45	1.72	67.62	8.97	0.35	0.56	3.14	1.01	6.94	2.74	0.00
74.588	64.158	11.066	4.45	1.69	68.66	9.09	0.32	0.55	3.06	1.02	7.01	2.31	0.01
74.593	64.158	11.064	4.30	1.64	67.67	9.16	0.35	0.56	2.99	1.04	6.95	2.76	0.00
74.598	64.158	11.068	4.99	4.13	65.68	9.99	0.74	0.62	2.80	1.13	7.50	2.95	0.00
74.603	64.158	11.066	4.36	1.65	67.84	9.01	0.33	0.57	3.15	1.04	7.08	2.76	0.00
74.608	64.158	11.068	4.37	1.65	68.21	8.98	0.33	0.58	2.86	1.03	7.17	2.89	0.01
74.613	64.158	11.066	4.34	1.66	67.18	8.97	0.32	0.55	3.04	1.02	7.09	3.13	0.01
74.618	64.158	11.068	4.37	1.70	67.58	8.88	0.33	0.59	2.87	1.04	7.15	3.11	0.00
74.623	64.158	11.065	4.34	1.70	67.05	8.88	0.36	0.54	2.72	1.04	7.09	3.04	0.02
74.628	64.158	11.065	4.27	1.60	66.69	9.10	0.31	0.52	2.82	1.05	7.06	3.24	0.01
74.633	64.158	11.067	4.36	1.64	67.42	8.98	0.33	0.57	2.67	1.03	7.17	2.90	0.00
74.638	64.158	11.067	4.36	1.65	67.84	9.01	0.33	0.57	3.15	1.04	7.08	2.76	0.00
74.643	64.158	11.065	4.37	1.65	68.21	8.98	0.33	0.58	2.86	1.03	7.17	2.89	0.01
74.648	64.158	11.065	4.34	1.66	67.18	8.97	0.32	0.55	3.04	1.02	7.09	3.13	0.01
74.653	64.158	11.067	4.37	3.05	67.15	8.49	0.75	0.50	3.01	0.97	6.95	2.38	0.00
74.658	64.158	11.066	0.29	28.76	54.29	0.67	8.10	0.08	2.91	0.13	2.93	0.00	0.00
74.663	64.158	11.066	0.34	29.19	54.49	1.02	8.40	0.09	2.97	0.20	3.05	0.00	0.00
74.668	64.158	11.066	4.00	5.23	64.01	8.40	0.69	0.45	3.95	1.00	6.80	2.53	0.01
74.673	64.158	11.066	1.01	23.28	57.27	2.47	7.48	0.15	3.32	0.35	3.83	0.00	0.01

Table 46 – (continued).

X (mm)	Y (mm)	Z (mm)	Al	Hf	Ni	Cr	Zr	Fe	Ta	Mo	Co	W	Ti
74.678	64.158	11.064	3.92	5.53	62.65	8.56	0.50	0.42	4.78	1.00	6.87	3.25	0.00
74.683	64.158	11.066	3.17	16.43	54.78	7.06	1.27	0.36	6.96	0.81	5.90	2.15	0.01
74.688	64.158	11.066	3.94	6.32	62.13	8.40	0.67	0.41	4.26	0.97	6.93	3.36	0.01
74.693	64.158	11.066	4.17	1.61	66.17	9.04	0.32	0.40	3.35	1.07	7.44	3.60	0.00
74.698	64.158	11.066	4.17	1.63	66.09	9.14	0.30	0.40	3.38	1.07	7.55	3.69	0.00
74.703	64.158	11.066	4.13	1.61	65.62	9.28	0.27	0.41	3.20	1.08	7.57	3.74	0.01
74.708	64.158	11.066	3.69	6.97	60.67	8.77	0.41	0.38	4.89	0.97	7.01	2.93	0.01
74.713	64.158	11.066	4.19	1.66	65.97	9.19	0.29	0.39	3.29	1.06	7.56	3.50	0.00
74.718	64.158	11.066	3.70	9.69	59.90	8.38	0.72	0.37	5.49	0.99	6.76	2.70	0.00
74.723	64.158	11.066	4.21	1.68	65.99	9.07	0.29	0.40	3.44	1.10	7.56	3.39	0.00
74.728	64.158	11.066	0.82	21.49	56.85	2.30	6.85	0.14	3.42	0.27	3.97	0.00	0.01
74.733	64.158	11.066	4.16	1.61	66.51	9.31	0.32	0.38	3.34	1.01	7.69	3.25	0.00
74.738	64.158	11.066	4.24	1.71	66.33	9.23	0.30	0.36	3.48	1.03	7.52	3.20	0.00
74.743	64.158	11.066	4.19	1.64	66.16	9.36	0.29	0.37	3.51	1.09	7.63	3.40	0.00
74.748	64.158	11.066	4.16	1.62	66.64	9.42	0.29	0.38	3.46	1.08	7.71	3.60	0.00
74.753	64.158	11.066	4.26	1.70	66.61	9.33	0.32	0.35	3.76	1.06	7.55	3.20	0.00
74.758	64.158	11.066	4.19	1.69	66.65	9.38	0.27	0.37	3.63	1.09	7.70	3.27	0.00
74.763	64.158	11.065	4.16	1.69	67.08	9.43	0.29	0.37	3.65	1.11	7.67	2.93	0.00
74.768	64.158	11.065	4.26	1.74	66.54	9.20	0.30	0.37	3.57	1.00	7.60	2.90	0.00
74.773	64.158	11.065	3.67	7.10	62.84	7.89	1.43	0.31	4.24	0.95	6.75	2.47	0.00
74.778	64.158	11.065	2.13	7.05	60.67	6.54	2.10	0.26	3.50	0.58	6.08	1.85	0.02
74.783	64.158	11.063	4.10	1.70	65.52	9.27	0.30	0.35	3.83	1.05	7.39	3.69	0.00
74.788	64.158	11.069	4.03	3.81	65.13	9.14	0.32	0.37	4.32	1.05	7.56	3.44	0.00
74.793	64.158	11.067	4.17	1.67	66.26	9.40	0.29	0.37	3.54	1.09	7.81	3.69	0.00
74.798	64.158	11.064	4.11	1.72	65.84	9.40	0.28	0.35	3.90	1.09	7.73	3.64	0.00
74.803	64.158	11.064	3.45	10.86	58.52	8.52	0.45	0.34	6.31	0.98	6.84	3.03	0.01
74.808	64.158	11.017	1.73	2.65	40.95	9.97	0.38	0.23	6.43	1.01	4.53	5.29	0.00
74.813	64.158	11.066	4.21	1.76	66.03	9.32	0.27	0.35	3.57	1.06	7.74	3.56	0.01

The line scan results shown in **Table 46** revealed the presence of three possible Hf-rich intermetallic phases, with a phase containing between 24% and 28% Hf being most prevalent. Other Hf-rich phases detected during the scan contained between 11 and 13% Hf, and 34 to 45% Hf. In order to perform a more detailed analysis of the intermetallic phases observed in the braze joint, three spot chemical analyses were performed within the intermetallic compound in the braze joint. Two backscatter electron images of the MarM247/Ni-Hf braze joint are shown in **Figure 145**, with the location of the three phase analyses highlighted. The results of the microprobe phase analyses, shown in **Table 47**, suggest that the intermetallic phase within the braze alloy contained between 31 and 36% Hf (wt.%). The binary Ni-Hf phase diagram, shown in **Figure 49**, indicates that the Ni_5Hf intermetallic phase contains approximately 38 wt.% Hf, whereas the Ni_7Hf_2 intermetallic compound contains about 46 wt.% Hf. The results shown in **Table 47** therefore suggest that the intermetallic phase in the braze joint is Ni_5Hf, rather than Ni_7Hf_2. It is, however, interesting to note that the Hf-rich phase identified in **Table 47**, as well as the phase containing between 24% and 28% Hf in **Table 46**, contained high levels of Zr (between 7.4% and 9.6%), probably present as a contaminant that segregated preferentially to the intermetallic phase on solidification, and approximately 3% Ta, which may be present as a result of dilution with the MarM247 powder particles during brazing. The presence of Zr and Ta may shift the composition of the Hf-rich intermetallic phase away from the equilibrium composition predicted by the phase diagram. If it is assumed that the intermetallic compound contains between 7.4% and 9.6% Zr in solution, as well as 3% Ta, its composition may well approach that of the Ni_7Hf_2 (or rather $Ni_7(Hf,Zr,Ta)_2$) intermetallic compound.

In order to study the distribution of various elements within the Ni-Cr-Hf braze microstructure, EMPA maps were constructed. These maps are shown in **Figure 146** (for Al, C, Ni and Cr), **Figure 147** (for Zr, Hf and Si), **Figure 148** (for Ru, Ta, Ti and W) and **Figure 149** (for Fe and Mo).

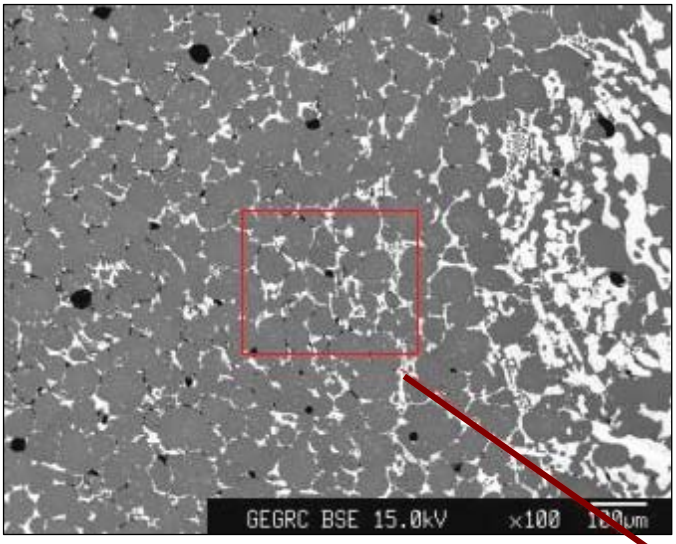

Figure 145(a) – Secondary electron image of the Ni-Cr-Hf alloy in the as-brazed condition.

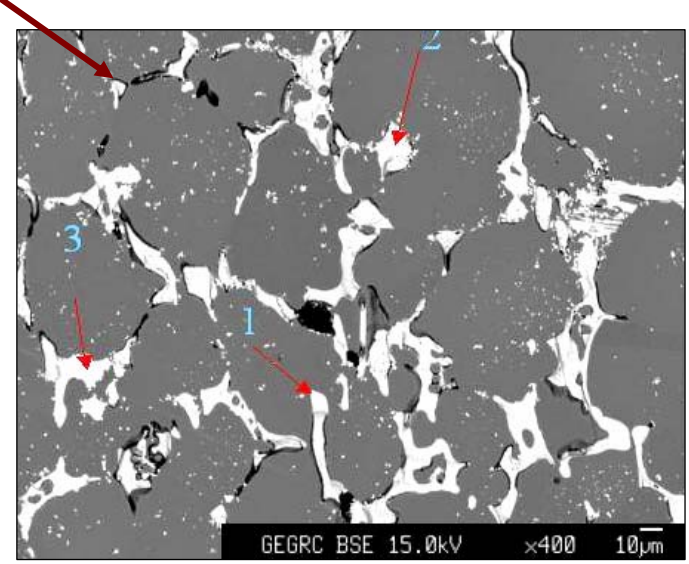

Figure 145(b) – Enlarged view of the secondary electron image of the Ni-Cr-Hf braze shown in Figure 145(a), highlighting the location of three spot chemical analyses of the intermetallic compound within the braze.

Table 47 - Quantitative EPMA data (taken at 15 keV and 80 nA with a focused spot beam) at three locations (indicated in Figure 145(b)) within the intermetallic phase. (Percentage by weight).

	Al	Hf	Ni	Cr	Zr	Fe	Ta	Mo	Co	W	Ti	Si
Phase 1	0.29	31.53	55.16	0.84	8.43	0.06	3.35	0.15	3.37	0.07	0.00	0.21
Phase 2	0.29	31.09	55.37	0.71	8.54	0.05	3.39	0.18	3.10	0.08	0.01	0.25
Phase 3	0.29	36.34	53.02	0.62	5.30	0.05	3.91	0.15	3.62	0.13	0.00	0.21

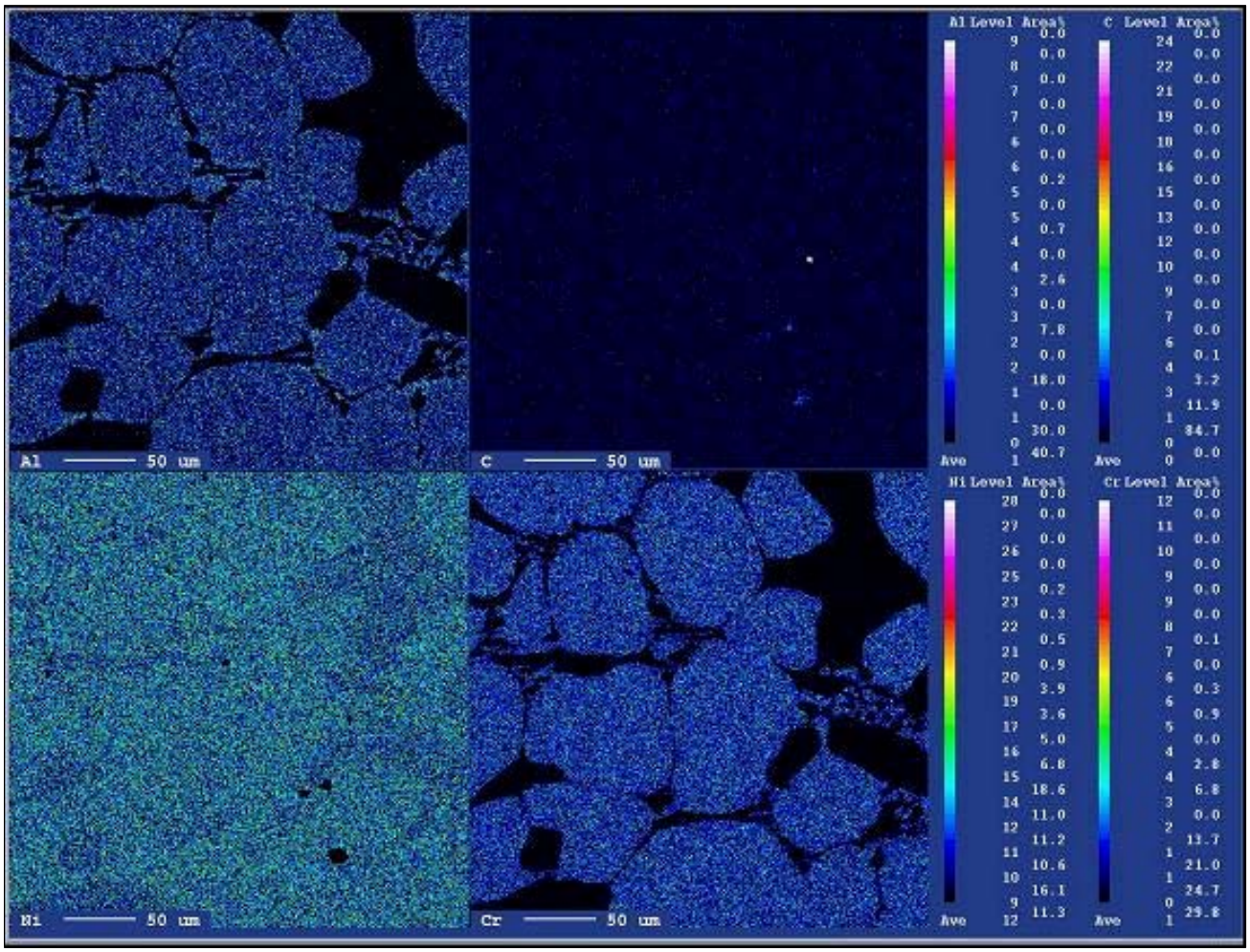

Figure 146 – EMPA maps displaying the distribution of Al, C, Ni and Cr within the MarM247/Ni-Cr-Hf braze microstructure (as-brazed condition).

The EMPA results shown in **Figure 146** indicate that Al and Cr partitioned strongly to the MarM247 powder particles during brazing. Given that the braze alloy contains 7% Cr and that a diffusion cycle was not applied, the low Cr concentration measured in the braze alloy between the MarM247 particles was surprising. Ni and C appeared to be fairly uniformly distributed between the braze alloy and the matrix, with a slightly higher Ni concentration measured in the MarM247 particles.

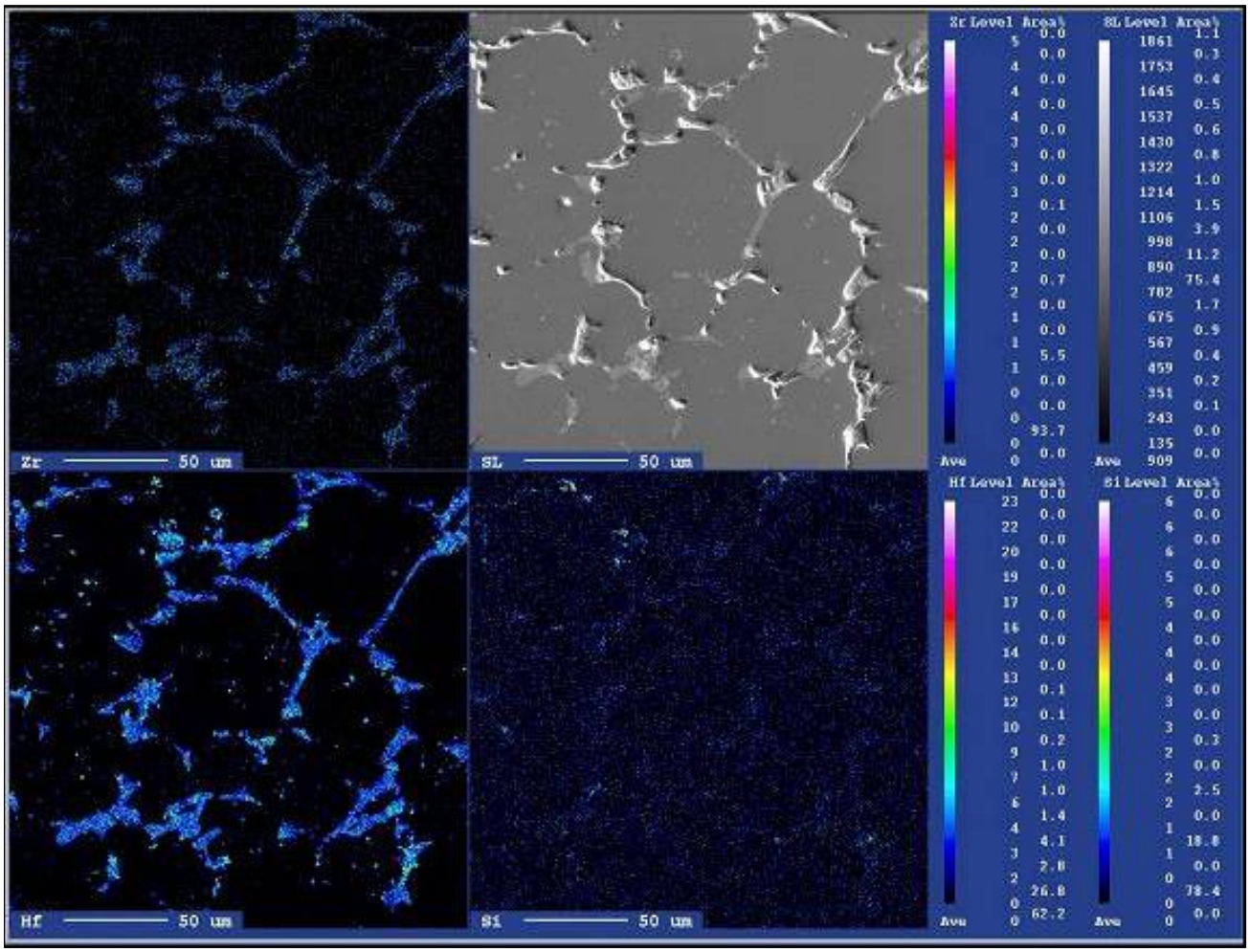

Figure 147 – EMPA maps displaying the distribution of Zr, Hf and Si within the MarM247/Ni-Cr-Hf braze microstructure (as-brazed condition).

The results shown in **Figure 147** suggest that both Hf and Zr partitioned strongly to the braze alloy, which confirms the results of the line and spot scans shown in **Tables 46 and 47**. Zr was not intentionally added to the braze alloy, and is almost completely absent from the MarM247 matrix particles (MarM247 has a nominal Zr content of 0.05 wt.%). A Zr content of 0.7 wt.% was measured in the binary Ni-Hf braze alloy as a result of contamination (see **Table 9**), but this is not considered high enough to cause the high Zr levels shown in **Tables 46 and 47**, and **Figure 147**. It is possible that the Cr powder used to make up the ternary Ni-Cr-Hf braze alloy contained a significant amount of Zr as contaminant. The Hf EMPA map confirms that the intermetallic phase within the braze joint is Hf-rich.

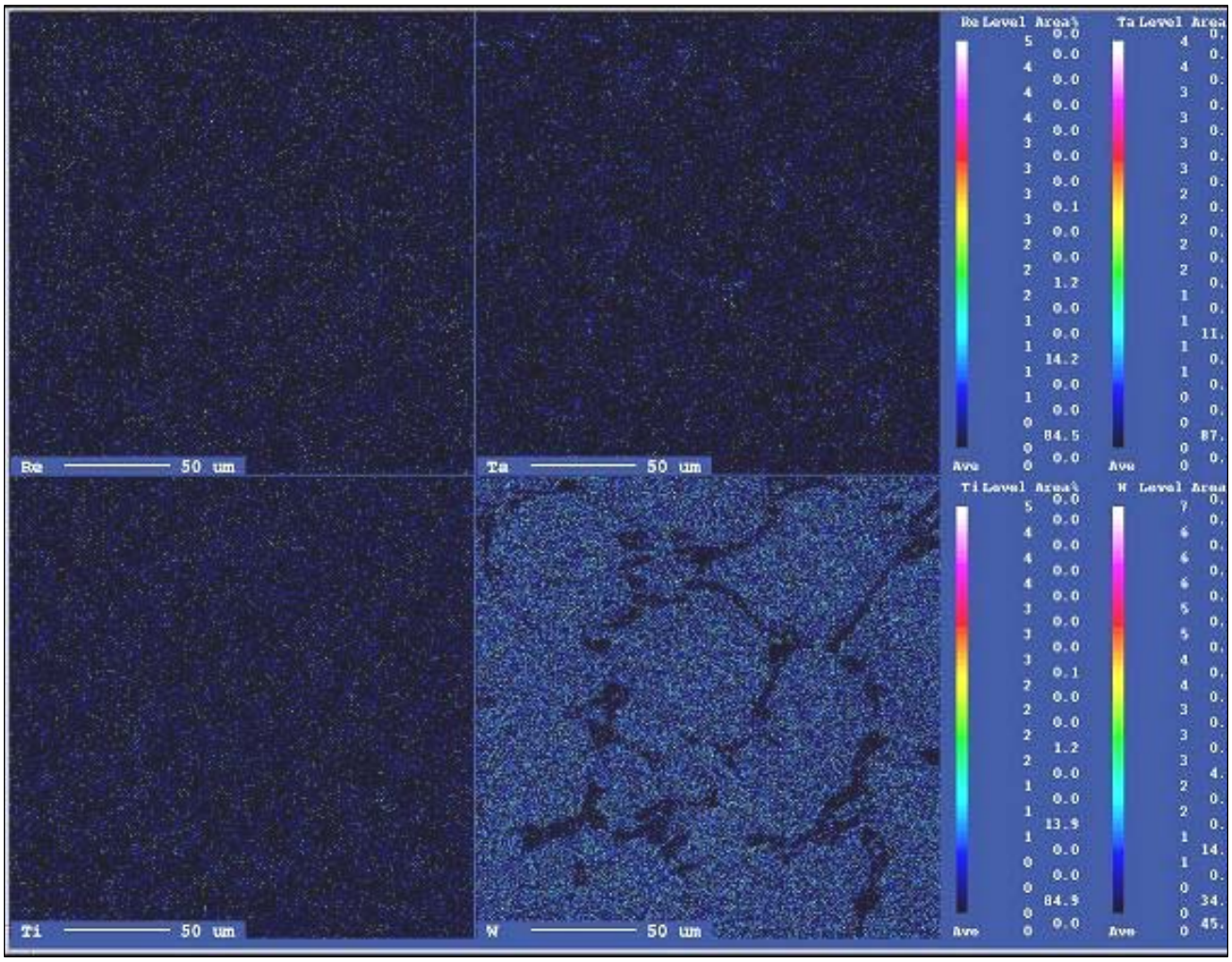

Figure 148 – EMPA maps displaying the distribution of Ru, Ta, Ti and W within the MarM247/Ni-Cr-Hf braze microstructure (as-brazed condition).

As shown in **Figure 148**, Ru, Ta and Ti were distributed fairly evenly between the braze alloy and the matrix. Tungsten, however, partitioned strongly to the MarM247 powder particles, suggesting low solubility within the intermetallic phase. The W appeared to be distributed evenly throughout the matrix particles, implying adequate solubility and little driving force for the precipitation of W-rich carbide particles or Laves phase.

The EMPA maps for Fe and Mo, shown in **Figure 149**, display preferential partitioning to the matrix particles, but due to the low levels of these elements within the MarM247 particles and the braze alloy, partitioning was weak.

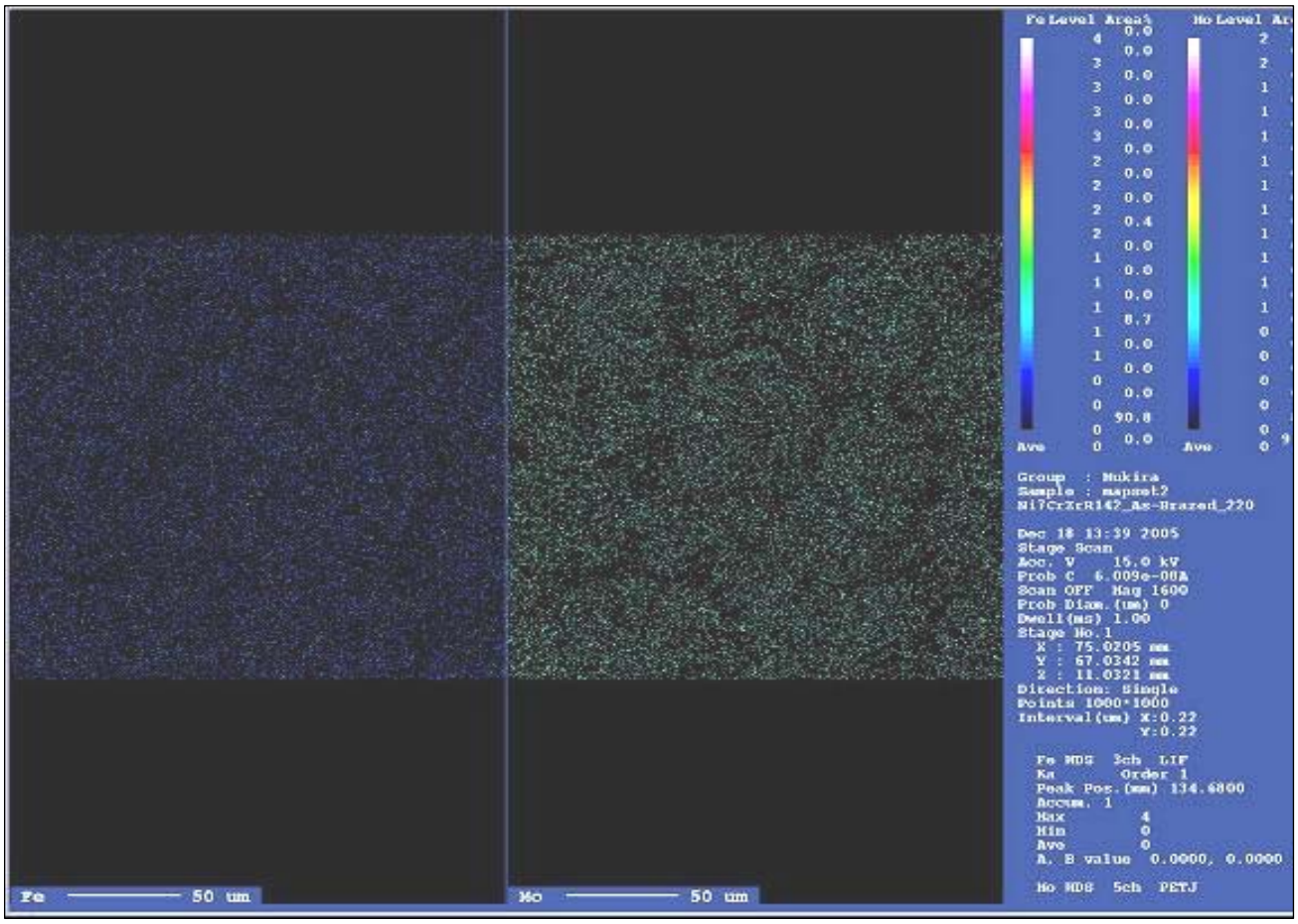

Figure 149 – EMPA maps displaying the distribution of Fe and Mo within the MarM247/Ni-Cr-Hf braze microstructure (as-brazed condition).

11.3.2 The MarM247/Ni-Zr braze joint produced using Ni-7Cr-13Zr braze filler (as-brazed condition):

Secondary and backscatter electron images of the MarM247/Ni-Zr joint produced using the experimental Ni-7Cr-13Zr braze filler metal are shown in **Figure 150** in the as-brazed condition. The arrow indicates the location and direction of the 2 μm stepped EPMA line scan. The results of the EMPA scan are shown in **Table 48**.

The line scan results shown in **Table 48** revealed the presence of a Zr-rich intermetallic phase, containing between 23% and 28% Zr. In order to perform a more detailed analysis of the intermetallic phase observed in the braze joint, four spot chemical analyses were performed within the intermetallic compound in the braze joint. Two backscatter electron images of the MarM247/Ni-Zr braze joint are shown in **Figure 151**, with the location of the four spot analyses highlighted. The results of the microprobe phase analyses, shown in **Table 49**, suggest that the intermetallic phase within the braze alloy contained between 27 and 29% Zr. The binary Ni-Zr phase diagram, shown in **Figure 50**, indicates that the Ni_7Zr_2 intermetallic phase contains approximately 30 wt.% Zr, whereas the Ni_5Zr intermetallic compound contains between 21 and 26 wt.% Zr. The results shown in **Table 49** are therefore inconclusive, suggesting that the intermetallic phase in the braze joint could be either Ni_5Zr or Ni_7Zr_2. Phase 3, shown in **Figure 145(b)**, is most likely the Ni-rich γ phase (with a composition shown in **Table 49**).

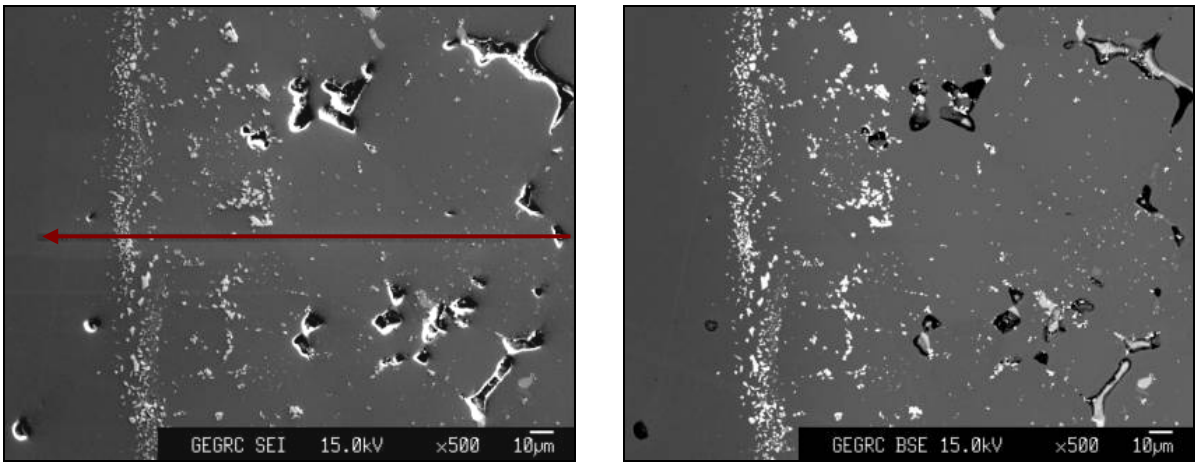

(a) (b)

Figure 150 – Secondary (a) and backscatter (b) electron images of the MarM247/Ni-7Cr-13Zr joint in the as-brazed condition (adjacent to the interface).

Table 48 – The results of the EMPA scan of the MarM247/Ni-7Cr-13Zr braze joint in the as-brazed condition. (All compositions given in wt.%).

X (mm)	Y (mm)	Z (mm)	Al	Hf	Ni	Cr	Zr	Fe	Ta	Mo	Co	W	Ti
76.613	65.076	11.043	4.45	2.01	64.25	7.85	0.21	0.62	4.39	1.34	8.94	3.84	0.00
76.615	65.076	11.043	4.46	2.22	64.32	7.71	0.25	0.66	4.31	1.30	8.91	4.08	0.00
76.617	65.076	11.043	4.37	2.30	64.17	7.81	0.29	0.67	4.26	1.32	8.99	3.75	0.00
76.619	65.076	11.043	4.46	2.00	64.08	7.77	0.24	0.67	4.48	1.37	8.76	4.02	0.00
76.621	65.076	11.043	4.48	2.06	63.94	7.71	0.27	0.68	4.41	1.31	8.75	3.86	0.00
76.623	65.076	11.045	4.40	3.48	63.34	7.48	0.55	0.70	5.15	1.32	8.60	3.73	0.00
76.625	65.076	11.043	4.14	4.85	60.39	7.44	0.89	0.69	6.02	1.30	8.34	3.61	0.00
76.627	65.076	11.043	4.32	2.58	63.11	7.80	0.36	0.75	4.23	1.43	8.81	3.91	0.00
76.629	65.076	11.043	4.54	2.04	64.22	7.74	0.24	0.72	4.02	1.33	8.61	4.03	0.00
76.631	65.076	11.043	4.41	1.95	63.21	7.94	0.22	0.81	3.95	1.37	8.76	4.19	0.00
76.633	65.076	11.043	4.46	2.06	63.96	7.94	0.27	0.84	4.09	1.38	8.71	4.02	0.00
76.635	65.076	11.043	4.41	1.87	64.25	7.99	0.24	0.85	4.21	1.36	8.84	3.82	0.00
76.637	65.076	11.045	4.18	4.88	61.14	7.61	0.59	0.83	5.57	1.28	8.40	3.56	0.01
76.639	65.076	11.043	4.44	2.25	63.61	7.78	0.28	0.83	4.32	1.34	8.71	3.94	0.00
76.641	65.076	11.045	4.52	1.99	64.14	7.80	0.25	0.86	3.86	1.38	8.84	4.04	0.00
76.643	65.076	11.043	4.47	2.01	63.15	7.73	0.24	0.88	4.07	1.35	8.66	3.87	0.00
76.645	65.076	11.043	4.41	1.91	63.34	7.82	0.23	0.89	3.77	1.42	8.84	3.87	0.00
76.647	65.076	11.043	4.36	1.91	63.75	7.84	0.24	0.91	4.09	1.35	8.81	4.07	0.00
76.649	65.076	11.043	4.45	2.00	63.77	7.74	0.24	0.88	4.10	1.40	8.75	4.27	0.00
76.651	65.076	11.043	4.40	1.92	63.55	7.82	0.23	0.94	3.90	1.41	8.82	4.35	0.00
76.653	65.076	11.043	4.34	1.91	63.37	7.79	0.28	0.93	3.87	1.44	8.77	4.13	0.00
76.655	65.076	11.043	4.32	1.85	63.62	7.81	0.25	0.93	3.75	1.43	8.87	3.96	0.00
76.657	65.076	11.043	4.40	1.90	63.30	7.76	0.21	0.98	3.79	1.35	8.81	4.19	0.01
76.659	65.076	11.043	4.36	1.83	63.90	7.83	0.20	1.01	3.50	1.44	8.89	3.90	0.00
76.661	65.076	11.043	4.37	1.87	64.21	7.83	0.24	1.01	3.55	1.50	8.77	4.05	0.00
76.663	65.076	11.043	4.49	2.05	64.23	7.72	0.22	0.97	3.77	1.37	8.70	4.23	0.01
76.665	65.076	11.043	4.43	2.01	64.16	7.70	0.25	1.01	3.74	1.41	8.65	3.67	0.01
76.667	65.076	11.043	4.42	1.96	64.26	7.74	0.22	1.00	3.72	1.42	8.72	3.97	0.00
76.669	65.076	11.043	4.48	2.00	64.48	7.69	0.24	0.97	3.64	1.45	8.57	3.74	0.00
76.671	65.076	11.043	4.45	1.96	64.21	7.77	0.26	1.01	3.62	1.42	8.74	3.54	0.00
76.673	65.076	11.042	4.36	1.95	64.01	7.80	0.19	1.00	3.79	1.42	8.72	3.87	0.00
76.675	65.076	11.042	4.38	1.95	63.79	7.81	0.22	0.98	3.77	1.40	8.71	3.90	0.00
76.677	65.076	11.043	4.45	2.00	64.28	7.74	0.22	1.00	3.65	1.41	8.73	3.71	0.00
76.679	65.076	11.043	4.40	1.96	64.36	7.73	0.24	1.00	3.92	1.39	8.73	3.69	0.00
76.681	65.076	11.043	4.38	1.97	64.19	7.70	0.20	1.04	3.63	1.40	8.68	3.56	0.00
76.683	65.076	11.043	4.41	1.97	64.20	7.68	0.23	1.04	3.79	1.44	8.73	3.90	0.02
76.685	65.076	11.043	4.38	1.94	64.42	7.59	0.24	1.03	3.85	1.44	8.78	3.88	0.00

Table 48 – (continued).

X (mm)	Y (mm)	Z (mm)	Al	Hf	Ni	Cr	Zr	Fe	Ta	Mo	Co	W	Ti
76.687	65.076	11.043	4.42	1.94	64.33	7.63	0.20	1.03	3.80	1.44	8.68	3.90	0.00
76.689	65.076	11.043	4.36	1.92	63.96	7.62	0.23	1.06	3.99	1.43	8.71	3.66	0.01
76.691	65.076	11.043	4.29	1.81	63.56	7.64	0.18	1.03	3.93	1.48	8.79	3.64	0.00
76.693	65.076	11.043	4.41	1.94	64.08	7.56	0.24	1.09	3.94	1.43	8.71	3.55	0.01
76.695	65.076	11.043	4.38	1.92	64.03	7.59	0.22	1.07	3.93	1.44	8.69	3.90	0.00
76.697	65.076	11.043	4.37	1.90	64.16	7.63	0.22	1.11	3.69	1.46	8.66	3.80	0.00
76.699	65.076	11.043	4.42	1.91	64.26	7.64	0.20	1.10	3.76	1.54	8.73	3.64	0.00
76.701	65.076	11.043	4.39	1.94	64.11	7.67	0.25	1.10	3.88	1.43	8.63	3.54	0.00
76.703	65.076	11.043	4.35	1.88	64.24	7.79	0.23	1.15	3.54	1.50	8.71	3.89	0.00
76.705	65.076	11.043	4.38	1.90	64.52	7.82	0.28	1.12	3.65	1.52	8.69	3.55	0.00
76.707	65.076	11.043	4.38	1.89	64.51	7.86	0.21	1.18	3.72	1.48	8.67	3.31	0.00
76.709	65.076	11.043	4.44	1.92	64.62	7.93	0.22	1.19	3.53	1.52	8.68	3.24	0.00
76.711	65.076	11.043	4.40	1.89	64.75	7.95	0.25	1.15	3.78	1.51	8.64	3.44	0.00
76.713	65.076	11.043	4.43	1.99	64.31	7.80	0.23	1.21	3.69	1.50	8.55	3.08	0.01
76.715	65.076	11.043	4.34	1.85	64.00	7.98	0.21	1.25	3.87	1.57	8.63	3.22	0.00
76.717	65.076	11.043	4.33	1.86	64.46	7.97	0.26	1.28	3.59	1.56	8.68	3.13	0.00
76.719	65.076	11.043	4.41	2.00	64.22	7.87	0.24	1.27	3.90	1.54	8.49	3.11	0.00
76.721	65.076	11.043	4.36	1.91	64.30	7.96	0.24	1.34	3.99	1.56	8.57	3.32	0.00
76.723	65.076	11.043	4.33	1.85	64.47	7.95	0.22	1.35	4.07	1.61	8.58	3.13	0.00
76.725	65.076	11.043	4.33	2.81	63.11	7.74	0.34	1.39	4.51	1.61	8.35	3.06	0.00
76.727	65.076	11.042	4.26	1.81	63.33	8.02	0.24	1.48	4.19	1.65	8.42	3.04	0.02
76.729	65.076	11.043	3.78	7.14	59.37	7.68	0.63	1.49	5.70	1.56	7.92	2.94	0.00
76.731	65.076	11.043	3.86	7.12	59.30	7.69	0.64	1.56	5.50	1.58	8.04	2.71	0.00
76.733	65.076	11.043	4.21	1.74	63.93	8.38	0.23	1.85	3.78	1.90	8.51	3.31	0.00
76.735	65.076	11.043	4.13	1.70	63.82	8.47	0.23	1.98	3.83	1.88	8.48	3.34	0.00
76.737	65.076	11.043	4.00	1.52	63.46	8.79	0.20	2.18	3.54	2.07	8.50	3.67	0.00
76.739	65.076	11.043	3.95	1.41	63.11	9.04	0.16	2.41	3.38	2.20	8.34	3.50	0.00
76.741	65.076	11.043	3.92	1.38	63.12	9.12	0.16	2.56	3.26	2.24	8.34	3.46	0.00
76.743	65.076	11.043	3.87	1.31	63.07	9.30	0.14	2.71	3.17	2.37	8.38	3.49	0.00
76.745	65.076	11.043	3.83	1.25	63.10	9.42	0.14	2.93	2.99	2.51	8.34	3.08	0.00
76.747	65.076	11.043	3.74	1.17	62.72	9.68	0.16	3.16	2.86	2.62	8.30	3.47	0.00
76.749	65.076	11.043	3.64	1.08	62.55	9.76	0.15	3.34	2.98	2.74	8.36	3.20	0.00
76.751	65.076	11.043	3.61	1.02	61.95	10.00	0.17	3.60	2.99	2.91	8.06	3.07	0.00
76.753	65.076	11.043	3.51	0.93	62.06	10.23	0.12	3.83	2.93	3.05	8.00	3.04	0.00
76.755	65.076	11.043	3.41	0.82	62.00	10.45	0.14	4.10	2.81	3.19	8.09	2.90	0.00
76.757	65.076	11.043	3.31	0.72	61.47	10.67	0.10	4.34	2.73	3.41	8.03	2.92	0.00
76.759	65.076	11.043	3.26	0.65	60.91	10.86	0.07	4.61	2.69	3.51	7.89	3.14	0.00
76.761	65.076	11.043	3.17	0.51	60.73	11.10	0.06	4.87	2.50	3.64	7.81	2.65	0.00
76.763	65.076	11.043	3.09	0.87	60.18	11.17	0.11	5.03	2.31	3.77	7.76	3.09	0.00
76.765	65.076	11.043	1.83	0.07	41.03	8.09	28.44	3.80	7.28	2.90	5.16	0.98	0.02
76.767	65.076	11.043	2.71	4.42	56.84	11.29	0.57	5.32	2.77	3.97	7.34	2.40	0.00
76.769	65.076	11.043	2.81	0.49	59.27	12.00	0.07	5.83	2.14	4.19	7.54	2.77	0.00
76.771	65.076	11.043	2.71	0.24	58.61	12.20	0.03	6.24	1.79	4.38	7.42	2.77	0.00
76.773	65.076	11.042	2.57	0.82	57.49	12.50	0.12	6.35	1.85	4.53	7.20	2.65	0.00
76.775	65.076	11.042	0.90	8.45	35.71	6.05	26.87	3.31	9.97	2.49	3.14	0.00	0.04
76.777	65.076	11.042	1.13	9.42	33.34	7.90	25.31	4.43	8.72	3.25	3.87	0.00	0.01
76.779	65.076	11.043	0.95	8.54	40.64	7.75	23.83	4.67	6.23	3.38	3.63	0.00	0.03
76.781	65.076	11.042	1.93	3.62	54.13	13.61	0.33	8.16	1.66	5.48	6.27	1.81	0.00
76.783	65.076	11.043	1.62	3.47	47.74	12.44	11.30	7.78	2.23	5.10	5.47	0.72	0.01
76.785	65.076	11.043	1.82	2.55	54.10	14.38	0.20	9.27	1.41	5.87	6.14	1.66	0.00
76.787	65.076	11.043	1.81	0.05	55.28	15.05	0.00	10.03	1.07	6.12	6.06	1.75	0.00
76.789	65.076	11.043	1.71	0.03	54.97	15.52	0.00	10.57	1.14	6.23	5.85	1.56	0.00
76.791	65.076	11.043	1.62	0.02	54.92	15.64	0.02	10.85	1.03	6.49	5.75	1.73	0.00
76.793	65.076	11.043	1.58	0.03	55.03	16.00	0.00	11.24	1.07	6.52	5.55	1.24	0.00
76.795	65.076	11.043	1.47	0.02	54.09	16.20	0.00	11.79	0.79	6.62	5.23	1.17	0.00
76.797	65.076	11.043	1.40	0.02	53.18	16.49	0.00	12.21	0.83	6.85	4.94	1.33	0.00
76.799	65.076	11.043	1.32	0.01	53.32	16.65	0.00	12.66	0.77	7.04	4.74	1.18	0.00
76.801	65.076	11.043	1.25	0.02	52.98	16.84	0.01	13.03	0.81	7.06	4.55	1.27	0.00
76.803	65.076	11.043	1.19	0.03	52.58	17.03	0.01	13.32	0.70	7.10	4.37	1.27	0.00
76.805	65.076	11.043	1.15	0.02	52.71	17.27	0.00	13.52	0.69	7.22	4.27	1.10	0.00

Table 48 – (continued).													
X (mm)	Y (mm)	Z (mm)	Al	Hf	Ni	Cr	Zr	Fe	Ta	Mo	Co	W	Ti
76.807	65.076	11.043	1.09	0.00	52.21	17.50	0.00	13.70	0.56	7.40	4.05	1.02	0.00
76.809	65.076	11.043	1.03	0.02	51.56	17.81	0.00	14.30	0.52	7.54	3.89	0.97	0.00
76.811	65.076	11.043	0.98	0.03	51.29	18.06	0.00	14.54	0.51	7.73	3.70	1.13	0.00
76.813	65.076	11.043	0.94	0.00	51.20	18.40	0.02	14.71	0.58	7.77	3.51	1.17	0.00

Table 49 - Quantitative EPMA data (taken at 15 keV and 80 nA with a focused spot beam) at four locations within the intermetallic phase (indicated in Figure 151(b)). (Percentage by weight).

	Al	Hf	Ni	Cr	Zr	Fe	Ta	Mo	Co	W	Ti	Si
Phase 1	0.20	0.0	66.81	1.34	27.54	0.12	1.32	0.19	2.31	0.03	0.62	0.26
Phase 2	0.22	0.0	66.64	1.15	27.83	0.08	1.11	0.21	2.23	0.00	0.64	0.28
Phase 3	3.83	0.0	74.46	9.70	0.82	0.49	1.00	0.95	4.39	0.35	3.61	0.18
Phase 4	0.65	0.0	70.43	6.80	9.74	0.26	0.66	0.81	4.42	0.02	2.07	0.15

In order to study the distribution of various elements within the Ni-Cr-Zr braze microstructure, EMPA maps were constructed. These maps are shown in **Figure 152** (for Al, C, Ni and Cr), **Figure 153** (for Zr, Hf and Si), **Figure 154** (for Ru, Ta, Ti and W) and **Figure 155** (for Fe and Mo).

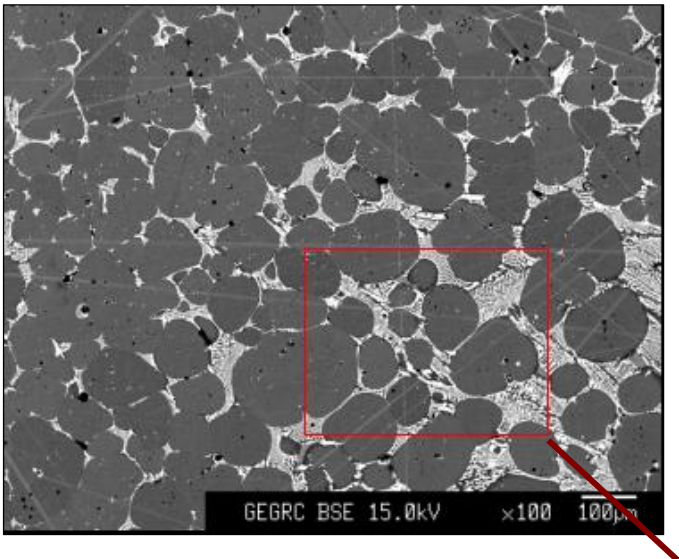

Figure 151(a) – Secondary electron image of the Ni-Cr-Zr alloy in the as-brazed condition.

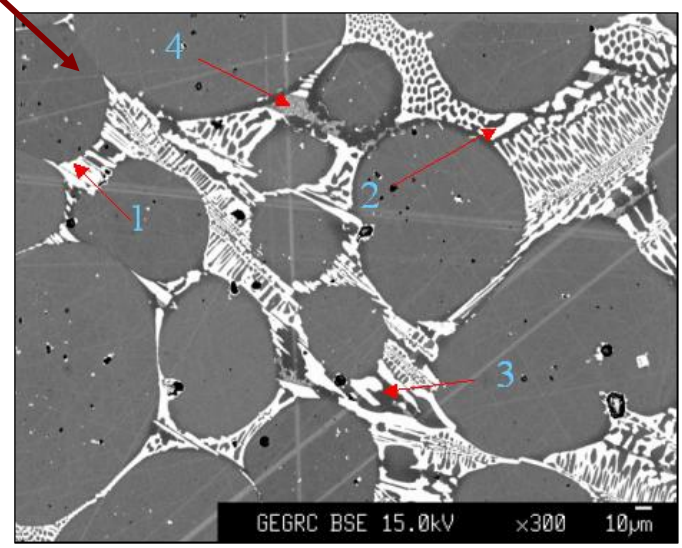

Figure 151(b) – Enlarged view of the secondary electron image of the Ni-Cr-Zr braze, shown in Figure 151(a), highlighting the location of four spot chemical analyses of the intermetallic compound within the braze.

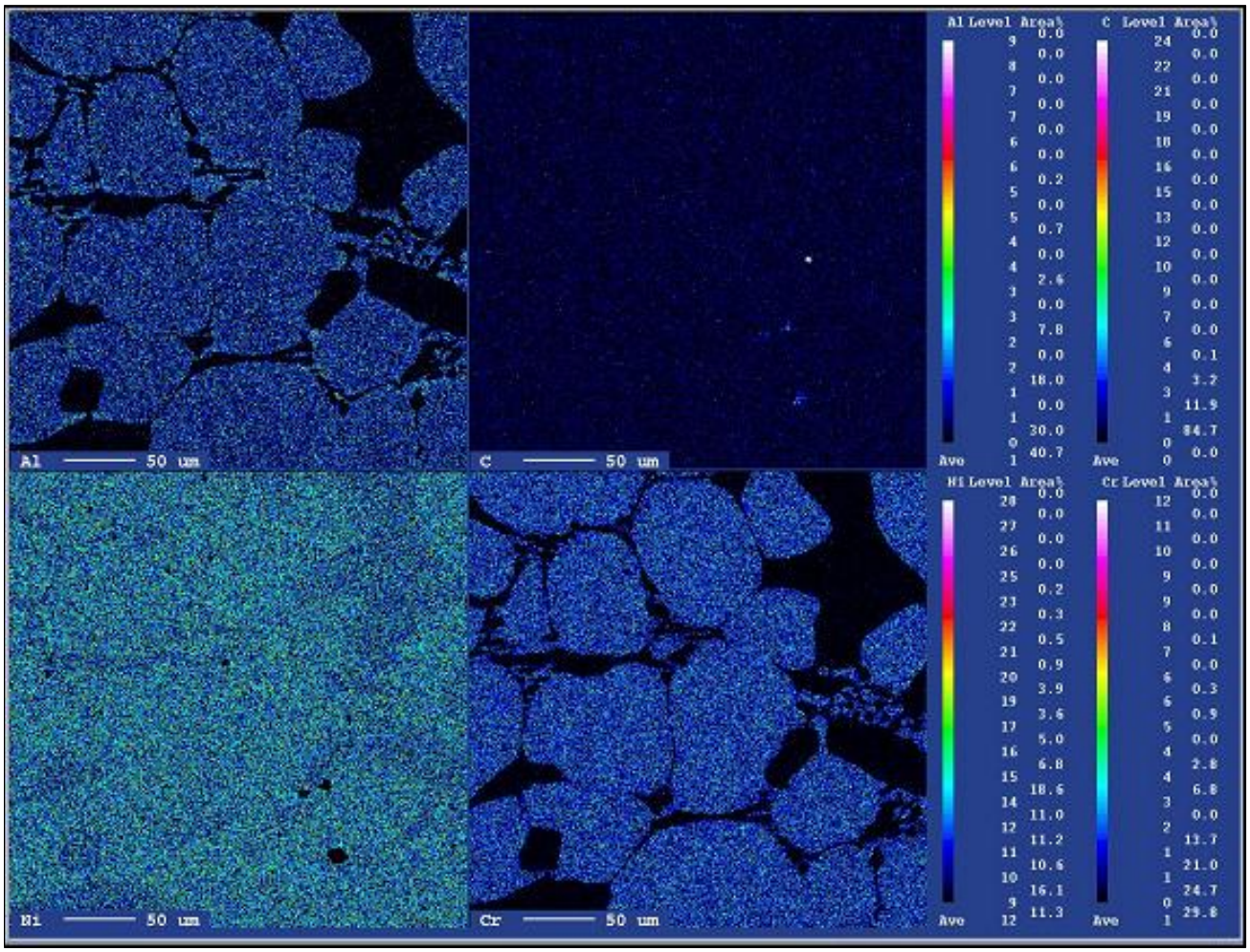

Figure 152 – EMPA maps displaying the distribution of Al, C, Ni and Cr within the MarM247/Ni-Cr-Zr braze microstructure (as-brazed condition).

The EMPA results shown in **Figure 152** indicate that in this braze Al and Cr also partitioned strongly to the MarM247 powder particles during brazing. Given that the braze alloy contains 7% Cr and that a diffusion cycle was not applied, the low Cr concentration measured in the braze alloy between the MarM247 particles was again surprising. Ni and C appeared to be fairly uniformly distributed between the braze alloy and the matrix, with a slightly higher Ni concentration measured in the MarM247 particles.

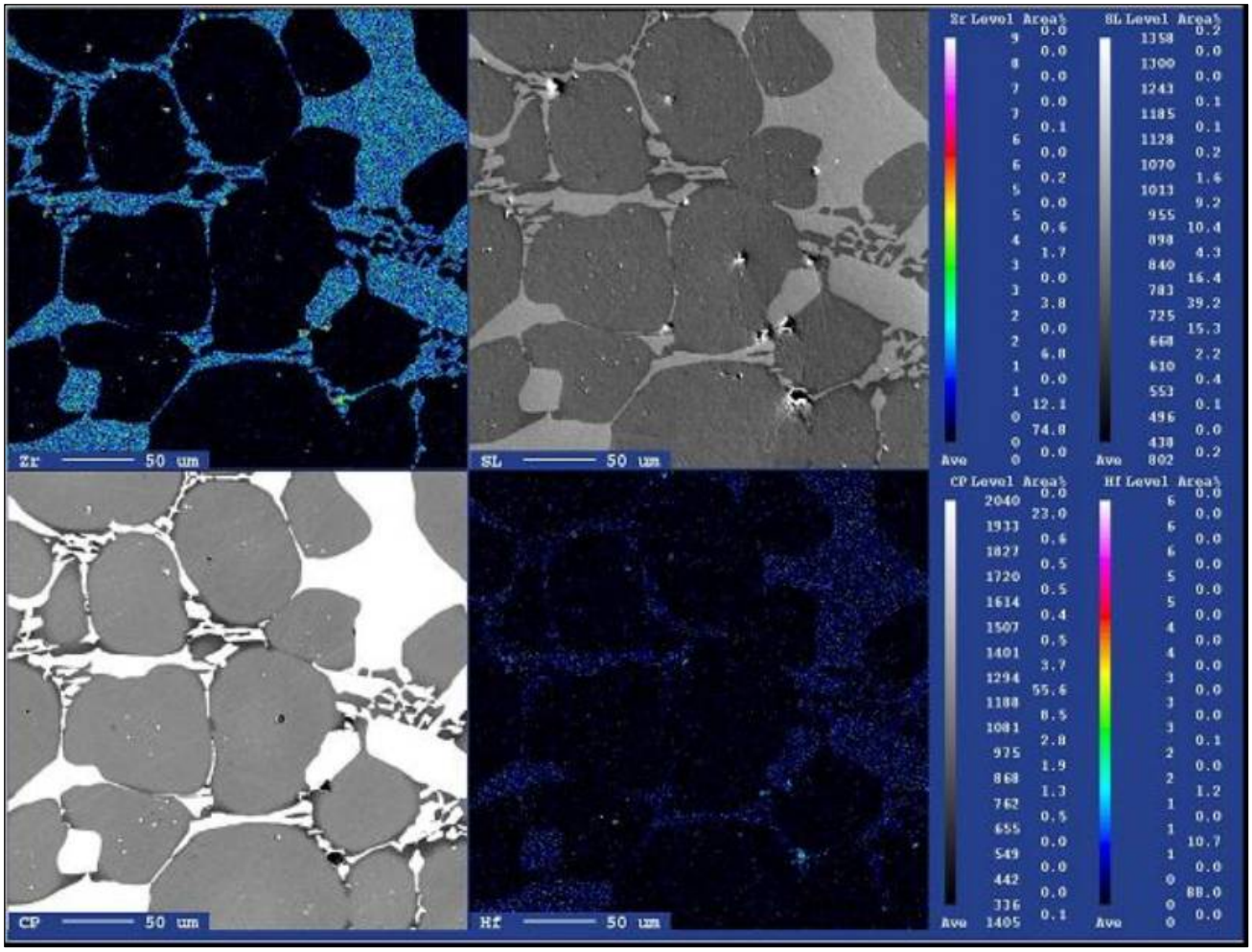

Figure 153 – EMPA maps displaying the distribution of Zr and Hf within the MarM247/Ni-Cr-Zr braze microstructure (as-brazed condition).

The results shown in **Figure 153** suggest that both Hf and Zr partitioned strongly to the braze alloy, which substantiates the results of the line and spot scans shown in **Tables 48 and 49**. The Zr EMPA map confirms that the intermetallic phase within the braze joint was Zr-rich, whereas Zr was almost completely absent from the MarM247 matrix particles (MarM247 has a nominal Zr content of 0.05 wt.%). Hf was not intentionally added to the braze alloy, and the binary eutectic Ni-Zr alloy analyzed in Chapter 3 (see **Table 9**) did not contain any Hf. The Hf detected in the Ni-Cr-Zr alloy may therefore be derived from the MarM247 powder particles (MarM247 has a nominal Hf content of 1.5 wt.%), or from the Cr powder used to make up the ternary alloy.

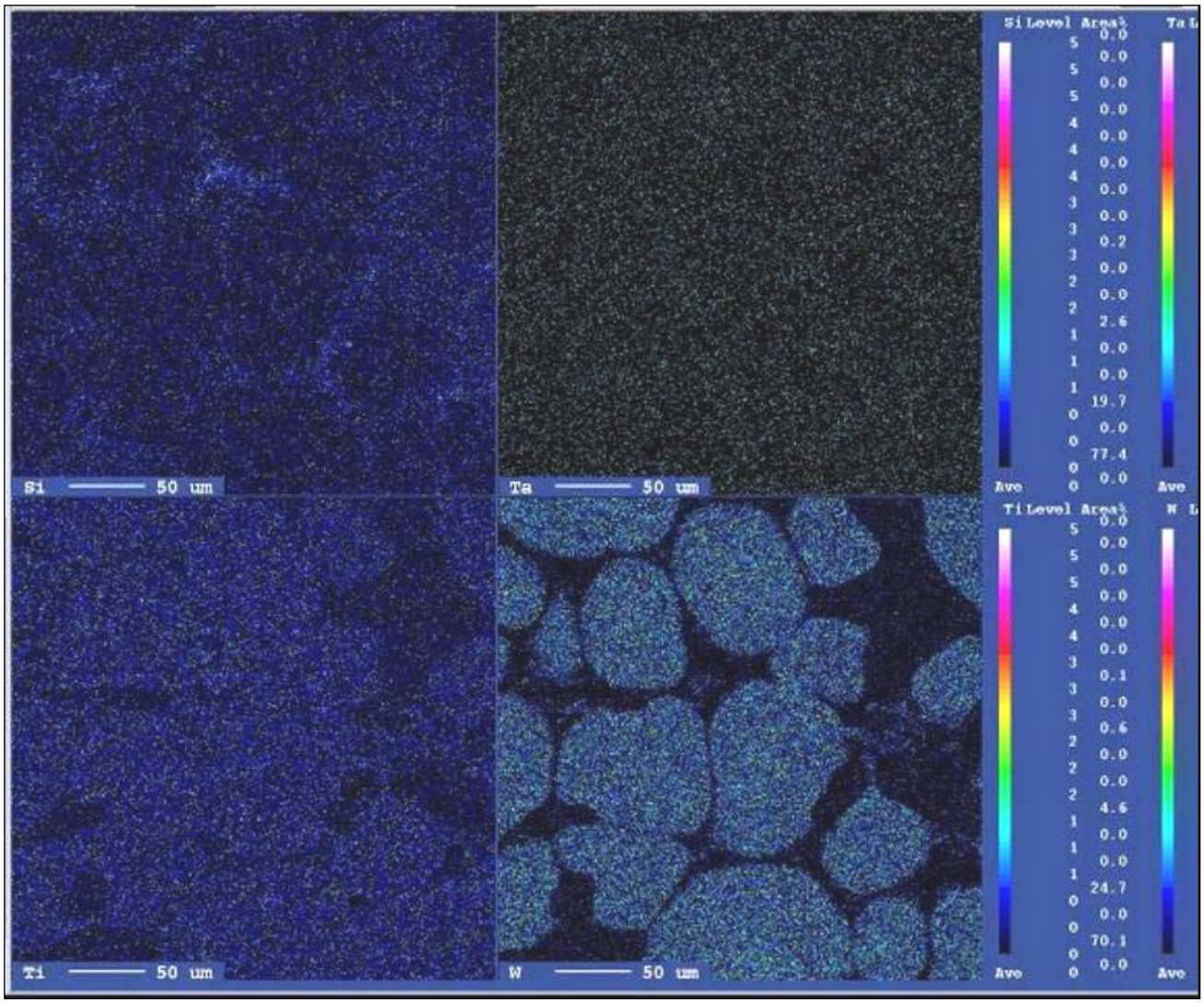

Figure 154 – EMPA maps displaying the distribution of Si, Ta, Ti and W within the MarM247/Ni-Cr-Zr braze microstructure (as-brazed condition).

As shown in **Figure 154**, Si, Ta and Ti were distributed fairly evenly between the braze alloy and the matrix. The Si apparently partitioned weakly to the intermetallic phase (suggesting limited solubility within the intermetallic compound), whereas Ti partitioned preferentially to the MarM247 powder particles. Tungsten, however, partitioned strongly to the MarM247 powder particles, suggesting low solubility within the intermetallic phase. The W appeared to be distributed evenly throughout the matrix particles, implying adequate solubility and little driving force for the precipitation of W-rich carbide particles or Laves phase.

The EMPA maps for Fe and Mo, shown in **Figure 155**, display weak partitioning to the matrix particles, but due to the low levels of these elements within the MarM247 particles and the braze alloy, this tendency was limited.

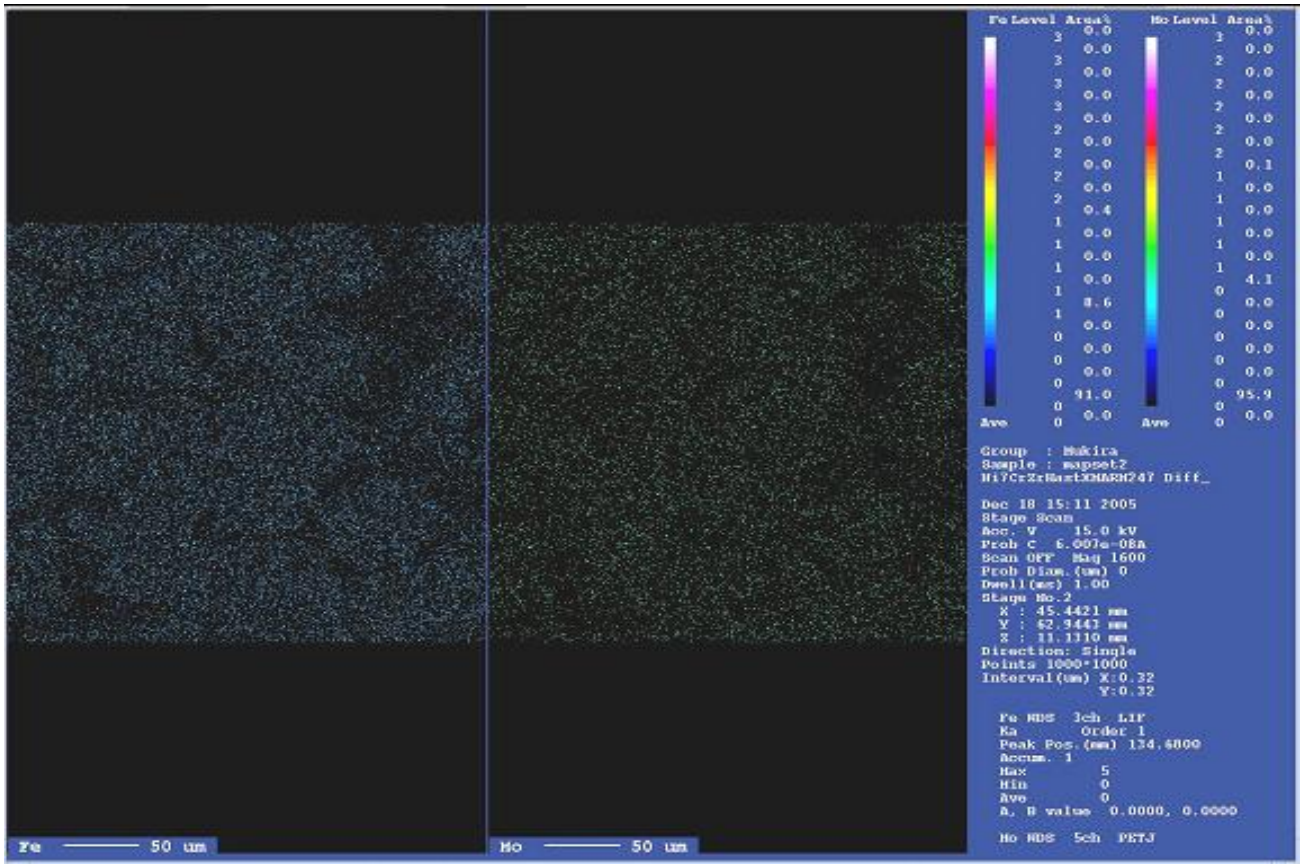

Figure 155 – EMPA maps displaying the distribution of Fe and Mo within the MarM247/Ni-Cr-Zr braze microstructure (as-brazed condition).

11.3.3 The MarM247/Ni-Zr braze joint produced using Ni-7Cr-13Zr braze filler (after an extended diffusion cycle):

Secondary and backscatter electron images of the MarM247/Ni-Zr joint produced using the experimental Ni-7Cr-13Zr braze filler metal are shown in **Figure 156** after an extended diffusion cycle at 1230°C for 12 hours. The arrow indicates the location and direction of the 2 μm stepped EPMA line scan. The results of the EMPA scan are shown in **Table 50**.

The line scan results shown in **Table 50** revealed the presence of Zr-rich intermetallic phases containing between 20% and 29% Zr, and occasionally between 10% and 18% Zr. In order to perform a more detailed analysis of the intermetallic phase observed in the braze joint, four spot chemical analyses were performed within the intermetallic compound in the braze joint. Two backscatter electron images of the MarM247/Ni-Zr braze joint are shown in **Figure 157**, with the location of the spot analyses highlighted. The results of the microprobe phase analyses, shown in **Table 51**, suggest that the intermetallic phase within the braze alloy (phases 1, 2 and 3) contained between 27 and 28% Zr, as well as some Hf, Ta and Co. Phase 4, shown in **Table 51**, was most likely the Ni-rich γ phase, with some Cr, Co and W in solution. The binary Ni-Zr phase diagram, shown in **Figure 50**, indicates that the Ni_7Zr_2 intermetallic phase contains approximately 30 wt.% Zr, whereas the Ni_5Zr intermetallic compound contains approximately between 21 and 26 wt.% Zr. The results shown in **Table 51** are therefore inconclusive, suggesting that the intermetallic phase in the braze joint could be either Ni_5Zr or Ni_7Zr_2. As a result of this uncertainty, another line scan was performed. The results of this line scan are described in §11.3.4.

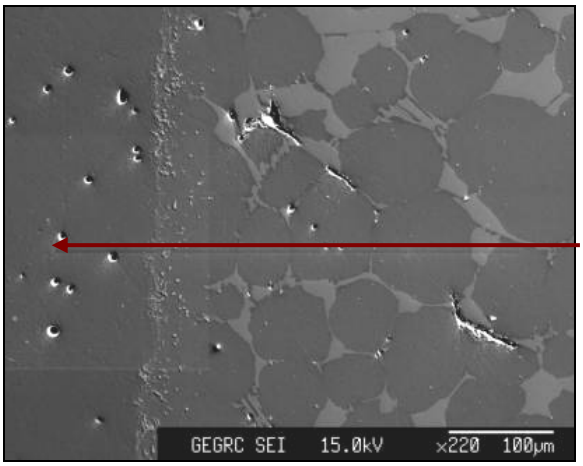

(a)

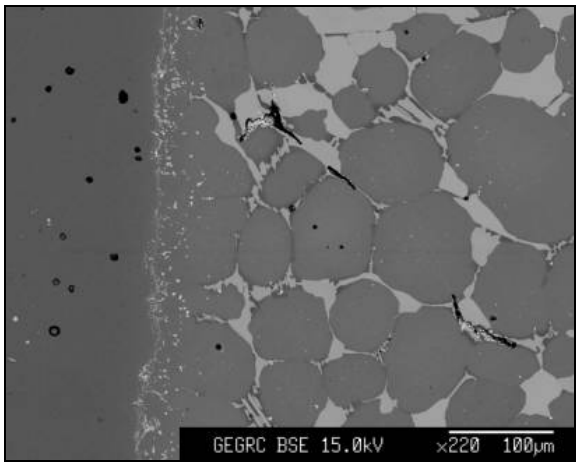

(b)

Figure 156 – Secondary (a) and backscatter (b) electron images of the MarM247/Ni-7Cr-13Zr joint after an extended diffusion cycle (adjacent to the interface).

Table 50 – The results of the EMPA scan of the MarM247/Ni-7Cr-13Zr braze joint after an extended diffusion cycle. (All compositions given in wt.%).

X (mm)	Y (mm)	Z (mm)	Al	Hf	Ni	Cr	Zr	Fe	Ta	Mo	Co	W	Ti
47.333	62.92	11.122	2.62	0.05	71.83	9.93	0.70	0.56	1.68	0.50	4.77	6.11	0.46
47.335	62.92	11.122	2.61	0.07	71.38	9.89	0.70	0.53	1.67	0.52	4.82	5.97	0.46
47.338	62.92	11.122	2.62	0.03	71.76	9.89	0.72	0.57	1.56	0.49	4.75	6.00	0.46
47.34	62.92	11.12	2.59	0.03	70.71	9.93	0.72	0.54	1.90	0.49	4.75	6.05	0.46
47.341	62.92	11.12	2.59	0.04	70.62	9.86	0.74	0.57	1.67	0.49	4.69	6.13	0.46
47.343	62.92	11.12	2.57	0.05	70.84	9.83	0.72	0.55	1.51	0.50	4.76	6.09	0.45
47.346	62.92	11.12	2.61	0.04	71.22	9.78	0.76	0.56	1.44	0.47	4.79	5.77	0.48
47.348	62.92	11.12	2.58	0.07	71.05	9.86	0.76	0.56	1.70	0.50	4.81	5.98	0.46
47.35	62.92	11.12	2.55	0.07	71.08	9.76	0.72	0.54	1.72	0.47	4.75	6.09	0.46
47.352	62.92	11.122	2.61	0.04	71.34	9.70	0.79	0.56	1.69	0.45	4.72	5.83	0.48
47.354	62.92	11.122	2.62	0.08	71.67	9.67	0.69	0.55	1.79	0.45	4.76	5.74	0.43
47.356	62.92	11.12	2.59	0.08	71.61	9.64	0.72	0.54	1.71	0.51	4.78	5.93	0.46
47.358	62.92	11.122	2.61	0.03	71.99	9.54	0.65	0.54	1.77	0.47	4.71	6.05	0.46
47.36	62.92	11.122	1.29	0.97	68.22	5.20	14.72	0.33	1.69	0.27	3.29	2.88	0.28
47.362	62.92	11.122	0.20	1.69	65.25	1.02	26.72	0.07	1.55	0.09	1.97	0.75	0.11
47.364	62.92	11.122	0.16	1.71	64.84	0.82	27.12	0.06	1.56	0.07	1.94	0.59	0.09
47.366	62.92	11.122	0.17	1.78	65.10	0.73	26.92	0.07	1.53	0.06	1.88	0.21	0.10
47.368	62.92	11.122	0.17	1.76	65.53	0.71	27.04	0.05	1.47	0.07	1.93	0.25	0.10
47.37	62.92	11.12	0.16	1.79	65.22	0.65	27.06	0.06	1.57	0.09	1.92	0.46	0.10
47.372	62.92	11.12	0.17	1.76	64.78	0.69	27.16	0.07	1.54	0.05	1.89	0.52	0.10
47.374	62.92	11.122	0.16	1.79	65.09	0.68	27.27	0.07	1.36	0.07	1.95	0.39	0.11
47.376	62.92	11.12	0.17	1.78	64.38	0.72	27.23	0.07	1.49	0.07	1.85	0.54	0.09
47.378	62.92	11.122	0.16	1.81	65.08	0.69	27.23	0.08	1.49	0.08	1.90	0.58	0.11
47.38	62.92	11.122	1.03	1.22	67.75	3.65	18.44	0.22	1.59	0.23	2.79	2.10	0.21
47.382	62.92	11.12	2.57	0.09	71.37	8.95	1.72	0.49	1.47	0.46	4.67	5.59	0.45
47.384	62.92	11.122	2.66	0.01	71.73	9.45	0.66	0.56	1.70	0.49	4.76	5.74	0.42
47.386	62.92	11.12	2.60	0.04	71.10	9.65	0.73	0.55	1.72	0.52	4.75	5.73	0.44
47.388	62.92	11.122	2.63	0.07	71.80	9.52	0.77	0.54	1.80	0.53	4.76	5.87	0.46
47.39	62.92	11.122	2.63	0.04	71.58	9.61	0.74	0.55	1.76	0.51	4.79	5.72	0.44
47.392	62.92	11.12	2.58	0.06	71.02	9.65	0.72	0.52	1.83	0.51	4.76	6.24	0.45
47.394	62.92	11.122	2.61	0.08	72.02	9.63	0.78	0.54	1.85	0.44	4.86	6.11	0.44
47.396	62.92	11.122	2.61	0.06	71.92	9.56	0.73	0.51	1.73	0.49	4.83	5.91	0.45
47.398	62.92	11.122	2.62	0.04	71.41	9.53	0.69	0.52	1.77	0.48	4.87	6.47	0.45
47.4	62.92	11.122	2.62	0.03	71.46	9.63	0.72	0.54	1.73	0.47	4.84	6.18	0.45
47.402	62.92	11.122	2.59	0.05	71.49	9.68	0.75	0.53	1.96	0.50	4.84	6.01	0.44
47.404	62.92	11.122	2.61	0.05	71.66	9.63	0.75	0.54	1.86	0.44	4.86	6.02	0.43
47.406	62.92	11.122	2.59	0.05	71.82	9.61	0.73	0.50	1.78	0.44	4.92	6.31	0.45

Table 50 – (continued).

X (mm)	Y (mm)	Z (mm)	Al	Hf	Ni	Cr	Zr	Fe	Ta	Mo	Co	W	Ti
47.408	62.92	11.122	2.59	0.05	71.68	9.70	0.75	0.51	1.88	0.47	4.88	6.10	0.45
47.41	62.92	11.12	2.57	0.05	70.88	9.71	0.75	0.51	1.76	0.45	4.87	6.46	0.45
47.412	62.92	11.122	2.60	0.05	71.21	9.71	0.75	0.50	1.77	0.47	4.90	6.41	0.47
47.414	62.92	11.122	2.57	0.06	70.97	9.66	0.74	0.51	1.70	0.43	4.84	6.70	0.43
47.416	62.92	11.122	2.59	0.06	71.50	9.74	0.73	0.51	1.89	0.46	4.94	6.28	0.45
47.418	62.92	11.122	2.59	0.03	71.51	9.65	0.75	0.52	1.82	0.46	4.94	6.16	0.44
47.42	62.92	11.122	2.60	0.05	71.74	9.62	0.70	0.48	1.72	0.44	4.91	6.23	0.45
47.422	62.92	11.12	2.48	0.05	70.20	9.63	0.72	0.49	1.96	0.52	4.83	6.13	0.44
47.424	62.92	11.12	2.55	0.05	70.49	9.56	0.71	0.48	1.81	0.49	4.86	6.18	0.46
47.426	62.92	11.122	2.58	0.05	71.49	9.60	0.70	0.50	1.94	0.46	4.91	6.07	0.44
47.428	62.92	11.12	2.53	0.05	70.61	9.56	0.68	0.49	1.97	0.46	4.89	6.48	0.45
47.43	62.92	11.122	2.55	0.06	71.19	9.47	0.72	0.46	2.03	0.47	4.99	6.33	0.44
47.432	62.92	11.12	2.36	1.77	67.34	9.20	2.77	0.47	2.27	0.48	4.65	6.64	0.44
47.434	62.92	11.12	2.51	0.05	70.29	9.61	0.76	0.49	2.15	0.51	4.91	6.65	0.44
47.436	62.92	11.12	2.52	0.05	70.50	9.60	0.77	0.47	2.04	0.47	4.90	6.70	0.43
47.438	62.92	11.122	2.55	0.10	71.45	9.56	0.67	0.49	2.06	0.48	4.85	6.53	0.44
47.44	62.92	11.122	2.57	0.06	71.73	9.57	0.68	0.48	1.81	0.45	5.00	6.66	0.44
47.442	62.92	11.122	2.59	0.06	71.42	9.71	0.77	0.49	2.03	0.47	4.90	6.54	0.46
47.444	62.92	11.122	2.56	0.07	70.87	9.69	0.83	0.48	2.05	0.46	4.97	6.63	0.43
47.446	62.92	11.12	2.23	0.70	64.10	8.98	6.50	0.42	3.50	0.45	4.42	6.40	0.44
47.448	62.92	11.122	2.54	0.21	69.71	9.59	1.74	0.50	2.44	0.49	4.87	6.72	0.43
47.45	62.92	11.122	2.56	0.03	71.11	9.77	0.69	0.50	1.78	0.50	4.90	6.64	0.45
47.452	62.92	11.12	2.53	0.04	71.08	9.86	0.72	0.51	1.92	0.50	4.89	7.11	0.44
47.454	62.92	11.12	2.54	0.03	70.91	9.83	0.74	0.50	1.89	0.47	4.90	7.04	0.46
47.456	62.92	11.12	2.53	0.06	70.46	9.86	0.76	0.50	1.96	0.47	4.84	6.85	0.46
47.458	62.92	11.122	2.58	0.07	71.35	9.79	0.71	0.53	1.72	0.50	4.87	6.44	0.45
47.46	62.92	11.12	2.57	0.04	70.46	9.82	0.67	0.52	2.13	0.50	4.79	6.39	0.44
47.462	62.92	11.122	2.59	0.05	71.32	9.84	0.73	0.55	1.85	0.47	4.89	6.26	0.45
47.464	62.92	11.122	2.58	0.06	71.64	9.83	0.75	0.54	1.95	0.47	4.92	6.07	0.44
47.466	62.92	11.122	2.62	0.04	71.78	9.93	0.71	0.53	1.87	0.47	4.87	5.76	0.44
47.468	62.92	11.12	2.54	0.06	70.81	10.04	0.69	0.55	2.06	0.47	4.85	6.32	0.44
47.47	62.92	11.12	2.56	0.05	70.93	10.05	0.77	0.55	2.25	0.49	4.82	6.20	0.47
47.472	62.92	11.122	2.62	0.03	71.40	9.88	0.70	0.59	2.04	0.49	4.79	5.99	0.44
47.474	62.92	11.122	2.83	0.04	72.11	9.65	0.61	0.57	1.79	0.49	4.77	5.69	0.49
47.476	62.92	11.12	2.17	0.45	71.35	7.02	9.44	0.44	1.35	0.30	3.75	2.28	0.45
47.478	62.92	11.122	2.87	0.04	72.69	9.62	0.60	0.53	1.69	0.46	4.78	5.38	0.49
47.48	62.92	11.12	2.62	0.05	70.86	9.89	0.72	0.58	1.82	0.48	4.89	6.28	0.46
47.482	62.92	11.122	2.60	0.03	71.48	9.79	0.75	0.58	1.94	0.47	4.88	6.20	0.43
47.484	62.92	11.122	2.57	0.04	71.12	9.77	0.73	0.57	1.85	0.49	4.83	6.20	0.45
47.486	62.92	11.12	2.52	0.06	70.49	9.83	0.71	0.57	1.80	0.49	4.84	6.73	0.46
47.488	62.92	11.122	2.58	0.17	71.20	9.68	0.73	0.55	1.90	0.48	4.85	6.44	0.45
47.49	62.92	11.12	2.52	0.38	70.46	9.64	0.92	0.52	2.15	0.51	4.85	6.60	0.46
47.492	62.92	11.122	2.55	0.07	71.46	9.64	0.79	0.51	2.17	0.48	4.94	6.31	0.44
47.494	62.92	11.12	2.51	0.05	70.14	9.78	0.72	0.53	1.99	0.49	4.90	6.86	0.46
47.496	62.92	11.12	2.54	0.04	70.88	9.78	0.70	0.53	2.00	0.46	4.90	7.00	0.44
47.498	62.92	11.12	2.53	0.05	70.78	9.77	0.70	0.51	1.78	0.49	4.87	7.16	0.44
47.5	62.92	11.122	2.57	0.04	71.07	9.62	0.72	0.53	1.72	0.48	4.92	7.03	0.44
47.502	62.92	11.12	2.54	0.03	70.78	9.63	0.69	0.51	1.66	0.52	4.98	7.42	0.46
47.504	62.92	11.122	2.57	0.05	71.01	9.58	0.71	0.51	1.65	0.50	5.04	7.24	0.46
47.506	62.92	11.12	2.54	0.04	70.16	9.65	0.69	0.49	1.69	0.47	4.95	7.35	0.44
47.508	62.92	11.12	2.50	0.07	70.61	9.57	0.75	0.52	1.71	0.48	5.01	7.25	0.45
47.51	62.92	11.12	2.49	0.04	70.57	9.60	0.66	0.50	1.55	0.47	4.98	6.98	0.44
47.512	62.92	11.122	2.44	0.16	69.53	9.42	1.53	0.52	1.94	0.48	4.94	6.96	0.45
47.514	62.92	11.12	2.50	0.02	70.72	9.58	0.68	0.49	1.66	0.49	5.01	7.21	0.43
47.516	62.92	11.12	2.49	0.15	68.94	9.48	1.24	0.50	2.02	0.46	4.96	7.22	0.44
47.518	62.92	11.12	2.51	0.08	69.86	9.57	0.84	0.50	1.83	0.45	4.97	7.12	0.45
47.52	62.92	11.12	2.53	0.05	70.54	9.64	0.76	0.50	1.94	0.52	4.97	7.13	0.45
47.522	62.92	11.12	2.53	0.04	70.39	9.58	0.62	0.50	1.88	0.50	5.03	7.32	0.42
47.524	62.92	11.12	2.47	0.05	70.26	9.67	0.60	0.53	1.73	0.48	4.98	7.17	0.44
47.526	62.92	11.12	2.50	0.05	70.67	9.57	0.71	0.53	1.69	0.51	5.03	7.26	0.44

Table 50 – (continued).

X (mm)	Y (mm)	Z (mm)	Al	Hf	Ni	Cr	Zr	Fe	Ta	Mo	Co	W	Ti
47.528	62.92	11.12	2.51	0.04	70.12	9.55	0.67	0.50	1.81	0.49	5.04	7.50	0.44
47.53	62.92	11.12	2.49	0.06	69.85	9.51	0.69	0.50	1.82	0.48	4.89	7.46	0.45
47.532	62.92	11.12	2.52	0.03	70.29	9.48	0.75	0.53	1.78	0.50	4.95	7.46	0.47
47.534	62.92	11.12	2.53	0.06	70.57	9.37	0.79	0.49	1.79	0.50	4.98	7.33	0.45
47.536	62.92	11.12	2.51	0.05	70.34	9.44	0.70	0.53	1.71	0.51	4.92	7.59	0.45
47.538	62.92	11.122	2.56	0.06	71.21	9.50	0.80	0.54	1.46	0.51	4.92	6.94	0.44
47.54	62.92	11.12	2.53	0.07	70.98	9.59	0.65	0.54	1.65	0.49	4.91	7.05	0.45
47.542	62.92	11.12	2.53	0.03	70.23	9.66	0.70	0.56	1.60	0.47	4.90	6.86	0.45
47.544	62.92	11.12	2.55	0.06	70.39	9.64	0.73	0.58	1.81	0.45	4.87	6.62	0.44
47.546	62.92	11.12	2.55	0.03	71.00	9.70	0.76	0.56	1.66	0.52	4.89	6.48	0.44
47.548	62.92	11.12	2.56	0.04	71.19	9.84	0.70	0.60	1.65	0.49	4.88	6.44	0.43
47.55	62.92	11.122	2.63	0.01	71.46	9.74	0.63	0.59	1.58	0.51	4.88	6.36	0.46
47.552	62.92	11.12	2.78	0.04	72.40	9.63	0.52	0.56	1.50	0.45	4.80	5.62	0.50
47.554	62.92	11.12	3.04	0.04	73.72	9.70	0.70	0.58	1.32	0.48	4.69	3.41	0.54
47.556	62.92	11.12	2.81	0.01	72.05	9.70	0.68	0.60	1.53	0.46	4.77	4.94	0.50
47.558	62.92	11.12	2.63	0.04	71.79	9.72	0.67	0.58	1.59	0.51	4.81	5.99	0.48
47.56	62.92	11.12	2.58	0.05	72.18	9.79	0.73	0.58	1.63	0.52	4.86	6.09	0.44
47.562	62.92	11.12	2.56	0.04	71.97	9.67	0.72	0.63	1.65	0.51	4.85	6.62	0.45
47.564	62.92	11.122	2.56	0.12	71.41	9.45	1.51	0.53	1.75	0.47	4.78	6.34	0.45
47.566	62.92	11.122	2.57	0.06	72.23	9.49	0.68	0.59	1.71	0.52	4.80	6.31	0.44
47.568	62.92	11.122	2.54	0.13	71.01	9.31	1.62	0.56	1.58	0.52	4.78	6.58	0.44
47.57	62.92	11.122	2.59	0.04	72.32	9.40	0.73	0.56	1.60	0.49	4.89	6.80	0.45
47.572	62.92	11.12	2.55	0.07	72.27	9.50	0.71	0.56	1.67	0.51	4.92	7.00	0.44
47.575	62.92	11.122	2.56	0.07	71.82	9.36	0.77	0.57	1.60	0.51	4.86	7.13	0.44
47.576	62.92	11.12	2.52	0.06	71.41	9.55	0.73	0.59	1.71	0.53	4.81	7.12	0.45
47.578	62.92	11.12	2.54	0.07	71.55	9.65	0.70	0.59	1.83	0.47	4.90	7.06	0.44
47.581	62.92	11.122	2.58	0.05	72.01	9.49	0.71	0.53	1.43	0.51	4.87	6.77	0.45
47.583	62.92	11.12	2.54	0.04	71.98	9.67	0.70	0.56	1.49	0.53	4.94	6.62	0.44
47.584	62.92	11.122	2.59	0.04	72.58	9.67	0.73	0.60	1.53	0.52	4.93	6.52	0.44
47.586	62.92	11.12	2.57	0.06	71.81	9.75	0.73	0.56	1.72	0.53	4.88	6.34	0.44
47.589	62.92	11.12	2.51	0.03	71.69	9.70	0.73	0.56	1.87	0.54	4.85	6.48	0.45
47.59	62.92	11.12	2.53	0.06	71.59	9.75	0.72	0.59	1.72	0.48	4.87	6.30	0.44
47.592	62.92	11.12	2.55	0.04	71.92	9.71	0.70	0.58	1.80	0.49	4.85	6.63	0.45
47.595	62.92	11.122	2.59	0.07	72.38	9.59	0.73	0.59	1.89	0.50	4.87	5.89	0.44
47.597	62.92	11.122	2.59	0.06	72.64	9.61	0.67	0.57	1.69	0.48	4.86	6.31	0.47
47.599	62.92	11.12	2.55	0.07	72.30	9.71	0.71	0.60	1.75	0.46	4.87	6.43	0.45
47.601	62.92	11.12	2.56	0.05	72.04	9.63	0.69	0.60	1.93	0.50	4.84	6.27	0.45
47.603	62.92	11.12	2.59	0.05	71.86	9.66	0.70	0.59	1.89	0.48	4.84	6.18	0.44
47.605	62.92	11.12	2.61	0.03	72.12	9.66	0.72	0.58	1.71	0.50	4.76	6.32	0.46
47.607	62.92	11.12	2.67	0.03	72.16	9.46	0.70	0.60	1.84	0.51	4.82	6.03	0.46
47.609	62.92	11.12	2.94	0.05	73.96	9.42	0.68	0.60	1.53	0.49	4.74	4.29	0.53
47.611	62.92	11.122	2.89	0.00	74.09	9.34	0.54	0.60	1.78	0.50	4.77	5.02	0.50
47.613	62.92	11.12	2.61	0.05	72.24	9.62	0.62	0.63	1.85	0.50	4.82	6.00	0.46
47.615	62.92	11.122	2.59	0.06	72.34	9.66	0.71	0.68	1.93	0.55	4.79	5.97	0.42
47.617	62.92	11.12	2.54	0.05	71.93	9.80	0.69	0.69	1.79	0.55	4.78	6.14	0.44
47.619	62.92	11.122	2.58	0.05	72.55	9.75	0.75	0.75	1.83	0.54	4.78	5.99	0.43
47.621	62.92	11.122	2.56	0.04	72.55	9.75	0.71	0.76	1.68	0.57	4.80	6.20	0.43
47.623	62.92	11.122	2.58	0.03	73.00	9.73	0.68	0.79	1.56	0.63	4.84	5.74	0.43
47.625	62.92	11.122	2.49	0.11	72.13	9.91	0.94	0.82	1.77	0.66	4.80	5.78	0.42
47.627	62.92	11.122	2.52	0.03	72.23	9.88	0.65	0.84	1.84	0.66	4.80	5.73	0.42
47.629	62.92	11.122	2.20	0.85	65.33	9.14	6.58	0.82	3.24	0.67	4.42	5.25	0.41
47.631	62.92	11.12	2.37	0.28	69.64	9.63	2.21	0.94	2.09	0.71	4.71	6.06	0.41
47.633	62.92	11.12	2.43	0.04	71.41	9.76	0.64	1.02	1.71	0.77	4.75	5.85	0.42
47.635	62.92	11.12	2.39	0.04	71.52	9.85	0.60	1.11	1.77	0.83	4.75	6.36	0.41
47.637	62.92	11.122	2.39	0.02	71.73	9.76	0.63	1.19	1.74	0.90	4.82	6.03	0.40
47.639	62.92	11.122	2.35	0.07	70.54	9.76	1.02	1.29	1.78	0.93	4.67	5.56	0.36
47.641	62.92	11.122	2.35	0.08	70.80	9.80	0.94	1.37	1.76	1.01	4.67	5.59	0.38
47.643	62.92	11.122	2.32	0.02	71.37	9.95	0.59	1.52	1.85	1.04	4.73	6.19	0.38
47.645	62.92	11.122	2.28	0.04	71.07	9.95	0.53	1.56	1.70	1.12	4.68	6.19	0.39
47.647	62.92	11.122	2.26	0.05	70.75	10.12	0.56	1.73	1.67	1.16	4.74	5.97	0.38

Table 50 – (continued).

X (mm)	Y (mm)	Z (mm)	Al	Hf	Ni	Cr	Zr	Fe	Ta	Mo	Co	W	Ti
47.649	62.92	11.122	2.23	0.03	70.37	10.16	0.57	1.85	1.45	1.25	4.68	6.13	0.34
47.651	62.92	11.122	2.17	0.03	69.91	10.27	0.53	1.95	1.83	1.36	4.65	5.98	0.35
47.653	62.92	11.122	2.13	0.03	69.66	10.41	0.45	2.15	1.59	1.46	4.61	6.15	0.36
47.655	62.92	11.122	2.06	0.14	68.70	10.41	1.81	2.30	1.67	1.52	4.51	5.73	0.33
47.657	62.92	11.122	2.05	0.02	69.91	10.83	0.43	2.62	1.28	1.77	4.55	5.95	0.31
47.659	62.92	11.122	2.01	0.00	69.86	11.13	0.43	2.82	1.36	1.84	4.59	5.33	0.32
47.661	62.92	11.122	2.00	0.03	69.28	11.27	0.43	3.01	1.30	1.97	4.53	5.38	0.29
47.663	62.92	11.122	1.93	0.00	68.83	11.41	0.37	3.17	1.35	2.09	4.45	5.33	0.29
47.665	62.92	11.122	1.90	0.00	68.45	11.53	0.33	3.36	1.40	2.18	4.37	5.02	0.28
47.667	62.92	11.122	1.83	0.01	68.75	11.70	0.28	3.56	1.26	2.34	4.33	4.99	0.27
47.669	62.92	11.122	1.79	0.02	68.58	11.74	0.28	3.84	1.40	2.47	4.40	4.86	0.25
47.671	62.92	11.122	1.75	0.00	68.48	11.92	0.19	4.11	1.48	2.63	4.32	4.56	0.24
47.673	62.92	11.12	1.52	0.43	63.72	11.60	5.46	4.07	1.67	2.64	3.99	4.04	0.25
47.675	62.92	11.12	0.96	1.88	47.72	9.21	23.85	3.62	2.96	2.34	3.00	2.84	0.33
47.677	62.92	11.122	1.06	1.74	51.00	9.87	20.56	4.08	2.20	2.61	3.15	3.14	0.40
47.679	62.92	11.122	0.99	1.66	50.60	10.18	20.07	4.48	2.03	2.90	3.13	3.29	0.40
47.681	62.92	11.122	1.36	0.00	65.94	12.92	0.34	5.85	1.35	3.62	4.01	4.10	0.18
47.683	62.92	11.12	1.30	0.02	64.65	13.10	0.33	6.15	1.27	3.84	3.94	4.03	0.17
47.685	62.92	11.122	1.26	0.00	64.76	13.35	0.10	6.63	1.24	4.04	3.96	3.94	0.15
47.687	62.92	11.122	1.21	0.03	63.69	13.63	0.24	6.82	1.16	4.17	3.84	3.67	0.15
47.689	62.92	11.122	1.09	0.40	60.40	13.37	3.19	6.98	1.46	4.18	3.66	3.20	0.19
47.691	62.92	11.12	1.06	0.22	60.67	13.85	2.05	7.32	0.90	4.43	3.65	3.41	0.18
47.693	62.92	11.122	0.87	1.37	53.20	12.39	10.50	6.73	1.83	4.07	3.15	2.67	0.34
47.695	62.92	11.122	0.80	1.73	51.11	12.36	12.66	7.03	1.83	4.20	3.02	2.58	0.36
47.697	62.92	11.12	0.90	0.43	58.27	14.44	3.23	8.38	0.92	4.93	3.42	3.03	0.24
47.699	62.92	11.12	0.87	0.07	59.55	15.03	0.80	9.04	0.71	5.33	3.38	2.67	0.12
47.701	62.92	11.12	0.85	0.01	59.91	15.41	0.10	9.44	0.52	5.46	3.38	2.48	0.10
47.703	62.92	11.122	0.81	0.00	59.78	15.53	0.17	9.80	0.65	5.50	3.33	2.19	0.10
47.705	62.92	11.12	0.78	0.00	59.52	15.85	0.01	9.94	0.68	5.67	3.25	1.87	0.08
47.707	62.92	11.12	0.74	0.00	59.02	15.93	0.02	10.30	0.58	5.86	3.14	1.90	0.09
47.709	62.92	11.122	0.72	0.00	58.68	16.07	0.00	10.84	0.73	5.95	3.08	1.72	0.06
47.711	62.92	11.122	0.67	0.00	57.97	16.20	0.02	11.17	0.65	6.06	3.00	1.59	0.07
47.713	62.92	11.12	0.63	0.00	57.60	16.39	0.01	11.34	0.74	6.17	2.93	1.53	0.06
47.715	62.92	11.122	0.60	0.01	57.29	16.53	0.00	11.80	0.67	6.41	2.81	1.37	0.05
47.717	62.92	11.12	0.56	0.00	56.56	16.79	0.01	12.11	0.72	6.40	2.73	1.70	0.06
47.719	62.92	11.122	0.55	0.00	56.47	16.90	0.00	12.41	0.77	6.58	2.61	1.55	0.04
47.721	62.92	11.122	0.52	0.00	55.53	16.94	0.00	12.80	0.62	6.69	2.53	1.50	0.04
47.723	62.92	11.122	0.49	0.00	55.37	16.98	0.01	12.98	0.44	6.70	2.48	1.36	0.04
47.725	62.92	11.122	0.47	0.00	55.51	16.98	0.00	13.17	0.57	6.86	2.41	1.35	0.03
47.727	62.92	11.122	0.45	0.01	54.70	17.13	0.02	13.44	0.45	6.95	2.35	1.28	0.02
47.729	62.92	11.12	0.42	0.01	54.12	17.23	0.02	13.57	0.30	6.97	2.23	1.30	0.02
47.731	62.92	11.122	0.44	0.00	54.30	17.22	0.01	13.75	0.41	6.95	2.13	1.23	0.02
47.733	62.92	11.12	0.40	0.00	53.15	17.62	0.01	14.16	0.34	7.17	2.09	1.27	0.02
47.735	62.92	11.118	0.36	0.00	52.29	17.92	0.03	14.33	0.36	7.35	1.99	1.04	0.01
47.737	62.92	11.116	0.34	0.00	51.72	18.34	0.01	14.48	0.47	7.41	1.91	1.17	0.02
47.739	62.92	11.118	0.33	0.00	51.83	18.50	0.01	14.83	0.41	7.58	1.84	1.20	0.01
47.741	62.92	11.116	0.32	0.00	51.16	18.69	0.03	15.02	0.57	7.54	1.78	0.94	0.01
47.743	62.92	11.12	0.32	0.01	51.89	18.44	0.01	15.38	0.30	7.65	1.82	0.83	0.01
47.745	62.92	11.12	0.30	0.00	51.65	18.87	0.00	15.46	0.32	7.83	1.71	0.86	0.00
47.747	62.92	11.12	0.29	0.00	50.87	18.79	0.00	15.81	0.22	7.82	1.64	0.87	0.01
47.749	62.92	11.12	0.27	0.00	50.58	18.82	0.01	16.00	0.31	7.85	1.63	0.73	0.00
47.751	62.92	11.122	0.26	0.00	50.84	18.81	0.00	16.13	0.44	7.90	1.59	0.95	0.01
47.753	62.92	11.12	0.24	0.00	50.47	19.01	0.00	16.25	0.38	7.94	1.55	0.34	0.01
47.755	62.92	11.122	0.24	0.00	50.36	19.07	0.00	16.48	0.57	8.06	1.57	0.64	0.00
47.757	62.92	11.122	0.23	0.00	50.17	18.92	0.00	16.59	0.48	8.21	1.48	0.51	0.01
47.759	62.92	11.122	0.22	0.00	49.50	18.92	0.00	16.69	0.42	8.12	1.46	0.54	0.01
47.761	62.92	11.122	0.21	0.00	49.52	19.18	0.00	16.90	0.62	8.19	1.44	0.58	0.00
47.763	62.92	11.122	0.21	0.00	49.53	19.26	0.00	16.80	0.62	8.21	1.44	0.73	0.00
47.765	62.92	11.122	0.20	0.00	49.41	19.31	0.00	17.08	0.53	8.27	1.40	0.47	0.01
47.767	62.92	11.12	0.19	0.00	48.90	19.61	0.02	17.10	0.69	8.28	1.39	0.66	0.00

Table 50 – (continued).

X (mm)	Y (mm)	Z (mm)	Al	Hf	Ni	Cr	Zr	Fe	Ta	Mo	Co	W	Ti
47.769	62.92	11.122	0.19	0.00	49.01	19.67	0.02	17.18	0.61	8.27	1.36	0.75	0.00
47.771	62.92	11.122	0.18	0.00	48.63	19.96	0.01	17.28	0.48	8.37	1.36	0.78	0.00
47.773	62.92	11.122	0.19	0.00	48.29	19.94	0.03	17.50	0.57	8.48	1.36	0.67	0.00
47.775	62.92	11.12	0.18	0.01	48.03	20.10	0.00	17.38	0.47	8.54	1.36	0.70	0.00
47.777	62.92	11.122	0.18	0.01	48.33	20.13	0.00	17.40	0.52	8.53	1.32	0.80	0.00
47.779	62.92	11.122	0.17	0.00	47.98	20.33	0.00	17.56	0.57	8.52	1.29	0.94	0.00
47.781	62.92	11.122	0.17	0.00	47.70	20.49	0.02	17.63	0.45	8.49	1.31	0.85	0.00
47.783	62.92	11.122	0.17	0.01	47.60	20.26	0.02	17.58	0.45	8.53	1.27	0.69	0.00

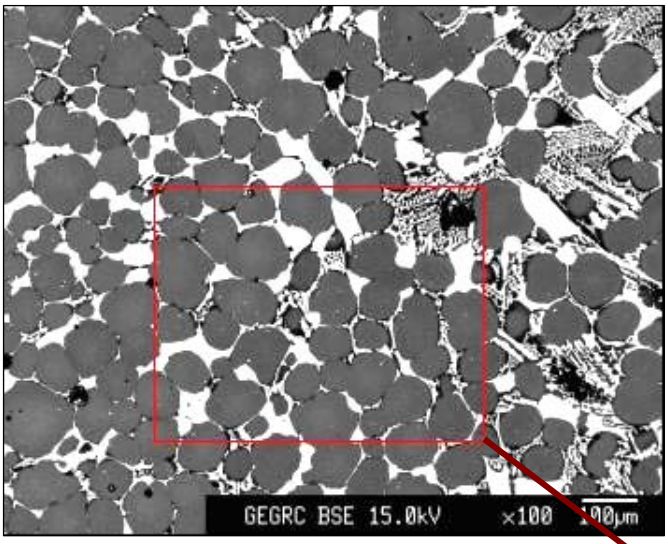

Figure 157(a) – Secondary electron image of the Ni-Cr-Zr alloy (after an extended brazing cycle).

Figure 157(b) – Enlarged view of the secondary electron image of the Ni-Cr-Zr braze, shown in Figure 157(a), highlighting the location of four spot chemical analyses of the intermetallic compound within the braze.

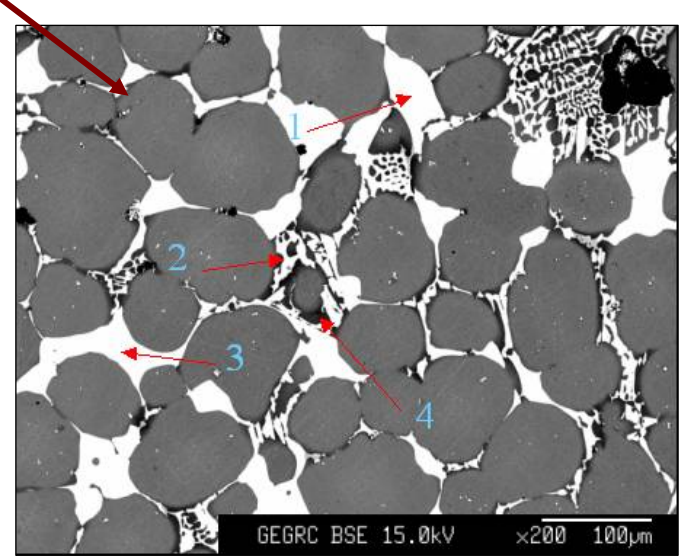

Table 51 - Quantitative EPMA data (taken at 15 keV and 80 nA with a focused spot beam) at four locations within the intermetallic phase (indicated in Figure 157(b)). (Percentage by weight).

	Al	Hf	Ni	Cr	Zr	Fe	Ta	Mo	Co	W	Ti	Si
Phase 1	0.18	1.60	66.77	0.60	27.87	0.06	1.39	0.05	1.83	0.35	0.08	0.16
Phase 2	0.19	1.43	66.83	0.77	27.97	0.08	1.33	0.07	1.81	0.07	0.14	0.24
Phase 3	0.17	1.71	66.22	0.61	27.65	0.06	1.81	0.09	1.85	0.45	0.10	0.17
Phase 4	3.16	0.04	75.05	9.13	0.63	0.54	1.58	0.42	4.53	3.35	0.55	0.19

In order to study the distribution of various elements within the Ni-Cr-Hf braze microstructure, EMPA maps were constructed. These maps are shown in **Figure 158** (for Al, C, Ni and Cr), **Figure 159** (for Zr, Hf and Si), **Figure 160** (for Ru, Ta, Ti and W) and **Figure 161** (for Fe and Mo).

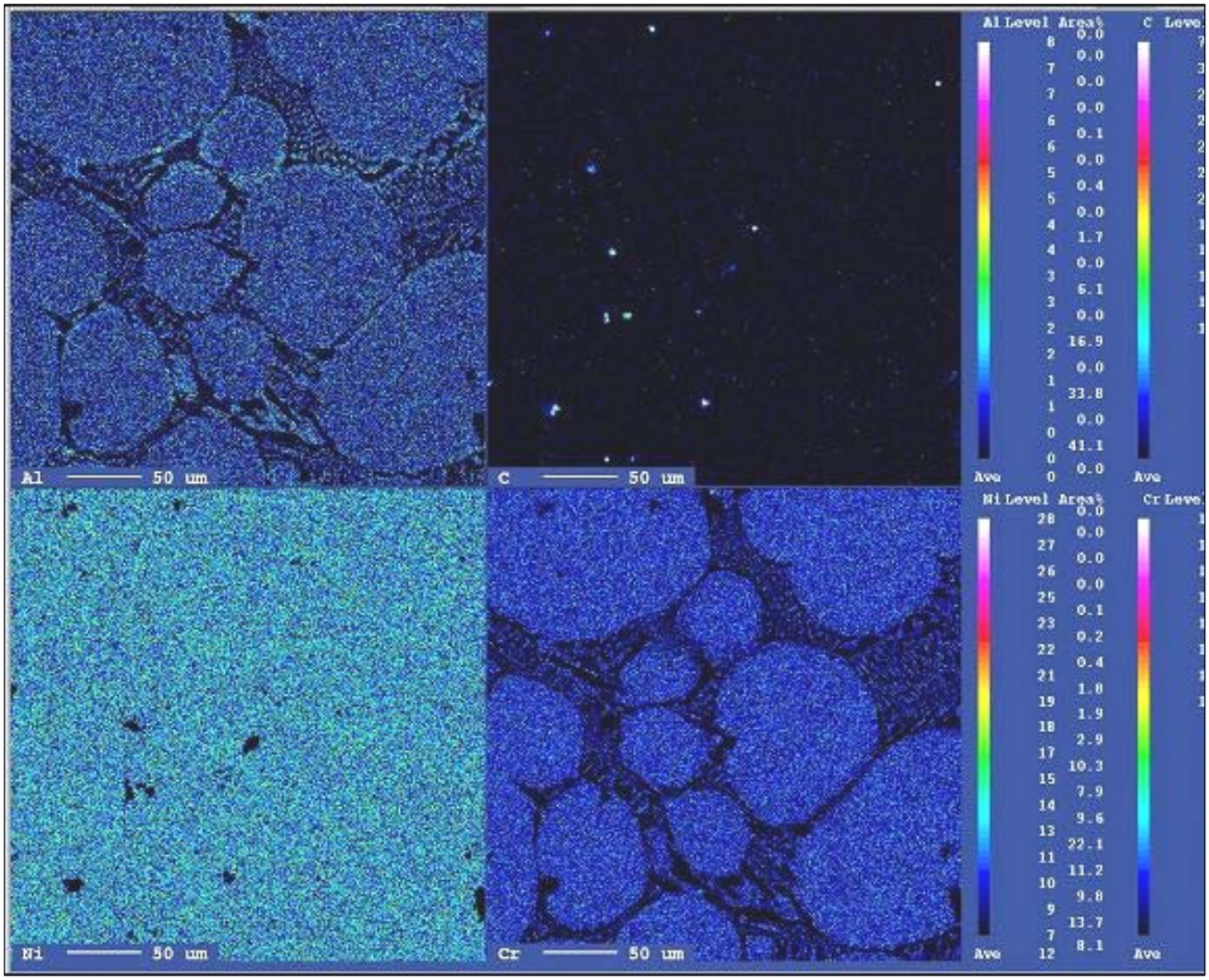

Figure 158 – EMPA maps displaying the distribution of Al, C, Ni and Cr within the MarM247/Ni-Cr-Zr braze microstructure (after an extended diffusion cycle).

The EMPA results shown in **Figure 158** indicate that Al and Cr partitioned strongly to the MarM247 powder particles and to one of the eutectic phases (most likely the Ni-rich γ phase) during the brazing and diffusion cycles. Both elements appeared to have limited solubility within the intermetallic phase in the eutectic component. The majority of the carbon within the structure was concentrated within small particles, probably carbides or pores saturated with C during the carbon coating process. Ni appeared to be fairly uniformly distributed between the braze alloy and the matrix.

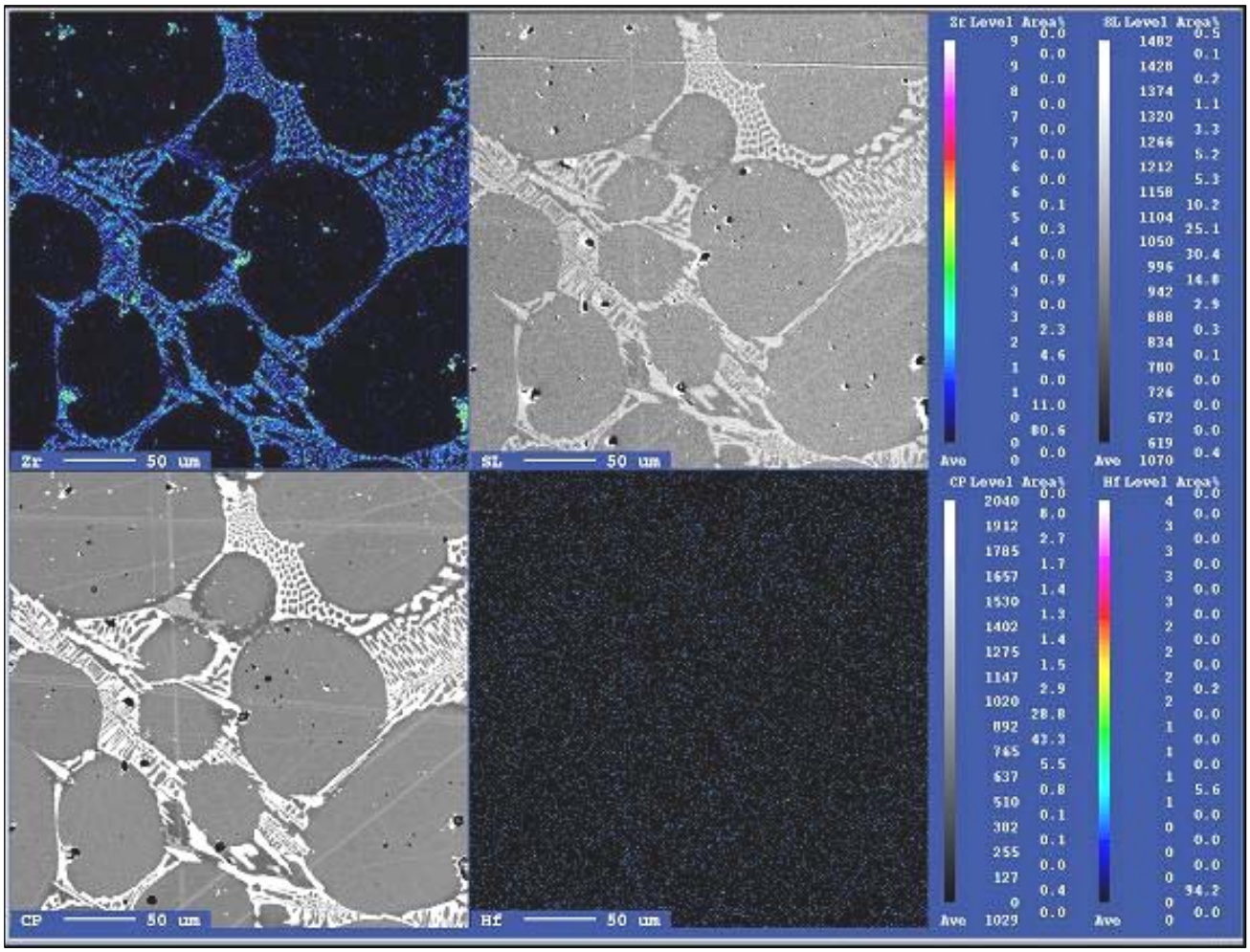

Figure 159 – EMPA maps displaying the distribution of Zr and Hf within the MarM247/Ni-Cr-Zr braze microstructure (after an extended diffusion cycle).

The results shown in **Figure 159** suggest that Zr partitioned strongly to the intermetallic phase within the braze alloy, which substantiates the results of the line and spot scans shown in **Tables 50 and 51**. The Zr EMPA map confirms that the intermetallic phase within the braze joint was Zr-rich, whereas Zr was almost completely absent from the MarM247 matrix particles. The Hf detected within the intermetallic compound in the Ni-Cr-Zr alloy after brazing (**Figure 153**) was not evident after the extended diffusion cycle, suggesting that the Hf diffused from the braze alloy into the MarM247 particles during heat treatment.

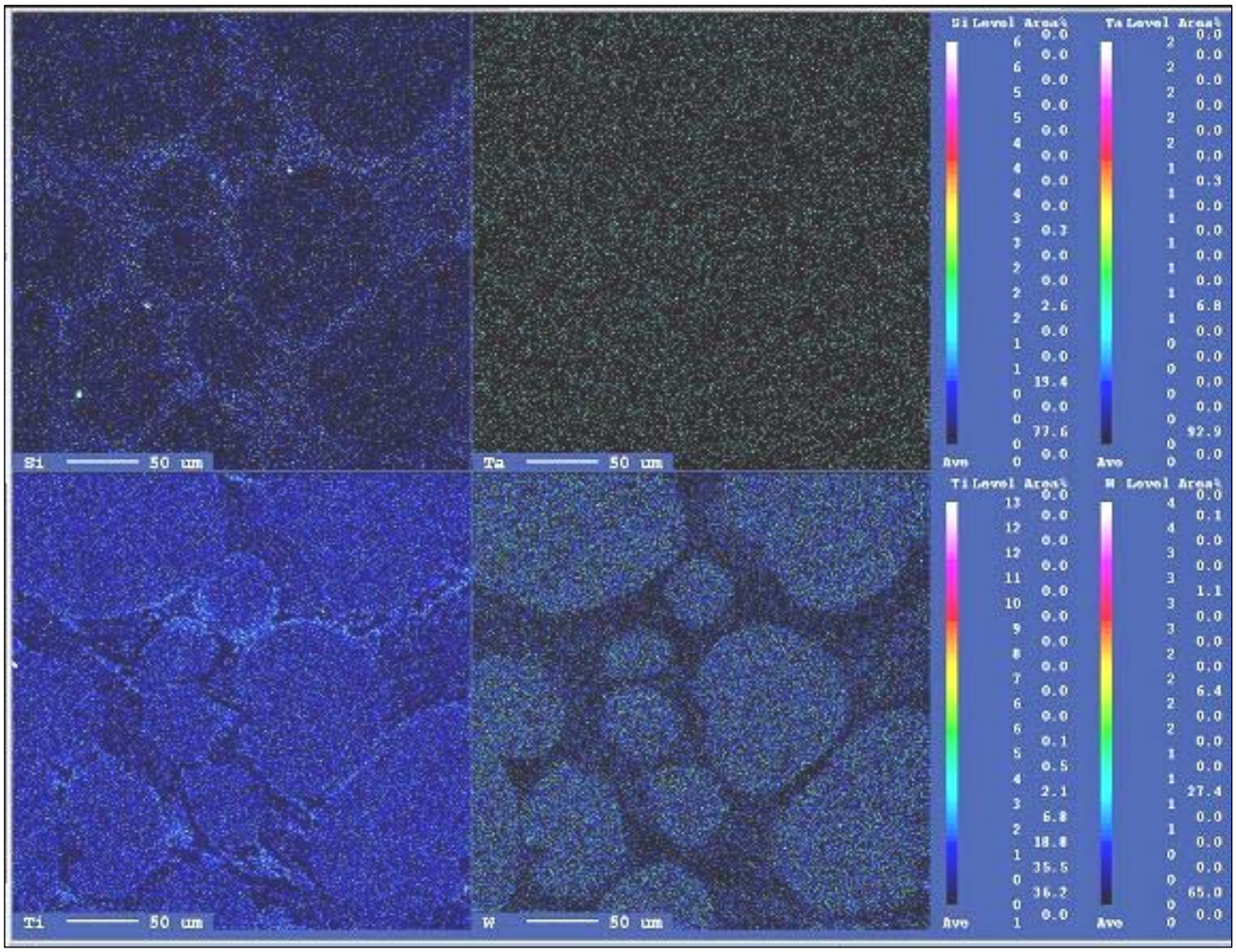

Figure 160 – EMPA maps displaying the distribution of Si, Ta, Ti and W within the MarM247/Ni-Cr-Zr braze microstructure (after an extended brazing cycle).

As shown in **Figure 160**, Si, Ta and Ti were distributed fairly evenly between the braze alloy and the matrix. Si apparently partitioned weakly to the intermetallic phase (suggesting limited solubility within the intermetallic compound), whereas Ti partitioned preferentially to the MarM247 powder particles. Tungsten, however, partitioned strongly to the MarM247 powder particles, suggesting low solubility within the intermetallic phase. The W appeared to be distributed evenly through the matrix phase.

The EMPA maps for Fe and Mo, shown in **Figure 161**, display weak partitioning to the matrix particles, but due to the low levels of these elements within the MarM247 particles and the braze alloy, this tendency was weak.

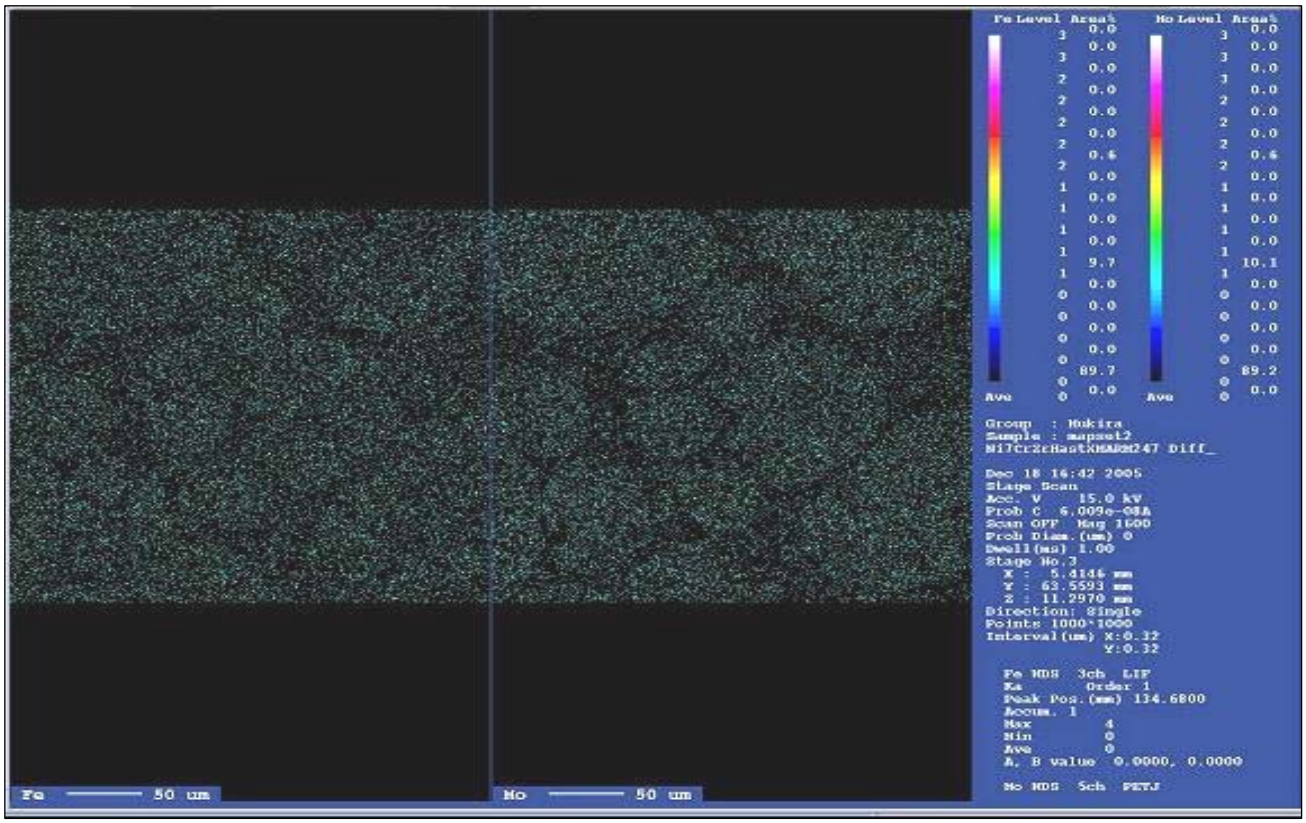

Figure 161 – EMPA maps displaying the distribution of Fe and Mo within the MarM247/Ni-Cr-Zr braze microstructure (as-brazed condition).

11.3.4 Repeat: The MarM247/Ni-Zr braze joint produced using Ni-7Cr-13Zr braze filler (after an extended diffusion cycle):

Secondary and backscatter electron images of the MarM247/Ni-Zr joint produced using the experimental Ni-7Cr-13Zr braze filler metal are shown in **Figure 162** after an extended diffusion cycle. The arrow highlights the location and direction of the 2 μm stepped EPMA line scan. The results of the EMPA scan are shown in **Table 52**.

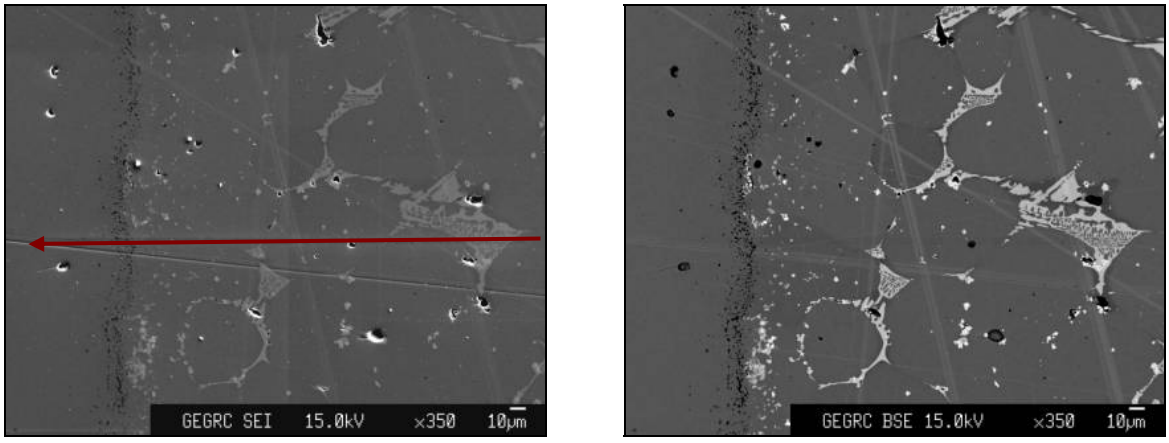

(a) (b)

Figure 162 – Secondary (a) and backscatter (b) electron images of the MarM247/Ni-7Cr-13Zr joint after an extended diffusion cycle (adjacent to the interface).

Table 52 – The results of the second EMPA scan of the MarM247/Ni-7Cr-13Zr braze joint after an extended diffusion cycle. (All compositions given in wt.%).

X (mm)	Y (mm)	Z (mm)	Al	Hf	Ni	Cr	Zr	Fe	Ta	Mo	Co	W	Ti
7.431	70.131	11.255	2.18	0.00	69.20	13.26	0.58	0.51	1.58	1.51	5.67	2.11	1.86
7.433	70.131	11.255	2.19	0.01	69.33	13.29	0.60	0.53	1.53	1.48	5.59	2.12	1.87
7.435	70.131	11.255	2.23	0.00	69.32	13.10	0.59	0.56	1.55	1.50	5.54	2.34	1.91
7.437	70.131	11.255	2.09	0.00	68.91	11.79	3.46	0.46	1.58	1.33	5.20	1.85	1.88
7.439	70.131	11.255	1.05	0.01	66.61	5.95	17.02	0.27	1.42	0.71	3.54	0.68	1.27
7.441	70.131	11.255	1.30	0.00	67.61	6.59	14.95	0.28	1.44	0.74	3.78	0.91	1.38
7.443	70.131	11.255	1.30	0.00	67.38	7.03	14.15	0.31	1.26	0.86	3.91	0.84	1.42
7.445	70.131	11.255	0.95	0.00	66.98	5.24	18.23	0.25	1.37	0.63	3.36	0.63	1.17
7.447	70.131	11.255	1.06	0.00	67.79	5.53	17.26	0.24	1.45	0.69	3.50	0.76	1.25
7.449	70.131	11.255	1.07	0.00	67.26	5.56	17.39	0.26	1.65	0.70	3.41	0.84	1.22
7.451	70.131	11.255	1.07	0.00	66.95	5.92	16.81	0.27	1.52	0.74	3.55	0.58	1.27
7.453	70.131	11.255	1.57	0.00	68.01	8.08	11.77	0.36	1.40	0.93	4.20	1.12	1.53
7.455	70.131	11.255	1.58	0.00	67.85	8.12	11.70	0.34	1.53	0.94	4.14	0.85	1.52
7.457	70.131	11.255	1.30	0.00	67.89	6.92	14.22	0.30	1.46	0.83	3.88	0.83	1.38
7.459	70.131	11.255	1.05	0.00	67.72	5.64	17.06	0.25	1.49	0.67	3.49	0.39	1.22
7.461	70.131	11.255	1.00	0.01	67.36	4.94	18.11	0.23	1.41	0.65	3.38	0.76	1.14
7.463	70.131	11.255	1.41	0.00	67.60	7.11	13.29	0.31	1.24	0.86	3.96	0.88	1.44
7.465	70.131	11.255	1.52	0.02	67.97	8.18	10.93	0.38	1.42	0.98	4.24	1.08	1.55
7.467	70.131	11.255	0.69	0.00	66.72	3.79	21.20	0.19	1.57	0.55	2.95	0.85	1.00
7.469	70.131	11.255	1.55	0.00	68.11	7.74	11.47	0.36	1.32	0.99	4.20	1.37	1.54
7.471	70.131	11.255	2.32	0.01	69.87	12.24	1.20	0.51	1.33	1.44	5.42	1.98	1.95
7.473	70.131	11.255	2.27	0.01	69.81	12.58	0.57	0.53	1.47	1.49	5.46	2.13	1.91
7.475	70.131	11.255	2.22	0.01	69.35	12.89	0.60	0.54	1.43	1.47	5.45	2.43	1.88
7.477	70.131	11.255	2.21	0.01	69.15	13.04	0.62	0.54	1.50	1.52	5.60	2.27	1.84
7.479	70.131	11.255	2.20	0.00	69.56	13.12	0.59	0.53	1.26	1.51	5.64	2.14	1.84
7.481	70.131	11.255	2.22	0.00	69.29	13.12	0.58	0.52	1.45	1.50	5.59	2.23	1.85
7.483	70.131	11.255	2.21	0.03	70.13	13.20	0.59	0.51	1.28	1.49	5.67	2.23	1.85
7.485	70.131	11.255	2.24	0.01	70.30	13.18	0.57	0.53	1.30	1.48	5.71	2.00	1.86
7.487	70.131	11.255	2.23	0.00	69.98	13.26	0.59	0.54	1.16	1.48	5.69	2.05	1.85
7.489	70.131	11.255	2.23	0.00	69.46	13.29	0.58	0.56	1.25	1.54	5.75	1.93	1.80
7.491	70.131	11.255	2.22	0.00	69.70	13.22	0.59	0.51	1.34	1.49	5.71	2.17	1.85
7.493	70.131	11.255	2.22	0.00	69.99	13.13	0.57	0.51	1.25	1.49	5.71	2.16	1.84
7.495	70.131	11.255	2.23	0.00	69.97	13.07	0.58	0.57	1.51	1.55	5.76	2.30	1.84
7.497	70.131	11.255	2.23	0.00	69.84	12.93	0.52	0.53	1.24	1.53	5.77	2.17	1.85
7.499	70.131	11.255	2.21	0.00	69.72	12.84	0.56	0.56	1.25	1.51	5.76	2.15	1.84
7.501	70.131	11.255	2.23	0.00	69.60	12.89	0.57	0.53	1.06	1.53	5.70	2.29	1.85
7.503	70.131	11.255	2.23	0.00	70.00	12.86	0.55	0.53	1.35	1.48	5.74	2.15	1.82
7.505	70.131	11.255	2.23	0.02	70.03	12.83	0.57	0.54	1.49	1.50	5.73	2.10	1.83
7.507	70.131	11.255	2.24	0.00	70.11	12.65	0.60	0.51	1.29	1.49	5.68	2.02	1.83
7.509	70.131	11.255	2.23	0.00	70.00	12.72	0.59	0.51	1.41	1.53	5.71	2.13	1.85
7.511	70.131	11.255	2.25	0.00	70.08	12.79	0.61	0.53	1.39	1.49	5.71	2.11	1.88
7.513	70.131	11.255	2.26	0.00	69.53	12.77	0.57	0.52	1.27	1.51	5.55	2.33	1.87
7.515	70.131	11.255	2.30	0.00	69.88	12.09	1.47	0.50	1.24	1.36	5.43	1.87	1.98
7.517	70.131	11.255	0.90	0.00	39.93	5.86	37.02	0.25	5.56	0.75	2.73	0.61	1.44
7.519	70.131	11.255	1.92	0.03	66.82	10.97	7.59	0.46	1.47	1.30	4.89	1.43	1.77
7.521	70.131	11.255	2.25	0.02	69.54	13.11	0.60	0.55	1.43	1.51	5.60	2.19	1.93
7.523	70.131	11.255	2.24	0.01	69.97	13.17	0.58	0.54	1.35	1.56	5.62	1.82	1.86
7.525	70.131	11.255	2.25	0.02	69.52	13.23	0.64	0.53	1.17	1.53	5.63	2.10	1.84
7.527	70.131	11.255	2.23	0.00	69.58	13.17	0.52	0.51	1.39	1.51	5.68	2.04	1.82
7.529	70.131	11.255	2.23	0.00	69.93	13.23	0.59	0.55	1.38	1.50	5.75	1.81	1.83
7.531	70.131	11.255	2.24	0.00	69.92	13.18	0.59	0.51	1.41	1.50	5.77	2.08	1.84
7.533	70.131	11.255	2.21	0.00	69.64	13.11	0.60	0.54	1.38	1.49	5.77	1.96	1.84
7.535	70.131	11.255	2.25	0.02	69.46	13.15	0.58	0.51	1.48	1.54	5.87	1.84	1.84
7.537	70.131	11.255	2.29	0.00	69.13	13.09	0.54	0.51	1.74	1.51	5.76	1.65	1.84
7.539	70.131	11.255	2.17	0.04	65.92	12.74	0.50	0.49	1.55	1.27	5.49	1.71	1.71
7.541	70.131	11.255	2.11	0.01	66.78	12.76	0.56	0.51	1.73	1.35	5.55	1.85	1.75
7.543	70.131	11.255	2.16	0.00	68.70	13.06	0.94	0.51	1.67	1.50	5.68	1.98	1.84
7.545	70.131	11.255	2.21	0.00	69.66	13.27	0.54	0.51	1.48	1.50	5.87	2.02	1.85
7.547	70.131	11.255	2.21	0.00	69.70	13.47	0.58	0.52	1.49	1.51	5.90	2.13	1.86

Table 52 – (continued).

X (mm)	Y (mm)	Z (mm)	Al	Hf	Ni	Cr	Zr	Fe	Ta	Mo	Co	W	Ti
7.549	70.131	11.255	2.22	0.01	69.54	13.37	0.59	0.51	1.41	1.53	5.86	1.99	1.87
7.551	70.131	11.255	2.22	0.00	69.15	13.41	0.58	0.52	1.56	1.54	5.84	1.88	1.86
7.553	70.131	11.252	2.19	0.00	68.86	13.56	0.56	0.51	1.48	1.58	5.84	1.85	1.84
7.555	70.131	11.255	2.21	0.00	69.48	13.45	0.56	0.53	1.52	1.58	5.88	2.18	1.82
7.557	70.131	11.255	2.20	0.00	69.67	13.55	0.54	0.50	1.54	1.51	5.89	2.14	1.85
7.559	70.131	11.255	2.21	0.00	69.37	13.57	0.56	0.51	1.36	1.54	5.96	2.19	1.85
7.561	70.131	11.255	2.21	0.02	69.59	13.56	0.55	0.52	1.48	1.56	5.90	2.22	1.87
7.563	70.131	11.255	2.22	0.00	69.11	13.62	0.53	0.50	1.38	1.57	5.86	2.03	1.83
7.565	70.131	11.255	2.23	0.00	69.26	13.54	0.55	0.52	1.58	1.54	5.89	1.87	1.87
7.567	70.131	11.255	2.22	0.00	69.61	13.72	0.53	0.49	1.69	1.54	5.93	1.79	1.83
7.569	70.131	11.255	2.20	0.00	69.50	13.50	0.55	0.53	1.61	1.57	5.93	2.09	1.83
7.571	70.131	11.255	2.23	0.02	69.38	13.59	0.54	0.53	1.57	1.54	5.92	1.98	1.81
7.573	70.131	11.255	2.22	0.00	69.32	13.51	0.56	0.51	1.62	1.53	5.87	2.16	1.82
7.575	70.131	11.255	2.23	0.00	69.45	13.44	0.51	0.50	1.50	1.50	5.88	1.93	1.86
7.577	70.131	11.255	2.24	0.00	69.61	13.50	0.56	0.52	1.50	1.56	5.82	1.86	1.83
7.579	70.131	11.255	2.21	0.02	69.94	13.50	0.56	0.54	1.46	1.51	5.87	2.33	1.84
7.581	70.131	11.255	2.22	0.00	70.09	13.40	0.57	0.55	1.70	1.46	5.76	2.06	1.82
7.583	70.131	11.255	2.22	0.00	69.80	13.44	0.52	0.51	1.60	1.51	5.72	1.96	1.86
7.585	70.131	11.255	2.22	0.00	70.03	13.28	0.56	0.55	1.37	1.52	5.69	2.12	1.84
7.587	70.131	11.255	2.21	0.00	69.73	13.42	0.55	0.54	1.50	1.54	5.74	2.53	1.83
7.589	70.131	11.255	2.22	0.00	69.89	13.29	0.57	0.54	1.07	1.57	5.61	2.43	1.83
7.591	70.131	11.255	2.24	0.00	69.93	13.34	0.55	0.55	1.37	1.49	5.63	2.07	1.88
7.593	70.131	11.255	2.23	0.00	70.27	13.34	0.56	0.57	1.45	1.58	5.65	1.92	1.84
7.595	70.131	11.255	2.22	0.00	70.06	13.32	0.55	0.57	1.34	1.52	5.56	2.19	1.85
7.597	70.131	11.255	2.09	0.01	69.85	12.24	3.08	0.52	1.32	1.44	5.21	1.85	1.85
7.599	70.131	11.255	2.19	0.00	70.21	12.83	1.71	0.53	1.45	1.40	5.35	1.87	1.90
7.601	70.131	11.255	2.25	0.00	70.33	13.39	0.59	0.59	1.50	1.51	5.50	1.75	1.89
7.603	70.131	11.255	2.25	0.00	70.38	13.41	0.58	0.57	1.46	1.47	5.59	1.83	1.85
7.605	70.131	11.255	2.23	0.00	70.32	13.60	0.57	0.57	1.40	1.49	5.51	2.25	1.84
7.607	70.131	11.255	2.25	0.00	70.42	13.39	0.59	0.58	1.53	1.51	5.63	1.74	1.86
7.609	70.131	11.255	2.22	0.01	70.14	13.42	0.52	0.59	1.29	1.51	5.55	2.06	1.85
7.611	70.131	11.255	2.23	0.00	70.12	13.31	0.55	0.58	1.44	1.52	5.61	2.17	1.82
7.613	70.131	11.255	2.21	0.01	70.17	13.37	0.57	0.60	1.39	1.50	5.47	2.05	1.85
7.615	70.131	11.255	2.22	0.00	69.97	13.17	0.57	0.64	1.67	1.54	5.54	2.20	1.84
7.617	70.131	11.255	2.22	0.01	70.34	13.20	0.52	0.65	1.35	1.55	5.59	2.26	1.81
7.619	70.131	11.255	2.19	0.00	69.74	13.22	0.57	0.67	1.52	1.59	5.57	2.03	1.80
7.621	70.131	11.255	2.21	0.00	69.90	13.16	0.55	0.70	1.44	1.60	5.57	2.23	1.79
7.623	70.131	11.255	2.20	0.00	69.75	13.22	0.50	0.77	1.46	1.62	5.63	2.51	1.78
7.625	70.131	11.255	2.18	0.00	69.29	13.43	0.52	0.87	1.48	1.71	5.68	2.40	1.76
7.627	70.131	11.255	2.17	0.00	69.55	13.41	0.55	0.94	1.17	1.72	5.75	2.05	1.71
7.629	70.131	11.255	2.13	0.01	69.17	13.54	0.51	1.08	1.12	1.73	5.70	2.48	1.69
7.631	70.131	11.255	2.12	0.00	68.82	13.62	0.46	1.17	1.29	1.83	5.80	2.58	1.63
7.633	70.131	11.255	2.07	0.00	68.36	13.83	0.44	1.29	1.10	1.96	5.81	2.53	1.61
7.635	70.131	11.255	2.05	0.00	68.08	13.95	0.39	1.44	1.08	2.05	5.81	2.13	1.54
7.637	70.131	11.255	2.04	0.00	67.86	14.10	0.40	1.62	1.04	2.09	5.89	2.42	1.53
7.639	70.131	11.255	2.00	0.00	67.59	14.10	0.32	1.76	1.24	2.20	5.87	2.16	1.48
7.641	70.131	11.252	1.96	0.00	67.14	14.24	0.33	1.88	1.14	2.28	5.85	2.35	1.46
7.643	70.131	11.255	1.97	0.00	67.27	14.15	0.33	2.05	1.07	2.40	5.85	2.30	1.43
7.645	70.131	11.255	1.93	0.01	66.73	14.35	0.28	2.16	1.09	2.44	5.82	2.20	1.38
7.647	70.131	11.255	1.91	0.00	66.30	14.41	0.24	2.40	1.08	2.60	5.84	2.25	1.33
7.649	70.131	11.255	1.87	0.00	66.22	14.63	0.24	2.64	1.00	2.75	5.93	2.05	1.27
7.652	70.131	11.255	1.85	0.00	66.12	14.72	0.23	2.77	0.93	2.81	5.85	1.91	1.20
7.654	70.131	11.255	1.82	0.00	65.55	14.77	0.21	3.04	1.08	2.87	5.83	2.17	1.18
7.655	70.131	11.255	1.45	0.00	55.42	12.92	10.59	2.88	2.90	2.67	4.89	1.57	1.63
7.657	70.131	11.255	1.26	0.01	51.72	12.41	13.76	2.97	2.88	2.69	4.65	1.59	1.65
7.66	70.131	11.255	1.68	0.01	64.13	15.24	0.13	3.86	1.14	3.30	5.73	1.77	1.01
7.661	70.131	11.255	1.62	0.00	62.95	14.98	1.42	4.00	1.19	3.40	5.63	2.11	1.06
7.663	70.131	11.255	1.39	0.00	56.23	13.64	8.52	3.82	1.99	3.18	4.92	1.54	1.73
7.666	70.131	11.255	1.55	0.00	62.67	15.42	0.66	4.53	1.09	3.62	5.57	2.06	0.94
7.668	70.131	11.255	1.55	0.00	62.77	15.90	0.07	4.92	1.00	3.83	5.59	1.90	0.81

Table 52 – (continued).

X (mm)	Y (mm)	Z (mm)	Al	Hf	Ni	Cr	Zr	Fe	Ta	Mo	Co	W	Ti
7.669	70.131	11.255	1.47	0.00	62.37	15.96	0.08	5.18	1.09	3.86	5.48	1.91	0.77
7.672	70.131	11.252	1.43	0.00	61.43	16.29	0.08	5.48	0.78	4.11	5.43	2.08	0.71
7.674	70.131	11.252	1.39	0.00	61.25	16.45	0.04	5.80	0.76	4.22	5.37	2.12	0.69
7.676	70.131	11.255	1.33	0.00	61.32	16.51	0.15	6.20	0.97	4.36	5.26	1.72	1.04
7.678	70.131	11.255	1.28	0.01	60.53	16.69	0.12	6.59	0.81	4.53	5.17	1.67	0.93
7.68	70.131	11.255	1.25	0.00	60.40	17.02	0.01	6.96	0.73	4.70	5.13	1.41	0.71
7.682	70.131	11.255	1.18	0.02	58.17	16.79	0.29	6.92	1.04	4.71	4.90	1.49	2.04
7.684	70.131	11.255	1.09	0.05	54.96	16.05	0.73	6.96	1.43	4.65	4.65	1.35	4.74
7.686	70.131	11.255	0.88	0.18	46.92	14.11	1.79	6.29	2.10	4.22	3.90	1.21	11.56
7.688	70.131	11.255	0.92	0.14	49.69	15.23	1.21	6.98	2.08	4.63	4.09	1.26	8.26
7.69	70.131	11.255	1.06	0.00	57.96	17.33	0.13	8.35	0.81	5.39	4.63	1.10	0.94
7.692	70.131	11.252	0.86	0.12	50.06	15.78	1.21	7.79	1.49	5.00	4.02	1.13	7.39
7.694	70.131	11.252	0.88	0.07	52.64	16.84	0.76	8.45	1.06	5.19	4.13	0.96	5.49
7.696	70.131	11.255	0.79	0.13	47.59	15.51	1.50	8.11	1.43	4.89	3.65	1.13	9.98
7.698	70.131	11.255	0.90	0.00	56.24	18.30	0.03	10.05	0.76	5.98	4.11	0.93	0.26
7.7	70.131	11.252	0.85	0.00	56.06	18.38	0.00	10.32	0.85	6.06	4.05	1.11	0.20
7.702	70.131	11.255	0.83	0.00	56.23	18.40	0.08	10.67	0.80	6.28	3.97	1.31	0.22
7.704	70.131	11.252	0.80	0.00	55.11	18.69	0.04	10.83	0.62	6.42	3.77	1.50	0.28
7.706	70.131	11.255	0.77	0.00	55.24	18.74	0.00	11.33	0.71	6.55	3.68	1.47	0.13
7.708	70.131	11.252	0.73	0.00	54.73	19.09	0.00	11.46	0.69	6.76	3.49	1.09	0.12
7.71	70.131	11.255	0.70	0.00	54.72	19.21	0.00	12.08	0.54	6.83	3.36	1.19	0.11
7.712	70.131	11.255	0.68	0.01	54.07	19.19	0.02	12.33	0.58	6.97	3.23	1.30	0.11
7.714	70.131	11.255	0.65	0.01	54.06	19.32	0.00	12.54	0.62	6.99	3.13	1.11	0.14
7.716	70.131	11.252	0.61	0.00	53.25	19.58	0.01	12.92	0.63	7.11	2.88	1.30	0.08
7.718	70.131	11.255	0.58	0.00	52.97	19.67	0.01	13.33	0.59	7.24	2.81	1.09	0.08
7.72	70.131	11.255	0.57	0.00	52.94	19.77	0.02	13.55	0.47	7.30	2.69	1.04	0.06
7.722	70.131	11.252	0.53	0.00	52.30	19.84	0.01	13.67	0.44	7.35	2.60	1.07	0.07
7.724	70.131	11.255	0.53	0.00	52.42	19.69	0.02	14.06	0.41	7.41	2.46	0.90	0.08
7.726	70.131	11.255	0.50	0.00	52.12	19.82	0.00	14.21	0.33	7.50	2.38	1.16	0.05
7.728	70.131	11.255	0.48	0.01	51.69	19.89	0.02	14.45	0.60	7.57	2.26	0.98	0.05
7.73	70.131	11.255	0.47	0.01	51.41	19.97	0.00	14.73	0.42	7.64	2.15	0.97	0.05
7.732	70.131	11.255	0.45	0.00	51.49	20.22	0.02	14.94	0.31	7.73	2.10	1.11	0.04
7.734	70.131	11.255	0.41	0.00	51.05	20.24	0.00	15.22	0.30	7.73	1.97	0.96	0.04
7.736	70.131	11.255	0.39	0.00	50.51	20.27	0.00	15.50	0.47	7.91	1.86	1.22	0.04
7.738	70.131	11.255	0.38	0.01	50.34	20.41	0.00	15.79	0.55	8.04	1.83	0.66	0.04
7.74	70.131	11.255	0.37	0.00	50.07	20.50	0.00	15.89	0.50	8.05	1.79	0.87	0.02

The line scan results shown in **Table 52** revealed the presence of Zr-rich intermetallic phases containing between 11% and 22% Zr, and occasionally containing approximately 37% Zr. The binary Ni-Zr phase diagram, shown in **Figure 50**, indicates that the Ni_7Zr_2 intermetallic phase contains approximately 30 wt.% Zr, whereas the Ni_5Zr intermetallic compound contains approximately between 21 and 26 wt.% Zr. The results shown in **Table 52** therefore suggest that the intermetallic phase in the braze joint was Ni_5Zr, rather than Ni_7Zr_2.

11.4) Conclusions

- The MarM247/Ni-7Cr-31Hf braze mixture in the as-brazed condition (prior to diffusion treatment) apparently contained a Hf-rich intermetallic phase with between 31 and 36% Hf. The binary Ni-Hf phase diagram predicts that the Ni_7Hf_2 phase contains approximately 46 wt.% Hf, whereas the Ni_5Hf phase contains approximately 38 wt.% Hf. The presence of significant amounts of Zr and Ta in solution in the intermetallic phase, however, complicates identification, shifting its composition away from the equilibrium composition predicted by the phase diagram. If it is assumed that the intermetallic compound contains between 7.4% and 9.6% Zr in solution, as well as 3% Ta, its

composition may well approach that of the Ni_7Hf_2 intermetallic compound, rather than that of the Ni_5Hf phase.

- The ternary MarM247/Ni-7Cr-13Zr braze mixture in the as-brazed condition (i.e. no diffusion heat treatment) was shown to contain an intermetallic compound with a Zr content ranging between 27 and 29%. The binary Ni-Zr phase diagram indicates that the Ni_7Zr_2 intermetallic phase contains approximately 30 wt.% Zr, whereas the Ni_5Zr intermetallic compound contains approximately between 21 and 26 wt.% Zr. This suggests that the intermetallic phase in the braze joint could be either Ni_5Zr or Ni_7Zr_2.

- The MarM247/Ni-7Cr-13Zr braze mixture contained a Zr-rich intermetallic phase with a Zr content of approximately 37 wt.% after an extended braze cycle. This suggests that the intermetallic phase in the braze joint is Ni_5Zr, rather than Ni_7Zr_2.

CHAPTER 12 – EXPERIMENT 10

DEVELOPMENT OF COMPLEX Ni-Cr-Hf BRAZE ALLOYS

12.1) Introduction

During the course of Experiment 8 (described in Chapter 10), the microstructures of a number of ternary Ni-Cr-Hf alloys, containing 13% Cr and between 15% and 25% Hf, were examined. The compositions of the eutectic component within these alloys were found to deviate from the predicted eutectic point in the binary Ni-Hf system (located at 30.5% Hf). The composition of the eutectic constituent observed in the Ni-13Cr-15Hf braze alloy was 65.2Ni-9.0Cr-25.8Hf (wt.%), the eutectic within the Ni-13Cr-20Hf braze alloy had a composition of 64.3Ni-10.5Cr-25.2Hf, whereas the eutectic component observed in the Ni-13Cr-25Hf braze alloy consisted of 63.1Ni-15.1Cr-21.8Hf (wt.%). The Hf content of the eutectic component in these alloys therefore ranged from approximately 21% Hf to 26% Hf.

This experiment aimed at developing and characterizing the microstructures of novel "near-eutectic" braze alloys in the as-cast condition, with or without additional alloying elements (Co, W, C, Ti and/or Al). An attempt was also made to identify the intermetallic phases and eutectic components observed in each alloy.

12.2) Experimental procedure

Five novel "near-eutectic" alloys, with chemical compositions given in **Table 53**, were melted at 1500^{o}C, and allowed to cool to form an ingot. In addition to Ni, Cr and Hf, deliberate additions of Co (for high temperature strength and oxidation resistance), W and C (for high temperature strength and to promote the formation of carbides), as well as Ti and Al (to facilitate the formation of γ' precipitates) were made to some of these alloys. The resultant as-cast microstructure of each alloy was analyzed using microprobe spot analysis techniques (as described in §11.2).

Table 53 – Chemical compositions (wt.%) of the novel "near-eutectic" alloys examined during the course of this investigation.

PV Heat	Cr	Co	W	Ti	Al	C	Hf	Ni
9020	8.5	-	-	-	-	-	25	66.5
9023	7.4	-	4.7	1.4	2.3	0.03	25.5	58.7
9025	8.4	-	5.4	1.6	6.1	-	14.5	64.0
9024	8.3	5.6	5.3	-	4.3	-	14.2	62.4
9026	7.9	5.4	5.0	1.5	4.1	0.04	20.3	55.8

12.3) Results and discussion

12.3.1 Alloy PV9020 (Ni-8.5Cr-25Hf):

Figure 163 displays photomicrographs at increasing magnification of the as-cast structure of alloy PV9020, with a chemical composition of Ni-8.5Cr-25Hf (wt.%).

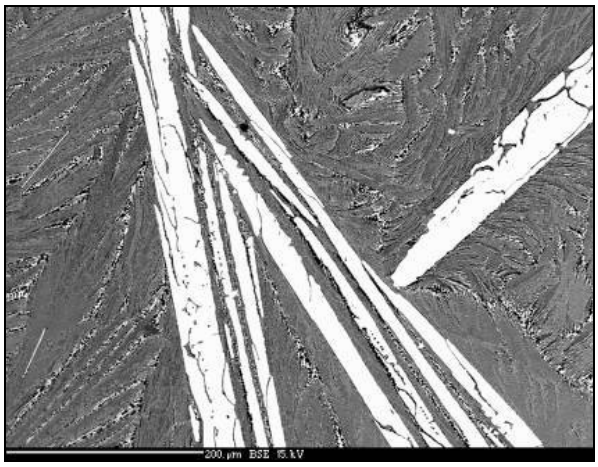

(a)

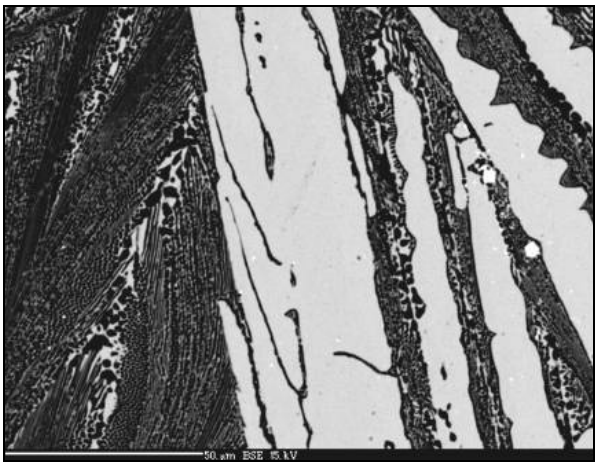

(b)

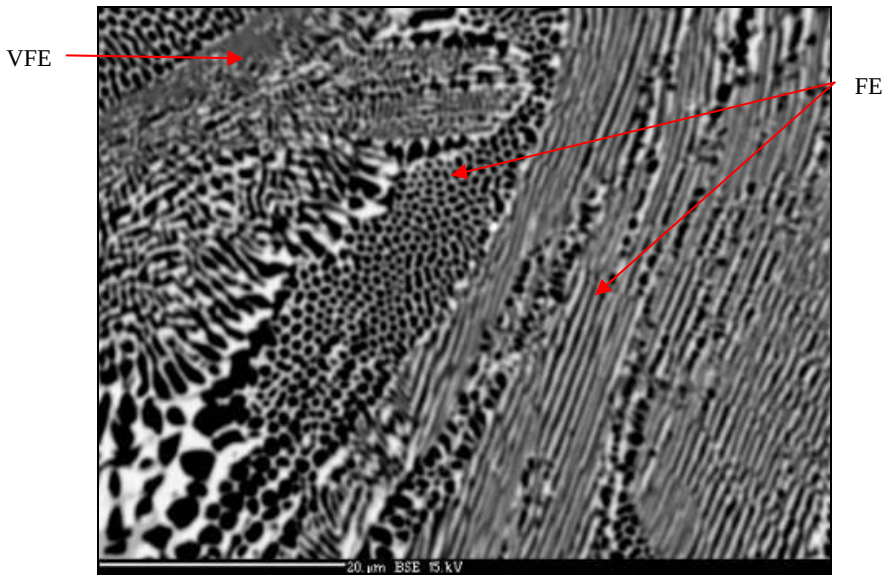

(c)

Figure 163 – Backscatter electron microprobe images of the Ni-8.5Cr-25Hf alloy in the as-cast condition (PV9020).

This alloy appears to be hypereutectic, with a needle-shaped primary Hf-rich intermetallic phase (light etching phase), consisting of 71.5Ni-1.5Cr-4.6Co-22.4Hf (at.%). This composition (given as atomic percentage) suggests that the intermetallic phase in **Figure 163** could be Ni_3Hf (a non-equilibrium phase) or Ni_7Hf_2 (more likely). The fine binary eutectic component evident in the micrographs was shown to consist of 76.3Ni-14.2Cr-9.4Hf (analyzed at the location labelled "VFE" in **Figure 163(c)**) and 76.5Ni-13.3Cr-10.1Hf (analyzed at the location labelled "FE" in **Figure 163(c)**). An attempt was made to analyze the individual phases within the eutectic component (see **Table 54**), but the results were inconsistent (probably due to the fine morphology of the eutectic component). It is assumed that the light phase within the eutectic component is the non-equilibrium Ni_3Hf or Ni_7Hf_2 intermetallic phase, and the dark component Ni-rich γ phase. This alloy had a solidus temperature of 1195°C and a liquidus temperature of 1281°C (ΔT = 86°C). This solidification temperature range makes the Ni-8.5Cr-25Hf alloy unsuitable for use in the repair of equiaxed Ni-base superalloys, such as In738 and MarM247. Single crystal Ni-base superalloys, however, can be processed at temperatures up to 1310°C, so this braze alloy may be suitable for use in repairing these materials.

Table 54 – EMPA results of the individual phases within the eutectic component observed in alloy PV9020 (wt.%).

	Ni	Cr	Hf
Dark eutectic phase (Analysis 1)	84.0	11.8	4.1
Dark eutectic phase (Analysis 2)	78.9	6.5	14.5
Light eutectic phase (Analysis 1)	92.7	2.9	4.3
Light eutectic phase (Analysis 2)	70.4	11.2	18.4

12.3.2 Alloy PV9023 (Ni-7.4Cr-4.7W-1.4Ti-2.3Al-0.03C-25.5Hf):

Figures 164(a) and (b) display photomicrographs at increasing magnification of the as-cast structure of alloy PV9023, with a chemical composition of Ni-7.4Cr-4.7W-1.4Ti-2.3Al-0.03C-25.5Hf (wt.%). The as-cast microstructure is considerably more complex than that of alloy PV9020, probably as a result of the deliberate addition of W, Al, Ti and C to this alloy. The white needle-shaped Hf-rich phase was shown to consist of 52.4Ni-1.1Cr-0.2W-0.4Ti-0.4Al-46.2Hf (at.%), suggesting a non-equilibrium NiHf or $Ni_{11}Hf_9$ intermetallic compound. The light to medium gray phase consisted of 61.0Ni-1.9Cr-2.1W-3.4Ti-3.2Al-28.9Hf (at.%) and 63.3Ni-2.8Cr-3.7W-3.8Ti-3.6Al-23.1Hf (at.%), suggesting a possible non-equilibrium Ni_3Hf or Ni_7Hf_2 intermetallic compound. The darkest phase contained 61.4Ni-21.2Cr-5.4W-2.0Ti-5.4Al-4.6Hf (at.%) and appears to be the Ni-rich γ phase with significant amounts of Cr, Al and W in solution. An attempt was made to analyze the individual phases within the eutectic component, yielding compositions of 61.7Ni-17.1Cr-11.3W-1.9Ti-3.8Al-4.2Hf for the dark eutectic phase (Ni-rich γ phase) and 52.6Ni-1.9Cr-0.4W-0.6Ti-0.8Al-44.4Hf for the light eutectic phase (possibly the non-equilibrium NiHf or $Ni_{11}Hf_9$ intermetallic compound). This alloy had a solidus temperature of 1140°C and a liquidus temperature of 1282°C (ΔT = 142°C). This solidification temperature range makes the Ni-7.4Cr-4.7W-1.4Ti-2.3Al-0.03C-25.5Hf alloy unsuitable for use in the repair of equiaxed Ni-base superalloy materials, such as In738 and MarM247, but this braze alloy may be suitable for use in repairing single crystal Ni-base superalloys.

12.3.3 Alloy PV9025 (Ni-8.4Cr-5.4W-1.6Ti-6.1Al-14.5Hf):

Figures 165(a) and (b) display photomicrographs of the as-cast structure of alloy PV9025, with a chemical composition of Ni-8.4Cr-5.4W-1.6Ti-6.1Al-14.5Hf (wt.%). This alloy appears to be hypo-eutectic, with primary Ni-rich γ dendrites consisting of Ni-7.1Cr-16.5Al-1.8W-2.6Ti-2.9Hf (at.%). The fine binary eutectic component between the dendrites was shown to consist of 61.2Ni-15.0Cr-13.3Al-0.6W-1.3Ti-8.6Hf (at.%). An attempt was made to analyze the individual phases within the eutectic component, yielding compositions of 56.4Ni-19.4Cr-17.6Al-0.7W-2.4Ti-3.5Hf for the dark eutectic phase (Ni-rich γ phase) and 64.4Ni-10.3Cr-6.8Al-1.1Ti-17.4Hf for the light eutectic phase (possibly the Ni_7Hf_2 intermetallic compound). **Figure 165(b)** also reveals the presence of a number of W-rich particles, probably (W,Cr) carbides or Laves phase. The solidus and liquidus temperatures of this alloy were 1049°C and 1119°C, respectively (ΔT = 70°C). Both the solidus and liquidus temperatures were therefore lower than those of the simple eutectic Ni-Hf braze alloy described in Chapter 3. This alloy shows great promise for the repair of equiaxed, directionally solidified and single crystal Ni-base superalloys.

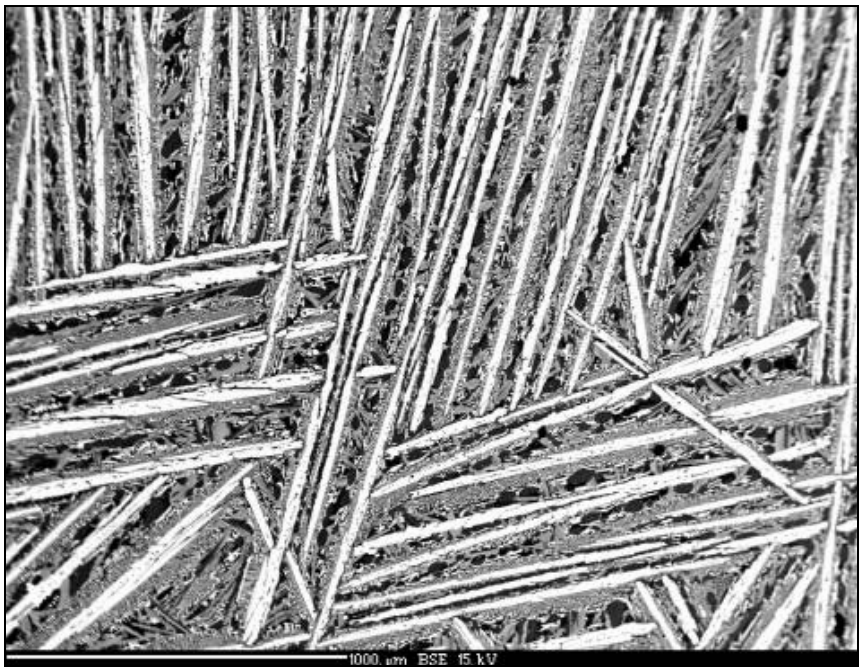

(a)

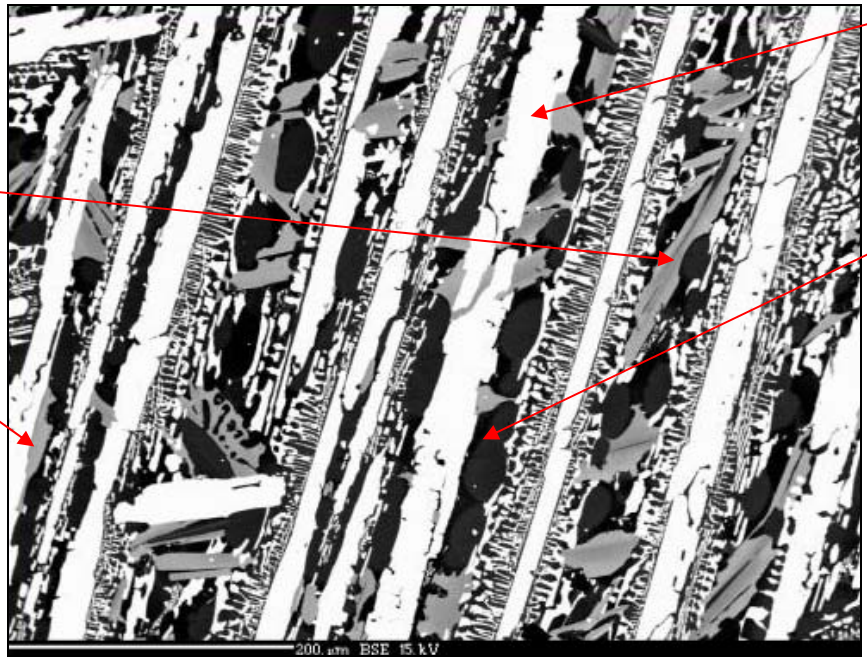

(b)

Figure 164 – Backscatter electron microprobe images of the Ni-7.4Cr-4.7W-1.4Ti-2.3Al-0.03C-25.5Hf alloy in the as-cast condition (PV9023). (All compositions given as atomic %).

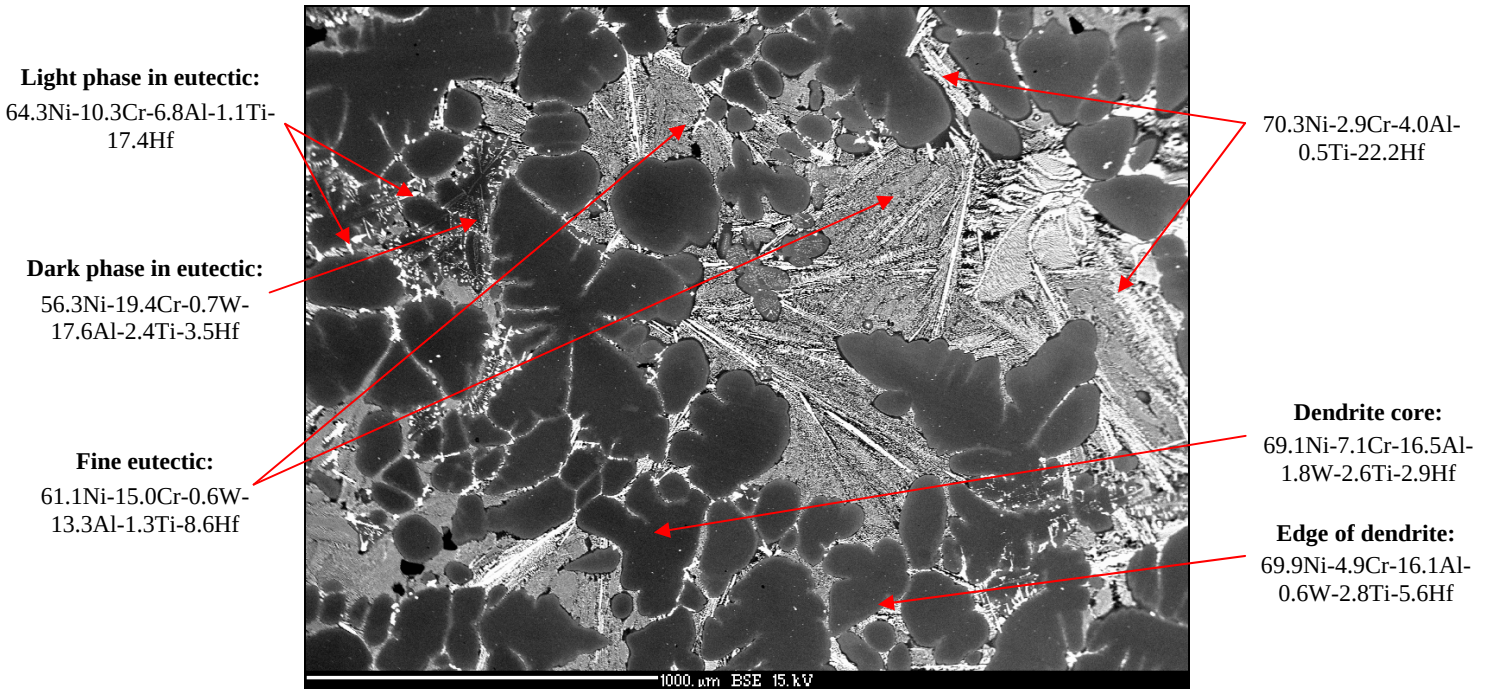

(a)

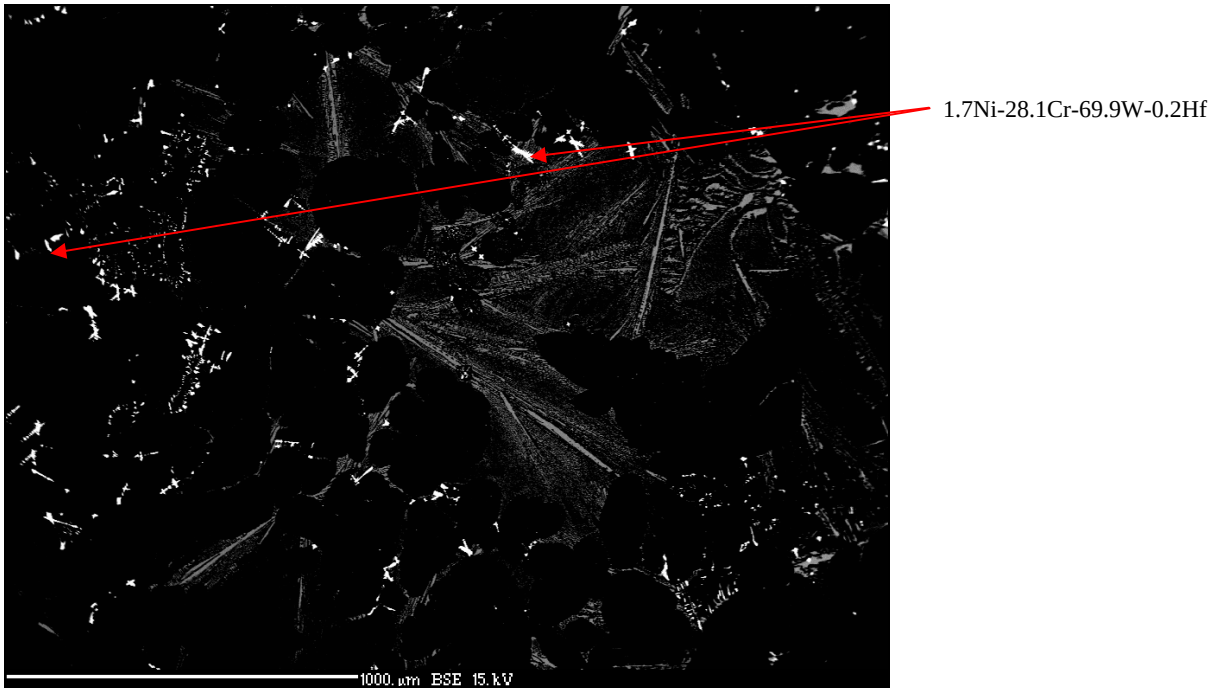

(b)

Figure 165 – Backscatter electron microprobe images of the Ni-8.4Cr-5.4W-1.6Ti-6.1Al-14.5Hf alloy in the as-cast condition (PV9025). (All compositions given as atomic %).

12.3.4 Alloy PV9024 (Ni-8.3Cr-5.6Co-5.3W-4.3Al-14.2Hf):

Figures 166(a) and (b) display photomicrographs of two different areas in the as-cast structure of alloy PV9024, with a chemical composition of Ni-8.3Cr-5.6Co-5.3W-4.3Al-14.2Hf (wt.%).

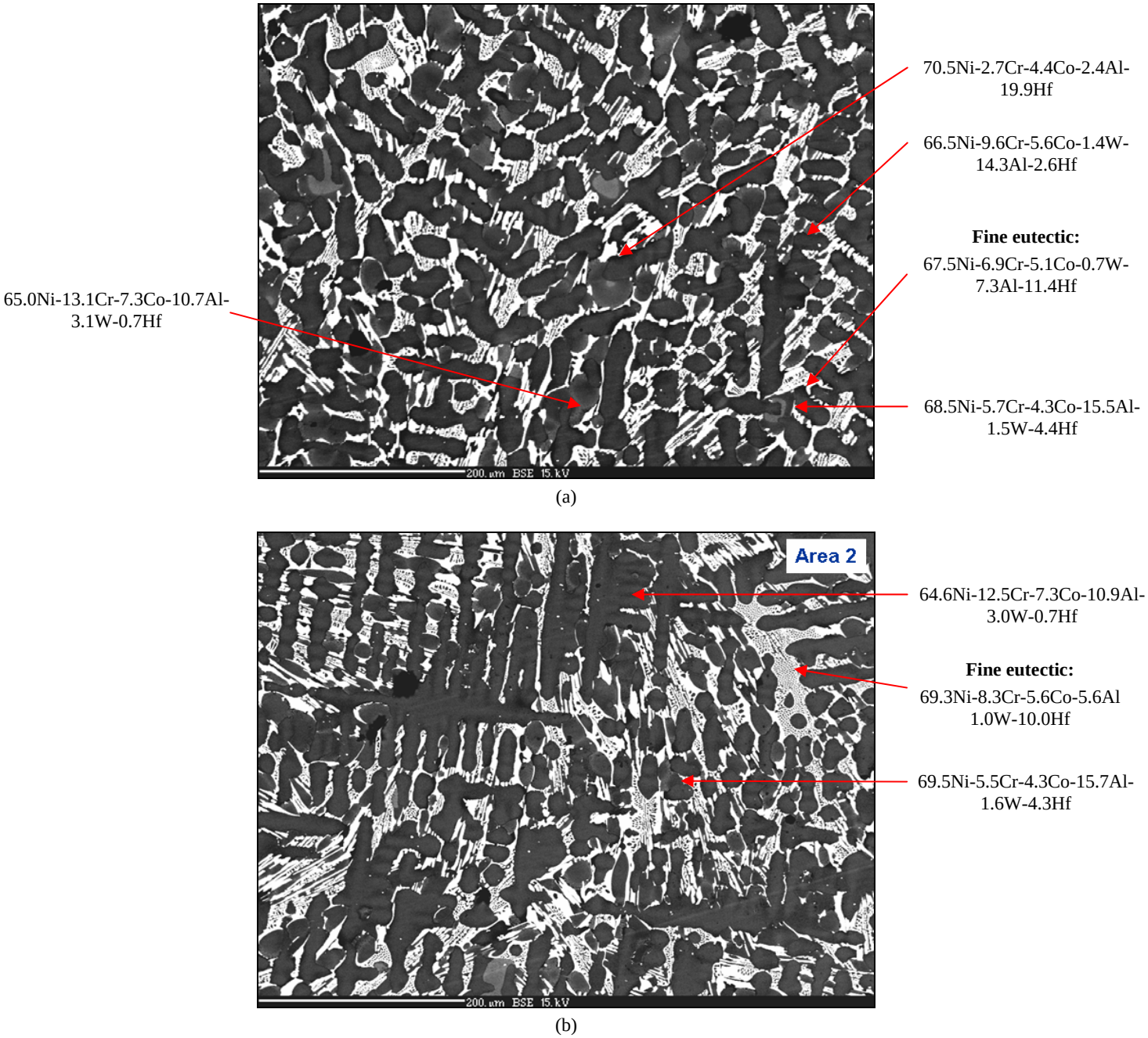

Figure 166 – Backscatter electron microprobe images of the Ni-8.3Cr-5.6Co-5.3W-4.3Al-14.2Hf alloy in the as-cast condition (PV9024). (All compositions given as atomic %).

This alloy also appears to be hypo-eutectic, with dark gray primary Ni-rich γ dendrites consisting of Ni-13.1Cr-7.3Co-10.7Al-3.1W-0.7Hf (at.%) in **Figure 166(a),** and Ni-17.5Cr-7.4Co-1.0W-11.5Al-0.7Hf (at.%) in **Figure 166(b)**. The fine binary eutectic component between the dendrites was shown to consist of 68.6Ni-6.9Cr-5.1Co-7.3Al-0.7W-11.4Hf

(**Figure 166(a)**), and 69.3Ni-8.3Cr-5.6Co-1.0W-5.6Al-10.0Hf (**Figure 166(b)**). Compositions of 70.6Ni-2.7Cr-4.4Co-2.4Al-19.9Hf (**Figure 166(a)**) and 74.5Ni-1.8Cr-4.5Co-1.4Al-21.8Hf (**Figure 166(b)**) were determined for the light eutectic phase (possibly the Ni_7Hf_2 intermetallic compound). The solidus and liquidus temperatures of this alloy were 1185°C and 1334°C, respectively (ΔT = 149°C). The liquidus temperature of this alloy was therefore too high to be of any practical use in the repair of the Ni-base superalloys utilized in production today, and the alloy is of no practical value in the short term.

12.3.5 Alloy PV9026 (Ni-7.9Cr-5.4Co-5W-1.5Ti-4.1Al-0.04C-20.3Hf):

Figure 167 displays a photomicrograph of the as-cast structure of alloy PV9026, with a chemical composition of Ni-7.9Cr-5.4Co-5W-1.5Ti-4.1Al-0.04C-20.3Hf (wt.%). This alloy appears to be hypo-eutectic, with dark gray primary Ni-rich γ dendrites consisting of Ni-9.8Cr-6.2Co-12.9Al-2.2W-2.7Ti-2.9Hf (at.%). The fine binary eutectic component between the dendrites was shown to consist of Ni-9.9Cr-6.4Co-7.8Al-1.5W-1.6Ti-10.2Hf (at.%). The coarse white phase was identified as the non-equilibrium Ni_3Hf or Ni_7Hf_2 intermetallic compound, consisting of 66.1Ni-2.4Cr-5.1Co-3.6Al-0.8Ti-22.0Hf (at.%). The composition of a number of white rosette-shaped particles (1.5Ni-11.4Cr-0.3Co-0.2Al-87.5W-0.1Ti-0.2Hf) suggests the presence of Laves phase or (W,Cr) carbides. Laves phase is not uncommon in some unstable Ni-base superalloys. Smaller dark particles observed in the microstructure were identified as Ni_3Al (γ') with a composition of 45.5Ni-6.2Cr-4.3Co-29.1Al-13.7Ti-1.2Hf. The solidus and liquidus temperatures of this alloy were 1034°C and 1210°C, respectively (ΔT = 176°C). Although the solidus and liquidus temperatures were lower than those of the simple eutectic Ni-Hf braze alloy described in Chapter 3, the potential of this alloy for the repair of equiaxed, directionally solidified and single crystal Ni-base superalloys may be limited by the presence of brittle Laves phase within the as-cast microstructure.

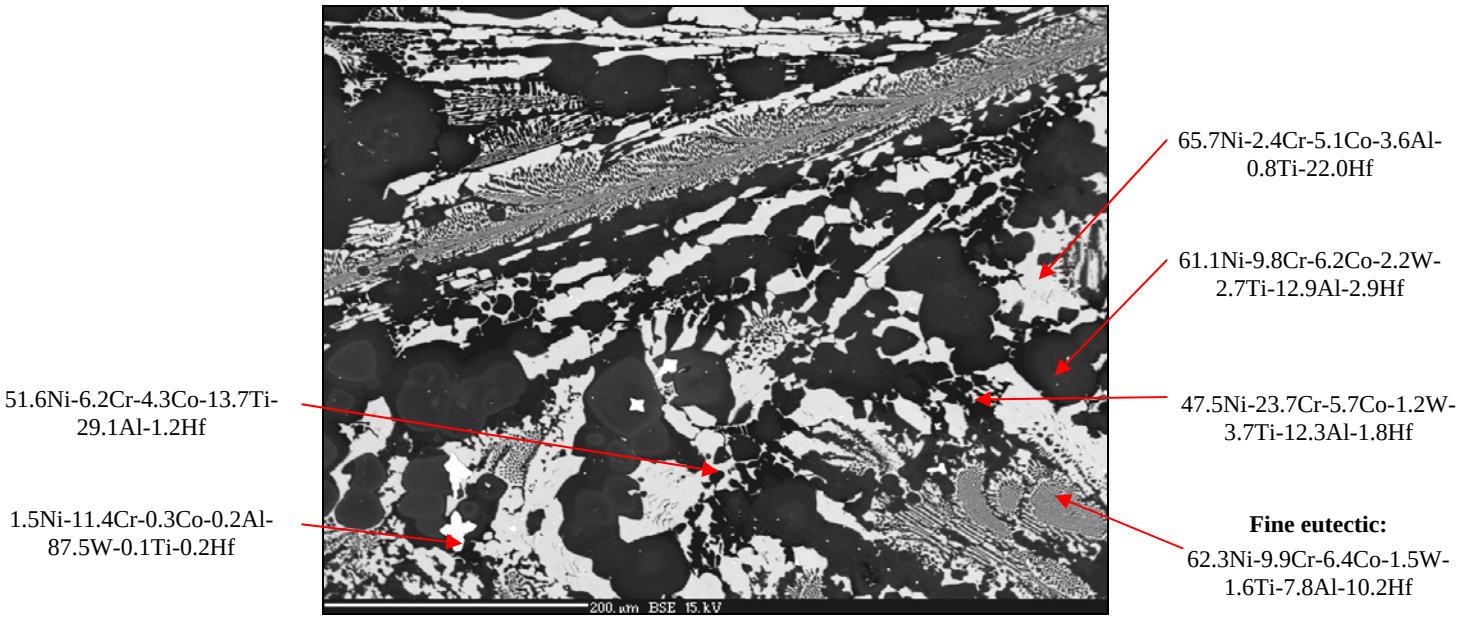

Figure 167 – Backscatter electron microprobe images of the Ni-7.9Cr-5.4Co-5W-1.5Ti-4.1Al-0.04C-20.3Hf alloy in the as-cast condition (PV9026). (All compositions given as atomic %).

12.4) Conclusions

- An alloy containing 66.5Ni-8.5Cr-25Hf (wt.%) appeared to be hypereutectic, with a needle-shaped primary Hf-rich intermetallic phase identified as non-equilibrium Ni_3Hf or Ni_7Hf_2, and a fine eutectic component consisting of Ni-rich γ and the Ni_3Hf or Ni_7Hf_2 intermetallic phase. This alloy had a solidus temperature of 1195°C and a liquidus temperature of 1281°C (ΔT = 86°C). This solidification temperature range makes the Ni-8.5Cr-25Hf alloy unsuitable for repairing equiaxed Ni-base superalloys, such as In738 and MarM247. Single crystal Ni-base superalloys, however, can be processed at temperatures up to 1310°C, so this braze alloy may be suitable for use in repairing these materials.

- An alloy with a chemical composition of Ni-7.4Cr-4.7W-1.4Ti-2.3Al-0.03C-25.5Hf (wt.%) displayed a complex microstructure consisting of a needle-shaped Hf-rich phase (identified as the non-equilibrium NiHf or $Ni_{11}Hf_9$ intermetallic compound), a non-equilibrium Ni_3Hf or Ni_7Hf_2 intermetallic compound, Ni-rich γ phase with a significant amount of Cr in solution, and a eutectic component consisting of Ni-rich γ and the non-equilibrium NiHf or $Ni_{11}Hf_9$ intermetallic compound. This alloy had a solidus temperature of 1140°C and a liquidus temperature of 1282°C (ΔT = 142°C). This solidification temperature range makes this material unsuitable for repairing equiaxed Ni-base superalloy materials, such as In738 and MarM247.

- Alloy PV9025, with a chemical composition of Ni-8.4Cr-5.4W-1.6Ti-6.1Al-14.5Hf (wt.%), appeared to be hypo-eutectic, with primary Ni-rich γ dendrites and a fine binary eutectic component consisting of Ni-rich γ phase and Ni_7Hf_2 intermetallic compound. A number of W-rich particles, probably (W,Cr) carbides or Laves phase, were also observed. The solidus and liquidus temperatures of this alloy were 1049°C and 1119°C, respectively (ΔT = 70°C). Both the solidus and liquidus temperatures were lower than those of the simple eutectic Ni-Hf braze alloy, and the alloy demonstrates great potential for the repair of equiaxed, directionally solidified and single crystal Ni-base superalloys.

- An alloy consisting of Ni-8.3Cr-5.6Co-5.3W-4.3Al-14.2Hf (wt.%) also appeared to be hypo-eutectic, with primary Ni-rich γ dendrites and a fine eutectic component consisting of Ni-rich γ and the Ni_7Hf_2 intermetallic compound. The solidus and liquidus temperatures of this alloy were 1185°C and 1334°C, respectively (ΔT = 149°C). The liquidus temperature of this alloy was therefore too high to be of any practical use in the repair of the Ni-base superalloys utilized in production today, and it is of no practical value as a braze alloy in the short term.

- The as-cast structure of alloy PV9026, with a chemical composition of Ni-7.9Cr-5.4Co-5W-1.5Ti-4.1Al-0.04C-20.3Hf (wt.%), appeared to be hypo-eutectic, with primary Ni-rich γ dendrites and a fine eutectic component between the dendrites. A coarse phase, (identified as the non-equilibrium Ni_3Hf or Ni_7Hf_2 intermetallic compound), a number of smaller rosette-shaped particles (identified as Laves phase), and small Ni_3Al particles were also observed. The solidus and liquidus temperatures of this alloy were 1034°C and 1210°C (ΔT = 176°C), respectively. Although the solidus and liquidus temperatures were lower than those of the simple eutectic Ni-Hf braze alloy, the potential of this alloy for the repair of equiaxed, directionally solidified and single crystal Ni-base superalloys may be limited by the presence of brittle Laves phase within the as-cast microstructure.

CHAPTER 13 - EXPERIMENT 11

CHARACTERIZATION OF THE MICROSTRUCTURE AND MECHANICAL PROPERTIES OF ADH BRAZE JOINTS IN FSX-414 COBALT-BASE SUPERALLOY NOZZLE SEGMENTS USING NOVEL BRAZE ALLOYS

13.1) Introduction

The preceding chapters focused on the use of binary and ternary Ni-Zr and Ni-Hf braze alloys for the repair of turbine components cast from Ni-base superalloys, such as Inconel 738 and MarM247. The promising mechanical properties of the novel braze joints in Ni-base superalloy components prompted an investigation into the use of novel braze alloys for repairing Co-base superalloy nozzle segments.

GE Energy Services, an OEM, currently produce a range of Industrial Gas Turbine (IGT) engines, including models such as the Frame7FA, Frame 7FA+ and Frame 7FA+e engines. All these engines contain first stage nozzle segments cast from FSX-414 cobalt-base superalloy. The chemical composition of FSX-414 is given in **Table 55**. This alloy is a solid solution strengthened alloy, in contrast to the γ' strengthened Ni-based superalloys (such as Inconel 738 and MarM247) considered in earlier chapters. A schematic illustration of a Frame7FA+e first stage nozzle segment with two airfoils is shown in **Figure 168**.

Table 55 – Nominal chemical compositions of the alloys considered in this investigation (wt.%).

Alloy	Co	Cr	Ni	W	Fe	Ta	Zr	Si	Mn	Ti	Al	Ce	C	B
FSX-414	Bal	29.0	10.0	7.5	1.0	-	-	-	-	-	-	-	0.25	0.01
Nozzalloy	Bal	29.0	20.0	-	-	7.0	0.01	-	-	-	-	0.06	0.05	-
X-40	Bal	25.5	10.0	7.5	-	-	-	0.7	0.7	-	-	-	0.5	-
D15	10.3	15.3	Bal	-	-	3.5	-	-	-	-	3.0	-	-	2.5
MarM509	Bal	23.5	10.0	7.0	-	3.5	0.5	-	-	0.2	-	-	0.6	-
MarM509B	Bal.	23.5	10.0	7.0	-	3.5	0.5	0.2	-	0.2	-	-	0.6	2.5
MarM918	Bal	20.0	20.0	-	-	7.5	0.1	-	-	-	-	-	0.05	-

Figure 168 - Schematic illustration of the first stage nozzle segment of a Frame7FA+e IGT engine.

Nozzle segments in IGT engines tend to degrade during engine service, with degradation modes ranging from craze cracking, oxidation, corrosion and creep, to foreign object damage. Examples of characteristic cracks in a first stage nozzle segment are shown in **Figure 169**. The cracks in this nozzle segment were originally repaired using manual arc welding with processes such as GTAW (gas tungsten arc welding) or PAW (plasma arc welding), and a Co-base filler metal known as Nozzalloy. The chemical composition of Nozzalloy is given in **Table 55**.

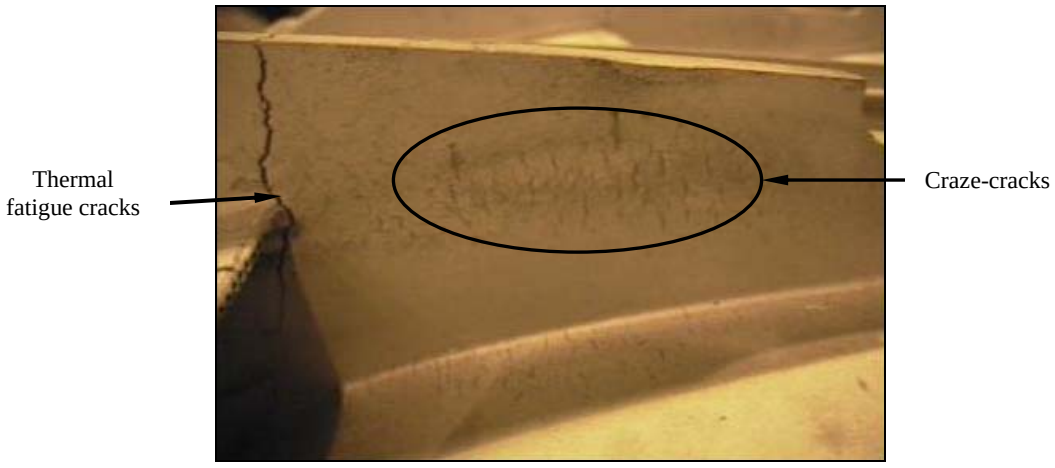

Figure 169 - An example of craze-cracks and large individual thermal fatigue cracks on the outer sidewall of a first stage nozzle segment.

Although as a solid solution strengthened alloy, FSX-414 is readily weldable, the extent of cracking displayed in **Figure 169** resulted in several hours of weld time. Extensive welding caused distortion of the nozzle segments to the extent that key dimensions were outside allowable tolerance limits. This resulted in the nozzle segments not fitting properly on return to the engine. Since brazing in a vacuum furnace involves uniform heating and cooling, resulting in minimal distortion, a vacuum braze repair was developed. The patented wide gap braze process known as ADH (activated diffusion healing), described in §1.5, was used. The ADH repair involved mixing equal parts (by weight) X-40 cobalt-base superalloy powder and a γ' strengthened Ni-base braze alloy known as D15 (containing 2.5% B as melt point depressant). The nominal compositions of X-40 and D15 are given in **Table 55**. The X-40/D15 mixture resulted in a hybrid braze mix with poor mechanical properties, and the joint cracked rapidly in service. As a result of the poor mechanical integrity of the braze joints, customers refused to have their nozzle segments ADH braze repaired, and insisted that the nozzle segments be welded.

The poor service performance of the X-40/D15 ADH braze repair prompted further investigation with the following objectives:

- To examine an alternative ADH braze mixture consisting of MarM509 Co-base superalloy powder and MarM509B braze alloy for crack repair of FSX-414 nozzle segments, with the aim of obtaining mechanical integrity equivalent or superior to the properties of Nozzalloy welds.
- To develop and test a novel Co-base braze alloy containing Hf instead of B as melt point depressant for the crack repair of FSX-414 nozzle segments.

Three properties are considered critical with respect to the quality of the braze joints: elevated temperature tensile properties, creep rupture properties and low cycle fatigue life. If a newly developed braze repair procedure ensures mechanical properties equivalent to those of a weld repair, the improved braze procedure would most likely be preferred by repair customers due to the lower risk of distortion.

In view of the stated requirements for an acceptable braze procedure, the X-40/D15 ADH braze mixture was changed to a MarM509/MarM509B braze. The chemical compositions of MarM509 and MarM509B are shown in **Table 55**. MarM509 is a Co-base superalloy with an excellent combination of mechanical properties, including high tensile strength, fatigue strength and creep rupture strength. MarM509B is a Co-base braze alloy with a nominal chemical composition virtually identical to that of MarM509, with 2.5 wt.% B added as melt point depressant. Certification documents for the MarM509B braze alloy assign a solidus temperature of 1121°C and a liquidus temperature of 1160°C to the alloy. Si is present as a trace element in MarM509B and is not added intentionally to lower the melting point.

The promising results described in earlier chapters for the binary and ternary eutectic Ni-Hf braze alloys encouraged the development of a novel Co-base braze alloy containing Hf as melt point depressant. The binary Co-Hf phase diagram [2], shown in **Figure 170**, illustrates that a eutectic point exists at a composition of 27.2%Hf and 72.8%Co (by weight), and a temperature of 1230°C. This investigation therefore included an evaluation of a novel ADH braze joint consisting of a mixture of MarM509 powder and the binary eutectic Co-Hf braze alloy.

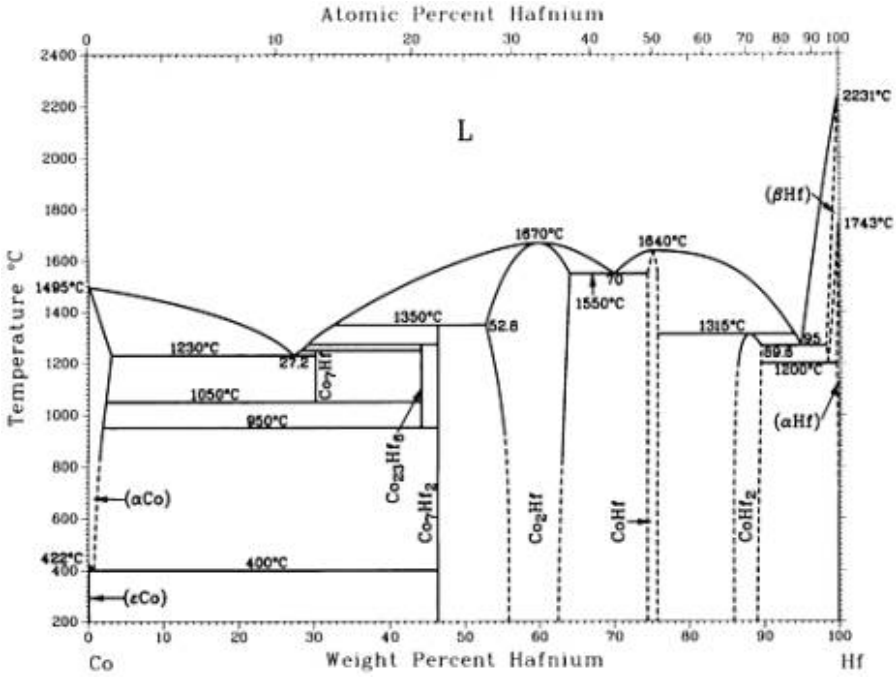

Figure 170 – The binary Co-Hf phase diagram [2].

13.2) Experimental procedure

Plates of FSX-414 with dimensions 248 mm long, 127 mm wide and 19 mm thick were investment cast for this experiment. A 1.5 mm wide groove was machined in the center of each plate, as illustrated in **Figure 171**. This gap width was selected on the basis of an investigation into the crack widths observed in 96 nozzle segments (four engine sets, with 24

nozzle segments in each engine set). The data revealed a mean crack width of 0.64 mm and a maximum crack width of 1.5 mm. The approval authority required that the new ADH process be capable of repairing up to the maximum crack width, i.e. 1.5 mm. The gap was only machined partially, leaving 0.5 mm of parent metal intact at the base of the groove (as shown in **Figure 172**). This was done to maintain the 1.5 mm gap width during brazing without the need for special fixturing. Since the mechanical test samples were machined to a gauge diameter of 6.4 mm, the 0.5 mm parent metal retained at the base of the groove was machined away after brazing and therefore did not affect the test results in any way.

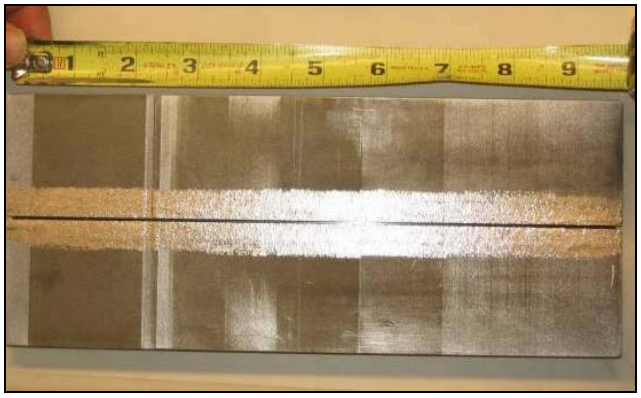

Figure 171 - The FSX-414 test plate with a 1.5 mm wide groove machined in the centre.

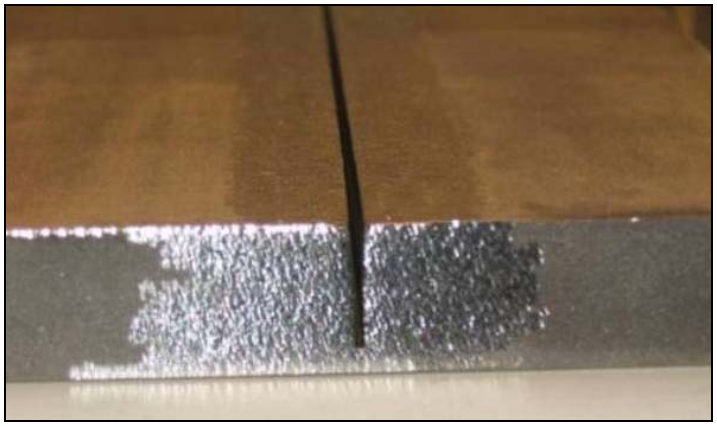

Figure 172 - Enlarged view of the machined groove in the braze test plate.

Two sets of braze samples were produced. The first set of samples was produced by filling the groove with a mixture of MarM509 powder and MarM509B braze powder (with compositions shown in **Table 55**). The powders were mixed in a ratio of 60% MarM509 and 40% MarM509B (by weight). The second set of samples was produced by filling the groove with a mixture of MarM509 powder and eutectic Co-Hf powder (containing 27.2% Hf) in a ratio of 60% MarM509 powder and 40% braze alloy. The plates were then processed in a vacuum furnace using the following braze cycle:

1) Evacuate the vacuum furnace to a pressure of $5x10^{-4}$ torr or lower.
2) Ramp up to a temperature of $450^{o}C \pm 14^{o}C$ at a rate between $8^{o}C$/minute and $14^{o}C$/minute.
3) Hold at $450^{o}C$ for a minimum of 40 minutes to allow the binder to burn off. Proceed to the next step once the vacuum level had returned to $1x10^{-3}$ torr or lower.

4) Ramp up to a temperature of 1093°C±14°C at a rate between 8°C/minute and 14°C/minute.
5) Hold at 1093°C for a minimum of 40 minutes to allow the samples to stabilize at this temperature.
6) Ramp up to the melting temperature of 1245°C±14°C at a rate between 8°C/minute and 14°C/minute.
7) Hold at 1245°C for a minimum of 30 minutes.
8) Furnace cool under vacuum to 1150°C±14°C.
9) Hold at 1150°C for a minimum of 240 minutes.
10) Ramp up to a temperature of 1177°C±14°C at a rate between 8°C/minute and 14°C/minute.
11) Hold at 1177°C for a minimum of 240 minutes.
12) Ramp up to a temperature of 1205°C±14°C at a rate between 8°C/minute and 14°C/minute.
13) Hold at 1205°C for a minimum of 240 minutes.
14) Gas quench with argon or helium gas to a safe temperature (about 90°C) before unloading the test plates.

A melting temperature of 1245°C was selected as it is above the liquidus temperatures of both the MarM509B ADH braze alloy and the novel Co-Hf braze alloy. The diffusion temperatures (1150°C, 1177°C and 1205°C) were selected to be below the liquidus temperatures of both braze alloys, but high enough to facilitate rapid diffusion of the melt point depressants, i.e. B or Hf, into the surrounding superalloy powder particles.

Photographs of the MarM509/Co-Hf and the MarM509/MarM509B ADH joints are shown in **Figures 173(a) and (b)**. The appearance of the joints suggests that the MarM509/MarM509B ADH braze alloy was more fluid than the MarM509/Co-Hf braze at the melting temperature. This is attributed to the amount of superheating above the liquidus temperature of the braze alloy, with the MarM509/MarM509B ADH braze being processed at a temperature 68°C higher than its liquidus temperature, whereas the MarM509/Co-Hf ADH braze was processed at a temperature only 16°C higher than its eutectic temperature.

(a) (b)

Figure 173 - Photographs of: (a) the MarM509/Co-Hf ADH test plate in the as-brazed condition; and (b) the MarM509/MarM509B ADH test plate in the as-brazed condition.

In order to compare the mechanical properties of the novel ADH braze joints with those of the welds currently preferred by repair customers, MarM509 plates were fusion welded using a

double V-weld preparation in the downhand position. The GTAW (gas tungsten arc welding) process was used with the following weld parameters:

- Welding current: 60 to 80 A
- Arc voltage: 10 to 15 V
- Welding speed: Manual
- Tungsten electrode: 2% Thoriated tungsten (classification: EWTh-2), 1.6 mm or 2.4 mm diameter
- Polarity: DCEN (direct current electrode negative)
- Filler wire diameter: 0.9 mm to 1.6 mm
- Shielding gas: 95% Ar + 5% H_2 (by volume)
- Preheat temperature: 10°C minimum
- Interpass temperature: 150°C maximum
- Welding technique: Stringer bead
- Gas cup size: 9.5 mm to 19 mm
- Filler metal: Nozzalloy or MarM918 (nominal chemical compositions are shown in **Table 55**).

Tensile tests, creep rupture tests and low cycle fatigue (LCF) tests were performed at various temperatures. An example of a mechanical test sample machined from the test plates is shown in **Figure 174**. The elevated temperature tensile tests were performed at 870°C. Creep rupture tests were performed at 760°C, 815°C, 870°C, 980°C, 1040°C and 1090°C at various applied stress levels. The LCF tests were performed at 870°C at various strain levels. Since the success of this investigation hinged mainly on the LCF properties of the joints, the Approval Repair Authority requested that the following LCF curves be generated:

a) FSX-414 base metal welded with MarM918 filler metal. This weld filler metal is used to salvage virgin castings with casting defects, such as hot tears or macroporosity. The chemical composition of MarM918 is given in **Table 55**.
b) FSX-414 welded with Nozzalloy filler metal. This weld filler metal is used to repair nozzle segments degraded during service.
c) FSX-414 brazed with the new MarM509/MarM509B wide gap braze mixture.
d) FSX-414 brazed with the new MarM509/Co-Hf ADH braze mixture.

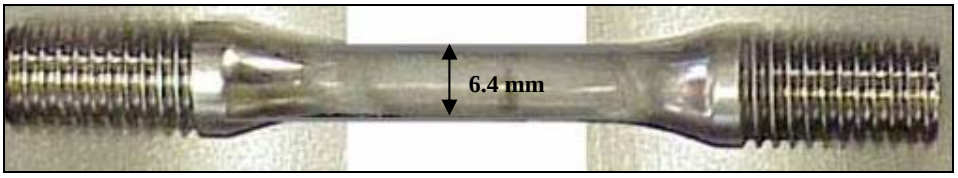

Figure 174 - Mechanical test sample machined from the braze test plates. The 1.5 mm wide braze joint is located in the centre of the gauge length.

13.3) Results and discussion

13.3.1 Mechanical test results:

The results of tensile tests performed at 870°C are shown in **Table 56** for the FSX-414 base metal, FSX-414 welded with Nozzalloy, FSX-414 ADH brazed with MarM509/MarM509B, and FSX-414 ADH brazed with the novel Co-Hf braze alloy.

Table 56 - Tensile properties at 870°C of FSX-414 base metal, FSX-414 welded with Nozzalloy, FSX-414 brazed with MarM509/MarM509B, and FSX-414 brazed with MarM509/Co-Hf. The test samples were produced with a joint gap of 1.5 mm to simulate a worst-case crack repair scenario.

Specimen identification	Failure location	Tensile strength, MPa	Yield stress, MPa	% Elongation	% Reduction in area
BLT-1T (FSX-414 base metal)	Base metal	291	168	32	32
BLT-2T (FSX-414 base metal)	Base metal	304	177	31	31
BLT-3T (FSX-414 base metal)	Base metal	296	167	44	44
BLT-4T (FSX-414 base metal)	Base metal	283	164	36	36
Average for the FSX-414 base metal	**-**	**295**	**169**	**35.8**	**35.8**
NOZ-1 (FSX-414 welded with Nozzalloy)	HAZ*	278	175	44	53
NOZ-7 (FSX-414 welded with Nozzalloy)	Base metal	274	179	46	45
NOZ-10 (FSX-414 welded with Nozzalloy)	Base metal	275	177	42	52
NOZ-16 (FSX-414 welded with Nozzalloy)	Base metal	275	178	38	43
Average for the FSX-414/Nozzalloy weld		**275**	**177**	**42.5**	**48.3**
509-1 (FSX-414 brazed with MarM509/MarM509B)	Base metal	277	190	48	46
509-7 (FSX-414 brazed with MarM509/MarM509B)	Base metal	282	189	28	44
509-10 (FSX-414 brazed with MarM509/MarM509B)	Base metal	268	178	30	38
509-16 (FSX-414 brazed with MarM509/MarM509B)	Base metal	284	179	29	48
Average for the MarM509/MarM509B ADH joint		**277**	**184**	**33.8**	**44.0**
ENH-1 (FSX-414 brazed with MarM509/Co-Hf)	Base metal	272	175	28	51
ENH-7 (FSX-414 brazed with MarM509/Co-Hf)	Base metal	268	175	50	59
ENH-10 (FSX-414 brazed with MarM509/Co-Hf)	Base metal	285	194	25	56
ENH-16 (FSX-414 brazed with MarM509/Co-Hf)	ADH joint	275	190	4.3	4.3
Average for the MarM509/Co-Hf ADH joint		**275**	**183**	**34.3**	**55.3**

* HAZ: Heat-affected zone.

It is evident from the tensile test results shown in **Table 56** that the FSX-414 samples fusion welded with Nozzalloy filler metal performed very well, with three of the four samples tested failing in the parent metal and the fourth failing in the heat-affected zone. The tensile strength, yield strength, elongation and reduction in area values were equivalent or even superior to those of the base metal.

FSX-414 brazed with the MarM509/MarM509B ADH material yielded similar results, with all the tensile samples failing in the base metal. The tensile test results shown in **Table 56** therefore represent the properties of the base metal, rather than those of the braze joint. It can, however, be concluded that the tensile properties of the MarM509/MarM509B braze joints were at least equivalent to those of the base metal.

The FSX-414 samples brazed with the MarM509/Co-Hf braze alloy yielded promising results, with three of the four samples failing in the base metal. It can be concluded that the tensile properties of these joints were at least equivalent to those of the base metal. The fourth sample failed in the braze joint, but displayed tensile and yield strength values equivalent to those of the base metal (as shown in **Table 56**). The elongation and reduction in area values of the fourth sample were, however, very low when compared with those of the base metal (4.3% elongation and reduction in area, compared with ±35%). Examination of the fractured sample revealed porosity on the fracture surface. It is assumed that the low ductility values measured during this tensile test were related to the presence of porosity in the braze joint.

A Larson-Miller plot comparing the creep rupture properties of the FSX-414 base metal, FSX-414 welded with Nozzalloy filler metal, and FSX-414 ADH brazed with MarM509/MarM509B, is shown in **Figure 175**. The Larson-Miller plot indicates that the MarM509/MarM509B braze samples outperformed the Nozzalloy welds. For example, at a Larson-Miller number of 49 (the dotted line in **Figure 175**), the MarM509/MarM509B samples exhibited 90% of the base metal's creep rupture properties, whereas the Nozzalloy samples displayed 75% of the base metal's properties. At higher test temperatures the creep rupture properties of the MarM509/MarM509B braze joints approached those of the base metal. On average the MarM509/MarM509B samples demonstrated 90% of the base metal's creep rupture properties, whereas the Nozzalloy samples displayed 72%.

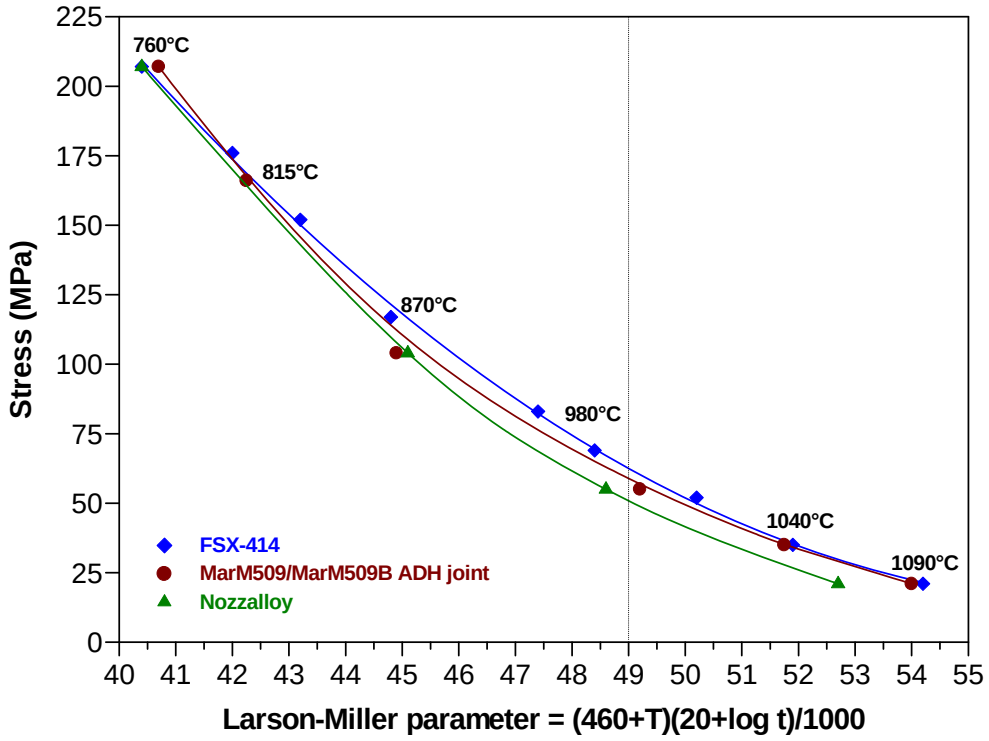

Figure 175 – Larson-Miller plot of FSX-414 base metal, the MarM509/MarM509B ADH braze joints, and the Nozzalloy weld.

The results of the low cycle fatigue (LCF) tests are shown in **Table 57**, and displayed graphically in **Figure 176**.

Although MarM918 filler metal is approved for salvaging virgin castings, all except one of the FSX-414 samples welded with MarM918 failed in the weld metal or heat-affected zone. The MarM918 welds displayed the poorest fatigue life of all the samples evaluated. The Nozzalloy welds performed marginally better, with four of the twelve samples failing in the weld or heat-affected zone. The remaining eight Nozzalloy samples failed in the base metal.

The MarM509/MarM509B braze joints displayed consistently higher LCF properties than the welded joints, with four of the twelve samples failing at the interface between the braze joint and the base metal. The remaining eight samples failed in the base metal.

Table 57 – Low cycle fatigue (LCF) data for FSX-414 base metal, FSX-414 welded with MarM918, FSX 414 welded with Nozzalloy, FSX-414 ADH brazed with MarM509/MarM509B, and FSX-414 ADH brazed with MarM509/Co-Hf.

Sample	Strain	Cycles to initiation	Cycles to failure	Failure location
FSX-414 base metal	0.60	1298	1460	Base metal
	0.60	1598	2099	Base metal
	0.50	2978	3563	Base metal
	0.50	3206	3773	Base metal
	0.46	6177	6375	Base metal
	0.40	4422	5787	Base metal
	0.40	7126	8765	Base metal
	0.35	8584	9087	Base metal
	0.35	11085	12972	Base metal
	0.33	14290	17141	Base metal
	0.30	22736	24712	Base metal
	0.30	49953	51066	Base metal
FSX-414 welded with MarM918	0.60	814	1013	Weld
	0.60	1212	1398	Weld
	0.50	1669	2039	HAZ*
	0.50	2153	2955	HAZ*
	0.45	1301	2056	HAZ*
	0.40	4194	4539	Weld
	0.40	3876	5302	Weld
	0.40	4885	5312	Weld
	0.35	8308	8768	Weld
	0.35	12006	12310	HAZ*
	0.30	10058	12310	Weld
	0.30	20999	26395	Base metal
FSX-414 welded with Nozzalloy	0.60	1920	1957	Base metal
	0.60	1871	2649	Base metal
	0.50	3036	3618	HAZ*
	0.50	2655	3294	Base metal
	0.45	2009	2357	Base metal
	0.40	2316	2924	Weld
	0.40	4989	6583	HAZ*
	0.40	6895	7163	Base metal
	0.35	6569	7372	HAZ*
	0.35	9947	11526	Base metal
	0.30	18243	20239	Base metal
	0.30	20206	22163	Base metal
FSX-414 ADH brazed with MarM509/MarM509B	0.69	989	1007	Interface**
	0.60	1156	1238	Interface**
	0.60	876	1360	Base metal
	0.50	1854	1912	Interface**
	0.50	2641	3010	Base metal
	0.45	3893	4939	Base metal
	0.44	4890	5289	Base metal
	0.40	3735	5189	Base metal
	0.40	5173	5556	Base metal
	0.35	8036	9188	Interface**
	0.35	11911	14986	Base metal
	0.30	26421	30221	Base metal

Table 57 – continued.

Sample	Strain	Cycles to initiation	Cycles to failure	Failure location
FSX-414 ADH brazed with MarM509/Co-Hf	0.70	1195	1588	Base metal
	0.60	1627	1970	Base metal
	0.60	2711	2927	Base metal
	0.50	2134	2248	Base metal
	0.50	3589	3914	Base metal
	0.45	3501	3898	Base metal
	0.45	3092	3906	Base metal
	0.40	4975	5771	Base metal
	0.40	5455	6849	Base metal
	0.35	16584	17726	Base metal
	0.35	23185	25365	Base metal
	0.30	40911	41754	Base metal

* HAZ: Heat-affected zone
** Interface: Joint line between the base metal and the ADH braze

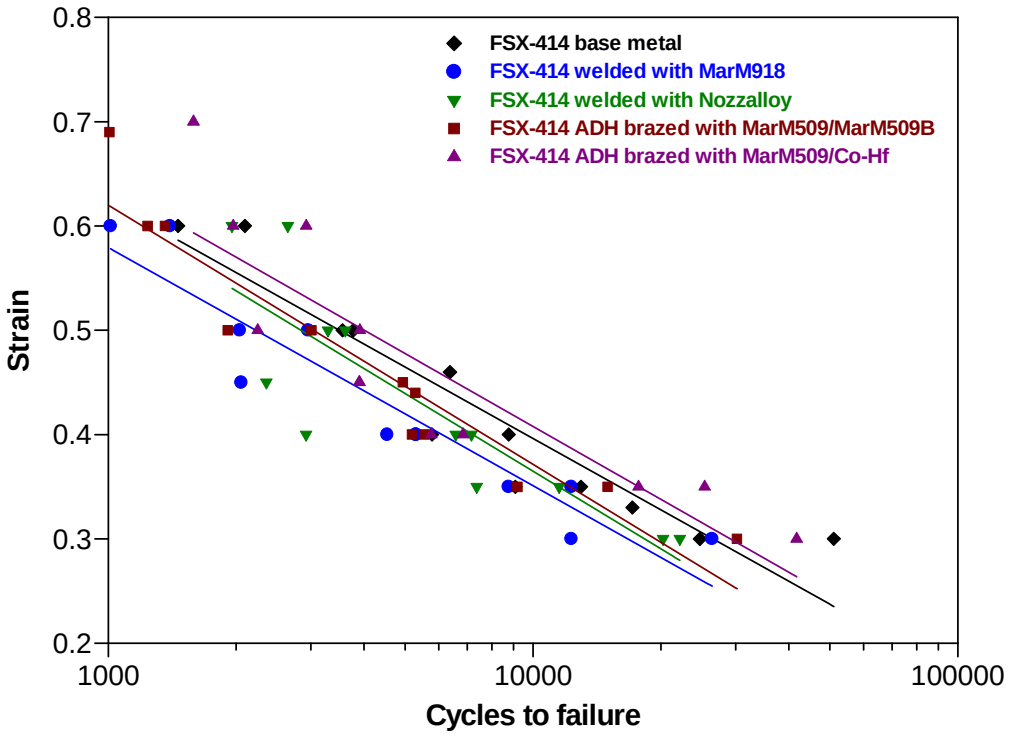

Figure 176 – Graphical representation of the LCF data determined for FSX-414 base metal, FSX-414 welded with MarM918 or Nozzalloy filler metal, FSX-414 ADH brazed with MarM509/MarM509B, and FSX-414 ADH brazed with MarM509/Co-Hf.

Figure 176 demonstrates that the MarM509/Co-Hf braze joint outperformed all the other repairs during LCF testing. It is also important to note that all the MarM509/Co-Hf samples failed in the base metal, and that the ADH braze joint displayed LCF properties superior to those even of the FSX-414 base metal. No publication in open literature has ever reported consistent base metal failure for braze joints. This resulted in consensus in both the aircraft and industrial gas turbine repair industries that braze joints are inherently brittle, and fail rapidly under conditions of applied strain. Joints produced using braze alloys with B as melt

point depressant have been shown to fail consistently in the braze joint under LCF test conditions.

Statistical analysis of the LCF results revealed that FSX-414 welded with MarM918 suffered a 38% reduction in LCF life, compared to the base metal. FSX-414 welded with Nozzalloy displayed a 27% reduction in LCF life (for the four samples that failed in the weld metal or heat-affected zone), whereas the four FSX-414 samples brazed with MarM509/MarM509B that failed at the joint interface suffered a 10% reduction in LCF life. All the FSX-414 samples brazed with MarM509/Co-Hf displayed LCF properties superior to those of the base metal.

13.3.2 Metallurgical examination:

Nozzle segments (especially first stage nozzle segments) endure the highest temperatures in a gas turbine engine and are exposed to fluctuating thermal strains which may result in thermal fatigue cracking. During engine service these thermal fatigue cracks can manifest as individual cracks or clusters of cracks, with the latter usually referred to as craze-cracks (shown earlier in **Figure 169**).

Thermal fatigue cracks develop surface oxide layers during service which must be removed prior to ADH brazing. These oxide layers are usually comprised of Cr-oxides, Ni-oxides or a combination of these compounds. The hydrogen cleaning process effectively reduces these oxides within cracks in Co-base superalloys. Simply stated, the hydrogen cleaning process pulses H_2 into a furnace at elevated temperature (around 1200°C) for a time of between 8 and 12 hours. The surface oxides are reduced at elevated temperature in this hydrogen-containing environment. **Figures 177(a) and (b)** compare the sidewalls of a crack before and after hydrogen cleaning, and illustrate the effectiveness of the cleaning process in removing surface oxide layers.

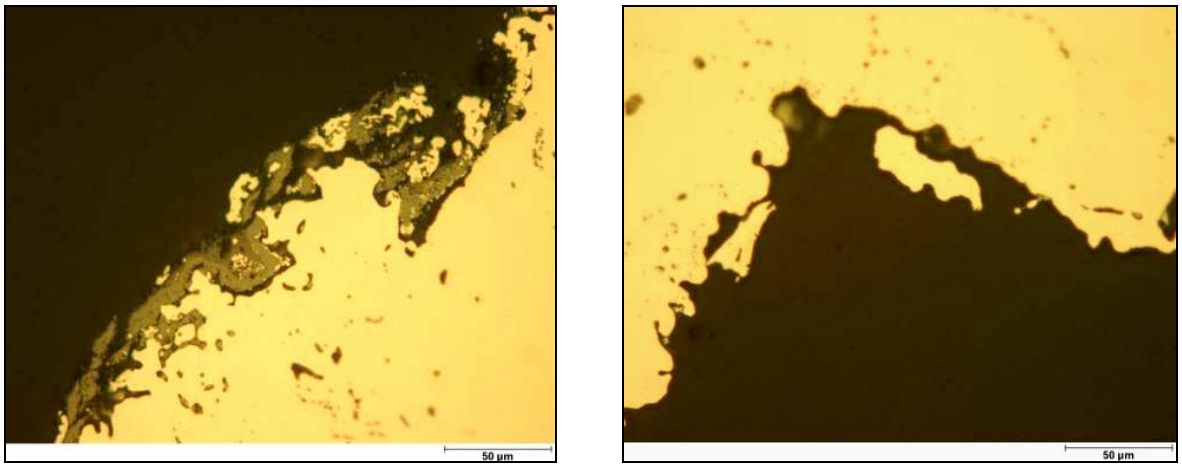

(a) (b)

Figure 177 – (a) Chromium oxides on the crack surface; and (b) oxide reduction on the sidewalls of the crack after H_2 cleaning.

Figure 178 displays a macrograph of craze-cracks successfully repaired using the MarM509/MarM509B braze alloy. This photograph illustrates that more than eleven small cracks had been filled with braze alloy. **Figure 179** shows an individual crack, also filled

with the MarM509/MarM509B braze. Some porosity is evident, but it amounts to less than 10% (by volume), which is the acceptance limit.

Figure 178 - Craze-cracks filled with the MarM509/MarM509B braze alloy.

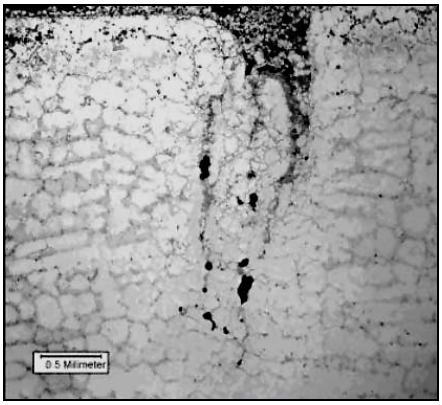

Figure 179 - Individual crack filled with the MarM509/MarM509B braze alloy.

Figures 180(a) and (b) demonstrate the ability of the MarM509/MarM509B braze alloy to repair deep cracks which had propagated from the concave to the convex surface of an airfoil during service. The structure is undiffused, i.e. the repair process had only progressed to the melting stage (1245°C for 30 minutes). As shown in **Figure 181**, good bonding of the braze filler metal to the sidewalls of the crack was obtained.

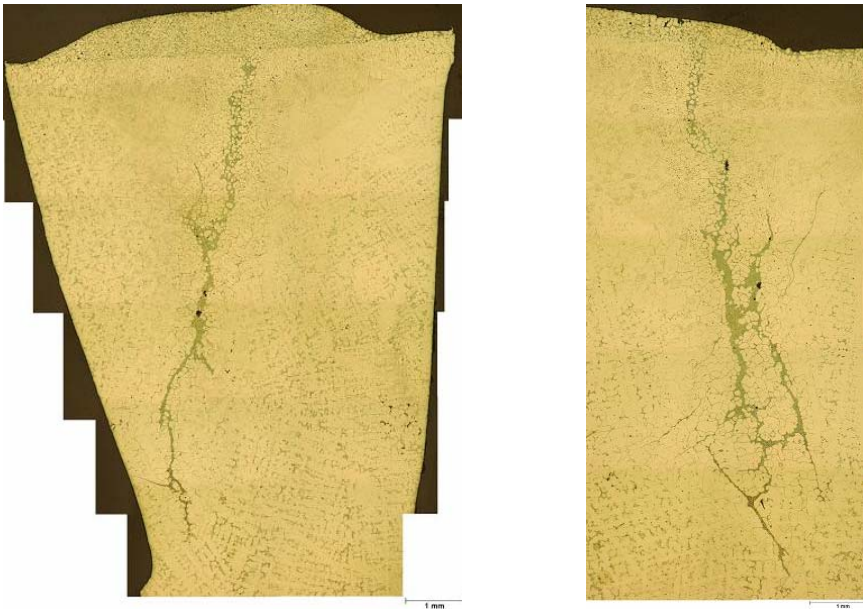

(a) (b)

Figure 180 – (a) Braze flow in a 7.5 mm deep crack; and (b) braze flow in an 11 mm deep crack.

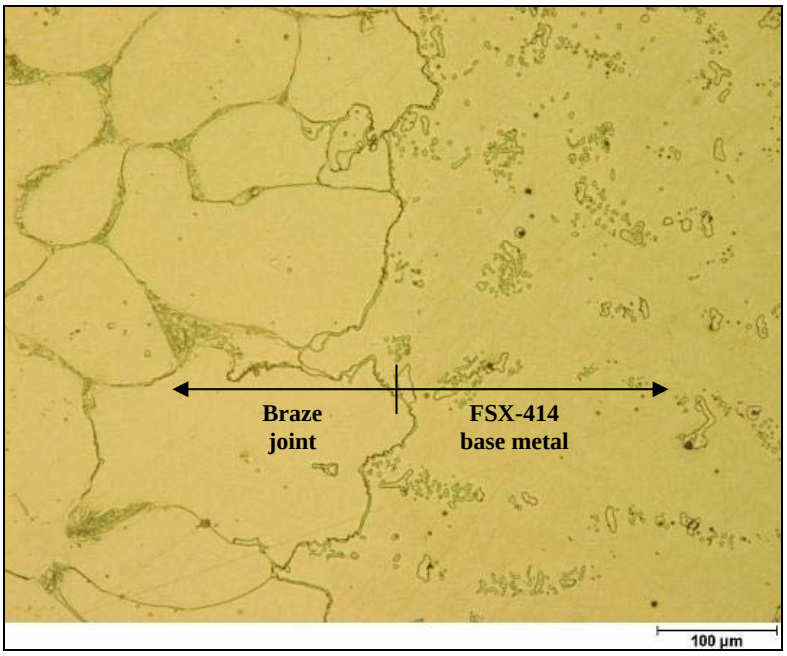

Figure 181 – Photomicrograph of the interface between the braze crack repair and the base metal.

Figures 182 and 183 display micrographs of braze joints used for craze-crack repair. These joints have undergone the full braze procedure, including the diffusion treatments. An equiaxed, homogenous structure, resembling that of the parent metal, is evident.

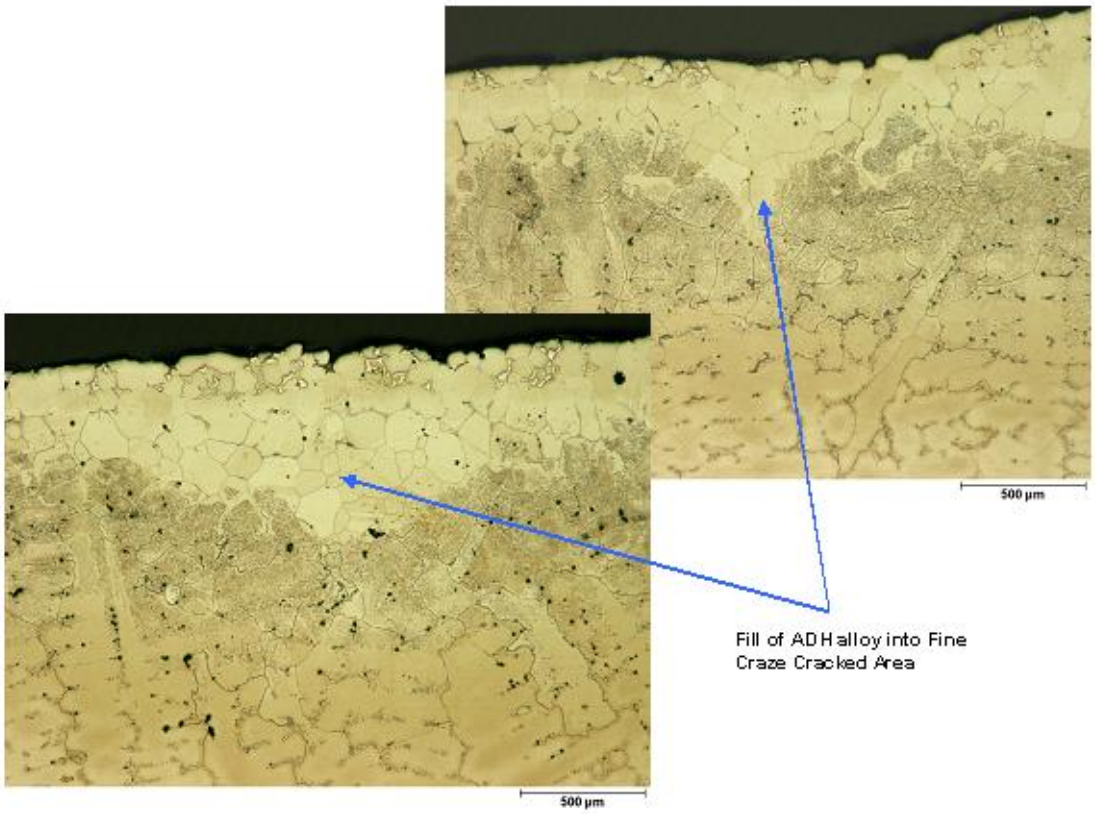

Figure 182 - Microstructure of the fully diffused braze repair of craze-cracks on a nozzle segment.

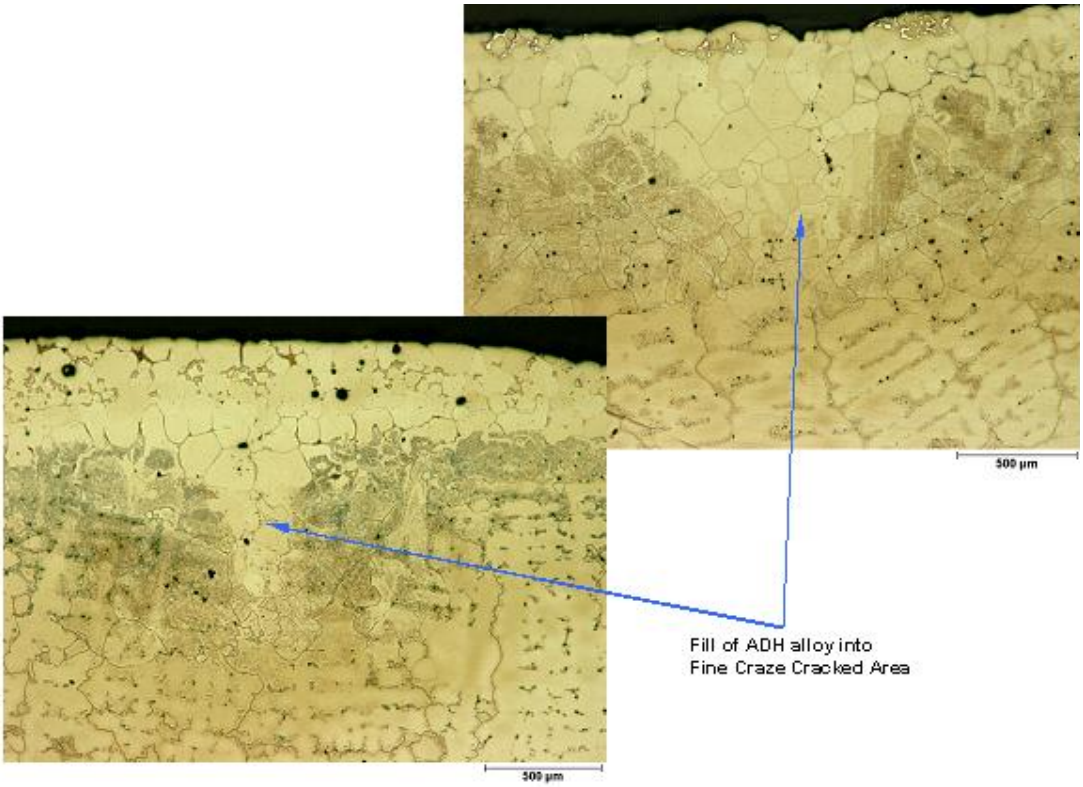

Figure 183 - Microstructure of the fully diffused braze repair of craze-cracks on a nozzle segment.

13.4) Conclusions

- This experiment examined the use of alternative ADH braze mixtures consisting of MarM509 Co-base superalloy powder and MarM509B braze alloy, or MarM509 powder and a eutectic Co-Hf braze alloy, for crack repair in FSX-414 Co-base superalloy nozzle segments. The aim of the investigation was to obtain mechanical integrity equivalent or superior to the properties of the fusion welds currently preferred by repair customers.

- Both the eutectic Co-Hf braze alloy (consisting of 27.2% Hf and 72.8% Co by weight) and the MarM509B braze were effective in repairing cracks in FSX-414 Co-base superalloy nozzle segments. Since nozzle segments have been shown to contain cracks up to 1.5 mm in width, the Co-Hf and MarM509B braze alloys had to be mixed with MarM509 superalloy powder to facilitate a wide gap ADH braze repair.

- The hydrogen cleaning process was effective in reducing the oxide layers typically found in thermal fatigue cracks in FSX-414 nozzle segments. Although the MarM509/Co-Hf braze alloy proved to be more sluggish than the MarM509/MarM509B alloy during brazing, the braze alloys filled craze-cracks and individual cracks, and bonded effectively to the sidewalls of the cracks.

- ADH braze repair of FSX-414 using the novel MarM509/MarM509B and MarM509/Co-Hf braze alloys resulted in high temperature tensile properties equivalent to those of weld repairs in the same parent material (using Nozzalloy filler metal). The creep rupture and low cycle fatigue (LCF) properties of the braze joints were superior to those of welds performed using Nozzalloy or MarM918 filler metal.

- FSX-414 samples braze repaired using the novel MarM509/Co-Hf braze alloy consistently failed in the base metal under low cycle fatigue conditions, implying that the LCF properties of the braze joint were superior to those of the base metal. This suggests that failure is likely to occur preferentially in the base metal if cracks in FSX-414 nozzle segments are ADH braze repaired using this braze alloy. A braze alloy consisting of a mixture of 60% MarM509 powder (by weight) and 40% eutectic Co-Hf powder therefore shows potential for crack repair of nozzle segments in industry.

- Statistical analysis of the LCF results revealed that FSX-414 welded with MarM918 suffered a 38% reduction in LCF life compared to the base metal. FSX-414 welded with Nozzalloy displayed a 27% reduction in LCF life (for four samples that failed in the weld metal or heat-affected zone), whereas the four FSX-414 samples brazed with MarM509/MarM509B that failed at the joint interface suffered a 10% reduction in LCF life. All the FSX-414 samples brazed with MarM509/Co-Hf displayed LCF properties superior to those of the base metal.

- Microstructural examination of brazed and fully diffused MarM509/MarM509B crack repairs revealed equiaxed braze microstructures with few boride particles.

CHAPTER 14 – FINAL CONCLUSIONS

This investigation was designed to:

- evaluate the use of two novel melt point depressants, namely Hf and Zr, in Ni- and Co-base braze filler metals, and
- optimize the liquid phase diffusion bonding process in conjunction with these novel braze filler metals with the aim of producing high strength joints with good ductility and mechanical properties at elevated temperature approaching those of the base metal.

This chapter describes the most important results obtained and the major conclusions drawn on completion of this project.

14.1 Liquid phase diffusion bonding of In738 Ni-base superalloy using binary eutectic Ni-Hf and Ni-Zr braze alloys

During the course of this investigation, the merit of two novel melt point depressants, namely Hf and Zr, was evaluated and the liquid phase bonding process optimized for the repair of wide cracks in Ni-base superalloy turbine components. The following conclusions were drawn:

- Hf and Zr were found to act as effective melt point depressants in Ni-base braze alloys. Binary eutectic Ni-Hf and Ni-Zr braze alloys melt and flow satisfactorily when processed at a melting temperature of 1230°C. In the as-brazed condition, the braze alloys were found to consist of a nickel-rich γ phase and an intermetallic compound (provisionally identified as Ni_2Hf_7 in the Ni-Hf braze alloy and Ni_5Zr in the Ni-Zr braze).
- In order to repair wide cracks in land-based turbine components, the binary Ni-Hf or Ni-Zr braze alloys need to be combined with a γ' strengthened Ni-base superalloy powder (such as MarM247) within the joint to form a liquid phase diffusion bond on brazing.
- A vacuum braze cycle consisting of melting at 1230°C, followed by an extended diffusion cycle of 24 hours at the same temperature, solution annealing at 1230°C, hot isostatic pressing at 1200°C and a full primary and secondary ageing cycle to precipitate γ' within the MarM247 particles, is recommended for obtaining optimal mechanical properties in the novel wide gap braze joints.
- Although the braze joints did not exhibit elevated temperature strength and creep rupture properties equivalent to those of the base metal, the novel wide gap braze joints consistently outperformed the commercially available B-containing braze alloys. The ductility of the novel braze alloys containing Hf or Zr as melt point depressant was significantly higher than the ductility of similar joints containing boron as melt point depressant.
- The Ni-Zr or Ni-Hf braze braze joints did not display LCF properties equivalent to those of the base metal, but the novel braze filler metals outperformed the commercially available B-containing brazes. Within the intermediate strain range where most cracks occur in nozzle segments (0.4% to 0.8% strain), the Ni-Zr and Ni-Hf braze joints displayed 70% and 74%, respectively, of the LCF properties of the base metal, compared to 11% for a B-containing braze alloy.

14.2 Liquid phase diffusion bonding of In738 Ni-base superalloy using more complex Ni-Hf and Ni-Zr braze alloys alloyed with chromium

In an attempt to further improve the performance of the novel braze filler metals, a series of more complex braze formulations containing chromium, in addition to various other deliberately added alloying elements, was produced. The microstructures of these formulations were examined in the as-cast, as-brazed or fully diffused condition, and electron microprobe analysis techniques were used to identify the phases observed in each alloy. The following conclusions were drawn:

- The addition of Cr to the novel Ni-Hf braze alloy shifted the eutectic composition to a lower Hf content.
- The boride particles which form in B-containing braze alloys were found to be considerably harder than the Ni_7Hf_2 intermetallic phase that forms in the novel Ni-Cr-Hf braze alloys. This difference in hardness may account for the high ductility and good LCF properties of the Ni-Hf braze joints, compared to those of B-containing braze alloys.
- Electron microprobe analysis of braze joints in complex alloys containing Hf or Zr as melt point depressants revealed that the intermetallic phases which form in the joints are most likely Ni_5Zr in Zr-containing brazes, and the nonequilibrium Ni_7Hf_2 phase in Hf-containing braze alloys. Dilution and contamination of the braze mixtures during production complicated identification of the intermetallic compounds.
- The high solidus and liquidus temperatures of many of the more complex alloys make them unsuitable for use in the repair of equiaxed Ni-base superalloy materials, such as In738 and MarM247. An alloy with a composition of Ni-8.4Cr-5.4W-1.6Ti-6.1Al-14.5Hf (wt.%), however, demonstrated great potential for the repair of equiaxed, directionally solidified and single crystal Ni-base superalloys.

14.3 Liquid phase diffusion bonding of FSX-414 Co-base superalloy using two novel ADH braze mixtures

The poor service performance of ADH braze joints currently used for refurbishing FSX-414 Co-base superalloy nozzle segments prompted an investigation into the use of alternative ADH braze mixtures in this application. The investigation examined ADH mixtures consisting of MarM509 Co-base superalloy powder and commercially available MarM509B braze alloy, and MarM509 powder and a eutectic Co-Hf braze alloy for FSX-414 crack repair, with the aim of obtaining mechanical integrity equivalent or superior to the properties of weld repairs. The following conclusions were drawn based on the results of the investigation:

- Both the eutectic Co-Hf braze alloy (consisting of 27.2% Hf and 72.8% Co by weight) and the MarM509B braze were effective in repairing cracks in FSX-414 Co-base superalloy nozzle segments. Since nozzle segments have been shown to contain cracks up to 1.5 mm in width, the Co-Hf and MarM509B braze alloys were mixed with MarM509 superalloy powder to facilitate a wide gap ADH braze repair.
- ADH braze repair of FSX-414 using the novel MarM509/MarM509B and MarM509/Co-Hf braze alloys resulted in high temperature tensile properties equivalent to those of weld repairs in the same parent material (using Nozzalloy filler metal). The creep rupture and low cycle fatigue (LCF) properties of the braze joints were superior to those of welds performed using Nozzalloy or MarM918 filler metal.

- Statistical analysis of the LCF results revealed that FSX-414 welded with MarM918 suffered a 38% reduction in LCF life compared to the base metal. FSX-414 welded with Nozzalloy displayed a 27% reduction in LCF life, whereas four FSX-414 samples brazed with MarM509/MarM509B failed at the joint interface and suffered a 10% reduction in LCF life.
- FSX-414 samples braze repaired using the novel MarM509/Co-Hf braze alloy consistently failed in the base metal under low cycle fatigue conditions, implying that the LCF properties of the braze joint were superior to those of the base metal. This suggests that failure is likely to occur preferentially in the base metal if cracks in FSX-414 nozzle segments are ADH braze repaired using this braze alloy. A braze alloy consisting of a mixture of 60% MarM509 powder (by weight) and 40% eutectic Co-Hf powder therefore has considerable potential for crack repair of nozzle segments in industry.

CHAPTER 15 – RECOMMENDATIONS FOR FUTURE WORK

- The results of SEM-EDS and electron microprobe analyses of the braze joints suggested that the intermetallic compound observed in the binary and more complex Ni-Hf joints was the nonequilibrium Ni_7Hf_2 phase, whereas the intermetallic phase observed in the Ni-Zr joints was most likely Ni_5Zr. In order to confirm the chemical composition and structure of the intermetallic phases observed in the braze joints, transmission electron microscopy work is recommended.

- Experiment 10, reported in Chapter 12, demonstrated that a complex Ni-base braze alloy with a composition of Ni-8.4Cr-5.4W-1.6Ti-6.1Al-14.5Hf (wt.%) (referred to as alloy PV9025) had solidus and liquidus temperatures below those of the simple eutectic Ni-Hf braze alloy evaluated in earlier experiments. This braze alloy therefore holds promise for the repair of equiaxed, directionally solidified and single crystal Ni-base superalloys. Since the microstructure of this complex Ni-base alloy was evaluated in the as-cast condition, it is recommended that the alloy be mixed with Ni-base superalloy powder and used to produce a wide gap liquid phase diffusion bond in a γ' strengthened Ni-base superalloy, such as In738. The properties of the braze samples should then be evaluated in the fully heat treated and aged condition. Such an evaluation should include examination of the joint microstructure using optical microscopy, scanning electron microscopy and electron microprobe techniques, and full mechanical testing (including elevated temperature tensile tests, creep rupture tests and low cycle fatigue tests).

- The results of Experiment 11, described in Chapter 13, revealed that ADH braze repair of wide cracks in FSX-414 cobalt-base superalloy nozzle segments using novel MarM509/MarM509B or MarM509/Co-Hf ADH braze mixtures resulted in excellent joint mechanical properties. The braze joints displayed tensile properties at elevated temperature equivalent to those of the base metal, and creep rupture properties superior to those of weld repairs in the same base metal. The low cycle fatigue properties of the MarM509/Co-Hf joints were shown to be at least equivalent to those of the FSX-414 base metal, with failure occurring in the base metal of all the joints evaluated. In order to further characterize these novel ADH braze alloys, it is recommended that the microstructures of MarM509/MarM509B and MarM509/Co-Hf joints be characterized using optical microscopy, scanning electron microscopy and electron microprobe analysis techniques.

- FSX-414, the Co-base superalloy currently used by GE Energy Services for casting nozzle segments, is recognized as having mechanical properties inferior to those of the Co-base superalloys used by a number of other original engine manufacturers (OEM's) for the same application. Siemens Westinghouse, an OEM, uses ECY 768 Co-base superalloy for nozzle segment casting, whereas Pratt & Whitney, Siemens and Alstom, also OEM's, use MarM509. Future work should evaluate the mechanical integrity of ADH braze joints produced using the novel MarM509/MarM509B and MarM509/Co-Hf ADH braze mixtures in these higher strength Co-base superalloys.

CHAPTER 16 – REFERENCES

[1] Sheward, G.E., and Bell, G.R. "Development and evaluation of a Ni-Cr-P brazing filler metal". *Welding Journal*, vol. 55, no. 10. October 1976. pp. 285s-292s.

[2] *ASM Handbook: Volume 3 - Alloy Phase Diagrams*. ASM International, Metals Park, OH. 1992. pp. 2.127 (Ni-Cd binary phase diagram), 2.143 (Co-Hf binary phase diagram), 2.241 (Ni-Hf binary phase diagram), 2.321 (Ni-Zn binary phase diagram) and 2.322 (Ni-Zr binary phase diagram).

[3] Lugscheider, E., and Kim D.-S. "New low-melting nickel-based high-temperature brazing alloys". *Schweissen und Schneiden*, vol. 43, no. 4. April 1991. pp. 222-226.

[4] Lugscheider, E., and Partz, K.-D. "High-temperature brazing of stainless steel with nickel-base filler metals BNi-2, BNi-5 and BNi-7". *Welding Journal*, vol. 62, no. 6. June 1983. pp. 160s-165s.

[5] Johnson, C. "The use of TETIG diagrams in high-temperature brazing". *Welding Journal*, vol. 60, no. 10. October 1981. pp. 185s-193s.

[6] Sakamoto, A., Fujiwara, C., Hattori, T, and Sakai, S. "Optimizing processing variables in high-temperature brazing with nickel-based filler metals". *Welding Journal*, vol. 68, no. 3. March 1989. pp. 63-71.

[7] Miyazawa, Y., and Ariga, T. "A study of the brazeability of nickel-based brazing filler metal foil for joining nickel base metal to mild steel base metal". *Welding Journal*, vol. 71, no. 7. July 1993. pp. 294s-300s.

[8] Kavishe, F.P.L., and Baker, T.J. "Influence of joint gap width on strength and fracture toughness of copper brazed steels". *Materials Science and Technology*, vol. 6, no. 2. February 1990. pp. 176-181.

[9] Lugscheider, E., and Krappitz, H. "The influence of brazing conditions on the impact strength of high-temperature brazed joints". *Welding Journal*, vol. 65, no. 10. October 1986. pp. 261s-267s.

[10] Draugelates, U., and Hartmann, K.-H. "Behaviour of brazed nickel alloy under cyclic and thermal load". *Welding Journal*, vol. 57, no. 10. October 1978. pp. 298s-302s.

[11] Tung, S.K., Lim, L.C., and Lai, M.O. "Solidification phenomena in nickel base brazes containing boron and silicon". *Scripta Materialia*, vol. 34, no. 5. March 1996. pp. 763-769.

[12] Johnson, R. "Microstructural aspects of brazing a ferritic steel with two Ni-Si-B braze filler metals". *Welding Journal*, vol. 57, no. 4. April 1978. pp. 93s-102s.

[13] Gale, W.F., and Wallach, E.R. "Influence of isothermal solidification on microstructural development in Ni-Si-B filler metals". *Materials Science and Technology*, vol. 7, no. 12. December 1991. pp. 1143-1148.

[14] Lasalmonie, A. "Diffusion brazing of nickel based superalloys: some basic aspects". *Annales de Chimie France*, vol. 12, no. 3. 1987. pp. 247-257.

[15] Savage, E.I., and Kane, J.J. "Microstructural characterisation of nickel braze joints as a function of thermal exposure". *Welding Journal*, vol. 63, no. 10. October 1984. pp. 316s-323s.

[16] Tung, S.K., Lim, L.C., and Lai, M.O. "Microstructural evolution and control in BNi-4 brazed joints of nickel 270". *Scripta Metallurgica et Materialia*, vol. 33, no. 8. October 1995. pp. 1253-1259.

[17] Lecomte-Martens. *Private communication* (repair company C.R.M., Belgium).

[18] Elder, J.E., Thamburaj, R., and Patnaik, P.C. "Braze repair of MA754 aero gas turbine engine nozzles". Proceedings of the *ASME Gas Turbine and Aeroengine Congress and Exposition* (Paper No. 89-GT-235). 4-8 June 1989. Toronto, Canada.

[19] Rose, D.P., Price, G., and Thyssen, J. "Development and evaluation of a repair for saddle cracks in a radial flow turbine wheel". Proceedings of the *Conference on Life Assessment & Repair: Technology for Combustion Turbine Hot Section Components*. 17-19 April 1990. Phoenix, Arizona, United States of America. pp. 271-286.

[20] Lee, J.W., McMurray, H.J., and Miller, J.A. "Development of a new brazing technique for repair of turbine engine components". *Welding Journal*, vol. 64, no. 10. October 1985. pp. 18-21.

[21] Hoppin, G.S., and Berry, T.F. "Activated Diffusion Bonding". *Welding Journal*, vol. 49, no. 11. November 1970. pp. 505s-509s.

[22] Demo, W.A., and Ferrigno, S.J. "Brazing method helps repair aircraft gas-turbine nozzles". *Advanced Materials & Processes*, vol. 131, no. 3. March 1992. pp. 43-45.

[23] Young, W.R. "Turbine airfoil repair". Proceedings of the *Conference on Materials Synergisms*. October 1978. Kiamesha Lake, New York, United States of America. pp. 924-938.

[24] Knotek, O., and Lugscheider, E. "Brazing filler metals based on reacting Ni-Cr-B-Si alloys". *Welding Journal*, vol. 55, no. 10. October 1976. pp. 314s-318s.

[25] Van Esch, H. "Braze repair techniques for gas turbine blades and vanes". *Turbomachinery International*, vol. 27, no. 7. September 1986. pp. 29-32.

[26] Su, C.Y., Chou, C.P., Wu, B.C., and Lih, W.C. "Microstructural characterisation of transient liquid phase zone of activated diffusion brazed nickel base superalloy". *Materials Science and Technology*, vol. 15, no. 3. March 1999. pp. 316-322.

[27] Chasteen, J.W., and Metzger, G.E. "Brazing of Hastelloy X with wide clearance butt joints". *Welding Journal*, vol. 58, no. 4. April 1979. pp. 111s-117s.

[28] Liburdi, J., Lowden, P., and Ellison, K. "Powder metallurgy repair technique." *US patent number US5156321*. 27 August 1990 (application date).

[29] Jahnke, B., and Demny, J. "Microstructural investigations of nickel-based repair coating processed by liquid phase diffusion sintering". *Thin Solid Films*, vol. 110, no. 3. December 1983. pp. 225-235.

[30] Miglietti, W.M., Curtis, R., Hall, B., and Lazarin, C.M. "Liquid phase diffusion bond repair of Westinghaus 501F, row 3 vanes". Proceedings of the *ASME Turbo Expo Conference 2000*. 2000. Münich, Germany.

[31] Miglietti, W.M., Kearney, J., and Pabon, L. "Liquid phase diffusion bond repair of Siemens V84.2, row 2 vanes and Alstom Tornado 2nd stage stator segments". Proceedings of the *ASME Turbo Expo Conference 2001*. 2001. New Orleans, United States of America.

[32] Miglietti, W.M.A. "Wide gap diffusion braze repair of Co-based industrial turbine vanes". Proceedings of the *International Brazing & Soldering Conference*. 2-5 April 2000. Albuquerque, New Mexico, United States of America. pp. 476-485.

[33] Miglietti, W.M.A. "Wide gap diffusion braze repair of Ni-based industrial turbine vanes". Proceedings of the *6th International Conference on Brazing, High Temperature Brazing and Diffusion Welding*. DVS Berichte, no. 212. 8-10 May 2001. Aachen, Germany. pp. 107-112.

APPENDIX A

MIGLIETTI, W.M., CURTIS, R., HALL, B., AND LAZARIN, C.M. "LIQUID PHASE DIFFUSION BOND REPAIR OF WESTINGHAUS 501F, ROW 3 VANES". PROCEEDINGS OF THE *ASME TURBO EXPO CONFERENCE 2000*. 2000. MÜNICH, GERMANY.

LIQUID PHASE DIFFUSION BOND REPAIR OF WESTINGHOUSE 501F, ROW 3 VANES

Warren M Miglietti , Rich Curtis, Brandon Hall and Christina M Lazarin
Sermatech International, Inc., Manchester, CT, 06040

ABSTRACT

During the industrial turbine engine operation of the W501F, Row3 Vanes, cracks develop as a result of thermal fatigue. Other damage found is pitting and dents resulting from corrosion/oxidation and FOD (foreign object damage) respectively. Erosion damage is also commonly found on the airfoils. Finally there is downstream deflection of the inner buttress/seal areas, as a result of axial creep. This paper describes the vacuum LPDB (liquid phase diffusion bond) repair process used to repair all of the above-mentioned damage, including LPDB build up and machining of the hook fit areas.

As a means of qualifying the high temperature diffusion bond process, both metallurgical and mechanical property evaluations were carried out. The metallurgical evaluation consisted of optical and scanning electron microscopy. The wide gap diffusion bonded area consisted of a fine-grained structure with carbide and boride phases dispersed both intergranularly and intragranularly. An EDAX analysis was also conducted and the results are reported.

The chemistry of the repaired area is similar to the base metal which may explain why mechanical tests revealed properties equivalent to that of the base metal. The mechanical evaluations undertaken were tensile tests at room temperature and elevated temperature, as well as stress rupture tests. These results were equivalent to mechanical properties of the X-45 Co-based superalloy, which is the base metal of the vane.

INTRODUCTION

Brazing has been utilised for decades now to repair aircraft engine vane and nozzle segments. It has only being the last 5 years that a variant of brazing has been utilised for Industrial Gas Turbine (IGT) vane and nozzle repairs. The wide gap brazing process was made popular by GE's and Pratt and Whitney's ADH (activated diffusion healing) (Demo and Ferrigno,1992) and Turbofix processes respectively. Many repair vendors have their own proprietary wide gap braze process such as SNECMA's RBD (rechargement per brasage diffusion), Howmet's ESR (effective structural repair) (Wustman and Smith,1996), and Chromalloy's SRB (surface reaction braze) (Bell,1985). Other wide gap joining processes available are LPDS (liquid phase diffusion sintering), Liburdi's LPM (Liburdi powder metallurgy) (Ellison, Lowden and Liburdi,1992) and Sermatech's "Sermafill" process. The latter 3 processes do not comply exactly with the definition of brazing as defined by the American Welding Society (AWS Welding Handbook, Vol. 2). Hence liquid phase diffusion sintering as referred to by Siemens/Westinghouse, powder metallurgy as referred to by Liburdi Engineering and liquid phase diffusion bonding (LPDB) as referred to by Sermatech are relatively new names appearing on the technological list of techniques to repair vanes and nozzles.

The object of this paper is to describe the use of the liquid phase diffusion bonding process, (which Sermatech have as their trademark the Sermafill process) for Westinghouse 501F, Row 3 vane repairs, and to compare this process with the traditional wide gap braze process. The former process is proprietary and hence exact precise temperatures and times, chemical compositions etc. cannot be documented; nevertheless, ranges of temperature and times are documented.

The LPDB process was qualified by undertaking a metallurgical evaluation and a mechanical property evaluation to show that metallurgically sound and high strength joints resulted. This LPDB process was used to restore wall thickness on the concave and convex surfaces of the airfoil, repair cracks,

pits/dents and build up the hook fit areas as a result of downstream deflection of the inner buttress/seal areas, as a result of axial creep. Figure 1 shows a typical example of a W501F, Row 3 vane with 3 airfoils. The vane is cast from a Cobalt superalloy referred to as X-45. Its chemical composition is Co-25.5Cr-10.5Ni-7W-0.25C-2(max)Fe-0.010B. The high Cr content contributes to corrosion, low temperature oxidation and sulphidation resistance.

Figure 2 shows typical cracking on the shroud and fillet areas as revealed by FPI (fluorescent particle inspection), while fig's 3, 4 and 5 show individual cracks in more detail. These cracks are wide 2.5mm (0.1'') and hence conventional narrow gap brazing cannot be utilised as a repair technique. The hook fit area, which needs to be rebuilt, is shown in fig 6.

Figure 1 – View of W501F, Row 3 vane

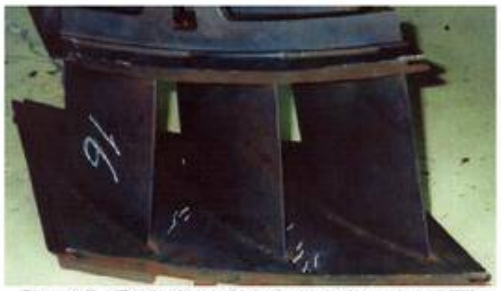

Figure 2 – Typical cracking on the shroud and fillet areas

The largest width of crack found on this engine set was 3.2mm (0.125''). Therefore for the process qualification the mechanical property tests (namely tensile and stress rupture) where undertaken on samples where the joint gap was 3.2mm (0.125''). The process is not limited to this gap and the largest gap repaired to date has been 10mm.

PROCESS EXPERIMENTAL PROCEDURE

Tensile tests at room temperature (21°C) and elevated

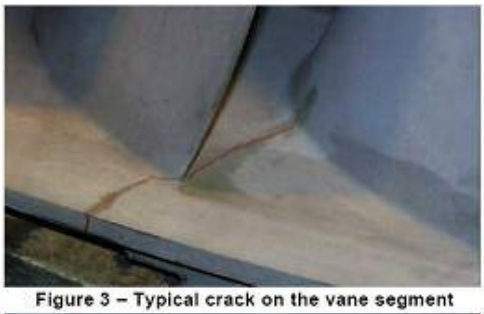

Figure 3 – Typical crack on the vane segment

Figure 4 – Typical crack on the vane segment

Figure 5 – Typical crack on the vane segment

Figure 6 – Hook fit area, which needs to be restored

temperatures, as well as stress rupture tests were undertaken. The test specimens were prepared in a butt joint configuration as seen in fig 7. The joint is in the centre of the gauge length and was 3.2mm wide.

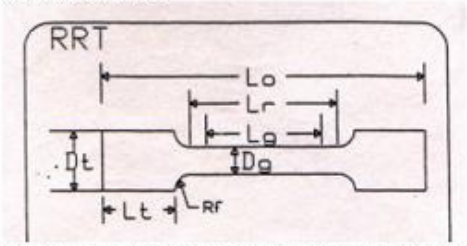

D_g=4.57mm, L_g=18.29mm, L_r=21.84mm, L_o=46.51mm, R_f =3.18mm, D_t=(5/16-24NF-2A inches) and L_t=9.53mm

Figure 7 – Configuration of tensile and stress rupture test specimens

Figure 8 shows the set up for the samples utilised for the metallographic evaluation. Molybdenum sheet stock was utilised to keep the joint gap uniform at 3.2mm in width. Conventional metallographic techniques were used for the metallurgical investigation.

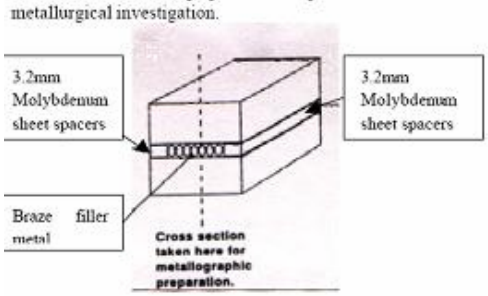

Figure 8 – Schematic representation of sample set for metallurgical evaluation

TENSILE AND STRESS RUPTURE TEST SPECIMEN PREPARATION

Mechanical test specimens according to the configuration shown in fig 7 were prepared as follows:

a) Obtain scrap vane and cut/grind away sections from the shroud area of the vane.
b) Machine rectangular sections of 12.5mm (0.5'') X 12.5mm (0.5'') X 55.9mm (2.2'')
c) Cut sample in half.
d) Grind the mating surfaces flat.
e) Grit blast surfaces with silicon carbide.
f) Shim gap at 3.2mm (0.125'').
g) Apply paste to the joint gap.
h) Place samples in fixture to maintain alignment.
i) Set in vacuum furnace.
j) Process between 1120°C (2048°F) and 1200°C (2192°F).
k) Isothermally process at the above-mentioned range for 4-20 hours.
l) Age at 982°C (1800°F) for 4hours.
m) Machine samples to the configuration shown in fig 7.
n) Send machined specimens for X-ray to determine if porosity greater than 1.3mm (0.050'') and for lack of bonding to the mating surfaces exist.

RESULTS AND DISCUSSION OF MECHANICAL PROPERTY TESTING

Table 1 below shows the results of the tensile tests undertaken at room temperature and elevated temperatures of 650°C, 760°C and 980°C. As can be seen the tensile and yield strengths are equivalent to the values quoted in the Metals Handbook. The ductility of the "Sermafill" joints appears low, and is typically 25-51% of the values quoted in the Metals Handbook.

Table 1: Tensile Strength of X-45 processed with "Sermafill"1 Filler Metal

TEMPERATURE		TENSILE STRENGTH		YIELD STRENGTH		ELONGATION	RA
°C	°F	MPa	ksi	MPa	Ksi	%	%
21	70	773	112	505	73.2	4.5	1.6
21	70	763	110	531	77	4.4	1.6
21	**70**	**745**	**108**	**525**	**76**	**8**	?
650	1200	520	75.4	304	46.8	6.4	7.1
650	1200	446	64.6	306	44.3	3.1	4.3
650	**1200**	**515**	**74.6**	**260**	**38**	**12**	?
760	1400	509	73.8	311	45.1	2.9	3.9
760	1400	451	65.4	315	45.7	3.6	3.6
760	1400	450	65.2	341	49.4	2.9	3.9
760	1400	448	64.9	311	45.1	3.3	3.1
760	**1400**	**485**	**70**	?	?	**9**	?
980	1800	214	31	?	?	4.9	?
980	**1800**	**200**	**29**	?	?	**16**	?

NOTE: **Values in Bold are for X-45 parent alloy (Metals Handbook Vol3, ninth edition)**

To verify if the elongation is as low as the data indicates, some X-45 material was taken from the shroud area of a vane. This material was machined to the configuration shown in fig 7 and subjected to the Sermafill heat treatment cycle. Table 2 shows the results of the X-45 specimens removed from the vane segment.

As seen in Table 2 the mechanical properties of the X-45 taken from the actual vane casting is lower than that quoted in the Metals Handbook, especially the ductility. Therefore the Sermafill joints have ductility in the order of 80% of the X-45 casting material. This is acceptable and the 20% loss in ductility

is attributed to the few brittle boride phases present in the 3.2mm (0.125") wide gap joint.

Table 2: Tensile strength of X-45 material taken from the vane

TEMPERATURE		TENSILE STRENGTH		YIELD STRENGTH		ELONGATION	RA
°C	°F	MPa	ksi	MPa	ksi	%	%
21	70	738	107	514	74.5	5.6	5.6
21	**70**	**745**	**108**	**525**	**76**	**8**	**?**

NOTE: **Values in Bold are for X-45 parent alloy (Metals Handbook Vol3, ninth edition)**

Table 3 shows the stress rupture properties of the "Sermafill 1" joints

Table 3: Stress rupture properties of X-45 processed with " Sermafill" 1 Filler Metal

TEMPERATURE		STRESS LEVEL		HOURS TO FAILURE	ELONGATION	RA
°C	°F	MPa	ksi	hrs	%	%
760	1400	260	38	92	?	?
760	**1400**	**260**	**38**	**100**	**?**	**?**
760	1400	193.2	28	513.9*	31.7	48.3
760	1400	193.2	28	566.5*	29.1	48.1
760	1400	193.2	28	507.1*	35.2	48.5
871	1600	103.5	15	365*	27.7	34.5
871	1600	103.5	15	344.2*	16.4	33.6
871	1600	103.5	15	336.3*	20.7	32

NOTE: **Values in Bold are for X-45 alloy (Metals Handbook Vol3, ninth edition)**

- **means that failure occurred in the base metal**

As seen in Table 3, the stress rupture properties of the joints are a minimum of 92% of the base metals stress rupture properties. In fact most of the failure occurred in the base metal, which is a good result.

To compare the results of the Sermafill wide gap joints with a more tradtional wide gap braze process, a 70%X-45 and 30%braze mixture was developed. Some samples were brazed with the same joint gap and at the same process parameters as those of the "Sermafill" joints. The 30% braze used in the mixture had a composition Co-40Ni-24.5Cr-3B.

Tables 4 and 5 show the tensile test results and stress rupture results respectively, of the joints brazed with the 70/30 mixture. As seen in these tables the strength of the brazed joint is 74%-80% of the base metals strength, the elongation is 50% of the cast X-45 vane material and the stress rupture life varies from 58-62% of the parent metals life. This is undesirable if the objective is to have a structural repair, where the properties of the repaired areas are equivalent to the base metal. Clearly the "Sermafill" type joints have superior mechanical properties when compared to a more traditional wide gap braze joint, and the properties are equivalent to the base metal as seen in Tables 1 and 3.

Table 4: Tensile strength of X-45 brazed with a traditional type filler metal

TEMPERATURE		TENSILE STRENGTH		YIELD STRENGTH		ELONGATION	RA
°C	°F	MPa	ksi	MPa	ksi	%	%
21	70	555.5	80.5	466.4	67.6	2.6	3.3
21	70	554.1	80.3	437.5	63.4	2.8	2.4
21	70	531.3	77.0	444.7	64.3	3.4	4.8
21	**70**	**745**	**108**	**525**	**76**	**9**	**?**
21	70	738	107	514	74.5	5.6	5.6
540	1004	405	58.7	254.6	36.9	3.1	2.6
540	1004	411.9	59.7	253.9	36.8	3.5	2.2
540	1004	380.9	55.2	285	41.3	4.9	1.9
540	1004	391	56.7	300.3	43.5	2.1	1.7
540	**1004**	**550**	**79.7**	**275**	**40**	**17**	**?**
650	1200	381.6	55.3	216.7	31.4	6.3	3.1
650	1200	391.2	56.7	216.7	31.4	3.4	1.7
650	1200	400.2	58	228.4	33.1	3.7	2.3
650	1200	393.3	57	227.7	33	3.6	2.2
650	**1200**	**515**	**74.6**	**260**	**38**	**12**	**?**

NOTE: **Values In Bold Are For X-45 Alloy (Metals Handbook Vol3, ninth edition)**

NOTE: Values underlined are from an actual cast vane

Table 5: Stress Rupture properties of X-45 brazed with a traditional type filler metal

TEMPERATURE		STRESS LEVEL		HOURS TO FAILURE	ELONGATION	RA
°C	°F	MPa	ksi	hrs	%	%
760	1400	260	38	61.4	?	?
760	1400	260	38	58.2	?	?
760	**1400**	**193.2**	**38**	**100**	**?**	**?**

NOTE: **Values in Bold are for X-45 alloy (Metals Handbook Vol3, ninth edition)**

RESULTS AND DISCUSSION OF THE METALLURGICAL EVALUATION

Figure 9 shows the microstructure of the base metal, which consists of a dendritic structure with Cr-carbides occurring intergranularly.

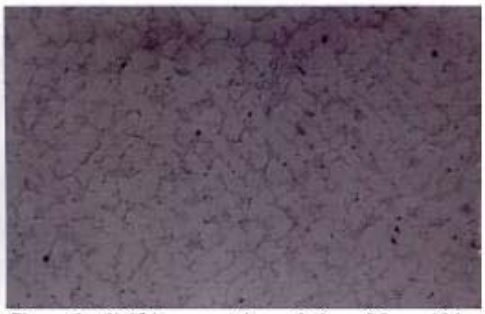

Figure 9 – X-45 base metal consisting of Cr-carbides dispersed intergranularly. Mag. 50X

Figures 10, 11, 12 and 13 all show the "Sermafill'ed" joint on the X-45 substrate, at increasing levels of magnification. Some boride phases can be seen in fig 13 and they resemble the Cr-carbide phases present in the base metal.

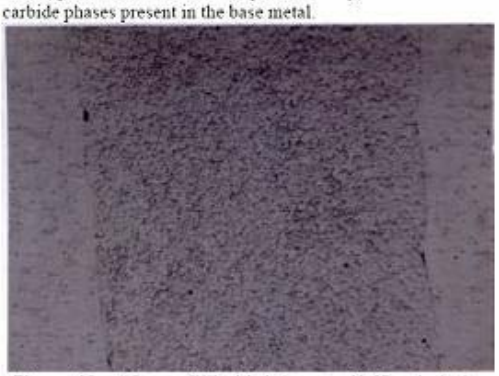

Figure 10 – "Sermafill'ed joint on an X-45 substrate. Mag. 50X

Figure 11 – LPD Bonded "Sermafill'ed joint on a X-45 substrate. Mag.100X

Figure 14 shows the joint interface. Clearly there is excellent bonding and adhesion to the mating surfaces.

A stress rupture sample (#3), which was tested at 760°C/193.2MPa and failed in the base metal, was subjected to a metallurgical evaluation using optical and scanning electron microscopy. Figure 15 shows the fractured piece, where the joint is intact. A semi quantitative and qualitative analyses on the base metal and joint can be seen in fig's 16 and 17. Essentially the elements of Co, Cr, Ni and W were found in the X-45 base metal, except the W concentration was higher than normal. (Perhaps the analysis was taken close to a W-carbide phase.) The LPD bonded joint had the same elements as the base metal, except for Ta, which is present in the chemistry of the "Sermafill" paste.

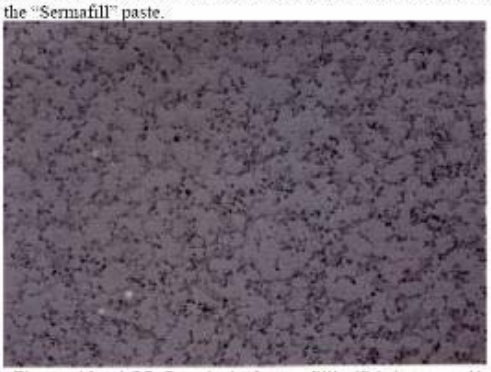

Figure 12 – LPD Bonded "Sermafill'ed" joint on a X-45 substrate. Mag. 200X

Figure 13 – LPD Bonded "Sermafill'ed" joint on a X-45 substrate. Mag. 500X

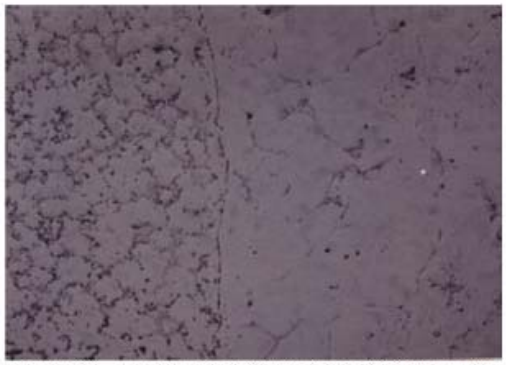

Figure 14 – LPD Bonded "Sermafill'ed" joint on a X-45 substrate. Mag. 200X

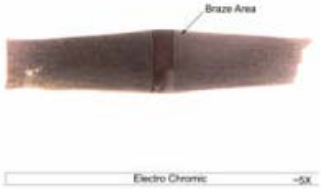

Figure 15 – Fractured stress rupture sample

Figure 16 – Semi-qualitative and semi-quantitative analylsis of the X-45 base metal

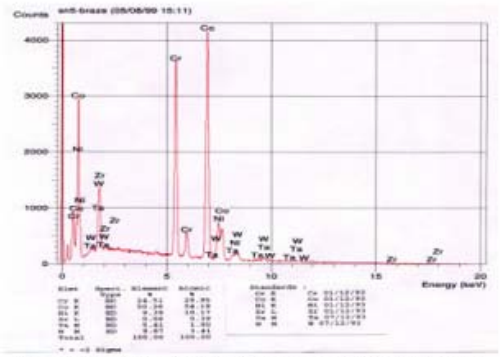

Figure 17 – Semi-qualitative and semi-quantitative analysis of the LPD bonded joint

Figures 18, 19, 20 and 21 show the above-mentioned stress ruptured LPD bonded joint at increasing magnifications. The phases seen on the grain boundaries in figure 22, are either Cr-borides or carbides, and W-borides or carbides respectively, as represented in the semi-qualitative and quantitative analyses seen in figures 23 and 24. As the EDAX system on the SEM could not detect either B or C it was difficult to precisely state the phases that formed in the joint.

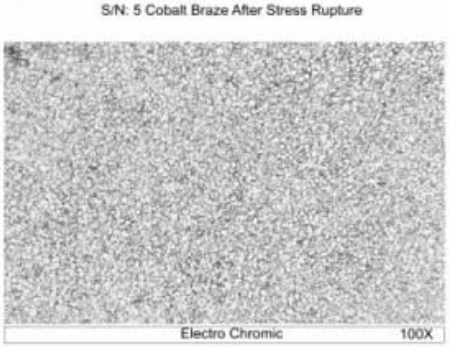

Figure 18 – Microstructure of a stress rupture tested, LPD bonded joint on a X-45 substrate. Mag. 100X

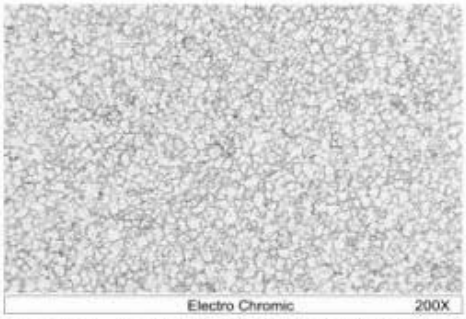

Figure 19 – Microstructure of a stress rupture tested, LPD Bonded joint on a X-45 substrate. Mag. 200X

S/N: 5 Cobalt Braze After Stress Rupture

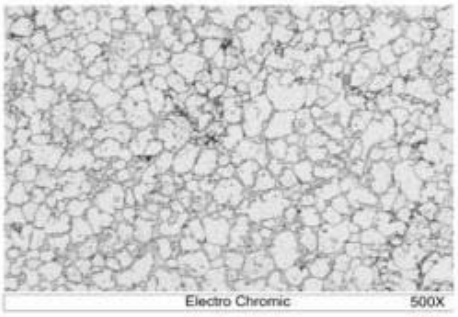

Figure 20 – Microstructure of a stress rupture tested, LPD Bonded joint on a X-45 substrate. Mag. 500X

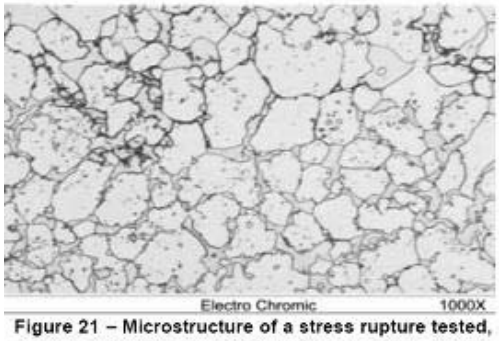

Figure 21 – Microstructure of a stress rupture tested, LPD Bonded joint on a X-45 substrate. Mag. 1000X

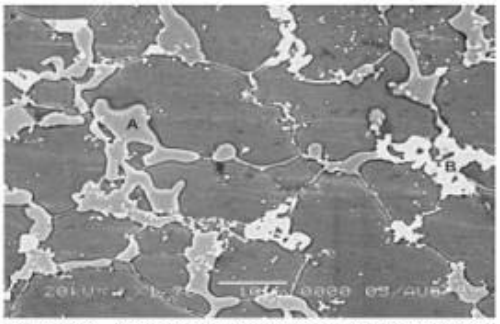

Figure 22 – Phases analysed on the grain boundaries of the LPD bonded joints.

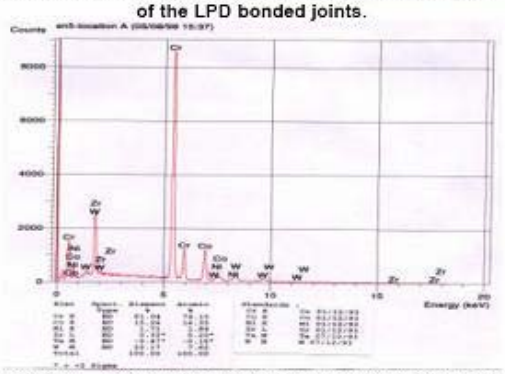

Figure 23 – Semi-qualitative and semi-quantitative analysis of the phase labeled "A" along the grain boundaries of a LPD bonded joint, after stress rupture testing.

The samples which, where wide gap brazed and the tensile and stress rupture test results were reported in Tables 4 and 5 respectively, were also metallographically examined to find a reason for the reduction in mechanical properties when compared to the LPD bonded joints. Figure 25 shows a macrograph of the brazed area. Figures 26, 27, 28 and 29 all show the wide gap braze joint at different magnifications. Clearly as seen in fig's 28 and 29, the grain boundaries of the joint consist of a large network/chain of elongated brittle boride phases. Comparing fig's 20 and 21, with 28 and 29, there is clear distinguishable difference as to the grain boundary morphology of the LPD bonded joints and the wide gap braze joints. The large network/chain of elongated brittle boride phases in the wide gap brazed joint is the predominant reason for the reduction in mechanical properties, including elongation.

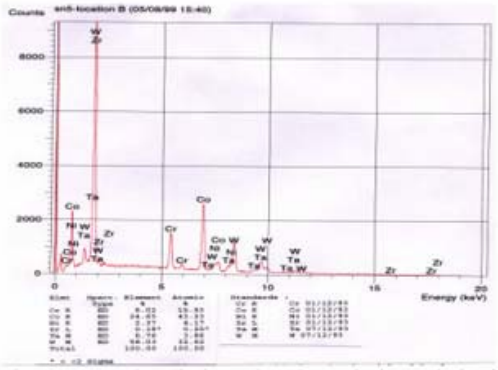

Figure 24 – Semi-qualitative and semi-quantitative analysis of the phase labeled "B" along the grain boundaries of a LPD bonded joint, after stress rupture testing.

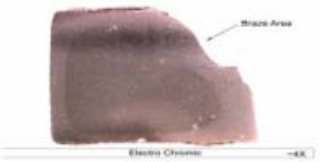

Figure 25 – Macrograph of the wide gap brazed joint.

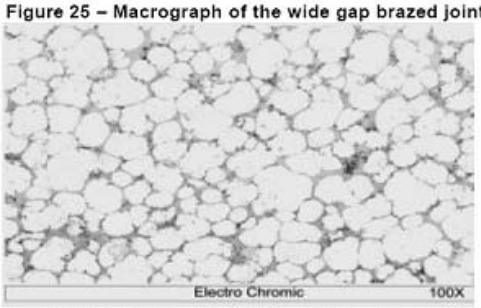

Figure 26 – Traditional type wide gap brazed joint on a X-45 substrate. Mag.100X

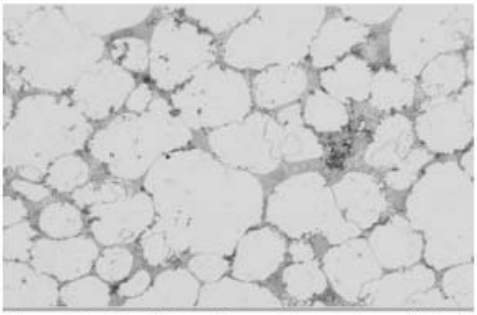

Figure 27 – Traditional type wide gap brazed joint on a X-45 substrate. Mag. 200X

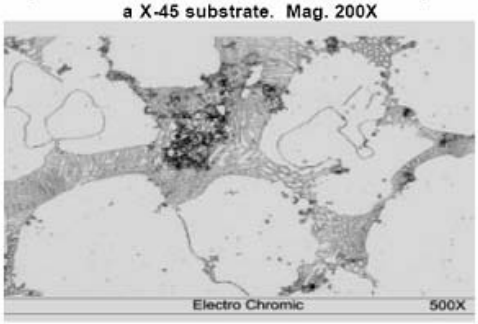

Figure 28 – Traditional type wide gap brazed joint on a X-45 substrate. Mag. 500X

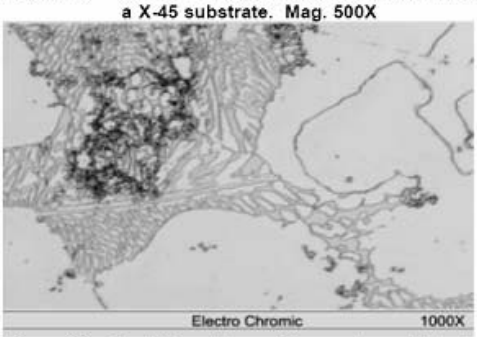

Figure 29 – Traditional type wide gap brazed joint on a X-45 substrate. Mag.1000X

Figure 30 shows an area in the wide gap brazed joint, along the grain boundary, where 3 phases were analysed. The braze area as seen in figure 31, contains Co, Cr, Ni, Ta and W, and the W and Ni percentages are higher than that present in the LPD bonded joints. The 3 phases identified were 2 Ta rich phases as seen in figures 32 and 33 (probably Ta-carbide) and a Cr, W rich phase as seen in figure 34 (probably a Cr, W boride).

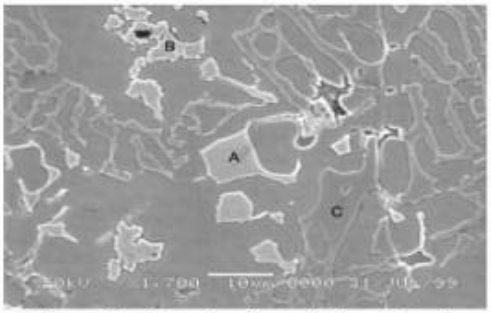

Figure 30 – Area along the grain boundary of a traditional wide gap braze where 3 phases where analysed.

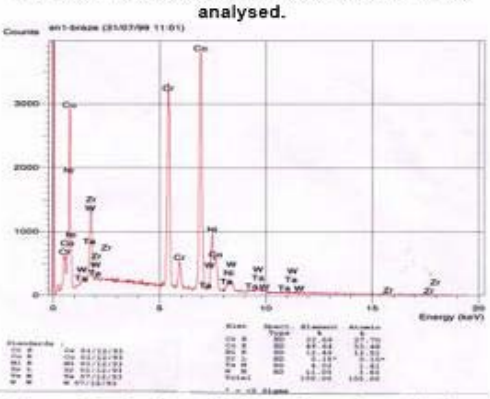

Figure 31 – Semi-qualitative and semi-quantitative analysis of the traditional type wide gap braze.

Figure 32 – Semi-qualitative and semi-quantitative analysis of the phase"A", along the grain boundary of a traditional type wide gap braze.

Figure 33 – Semi-qualitative and semi-quantitative analysis of the phase"B", along the grain boundary of a traditional type wide gap braze.

Figure 34 – Semi-qualitative and semi-quantitative analysis of the phase"C", along the grain boundary of a traditional type wide gap braze.

FIRST ARTICLE REPAIR DEMONSTRATION

An engine run vane with the types of damage shown in fig's 2-6 was obtained. The cracks were ground/routed out and then were repaired using the LPDB process "Sermafill". Figures 35 (a and b), 36 (a and b), 37 (a, and b), 38 (a and b), 39 (a and b), 40 (a and b) and 41 (a, b, c and d) all show the routed cracks and the very same repaired area. The crack in fig 41 is a through wall crack, hence fig's 41(c) and (d) are photographs taken from the opposite side of the through wall crack.

Figure 35(a) – Routed crack

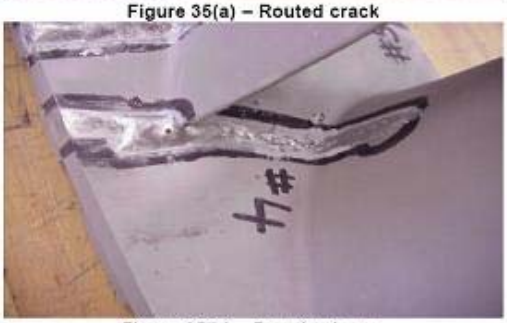

Figure 35(b) – Repaired area

Figure 36(a) – Routed crack

Figure 36(b) – Repaired area

Figure 37(a) – Routed crack

Figure 37(b) – repaired area

Figure 38(a) – Routed crack

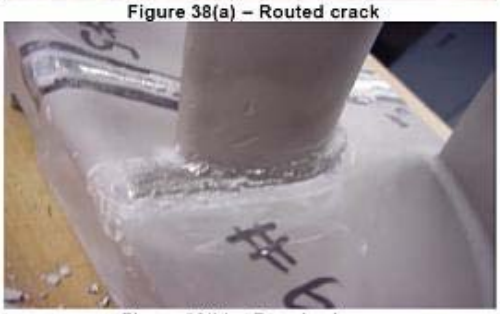

Figure 38(b) – Repaired area

Figure 39(a) – Routed crack

Figure 39(b) – Repaired area

Figure 40(a) – Routed crack

Figure 40(b) – Repaired area

Figure 41(a) – Routed crack

Figure 41(b) – Repaired area

Figure 41 (c) – Repaired area

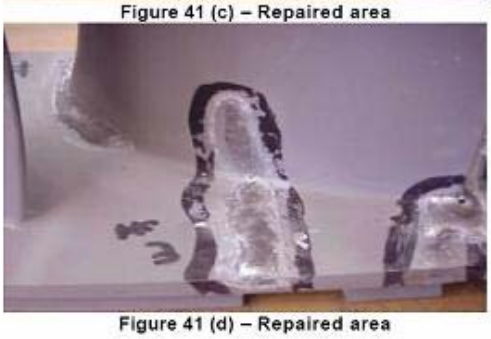

Figure 41 (d) – Repaired area

Figures 42(a) and (b) show the build up of the hook fit areas, which was required because of downstream deflection of the inner buttress/seal areas, as a result of axial creep.

Figure 42(a) – Hook fit restoration, using paste.

Figure 42(b) – Hook fit restoration, using pre-sintered plate.

METALLURGICAL EVALUATION OF FIRST ARTICLE REPAIR DEMONSTRATION

The cracks repaired (in fig's 35 – 41) using the LPDB process, were sectioned and a conventional metallurgical analysis was conducted. Figure 43 shows a macrograph taken through the crack. The paste has filled the complete cavity of the crack and there is good bonding to the sidewalls of the routed out crack. A semi-quantitative and qualitative analyses on the base metal and joint can be seen in fig's 44 and 45. Essentially the elements of Co, Cr, Ni and W were found in the X-45 base metal as seen in figure 44. The LPD bonded repaired joint not only had the same elements as the base metal, (except for Ta, which is present in the chemistry of the "Sermafill" paste) but the elements only differed by 1% when comparing the chemistry of the 2 regions.

Figure 43 – Macrograph taken through a crack repaired with the "Sermafill" process

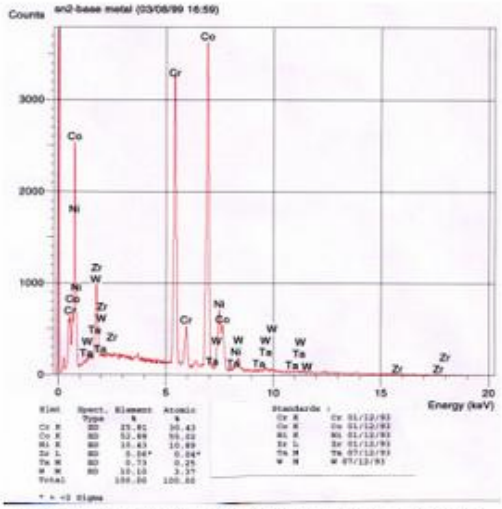

Figure 44 – Semi-qualitative and semi-quantitative analysis of the X-45 base metal.

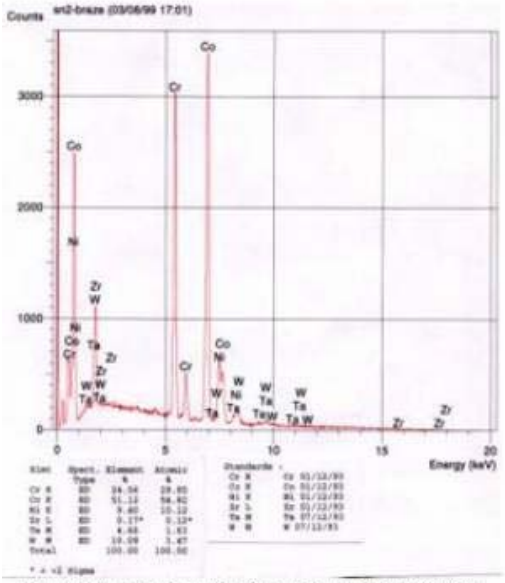

Figure 45 – Semi-qualitative and semi-quantitative analysis of the crack repaired region i.e. the "Sermafill'ed" joint.

Figures 46, 47 and 48 show at different magnifications, the microstructure of the repaired crack region using the "Sermafill" process. The microstructure is similar to that present in figures 11, 12 and 13 or figures 18, 19 and 20.

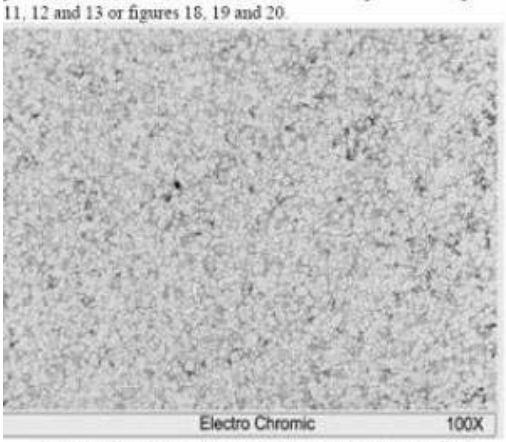

Figure 46 – Microstructure of the crack repaired region using the LPDB/"Sermafill" process. Mag. 100X

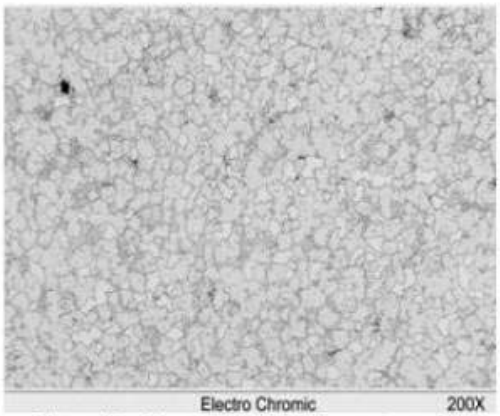

Figure 47 – Microstructure of the crack repaired region using the LPDB/ "Sermafill" process. Mag. 200X

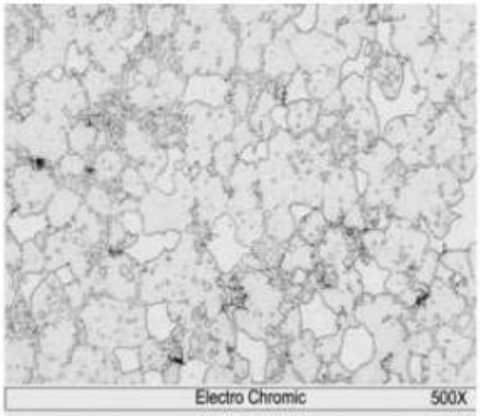

Figure 48 – Microstructure of the crack repaired region using the LPDB/ "Sermafill" process. Mag 500X

The phases seen on the grain boundaries in fig 49, are either W-borides or carbides, and Cr-borides or carbides respectively, as represented in the semi-qualitative and quantitative analyses seen in fig's 50 and 51. As the EDAX system on the SEM could not detect either B or C it was difficult to precisely state the phases that formed in the joint. From the phase morphology it is probably a Cr-carbide phase and W-boride phase that is present in the repaired area.

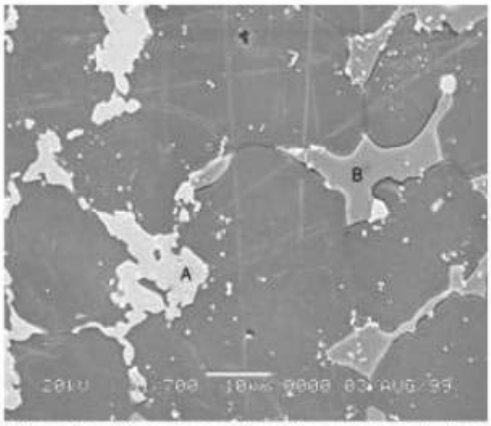

Figure 49 – Phases present on the grain boundaries of a crack repaired area

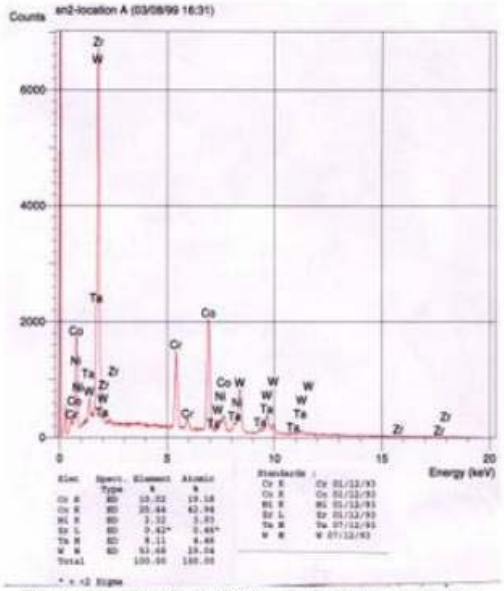

Figure 50 – Semi-qualitative and semi-quantitative analysis of the phase "A", along the grain boundary of a repaired crack using the LPDB/ "Sermafill" process.

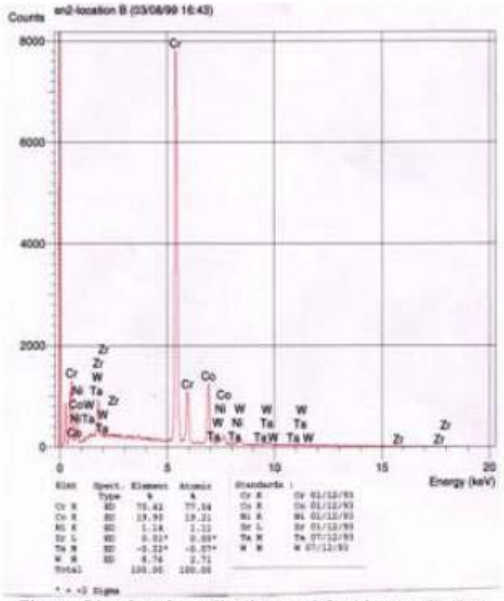

Figure 51 – Semi-qualitative and Semi-quantitative analysis of the phase "B", along the grain boundary of a repaired crack using the LPDB/ "Sermafill" process.

POSSIBLE WORKSCOPE FOR REPAIR OF W501F, ROW 3 VANES

- Incoming inspection for damage
- Inspect cooling holes for damage
- Airflow a percentage of the vanes
- Disassemble the vanes
- Vibropeen appropriate parts
- Rout out cracks and appropriate indications
- Grit blast
- Acetone clean
- Repair all areas including the hook fit region, using the "Sermafill" process. Note this process incorporates a heat treatment at 1150°C (2100°F) for 4 hours
- Blend repaired area to proper contour
- EDM cooling holes
- Inspection
- Heat treat at 982°C (1800°F) for 4 hours
- Blast clean
- Machine vane segments
- Record final dimensions
- Assemble the vanes
- Airflow the vanes
- Final inspection

SUMMARY AND CONCLUSIONS

- The use of the LPDB ("Sermafill") process, results in a repaired joint, which has mechanical properties (tensile and stress rupture) equivalent to that of the base metal.
- The microstructure of the joint shows no signs of large networks of brittle boride phases, known to significantly reduce mechanical properties and ductility. Only isolated boride phases were seen in the repaired area.
- The LPDB process yields superior mechanical properties when comparing with the traditional wide gap brazing process.
- Based on the metallurgical and mechanical results obtained in this in-house research project, the use of the LPDB ("Sermafill") process is a suitable alternative to the traditional Gas Tungsten Arc weld approved repair process specified by the OEM.
- At the time of drafting this document, approval has been granted by the OEM for the LPDB repair of only the hook fit areas of this vane segment. Therefore at this stage the crack repair has nearly completed its developmental stage and is therefore not in production.
- The LPBD ("Sermafill") process is ideally suited for crack repair, wall thickness repair of the convex and concave surfaces and dimensional restoration of the hook fit and race track areas of all Co-based vanes.
- This process also works well on Ni-base superalloy components and this will form the basis of a paper in the near future.

ACKNOWLEDGMENTS

The authors acknowledge the help of Jan Williams and Kevin Pelletier of Dirats Laboratory for the mechanical testing and metallographic work.

REFERENCES

Demo, W.A and Ferrigno, S.J, 1992, "Brazing method helps repair aircraft gas –turbine nozzles", Advanced Materials and Processes, Vol 141, No.3, pp43-45

Wustman, R.D and Smith, J.S, 1996, "High strength diffusion braze repairs for gas turbine components", ASME paper 96-GT-427

Bell, S, 1985, "Repair and Rejuvenation procedures for aero gas-turbine hot section components", Material Science and Technology, Aug, Vol 1, pp629

Ellison, K.A, Lowden, P and Liburdi, J, 1992, "Powder metallurgy Repair of Turbine Components", ASME paper 92-GT-312

AWS Welding Handbook, Vol2, 8th edition, pp380

Metals Handbook, Vol3, 9th edition

APPENDIX B

MIGLIETTI, W.M., KEARNEY, J., AND PABON, L. "LIQUID PHASE DIFFUSION BOND REPAIR OF SIEMENS V84.2, ROW 2 VANES AND ALSTOM TORNADO 2ND STAGE STATOR SEGMENTS". PROCEEDINGS OF THE *ASME TURBO EXPO CONFERENCE 2001*. 2001. NEW ORLEANS, USA.

LIQUID PHASE DIFFUSION BOND REPAIR OF SIEMENS V84.2, ROW 2 VANES AND ALSTOM TORNADO, 2ND STAGE STATOR SEGMENTS

Warren M Miglietti , John Kearney and Luis Pabon
Sermatech International, Inc., Manchester, CT, 06040

ABSTRACT

During the industrial turbine engine operation of the Siemens V84.2, Row 2 vanes, and the Alstom Tornado, 2nd stage stator segments, "craze-cracking" and isolated thermal fatigue cracks develop during engine operation. Other damages found include pitting and dents resulting from corrosion/erosion and FOD (foreign object damage), respectively. Erosion and oxidation damage is also commonly found on the airfoils. This paper describes the vacuum LPDB (liquid phase diffusion bond) repair process used to repair all of the above-mentioned damage.

As a means of qualifying the high temperature diffusion bond process, both metallurgical and mechanical property evaluations were carried out. The metallurgical evaluation consisted of optical and scanning electron microscopy. The wide gap diffusion bonded area consisted of a fine-grained structure with intermetallic phases dispersed both intergranularly and intragranularly. An Energy Dispersive X-ray analysis was also conducted and the results are reported.

The chemistry of the repaired area is similar to the base metal which may explain why mechanical tests revealed properties equivalent to that of the base metal. The mechanical evaluations undertaken were tensile tests at room temperature and elevated temperature, as well as stress rupture tests. These results were equivalent to mechanical properties of the IN738 and IN939 Ni-based superalloys, which is the base metal that the above mentioned vanes and stator segments are manufactured from.

INTRODUCTION

Brazing has been utilised for decades, to repair aircraft engine vane and nozzle segments. It has only been the last five years that a variant of brazing has been utilised for Industrial Gas Turbine (IGT) vane and nozzle repairs. The traditional wide gap brazing process was made popular by GE's and Pratt and Whitney's ADH (activated diffusion healing) (Demo and Ferrigno, 1992) and Turbofix processes respectively. Many repair vendors have their own proprietary wide gap braze process such as SNECMA's RBD (rechargement per brasage diffusion), Howmet's ESR (effective structural repair) (Wustman and Smith, 1996), and Chromalloy's SRB (surface reaction braze) (Bell, 1985). Other wide gap joining processes available are LPDS (liquid phase diffusion sintering), Liburdi's LPM (Liburdi powder metallurgy) (Ellison, Lowden and Liburdi, 1992) and Sermatech's "SermaFill" process. The latter three processes do not comply exactly with the definition of brazing as defined by the American Welding Society (AWS Welding Handbook, Vol. 2). Hence liquid phase diffusion sintering as referred to by Siemens/Westinghouse, powder metallurgy as referred to by Liburdi Engineering and liquid phase diffusion bonding (LPDB) as referred to by Sermatech are relatively new names appearing on the technological list of techniques to repair vanes and nozzles.

The object of this paper is to describe the use of the liquid phase diffusion bonding process, (which Sermatech have as their trademark the SermaFill process) for Siemens V84.2, Row 2 vane and Alstom Tornado 2nd stage stator segment repairs. This SermaFill process was also compared with the traditional wide gap braze process. The former process is proprietary and in the process of being patented, hence exact precise temperatures and times, chemical compositions etc. cannot be revealed in this paper; nevertheless, ranges of temperature and times are reported here.

The LPDB process was qualified by undertaking a metallurgical evaluation and a mechanical property evaluation to show that metallurgically sound and high strength joints resulted. This LPDB process was used to restore wall thickness on the concave and convex surfaces of the airfoil on the 2nd

stage stator segments as well as to repair cracks and pits/dents. The process was also used to repair craze cracking on the Row 2 vanes. Figures 1-4 show typical examples of the cracking on both components. The Row 2 vanes and 2nd stage stator segments are cast from IN738 and IN939, respectively. The nominal composition of IN738 and IN939 is Ni-16Cr-8.5Co-1.75Mo-2.6W-1.75Ta-0.9Nb-3.4Al-3.4Ti-0.1Zr-0.17C and Ni-22.4Cr-19Co-2W-1.4Ta-1Nb-1.9Al-3.7Ti-0.1Zr-0.15C, respectively. These cracks are wide; therefore conventional narrow gap brazing cannot be utilised as a repair technique.

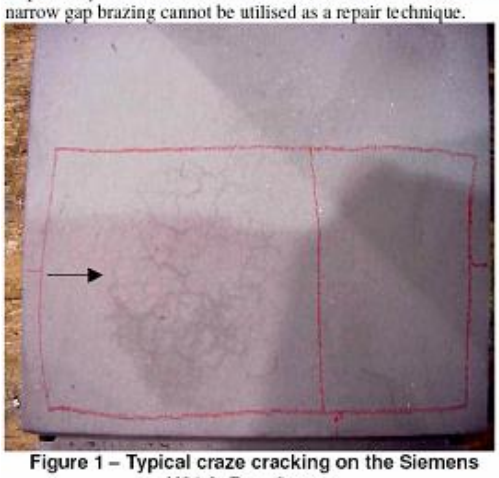

Figure 1 – Typical craze cracking on the Siemens V84.2, Row 2 vane.

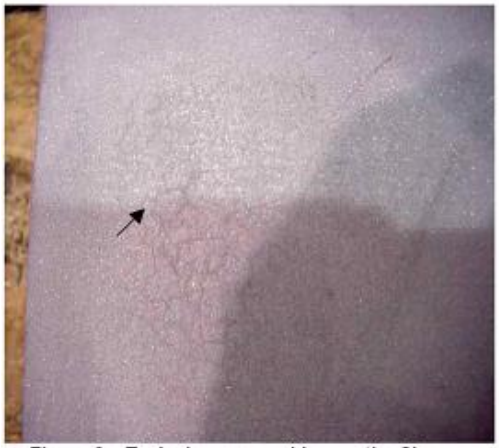

Figure 2 – Typical craze cracking on the Siemens V84.2, Row 2 vane.

The largest width of cracks found on these engine sets was 1.5mm (0.059''). Therefore for the process qualification the mechanical property tests (namely tensile and stress rupture) were undertaken on samples where the joint gap was 1.5mm (0.059''). The process is not limited to this gap and the largest gap repaired to date has been 10mm.

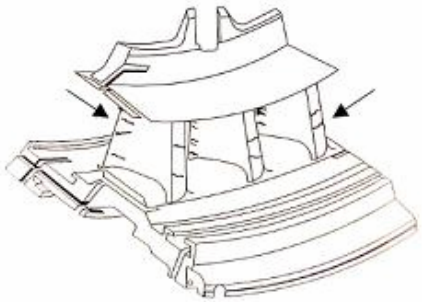

Figure 3 – Typical view from the concave side, showing leading, trailing and shroud/buttress cracking on the Alstom Tornado 2nd stage stator segment.

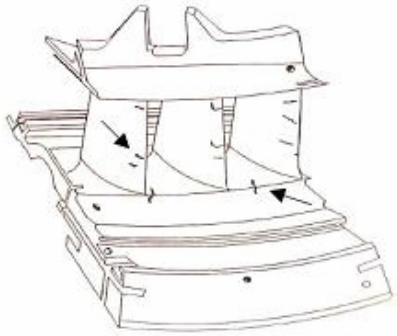

Figure 4 – Typical view from the convex side, showing leading, trailing and shroud/buttress cracking on the Alstom Tornado 2nd stage stator segment.

PROCESS EXPERIMENTAL PROCEDURE

Tensile tests at room temperature (21°C) and elevated temperatures, as well as stress rupture tests were undertaken. The test specimens were prepared in a butt joint configuration as seen in Fig. 5. The joint is in the centre of the gauge length and was 1.5mm wide.

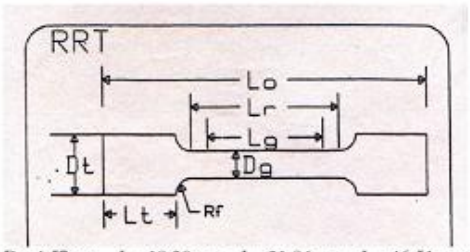

D_g=4.57mm, L_g=18.29mm, L_t=21.84mm, L_o=46.51mm, R_f =3.18mm, D_t=(5/16-24NF-2A inches) and L_t=9.53mm

Figure 5 – Configuration of tensile and stress rupture test specimens

Figure 6 shows the set up for the samples utilised for the metallographic evaluation. Molybdenum sheet stock was utilised to keep the joint gap uniform at 1.5mm in width. Conventional metallographic techniques were used for the metallurgical investigation.

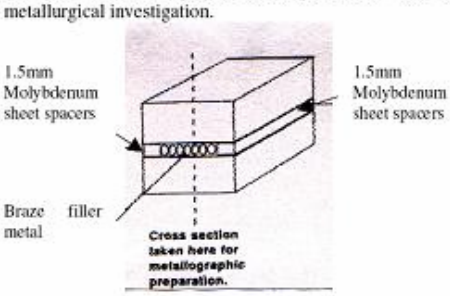

Figure 6 – Schematic representation of sample set for metallurgical evaluation

TENSILE AND STRESS RUPTURE TEST SPECIMEN PREPARATION

Mechanical test specimens according to the configuration shown in Fig. 5 were prepared as follows:

a) Obtain investment cast IN738 and IN939 material.
b) Machine rectangular sections of 12.5mm (0.5'') X 12.5mm (0.5'') X 55.9mm (2.2'')
c) Cut sample in half.
d) Grind the mating surfaces flat.
e) Grit blast surfaces with silicon carbide.
f) Shim gap at 1.5mm (0.059'').
g) Apply paste to the joint gap.
h) Place samples in fixture to maintain alignment.
i) Set in vacuum furnace.
j) Process between 1120°C (2048°F) and 1200°C (2192°F).
k) Isothermally process at the above-mentioned range for 4-20 hours.
l) Age at 843°C (1550°F) for 24hours for IN738 or age at 900°C (1650°F) for 24hours + 700°C (1300°F) for 16 hours for IN939.
m) Machine samples to the configuration shown in Fig. 5.
n) Send the machined specimens for X-ray analysis to determine if porosity greater than 0.4mm (0.016'') exists and for lack of bonding to the mating surfaces.

RESULTS AND DISCUSSION OF MECHANICAL PROPERTY TESTING

Table 1 below shows the results of the tensile tests undertaken at room temperature, and elevated temperatures of 650°C, 760°C and 982°C on the LPDB joints for IN738. As can be seen the tensile and yield strengths are extremely close to the values quoted in the Metals Handbook. The elongation of the LPDB joints appears low, when compared to the values quoted in the Metals Handbook. There is a good explanation for this, which will be discussed later. Nevertheless the RA values are equivalent to the base metals values and hence the joints possess reasonable ductility.

Table 1: Tensile Strength of IN738 processed with "SermaFill"5 Filler Metal

TEMPERATURE		TENSILE STRENGTH		YIELD STRENGTH		ELONGATION	RA
°C	°F	MPa	ksi	MPa	ksi	%	%
21	70	1011	146.5	882	127.8	3.1	4.7
21	70	886	128.4	866	125.5	1.4	3.6
21	**70**	**1050**	**152**	**865**	**125.4**	**5**	**5**
650	1200	827	120	671	97.3	6.0	5.6
650	1200	765	111	661	95.8	3.3	4.0
650	1200	753	109	682	98.9	4.1	3.7
650	**1200**	**850**	**123**	**655**	**95**	**5**	**5**
760	1400	908	131.6	747	108.3	3.9	5.9
760	1400	944	136.8	768	111.3	3.8	5.6
760	**1400**	**965**	**140**	**795**	**115**	**6**	**NR**
982	1800	412	59.7	319	46.2	2.0	8.2
982	1800	372	53.9	317	45.9	1.6	6.1
982	**1800**	**435**	**63**	**325**	**47.1**	**6.5**	**NR**

NOTE: **Values in Bold are for IN738 parent alloy (Metals Handbook Vol.3, ninth edition) NR = Not Reported**

To verify if the elongation is as low as the data indicates, some IN738 material was taken from the root area of a W501F, 1st stage blade. This material was machined to the configuration shown in Fig. 5. Table 2 shows the results of the IN738 specimens removed from the blade root.

As seen in Table 2 the mechanical properties of the IN738 taken from the actual blade casting is lower than that quoted in the Metals Handbook, including the ductility. Therefore the LPDB joints have ductility in the order of 80% of the IN738 casting material. This is acceptable and the 20% loss in ductility is attributed to the few brittle intermetallic phases present in the 1.5mm (0.059'') wide gap joint.

Table 2: Tensile strength of IN738 material taken from the root of a blade

TEMPERATURE		TENSILE STRENGTH		YIELD STRENGTH		ELONGATION	RA
°C	°F	MPa	ksi	MPa	ksi	%	%
21	70	828	120	759	110	3	3
21	**70**	**1050**	**152**	**865**	**125.4**	**5**	**5**

NOTE: **Values in Bold are for IN738 parent alloy (Metals Handbook Vol.3, ninth edition)**

Table 3 shows the stress rupture properties of the LPDB joints

Table 3: Stress rupture properties of IN738 processed with " SermaFill" 5 Filler Metal

TEMPERATURE		STRESS LEVEL		HOURS TO FAILURE	ELONGATION	RA
°C	°F	MPa	ksi	hrs	%	%
843	1550	345	50	190.3	1.7	NR
843	1550	345	50	93.7	1.9	NR
843	1550	345	50	89	2.3	NR
843	1550	345	50	97.3	1.8	NR
843	**1550**	**345**	**50**	**100**	**5**	**5**
829	1525	345	50	203.37	4.4	NR
829	**1525**	**345**	**50**	**223.02**	**6.7**	**NR**
982	1800	124.2	18	453.2*	5.5	NR
982	**1800**	**124.2**	**18**	**807.2**	**5.2**	**NR**

NOTE: **Values in bold are for IN738 material, taken from the root of a blade. NR = Not Reported**
*** means that failure occurred in the base metal**

As seen in Table 3, the stress rupture properties of the joints are a minimum of 89% of the base metals stress rupture properties.

For those readers who prefer the results shown in graphical form, Figs. 7 and 8 show the tensile and Larson Miller stress rupture data of the LPDB joints.

To compare the results of the LPDB wide gap joints with a more traditional wide gap braze process, a 50%IN738 and 50% BRB braze mixture was developed. Some samples were brazed with the same joint gap and at the same process parameters as those of the LPDB joints. The 50% braze used in the mixture had a composition Ni-13.5Cr-7.5Co-4Al-2.5B.

Tables 4 and 5 show the tensile test results and stress rupture results respectively, of the joints brazed with the 50/50 mixture. As seen in these tables the strength of the brazed joint is 40%-53% of the base metal's strength, the elongation is 33-50% of the cast IN738 blade material and the stress rupture life varies from 7.4-11.9% of the parent metals life. This is undesirable if the objective is to have a structural repair, where the properties of the repaired areas are equivalent to the base metal. Clearly the LPDB type joints have superior mechanical properties when compared to a more traditional wide gap braze joint, and the properties are equivalent to the base metal as seen in Tables 1 and 3.

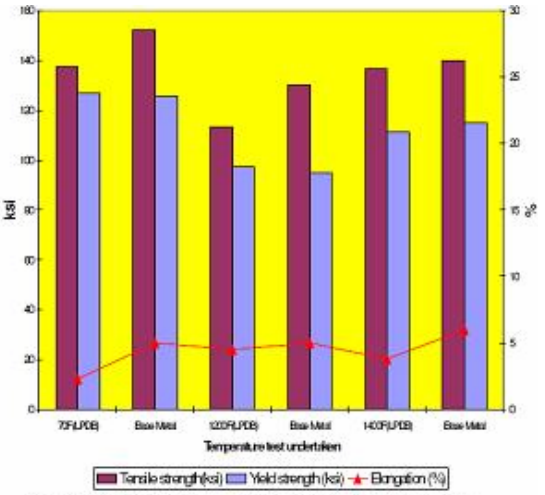

Figure 7 – Tensile properties of the LPDB joints for IN738 Nickel Base superalloy. °C = (°F – 32) / 1.8
MPa = ksi X 6.9

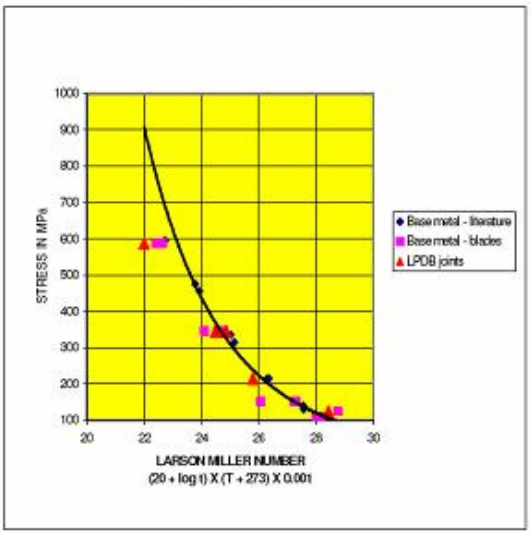

Figure 8 – Larson Miller plot of the stress rupture properties of the LPDB joints for IN738 superalloy.

Table 4: Tensile strength of IN738 brazed with a traditional type filler metal (50%IN738 + 50%BRB)

TEMPERATURE		TENSILE STRENGTH		YIELD STRENGTH		ELONGATION	RA
°C	°F	MPa	ksi	MPa	ksi	%	%
21	70	527	76.4	527	76.4	1.4	2.4
21	70	502	72.8	502	72.8	1.8	2.2
21	70	559	81	559	81	1.0	2.9
21	**70**	**1050**	**152**	**865**	**125.4**	**5**	**5**
650	1200	322	46.7	322	46.7	2.5	1.6
650	1200	441	63.9	441	63.9	1.2	1.9
650	1200	338	49	338	49	1.9	5.2
650	**1200**	**850**	**123**	**655**	**95**	**5**	**5**

NOTE: Values In Bold Are For IN738 Alloy (Metals Handbook Vol.3, ninth edition)

Table 5: Stress Rupture properties of IN738 brazed with a traditional type filler metal (50%IN738 + 50%BRB)

TEMPERATURE		STRESS LEVEL		HOURS TO FAILURE	ELONGATION	RA
°C	°F	MPa	ksi	hrs	%	%
843	1550	345	50	11.9	NR	NR
843	1550	345	50	7.4	NR	NR
843	**1550**	**345**	**50**	**100**	**5**	**5**

NOTE: Values in Bold are for X-45 alloy (Metals Handbook Vol.3, ninth edition) NR = Not Reported

Table 6 and Fig. 9 show the results of the tensile tests undertaken at room temperature and 650°C (1200°F) on the LPDB joints for IN939. As can be seen the tensile and yield strengths are equivalent to the values of the cast material. The elongation of the LPDB joints is 50-73% of the base metals values. This is attributed to the intermetallic phases present in the joint. The RA values are however equivalent to that of the base metal, hence the joints do possess reasonable ductility. As seen in Fig. 10, the stress rupture properties of the joints are a minimum of 90% of the base metal.

Table 6: Tensile Strength of IN939 processed with "SermaFill"3 Filler Metal

TEMPERATURE		TENSILE STRENGTH		YIELD STRENGTH		ELONGATION	RA
°C	°F	MPa	ksi	MPa	ksi	%	%
21	70	920	133.3	670	97.1	2.2	3.6
21	70	859	124.5	696	100.9	1.8	4.3
21	70	817	118.4	750	108.7	1.7	7.7
21	70	999	144.8	651	94.3	1.5	3.0
21	**70**	**897**	**130**	**690**	**100**	**3**	**5.0**
650	1200	768	111.3	625	90.6	1.5	4.0
650	1200	860	124.7	654	94.8	2.1	5.1
650	**1200**	**863**	**125.1**	**621**	**90**	**3**	**5.0**

NOTE: Values in bold are for cast IN939 material taken from a shroud buttress section.

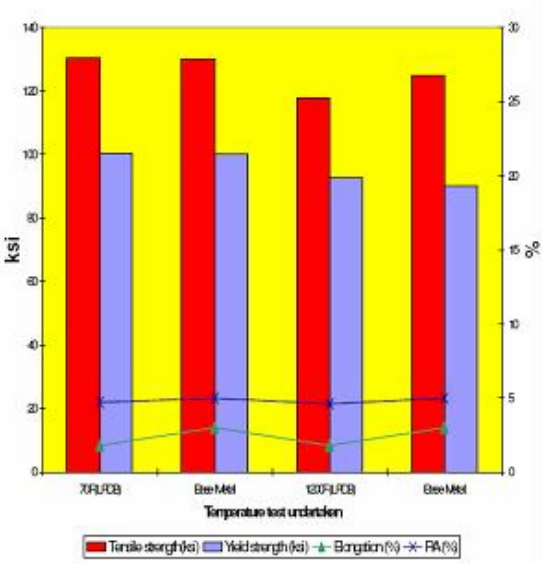

Figure 9 – Tensile properties of the LPDB joints for IN939 Nickel Base superalloy. °C = (°F – 32) / 1.8 MPa = ksi X 6.9

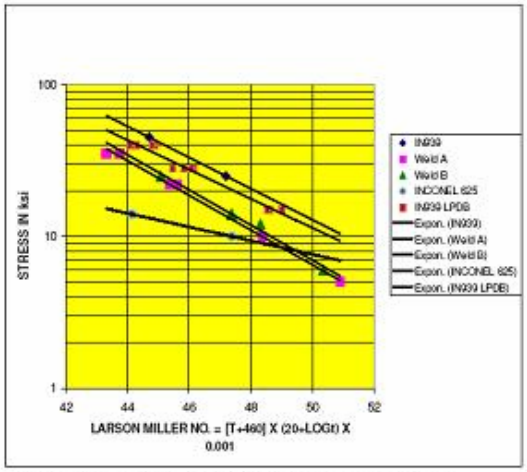

Figure 10 – Larson Miller plot of the stress rupture properties of the LPDB joints for IN939 superalloy. °C = (°F – 32) / 1.8 and MPa = ksi X 6.9

In fact Fig. 10 also shows that the LPDB joints have superior stress rupture lives when compared to three different weld filler metals viz. IN625, Weld A and Weld B. IN625 is well utilised as a filler metal for non-structural repair applications, because of its good ductility and ease of welding. However as can be seen, this filler metal has poor stress rupture life when compared to IN939. Two proprietary higher strength weld filler metals based on the elements Ni-Cr-Co-Mo-W-Ti-Al-C were developed as substitutes for IN625, and even these filler metals, did not even have the stress rupture properties equivalent to those of the LPDB joints.

IN939 as a result of its high Al + Ti content is not readily weldable and suffers from strain age cracking, as seen in Figs. 11 and 12.

Figure 11 – Strain age cracking, on the airfoil, after initial attempts at a weld repair.

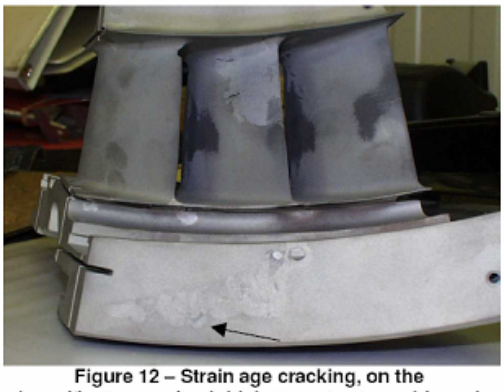

Figure 12 – Strain age cracking, on the shroud/buttress, after initial attempts at a weld repair.

RESULTS AND DISCUSSION OF THE METALLURGICAL EVALUATION

Figure 13 shows the macrograph of a cross section taken through the LPDB repair of the V84.2, row 2 vane. As can be seen the "craze-cracked" area was machined away and this area was filled with the LPDB filler metal.

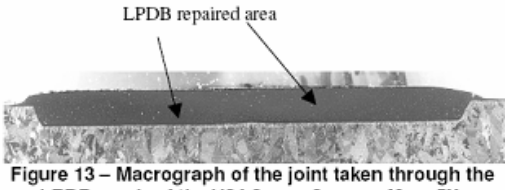

Figure 13 – Macrograph of the joint taken through the LPDB repair of the V84.2, row 2 vane. Mag. 5X

Figures 14 and 15 show the excellent bonding/ adhesion to the vane material. A fine-grained microstructure is evident. Some minor microporosity can be seen in the micrograph, but this microporosity level is considered to be acceptable.

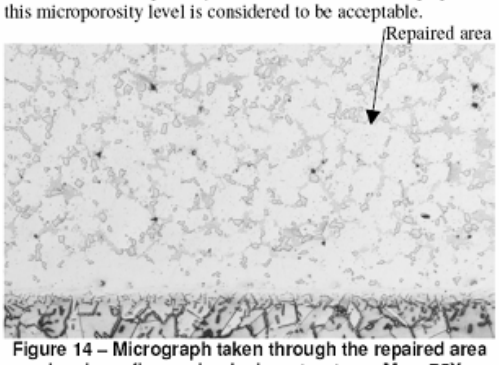

Figure 14 – Micrograph taken through the repaired area showing a fine-grained microstructure. Mag. 75X

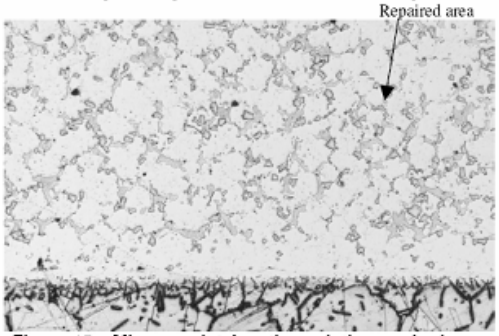

Figure 15 – Micrograph taken through the repaired area showing excellent bonding to the vane material. Mag. 75X

Figures 16 and 17 show the fine-grained structure of the LPDB joint, with intermetallic phases dispersed intergranularly.

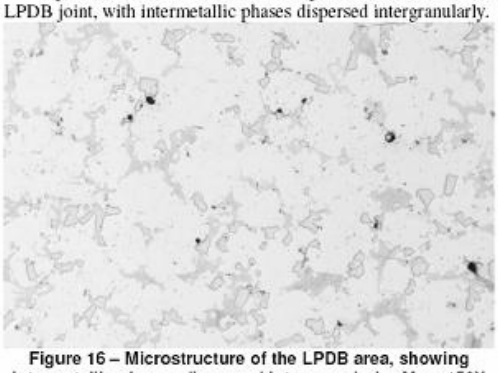

Figure 16 – Microstructure of the LPDB area, showing intermetallic phases dispersed intergranularly. Mag. 150X

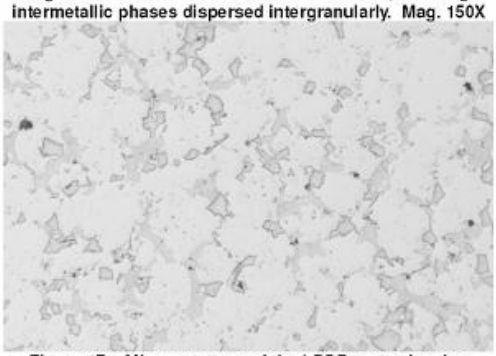

Figure 17 – Microstructure of the LPDB area, showing intermetallic phases dispersed intergranularly. Mag. 150X

Figures 18 and 19 show the intermetallic phases that are present in more detail.

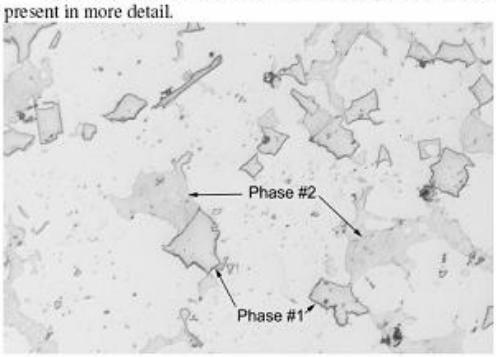

Figure 18 – Intermetallic phases present in the joint. Mag.400X

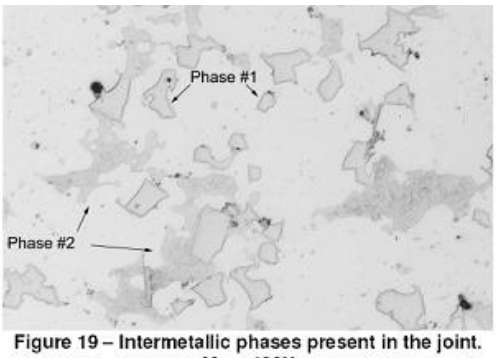

Figure 19 – Intermetallic phases present in the joint. Mag. 400X

Figures 20 and 21 show semi-qualitative analyses of the phases labeled phase #1 and phase #2 in Figs. 18 and 19. Table 7, shows the semi-quantitative analyses of the phases labeled phase #1 and phase #2 in Figs. 18 and 19. As can be seen in Fig. 20 and Table 7, the "blocky" phases #1 are Cr/W rich phases; whereas, the phases #2 are Ni rich phases as seen in Fig. 21 and Table 7. Energy dispersive spectrometry was utilised for this work, and hence neither Boron nor Carbon could be detected. Therefore it is difficult to precisely state what phase is present in the joint. Nevertheless, it is probably a boride or carbide phase that formed. Unfortunately there was no thin window on the EDAX to detect Carbon or Boron.

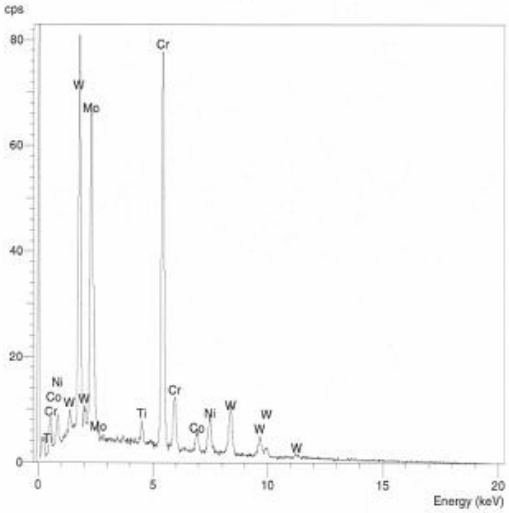

Figure 20 – Semi-qualitative analysis of the phase #1 shown in Figs. 18 and 19.

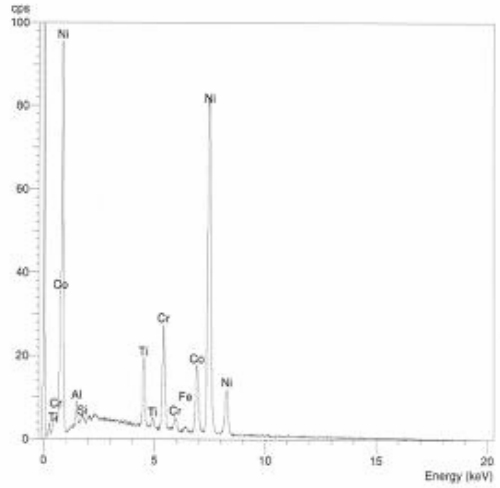

Figure 21 – Semi-qualitative analysis of the phase #2 shown in Figs. 18 and 19

Table 7: Semi-quantitative analysis of the phases present in the joint.

Intermetallic phase	Ni	Cr	W	Mo	Co	Ti	Al
Phase #1	5.4	30.7	30.5	29.0	2.7	1.3	0.5
Phase #2	69.4	10.5	0	0	11.9	5.9	2.1

Figure 22 shows the macrograph of a cross section taken through the LPDB repair of the Tornado 2nd stage stator segment. As can be seen the filler metal has flowed completely down to the bottom of the crack and has bonded excellently to the sidewalls of the routed out crack. Figure 23 shows a cross section taken through a "through" crack at the trailing edge of the airfoil. Once again there is good bonding to the sidewalls of the routed out crack.

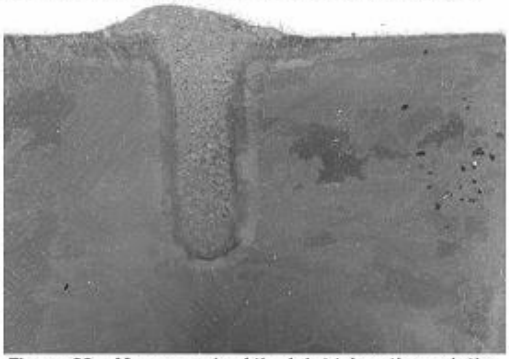

Figure 22 – Macrograph of the joint taken through the LPDB repair of the Tornado, 2nd stage stator segment. Mag. 5X

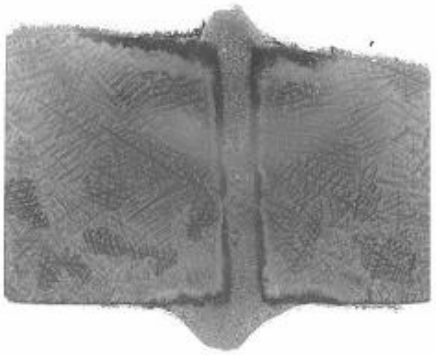

Figure 23 - Macrograph of the joint taken through the LPDB repair of the Tornado, 2nd stage stator segment. Mag. 5X

Figure 24 shows the microstructure of the repaired area. It consists of a fine-grained structure and there is good bonding/adhesion to the sidewalls. The joint interface can be clearly seen in Fig. 25 and there is no lack of sidewall bonding. Figure 26 shows the joint to consist of equiaxed grains with intermetallic phases dispersed intergranularly. These intermetallic phases can be clearly seen in Fig. 27. These "bright blocky" phases were determined to be Cr-rich intermetallic phases as seen in Fig. 28 and Table 8. Energy dispersive spectrometry was utilised for this work, and hence neither Boron nor Carbon could be detected. Therefore it is difficult to precisely state what phase is present in the joint. Nevertheless, it is probably a boride or carbide phase.

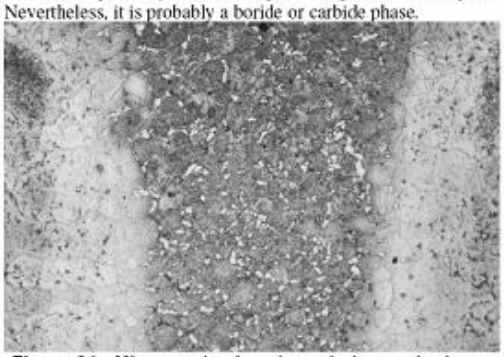

Figure 24 - Micrograph taken through the repaired area showing a fine-grained microstructure. Mag. 45X

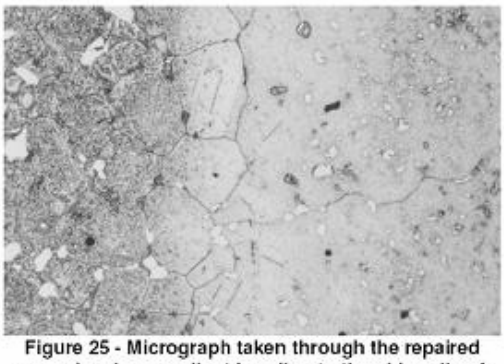

Figure 25 - Micrograph taken through the repaired area showing excellent bonding to the sidewalls of the routed out crack. Mag. 150X

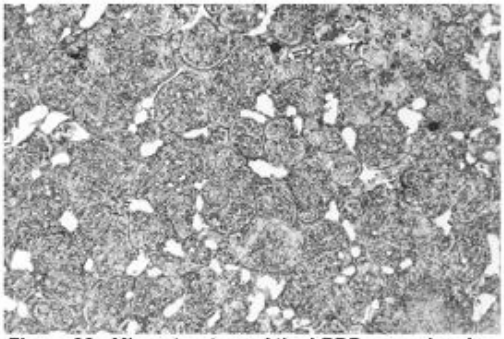

Figure 26 - Microstructure of the LPDB area, showing intergranular intermetallic phases. Mag. 150X

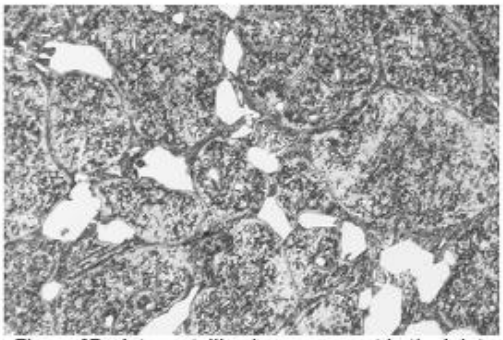

Figure 27 – Intermetallic phases present in the joint. Mag. 400X

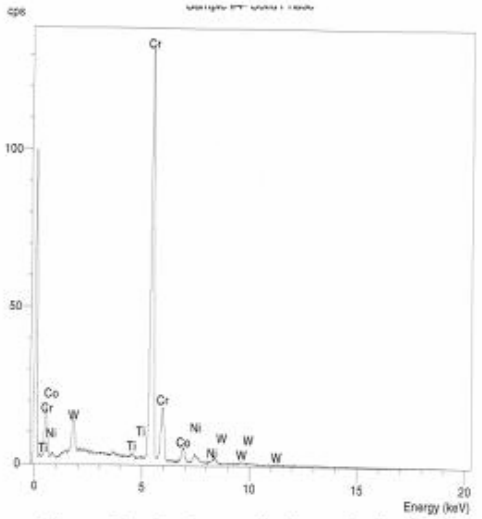

Figure 28 – Semi-quantitative analysis of the intermetallic phases, which are dispersed intergranularly.

Table 8: Semi-quantitative analysis of the phase present in the joint.

Intermetallic phase	Ni	Cr	W	Co	Ti	Al
Intergranular phase	2.7	83.7	8.4	4.7	0.5	0.1

The samples used to produce the mechanical test results shown in Tables 4 and 5, were also analysed. As a reminder a filler metal of 50% IN738 powder and 50%BRB braze was utilised. As seen in Fig. 29 the joint in the stress rupture sample consist of a mixture of fine and coarse grains with a continuous layer of intergranular intermetallic phases. This is in contrast to the discrete isolated and discontinuous intermetallic phases that were present in the joints seen in Figs. 24-27. Figure 30 shows that the traditional type wide gap braze bonded well to the sidewalls of the stress rupture sample and in fact failure did not occur in this region, but through the centre of the joint. Figure 31 shows the continuous intergranular intermetallic phases present in the joint. The bright "blocky and dark grey intermetallic phases can be clearly seen along the grain boundaries. Figure 32 shows these intergranular intermetallic phases more clearly and the phases labeled phase #1 and phase #2 were analysed.

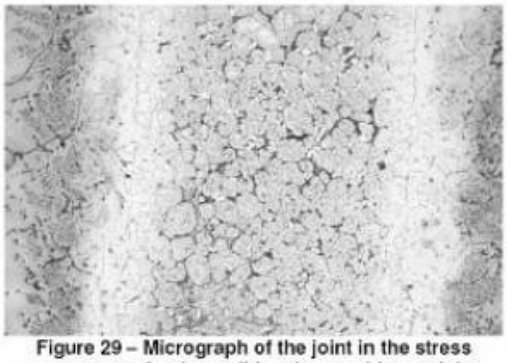

Figure 29 – Micrograph of the joint in the stress rupture sample of a traditional type wide gap joint. Mag. 45X

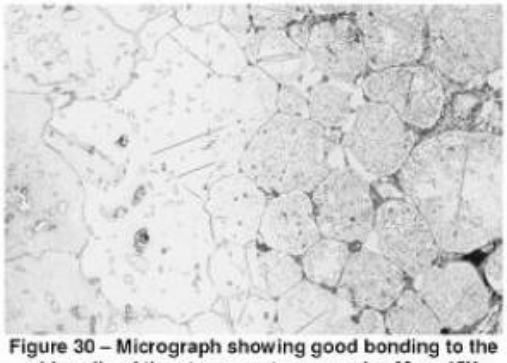

Figure 30 – Micrograph showing good bonding to the sidewalls of the stress rupture sample. Mag. 45X

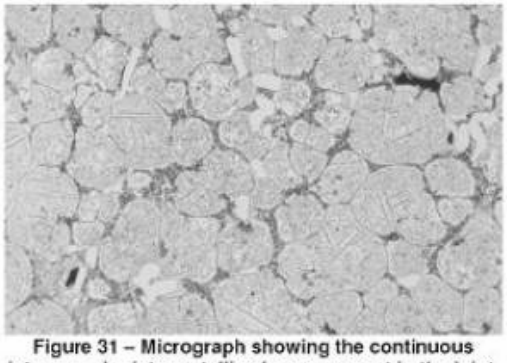

Figure 31 – Micrograph showing the continuous intergranular intermetallic phases present in the joint. Mag. 150X

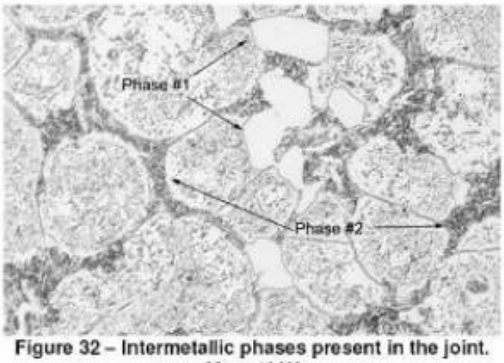

Figure 32 – Intermetallic phases present in the joint. Mag. 400X

Figures 33 and 34 show semi-qualitative analyses of the phases labeled phase #1 and phase #2 in Fig. 32. Table 9, shows the semi-quantitative analyses of the phases labeled phase #1 and phase #2 in Fig. 32. As can be seen in Fig. 33 and Table 9, the "blocky" phases #1 are Cr rich phases; whereas, the phases #2 are Ni rich phases as seen in Fig. 34 and Table 9. Energy dispersive spectrometry was utilised for this work, and hence neither Boron nor Carbon could be detected. Therefore it is difficult to precisely state what phase is present in the joint. Nevertheless, it is probably a boride or carbide phase that formed. Unfortunately there was no thin window on the EDAX to detect Carbon or Boron.

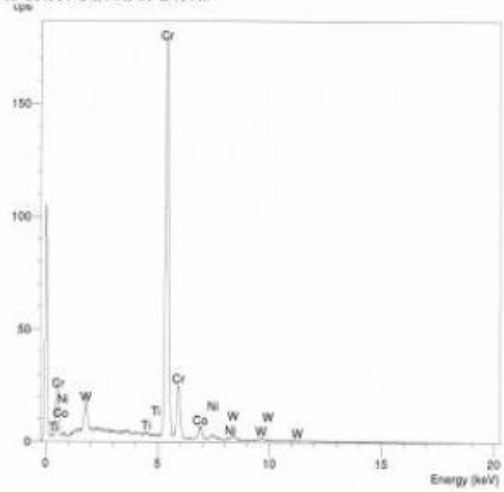

Figure 33 – Semi-qualitative analysis of the phase #1 shown in figure 32.

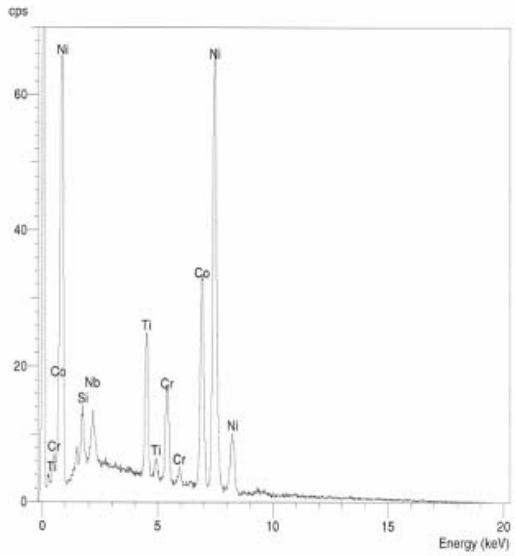

Figure 34 – Semi-qualitative analysis of the phase #2 shown in figure 32.

Table 9: Semi-quantitative analysis of the phases present in the joint.

Intermetallic phase	Ni	Cr	W	Nb	Co	Ti	Al
Phase #1	1.9	85.2	8.3	0	4.3	0.3	0.1
Phase #2	55.5	8.2	0	3.1	25.1	6.3	1.9

FIRST ARTICLE REPAIR DEMONSTRATION

Figures 35 and 36 show areas on the V84.2, row 2 vanes, which were routed out and processed with the LPDB material. Figure 37 shows the V84.2 row 2 vane after complete repair including heat treatment and MCrAlY coating.

Figures 38 and 39 show the Tornado, 2nd stage stator segment after complete repair including heat treatment and Sermaloy J coating. (Sermaloy J is an aluminide coating that is proprietary to Sermatech International, Inc.)

Figure 35 – V84.2, row 2 vanes repaired with the LPDB process.

Figure 36 – V84.2, row 2 vanes repaired with the LPDB process.

Figure 37 - V84.2 row 2 vane after complete repair including heat treatment and MCrAlY coating.

POSSIBLE WORKSCOPE FOR REPAIR OF V84.2 ROW 2 VANES

- Incoming inspection for damage
- Inspect cooling holes for damage
- Airflow a percentage of the vanes
- Disassemble the vanes
- Vibropeen appropriate parts
- Wax mask internal passages and any uncoated external areas
- Strip existing MCrAlY coating
- Grit blast
- Check cooling holes
- Heat tint
- Inspect to ensure that there is no residual coating.
- Measure trailing edge thickness and cooling hole to wall thickness
- FPI
- Rout out indications
- Apply SermaFill 5 filler metal
- Process in vacuum and incorporate the solution heat treat

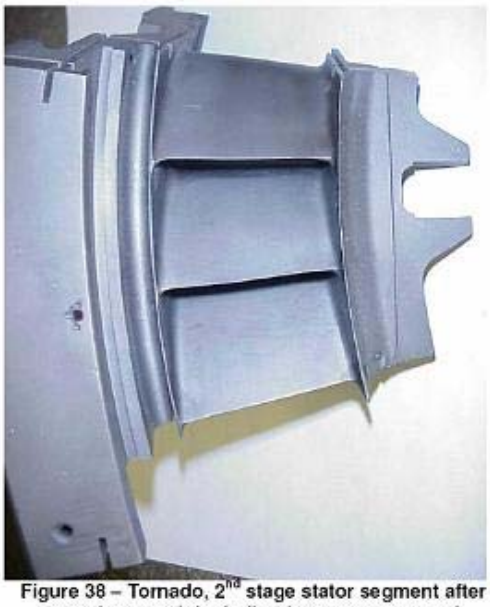

Figure 38 – Tornado, 2nd stage stator segment after complete repair including heat treatment and Sermaloy J coating.

Figure 39 – Tornado, 2nd stage stator segment after complete repair including heat treatment and Sermaloy J coating.

cycle at 2175°F (1191°C) /4hrs
- Blend to proper contour and thickness
- EDM plugged cooling holes
- Apply MCrAlY and TBC coatings
- Diffuse MCrAlY at 2050°F (1121°C) /2hrs
- Age heat treat at 1550°F (843°C) /24hrs
- Install cooling inserts
- Airflow the vanes
- Fixture check
- Final inspection

POSSIBLE WORKSCOPE FOR REPAIR OF TORNADO 2ND STAGE STATOR SEGMENT

- Incoming inspection for damage
- Remove seals and pins
- Grit blast
- Chemically strip
- Heat tint
- Inspect to ensure that there is no residual coating.
- FPI
- Measure trailing edge thickness
- Rout out indications and apply SermaFill 3 filler metal
- Process in vacuum and incorporate the solution heat treat cycle at 2120°F (1160°C) /4hrs
- Blend to proper contour and thickness
- Stabilisation and age at 1830°F (1000°C) /6hrs + 1650°F (900°C) /24hrs
- Apply Sermaloy J coatings
- Diffuse Sermaloy J coating at 1600°F (871°C) /2hrs
- Final age heat treat at 1300°F (704°C) /16hrs
- Install seals and pins if needed
- Airflow the vanes
- Fixture check
- Final inspection

OVERALL DISCUSSION

The results of the mechanical tests showed that the tensile strength values of the LPDB joints on both the IN738 and IN939 base metals, were a minimum of 85% of the base metals tensile strength. The yield strength was equivalent to that of the base metal. The elongation values varied from 30% - 100% of those of the base metal. The RA values varied from 60% - 100% of those of the base metal. The loss in elongation is attributed to the intermetallic phases present in the joint. The stress rupture properties were a minimum of 90% of the base metals properties. Based on the mechanical properties achieved in this study, the use of the LPDB process is considered to be suitable for structural repairs on both the V84.2, row 2 vane and Tornado, 2nd stage stator segment.

The mechanical tests undertaken showed that the traditional type wide gap joints had tensile properties approximately half of the base metals value and stress rupture properties of approximately 10% of the base metals properties. Therefore the use of this type of wide gap filler metal is considered to be unsuitable for 1.5mm wide defects and structural repairs. This type of traditional wide gap braze repair should be confined to non-structural applications.

The LPDB joints consisted of a fine-grained microstructure, with discrete intergranular intermetallic phases. For the IN738 base metal, Cr/W and Ni-rich intermetallic phases existed; whereas, for the IN939 base metal, Cr-rich intermetallic phases existed.

The traditional wide gap braze joints consisted of a mixture of fine and coarse grains. There were continuous intergranular intermetallic phases present, which were Cr and Ni-rich.

First article production repairs showed no coating/bonding interactions.

CONCLUSIONS

- The LPDB ("SermaFill") process, produces a repaired joint having mechanical properties (tensile and stress rupture) equivalent to those of the base metal.
- The microstructure of the joint was found to reveal no signs of large networks of brittle boride phases, known to significantly reduce mechanical properties and ductility. Only isolated and discrete intermetallic phases were seen in the repaired area.
- The LPDB process yields superior mechanical properties when comparing with the traditional type wide gap brazing process.
- Based on the metallurgical and mechanical results obtained in this in-house research project, the use of the LPDB ("SermaFill") process is a suitable alternative to the traditional Gas Tungsten Arc weld approved repair process.
- The LPBD ("SermaFill") process is ideally suited for crack repair, including "craze cracking", wall thickness repair of the convex and concave surfaces and dimensional restoration of the Siemens V84.2, row 2 vane and Alstom Tornado, 2nd stage stator segment.

ACKNOWLEDGMENTS

The authors acknowledge the help of Jan Williams and Kevin Pelletier of Dirats Laboratory for the mechanical testing and metallographic work.

REFERENCES

Demo, W.A and Ferrigno, S.J, 1992, "Brazing method helps repair aircraft gas –turbine nozzles", Advanced Materials and Processes, Vol. 141, No.3, pp43-45

Wustman, R.D and Smith, J.S, 1996, "High strength diffusion braze repairs for gas turbine components", ASME paper 96-GT-427

Bell, S, 1985, "Repair and Rejuvenation procedures for aero gas-turbine hot section components", Material Science and Technology, Aug, Vol. 1, pp629

Ellison, K.A, Lowden, P and Liburdi, J, 1992, "Powder metallurgy Repair of Turbine Components", ASME paper 92-GT-312

AWS Welding Handbook, Vol2, 8th edition, pp380

Metals Handbook, Vol3, 9th edition

APPENDIX C

MIGLIETTI, W.M.A. "WIDE GAP DIFFUSION BRAZE REPAIR OF CO-BASED INDUSTRIAL TURBINE VANES". PROCEEDINGS OF THE *INTERNATIONAL BRAZING & SOLDERING CONFERENCE*. 2-5 APRIL 2000. ALBUQUERQUE, NEW MEXICO, USA. PP. 476-485.

WIDE GAP DIFFUSION BRAZE REPAIR OF Co-BASED INDUSTRIAL TURBINE VANES

W.M.A. Miglietti*

ABSTRACT

During the industrial turbine engine operation, cracks develop on the vanes as a result of thermal fatigue. Other damage found is pitting and dents resulting from corrosion/oxidation and FOD (foreign object damage) respectively. Erosion damage is also commonly found on the airfoils. Finally there is downstream deflection of the inner buttress/seal areas, as a result of axial creep. This paper describes the vacuum wide gap diffusion brazing repair process used to repair all of the above-mentioned damage, including braze build up and machining of the hook fit areas.
As a means of qualifying the high temperature diffusion braze process, both metallurgical and mechanical property evaluations were carried out. The metallurgical evaluation consisted of optical and scanning electron microscopy. The wide gap diffusion brazed area consisted of a fine-grained structure with carbide and boride phases dispersed both intergranularly and intragranularly. An EDAX analysis was also conducted and the results are reported. The microstructure of the repaired area is similar to the base metal which may explain why mechanical tests revealed properties equivalent to that of the base metal. The mechanical evaluations undertaken were tensile tests at room temperature and elevated temperature, as well as stress rupture tests. These results were equivalent to mechanical properties of the X-45, X-40, and FSX-414 Co-based superalloys, which are the base metals that many of the vanes are cast from.

KEYWORDS

Wide Gap Diffusion Brazing, Repair of Industrial Gas Turbine Vanes, Co-based superalloys

INTRODUCTION

Narrow gap brazing has been utilized for decades now to repair aircraft engine vane and nozzle segments. It has only being the last 5 years that wide gap brazing has been utilized for Industrial Gas Turbine (IGT) vane and nozzle repairs. The wide gap brazing process was made popular by GE's and Pratt and Whitney's ADH (activated diffusion healing) by Demo and Ferrigno, 1992 (Ref 1) and Turbofix processes respectively. Many repair vendors have their own proprietary wide gap braze process such as SNECMA's RBD (rechargement per brasage diffusion), Howmet's ESR (effective structural repair) by Wustman and Smith, 1996 (Ref 2) and Chromalloy's SRB (surface reaction braze) by Bell, 1985 (Ref 3). Other wide gap joining processes available are LPDS (liquid phase diffusion sintering), Liburdi's LPM (Liburdi powder metallurgy) by Ellison, Lowden and Liburdi, 1992 (Ref 4) and Sermatech's "Sermafill" process.

*Sermatech International, Inc., 1366 Tolland Turnpike, Manchester, CT, 06040

The objective of this paper is to describe the use of an alternative wide gap braze process for IGT vane repairs, and to compare this process with the traditional wide gap braze process. A traditional wide gap process is referred to as, when a mixture/blend of superalloy powder and braze powder is utilized. The mixtures are usually a 40/60, 50/50 or a 60/40 blend by weight. The alternative wide gap process is proprietary and hence exact precise temperatures and times, chemical compositions etc. cannot be documented; nevertheless, ranges of temperature and times are documented. This process was qualified by undertaking a metallurgical evaluation and a mechanical property evaluation to show that metallurgically sound and high strength joints resulted. This alternative process was used to restore wall thickness on the concave and convex surfaces of the airfoil, repair cracks, pits/dents and build up the hook fit areas, because of downstream deflection of the inner buttress/seal areas, as a result of axial creep.

Many of the IGT vanes are manufactured from Co-based alloys like X-40, X-45 and FSX 414. The chemical composition of the materials is given in Table 1. The high Cr content contributes to corrosion, low temperature oxidation and sulphidation resistance. Figures 1, 2 and 3 show typical examples of ground out cracks on an X-45, W501F, Row 3 vane with 3 airfoils and an FSX-414, GE Frame7EA, Row 1 vane with 2 airfoils. The largest width of crack found on these engine sets was 3.2mm (0.125''), although after grinding through the cracks with grinding discs and burrs, the crack length can vary in width from 6mm-15mm (0.236''--0.600"). As a result of these large gaps, conventional narrow gap brazing cannot be utilised as a repair technique. The hook fit area, which needs to be rebuilt, is shown in Figure 4. For the crack repair, paste is used as the medium for the repair; whereas, with the hook fit repair a tape is utilized.

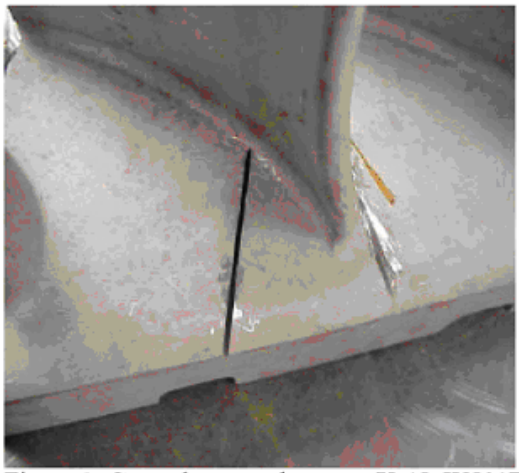

Figure 1: Ground out cracks on an X-45, W501F, Row 3 vane.

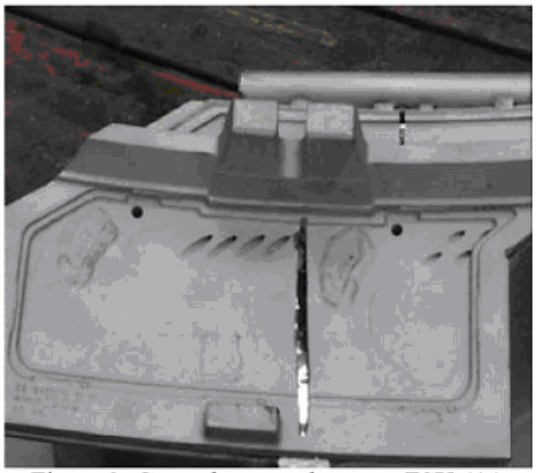

Figure 2: Ground out cracks on an FSX-414, GE Frame 7EA vane.

Element	C	Cr	Ni	W	B	Fe	Si	Zr	Co
X-40	0.5	25	10	7.5	0	1.5	0.4	0.17	Bal
X-45	0.25	25.5	10.5	7	0.012	2 max	0	0	Bal
FSX-414	0.25	29.5	10.5	7	0.012	2 max	0	0	Bal

Table 1: Nominal chemical compositions of some common Co-based superalloys.

Figure 3: Ground out cracks on an X-45, W501F, Row 3 vane.

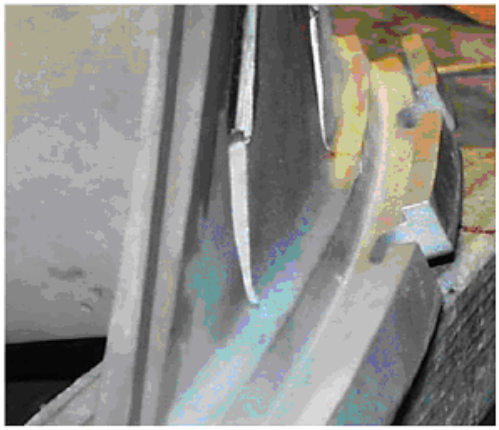

Figure 4: Hook fit area, which need to be built up.

EXPERIMENTAL PROCEDURE

Tensile tests at room temperature and elevated temperature, as well as stress rupture tests were undertaken. The test specimens were prepared in a butt joint configuration as seen in Figure 5. The joint is in the center of the gauge length and is 3.2mm wide. Conventional metallographic techniques were utilised for the metallurgical evaluation. For the traditional type wide gap joints a mixture of 60%Co-based powder (X-40 or X-45) and 40% Co-40Ni-24.5Cr-3B was utilised.

Tensile and Stress Rupture Test Specimen Preparation

Mechanical test specimens according to the configuration shown in Figure 5 were prepared as follows:

a) Obtain scrap vane and cut/grind away sections from the shroud area of the vane.
b) Machine rectangular sections of 12.5mm (0.5'') X 12.5mm (0.5'') X 55.9mm (2.2'')
c) Cut sample in half.
d) Grind the mating surfaces flat.
e) Grit blast surfaces with silicon carbide.
f) Shim gap at 3.2mm (0.125'').
g) Apply paste to the joint gap.
h) Place samples in fixture to maintain alignment.
i) Set in vacuum furnace.
j) Process between 1120°C (2048°F) and 1200°C (2192°F).
k) Isothermally process at the above-mentioned range for 4-20 hours.
l) Age at 982°C (1800°F) for 4hours.
m) Machine samples to the configuration shown in Figure 5.
n) Send machined specimens for X-ray to determine if porosity greater than 1.3mm (0.050'') and for lack of bonding to the mating surfaces exist.

Figure 5: Configuration of Tensile and Stress rupture Test Specimens

RESULTS

Tensile and Stress Rupture Results of the Traditional Type Wide Gap Brazed Joints Base Metal is X-40

Table 2 shows the tensile results of the wide gap joints brazed with 60%X-40/40%braze alloy, where the braze composition was Co-40Ni-24.5Cr-3B.

Temperature		Tensile Strength		Yield Strength		Elongation	RA
°C	°F	MPa	ksi	MPa	ksi	%	%
21	70	555.5	80.5	466.4	67.6	2.6	3.3
21	70	554.1	80.3	437.5	63.4	2.8	2.4
21	70	531.3	77.0	444.7	64.3	3.4	4.8
21	**70**	**745**	**108**	**525**	**76**	**9**	**?**
540	1004	405	58.7	254.6	36.9	3.1	2.6
540	1004	411.9	59.7	253.9	36.8	3.5	2.2
540	1004	380.9	55.2	285	41.3	4.9	1.9
540	1004	391.2	56.7	300.3	43.5	2.1	1.7
540	**1004**	**550**	**79.7**	**275**	**40**	**17**	**?**
650	1200	381.6	55.3	216.7	31.4	6.3	3.1
650	1200	391.2	56.7	216.7	31.4	3.4	1.7
650	1200	400.2	58	228.4	33.1	3.7	2.3
650	1200	393.3	57	227.7	33	3.6	2.2
650	**1200**	**515**	**74.6**	**260**	**38**	**12**	**?**

Table 2. Tensile test results of a wide gap joint brazed with a 60/40 ratio of superalloy powder/braze alloy.
Note: Values in bold are for X-40 base metal taken from the Metals Handbook. (Ref 5)
? means that the RA value was not measured.

As seen in Table 2, the tensile strength of the traditional type wide gap joints is only 70-80% of the base metals strength. Table 3 shows the stress rupture results of the above mentioned joints.

Temperature		Stress Level		Hours to Rupture	Elongation
°C	°F	MPa	ksi	hrs	%
760	1400	260	38	61.4	?
760	1400	260	38	58.2	?
760	**1400**	**260**	**38**	**100**	**?**

Table 3. Stress rupture results of a wide gap joint brazed with a 60/40 ratio of superalloy powder/braze alloy.
Note: Values in bold are for X-40 base metal taken from the Metals Handbook. (Ref 5)
? means that the elongation value was not measured.

As seen in Table 3, the stress rupture strength of the traditional type wide gap joints is typically only 60% of the base metals stress rupture strength. Therefore based on the results in Tables 2 and 3, the traditional type wide gap brazed joints cannot be utilised for high strength repairs, where properties close or equivalent to the base metal is desirable.

Tensile and Stress Rupture Results of the Alternative Type Wide Gap Brazed Joints Base Metal is X-40

Table 4 shows the tensile results of the alternative type, wide gap brazed joints.

Temperature		Tensile Strength		Yield Strength		Elongation	RA
°C	°F	MPa	ksi	MPa	ksi	%	%
21	70	701.4	101.6	508.6	73.7	2.4	3.8
21	70	738.3	107.0	490.7	71.1	2.0	3.4
21	**70**	**745**	**108**	**525**	**76**	**9**	**?**
540	1004	520	75.4	260.3	37,7	2.1	?
540	1004	539.8	78.2	259.9	37.6	2.0	?
540	**1004**	**550**	**79.7**	**275**	**40**	**17**	**?**
650	1200	450	65.2	341	49.4	2.9	3.9
650	1200	509	73.8	311	45.1	6.2	7.8
650	1200	451	65.4	315	45.7	3.6	3.6
650	1200	448	64.9	311	45.1	3.3	3.1
650	**1200**	**515**	**74.6**	**260**	**38**	**12**	**?**

Table 4. Tensile test results of the alternative type wide gap brazed joints.
Note: Values in bold are for X-40 base metal taken from the Metals Handbook. (Ref 5)
? means that the RA value was not measured.

As seen in Table 4, the tensile strength of the alternative type wide gap brazed joints is 87-99% of the base metals strength. Table 5 shows the stress rupture results of the above mentioned joints.

Temperature		Stress Level		Hours to Rupture	Elongation
°C	°F	MPa	ksi	hrs	%
760	1400	260	38	92	?
760	1400	260	38	97.1	?
760	**1400**	**260**	**38**	**100**	**?**

Table 5. Stress Rupture test results of an alternative type wide gap brazed joint.
Note: Values in bold are for X-40 base metal taken from the Metals Handbook. (Ref 5)
? means that the elongation value was not measured.

As seen in Table 5, the stress rupture strength of the alternative type wide gap brazed joints is typically 92-97% of the base metals stress rupture strength. As can be seen comparing the data in Tables 2 and 3, with those of Tables 4 and 5, it can be concluded that the alternative type wide gap brazed joints yield significantly higher tensile and stress rupture strengths, when comparing with the traditional type wide gap brazed joints.

Tensile and Stress Rupture Results of the Alternative Type Wide Gap Brazed Joints Base Metal is FSX-414

Table 6 shows the tensile test results of the alternative type, wide gap brazed joints. The base metal is FSX-414.

Temperature		Tensile Strength		Yield Strength		Elongation	RA
°C	°F	MPa	ksi	MPa	ksi	%	%
21	70	659	95.5	502	72.8	5.5	4.1
21	70	628	91	474	68.7	3.3	16.8
21	70	688	99.7	489	70.9	6.1	13.8
21	**70**	**740**	**107**	**440**	**64**	**11**	**?**
650	1200	503*	72.9	253	36.7	11.4	4.5
650	1200	441*	63.9	274	39.7	8.1	4.8
650	1200	498*	72.2	288	41.7	8.5	7.8
650	**1200**	**485**	**70**	**215**	**31**	**15**	**?**
870	1600	324*	47	311	45.1	25.1	51.9
870	1600	338*	49	233	33.8	31	54
870	1600	330*	47.8	255	37	26.1	49
870	**1600**	**310**	**45**	**165**	**24**	**23**	**?**

Table 6. Tensile test results of the alternative type wide gap brazed joints.
Note: Values in bold are for FSX-414 base metal taken from the Metals Handbook. (Ref 5)
? means that the RA value was not measured. * means failure occurred in the base meta

As seen in Table 6, the tensile strength of the alternative type wide gap brazed joints at roo temperature is 85-93% of the base metals strength. However, at test temperatures above roo temperature failure occurred in the base metal. This implies that the brazed joints at elevat temperature have tensile properties equivalent to the FSX-414 base metal.

Tensile and Stress Rupture Results of the Alternative Type Wide Gap Brazed Joints Base Metal is X-45

Table 7 shows the tensile results of the alternative type, wide gap brazed joints.

Temperature		Tensile Strength		Yield Strength		Elongation	RA
°C	°F	MPa	ksi	MPa	ksi	%	%
21	70	773*	112.0	505	73.2	4.5	1.6
21	70	763*	110.6	531	77	4.4	1.6
21	**70**	**745**	**108**	**525**	**76**	**8**	**?**
650	1200	520*	75.4	304	46.8	6.4	7.1
650	1200	446	64.6	306	44.3	3.1	4.3
650	**1200**	**515**	**74.6**	**260**	**38**	**12**	**?**
760	1400	509*	73.8	311	45.1	2.9	3.9
760	1400	451*	65.4	315	45.7	3.6	3.6
760	1400	450*	65.2	341	49.4	2.9	3.9
760	1400	448*	64.9	311	45.1	3.3	3.1
760	**1400**	**485**	**70**	**?**	**?**	**9**	**?**
980	1800	214*	31	128.4	18.6	4.9	11
980	**1800**	**200**	**29**	**?**	**?**	**16**	**?**

Table 7. Tensile test results of the alternative type wide gap brazed joints.
Note: Values in bold are for X-45 base metal taken from the Metals Handbook. (Ref 5)
? means that the RA value was not measured. *means failure occurred in the base metal.

As seen in Table 7, the tensile strength of the alternative type wide gap brazed joints is superior to that of the base metal, since fracture occurred in the base metal. In many cases the tensile and yield strengths were higher than that quoted in the Metals Handbook and the elongation values were lower than that quoted in the Metals Handbook.

To verify if the elongation is as low as the data indicated, some X-45 material was removed from the shroud area of an actual service exposed W501, Row 3 vane. This material was machined to the configuration shown in Figure 5. The material was then heat treated at 1150°C (2100°F) for 4hours + 982°C (1800°F) for 4hours. Table 8 shows the result of the tensile tests of the X-45 material removed from the vane.

Temperature		Tensile Strength		Yield Strength		Elongation	RA
°C	°F	MPa	ksi	MPa	ksi	%	%
21	70	738	107	514	74.5	5.6	5.6
21	**70**	**745**	**108**	**525**	**76**	**8**	**?**

Table 8. Tensile strength of X-45 material taken from the vane and heat treated.
Note: Values in bold are for X-45 base metal taken from the Metals Handbook. (Ref 5)
? means that the RA value was not measured.

As seen in Table 8, the mechanical properties of X-45, taken from the actual vane casting, is lower than that quoted in the Metals Handbook, especially the ductility. Therefore the alternative type wide gap brazed joints have ductility in the order of 80% of the X-45 casting material. This is acceptable and the 20% loss in ductility is attributed to the few brittle boride phases present in the joint.

Table 9 shows the stress rupture test results for the above alternative type wide gap joints on an X-45 substrate.

Temperature		Stress Level		Hours to Rupture	Elongation	RA
°C	°F	MPa	ksi	hrs	%	%
760	1400	193.2	28	513.9*	31.7	48.3
760	1400	193.2	28	566.5*	29.1	48.1
760	1400	193.2	28	507.1*	35.2	48.5
871	1600	103.5	15	365*	27.7	34.5
871	1600	103.5	15	344.2*	16.4	33.6
871	1600	103.5	15	336.3*	20.7	32

Table 9. Stress Rupture test results of an alternative type wide gap brazed joint.
Note: *means that failure occurred in the base metal.

As seen in Table 9, the stress rupture strength of the alternative type wide gap brazed joints is superior to that of the base metal, since all of the fracture occurred in the base metal.

Figure 6 shows the Larson Miller plot of the alternative type wide gap brazed joints. As can be seen the stress rupture strengths of the joint lie within the scatterband of the base metals rupture strength.

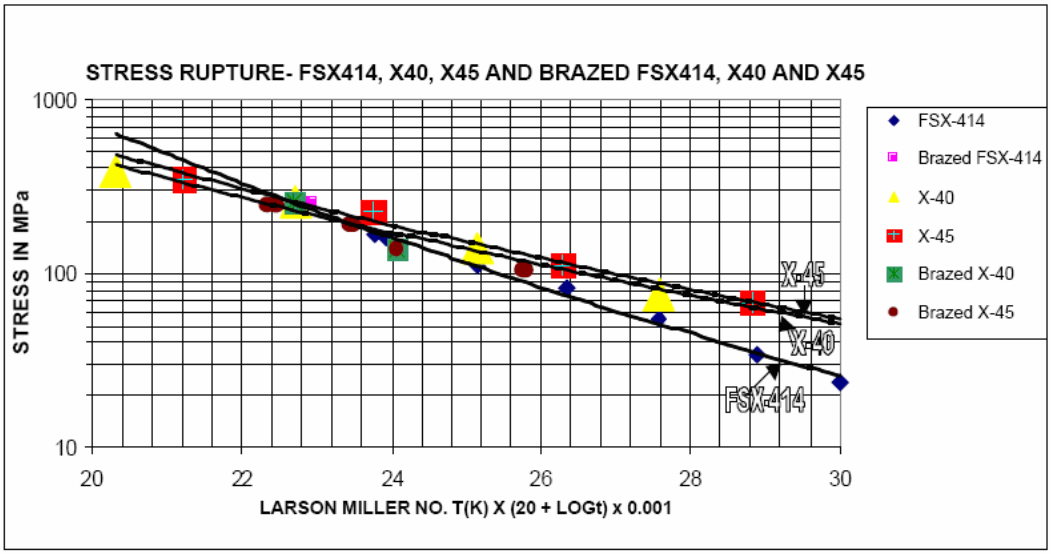

Figure 6: Stress Rupture plot of the brazed joints and base metal for X-45, X-40 and FSX-414.

Metallurgical Results
Traditional Type Wide Gap Brazed Joints

Figures 7 and 8 shows the microstructure of the traditional type wide gap brazed joint on an X-45 base metal. The X-45 powder particles are surrounded with a network of elongated brittle boride phases. This network of brittle boride phases in the wide gap joint, is the predominant reason for the reduction in mechanical properties, including elongation. Figure 9 shows an area in the wide gap brazed joint, along the grain boundary, where 3 phases were analysed. The 3 phases identified were 2, Ta-rich phases (probably Ta-carbide) and a Cr-W rich boride phase as seen in Table10. (The EDAX system on the SEM could not detect the elements C and B).

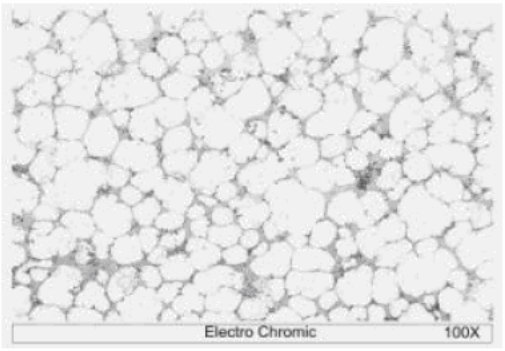

Figure 7: Traditional type wide gap joint on an X-45 substrate.

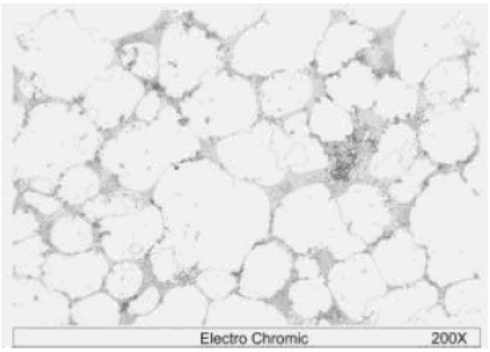

Figure 8: Traditional type wide gap joint on on an X-45 substrate.

Element	Phase A	Phase B	Phase C
Cr (at.%)	8.30	5.97	40.55
Co (at.%)	4.52	7.67	40.28
Ni (at.%)	0.91	1.66	9.02
Zr (at.%)	8.76	13.14	0.13
Ta (at.%)	68.70	67.04	0.23
W (at.%)	8.81	4.52	9.79

Table 10. Semi-quantitative analysis of the phases present in the traditional type wide gap braze

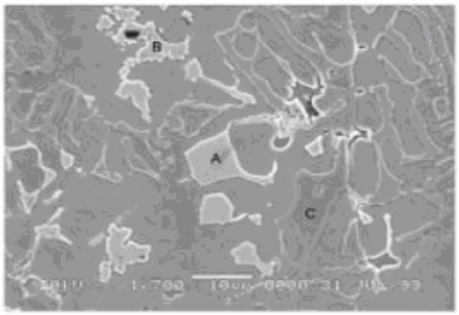

Figure 9: Location where the phases were identified.

Alternative Type Wide Gap Brazed Joints

Figures 10 and 11 shows the microstructure of the alternative type wide gap brazed joint on X-45 base metal. The wide gap brazed area is a finer grained structure (as seen in Figures 10 and 11) when comparing with Figures 7 and 8. The boride phases are discrete phases as seen in figure 11, and are not a network of elongated brittle boride phases as compared with those in Figure 8. The absence of the network of brittle boride phases in the wide gap joint, is the predominant reason for the increase in mechanical properties, including elongation. Figure 12 shows an area in the wide gap brazed joint, along the grain boundary, where 2 phases were analysed. The 2 phases identified were probably a W-Cr rich boride phase and a Cr carbide phase as seen in Table11. (The EDAX system on the SEM could not detect the elements C and B).

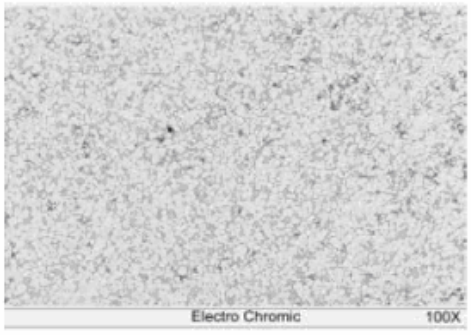

Figure 10: Alternative type wide gap joint on an X-45 substrate.

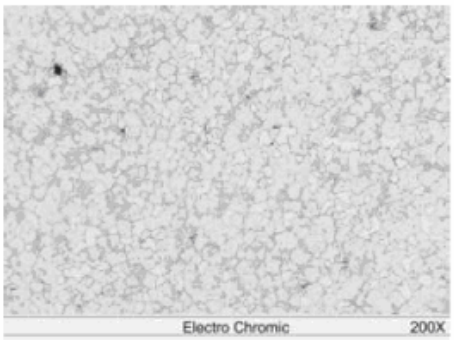

Figure 11: Alternative type wide gap joint on an X-45 substrate.

Element	Phase A	Phase B
Cr (at.%)	19.18	77.04
Co (at.%)	42.94	19.21
Ni (at.%)	3.93	1.11
Zr (at.%)	0.46	0
Ta (at.%)	4.46	0
W (at.%)	29.04	2.64

Table 11. Semi-quantitative analysis of the phases present in the alternative type wide gap braze

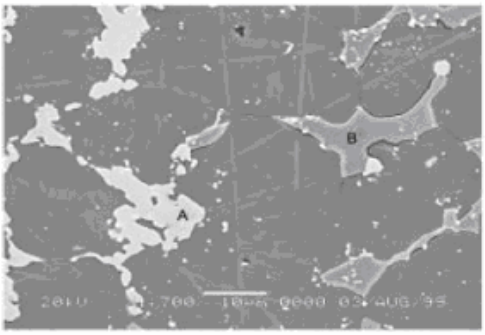

Figure 12: Location where the phases were identified.

PROCESS DEMONSTRATION

Figures 13 and 14 show the brazed repaired cracked areas, which were routed out in Figures 1 and 3. Figure 15 shows the brazed built up hook-fit region previously shown in Figure 4.

Figure 13: Brazed repaired region.

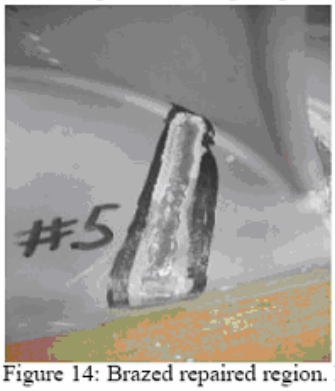

Figure 14: Brazed repaired region.

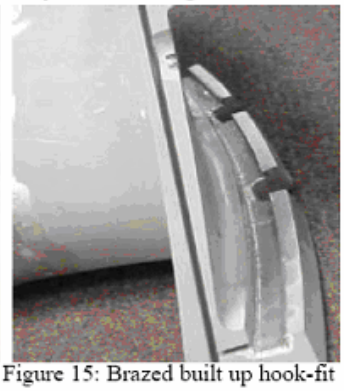

Figure 15: Brazed built up hook-fit

SUMMARY AND CONCLUSIONS

- The use of the alternative wide gap braze process, results in a repaired joint, which has mechanical properties (tensile and stress rupture) equivalent to that of the base metal.
- The microstructure of the joint shows no signs of large networks of brittle boride phases, known to significantly reduce mechanical properties and ductility. Only isolated boride phases were seen in the repaired area.
- The alternative wide gap braze process yields superior mechanical properties when comparing with the traditional wide gap brazing process.
- Based on the metallurgical and mechanical results obtained in this research project, the use of the alternative wide gap braze process is a suitable alternative to the Gas Tungsten Arc (GTA) weld approved repair process specified by the original engine manufacturer (OEM).
- The alternative process is ideally suited for crack repair, wall thickness repair of the convex and concave surfaces and dimensional restoration of the hook fit and race track areas of all Co-based vanes.
- This alternative process also works well on Ni-base superalloy components and this will form the basis of a paper in the near future.

REFERENCES

1. Demo, W.A and Ferrigno, S.J, 1992, "Brazing method helps repair aircraft gas – turbine nozzles", Advanced Materials and Processes, Vol 141, No.3, pp43-45
2. Wustman, R.D and Smith, J.S, 1996, "High strength diffusion braze repairs for gas turbine components", ASME paper 96-GT-427
3. Bell, S, 1985, "Repair and Rejuvenation procedures for aero gas-turbine hot section components", Material Science and Technology, Aug, Vol 1, pp629
4. Ellison, K.A, Lowden, P and Liburdi, J, 1992, "Powder metallurgy Repair of Turbine Components", ASME paper 92-GT-312
5. Metals Handbook, Vol 3, 9th edition, pp. 258 and 268, ASM International

APPENDIX D

MIGLIETTI, W.M.A. "WIDE GAP DIFFUSION BRAZE REPAIR OF NI-BASED INDUSTRIAL TURBINE VANES". PROCEEDINGS OF THE 6^{TH} *INTERNATIONAL CONFERENCE ON BRAZING, HIGH TEMPERATURE BRAZING AND DIFFUSION WELDING*. DVS BERICHTE, NO. 212. 8-10 MAY 2001. AACHEN, GERMANY. PP. 107-112.

WIDE GAP DIFFUSION BRAZE REPAIR OF Ni-BASED INDUSTRIAL TURBINE VANES

W.M.A. Miglietti - Sermatech International, Inc.

ABSTRACT

During the industrial turbine engine operation, cracks develop on the vanes as a result of thermal fatigue. Other damage found includes pitting and dents resulting from corrosion/oxidation and FOD (foreign object damage) respectively. Erosion damage is also commonly found on the airfoils. This paper describes the vacuum wide gap diffusion brazing repair process used to repair all of the above-mentioned damage, including braze build up. As a means of qualifying the high temperature diffusion braze process, both metallurgical and mechanical property evaluations were carried out. The metallurgical evaluation consisted of optical and scanning electron microscopy. The wide gap diffusion brazed area consisted of a fine-grained structure with carbide and intermetallic phases dispersed both intergranularly and intragranularly. The mechanical evaluations undertaken were tensile tests, stress rupture tests and low and high cycle fatigue tests. These results were equivalent to mechanical properties of the IN738, IN939, and Rene 80 Ni-based superalloys, which are the base metals that many of the vanes are cast from.

1. INTRODUCTION

Narrow gap brazing has been utilised for decades now to repair aircraft engine vane and nozzle segments. It has only being the last 5 years that wide gap brazing has been utilised for Industrial Gas Turbine (IGT) vane and nozzle repairs. The wide gap brazing process was made popular by GE's and Pratt and Whitney's ADH (activated diffusion healing) [1] and Turbofix processes respectively. Many repair vendors have their own proprietary wide gap braze process such as SNECMA's RBD (rechargement per brasage diffusion), Howmet's ESR (effective structural repair) [2] and Chromalloy's SRB (surface reaction braze) [3]. Other wide gap joining processes available are LPDS (liquid phase diffusion sintering), Liburdi's LPM (Liburdi powder metallurgy) [4] and Sermatech's "SermaFill" process [5]. The objective of this paper is to describe the use of an alternative wide gap braze process for IGT vane repairs, and to compare this process with the traditional wide gap braze process. A traditional wide gap process is referred to as, when a mixture/blend of superalloy powder and braze powder is utilised. The mixtures are usually a 40/60, 50/50 or a 60/40 blend by weight. The alternative wide gap process is proprietary and hence exact precise temperatures and times, chemical compositions etc. cannot be documented; nevertheless, ranges of temperature and times are documented. This process was qualified by undertaking a metallurgical evaluation and a mechanical property evaluation to show that metallurgically sound and high strength joints resulted. This alternative process was used to restore wall thickness on the concave and convex surfaces of the airfoil, and repair cracks, pits and dents.

Many of the IGT vanes are manufactured from Ni-based alloys like IN738, IN939 and Rene80. The chemical composition of the materials is given in **Table 1.** The high volume fraction of gamma prime (γ'), a Ni_3Al phase, enables these alloys to possess remarkable mechanical properties at elevated temperatures. **Figures 1 and 2** show typical examples of "craze" cracking and leading and trailing edge cracking on an IN738, Siemens V84.2, Row 2 vane and an Alstom, Tornado, CT2, stator segement, respectively. The largest width of crack found on these engine sets was 1.5mm. As a result of these large gaps, conventional narrow gap brazing cannot be utilised as a repair technique. For the crack repair, paste is used as the medium for the repair; whereas, for concave and convex dimensional build up, tape is utilised. The largest width of cracks found on these engine sets was 1.5mm. Therefore for the process qualification, the mechanical property tests

Table 1: Base Metals (BM) Composition, Wt. %

Alloy	C	Co	Cr	Ni	Mo	Al	W	Ta	Nb	Ti	Zr
IN738	0.17	8.5	16	Bal	1.7	3.4	2.6	1.7	0.9	3.4	0.1
IN939	0.15	19	22.5	Bal	0	1.9	2.0	1.4	0	3.7	0.1
Rene80	0.17	9.5	14	Bal	4	3	4	0	0	5	0.1

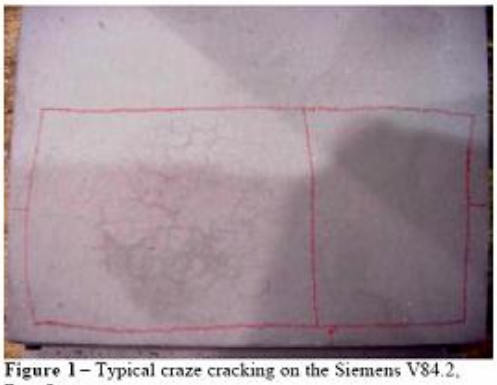

Figure 1 – Typical craze cracking on the Siemens V84.2, Row 2 vane.

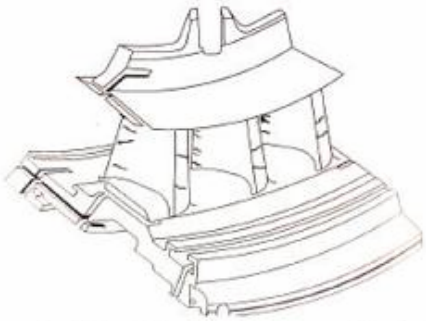

Figure 2 – Typical view from the concave side, showing leading edge, trailing edge and shroud/buttress cracking on the Alstom Tornado 2nd stage stator segment.

(namely tensile, stress rupture and fatigue) where undertaken on samples where the joint gap was 1.5mm. The process is not limited to this gap and the largest gap repaired to date has been 10mm.

2. EXPERMENTAL PROCEDURE

Tensile tests at room temperature (21°C) and elevated temperatures, as well as stress rupture and low and high cycle fatigue tests were undertaken. The test specimens were prepared in a butt joint configuration as seen in **fig 3**. The joint is in the centre of the gauge length and was 1.5mm wide.

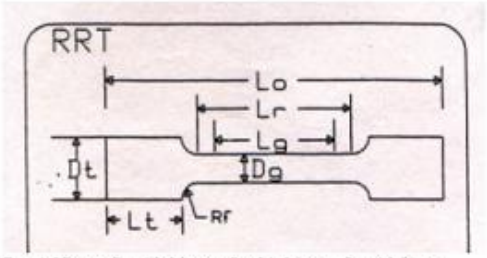

D_g=4.57mm, L_g=18.29mm, L_r=21.84mm, L_o=46.51mm, R_f=3.18mm, D_t=(5/16-24NF-2A inches) and L_t=9.53mm

Figure 3 – Configuration for the mechanical test specimens.

3. MECHANICAL TEST SPECIMEN PREPA RATION

Mechanical test specimens according to the configuration shown in **fig 3** were prepared as follows:

a) Obtain investment cast IN738, IN939 and Rene80 material.
b) Machine rectangular sections of 12.5mm X 12.5mm X 55.9mm.
c) Cut sample in half.
d) Grind the mat ing surfaces flat.
e) Grit blast surfaces with silicon carbide.
f) Shim gap at 1.5mm .
g) Apply paste to the joint gap.
h) Place samples in fixture to maintain alignment.
i) Set in vacuum furnace.
j) Process between 1120°C and 1200°C.
k) Isothermally process for 4-20 hours.
l) Age at 843°C/ 24 hours for IN738 or age at 900°C/ 24 hours + 700°C/16 hours for IN939, or age at 1050°C/ 4 hours + 845°C/16 hours for Rene80.
m) Machine samples to the configuration shown in **fig 3**.
n) Send the machined specimens for X-ray analysis to determine if porosity greater than 0.5mm exists and for lack of bonding to the mating surfaces.

4. RESULTS AND DISCUSSION OF MECHANICAL PROPERTY TESTING

Table 2 below shows the results of the tensile tests undertaken at room temperature and elevated temperatures of 650°C, 760°C and 982°C on the alternative wide gap brazed joints for IN738. As can be seen the tensile and yield strengths are equivalent to the values quoted in the Metals Handbook. The elongation of the alternative type wide gap brazed joints appears low, when compared to the values quoted in the Metals Handbook. There is a good explanation for this, which will be discussed later. Nevertheless the RA values are equivalent to the base metals values and hence the joints possess reasonable ductility.

Table 2: Tensile Strength of IN738 processedwith "SermaFill"5 Filler Metal

TEMPERA - TURE		TENSILE STRENGTH		YIELD STRENGTH		ELONG ATION	RA
°C	°F	MPa	ksi	MPa	ksi	%	%
21	70	1011	146.5	882	127.8	3.1	4.7
21	70	886	128.4	866	125.5	1.4	3.6
21	**70**	**1050**	**152**	**865**	**125.4**	**5**	**5**
650	1200	827	120	671	97.3	6.0	5.6
650	1200	765	111	661	95.8	3.3	4.0
650	1200	753	109	682	98.9	4.1	3.7
650	**1200**	**850**	**123**	**655**	**95**	**5**	**5**
760	1400	908	131.6	747	108.3	3.9	5.9
760	1400	944	136.8	768	111.3	3.8	5.6
760	**1400**	**965**	**140**	**795**	**115**	**6**	**?**
982	1800	412	59.7	319	46.2	2.0	8.2
982	1800	372	53.9	317	45.9	1.6	6.1
982	**1800**	**435**	**63**	**325**	**47.1**	**6.5**	**?**

NOTE Values in Bold are for IN738 parent alloy (Metals Handbook Vol3, ninth edition)

To verify if the elongation is as low as the data indicates, some IN738 material was taken from the root area of a W501F, 1st stage blade. This material was machined to the configuration shown in **fig 3**.

Table 3 shows the results of the IN738 specimens removed from the blade root. As seen in **Table 3** the mechanical properties of the IN738 taken from the actual blade casting is lower than that quoted in the Metals Handbook, including the ductility. Therefore the alternative wide gap brazed joints have ductility in the order of 80% of the IN738 casting material. This is acceptable and the 20% loss in ductility is attributed to the few brittle intermetallic phases present in the 1.5mm wide gap joint.

Table 3: Tensile strength of IN738 material taken from the root of a blade.

TEMPERA - TURE		TENSILE STRENGTH		YIELD STRENGTH		ELONG ATION	RA
°C	°F	MPa	ksi	MPa	ksi	%	%
21	70	828	120	759	110	3	3
21	**70**	**1050**	**152**	**865**	**125.4**	**5**	**5**

NOTE Values in Bold are for IN738 parent alloy (Metals Handbook Vol3, ninth edition)

Table 4, shows the stress rupture properties of the alternative type wide gap joints for IN738. As seen in **Table 4**, the stress rupture properties of the joints are a minimum of 89% of the base metals stress rupture properties.

To compare the results of the alternative type wide gap joints with a more traditional wide gap braze process, a 50% IN738 and 50% BRB braze (Ni-13.5Cr-7.5Co-4Al-2.5B) mixture was developed. Some samples were brazed with the same joint gap and at the same process parameters as those of the alternative type wide gap brazed joints.

Tables 5 and 6 show the tensile test results and stress rupture results respectively, of the joints brazed with the 50/50 mixture. As seen in these tables, the strength of the brazed joint is 40%–53% of the base metals strength, the elongation is 33%--50% of the cast IN738 blade material

Table 4: Stress rupture properties of IN738 processed with "Sermafill" 5 Filler Metal

TEMPERATURE		STRESS	HOURS TO FAILURE	ELONGATION	RA
°C	°F	MPa	hrs	%	%
843	1550	345	190.3	1.7	?
843	1550	345	93.7	1.9	?
843	1550	345	89	2.3	?
843	1550	345	97.3	1.8	?
843	**1550**	**345**	**100**	**5**	**5**
829	1525	345	203.37	4.4	?
829	**1525**	**345**	**223.02**	**6.7**	**?**
982	1800	124.2	453.2*	5.5	?
982	**1800**	**124.2**	**807.2**	**5.2**	**?**

NOTE: Values in Bold are for IN738 material, taken from the root of a blade

* means that failure occurred in the base metal

and the stress rupture life varies from 7.4-11.9% of the parent metals life. This is undesirable if the objective is to have a structural repair, where the properties of the repaired areas are equivalent to the base metal. Clearly the alternative wide gap type joints have superior mechanical properties when compared to a more traditional type wide gap braze joint, and the properties are equivalent to the base metal as seen in **Tables 2 and 4.**

Table 5: Tensile strength of IN738 brazed with a traditional type filler metal (50%IN738 + 50%BRB)

TEMPERATURE		TENSILE STRENGTH		YIELD STRENGTH		ELONGATION	RA
°C	°F	MPa	ksi	MPa	ksi	%	%
21	70	527	76.4	527	76.4	1.4	2.4
21	70	502	72.8	502	72.8	1.8	2.2
21	70	559	81	559	81	1.0	2.9
21	**70**	**1050**	**152**	**865**	**125.4**	**5**	**5**
650	1200	322	46.7	322	46.7	2.5	1.6
650	1200	441	63.9	441	63.9	1.2	1.9
650	1200	338	49	338	49	1.9	5.2
650	**1200**	**850**	**123**	**655**	**95**	**5**	**5**

NOTE: Values in Bold are for IN738 Alloy (Metals Handbook, Vol. 3, ninth edition)

Table 6: Stress Rupture properties of IN738 brazed with a traditional type filler metal (50%IN738 + 50%BRB)

TEMPERATURE		STRESS LEVEL		HRS TO FAILURE	ELONGATION	RA
°C	°F	MPa	ksi	hrs	%	%
843	1550	345	50	11.9	?	?
843	1550	345	50	7.4	?	?
843	**1550**	**345**	**50**	**100**	**5**	**5**

NOTE: Values in Bold are for X-45 alloy (Metals Handbook, Vol3, ninth edition)

Table 7, shows the results of the tensile tests undertaken at room temperature and elevated temperature of 650°C, on the alternative type joints for IN939. As can be seen the tensile and yield strengths are equivalent to the values of the cast material. The elongation of the joints is 50-73% of the base metals values. This is attributed to the intermetallic phases present in the joint. The RA values are however equivalent to that of the base metal, hence the joints do possess reasonable ductility. As seen in **fig 4** the stress rupture properties of the joints are a minimum of 90% of the base metals.

Table 7: Tensile Strength of IN939 processed with "SermaFill"3 Filler Metal

TEMPERATURE		TENSILE STRENGTH		YIELD STRENGTH		ELONGATION	RA
°C	°F	MPa	ksi	MPa	ksi	%	%
21	70	920	133.3	670	97.1	2.2	3.6
21	70	859	124.5	696	100.9	1.8	4.3
21	70	817	118.4	750	108.7	1.7	7.7
21	70	999	144.8	651	94.3	1.5	3.0
21	**70**	**897**	**130**	**690**	**100**	**3**	**5.0**
650	1200	768	111.3	625	90.6	1.5	4.0
650	1200	860	124.7	654	94.8	2.1	5.1
650	**1200**	**863**	**125.1**	**621**	**90**	**3**	**5.0**

NOTE: Values in bold are for cast IN939 material taken from a shroud buttress section.

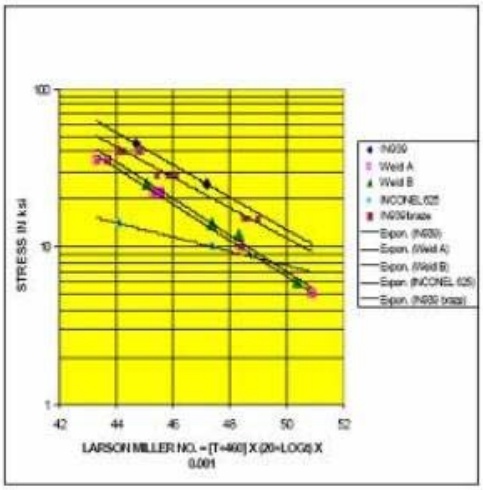

Figure 4 – Larson Miller Plot of the stress rupture properties of the alternative type wide gap joints versus a number of weld filler metals.

In fact **fig 4,** also shows that the alternative wide gap brazed joints have superior stress rupture lives when compared to 3 different weld filler metals viz. IN625, Weld A and Weld B. IN625 is well utilised as a filler metal for non-structural repair applications, because of its good ductility and ease of welding. However as can be seen, this filler metal has poor stress rupture life when compared to IN939. Two proprietary higher strength weld filler metals based on the elements Ni-Cr-Co-Mo-W-Ti-Al-C were developed as substitutes for IN625, and even these filler metals, did not even have the stress rupture properties equivalent to those of the LPDB joints. It should be realised that IN939, as a result of its high total Al + Ti content is not readily weldable and suffers from strain age cracking.

A similar trend of the results for the alternative wide gap brazed joints of IN738 and IN939 was obtained for Rene80. As seen in **Tables 8, 9 and 10**, the mechanical properties of the wide gap brazed joints are equivalent to that of the base metal.

Table 8 Tensile properties at 25°C of Rene80 and Rene80 alternative wide gap brazed joints.

Property	80 Sermafill	Rene80*
Tensile (MPa)	892.9	870.1
Yield (MPa)	857.7	700.4
Elongation (%)	0.6	1.8
RA (%)	1.5	3.5

- *specimens were in the solution and aged condition and not in the Hipped, solution and aged condition

Table 9: Tensile properties at 871°C of Rene80 and Rene80 altemative wide gap brazed joints.

Property	80 SermaFill	Rene 80*
Tensile (MPa)	103.2	91.9
Yield (MPa)	86.6	63.2
Elongation (%)	1.9	6.6
RA (%)	1.2	8.1

- *specimens were in the solution and aged condition and not in the Hipped, solution and age d condition

Table 10: Stress rupture properties of Rene80 and Rene80 wide gap braze.

Alloy	Cond-ition	Test temp	Stress (MPa)	Hrs	Elong %	RA %
80 Serma fill	Brazed + Solution + aged	871°C	345	22.6	4.9	6.4
		871°C	311	59	3.9	7.7
		871°C	276	124	3.0	11.3
		927°C	242	26.1	3.7	7.4
Rene 80* base metal	Solution + aged	871°C	345	18.1	?	?
		871°C	311	44	10.2	18.4
		871°C	276	122.6	?	?
		927°C	242	31.5	?	?

- *specimens were in the solution and aged condition and not in the Hipped, solution and aged condition

In summary the tensile and stress rupture data of the alternative wide gap brazed joints for IN738, IN939 and Rene80 are equivalent to that of the base metal.

Figure 5 shows the stress controlled, high cycle fatigue results generated at 760°C on IN738 base metal, which were undertaken at a frequency of 10Hz, with the minimum stress (σ_{min}=0); therefore maximum stress = total stress (σ_{max} = σ_{total}). As can be seen in **fig 5**, the endurance limit defined as the stress corresponding to 10^7 cycles is 345MPa (50ksi), even though at 414MPa (60ksi) the samples at 5000000 cycles had not failed.

Figure 6 shows the strain controlled low cycle fatigue results generated at 870°C on IN738 base metal, which were undertaken at a constant strain rate of 0.01 S^{-1}, with a symmetrical triangular wave form. The LCF tests were conducted between total strain values of 0.5% and 1.5%, and a corresponding test frequency ranging between 1Hz and 0.33Hz. At strain levels of 0.6% and higher the LCF life is 50%--75% of the base metals life. At strain levels less than 0.6%, the LCF life is equivalent to that of the base metal.

In summary the high cycle fatigue properties, i.e. the endurance limit corresponding to 10^7 cycles, of the alternative wide gap brazed joints is equivalent to that of the base metal. At strain levels of less than 0.6%, the low cycle fatigue life is equivalent to that of the base metal.

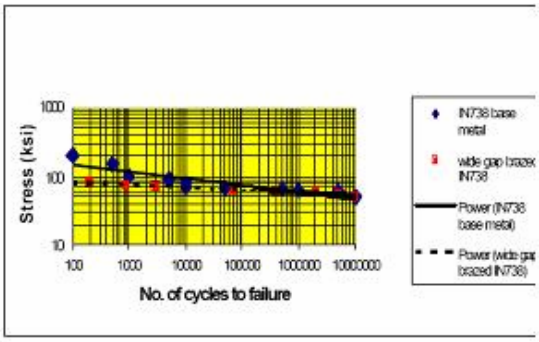

Figure 5 - High cycle fatigue properties at 760°C of IN738 and the alternative wide gap brazed IN738.

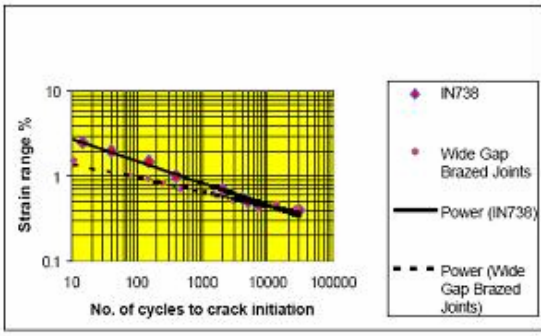

Figure 6 - LCF properties at 870°C of IN738 and the alternative wide gap diffusion brazed IN738.

5. METALLURGICAL RESULTS AND DISCUSSION

Figure 7 shows the macrograph of a cross section taken through the alternative type wide gap braze repair of the IN738, V84.2, row 2 vane. As can be seen the "craze-cracked" area was machined away and this area was filled with the alternative wide gap braze filler metal

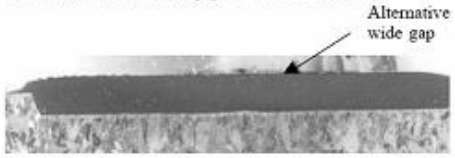

Figure 7 – Macrograph taken through the alternative wide gap braze repaired area of the V84.2, row 2 vane. Mag. 5X

Figure 8 shows the excellent bonding/ adhesion to the IN738 vane material. A fine-grained microstructure is evident. Some minor microporosity can be seen in the micrograph, but this microporosity level is acceptable. **Figure 9** shows the fine grained structure of the alternative type wide gap brazed joint, with intermetallic phases dispersed intergranularly.

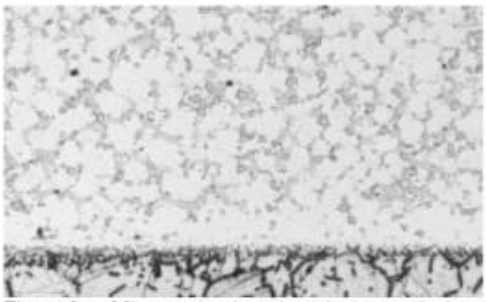

Figure 8 – Micrograph taken through the repaired area showing excellent bonding to the vane material. Mag. 75X

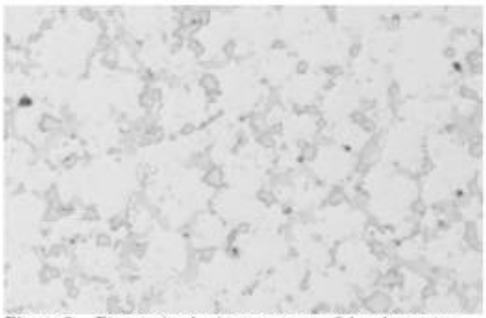

Figure 9 – Fine grained microstructure of the alternative wide gap brazed joint with intermetallic phases dispersed intergranularly. Mag. 150X

Figure 10 shows the macrograph of a cross section taken through the alternative wide gap braze repair of the IN939, Tornado 2nd stage stator segment. As can be seen the filler metal has flowed completely down to the bottom of the crack and has bonded excellently to the sidewalls of the routed out crack. Also the microporosity is less in the joint, when compared to that of the base metal.

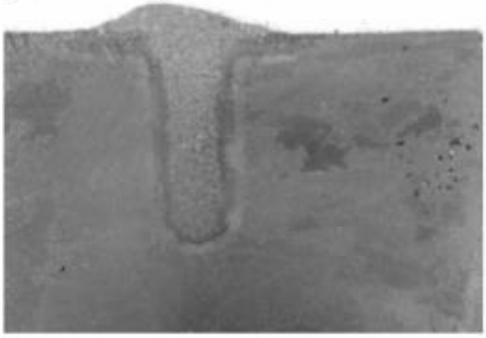

Figure 10 – Macrograph of the joint taken through the alternative wide gap braze repair of the Tornado, 2nd stage stator segment. Mag. 5X

Figure 11 shows a cross section taken through a "through" crack at the trailing edge of the airfoil. Once again there is good bonding to the sidewalls of the routed out crack.

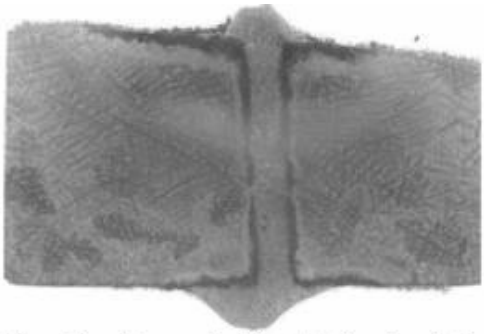

Figure 11 – Macrograph of the joint taken through the alternative wide gap braze repaired area of the Tornado, 2nd stage stator segment. Mag 5X

Figure 12 shows the micrograph of the repaired area. It consists of a fine-grained structure and there is good bonding/adhesion to the sidewalls. **Figure 13** shows the joint to consist of equiaxed grains with intermetallic phases dispersed intergranularly.

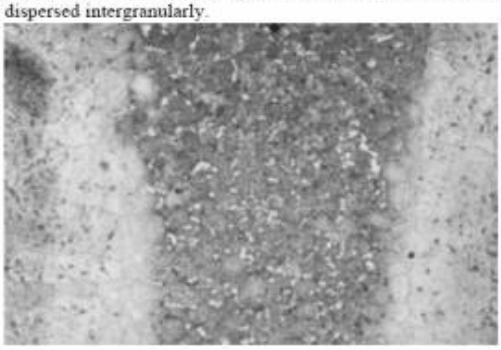

Figure 12 - Micrograph taken through the repaired area showing a fine-grained microstructure. Mag. 45X

The traditional wide gap brazed samples used to produce the mechanical test results shown in **Tables 5 and 6**, were also analysed. As a reminder a filler metal of 50% IN738 powder and 50%BRB braze was utilised. As seen in **fig 14** the joint in the stress rupture sample consist of a mixture of fine and coarse grains with a continuous layer of intergranular intermetallic phases. This is in contrast to the discrete isolated and discontinuous intermetallic phases that were present in the joints seen in **fig's 12-13. Figure 15** shows the continuous intergranular intermetallic phases present in the joint. The bright "blocky and dark grey intermetallic phases can be clearly seen along the grain boundaries.

6. FIRST ARTICLE REPAIR DEMONSTRATION

Figure 16 shows areas on the V84.2, row 2 vanes, which were routed out and processed with the alternative wide gap filler metal, plus subsequent heat treatment **Figure 17** shows the Tornado, 2nd stage stator segment after complete repair including heat treatment and Sermaloy J coating. (Sermaloy J is an aluminide coating that is proprietary to Sermatech International, Inc.)

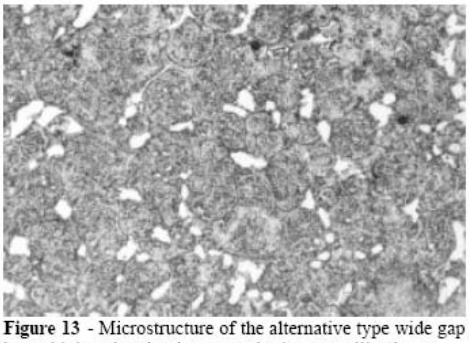

Figure 13 - Microstructure of the alternative type wide gap brazed joint, showing intergranular intermetallic phases. Mag. 150X

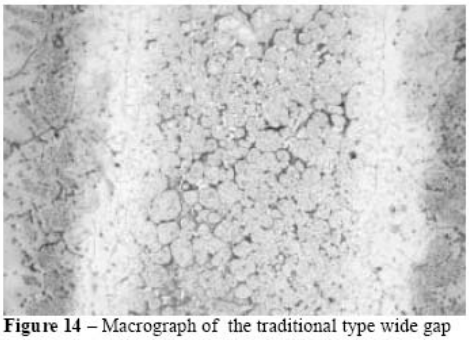

Figure 14 – Macrograph of the traditional type wide gap brazed joint taken from a stress rupture sample. Mag. 45X

7. CONCLUSIONS

The use of the alternative wide gap braze process, results in a repaired joint, which has mechanical properties (tensile, stress rupture and fatigue) equivalent to that of the base metal. These properties are far superior to those of traditional and conventional wide gap braze processes.

The microstructure of the joint shows no signs of large networks of brittle boride phases, known to significantly reduce mechanical properties and ductility. Only isolated and discrete intermetallic phases were seen in the repaired area.

Based on the metallurgical and mechanical results obtained in this research project, the use of the alternative wide gap braze process (which Sermatech International, Inc. has as there trademark "SermaFill") is a suitable alternative to the traditional Gas Tungsten Arc weld approved repair process.

This alternative wide gap braze process ("SermaFill") is ideally suited for crack repair, including "craze cracking", wall thickness repair of the convex and concave surfaces and dimensional restoration of Ni and Co-based IGT vanes.

8. REFERENCES

[1] Demo, W.A. and Ferrigno, S.J., 1992, "Brazing method helps repair aircraft gas –turbine nozzles", Advanced Materials and Processes, Vol. 141, No.3, pp43-45.

[2] Wustman, R.D. and Smith, J.S., 1996, "High strength diffusion braze repairs for gas turbine components", ASME paper 96-GT-427.

[3] Bell, S., 1985, "Repair and Rejuvenation procedures for aero gas-turbine hot section components", Material Science and Technology, Aug, Vol. 1, pp629

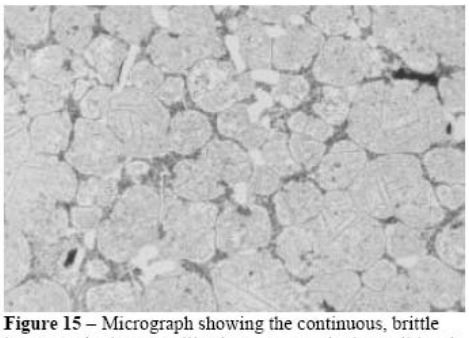

Figure 15 – Micrograph showing the continuous, brittle intergranular intermetallic phases present in the traditional type wide gap brazed joints. Mag. 150X

Figure 16 – V84.2, row 2 vanes repaired with the alternative wide gap braze process.

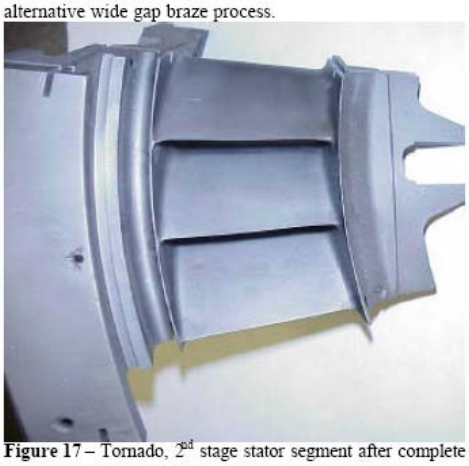

Figure 17 – Tornado, 2nd stage stator segment after complete repair including heat treatment and Sermaloy J coating.